Evaluation of Tsunami Sources with the Potential to Impact the U.S. Atlantic and Gulf Coasts

An Updated Report to the Nuclear Regulatory Commission

By Atlantic and Gulf of Mexico Tsunami Hazard Assessment Group

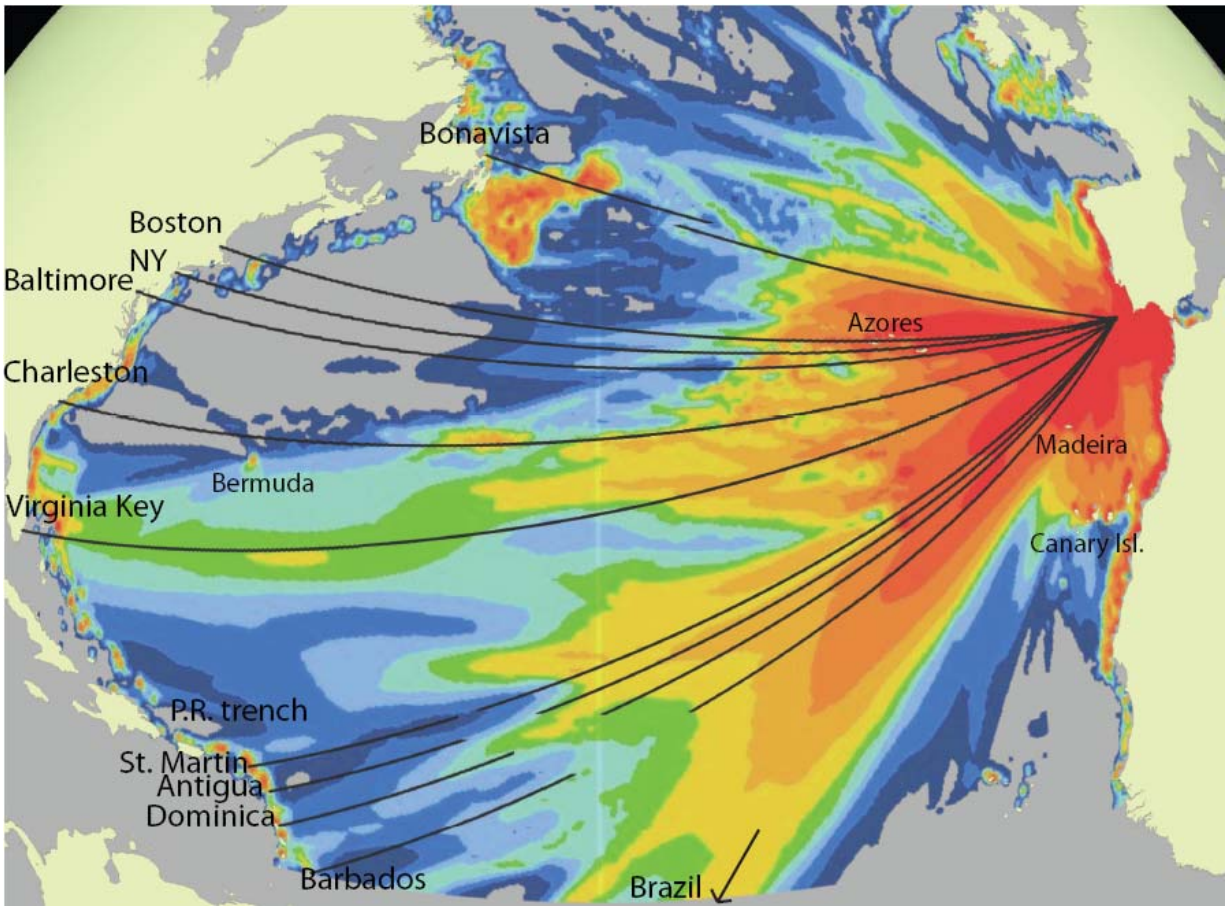

USGS
science for a changing world

Evaluation of Tsunami Sources with the Potential to Impact the U.S. Atlantic and Gulf Coasts

An Updated Report to the Nuclear Regulatory Commission

By Atlantic and Gulf of Mexico Tsunami Hazard Assessment Group:

Uri ten Brink[1], David Twichell[1], Eric Geist[2], Jason Chaytor[1,3], Jacques Locat[4], Homa Lee[2], Brian Buczkowski[1], Roy Barkan[5], Andrew Solow[3], Brian Andrews[1], Tom Parsons[2], Patrick Lynett[6], Jian Lin[3], and Mylène Sansoucy[4]

[1] U.S. Geological Survey, Woods Hole Science Center, Woods Hole, Massachusetts, USA
[2] U.S. Geological Survey, Menlo Park, California, USA
[3] Woods Hole Oceanographic Institution, Woods Hole, Massachusetts, USA
[4] Department of Geology and Geological Engineering, Université Laval, Sainte-Foy, Québec, Canada
[5] Department of Geophysics and Planetary Sciences, Tel Aviv University, Ramat Aviv, Israel
[6] Department of Civil Engineering, Texas A&M University, College Station, Texas, USA

This report supersedes *The Current State of Knowledge Regarding Potential Tsunami Sources Affecting U.S. Atlantic and Gulf Coasts*, submitted to the Nuclear Regulatory Commission on September 30, 2007

April 30, 2007
Revised September 30, 2007
Revised August 22, 2008

NOTICE from USGS

This report should be cited as:

Atlantic and Gulf of Mexico Tsunami Hazard Assessment Group, 2008, Evaluation of Tsunami Sources with the Potential to Impact the U.S. Atlantic and Gulf Coasts - A Report to the Nuclear Regulatory Commission: U.S. Geological Survey Administrative Report.

This report was compiled for the Nuclear Regulatory Commission under NRC Job Nº: N6480

Acknowledgements:

We would like to thank Thierry Mulder, David Piper, Bill Normark, Brian McAdoo, Roger Urgeles, Brian Collins, David Mosher, Rob Kayen, Dave Tappin, Valerie Paskevich, VeeAnn Cross and many others who have contributed their thoughts, insights, technical assistance and reviews on the various papers included in this volume.

Cover: Maximum wave amplitude projected on a sphere from our preferred location of the 1755 Lisbon Earthquake. Warm colors indicate high amplitudes and cold colors low amplitudes. Black lines are Great Circle paths between the source and various locations along the U.S. East Coast and the Caribbean. Note the predicted low amplitude along most of the U.S. East Coast (with the exception of Florida) due to the scattering of energy by submarine topography in the Eastern Atlantic Basin.

Executive Summary

The 2004 Sumatra tsunami, which took place in an area with no historical record of a similar event, has brought awareness to the possibility of tsunamis along the U.S. Atlantic and Gulf of Mexico coasts. While these rare events may not have an impact on tsunami probability calculations for flood insurance rates, they need to be considered in long-range planning, such as for the placement of nuclear power plants. The U.S. Geological Survey was tasked by the Nuclear Regulatory Commission to prepare an evaluation of tsunami sources and their probability to impact the U.S. Atlantic and Gulf of Mexico coasts. This report is an updated evaluation based on additional data analysis and modeling. It provides a general review of potential tsunami sources, and provides a geotechnical analysis and hydrodynamic model for one landslide offshore North Carolina. The evaluation also identifies geographical areas with limited information and topic for further study. Finally, the updated report present new theoretical developments that may aid in quantitative evaluation of tsunami probability.

The work included in this report represents both review of published work and original work. Eight of the 14 topical chapters in this report represent original work, and the remaining 6 chapters are based on literature reviews. The original work is in the process of being published as eight papers in a special issue of Marine Geology, an international peer-reviewed scientific journal.

The main findings of the study so far include:

1. Landslides along the U.S. Atlantic margin have the potential to cause tsunami locally. These landslides are concentrated along the New England and Long Island sections of the margin, outward of major ancient rivers in the mid-Atlantic margin and in the salt dome province offshore North Carolina. The landslides generally removed a relatively thin (a few 10s of meters) layer of mostly unconsolidated sediments. The mapped landslides follow a log-normal size distribution centered at a volume of about 1 km^3. However, some parts of the upper continental slope, particularly off Long Island New England, have not yet been mapped in detail. Relatively few large landslides from the entire mapped inventory (9 landslides over 500 km^2 and 16 landslides over 10 km^3) could have caused a damaging tsunami. The criteria for devastating tsunami is presently based solely on modeling of the Currituck slide offshore North Carolina. Additional simulations off New England are needed to refine the threshold for damaging tsunamis. A review of known ages of submarine landslides around the Atlantic Ocean and worldwide

shows a factor of 1.7-3.5 lower frequency of occurrence during the past 5000 years relative to the last glacial period and the first 5000 years after the end of glaciation, suggesting that the majority of the observed landslides along the U.S. Atlantic margin are older than 5000 years.

2. Earthquake sources that can generate trans-oceanic tsunamis, are located west of Gibraltar and in the Puerto Rico trench. Tsunami simulations from the 1755 Lisbon earthquake show that seafloor topography between the source area and the Azores Islands plays a major role in scattering the wave energy traveling toward the U.S. East Coast. This conclusion matches the lack of tsunami reports from parts of the U.S. East coast that were populated at the time (Boston, New York, Chesapeake Bay, Savannah, Charleston). However, simulations show that should a large tsunamigenic earthquake take place in the Puerto Rico trench, the resultant tusnami may be destructive to many parts of the U.S. East Coast. To date, no evidence was found for large historical or pre-historical earthquakes in the Puerto Rico trench, and the ability of this plate boundary to generate large earthquakes is being investigated.
3. Far-field landslides, such as in the Canary Islands, are not expected to cause a devastating tsunami along the U.S. Atlantic coast.
4. Large landslides in the Gulf of Mexico are found in the submarine canyon and fan provinces extending from present Mississippi and other former larger rivers that emptied into the Gulf. These large landslides were probably active before 7500 years ago. In other areas, landslides continue to be active, probably because of salt movement, but are small and may not pose tsunami hazard. Very little is known about the threat of landslide-generated tsunamis from the Mexican coast, particularly the Campeche escarpment. Tsunamis generated by earthquakes do not appear to impact the Gulf of Mexico coast.
5. Several approaches to quantitatively calculate the probability of tsunamis impacting the U.S. East and Gulf Coasts have been developed, but their accuracy depends in large part on the available of observations of size distribution, recurrence interval, and geotechnical parameters of the sea floor.

Contents

Section 2: Earthquakes

Section 3: Case Study

Section 4: Toward the Development of Quantitative Probabilistic Hazard Assessment

Section 5: Summary and Future Directions

Chapter 1: Introduction and Background

The devastation caused by the 2004 Indian Ocean tsunami has brought about a heightened awareness of the dangers posed by tsunamis. Long known as a hazard in the Pacific Ocean, the 2004 event highlighted the fact the tsunamis can occur in other oceans that are less prepared for this rare phenomenon. The M~9.2 2004 Sumatra-Andaman earthquake was unusual from a geologic/tectonic perspective as well. This massive earthquake occurred along a highly oblique subduction zone, where the convergence rate is low (~7-14 mm/yr). In the decades leading up to this event, highly oblique subduction zones were thought to be unlikely places for a M~9 earthquake to occur. The 2004 Sumatra-Andaman earthquake has therefore brought about the need to reassess tsunamigenic potential for similar tectonic regimes, particularly in the Caribbean Sea, Atlantic Ocean, and the Gulf of Mexico.

As in the 2004 earthquake, where the recurrence interval for earthquakes of similar magnitude is greater than 1,000 years, many of the tsunamigenic fault zones in the Caribbean and Atlantic are characterized by low convergence rates. While these events have less impact on tsunami probability calculations for some applications (*e.g.*, FEMA flood insurance rate maps), it is critical to define the tsunami hazard at longer return times for nuclear power facilities. The Atlantic and Gulf of Mexico coasts are highly vulnerable to tsunamis when they do occur because major population centers and industrial faculties are located near the shoreline at low-lying elevations, and often in estuaries. This is in comparison to the Pacific coast where tsunamis are more frequent but the coastline is more sparsely populated and most sections have much more relief.

Following the Sumatra 2004 earthquake, a major concern was raised about a similar plate tectonic geometry existing in the Puerto Rico trench with a potential impact on the U.S. East Coast. The Puerto Rico trench is a curved subduction zone where, similar to the Sumatra trench, relative plate motion is strike slip with only a small component of subduction. Tsunami hazard due to thrust earthquakes was underestimated in the Sumatra trench because of the large component of strike slip. The USGS has recently carried out extensive fieldwork in the Puerto Rico trench (See attached publication list) and is therefore in a position to provide an evaluation for this source.

Submarine landslides have also historically generated destructive tsunamis, although the extent of damaging wave generated by landslides is generally smaller. Along coastlines proximal to catastrophic submarine landslides, tsunami run-up can be significant as exemplified by the 1929

Grand Banks tsunami, which likely had a significant landslide-generated component. Less is generally known about submarine landslides as tsunami triggers in comparison to their earthquake counterparts.

This report represents the combined effort of a diverse group of marine geologists, geophysicists, geotechnical engineers, and hydrodynamic modelers to evaluate tsunami sources that have the potential to impact the US East and Gulf coasts. The report was commissioned by the Nuclear Regulatory Commission and was prepared between September 2006 and August 2008. It supersedes a previous version of the report titled "The current state of knowledge regarding potential tsunami sources affecting U.S. Atlantic and Gulf Coasts", which was submitted to the US-NRC on September 30, 2007.

The report is divided into five sections: Section 1 deals with tsunamigenic submarine landslide hazard and has chapters covering landslides along the Atlantic continental slope (Chapter 2), the Gulf of Mexico (Chapter 3) and far-field landslides (Chapter 4). Section 2 deals with tsunmigenic earthquakes and includes chapters on simulations of the 1755 Lisbon earthquake (Chapter 5), review of other earthquake sources that may affect the U.S. Atlantic (Chapter 6) and Gulf of Mexico (Chapter 7) coasts, and simulations of the propagation patterns from the Puerto Rico trench and other Caribbean earthquakes (Chapter 8). Section 3 presents a case study of the Currituck submarine landslide off North Carolina and includes a geotechnical analysis of the slide (Chapter 9) and tsunami simulations of the landslide using parameters from this analysis (Chapter 10). Section 4 develops tools that can help in a quantitative probability estimate of tsunamis along the U.S. East coast. These tools include using the relationship between earthquakes and landslides to assess landslide size and recurrence interval (Chapter 11), a quantitative size distribution analysis of submarine landslides (Chapter 12), a survey of the timing of occurrence of presently dated landslides (Chapter 13), and the development of a framework for probabilistic tsunami hazard analsys (Chapter 14). Section 5 includes summary of each of the chapters (Chapter 15), and future directions necessary to fill knowledge gaps, which were identified as a result of the preparation of this report (Chapter 16).

Section 1:

Landslides

Chapter 2: Geologic Controls on the Distribution of Submarine Landslides along the U.S. Atlantic Continental Margin

Introduction

While it has long been known that landslides and turbidity currents play a role in the development of passive margins, recent advances in sea floor imaging techniques are improving our ability to image and map geomorphic features generated by these processes. One of the early observed examples of submarine slope failures was the landslides and related turbidity currents generated by the 1929 earthquake near the Grand Banks offshore of Nova Scotia, Canada (Heezen and Ewing, 1952). With the availability of sidescan sonar and multibeam bathymetric images the extent and nature of the landslides generated by the Grand Banks earthquake has been realized (Piper *et al.*, 1988; Shor and Piper, 1989; Mosher *et al.*, 2004).

The 2004 Sumatra tsunami drew attention to the devastation they can cause in tectonically active settings, yet studies of tsunami generated by large landslides (Mader, 2001; Bondevik *et al.*, 2005; and Gisler *et al.*, 2006) indicate that even passive margins are not spared from this hazard. The extent of submarine landslides on the passive margins of the North Atlantic Ocean has been summarized by several authors (*i.e.* Embley and Jacobi, 1986; Booth *et al.*, 1993; Weaver *et al.*, 2000; Piper and McCall, 2003; Huhnerbach *et al.*, 2004; and Masson *et al.*, 2006). Along the Atlantic margin of the United States, landslides were first mapped by means of widely-spaced seismic profiles and piston cores (see summaries by Embley and Jacobi, 1986; Booth *et al.*, 1988; and Pratson and Laine, 1989). Knowledge of their distribution was further refined using GLORIA sidescan sonar imagery (EEZ-SCAN 87, 1991; Booth and O'Leary, 1991; Booth *et al.*, 1993). However, the acquisition of multibeam bathymetry over large portions of the U.S. Atlantic continental slope and rise between the eastern end of Georges Bank and the Blake Spur (Figure 2-1) has provided a valuable new view of this margin (Gardner *et al.*, 2006; Chaytor *et al.*, 2007), and warrants revisiting and refining the extent and distribution of landslides. In addition to the acquisition of improved sea floor imagery, many investigations have advanced our knowledge of the geologic evolution of this margin (Austin *et al.*, 1980; Schlee and Fristch, 1983; Vogt and Tucholke, 1986; Poag and Sevon, 1989; Poag, 1992). Based on this new information, we can now assess the distribution and style of

submarine landslides on the U.S. Atlantic continental margin, and discuss their distribution in the context of variations in the geologic conditions along the margin.

Geologic Setting

The U.S. Atlantic continental margin is a passive margin that rifted asynchronously from south to north during the Mesozoic (Klitgord *et al.*, 1988). Three basins associated with this initial rifting lie shoreward of the study area (Figure 2-1). Salt deposition was probably extensive during early stages of rifting, but salt domes have formed only in the Carolina Trough offshore of North and South Carolina (Dillon *et al.*, 1982). A nearly continuous carbonate platform and barrier reef system formed during the early Middle Jurassic (Poag, 1991), which stopped forming in the Early Cretaceous. Deposition during the Cenozoic consisted primarily of siliciclastic sediments (Tucholke and Mountain, 1986; Poag and Sevon, 1989) except during the Eocene, when calcareous chalk was deposited along much of the margin. This chalk is still exposed discontinuously on the lower slope off Georges Bank, southern New England and New Jersey (Weed *et al.*, 1974; Ryan *et al.*, 1978; Robb *et al.*, 1981; Tucholke and Mountain, 1986). South of the study area, Middle Cretaceous and older limestone is exposed along the Blake Spur and Blake Escarpment (Dillon *et al.*, 1993).

The Quaternary saw large volumes of sediment eroded from the North American continent by glacial processes and redistributed unevenly along this margin (Poag and Sevon, 1989). North of the study area, off Nova Scotia, continental glaciers reached the shelf edge, and supplied sediment directly on the outer shelf and upper slope (Jenner *et al.*, 2007). Off New England the glaciers extended southward and eastward to the northern edge of Georges Bank and the present southern New England and New York coasts (Figure 2-1; Oldale, 1992). Beyond the moraines, rivers transported sediment eroded by the glaciers to the shelf edge. Large rivers crossed the shelf at both ends of Georges Bank (Austin *et al.*, 1980; Schlee and Fritsch, 1983) and south of New England (McMaster and Ashraf, 1973). Deltas formed along much of this shelf edge in response to the huge sediment supply from glaciers. These shelf-edge deltas reached thicknesses of 400-800 m on the outer shelf and upper slope, and thin or locally are absent on the lower slope (Poag and Sevon, 1989; Poag, 1992). South of this glacially-influenced region, several large rivers crossed the shelf and in some cases built shelf-edge deltas (Figure 2-1), while elsewhere supplying sediment to deep-sea fans on the upper rise (Poag, 1992). Thick Quaternary shelf-edge deposits are found offshore of the paleo-Hudson, Susquehanna and James Rivers, and deep-sea fans formed on the rise off the Hudson and Susquehanna Rivers (Poag, 1992). Sediment accumulation rates on this margin were higher during the Quaternary than during any other time since the opening of the Atlantic Ocean (Poag and Sevon, 1989).

Uchupi (1967) published the first study of submarine landslides along the U.S. Atlantic margin. Landslide studies flourished into the 1990s (McGregor

and Bennett, 1977; 1979; Knebel and Carson, 1979; MacIlvaine and Ross, 1979; Bunn and McGregor, 1980; Embley, 1980; Malahoff *et al.*, 1980; Robb *et al.*, 1981; Farre *et al.*, 1983; Knebel, 1984; Prior *et al.*, 1984; 1986; Cashman and Popenoe, 1985; O'Leary, 1986, 1991, 1993, 1996; Schlee and Robb, 1991; Popenoe *et al.*, 1993; Popenoe and Dillon, 1996; McAdoo *et al.*, 2000). Several regional syntheses of their distribution were compiled using echo-sounder profiles and cores (Embley, 1980; Embley and Jacobi, 1986; Booth *et al.*, 1988; Booth and O'Leary, 1991; Pratson and Laine, 1989; and Huhnerbach *et al.*, 2004). The first comprehensive survey of the U.S. Atlantic continental slope and rise by the GLORIA long-range sidescan sonar was completed in 1987 (EEZ-SCAN87, 1991). Booth and O'Leary (1991) and Booth *et al.* (1993) provided a summary of the distribution and attributes of landslides and tabulated published information on the dimensions of these features, characteristics of the source areas, and styles of failure.

Methods

Available bathymetry, sidescan sonar imagery, subbottom seismic profiles, and core data were incorporated into a GIS and the integration of these data provide the basis for this interpretation of landslides.

Bathymetry

Data used in the compilation of the bathymetry for this analysis were acquired from several sources and vary in age, sounding density, and positional accuracy. The primary data set was acquired during 2004 and 2005 by the University of New Hampshire (UNH) in support of potential U.S. claims under the United Nations Convention on the Law of the Sea (Gardner *et al.*, 2006). This data set provides near-continuous multibeam coverage from the base of the continental slope down to abyssal plain depths (~ 1,500 m and 5,000 m) between the eastern end of Georges Bank and 33°N in the central Carolina Trough (Figure 2-2). Other multibeam data sets provide coverage of portions of the continental slope and rise not covered by the UNH data set. These data were collected by Woods Hole Oceanographic Institution ships R/V Knorr (14 cruises) and R/V Atlantis (13 cruises), Lamont-Doherty Earth Observatory ships R/V Ewing (11 cruises) and R/V Robert Conrad (1 cruise), and NOAA ships as part of the U.S. EEZ mapping surveys (13 cruises). Areas where multibeam soundings were not available include large sections of the continental slope off Georges Bank and southern New England, smaller sections of the slope off the Middle Atlantic States, and a large section of the slope and rise offshore northern Florida and southern Georgia (Figure 2-2). Multibeam coverage in these areas includes only widely separated transit lines except in the area off northern Florida and southern Georgia where complete coverage is available around some of the salt domes (Hornbach *et al.*, 2007). Where multibeam data are not available, sounding data from the National Ocean Service

hydrographic database provided bathymetric coverage of the continental slope. The final map covers the ocean floor from the shoreline to depths greater than 5,000 m, and has a horizontal pixel resolution of 100 m.

GLORIA sidescan

GLORIA (Geologic Long-Range Inclined Asdic) sidescan sonar data collected in 1987 (EEZ-SCAN 87, 1991) provide almost total coverage of the sea floor at a pixel resolution of 50 m from the shelf edge out to 200 miles from shore, between 28 and 42 degrees north latitude (Figure 2-2).

Subbottom profiles

Analog records of 3.5-kHz profiles, co-acquired with the GLORIA sidescan imagery, resolve the shallow stratigraphy of landslide features along lines spaced 10-35 km apart. These profiles provided information on the thicknesses of some of the deposits, but had insufficient penetration into other deposits. Consequently the thicknesses, and thus volumes of only selected landslide deposits could be measured, and these most likely are minimum estimates.

Cores

Over 1,400 cores have been collected from the study area, and brief descriptions of the overall lithology and sedimentary structures in cores are available from the National Geophysical Data Center core repository (`http://www.ngdc.noaa.gov/mgg/curator/curator.html`) and more detailed descriptions of some cores are available from the literature (Embley, 1980; Prior *et al.*, 1984, 1986;). Of these, approximately 1000 have been visually described, and 145 of them have ages assigned based on faunal content. Radiocarbon dates are scarce, and the published dates are summarized by Lee (this volume).

Landslide mapping

The mapping of landslide-affected areas was broken into several steps. First, the headwall scarps were identified and mapped in a GIS. These scarps were identified based on interpretation of shaded-relief images and slope maps derived from the bathymetric data. Gullies that are prevalent along canyon walls and that have been attributed to mass movements (Twichell and Roberts, 1982; Scanlon, 1984) were not mapped individually because of their huge number and small size. Second, the areas downslope of the scarps affected by landslides were digitized in a GIS. The shaded-relief imagery, backscatter imagery from multibeam systems (where available), and GLORIA imagery were used to identify these areas. The surfaces of most landslides have a high-backscatter signature. Offshore the Carolinas, where the multibeam coverage was incomplete (Figure 2-2), the extent of the

landslide areas was based on the GLORIA imagery alone. Third, the thicknesses of the landslide deposits were measured on the 3.5-kHz profiles and an average thickness, based on available profiles, was assigned to each deposit. The ability to resolve the thickness of landslide deposits was variable. In some cases the thickness was clearly imaged, in others a highly-reflective sea floor did not allow any subbottom penetration, and in still other cases the base of the deposit was deeper than could be penetrated by the subbottom profiling system. The fourth and final step was to merge the thicknesses measured on the subbottom profiles with the areal extents of landslides to estimate the volumes of landslide deposits. The volumes of the landslide deposits are minimum estimates because of our inability to resolve some of the landslide thicknesses from the 3.5-kHz profiles.

Results

A total of 48 distinct areas affected by landslides were mapped between the eastern end of Georges Bank and the Blake Spur (Figure 2-3). Each of these areas outlines the source area and the extent of the deposits derived from the source area. In most cases more than one headwall scarp was present and in these cases the deposits appear to be made up of several smaller units. These areas are described as composite landslides (Figure 2-3) because they are made up of several failures derived from the same general source area. The number of landslides that we mapped is considerably less than the 179 tabulated by Booth *et al.* (1988, 1993) and Booth and O'Leary (1991). The reason for the difference is largely because many of the landslides that Booth *et al.* (1988) summarized were identified on widely spaced seismic lines. When the locations compiled by them are compared to the multibeam data, many fall within the larger landslide complexes that can now be identified.

The types of landslides were interpreted from the morphology of the deposits as well as from their internal character, and were classified by the scheme proposed by Locat and Lee (2002). Rotational slides, translational slides, debris flows, and composite landslides were identified, and their distributions are shown in Figure 2-3. Most of the landslides have several scarps in the source area, suggesting that they consist of multiple failures rather than a single event (Figure 2-4A). In some cases the surficial morphology suggests that the deposits consist of several smaller deposits (Figure 2-4A). Subbottom profiles show a rough, possibly eroded, sea floor downslope of the headwall scarp (Figure 2-4B) and thin acoustically transparent deposits farther downslope (Figure 2-4C). Many of the large landslides are considered to be composite landslides that can contain different types of failures. The extent of these composite landslides is now well mapped, but when they occurred and the length of time it took each to form are still poorly known because of the limited availability of age dates (Lee, this volume). Turbidity currents are known to have transported large amounts of sediment downslope in this area (Pratson and Laine, 1989), but turbidites are not included in this discussion because they are not uniquely identifiable from the imagery available to us.

An example of one of the rotational slides offshore of Wilmington Canyon is shown in Figure 2-5. Reflections have continuity within the deposit although they have been gently folded. The two rotational slides in this area are relatively old as their toes are buried by younger sediment (Figure 2-5B). Translational slides are slab-like deposits that have been translated a short distance downslope (Figure 2-6). No seismic profiles cross this example, so the internal structure cannot be described. The headwall scarps are less than 5 km from the deposit and have a shape similar to the deposit's upper edge indicating a short translation distance. Debris flows have clearly defined headwall scarps, acoustically transparent lens-shaped deposits (Figure 2-4C), and can extend more than 200 km downslope to the distal end of the deposit (Figure 2-3). The acoustically transparent nature of these deposits suggests complete disintegration of the failed material during transport. Debris flows appear to be the most common form of failure based on the nature of the deposits. Virtually all of the composite landslides have acoustically transparent deposits suggesting disintegration of the failed material during the process of transport (Figure 2-3).

The general characteristics of the mapped landslides are given in Table 2-1. Their areas ranged from 9 to 15,241 km^2 with a mean area of 1,880 km^2. The total area affected by landslides is approximately 18% of the entire study area. Composite landslides as well as individual debris flows (where they could be identified) are about 4 times as long as they are wide and have a mean length of 85 km. The water depth of the source area for landslides was defined as the shallowest scarp upslope of the landslide. Depths of these scarps could only be measured at 33 of the 48 identified landslide areas because of inadequate bathymetric data on some parts of the continental slope. The depth of the headwall scarps ranged from 92 to 3,263 m with a mean depth of 1,630 m; 50% of these scarps occurred on the middle and lower slope in 1,200-2,250 m water depths. Our estimate of this range of source area depths may change once multibeam bathymetry becomes available for the upper continental slope offshore of Georges Bank and southern New England (Figure 2-2). Yet Booth *et al.* (1988, 1993) reported 900 m as the most common source depth for landslides. This discrepancy between our estimate for source depth and that by Booth *et al.* (1988, 1993) is attributed to the improved mapping allowed by the multibeam bathymetric data. The mean height of the headwall scarps that could be measured was 90 m, and of the 33 that were measured only 5 had relief in excess of 200 m. The toes of all of the landslide deposits that spread onto the continental rise were in water depths greater than 2,126 m. Some of the landslides extended beyond the limit of the data coverage, so the maximum toe depth is unknown. The mean toe depth of those that fell entirely within the study bounds is 3,101 m.

The distribution of landslides is not uniform along this margin (Figure 2-3) nor is their size (Figure 2-7). Most areas covered by landslides are less than 2,000 km^2, but one exceeds 15,000 km^2. Fifteen landslides and composite landslides cover 33% of the area off Georges Bank and southern New England. In this area, 7 of them cover areas exceeding 2,000 km^2, and the largest covers 13,939 km^2. Between Hudson Canyon and Cape Hatteras,

off the Middle Atlantic States, 31 landslides and composite landslides were mapped, but they cover only 16% of this part of the study area. In this area, 5 of them cover areas exceeding 2,000 km^2, and the largest covers 5,322 km^2. South of Cape Hatteras, off the Carolina Trough, only 2 areas subjected to landslides are present; they exceed 7,492 and 15,241 km^2 in area, respectively. Together, they cover 13% of this part of the study area.

Booth *et al.* (1993) were the first to recognize that landslides fall into two categories on this margin: those with source areas on the open slope and those that are sourced in submarine canyons. Landslides with open slope sources are concentrated on the southern New England margin, off Chesapeake Bay, and in the Carolina Trough (Figure 2-8). Many of the landslides off Georges Bank appear to have a combination of canyon and the open slope sources, but existing bathymetry on this section of the slope is inadequate to fully map the source areas. Where multibeam bathymetry is available off Georges Bank, scarps are present on the middle to lower slope well removed from canyons. This observation indicates that at least part of the source for landslides in this area is from open-slope settings. The landslides with source areas in submarine canyons are concentrated between Hudson and Norfolk Canyons, and offshore of Cape Hatteras.

The thicknesses of landslide deposits, where they could be measured, ranged from 5-70 m with a mean of approximately 20 m. In places the seismic data did not penetrate to the base of the landslide deposits; consequently the volumes are minimum estimates. The thickest deposits were found on the southern New England rise, and in the Carolina Trough area. The total volumes of the deposits can be huge (Figure 2-9), but many are composite landslides, and thus the deposit associated with any one failure would be considerably smaller. For example, the Currituck landslide deposit has a total volume of at least 84 km^3 (based on an average thickness of 20 m derived from 5 profiles across the middle and distal part of the deposit), but the imagery suggests the deposit can be divided into several sections that range in volume from 1.7-38.5 km^3 (Figure 2-4A). Of the largest landslide complexes, two are slope-sourced landslides in the southern New England region with deposits having minimum volumes of 190 and >392 km^3 and two are sourced around salt domes in the Carolina Trough area (minimum volumes of 114 and 150 km^3). By contrast, the largest canyon-sourced landslide deposits, which are also composite landslides, have volumes less than 10 km^3 (Figure 2-9).

The ages of the landslides on the U.S. Atlantic margin are poorly known because of the lack of reliable dates. Of those that have been dated, most are older than 7,000 yr BP (Prior *et al.*, 1984, 1986; Popenoe *et al.*, 1993; Schmuck and Paull, 1993; Embley and Jacobi, 1986; Lee, this volume). In two cases, sediment immediately above failure deposits had ages of 5,000 and 6,680 yr BP (Embley, 1980). The landslide deposits themselves, as defined by 30 cores, are composed of Pleistocene material in all but three cases (Figure 2-3). The relatively young age of the sediment comprising the deposits indicates that most failures removed only a surficial skin of Quaternary sediment from the source area. Limited amounts of older material have been recovered from within some landslide deposits off southern New England

and between Hudson and Lindenkohl Canyons where Tertiary strata presently are exposed on the lower slope (Robb *et al.*, 1981; Tucholke and Mountain, 1986). The Currituck slide is another place where older strata may have been incorporated in the failures. The headwall scarp has the most relief of all failures (404 m), a core from the headwall area recovered Early Pleistocene dry friable clay (Bunn and McGregor, 1980; Prior *et al.*, 1986), and the blocky nature of parts of the deposit's surface (Figure 2-4A) suggests that more lithified material was excavated from the source area and did not completely disintegrate during transport.

Discussion

The distribution of submarine landslides along the Atlantic margin is strongly, although not exclusively, controlled by proximity to continental glaciers. The U.S. Atlantic margin can be divided into three sub-regions based on proximity to glaciers: a northern glacially influenced region, a central fluvially influenced region, and a southern region with limited direct input of continental sediment during the Quaternary. Farther north, off Nova Scotia, glaciers reached the shelf edge and directly supplied sediment to the slope (Piper and McCall, 2003, Jenner *et al.*, 2007). Here 40% of the slope is estimated to be covered by landslides (Piper, 1991). Based on the landslide mapping conducted as part of the present study, we calculated the portion of the sea floor covered by landslides off Georges Bank and southern New England, where glaciers did not reach the shelf edge, to be 33% of this area (Figure 2-8). In this glacially-influenced setting shelf-edge deltas are extensive. Farther south, between Hudson Canyon and Cape Hatteras, 16% of the sea floor is covered by landslides. Here, sediment supply to the shelf edge was through widely-separated rivers (Figure 2-8). Between areas occupied by Quaternary shelf-edge deltas, Quaternary sediment cover on the upper slope is thinner (Poag and Sevon, 1989) and absent from large parts of the lower slope (Robb *et al.*, 1981; Tucholke and Mountain, 1986). The southern region extends from just south of Cape Hatteras to the Blake Spur, and here 13% of the sea floor is covered by landslides. This southern region is well removed from glacial sources and had minimal direct sediment input from the continent during Quaternary lowstands of sea level. In part, the diminished continental sediment input occurs because of the presence of Blake Plateau, a broad terrace which separates the shelf from the lower slope (Figure 2-1). The two composite landslides appear to be influenced by different geologic processes as they both originate near a string of salt domes (Hornbach *et al.*, 2007) along a section of the Atlantic margin where shallow low-magnitude earthquakes have been periodically recorded (Ekström, 2006).

Landslides are most extensive off areas affected by continental glaciers and large river systems during the last glaciation, and it appears that the shallow stratigraphy in these areas has a strong control on landslide distribution. Seismic profiles show variations in aggradation of the shelf and progradation of the slope along this margin during the late Cenozoic and

Quaternary. Off Georges Bank and southern New England most profiles show reflecting horizons with dips parallel to the sea floor (Uchupi and Emery, 1967; Uchupi, 1970; Klitgord *et al.*, 1994). This geometry presumably is due to the aggradation and progradation of shelf-edge deltas. Much of the continental slope between Hudson and Lindenkohl Canyons shows Eocene and Miocene strata that are truncated on the middle and lower slope either by the sea floor or a shallow unconformity that is buried by a thin veneer of more recent sediment (Robb *et al.*, 1981; Tucholke and Mountain, 1986). South of Norfolk Canyon reflecting horizons generally parallel the sea floor under the slope (Uchupi and Emery, 1967; McGregor, 1981). Off Cape Hatteras again older strata are truncated by the slope (Rona, 1969). Rona (1969), McGregor (1981), and O'Leary (1986) have all suggested that the seaward dip of the underlying strata enhances the chance of failure. O'Leary (1991, 1993) suggested that the presence of weak layers within these seaward dipping slope deposits further enhanced the possibility of failure.

The area south of Cape Hatteras which was isolated from river systems by the Blake Plateau has only 13% landslide cover. The two landslides in the Carolina Trough are in a different geologic setting, and different processes contributed to their formation (Figure 2-8). The headwall scarps of these failures are near salt domes and the tectonic activity of the salt domes has been suggested as a triggering mechanism (Dillon *et al.*, 1982; Popenoe *et al.*, 1993; Cashman and Popenoe, 1985; Hornbach *et al.*, 2007). The decomposition of gas hydrates due to changes in sea level has also been suggested to have contributed to triggering these failures (Popenoe *et al.*, 1993; Schmuck and Paull, 1993). The recent observation of small, shallow earthquakes along this section of the continental margin (Ekström, 2006) suggests that seismic activity may have also contributed to the formation of these landslides.

The triggering mechanism for landslides has been attributed primarily to earthquakes (Booth *et al.*, 1993); however other processes may have pre-conditioned the material for failure. Booth *et al.* (1993) and Popenoe *et al.* (1993) suggested decomposition of gas hydrates during periods of lowered sea level might have contributed to triggering landslides. However, Maslin *et al.* (2004) and Hornbach *et al.* (2007) point out that gas hydrates are most susceptible to decomposition in response to lowered sea level if they occur in 200-600 m water depths. Our mapping shows that the headwalls of landslides are concentrated on the lower slope along this margin (Table 2-1); a depth at which hydrate decomposition due to changes in sea level would be less significant. Evidence and modeling of fluid discharge on the lower slope suggests this process may make the lower slope more prone to failure. Along the New Jersey margin Robb (1984) suggested that groundwater discharge during periods of lower sea level caused slumping on the lower slope. Dugan and Flemings (2000) suggested that rapid loading of permeable Miocene beds by Pleistocene sediment increased the pore pressure in these beds with one consequence being increased slope failure where Miocene strata underlie the middle and lower slope. Hydrogeologic modeling of fresh water in Miocene strata under the southern New England shelf suggests that subglacial recharge from the Laurentide ice sheet would have extended offshore as far

as the lower slope (Person *et al.*, 2003). O'Leary (1993) speculated that weak layers existed within the seaward dipping deposits under the southern New England and Georges Bank slope and suggested that failures were more likely to occur along layer boundaries where one of the layers is weak. These weak layers may be overpressured beds due to ground water recharge during glacial times or to rapid sediment loading during the Quaternary. While beds with excess pore pressure may not have triggered the landslides, they may have reduced the stability of slope deposits sufficiently that small earthquakes associated with glacial rebound could trigger these large failures. Stein *et al.* (1979) and Wu and Johnston (2000) noted that, in eastern Canada, zones weakened by previous faults may be reactivated by glacial unloading.

The dominant style of mass-wasting identified along the U.S. Atlantic margin appears to be composite landslides (Figure 2-3). The subbottom profiles show that nearly all the composite landslide deposits are acoustically transparent suggesting that these landslides underwent disintegration and probably were transported primarily as debris flows. In part, the reason for the prevalence of this type of failure may be because the bulk of the sediment recovered from mass-wasting deposits was Quaternary in age (Figure 2-3). Thus sediment in the source areas was largely unconsolidated to semi-lithified, and might have had a propensity to disintegrate as it fails. The height of scarps in most landslide source regions have less than 75 m relief indicating that in most places only parts of the Quaternary section were removed (Table 2-1).

We find that the open-slope sourced landslides are larger in overall volume than canyon-sourced ones, and as such, are the dominant means of rapid large-scale margin modification (Figure 2-9). Because of the large volumes associated with these open-slope sourced landslides, they have the most potential to initiate tsunamis (Murty, 2003); however their significance may be diminished depending on the mode of failure and the rate at which it occurs. The presence of several headwall scarps above many of these large landslides (Figures 2-4 and 2-6) points to their being the result of multiple retrogressive failures rather than a single event. Even so, the volume of material that was removed to form an individual scarp can in some cases be large enough to generate a tsunami (Hornbach *et al.*, 2007; Geist *et al.*, this volume; Locat, this volume). Whereas conditions related to glaciation, including oversteepening and weak layers associated with deltaic sedimentation (O'Leary, 1991, 1993), excess pore pressures in response to sediment loading or glacial recharge (Dugan and Flemings, 2000; Person *et al.*, 2003), and earthquakes associated with glacial rebound (ten Brink *et al.*, this volume), appear to have contributed to the abundance of landslides off the glacially influenced part of the margin, these are not the only processes that have been instrumental. Off the Middle Atlantic States, the large open-slope-sourced landslides occur only off more localized river-fed shelf-edge deltas (Figure 2-8). Here, depositional processes and excess pore pressure conditions would be similar to those on glacially influenced margins, but earthquakes would not be as readily associated with glacial rebound. The large landslides off the Carolina Trough are well removed from glaciated areas, and here the upward migration of salt along normal faults could lead to

oversteepening of the sea floor and repeated slope failures (Hornbach *et al.*, 2007).

Table

Table 2-1: Characteristics of landslides on the Atlantic margin.

Dimension	Minimum	Maximum	Mean	Median
Area (km^2)	9	15,241	1,880	424
Length (km)	2.7	>291	85	51
Width (km)	2.1	151	21	12
Source depth (m)	92	3,263	1,630	1,785
Toe depth (m)	2,126	4,735	3,101	2,991
Scarp height (m)	3	410	90	63

Figures

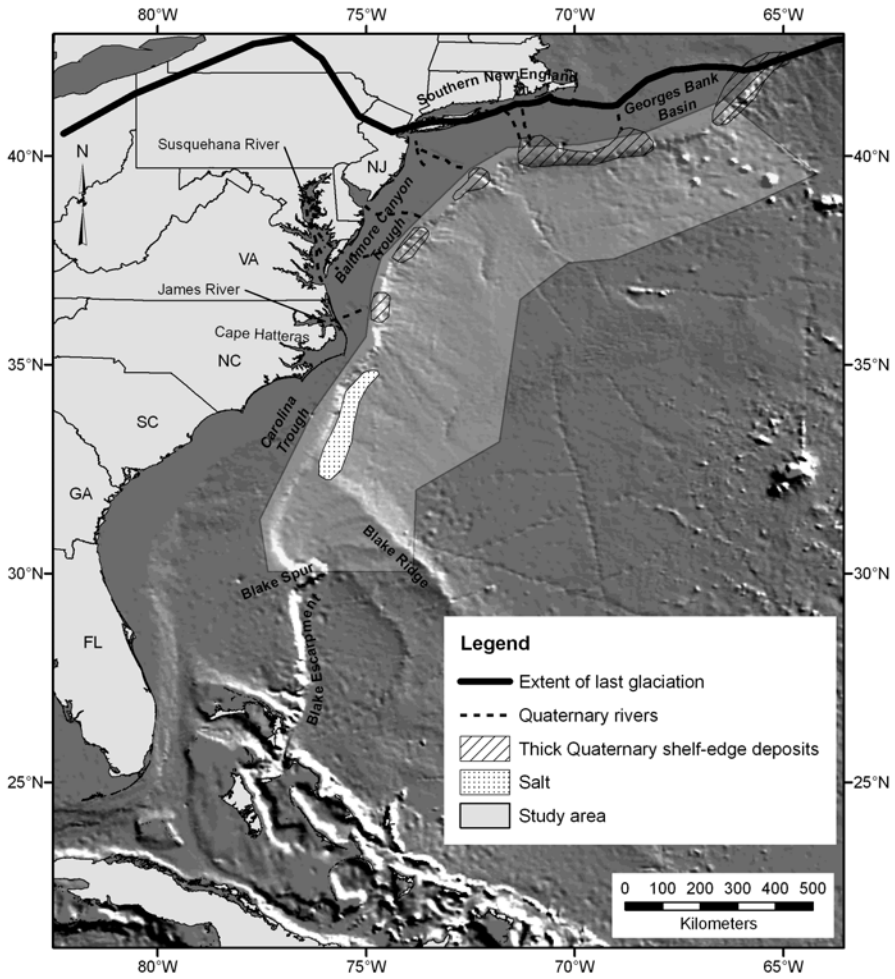

Figure 2-1: Location map showing the extent of the study area, the names of areas referenced in the text and geologic features that may influence landslide distribution along the U.S. Atlantic margin. The limit of the Laurentide ice sheet is taken from Oldale (1992), the distribution of rivers and shelf-edge deltas comes from McMaster and Ashraf (1973), Schlee and Fristch (1983), and Poag and Sevon (1989), and the extent of salt domes is taken from Dillon *et al.* (1982).

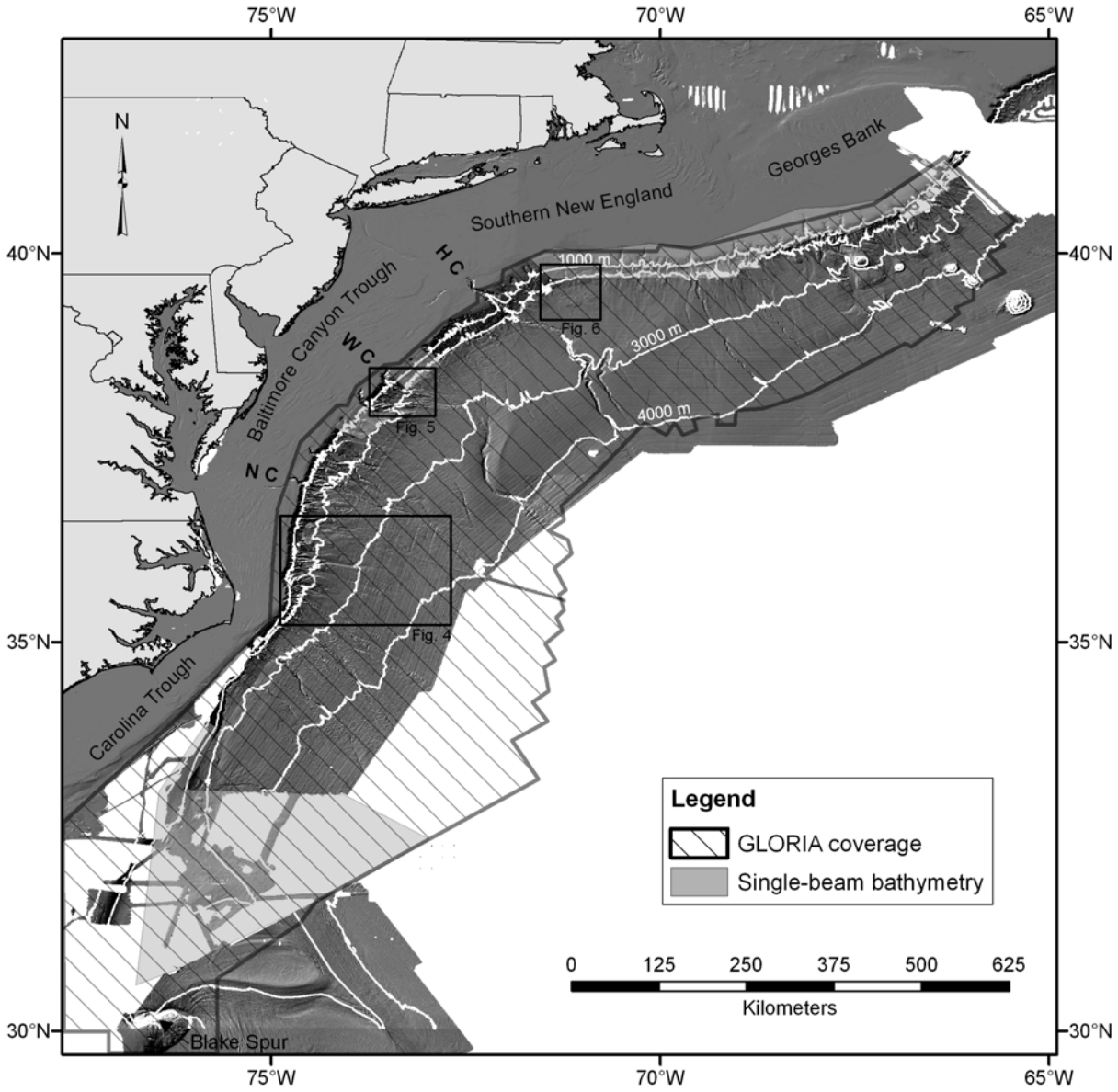

Figure 2-2: Extent of the study area and available data used in this analysis of landslides. Contours are in meters and abbreviations refer to Hudson Canyon (HC), Wilmington Canyon (WC), and Norfolk Canyon (NC). Boxes show locations of Figures 4, 5, and 6. The light-gray shaded polygons outline areas where multibeam bathymetry is not yet available.

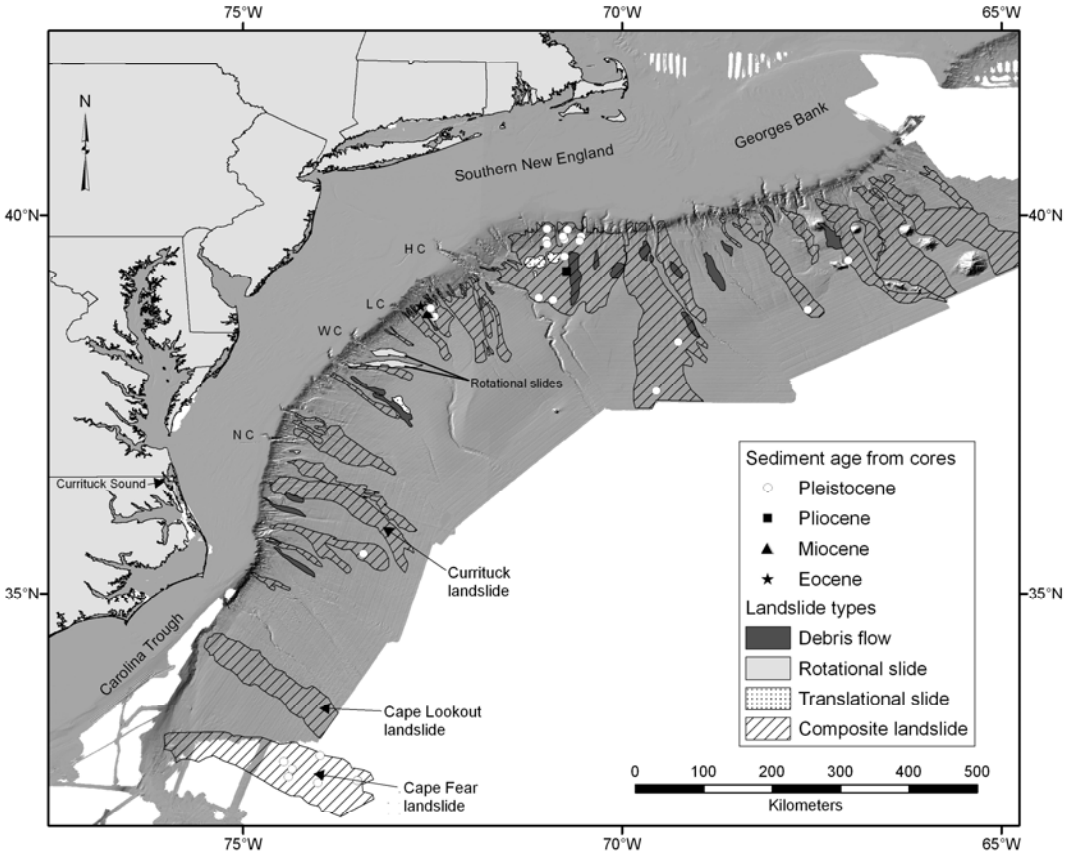

Figure 2-3: Distribution of different landslide types along the U.S. Atlantic continental slope and rise between the eastern end of Georges Bank and the southern edge of the Carolina Trough, and age of failed sediment recovered from cores collected in landslide deposits. Abbreviations identify some of the submarine canyons along this margin: HC = Hudson Canyon, LC = Lindenkohl Canyon, WC = Wilmington Canyon, NC = Norfolk Canyon. Three of the major landslides discussed in the text are labeled.

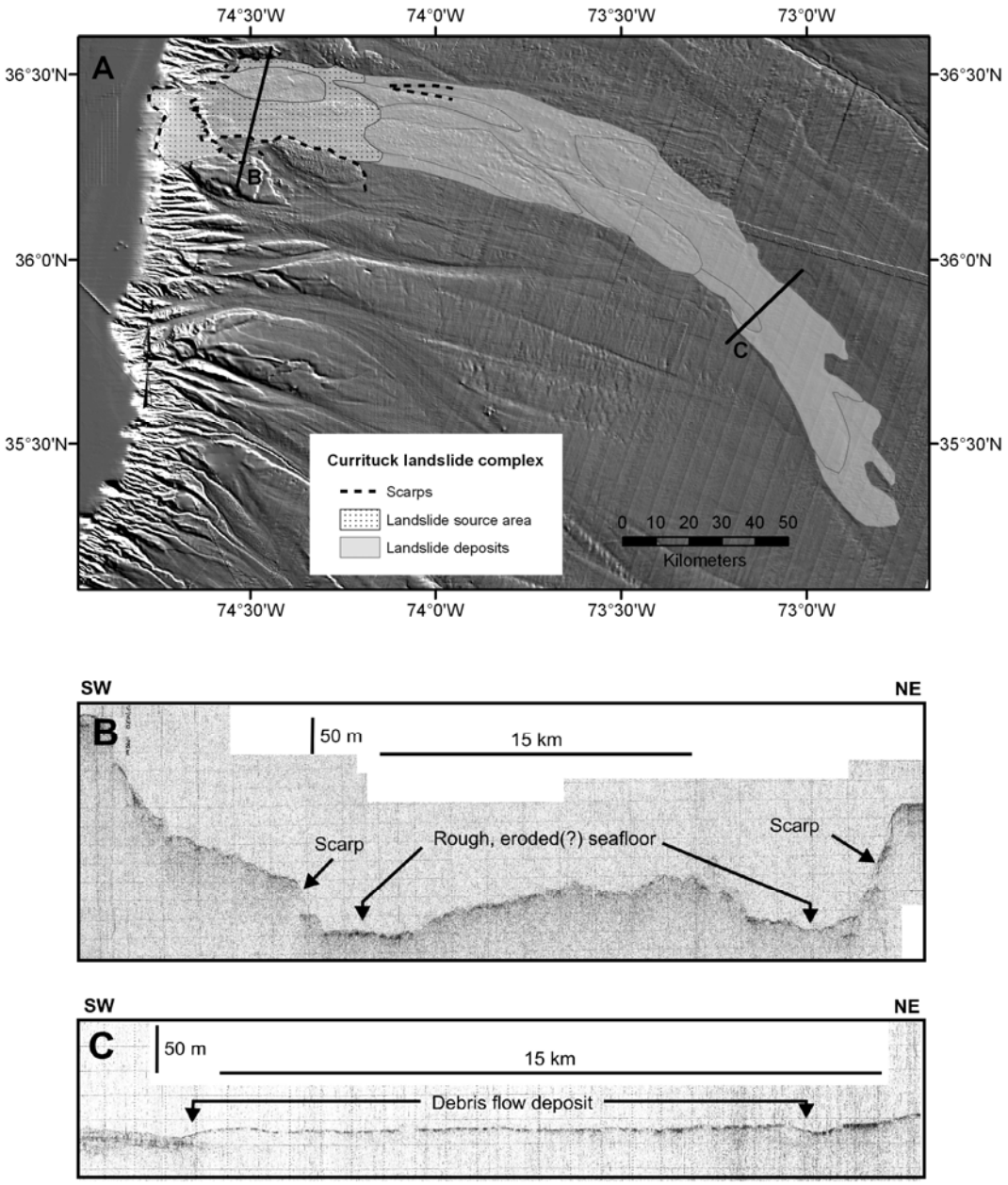

Figure 2-4: Detailed view of the Currituck landslide complex: (A) shaded relief image showing the extent of the landslide, the two headwall scarps and the outlines of subunits that comprise this composite landslide, (B) 3.5-kHz profile across one of the headwall scarps and the proximal part of the landslide, and (C) 3.5-kHz profile across the toe of the deposit, which is acoustically transparent and its surface is slightly mounded. Whereas the cumulative volume of the entire complex is 84 km^3, individual deposits are less than 38.5 km^3. The locations of the two profiles are shown in A, and the location of A is shown in Figure 2-2.

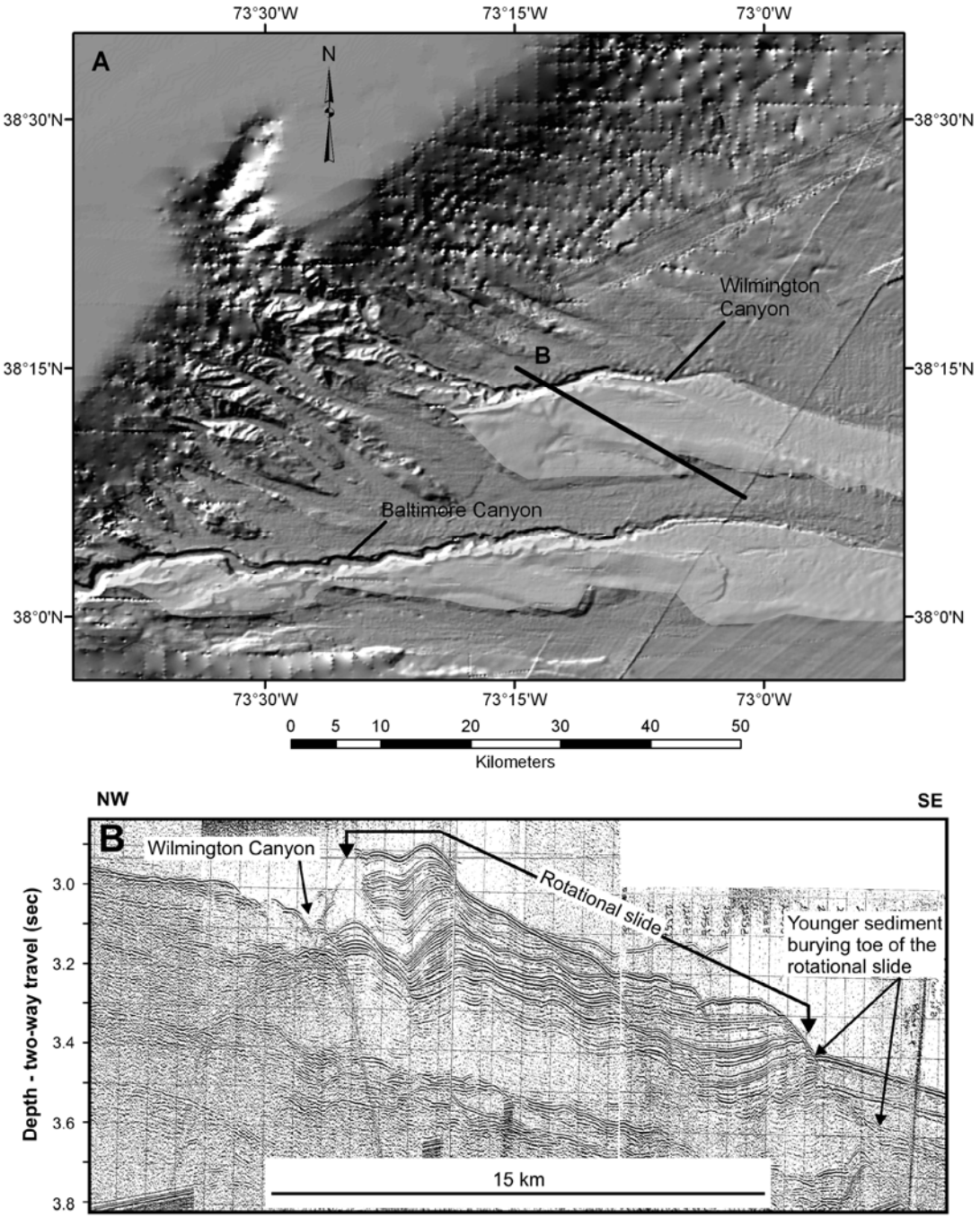

Figure 2-5: Examples of rotational slides: (A) shaded-relief image of two rotational slide blocks (high lighted in light gray) downslope of Wilmington and Baltimore Canyons, and (B) airgun seismic profile showing the rotational slide downslope of Wilmington Canyon whose toe has been buried by ~0.2 sec. of younger sediment. Profile location shown in A, and the location of A is shown in Figure 2-2.

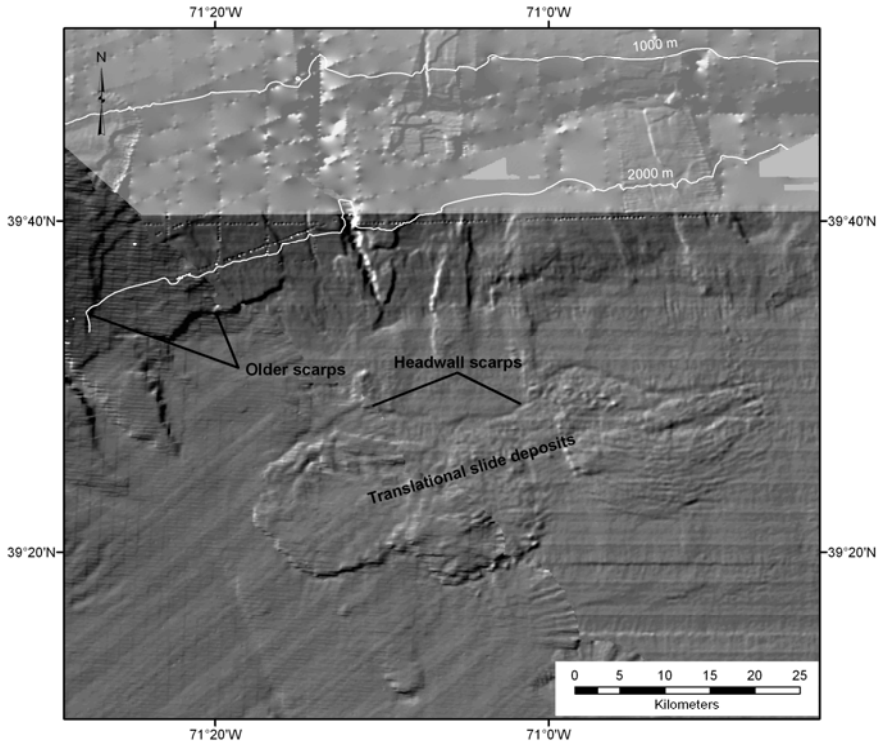

Figure 2-6: Shaded-relief image of translational slide on the southern New England upper rise (location shown in Figure 2-2). The headwall scarps and deposits are shown as well as some other scarps presumably formed by older landslides. Light gray shaded area at the top of the figure outlines a part of the southern New England slope where multibeam bathymetry is not available. Location of this figure is shown in Figure 2-2.

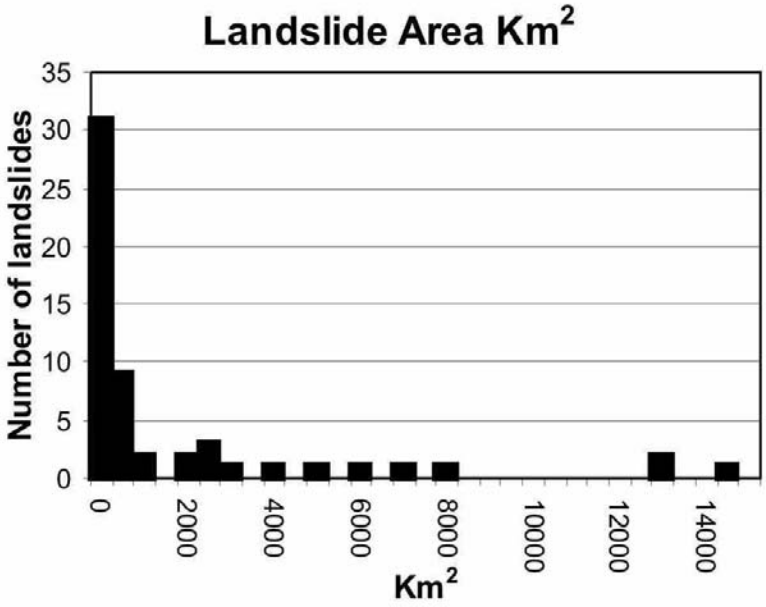

Figure 2-7: Graph showing the number landslides within each 500 km² grouping. Most of the landslides cover areas less than 2000 km².

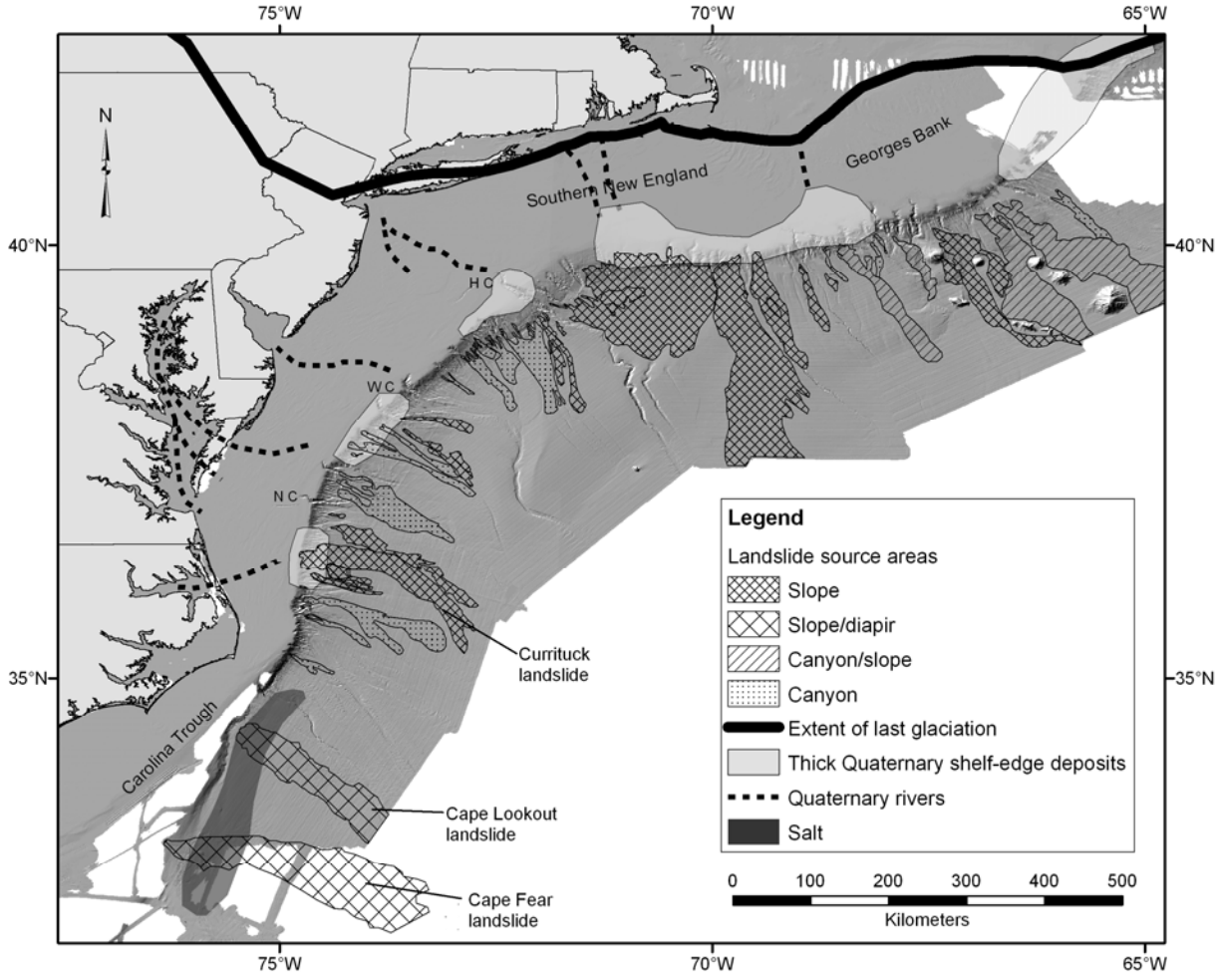

Figure 2-8: Map showing the distribution of landslides by source area, and their relationship to underlying geologic features. The largest landslides have open-slope source areas: off Georges Bank and southern New England many are downslope of shelf-edge deltas, and in the Carolina Trough area they are associated with salt domes. The landslides off Georges Bank have contributions from both canyon and open-slope sources; improved bathymetry in this area will allow assessing the importance of the two source areas. Landslides with submarine canyons as their source areas are smaller in area and shorter in their runout than the slope-sourced failures, and mostly are found between Hudson and Norfolk Canyons.

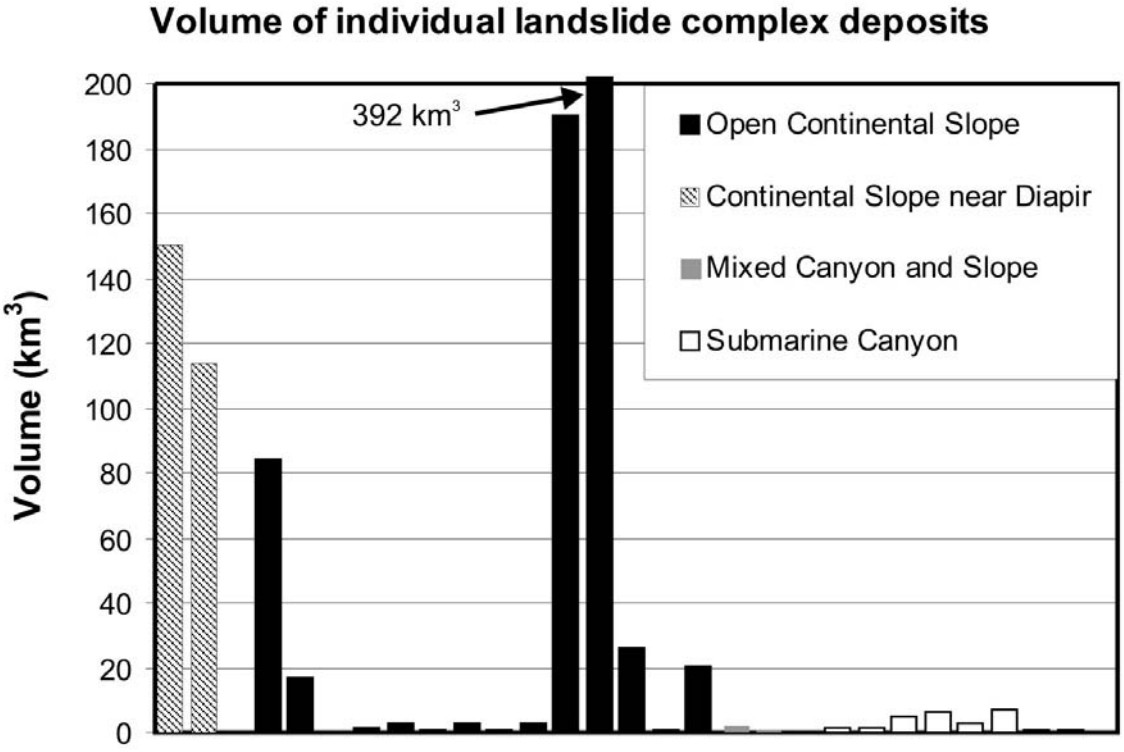

Figure 2-9: Graph showing the volume of 29 of the landslide complexes based on their source area type. The largest ones (by volume) have sources on the open slope (15 measured with volumes ranging from 0.2-392 km^3) or on the open slope near salt domes (2 measured with volumes of 114 and 150 km^3). The smallest ones have sources in submarine canyons (9 measured with volumes of 0.2-6.7 km^3) or in mixed canyon and slope settings (3 measured with volumes of 0.3-2.1 km^3). The largest landslide complex deposit is found on the southern New England rise and contains 392 km^3.

References

Austin, J.A., Uchupi, E., Shaughnessy, D.R., and Ballard, R.D., 1980, Geology of New England passive margin: *American Association of Petroleum Geologists Bulletin*, *v. 64*, p. 501-526.

Bondevik, S., Lovholt, F., Harbitz, C.B., Mangerud, J., Dawson, A., and Svendsen, J.I., 2005, The Storegga Slide tsunami; comparing field observations with numerical simulations: *Marine and Petroleum Geology*, *v. 22*, p. 195-208.

Booth, J.S., O'Leary, D.W., Popenoe, P., Robb, J.M., and McGregor, B.A., 1988, Map and tabulation of Quaternary mass movements along the United States-Canadian Atlantic continental slope from 32° 00' to 47° 00' N latitude: U.S. Geological Survey Miscelaneous Field Studies Map MF-2027.

Booth, J.S., and O'Leary, D.W., 1991, A statistical overview of mass movement characteristics on the North American Atlantic outer continental margin: *Marine Geotechnology*, *v. 10*, p. 10-18.

Booth, J.S., O'Leary, D.W., Popenoe, P., and Danforth, W.W., 1993, U.S. Atlantic continental slope landslides: Their distribution, general attributes, and implications, *in* Schwab, W.C., Lee, H.J., and Twichell, D.C. (Editors), Submarine landslides: Selected studies in the U.S. Exclusive Economic Zone: U.S. Geological Survey Bulletin no. 2002, p. 14-22.

Bunn, A.R., and McGregor, B.A., 1980, Morphology of the North Carolina slope, western North Atlantic, shaped by deltaic sedimentation and slumping: *Marine Geology*, *v. 37*, p. 253-266.

Cashman, K.V., and Popenoe, P., 1985, Slumping and shallow faulting related to the presence of salt on the continental slope and rise off North Carolina: *Marine and Petroleum Geology*, *v. 2*, p. 260-271.

Chaytor, J.D., Twichell, D.C., ten Brink, U.S., Buczkowski, B.J., and Andrews, B.D., 2007, Revisiting submarine mass movements along the U.S. Atlantic continental margin: Implications for tsunami hazards, *in* V. Lykousis, D. Sakellariou, and J. Locat (Editors), Submarine Mass Movements and Their Consequences: Springer, Netherlands, p. 395-403.

Dillon, W.P., Risch, J.S., Scanlon, K.M., Valentine, P.C., and Huggett, Q.J., 1993, Ancient crustal fractures control the location and size of collapsed blocks at the Blake Escarpment, East of Florida, *in* Schwab, W.C., Lee, H.J., and Twichell, D.C. (Editors), Submarine landslides: Selected studies in the U.S. Exclusive Economic Zone: U.S. Geological Survey Bulletin no. 2002, p. 40-53..

Dillon, W.P., Popenoe, P., Grow, J.A., Klitgord, K.D., Swift, B.A., Paull, C.K., and Cashman, K.V., 1982, Growth faulting and salt diapirism: Their relationship and control in the Carolina Trough, eastern North America, *in* J.S. Watkins and C.L. Drake (Editors), Studies in continental margin geology: American Association of Petroleum Geologists Memoir 34, p. 21-46.

Dugan, B., and Flemings, P.B., 2000, Overpressure and fluid flow in the New Jersey continental slope: Implications for slope failure and cold seeps: *Science*, *v. 289*, p. 288-291.

EEZ-SCAN 87, 1991, Atlas of the U.S. Exclusive Economic Zone, Atlantic continental margin: U.S. Geological Survey Miscelaneous Investigations Series I-2054, 174 pp.

Ekström, G., 2006, Global detection and location of seismic sources by using surface waves: *Bulletin of the Seismological Society of America*, *v. 96*, p. 1201-1212.

Embley, R.W., 1980, The role of mass transport in the distribution and character of deep ocean sediments with special reference to the North Atlantic: *Marine Geology*, *v. 38*, p. 23-50.

Embley, R.W. and Jacobi, R.D., 1986, Mass wasting in the western North Atlantic, *in* Vogt, P.R. and Tucholke, B.E., (Editors), The western North Atlantic region: Geological Society of America, Boulder, CO, Geology of North America, v. M, p. 479-490.

Farre, J.A., McGregor, B.A., Ryan, W.B.F., and Robb, J.M., 1983, Breaching the shelfbreak: Passage from youthful to mature phase in submarine canyon evolution, *in* Stanley, D.J., Moore, G.T. (Editors), The shelfbreak:

Critical interface on continental margins: *SEPM Special Publication*, *No. 33*, p. 25-39.

Gardner, J.V., Mayer, L.A., and Armstrong, A.A., 2006, Mapping supports potential submission to U.N. Law of the Sea: *EOS Transactions of American Geophysical Union*, *v. 87*, p. 157-159.

Geist, E.L., Lynett, P.J., and Chaytor, J.D., this volume, Hydrodynamic modeling of tsunamis from the Currituck Landslide.

Gisler, G., Weaver, R., and Gittings, M.L., 2006, SAGE calculations of the tsunami threat from La Palma: *Science of Tsunami Hazards*, *v. 24*, p. 288-301.

Heezen, B.C., and Ewing, M., 1952, Turbidity currents and submarine slumps, and the Grand Banks earthquake: *American Journal of Science*, *v. 250*, p. 849-873.

Hornbach, M., Lavier, L., and Ruppel, C., 2007, Triggering mechanism and tsunamogenic potential of the Cape Fear Slide complex, U.S. Atlantic coastal margin: *Geochemistry, Geophysics, and Geosystems*, *v. 8*, doi:10.1029/2007GC001722, 16 pp.

Huhnerbach, V., Masson, D.G., and partners of the COSTA-Project, 2004, Landslides in the North Atlantic and its adjacent seas: an analysis of their morphology, setting and behavior: *Marine Geology*, *v. 213*, p. 343-362.

Jenner, K.A., Piper, D.J.W., Campbell, D.C., and Mosher, D.C., 2007, Lithofacies and origin of late Quaternary mass transport deposits in submarine canyons, central Scotian Slope, Canada: *Sedimentology*, *v. 54*, p. 19-38.

Klitgord, K.D., Hutchinson, D.R., and Schouten, H., 1988, U.S. Atlantic continental margin: structural and tectonic framework, *in* Sheridan, R.E., and Grow, J.A., (Editors), The Geology of North America, v. I-2, The Atlantic Continental Margin: U.S. Geological Society of America, Boulder, CO, p. 19-55.

Klitgord, K. D., Poag, C. W., Schneider, C. M., and North, L., 1994, Geophysical database of the East Coast of the United States northern Atlantic margin--cross sections and gridded database (Georges Bank Basin, Long Island Platform, and Baltimore Canyon Trough): USGS Open-File Report 94-637, 190 pp.

Knebel, H.J., 1984. Sedimentary processes on the Atlantic continental slope of the United States: *Marine Geology*, *v. 61*, p. 43-74.

Knebel, H.J., and Carson, B., 1979, Small-scale slump deposits, Middle Atlantic continental slope, off eastern United States: *Marine Geology*, *v. 29*, p. 221-236.

Lee, H.J., this volume, Timing of occurrence of large submarine landslides on the Atlantic Ocean margin.

Locat, J., Lee, H., ten Brink, U., Twichell, D., Geist, E., and Sansoucy, M., this volume, Geomorphology, stability and mobility of the Currituck Slide.

Locat, J., and Lee, H. J., 2002, Submarine landslides: advances and challenges: *Canadian Geotechnical Journal*, *v. 39*, p. 193-212.

MacIlvaine, J.C., and Ross, D.A., 1979, Sedimentary processes on the continental slope of New England: *Journal of Sedimentary Petrology*, *v. 49*, p. 563-574.

Mader, C.L., 2001, Modeling the La Palma landslide tsunami: *Science of Tsunami Hazards*, *v. 19*, p. 150-170.

Malahoff, A., Embley, R.W., Perry, R.B., and Fefe, C., 1980, Submarine mass-wasting of sediments on the continental slope and upper rise south of Baltimore Canyon: *Earth and Planetary Science Letters*, *v. 49*, p. 1-7.

Maslin, M., Owen, M., Day, S., and Long, D., 2004, Linking continental-slope failures and climate change: Testing the clathrate gun hypothesis: *Geology*, *v. 32*, p. 53-56.

Masson, D.G., Harbitz, C.B., Wynn, R.B., Pedersen, G., and Lovholt, F., 2006, Submarine landslides: Processes, triggers, and hazard prediction: *Philosophical Transactions of the Royal Society A*, *v. 364*, p. 2009-2039.

McAdoo, B.G., Pratson, L.F., and Orange, D.L., 2000, Submarine landslide geomorphology, U.S. continental slope: *Marine Geology*, *v. 169*, p. 103-136.

McGregor, B.A., and Bennett, R.H., 1977, Continental slope sediment instability northeast of Wilmington Canyon: *American Association of Petroleum Geology Bulletin*, *v. 61*, p. 918-928.

McGregor, B.A., and Bennett, R.H., 1979, Mass movement of sediment on the continental slope and rise seaward of the Baltimore Canyon Trough: *Marine Geology*, *v. 33*, p. 163-174.

McGregor, B.A., 1981, Smooth seaward-dipping horizons – an important factor in sea-floor stability?: *Marine Geology*, *v. 39*, p. M89-M98.

McMaster, R.L., and Ashraf, A., 1973, Drowned and buried valleys on the southern New England continental shelf: *Marine Geology*, *v. 15*, p. 249-268.

Mosher, D.C., Piper, D.J.W., Campbell, C., Jenner, K.A., 2004, Near surface geology and sediment-failure geohazards of the central Scotian slope: *American Association of Petroleum Geology Bulletin*, *v. 88*, p. 703-723.

Murty, T. S., 2003, Tsunami wave height dependence on landslide volume: *Pure and Applied Geophysics*, *v. 160*, p. 2147-2153.

Oldale, R.N., 1992, Cape Cod and the Islands: The Geologic Story: Parnassus Imprints, East Orleans, MA, 208 pp.

O'Leary, D.W., 1986, The Munson-Nygren slide: A major lower-slope slide off Georges Bank: *Marine Geology*, *v. 72*, p. 101-114.

O'Leary, D.W., 1991, Structure and morphology of submarine slab slides: Clues to origin and behavior: *Marine Geotechnology*, *v. 10*, p. 53-69.

O'Leary, D.W., 1993, Submarine mass movement, a formative process of passive continental margins: the Munson-Nygren landslide complex and the southeast New England landslide complex, *in* Schwab, W.C., Lee, H.J., and Twichell, D.C. (Editors), Submarine landslides: Selected studies in the U.S. Exclusive Economic Zone. USGS Bulletin No. 2002, p. 23-39.

O'Leary, D.W., 1996, The timing and spatial relations of submarine canyon erosion and mass movement on the New England continental slope and rise, *in* Gardner, J.V., Field, M.E., and Twichell, D.C., (Editors), Geology of the United States Seafloor: The view from GLORIA: Cambridge University Press, Cambridge, UK, p. 47-58.

Person, M., Dugan, B., Swenson, J.B., Urbano, L., Stott, C., Taylor, J., and Willett, M, 2003, Pleistocene hydrogeology of the Atlantic continental shelf, New England: *Geological Society of America Bulletin*, *v. 115*, p. 1324-1343.

Piper, D.J.W., 1991, Surficial geology and physical properties 6 – Deep-water surficial geology, East Coast Basin Atlas Series: Scotian Shelf: Geological Survey of Canada, 121 pp.

Piper, D.J.W., and McCall, C., 2003, A synthesis of the distribution of submarine mass movements on the eastern Canadian margin, *in* J. Locat, and Mienert, J. (Editors), Submarine Mass Movements and their Consequences: Kluwer, Dordrecht, Netherlands, p. 291-298.

Piper, D.J.W., Shor, A.N., and Hughes Clarke, J.E., 1988, The 1929 Grand Banks earthquake, slump and turbidity current, *in* H.E. Clifton (Editor), Sedimentologic consequences of convulsive geologic events. Geological Society of America Special Paper 229, p. 77-92.

Poag, C.W., 1991, Rise and demise of the Bahama-Grand Banks gigaplatform, northern margin of the Jurassic proto-Atlantic seaway: *Marine Geology*, *v. 102*, p. 63-130.

Poag, C.W., 1992, U.S. Middle Atlantic continental rise: Provenance, dispersal, and deposition of Jurassic to Quaternary sediments, *in* Poag, C.W., and de Graciansky, P.C. (Editors), Geologic evolution of Atlantic Continental Rises: Van Nostrand Reinhold, New York, p. 100-156.

Poag, C.W., and Sevon, W.D., 1989, A record of Appalachian denudation in postrift Mesozoic and Cenozoic sedimentary deposits of the U.S. middle Atlantic continental margin: *Geomorphology*, *v. 2*, p. 119-157.

Popenoe, P., Schmuck, E.A., and Dillon, W.P., 1993, The Cape Fear Landslide: Slope failure associated with salt diapirism and gas hydrate decomposition., *in* Schwab, W.C., Lee, H.J., and Twichell, D.C. (Editors), Submarine landslides: Selected studies in the U.S. Exclusive Economic Zone. USGS Bulletin No. 2002, p. 40-53.

Popenoe, P., and Dillon, W.P., 1996, Characteristics of the continental slope and rise off North Carolina from GLORIA and seismic-reflection data: The interaction of downslope and contour current processes, *in* Gardner, J.V., Field, M.E., and Twichell, D.C.(Editors), Geology of the United States Seafloor: The view from GLORIA: Cambridge University Press, Cambridge, UK, p. 59-79.

Pratson, L.F., and Laine, E.P., 1989, The relative importance of gravity-induced versus current-controlled sedimentation during the Quaternary along the mideast U.S. Outer continental margin revealed by 3.5 kHz echo character: *Marine Geology*, *v. 89*, p. 87-126.

Prior, D.B., Doyle, E.H., and Neurauter, T., 1986, The Currituck Slide, Mid-Atlantic continental slope; revisited: *Marine Geology*, *v. 73*, p. 25-45.

Prior, D.B., Coleman, J.M., and Doyle, E.H., 1984, Antiquity of the continental slope along the Middle-Atlantic margin of the United States: *Science*, *v. 223*, p. 926-928.

Robb, J.M., Hampson, J.C., and Twichell, D.C., 1981, Geomorphology and sediment stability of a segment of the U.S. Continental Slope off New Jersey: *Science*, *v. 211*, p. 935-937.

Robb, J.M., 1984, Spring sapping on the lower continental slope, offshore New Jersey: *Geology*, *v. 12*, p. 278-282.

Rona, P.A., 1969, Middle Atlantic Continental Slope of United States: Deposition and erosion: *American Association of Petroleum Geologists Bulletin*, *v. 53*, p. 1453-1465.

Ryan, W.B.F., Cita, M.B., Miller, E.L., Hanselman, D., Nesterhoff, W.D., Hecker, B., and Nibbelink, M., 1978, Bedrock geology in New England submarine canyons: *Oceanologica Acta*, *v. 1*, p. 233-254.

Scanlon, K.M., 1984, The continental slope off New England: A long-range sidescan-sonar perspective: *Geo-Marine Letters*, *v. 4*, p. 1-4.

Schlee, J.S., and Fritsch, J., 1983, Seismic stratigraphy of the Georges Bank basin complex, offshore New England, *in* Watkins, J.S., and Drake, C.L. (Editors), Studies in continental margin geology: American Association of Petroleum Geologists Memoir 34, p. 223-251.

Schlee, J.S., and Robb, J.M., 1991, Submarine processes of the middle Atlantic continental rise based on GLORIA imagery: *Geological Society of America Bulletin*, *v. 103*, p. 1090-1103.

Schmuck, E.A., and Paull, C.K., 1993, Evidence for gas accumulation associated with diapirism and gas hydrates at the head of the Cape Fear Slide: *Geo-Marine Letters*, *v. 13*, p. 145-152.

Shor, A.N. Piper, D.J.W., 1989, A large Late Pleistocene blocky debris flow on the central Scotian Slope: *Geo-Marine Letters*, *v. 9*, p. 153-160.

Stein, S., Sleep, N.H., Geller, R.J., Wang, S.C., and Kroeger, G.C., 1979, Earthquakes along the passive margin of eastern Canada: *Geophysical Research Letters*, *v. 6*, p. 537-540.

ten Brink, U.S., Lee, H.J., Geist, E.L., and Twichell, D.C., this volume, Assessment of tsunami hazard to the U.S. East Coast using relationships between submarine landslides and earthquakes.

Tucholke, B.E. Mountain, G.S., 1986, Tertiary paleoceanography of the western North Atlantic Ocean, *in* Vogt, P.R., and Tucholke, B.E. (Editors), The Geology of North America, Volume M, The Western North Atlantic Region: Geological Society of America, p. 631-650.

Twichell, D.C. and Roberts, D.G., 1982, Morphology, distribution, and development of submarine canyons on the U.S. Atlantic Continental Slope between Hudson and Baltimore Canyons: *Geology*, *v. 10*, p. 408-412.

Uchupi, E., 1967. Slumping on the continental margin southeast of Long Island, New York: *Deep-Sea Research*, *v. 14*, p. 635-639.

Uchupi, E., 1970, Atlantic continental shelf and slope of the United States – Shallow structure: USGS Professional Paper 529-I, 44 pp.

Uchupi, E., and Emery, K.O., 1967, Structure of continental margin off Atlantic coast of United States: *American Association of Petroleum Geologists Bulletin*, *v. 51*, p. 223-234.

Vogt, P.R., and Tucholke, B.E. (Editors), 1986, The Geology of North America, Volume M, The Western North Atlantic Region: Geological Society of America, Boulder, CO, 696 pp.

Weaver, P.P.E., Wynn, R.B., Kenyon, N.H., and Evans, J., 2000, Continental margin sedimentation, with special reference to the north-east Atlantic margin: *Sedimentology*, *v. 47*, p. 239-256.

Weed, E.G.A., Minard, J.P., Perry, W.J., Rhodehamel, E.C., and Robbins, E.I., 1974, Generalized pre-Pleistocene geologic map of the northern United States Atlantic continental margin: USGS Miscelaneous Investigations Series I-861, scale 1:1,000,000.

Wu, P., and Johnston, P., 2000, Can deglaciation trigger earthquakes in N. America? *Geophysical Research Letters*, *v. 27*, p. 1323-1326.

Chapter 3: Distribution of Submarine Landslides in the Gulf of Mexico

Introduction

Submarine landslides have been studied in the Gulf of Mexico for two reasons: first they can pose a hazard to offshore platforms and pipelines for hydrocarbon extraction and transportation and second, when more deeply buried they can serve either as hydrocarbon reservoirs or barriers in reservoirs depending on their composition. The threat of submarine landslides as a generator of tsunamis has not been addressed for the Gulf of Mexico region. Here we present a brief review of the literature on the distribution and style of submarine landslides that have occurred in the Gulf of Mexico during the Quaternary. This review will focus on landslides that have occurred in on the continental slope and rise in the Gulf of Mexico; with much of the discussion focused on the part of the basin within the U.S. EEZ due to the availability of a greater number of publications from this region.

Setting

The Gulf of Mexico is a small, geologically diverse ocean basin that includes three distinct geologic provinces: a carbonate province, a salt province, and canyon to deep-sea fan province (Figure 3-1a). The basement under the deep Gulf of Mexico is Upper Triassic to Lower Jurassic oceanic or transitional crust (Sawyer *et al.*, 1991). The stratigraphy of the overlying deposits records the subsequent evolution of this small ocean basin (Buffler, 1991). Three particular aspects of the basin's evolution that should be considered in an assessment of landslide activity within the basin are the Jurassic-aged salt that was deposited during the early stages of the opening of this ocean basin (Salvador, 1991a), the development and growth of extensive carbonate reef tracts during the late Jurassic and Cretaceous (Bryant *et al.*, 1991), and the siliciclastic sediment input from the North American continent during the latest Mesozoic and Cenozoic (Buffler, 1991).

Salt deposited in the late Jurassic Gulf of Mexico basin, the Louann salt, originally underlay large parts of Louisiana, southern Texas, and the area offshore of Mexico in the Bay of Campeche (Salvador, 1991a). As sediment eroded from the North American continent was deposited on this salt sheet

throughout the Mesozoic and Cenozoic, the increased load caused the salt to flow with it migrating southward from the source area into the northern Gulf of Mexico (Salvador, 1991b; Diegel *et al.*, 1995). Presently the Louann salt underlies large parts of the northern Gulf of Mexico continental shelf and continental slope. South of Louisiana and Texas, the Sigsbee Escarpment is a pronounced cliff that marks the seaward limit of the shallowest salt tongue (Bryant *et al.*, 1991). As the salt is loaded, it flows both seaward and also upward through the overlying sediment column as cylindrical salt domes. The morphology of the salt sheet varies considerably across the margin. Salt domes are most common under the continental shelf, and most of the original salt sheet between individual domes in this region has been removed in response to the sediment loading, and migrated farther seaward. Under the upper and middle continental slope the salt is shaped into a network of ridges and narrow salt sheets that are interrupted by sub circular basins, (referred to in this chapter as mini-basins) which have thin salt or no salt underlying them. Farther down slope, immediately north of the Sigsbee Escarpment, the salt is more sheet-like in appearance and has a thin sediment cover over it (Diegel *et al.*, 1995). Rates of salt movement are largely due to the confining pressure of sediment deposition. Calculated rates of salt motion range from as high as 17 cm/year to as low as only a few cms/1,000 yrs (Lowrie *et al.*, 1991).

In the southwestern corner of the Gulf, in the Bay of Campeche, the seafloor has an irregular morphology that is similar to that of the northern Gulf of Mexico slope and appears to be the result of sediment loading an underlying salt deposit (Figure 3-1a; Worzel *et al.*, 1968; Martin and Bouma, 1978).

During the Mesozoic, an extensive reef system developed around much of the margin of the Gulf of Mexico Basin by the vertical growth of reefs and carbonate shelf edge banks (Bryant *et al.*, 1969; Sohl *et al.*, 1991). This reef system is exposed along the Florida Escarpment and the Campeche Escarpment that fringe the eastern and southern margins of this basin (Figure 3-1a). These escarpments stand as much as 1,500 m above the abyssal plain floor, and have average gradients that commonly exceed 20° and locally are vertical (Jordan and Stewart, 1959; Paull *et al.*, 1990a). Reef growth ended during the Middle Cretaceous (Freeman-Lynde, 1983; Locker and Buffler, 1984; Paull *et al.*, 1990b), and subsequently the platform edges have been sculpted and steepened by a variety of erosional processes (Freeman-Lynde, 1983; Corso *et al.*, 1989; Paull *et al.*, 1991; Twichell *et al.*, 1996). The tops of the steep escarpments are in 1,500-2,500 m of water, and above these steep cliffs is a slope with a markedly gentler gradient (Figure 3-2a).

A huge volume of continental sediment has been supplied to the deep Gulf of Mexico basin from the North American continent during the Cenozoic through submarine canyons. These sediments were deposited in the central deep part of the Gulf of Mexico as a series of deep-sea fans. The oldest were deposited in the western part of the basin, and the depocenter shifted progressively eastward (Buffler, 1991). Three fan systems formed during the Pliocene and Pleistocene: Bryant Fan (Lee *et al.*, 1996; Twichell *et*

al., 2000), Mississippi Fan (Weimer, 1989), and Eastern Mississippi Fan (Weimer and Dixon, 1994). The Mississippi Fan is the largest of these three fans, and covers most of the eastern half of the deep Gulf of Mexico basin and reaches 4 km in thickness under the upper fan off the mouth of the Mississippi Canyon (Weimer, 1989; 1991). Sediment was supplied to the Mississippi Fan through the Mississippi Canyon which has retained its morphologic expression on the slope (Figure 3-1a). The canyons that supplied sediment to Bryant and Eastern Mississippi Fans have been largely erased by salt movement (Weimer and Dixon, 1994; Lee *et al.*, 1996; Twichell *et al.*, 2000).

Types of Submarine Mass Movements

Several classification schemes exist for submarine mass movements. For this report we use one presented by Locat and Lee (2002) that was adapted from the classification of subaerial mass movements proposed by the International Society for Soil Mechanics and Geotechnical Engineering (ISSMGE) Technical Committee on Landslides. While it has been observed that one type of mass movement can lead to another, here we briefly describe the end-member types.

- **Topples** – The displaced material usually is lithified rock that descends mainly through water as a coherent block that does not disintegrate during movement. Topples result in minimal lateral displacement.
- **Falls** – The displaced material mostly is lithified to semi-lithified material that is broken into smaller blocks and rubble during the failure process and descends mainly through water by falling, bouncing, and rolling. Falls also result in minimal lateral displacement.
- **Rotational slides** – The failed material undergoes rotation along a curved slip surface during displacement. This material tends to be rigid although in some cases beds within the failed mass are folded but do not undergo disintegration during translation.
- **Translational slides** – The failed material is translated along a discrete, flat slip surface. The material is rigid, and thus maintains its internal stratigraphy; however displacement can be great distances.
- **Debris flows** – Mass movements in which the failed material disintegrated during transport, and results in the deposit being a heterogeneous mix of clasts supported in a matrix of fine sediment. The clasts in debris flows vary in size and sediment texture.
- **Mudflows** – Mass movements of predominantly fine-grained material. These are similar to debris flows, but because of the more uniform texture their internal structure is not as clearly defined.
- **Turbidity currents** – Mass movements that involve the down slope movement of a relatively dilute suspension of sediment grains that are supported by the upward component of fluid turbulence.

Distribution of Submarine Landslides

Submarine landslides have occurred in each of the three provinces of the Gulf of Mexico basin although they vary in style and size among these different provinces. Landslides also have been active throughout much of the history of this basin, but this report will focus mostly on those that occurred during the Quaternary Period, up to the present.

Carbonate province

Landslides in the carbonate provinces that fringe the eastern and southern Gulf of Mexico appear to have been derived from both the steep West Florida and Campeche Escarpments as well as from the gentler slopes above these escarpments (Figure 3-2a). On the escarpments themselves, the amount and style of erosion varies along their lengths. Landslides have removed material from the gentler slope above the Florida Escarpment as well, but this process apparently has acted on different parts of the West Florida Slope at different times. No information could be found on the processes acting on the slope above the Campeche Escarpment.

The presence of reef structures under the northern part of the Florida Escarpment suggests this part of the cliff has undergone little erosion since it originally formed during the Cretaceous (Locker and Buffler, 1984; Corso *et al.*, 1989; Twichell *et al.*, 1990). In fact, sidescan sonar imagery suggest that the only erosion along this section of the escarpment is the removal of a thin veneer of younger sediment that has accumulated as thin turbidity current or debris flow deposits at the foot of the escarpment (Figure 3-2b).

The carbonate platform edge that is exposed along the southern part of the Florida Escarpment and the Campeche Escarpment has been eroded since its initial formation and lagoonal facies are now exposed on the cliff face (Freeman-Lynde, 1983; Paull *et al.*, 1990b). The present morphology of these sections of the escarpments is quite different from the northern part of the Florida Escarpment (Figure 3-2a). Here canyons with steep sides and near-vertical headwalls, called box canyons (Paull *et al.*, 1991), incise these parts of the escarpments. These box canyons may be the result of dissolution of the limestone by discharge of acidic groundwater at the base of the escarpment in the canyon heads that resulted in collapse of the steep canyon headwalls (Paull *et al.*, 1990a). A large talus deposit has been identified in seismic profiles along the base of the Campeche Escarpment that was deposited prior to the mid-Cretaceous (Schlager *et al.*, 1984; Locker and Buffler, 1984). The full extent of this deposit is unknown because of limited seismic coverage. Breccia recovered from a DSDP hole near the base of the Campeche Escarpment (Schlager *et al.*, 1984; Halley *et al.*, 1984) presumably is the result of topples and falls from the escarpment face. The amount of material associated with an individual failure is unknown. Talus blocks up to 5-m across and rubble have been observed on the seafloor along the base of the southern part of the Florida Escarpment which suggests this cliff has recently undergone erosion (Paull *et al.*, 1990a; Twichell

et al., 1990). The talus deposits in the heads of some of the box canyons cover areas less than 15 km^2, and their thickness is unknown. Published information suggests that the recent falls and topples were limited to the southern part of the Florida Escarpment and perhaps the Campeche Escarpment (Twichell *et al.*, 1996), but those that have been mapped are of limited aerial extent and are concentrated in the heads of box canyons (Figure 3-2b).

Landslides on the West Florida Slope above the Florida Escarpment are sourced in Tertiary and Quaternary carbonate deposits. Mullins *et al.* (1986) mapped large collapse scars along the central part of the West Florida Slope near the latitude of Tampa, FL (Figure 3-2b). The entire slide scar is 120 km long, 30 km wide, and has 300-350 m relief. While the total volume of material removed is around 1,000 km^3, there were at least 3 generations of failures with most of the sediment removal occurring prior to the middle Miocene. Presently these landslide scarps are buried and only local episodic failures have subsequently occurred along this section of the slope (Doyle and Holmes, 1985). Along the southern part of the West Florida Slope, Doyle and Holmes (1985) and Twichell *et al.* (1993) have mapped another extensive area of the slope that has undergone collapse (Figure 3-2b). Here the scarps are still exposed on the seafloor and have 50-150 m relief and are 10-70 km in length. Some of the mass-movement deposits are on the slope above the Florida Escarpment, but it is unknown how much of the failed material was transported farther and deposited at the base of the Florida Escarpment. The cross-cutting of the headwall scarps indicates that these landslides are composed of several smaller failure events (Twichell *et al.*, 1993). The age of these failures is not known, but Mullins *et al.* (1986) and Doyle and Holmes (1985) suggest periods of increased mass wasting which are probably associated with periods of higher sedimentation rates. If this is the case, then the landslides along the southern part of the West Florida Slope are most likely early Holocene or older in age (Doyle and Holmes, 1985).

Salt province

No published information has been found on landslides in the salt province in the Bay of Campeche, so this discussion will focus on the northern Gulf of Mexico slope where good information is available on landslides. Presumably the northern Gulf is an appropriate analogue for the Bay of Campeche area (Figure 3-1a). Detailed bathymetric mapping of the salt province in the northern Gulf of Mexico shows that it has a unique morphology characterized by relatively small sub-circular basins that are 3-33 km long and have areas of 5-312 km^2 (Figure 3-3). These basins are bordered by narrow salt-cored ridges that stand 50-521 m above the basin floors (Pratson and Ryan, 1994).

Landslide deposits have been mapped in several of the mini-basins using GLORIA imagery (Rothwell *et al.*, 1991; Twichell *et al.*, 2000; Twichell *et al.*, 2005) as well as with high-resolution sidescan sonar, high resolution seismic profiles, and cores (Behrens, 1988; Lee and George, 2004; Orange *et al.*, 2003;

2004; Sager *et al.*, 2004, Silva *et al.*, 2004; Tripsanas *et al.*, 2004a; 2004b). The GLORIA imagery provides a regional perspective on the size and distribution of landslides, while the detailed studies provide more information on the types of failures. The GLORIA imagery identified 37 landslides in the salt province and along the base of the Sigsbee Escarpment (Figure 3-3a). The largest of these failures occurs in the northwestern Gulf of Mexico, is 114 km long, 53 km wide, covers about 2,250 km^2, and has been interpreted to consist of at least two debris flows (Rothwell *et al.*, 1991; McGregor *et al.*, 1993). This landslide lies offshore of the Rio Grande River system and Rothwell *et al.* (1991) suggest it is the result of failure of the shelf edge delta that formed off this river during the last lowstand of sea level.

The remaining landslides within the salt province are considerably smaller and cover areas ranging from 4-273 km^2 (Figure 3-3b). Most have sources on the walls of the mini-basins or on the Sigsbee Escarpment. The detailed studies indicate a wide variety of landslide types that include translational slides, rotational slides, debris flows, and creep movements (Lee and George, 2004; Orange *et al.*, 2004; Silva *et al.*, 2004). It has been suggested that triggering mechanisms for these landslides include shallow stratigraphic layers with overpressured pore waters (Orange *et al.*, 2003), salt movement (Lee and George, 2004; Tripsanas *et al.*, 2004a), oversteepening of shelf edge deltas (Tripsanas *et al.*, 2004b), and possibly gas hydrates (Twichell and Cooper, 2000).

Information is limited on the age of landslides in the salt province. The most extensive study (Tripsanas *et al.*, 2004a; b) indicates that most of the youngest landslides sampled in the salt province occurred during oxygen isotope stages 2, 3, and 4 (18,170-71,000 yr BP) when salt movement due to sediment loading was most active. One unpublished age date of a sample below a thin landslide deposit (<3 m thick) indicates that it is younger than 6,360 yr BP (H. Nelson, personal communication). Localized failure of mini-basin walls may continue to be active, but available data suggests these small failures were more prevalent during the last lowstand of sea level.

Canyon/fan province

Three canyon/fan systems formed during the Quaternary period; the Bryant, Mississippi, and Eastern Mississippi systems (Figure 3-1a). Of these three systems, the Mississippi is the largest and youngest (Weimer, 1989). During the latest Pleistocene, sediment was supplied to the Mississippi Fan from a point source, the Mississippi Canyon (Bryant *et al*, 1991). Regional seismic stratigraphic analysis has been used to divide the Mississippi Fan into 17 seismic sequences (Weimer, 1989): most contain a basal chaotic unit inferred to be mass-transport deposits. The mass-transport deposits are overlain by channel-levee complexes, which are capped by a thin interval of hemipelagic sediment that represents a period of limited sediment input. Depositional style within each sequence has been attributed to changes in sea level: the mass-transport complexes were deposited during falling sea level and the initial part of the lowstand; the channel-levee complexes formed during the lowstand and the onset of the transgression; and condensed sections were

deposited during highstands (Weimer, 1989). According to this interpretation, the Holocene should have been a period of quiescence.

However, studies of the Mississippi Canyon and present surface of the Mississippi Fan indicate a different stratigraphic progression (Twichell *et al.*, 1990; Twichell *et al.*, in press) and reveal evidence of landslides at several scales. Turbidity current deposits and thin debris flow deposits associated with channel-levee development have been mapped and sampled on the distal fan (Twichell *et al.*, 1990; Twichell *et al.*, 1992; Nelson *et al.*, 1992; Schwab *et al.*, 1996). Some of these deposits have been mapped with sidescan sonar and cores and are relatively small: covering areas less than 331 km^2, and having volumes less than 1 km^3 (Twichell *et al.*, in press). At the other extreme is a large landslide complex that covers approximately 23,000 km^2 of the middle and upper fan (Figure 3-4) and reaches 100 m in thickness (Walker and Massingill, 1970; Normark *et al.*, 1986; Twichell *et a*l., 1992). The total volume of this deposit cannot be accurately estimated because of inadequate seismic coverage. Seismic profiles and GLORIA imagery suggest that this feature consists of at least two separate events (Twichell *et al.*, in press). The Mississippi Canyon appears to have the source area for these landslide deposits (Walker and Massingill, 1970; Coleman *et al.*, 1983; Goodwin and Prior, 1989; Lowrie *et al.*, 2004). Borings and seismic data from the head of Mississippi Canyon (Goodwin and Prior, 1989) indicate that there were alternating episodes of canyon filling and excavation between 19,000 and 7,500 yr BP, and Coleman *et al.* (1983) estimate total volume of sediment removed was approximately 8,600 km^3. One DSDP hole through this landslide deposit penetrated thick sections of tilted beds (Normark *et al.*, 1986). This information in conjunction with the GLORIA imagery which shows a swirling pattern on the surface of the youngest part of this failure suggests it may be a translational slide that has undergone deformation but not complete disintegration as it moved (Figure 3-4).

The timing of these landslides needs to be refined to determine whether they are associated with glacial meltwater floods that discharged into the Gulf of Mexico (Laventer *et al.*, 1982; Marchitto and Wei, 1995, Aharon, 2003), or whether they occurred more recently. Available age dates indicate that this large landslide complex is younger than 11,100 yr BP, when turbidity current and debris flow transport to the distal fan ceased due to the channel being blocked by part of this landslide (Schwab *et al.*, 1996; Twichell *et al.*, in press). This large landslide is older than 7,500 yr BP, when hemipelagic sedimentation resumed in Mississippi Canyon and covered the headwall scarps of the failures (Prior *et al.*, 1989). Meltwater discharge to the Gulf of Mexico ceased about 9,000 yr BP (Marchitto and Wei, 1995; Aharon, 2003). Refining the timing of these large landslides is needed to determine if they are associated with meltwater floods or are younger than the floods and formed under conditions similar to the present.

The Bryant and Eastern Mississippi Fans may both have canyon head failures associated with them as well. The Bryant Canyon system was immediately downslope of a shelf edge delta system (Morton and Sutter, 1996), and failure of this system has been proposed as the explanation for thick chaotic deposits in mini basins along the path of this canyon system

(Lee *et al.*, 1996; Prather *et al.*, 1998; Twichell *et al.*, 2000; Tripsanas *et al.*, 2004a). Debris from the failure of the shelf edge delta was transported down the Bryant Canyon system (Lee *et al.*, 1996; Prather *et al.*, 1998), but these landslide deposits predate and are buried by the smaller landslides off the mini-basin walls that are shown in Figure 3-3 (Twichell *et al.*, 2000).

The Eastern Mississippi Fan system also has a relatively large landslide that partially buries the fan channel that supplied this fan (Figure 3-4). This landslide deposit is approximately 154 km long, as much as 22 km wide, and covers an area of 2,410 km^2. The volume of the deposit and its age are unknown.

Summary

Landslides occur in all three provinces (carbonate, salt, and canyon/fan) in the Gulf of Mexico. The largest failures are found in the canyon/fan province. More information is needed on the timing of the large failures that filled the Bryant Canyon and covered the upper parts of the Mississippi and Eastern Mississippi Fans (Figure 3-5). The resumption of hemipelagic sedimentation in the head of Mississippi Canyon by 7,500 yr BP (Goodwin and Prior, 1988) indicates that at least the largest of these landslide complexes had ceased being active by mid-Holocene time. Further age dating is needed to refine the timing of the landslides derived from the Mississippi Canyon area to determine if they are associated with meltwater floods discharged into the Gulf of Mexico during the early part of the Holocene or whether they were triggered by other processes at a later time.

Preliminary Mapping and Analysis of Three Potential Landslide-generated Tsunamigenic Sources

Potential tsunami sources for the Gulf of Mexico are submarine landslides within the Gulf of Mexico and earthquakes along Caribbean plate boundary faults. Subaerial landslides, volcanogenic sources, and near-field intraplate earthquakes are unlikely to be the causative tsunami generator for damaging tsunamis in the Gulf of Mexico region. We focus initially on submarine landslide sources. Offshore tsunami amplitudes from Carribbean earthquakes are estimated in Chapter 8 of this volume, and can be used in comparison to tsunami amplitudes determined for submarine landslides in establishing the potential maximum tsunami.

Submarine landslides in the Gulf of Mexico are considered a potential tsunami hazard for two reasons: (1) some dated landslides in the Gulf of Mexico have post-glacial ages (Coleman *et al.*, 1983) and (2) recent suggestions from seismic records of small-scale energetic landslides in the Gulf of Mexico.

With regard to (1), the Mississippi Canyon landslide dated 7,500-11,000 years before present (ybp) (Coleman *et al.*, 1983; this chapter) and the East Breaks landslide dated 15,900 ± 500 ybp (Piper and Behrens, 2003), these are among the largest landslides in the Gulf of Mexico. Although landslide

activity along the passive margins of North America may be decreasing with time since the last glacial period, the 1929 Grand Banks landslide is a historic example of such an event that produced a destructive tsunami (Fine *et al.*, 2005). In addition, the Mississippi River continues to dump large quantities of water-saturated sediments on the continental shelf and slope, making them vulnerable to over-pressurization and slope failure

With regard to (2), seismic recordings of the Green Canyon event that occurred on February 10, 2006 offshore southern Louisiana, Dewey and Dellinger, (2008) suggest that energetic landslides continue to occur in the Gulf of Mexico. Although most landslides affected by salt tectonics are small in size (*e.g.*, in comparison to the East Breaks landslide; this chapter) and unlikely to be tsunamigenic, because the 2006 event generated seismic energy, it had to have occurred rapidly. This event is evidence for present-day slope instability. Shown below is the multibeam bathymetry near the Green Canyon event and 3 seismograms and accompanying spectrograms: the first for a typical earthquake, the second for a known landslide in SE Alaska, and the third for the 2006 Gulf of Mexico event (P. Whitmore, personal communication).

Maximum Credible Submarine Landslides

We define 4 geological provinces in the Gulf of Mexico that are likely to be the origin of submarine landslides. Three additional provinces defined in this chapter are not likely to be sites of major tsunamigenic landslides. The four provinces defined for the analysis are the Northwest Gulf of Mexico, Mississippi Canyon, Florida Escarpment, and Campeche Escarpment. The first two are canyon/fan provinces involving failure of terrigenous and hemipelagic sediment, whereas the third and fourth are carbonate provinces formed from reef structures and characterized by having steep slopes (*i.e.*, escarpments). The U.S. south coast would be affected primarily be the back-going tsunami emanating from the Northwest Gulf of Mexico (East Breaks) and Mississippi Canyon landslides, and would be affected primarily by the outgoing tsunami from a landslide sourced from above the Campeche or Florida Escarpments. For the latter tsunami, there is a significant directivity effect that scales with the speed of downslope motion of the landslide (up to the phase speed of the tsunami). The characteristics and the parameters that define the maximum credible landslide are given below for the East Breaks Landslide in the Northwest Gulf of Mexico and the Mississippi Canyon and Florida Escarpment provinces.

Landslide volume calculations were based on measuring the volume of material removed from the landslide source area using a technique similar to that applied by ten Brink *et al.* (2006). Briefly stated, the approach involves using the multibeam bathymetry to outline the extent of the source area, interpolating a smooth surface through the polygons that define the edges of the slide to provide an estimate of the pre-slide slope surface, and subtracting this surface from the present seafloor surface. These calculations were only completed for part of the East Breaks landslide, the Mississippi Canyon

landslide, and a Florida Escarpment landslide. No calculations were made for failures above the Campeche Escarpment because available bathymetric data is inadequate. In the case of the East Breaks landslide, the source area may be somewhat larger, but multibeam bathymetry is not available for the entire source area.

East Breaks landslide

Geologic Setting: River delta
Post Failure Sedimentation: Canyon appears to be partially filled (predominantly failure deposits with some post-failure sedimentation)
Age: 10,000 – 25,000 years (Piper, 1997)
Maximum Credible Single Event (East Breaks landslide):
Max
Volume: 21.95 km^3
Area: 519.52 km^2
Min
Volume: 20.80 km^3
Area: 420.98 km^2
Other Reported Volumes: 50-60 km^3 (Trabant *et al.*, 2001)
Excavation depth: ~160 m (shelf to base of headwall scarp)
Run out distance: 91 km from end of excavation and 130 km from headwall based on GLORIA mapping (Rothwell *et al.*, 1991) (See Figure 11).
Other reported run-out distance: 160 km (Trabant *et al.*, 2001)

Mississippi Canyon

Geologic Setting: River delta and fan system
Post Failure Sedimentation: Canyon appears to be partially filled (failure deposits or post-failure sedimentation)
Age: 7,500 to 11,000 years (Coleman *et al.*, 1983; this chapter)
Maximum Credible Single Event:
Volume: 425.54 km^3
Other reported volumes – 1750 km^3 (this chapter); 1500-2000 km^3 (Coleman *et al.*, 1983)
Area: 3687.26 km^2
Excavation depth: ~300 m (in the upper canyon)
Runout distance: 297 km from toe of excavation area and 442 km from the headwall scarp (see Figure 13).

Florida Escarpment

Geologic Setting: Edge of a carbonate platform
Post Failure Sedimentation: None visible on multibeam images or on available high-resolution seismic profiles (Twichell *et al.*, 1993).
Age: Early Holocene or older (Doyle and Holmes, 1985)

Maximum Credible Single Event:

Volume: 16.2 km^3

Area: 647.57 km^2

Excavation depth: ~150 m, but quite variable

Runout distance: Uncertain. The landslide deposit is at the base of the Florida Escarpment buried under younger Mississippi Fan deposits.

Campeche Escarpment

Geologic Setting: Carbonate platform

One of the persistent issues during the independent confirmatory analysis is acquiring sufficient geologic information about the Campeche Escarpment with which to estimate the maximum credible landslide parameters as with the other Gulf of Mexico provinces. Plans to conduct multibeam bathymetry surveys have been funded outside this task order and are pending State Department approval. Presently, there is no published information showing the detailed bathymetry, nor distribution of landslides on or above the Campeche Escarpment.

Mobility Analysis

We have conducted a preliminary mobility analysis of the East Breaks landslide to determine the time scale of landslide dynamics as input into the tsunami generation and propagation model (COULWAVE). We use the method set forth by Locat, *et al.* (2004) for the Palos Verdes debris avalanche offshore southern California and in Chapter 8 of this volume for the Currituck landslide offshore North Carolina.

Submarine landslide mobility is modeled using a bilinear rheology that combines characteristics of Newtonian and Bingham viscoplastic behaviors. The rheology is parameterized by an apparent yield strength (τ_{ya}), a reference strain rate

$$\gamma_r = \frac{\tau_{ya}}{\mu_{dh}} \qquad (1)$$

where μ_{dh} is the plastic viscosity, and the ratio of strain rates

$$r = \frac{\gamma_r}{\gamma_o} \qquad (2)$$

where γ_o is the shear strain rate at the transition from Newtonian to Bingham behavior. The apparent yield strength is estimated using the following equation (Johnson, 1984):

$$\tau_{ya} = H_f \gamma' \sin\beta_f \quad (3)$$

where H_f is the final flow thickness, γ' is the buoyant unit weight (kN/m^3), and β_f is the slope angle where the debris flow comes to rest. A reference strain rate of 1000 is used according to the estimate for clayey sediment by Jeong *et al.* (2007). As in the previous studies, we use the program BING (Imran *et al.*, 2001) to carry out the numerical computations of landslide dynamics in 1D.

Using a seafloor profile along the flank of the East Breaks landslide (*i.e.*, pre-slide conditions), we preliminarily estimate that $\tau_{ya} = 3000$ Pa based on the runout distance and final flow thickness. This estimate is slightly smaller than that for the Palos Verdes debris avalanche (5000 Pa) and slightly larger than for the Currituck landslide (2000 Pa). The ratio of strain rates (r) is determined from a best fit to the runout length. Figure 15 below shows the initial parabolic thickness profile and thickness profile 30 minutes after failure.

In the region of excavation, the duration of vertical movement (defined as the time to reach a 90% reduction in thickness) is approximately 10 minutes. In the region of deposition, the duration of vertical movement is approximately 22 minutes. The phenomenon of hydroplaning during failure (De Blasio *et al.*, 2004; Elverhøi *et al.*, 2005) may increase the mobility of debris flows and result in shorter durations that estimated here. For comparison, a conservative value of 7.2 minutes was used for duration in modeling the Currituck landslide tsunami (Chapter 9 in this volume)

This modeling will be further refined during the independent confirmatory analysis and performed for the other landslide provinces in the Gulf of Mexico.

Interim Findings

In summary, we list the following interim findings of the independent confirmatory analysis below:

- There is sufficient evidence to consider submarine landslides in the Gulf of Mexico as a present-day tsunami hazard.
- Four geologic landslide provinces are defined in the Gulf of Mexico: Northwest Gulf of Mexico, Mississippi Canyon, Florida Escarpment, and Campeche Escarpment.
- Parameters for the maximum credible submarine landslide were determined for each of the provinces, except for the Campeche Escarpment where we are awaiting additional data.
- Our estimate for the volume of the East Breaks landslide is smaller than that estimated by Trabant *et al.* (2001).

- Mobility analysis suggests that constitutive parameters of the East Breaks landslide are similar to the parameters for other landslides that have recently been analyzed (Palos Verdes and Currituck)

Future Directions

The Gulf of Mexico is one of the most intensely studied ocean basins because of the energy resources it contains, but information for understanding the timing, style, and distribution of landslides is still incomplete. Little published information could be found on landslides along the Mexican margin, and this region needs to be addressed. In addition to the Mexican Margin, other sections of the margin surrounding this ocean basin have not been surveyed with multibeam techniques. Published multibeam bathymetry is not available for the northern part of the Florida Escarpment, the West Florida Slope, or the slope in the northwestern corner of the Gulf of Mexico. Acquisition of this bathymetric data set would improve our understanding of recent landslide source areas and triggering mechanisms.

Figures

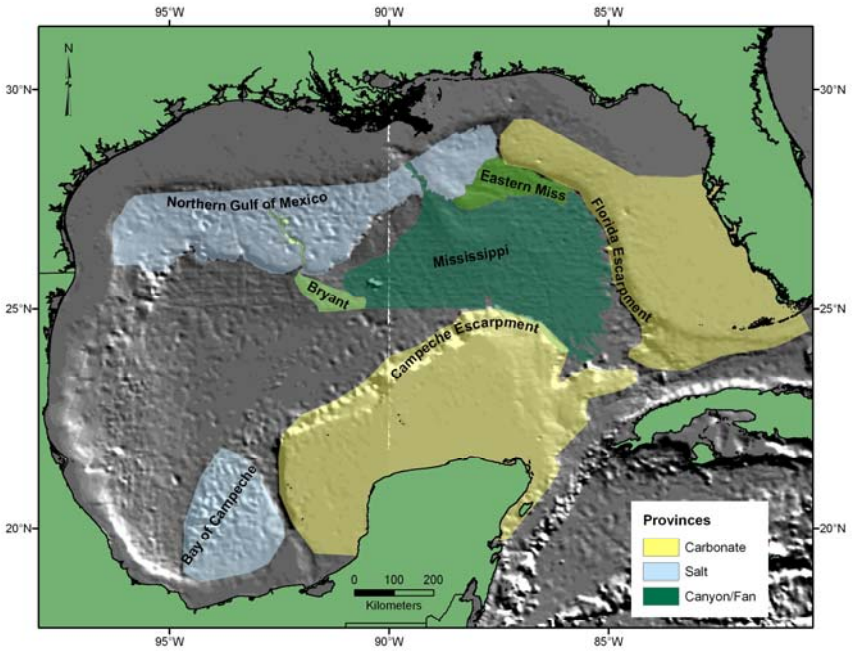

Figure 3-1a: Location map showing the extent of the carbonate, salt, and canyon/fan provinces in the Gulf of Mexico basin. The Bryant, Mississippi, and Eastern Mississippi Fans are the three youngest fans in the Gulf of Mexico, and, of these, the Mississippi is youngest.

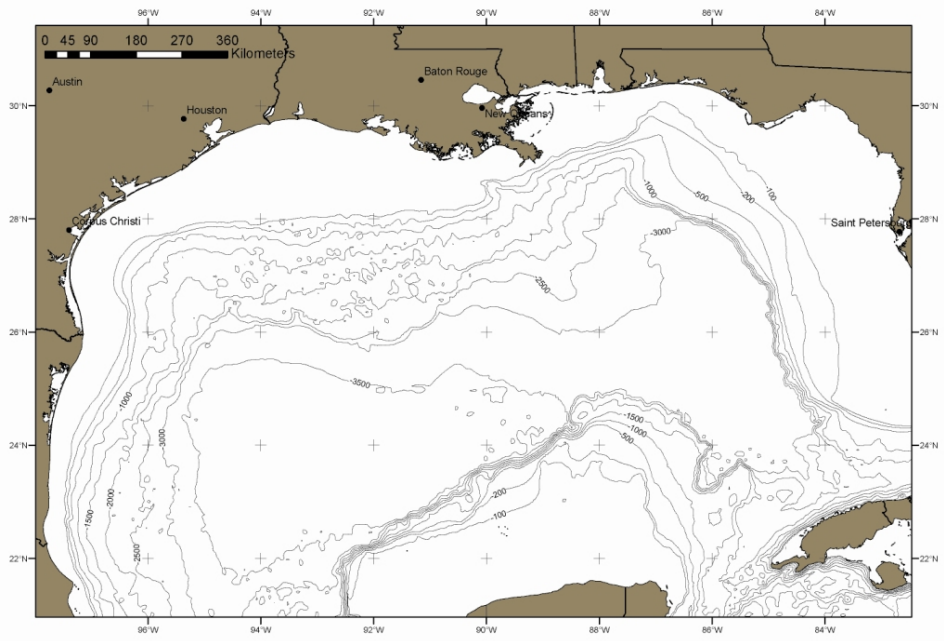

Figure 3-1b: Bathymetric map of the Gulf of Mexico.

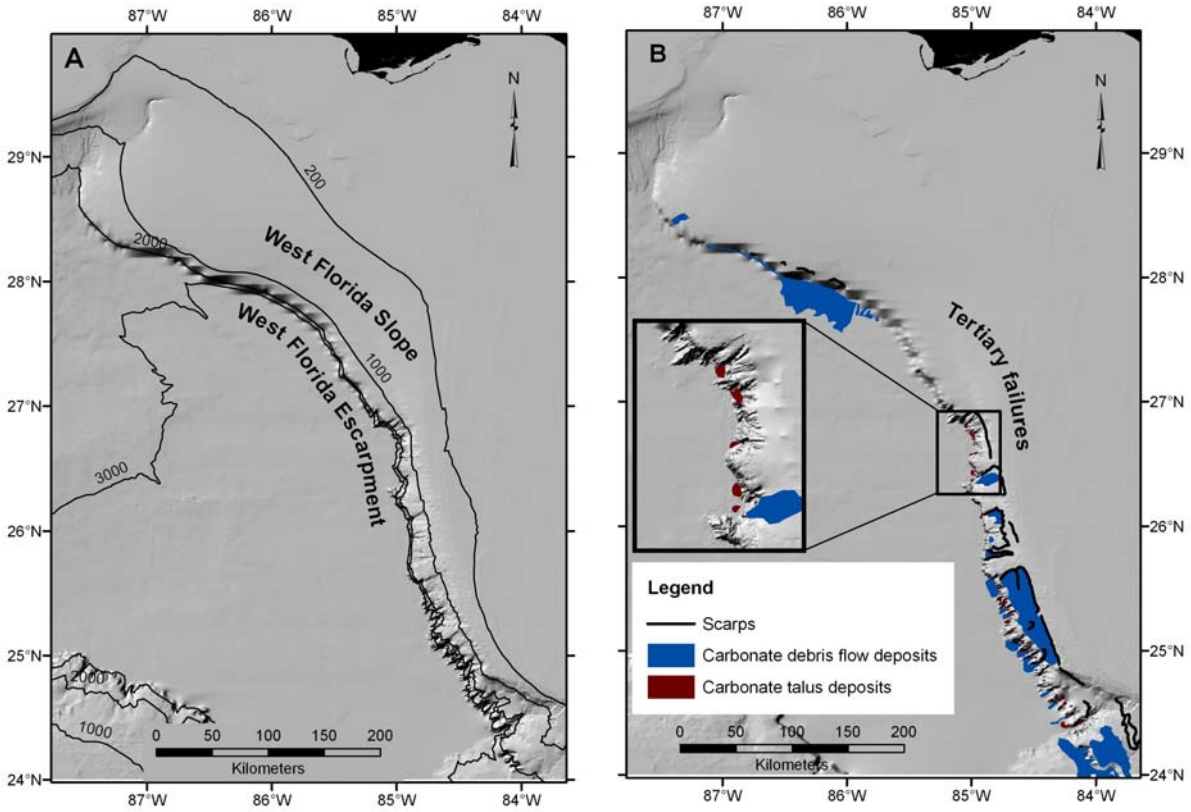

Figure 3-2: (A) Morphology of the West Florida Escarpment and the West Florida Slope, and (B) the extent and distribution of carbonate debris flow deposits and talus deposits derived from this part of the carbonate province. "Tertiary failures" marks the general location of older landslides mapped by Mullins *et al.* (1986) that now have been completely buried. Inset box shows a detailed view of some of the carbonate talus deposits. Equivalent information is not available for the slope above the Campeche Escarpment.

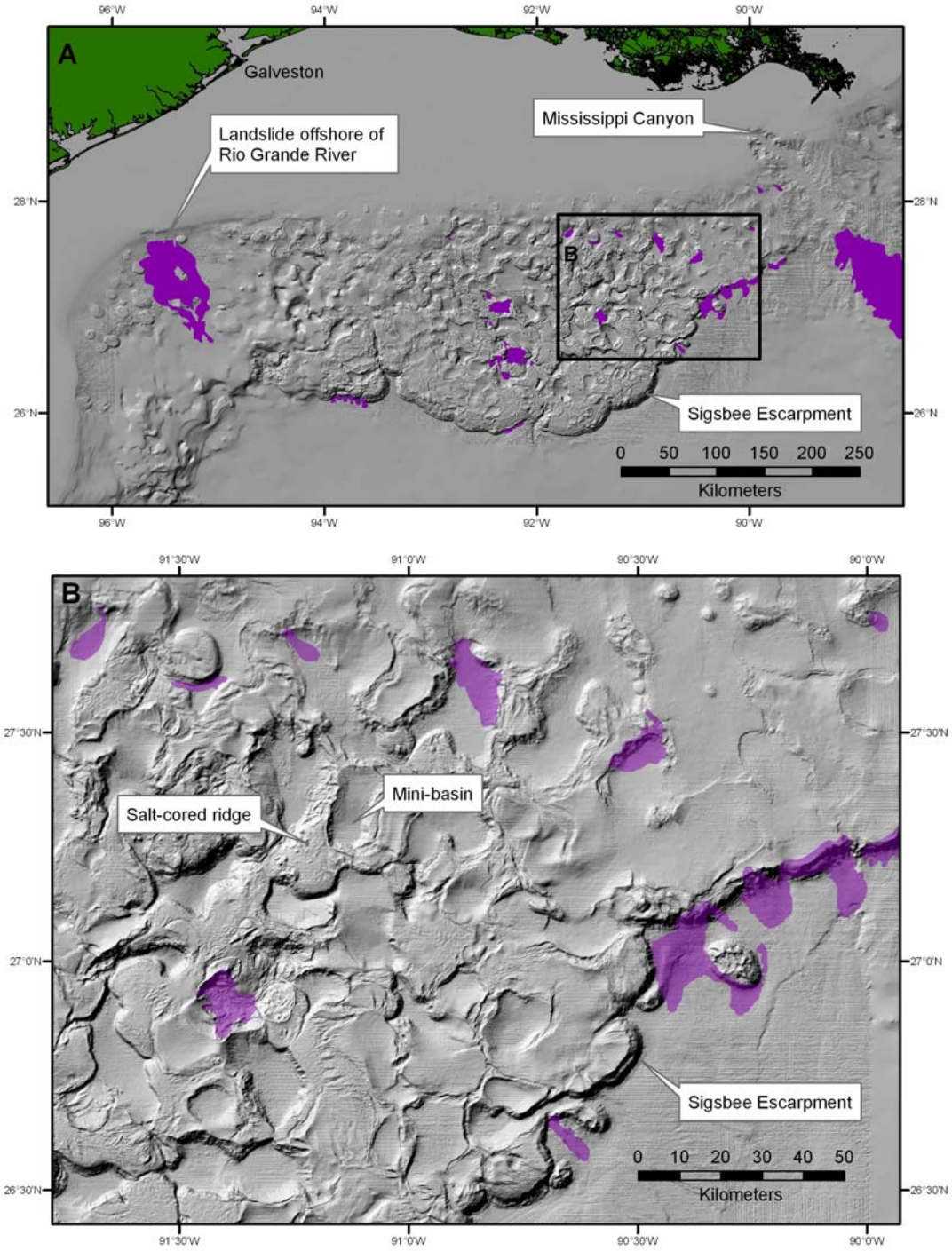

Figure 3-3: (A) Shaded relief image of a large part of the northern Gulf of Mexico salt deformation province west of Mississippi Canyon showing the irregular morphology of this continental slope and the distribution of landslides (purple areas), and (B) an enlarged view of part of this region showing the relation of landslides (purple areas) to the mini basins and the Sigsbee Escarpment.

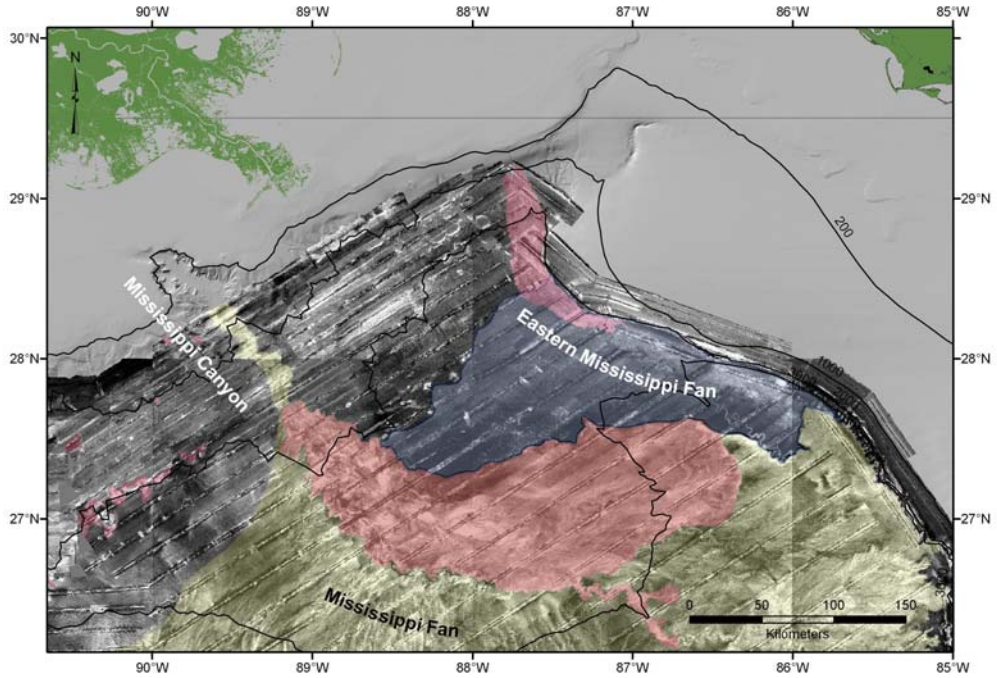

Figure 3-4: GLORIA sidescan sonar imagery showing part of the Mississippi Fan (yellow) and Eastern Mississippi Fan (blue) and two large landslide areas (red) that spread across the upper parts of these two fans. The landslide on the upper Mississippi Fan was sourced from the Mississippi Canyon region (Coleman *et al.*, 1983) and is the largest Quaternary landslide found in the Gulf of Mexico.

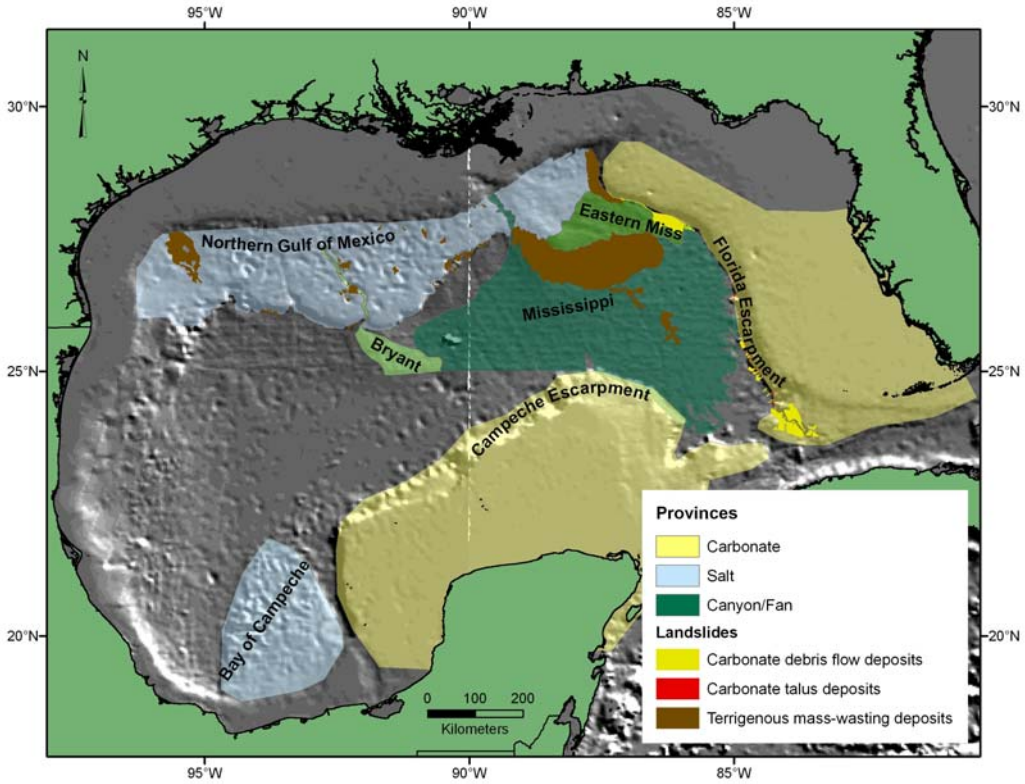

Figure 3-5: Summary map showing the size, distribution, and composition of landslides in the three provinces. Carbonate talus deposits are too small to show at this scale.

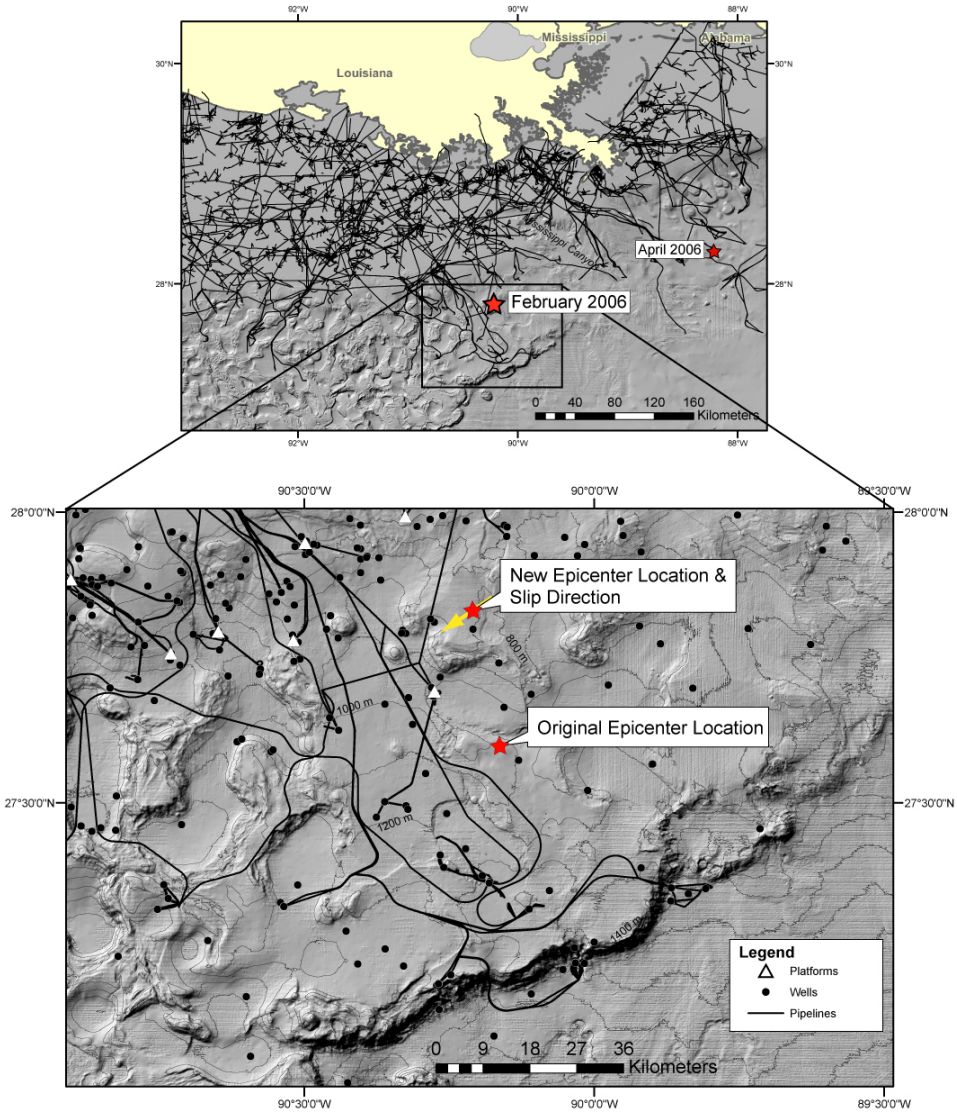

Figure 3-6: Multibeam bathymetry near the February 10, 2006 Green Canyon event in the Gulf of Mexico that was seismically recorded.

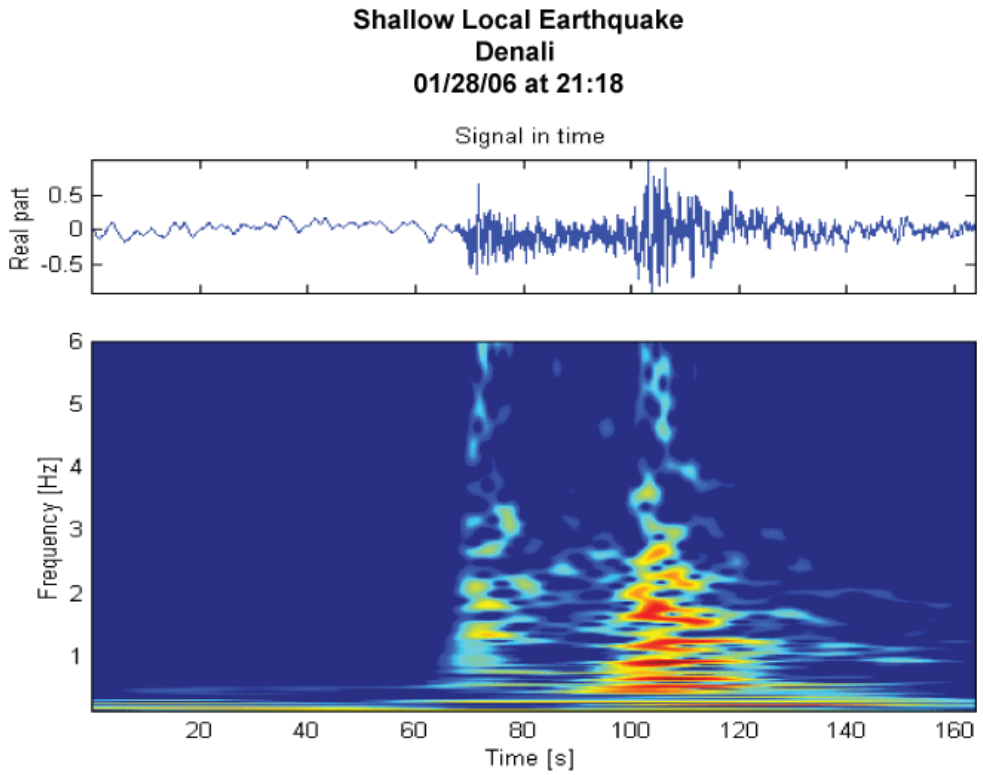

Figure 3-7: Seismogram (top) and spectrogram of a typical shallow earthquake (M 3.9 January 27, 2006 Denali earthquake)

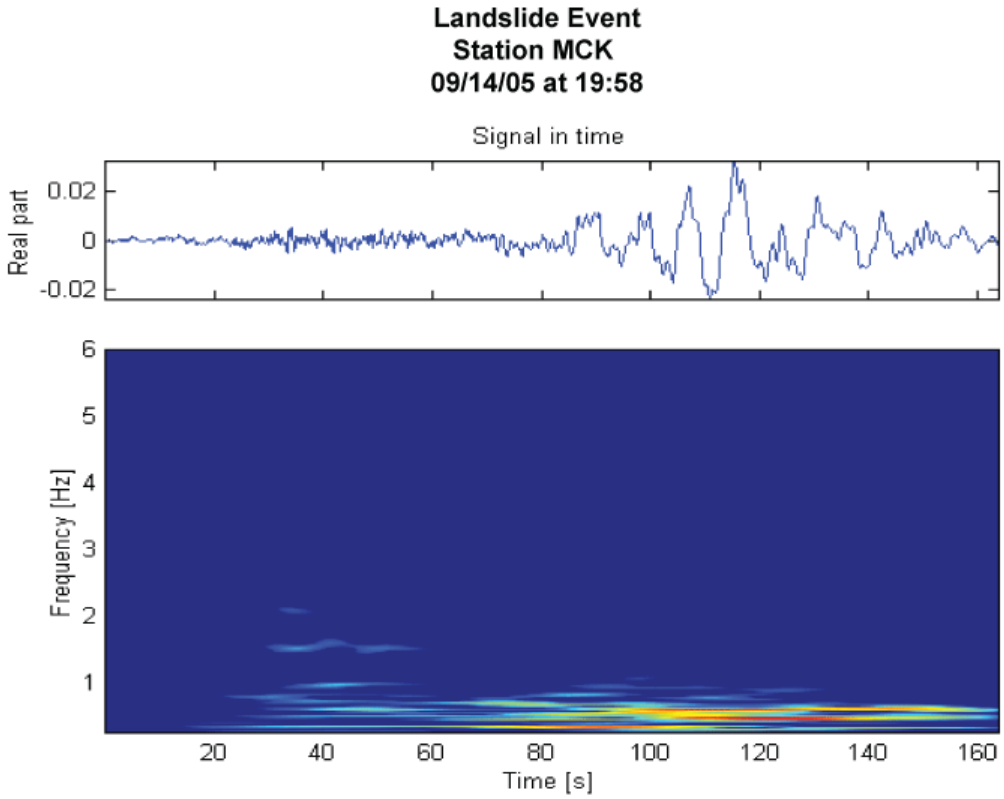

Figure 3-8: Seismogram (top) and spectrogram of a known subaerial landslide in SE Alaska. MCK: McKinley Park seismic station.

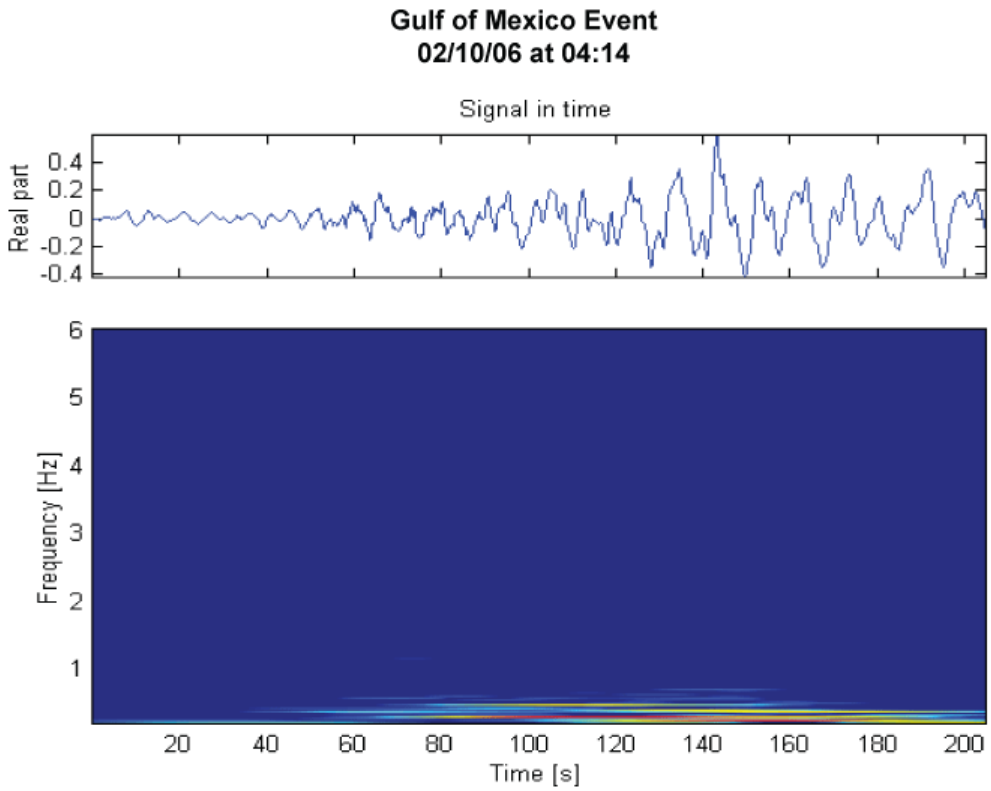

Figure 3-9: Seismogram (top) and spectrogram of the February 10, 2006 Gulf of Mexico Green Canyon event (see Figure 3-6 for location). Note the similarity with Figure 3-8 (landslide) and the dissimilarity with Figure 3-7 (earthquake).

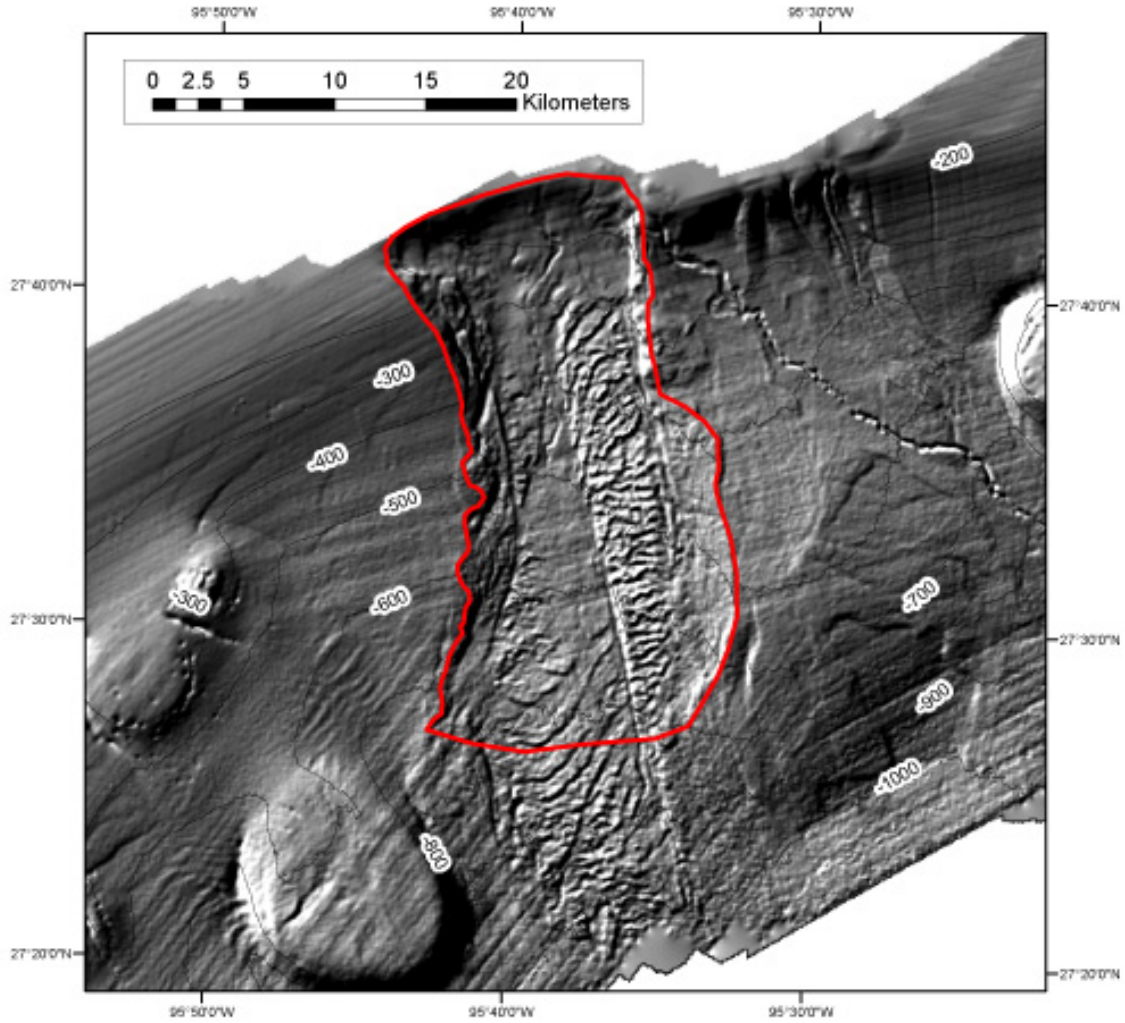

Figure 3-10: Outline (red) of excavation area for the East Breaks landslide based on available multibeam bathymetric data.

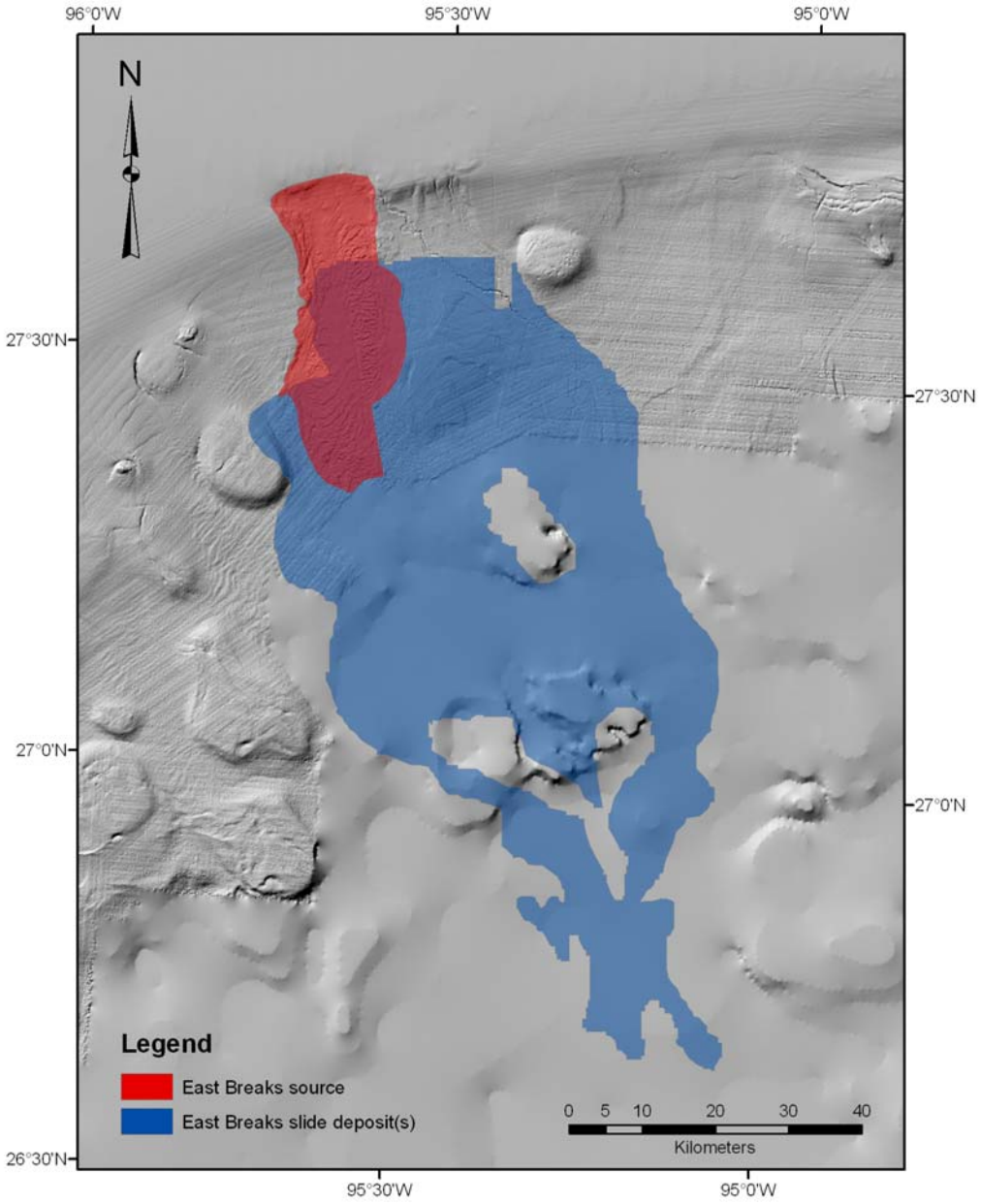

Figure 3-11: Comparison of excavation area (red) and depositional area (blue) for the East Breaks landslide. The extent of the landslide deposit was mapped using GLORIA sidescan sonar imagery (Rothwell *et al.*, 1991).

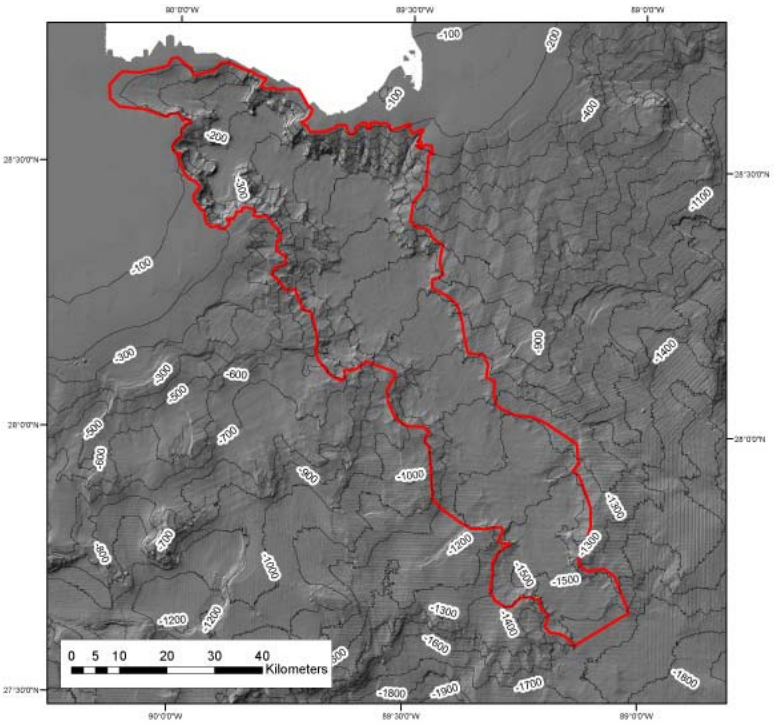

Figure 3-12: Outline (red) of excavation area for the Mississippi Canyon landslide based on multibeam bathymetric data and reports by Coleman and others (1983) and Goodwin and Prior (1989).

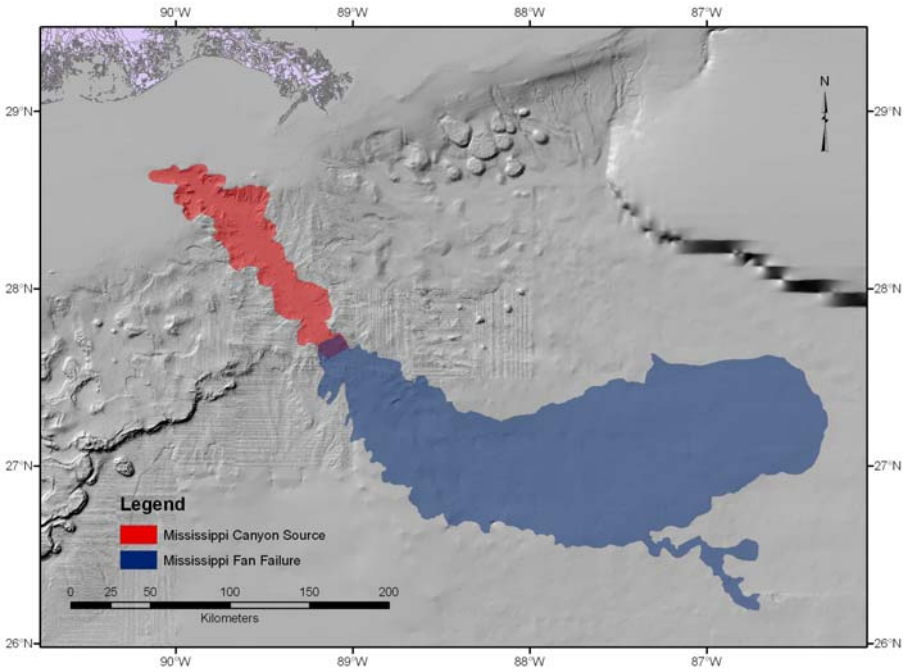

Figure 3-13: Comparison of excavation area (red) and depositional area (blue) for the Mississippi Canyon landslide. The extent of the landslide deposit is based on GLORIA sidescan sonar imagery (Twichell *et al.*, 1991).

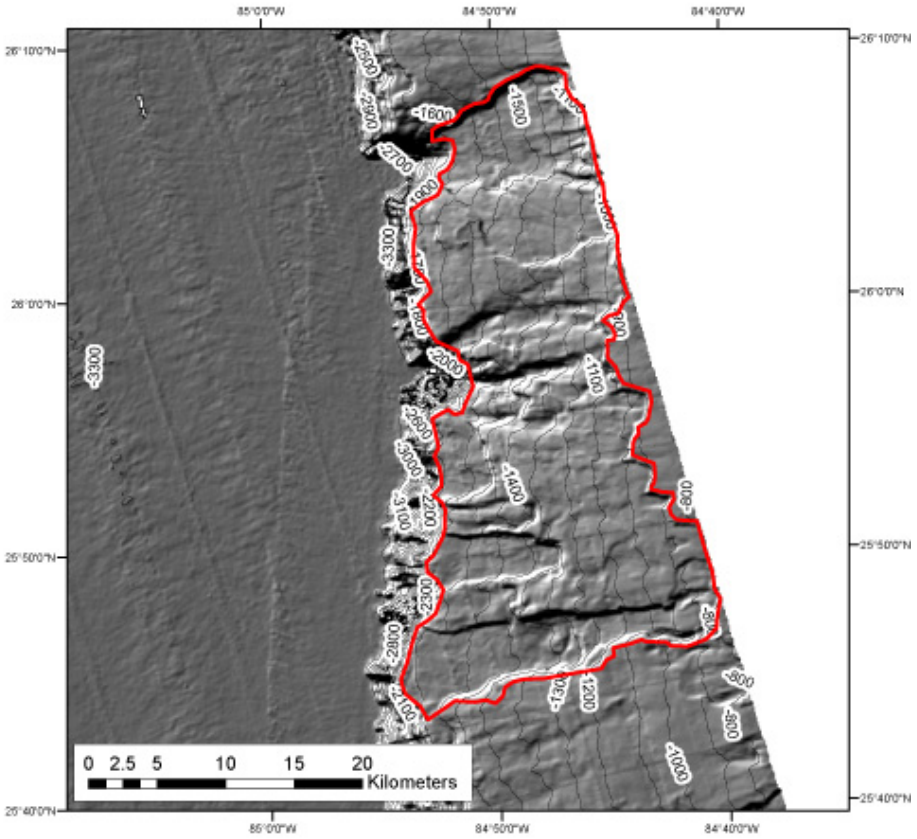

Figure 3-14: Outline (red) of excavation area for the maximum credible landslide above the Florida Escarpment from multibeam bathymetric data.

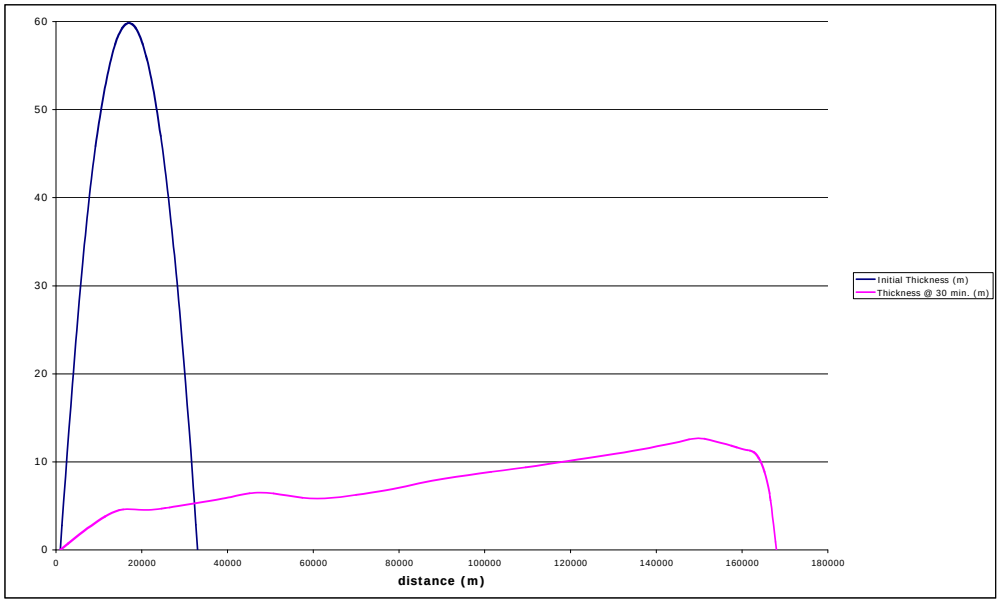

Figure 3-15: The initial parabolic thickness profile and thickness profile 30 minutes after failure**.**

References

Aharon, P., 2003, Meltwater flooding events in the Gulf of Mexico revisited: Implications for rapid climate changes during the last deglaciation: *Paleoceanography, v. 18*, 1079, doi: 10.1029/2002PA000840.

Behrens, W.E., 1988, Geology of a continental slope oil seep, northern Gulf of Mexico: *American Association of Petroleum Geologists Bulletin, v. 72*, p. 105-114.

Bryant, W.R., Meyerhoff, A.A., Brown, N.K., Furrer, M.A., Pyle, T.E., and Antoine, J.W., 1969, Escarpments, reef trends, and diapiric structures, eastern Gulf of Mexico: *American Association of Petroleum Geologists Bulletin, v. 53*, p. 2506-2542.

Bryant, W.R., Lugo, J., Cordova, C., and Slavador, A., 1991, Physiography and bathymetry, *in* Salvador, A. (Editor), The Geology of North America, Vol. J, Gulf of Mexico Basin: Geological Society of America, Boulder, CO, p. 13-30.

Buffler, R.T., 1991, Seismic stratigraphy of the deep Gulf of Mexico basin and adjacent margins, *in* Salvador, A. (Editor), The Geology of North America, Vol. J, Gulf of Mexico Basin: Geological Society of America, Boulder, CO, p. 353-387.

Coleman, J.M., Prior, D.B., and Lindsay, J.F., 1983, Deltaic influences on shelf edge instability processes, *in* Stanley, D.J., and Moore, G.T. (Editors), The shelfbreak: Critical interface on continental margins: Society of Economic Paleontologists and Mineralogists Special Publication 33, p. 121-137.

Corso, W., Austin, J.A., and Buffler, R.T., 1989, The early Cretaceous platform off northwest Florida: Controls on morphologic development of carbonate margins: *Marine Geology, v. 86*, p. 1-14.

De Blasio, F.V., Ilstad, T., Elverhøi, A., Issler, D., and Harbitz, C., 2004, High mobility of subaqueous debris flows and the lubricating-layer model, in 2004 Offshore Technology Conference, Houston, TX, p. OTC 16747.

Dewey, J.W., and Dellinger, J.A., 2008, Location of the Green Canyon (offshore southern Louisiana) seismic event of February 10, 2006: U.S. Geological Survey, Open-File Report 2008-1184, 30 pp.

Diegel, F.A., Karlo, J.F., Schuster, D.C., Shoup, R.C., and Tauvers, P.R., 1995, Cenozoic structural evolution and tectono-stratigraphic framework of the northern Gulf Coast continental margin, *in* Jackson, M.P.A., Roberts, D.G., and Snelson, S. (Editors), Salt tectonics: A global perspective: AAPG Memoir 65, p. 109-151.

Doyle, L.J., and Holmes, C.W., 1985, Shallow structure, stratigraphy, and carbonate sedimentary processes of West Florida Continental Slope: *American Association of Petroleum Geologists Bulletin, v. 69*, p. 1133-1144.

Elverhøi, A., Issler, D., De Blasio, F.V., Ilstad, T., Harbitz, C.B., and Gauer, P., 2005, Emerging insights into the dynamics of submarine debris flows: *Natural Hazards and Earth System Sciences*, *v. 5*, p. 633-648.

Fine, I.V., Rabinovich, A.B., Bornhold, B.D., Thomson, R., and Kulikov, E.A., 2005, The Grand Banks landslide-generated tsunami of November 18, 1929: preliminary analysis and numerical modeling: *Marine Geology*, *v. 215*, p. 45-57.

Freeman-Lynde, R.P., 1983, Cretaceous and Tertiary samples dredged from the Florida Escarpment, eastern Gulf of Mexico: *Transactions Gulf Coast Association of Geological Societies, v. 33*, p. 91-99.

Goodwin, R.H., and Prior, D.B., 1989, Geometry and depositional sequences of the Mississippi Canyon, Gulf of Mexico: *Journal of Sedimentary Petrology, v. 59*, p. 318-329.

Halley, R.B., Pierson, B.J., and Schlager, W., 1984, Alternative diagenetic models for Cretaceous talus deposits, Deep Sea Drilling Project site 536, Gulf of Mexico, *in*, Buffler, R.T., Schlager, W. *et al.*, Initial Reports of the Deep Sea Drilling Project v. 77, Washington DC, U.S. Government Printing Office, p. 397-408.

Imran, J., Parker, G., Locat, J., and Lee, H., 2001, A 1-D numerical model of muddy subaqueous and subaerial debris flows: *Journal of Hydraulic Engineering*, *v. 127*, p. 959-958.

Jeong, S.W., Locat, J., Leroueil, S., and Malet, J.-P., 2007, *in* Lykousis, V., Sakellariou, D., and Locat, J., (Editors)., Submarine Mass Movements and Their Consequences: Springer, p. 191-198.

Johnson, A.M., 1984, Debris flows, *in* Brunsdum, D., and Prior, D.B., (Editors), Slope Instability: Chichester West Sussex, Wiley, p. 257-361.

Jordan, G.F., and Stewart, H.B., 1959, Continental slope off southwest Florida: *American Association of Petroleum Geologists Bulletin, v. 43*, p. 974-991.

Laventer, A., Williams, D.F., and Kennett, J.P., 1982, Dynamics of the Laurentide Ice Sheet during the last deglaciation: Evidence from the Gulf of Mexico: *Earth and Planetary Science Letters, v. 59*, p. 11-17.

Lee, G.W., Watkins, J.S., and Bryant, W.R., 1996, Bryant Canyon fan system: An unconfined large river-sourced system in the northwestern Gulf of Mexico: *American Association of Petroleum Geologists Bulletin, v. 80*, p. 340-358.

Lee, E.Y.D., and George, R.A., 2004, High-resolution geological AUV survey results across a portion of the eastern Sigsbee Escarpment: *American Association of Petroleum Geologists Bulletin, v. 88*, p. 747-764.

Locat, J., and Lee, H. J., 2002, Submarine landslides: advances and challenges: *Canadian Geotechnical Journal, v. 39*, p. 193-212.

Locat, J., Lee, H.J., Locat, P., and Imran, J., 2004, Numerical analysis of the mobility of the Palos Verdes debris avalanche, California, and its implication for the generation of tsunmis: *Marine Geology*, *v. 203*, p. 269-280.

Locker, S.D. and Buffler, R.T., 1984, Comparison of Lower Cretaceous carbonate shelf margins, northern Campeche Escarpment and northern Florida Escarpment, Gulf of Mexico, *in* Bally, P.W. (Editor), Seismic Expression of Structural Styles – A Picture and Work Atlas, American Association of Petroleum Geologists Studies in Geology Series, No. 15, v. 2, p. 123-128.

Lowrie, A., Lutken, C.B., and McGee, T.M., 2004, Multiple outer shelf deltas and downslope massive mass-wastings characterize the Mississippi Canyon, northern Gulf of Mexico: *Transactions Gulf Coast Association of Geological Societies, v. 54*, p. 383-392.

Lowrie, A., Yu, Z., and Lerche, I., 1991, Hydrocarbon trap types and deformation styles modeled using quantified rates of salt movement, Louisiana margin: *Transactions-Gulf Coast Association of Geological Societies, v. 41,* p. 445-459.

Marchitto, T.M., and Wei, K., 1995, History of Laurentide meltwater flow to the Gulf of Mexico during the last deglaciation, as revealed by reworked calcareous nannofossils: *Geology, v. 23*, p. 779-782.

Martin, R.G., and Bouma, A.H., 1978, Physiography of Gulf of Mexico, *in* Bouma, A.H., Moore, G.T., and Coleman, J.M., eds., Framework, facies, and oil-trapping characteristics of the upper continental margin: American Association of Petroleum Geologists Studies in Geology no. 7, p. 3-19.

McGregor, B.A., Rothwell, R.G., Kenyon, N.H., and Twichell, D.C., 1993, Salt tectonics and slope failure in an area of salt domes in the northwestern Gulf of Mexico, *in* Schwab, W.C., Lee, H.J., and Twichell, D.C. (Editors), Submarine Landslides: Selected Studies in the U.S. Exclusive Economic Zone: U.S. Geological Survey Bulletin, 2002, p. 92-96.

Morton, R.A., and Suter, J.R., 1996, Sequence stratigraphy and composition of Late Quaternary shelf-margin deltas, northern Gulf of Mexico: *American Association of Petroleum Geologists Bulletin, v. 80*, p. 505-530.

Mullins, H.T., Gardulski, A.F., and Hine, A.C., 1986, Catastrophic collapse of the West Florida carbonate platform margin: *Geology, v. 14*, p. 167-170.

Nelson, C.H., Twichell, D.C., Schwab, W.C., Lee, H.J., and Kenyon, N.H., 1992, Late Pleistocene turbidite sand beds and chaotic silt beds in the channelized distal outer fan lobes of Mississippi Fan: *Geology, v. 20*, p. 693-696.

Normark, W.R., Meyer, A.H., Cremer, M., Droz, L., O'Connell, S., Pickering, K.T., Stelting, C.E., Stow, D.A.V., Brooks, G.R., Mazzullo, J., Roberts, H., and Thayer, P., 1986, Summary of drilling results for the Mississippi Fan and considerations for application to other turbidite systems, *in* Bouma, A.H., Coleman, J.M., Meyer, A.W., *et al.* (Editors), Initial Reports of the Deep Sea Drilling Project: U.S. Government Printing Office, Washington, D.C., v. 96, p. 425-436.

Orange, D.L., Saffer, D., Jeanjean, P., Khafaji, Z.A., Humphrey, G., and Riley, G., 2003, Measurements and modeling of the shallow pore pressure regime at the Sigsbee Escarpment: Successful prediction of overpressure and ground-truthing with borehole measurements: *The Leading Edge, v. 22*, p. 906-913.

Orange, D.L., Angell, M.M., Brand, J.R., Thomson, J., Buddin, T., Williams, M., Hart, W., Berger, W.J., 2004, Geologic and shallow salt tectonic setting of the Mad Dog and Atlantis fields: Relationship between salt, faults, and seafloor geomorphology: *The Leading Edge, v. 23*, p. 354-365.

Paull, C.K., Spiess, F.N., Curray, J.R., and Twichell, D.C., 1990a, Origin of Florida Canyon and the role of spring sapping on the formation of submarine box canyons: *Geological Society of America Bulletin, v. 102*, p. 502-515.

Paull, C.K., Freeman-Lynde, R.P., Bralower, T.J., Gardemal, J.M., Neumann, A.C., D'Argenio, B., and Marsella, E., 1990b, Geology of the strata exposed on the Florida Escarpment: *Marine Geology, v. 91*, p. 177-194.

Paull, C.K., Twichell, D.C., Spiess, F.N., and Curray, J.R., 1991, Morphological development of the Florida Escarpment: Observations on the generation of time transgressive unconformities in carbonate terrains: *Marine Geology, v. 101*, p. 181-201.

Piper, J.N., 1997, Downslope sediment transport processes and sediment distributions at the East Breaks, northwest Gulf of Mexico: Austin, University of Texas, Thesis.

Piper, J.N., and Behrens, W.E., 2003, Downslope sediment transport processes and sediment distributions at the East Breaks, northwest Gulf of Mexico, in Proceedings of the 23rd Annual Gulf Coast Section SEPM Research Conference, Houston, TX, p. 359-385.

Prather, B.E., Booth, J.R., Steffens, G.S., and Craig, P.A., 1998, Classification, lithologic calibration, and stratigraphic succession of seismic facies of intraslope basins, deep-water Gulf of Mexico: *American Association of Petroleum Geologists Bulletin, v. 82*, p. 701-728.

Pratson. L.F., and Ryan, W.B.F., 1994, Pliocene to Recent infilling and subsidence of intraslope basins offshore Louisiana: *American Association of Petroleum Geologists Bulletin, v. 78*, p. 1483-1506.

Rothwell, R.G., Kenyon, N.H., and McGregor, B.A., 1991, Sedimentary features of the south Texas continental slope as revealed by side-scan sonar and high-resolution seismic data: *American Association of Petroleum Geologists Bulletin, v. 75*, p. 298-312.

Sager, W.W., and MacDonald, I.R., and Hou, R., 2004; Side-scan sonar imaging of hydrocarbon seeps on the Louisiana continental slope: *American Association of Petroleum Geologists Bulletin, v. 88*, p. 725-746.

Salvador, A., 1991a, Triassic-Jurassic: *in* Salvador, A. (Editor), The Geology of North America, Vol. J., The Gulf of Mexico Basin, Geological Society of America, Boulder, CO, p. 131-180.

Salvador, A., 1991b, Origin and development of the Gulf of Mexico basin: *in* Salvador, A. (Editor), The Geology of North America, Vol. J., The Gulf of Mexico Basin, Geological Society of America, Boulder, CO, p. 389-444.

Sawyer, D.S., Buffler, R.T., and Pilger, R.H., 1991, The crust under the Gulf of Mexico basin, *in* Salvador, A. (Editor), The Geology of North America, Vol. J, Gulf of Mexico Basin: Geological Society of America, Boulder, CO, p. 53-72.

Schlager, W., Buffler, R.T., and Scientific Party of DSDP Leg 77, 1984, DSDP Leg 77; Early history of the Gulf of Mexico: *Geological Society of America Bulletin, v. 95*, p. 226-236.

Schwab, W.C., Lee, H.J., Twichell, D.C., Locat, J., Nelson, C.H., McArthur, W.G., and Kenyon, N.H., 1996, Sediment mass-flow processes on a

depositional lobe, outer Mississippi Fan: *Journal of Sedimentary Research, v. 66*, p. 916-927.

Silva, A.J., Baxter, C.D.P., LaRosa, P.T., and Bryant, W.R., 2004, Investigation of mass wasting on the continental slope and rise: *Marine Geology, v. 203*, p. 355-366.

Sohl, N., Martinez, E., Salmeron-Urena, P., and Soto-Jaramillo, F., 1991, Upper Cretaceous, *in* Salvador, A. (Editor), The Geology of North America, Vol. J., The Gulf of Mexico Basin, Geological Society of America, Boulder, CO, p. 205-244.

ten Brink, U.S., Geist, E.L., and Andrews, B.D., 2006, Size distribution of submarine landslides and its implication to tsunami hazard in Puerto Rico: Geophysical Research Letters, v. 33, p. doi:10.1029/ 2006GL026125.

ten Brink, U.S., Twichell, D., Geist, E.L., Chaytor, J., Locat, J., Lee, H., Buczkowski, B., and Sansoucy, M., 2007, The current state of knowledge regarding potential tsunami sources affecting U.S. Atlantic and Gulf Coasts, U.S. Geological Survey Administrative Report, 154 p.

Trabant, P., Watts, P., Lettieri, F.L., and Jamieson, A., 2001, East Breaks slump, northwest Gulf of Mexico, OTC 12960, in 2001 Offshore Technology Conference, Houston, TX, p. 231-238.

Tripsanas, E.K., Bryant, W.R., and Phaneuf, B.A., 2004, Slope-instability processes caused by salt movements in a complex deep-water environment, Bryant Canyon area, northwest Gulf of Mexico: *American Association of Petroleum Geologists Bulletin, v. 88*, p. 801-824.

Tripsanas, E.K., Bryant, W.R., and Phaneuf, B.A., 2004, Depositional processes of uniform mud deposits (unifites), Hedberg Basin, northwest Gulf of Mexico: New perspectives: *American Association of Petroleum Geologists Bulletin, v. 88*, p. 825-840.

Twichell, D.C., Parson, L.M., and Paull, C.K., 1990, Variations in the styles of erosion along the Florida Escarpment, eastern Gulf of Mexico: *Marine and Petroleum Geology, v. 7*, p. 253-266.

Twichell, D.C., Kenyon, N.H., Parson, L.M., and McGregor, B.A., 1991, Depositional patterns of the Mississippi Fan surface: Evidence from GLORIA II and high-resolution seismic profiles, *in* Weimer, P., and Link, M.H. (Editors), Seismic Facies and Sedimentary Processes of Submarine Fans and Turbidite Systems, Springer-Verlag, New York, p. 349-363.

Twichell, D.C., Schwab, W.C., Nelson, C.H., Lee, H.J., and Kenyon, N.H., 1992, Characteristics of a sandy depositional lobe on the outer Mississippi Fan from SeaMARC IA sidescan sonar images: *Geology, v. 20*, p. 689-692.

Twichell, D.C., Valentine, P.C., and Parson, L.M., 1993, Slope failure of carbonate sediment on the West Florida Slope, *in*, Schwab, W.C., Lee, H.J., and Twichell, D.C. (Editors), Submarine landslides: Selected studies in the U.S. Exclusive Economic Zone, U. S. Geological Survey Bulletin 2002, p. 69-78.

Twichell, D.C., Dillon, W.P., Paull, C.K., and Kenyon, N.H., 1996, Morphology of carbonate escarpments as an indicator of erosional

processes, *in* Gardner, J. V. Field, M.E., and Twichell, D.C. (Editors), Geology of the United States' Seafloor: The view from GLORIA, Cambridge University Press, p. 97-107.

Twichell, D.C., and Cooper, A.K., 2000, Relation between sea floor failures and gas hydrates in the Gulf of Mexico; a regional comparison: *American Association of Petroleum Geologists Annual Convention, v. 9*, p. A150.

Twichell, D.C., Nelson, C.H., and Damuth, J.E., 2000, Late-stage development of the Bryant Canyon turbidite pathway on the Louisiana continental slope, *in* Weimer, P., Slatt, R.M., Coleman, J., Rosen, N.C., Nelson, H., Bouma, A.H., Styzen, M.J., and Lawrence, D.T. (Editors), Deep-Water Reservoirs of the World: Proceedings of the Gulf Coast Section SEPM, p. 1032-1044, CD-ROM.

Twichell, D.C., Cross, V.A., Paskevich, V.F., Hutchinson, D.R., Winters, W.J., and Hart, P.E., 2005, GIS of selected geophysical and core data in the northern Gulf of Mexico continental slope collected by the U.S. Geological Survey: U.S. Geological Survey Open-File Report 2005-1071, 1 DVD-ROM.

Twichell, D.C., Nelson, C.H., Kenyon, N. and Schwab, W., in press, The influence of external processes on the latest Pleistocene and Holocene evolution of the Mississippi Fan, *in,* Kneller, B., McCaffrey, W., Martinsen, O., and Posamentier, H. (Editors), External Controls on Deep Water Depositional Systems: Climate, sea-level, and Sediment Flux, SEPM Special Publication.

Walker, J.R., and Massingill, J.V., 1970, Slump features on the Mississippi Fan, northeastern Gulf of Mexico: *Geological Society of America Bulletin, v. 81*, p. 3101-3108.

Weimer, P., 1989, Sequence stratigraphy of the Mississippi Fan (Plio-Pleistocene), Gulf of Mexico: *Geo-Marine Letters, v. 9*, p. 185-272.

Weimer, P., 1991, Seismic facies, characteristics, and variations in channel evolution, Mississippi Fan (Plio-Pleistocene), Gulf of Mexico, *in* Weimer, P., and Link, M.H. (Editors), Seismic Facies and Sedimentary Processes of Submarine Fans and Turbidite Systems, Springer-Verlag, New York, p. 323-347.

Weimer, P. and Dixon, B.T., 1994, Regional sequence stratigraphic setting of the Mississippi Fan complex, northern deep Gulf of Mexico: Implications for evolution of the northern Gulf basin margin, *in* Weimer, P., Bouma, A.H., and Perkins, B.F. (Editors), Submarine fans and turbidite systems: Sequence stratigraphy, reservoir architecture and production characteristics, GCSEPM Foundation 15th Annual Research Conference, p. 373-381.

Worzel, J.L., Leyden, R., and Ewing, M., 1968, Newly discovered diapirs in the Gulf of Mexico: *American Association of Petroleum Geologists Bulletin, v. 52*, p. 1194-1203.

Chapter 4: Far-field Submarine Landslide Sources

Numerous debris deposits from subaerial and submarine landslide have been identified along the Canadian, European and African coasts of the Atlantic Ocean (*e.g.*, Canals *et al.*, 2004; Piper and McCall, 2003; Weaver and Mienert, 2003).

Canary Islands

Perhaps the most publicized hazard is that of a possible collapse of Cumbre Vieja, a volcano on the Canary island of La Palma (Ward and Day, 2001). As envisioned by Ward and Day (2001), a flank collapse of the volcano may drop a rock volume of up to 500 km^3 into the surrounding ocean. The ensuing submarine slide, which was assumed to propagate at a speed of 100 m/s, will generate a strong tsunami with amplitudes of 25 m in Florida. In addition, they claimed that the collapse of Cumbre Vieja is imminent.

In our opinion, the danger to the U.S. Atlantic coast from the possible collapse of Cumbre Vieja is exaggerated. Mader (2001) pointed out that Ward and Day's (2001) assumption of linear propagation of shallow water waves is incorrect, because it only describes the geometrical spreading of the wave and neglects dispersion effects. A more rigorous hydrodynamic modeling by Gisler *et al.* (2006), confirms Mader's criticism. Their simulations show significant wave dispersion and predict amplitude decay proportional to r^{-1} for a 3-dimensional model and $r^{-1.85}$ for a 2-D model. (r is distance). Their predicted wave amplitude for Florida is between 1-77 cm. They uses slightly smaller volume, 375 km^3, than Ward and Day (2001), but a much higher slide speed, that is much closer to the phase speed for tsunamis in the deep ocean (4,000 m of water). The amplitude in Ward and Day (2001) model scales proportionally with rock volume times slide speed. Hence, the much smaller predicted amplitude of Gisler *et al.* (2006) for the Florida coast cannot be attributed to the smaller slide volume. Moreover, typical speeds of landslides are thought to be 20-80 m/s, slower than assumed by either model (ten Brink *et al.*, 2006a, and references therein).

Masson *et al.* (2002) have identified at least 14 landslides with volumes ranging between 50-500 km^3 taking place within the last 1.3 m.y., or an average of 1 slide per 10^{-5} yr. However, volcanoclastic turbidites that are correlated with the two most recent landslides in the Canary Islands shows stacked sub-units within the turbidite bed, which may indicate multiple stages of landslide failures, not a single catastrophic collapse (Wynn and Masson,

2003). Therefore, the recurrence interval may be shorter than 10^{-5} yr but the landslide volumes are also smaller.

Other landslide sources along the continental margin

Many submarine landslides have been discovered along the glaciated margins of northern Europe and Canada (Canals *et al.*, 2004; Piper and McCall, 2003; Weaver and Mienert, 2003, Leynaud *et al.*, submitted).

The largest of these landslides is the Storegga landslide (Figure 4-1), which caused a tsunami that impacted the coasts of Norway (runup of ≤13 m), the Faeroes islands (>14m), Shetland islands (>20 m), Scotland and northern England (3-6 m), and Iceland (Bondevik *et al.*, 2005). The impacted areas are all within 600 km of the slide. The runup observations were fit with a retrogressive slide source with a relatively low slide speed (25-30 m/s) (Bondevik *et al.*, 2005). The Storegga slide is a composite failure with 7 slides occurring during the past 0.5 Ma, when the ice sheet started advancing across the continental shelf (Solheim *et al.*, 2005, and ref. within). The latest and largest landslide, which also caused the tsunami, is dated at 8150 yr BP. The total volume of the latest slide is 2,500-3,000 km^2, the area of the slide scar is 27,000 km^2 and the length of the headwall is 290 km. The repeated failures within the same area are explained by excess pore pressure in the sediments due to rapid loading from glacial deposits, followed by triggering by earthquakes (Bryn *et al.*, 2005).

Several scarps, disturbances in glacial sediments, and debris flow were also identified along the Scotia margin, immediately NE of the U.S. border (Piper and McCall, 2003). A very large failure event in the eastern Scotian margin at 0.15 Ma has released perhaps 10 times the volume of sediments released during the 1929 Grand Banks landslide (Piper and Ingram, 2003). Increased deposition and perhaps slope failure on the Scotian margin occurred at 0.5 Ma when the glacial advance reached close to the shelf edge (Piper *et al.*, 2003). Deposition rate on the slope decreased about 8,000 years ago by a factor of 20-50 as deglaciation came to and end (Piper *et al.*, 2003). Among the 23 dated slope failures in the Grand Banks and the Scotia shelf, only two postdate the Holocene, one of them being the 1929 Grand Banks failure (Piper *et al.*, 2003).

Other submarine landslides were identified along the northern European margin (Kenyon, 1987), and the Puerto Rico trench (ten Brink *et al.*, 2006a, b), but to our knowledge, none of them are associated with very large deposit volumes. The Puerto Rico landslide scarps are generally in deep (>3,000 m) water, but are located on steep carbonate slopes, and have the characteristics of rock falls (ten Brink *et al.*, 2006a). Hence, the initial slide acceleration of falling competent blocks may be higher than along most other margins described above, although this is only a conjecture.

The mid-Atlantic ridge

The mid-Atlantic ridge is one of the few tectonic features in the Atlantic Ocean, which is associated with frequent earthquake activity. Two magnitude 7+ earthquakes took place on the ridge between latitudes 10°-50° during the last 34 years. High seafloor slope angles and relatively fractured basaltic and gabbroic rocks are often encountered along both the rift valley and the transform valley, and they may be susceptible to landslides. A scarp and debris field at a depth of 2700 – 3100 m were found at latitude 26°27'N in an area of steep slopes (14-23°) (Tucholke, 1992). The estimated slide volume is 19km^3 and the slide took place within the past 0.45 my (Tucholke, 1992). Massive slumps of gabbroic bedrock on steep slopes (~30°) were observed at the intersection between the Kane Transform and the ridge at 23°38'N (Gao, 2006). However, about 3/4 of the ridge length between 10°-45°N are not yet surveyed in detail (Marine Geoscience Data Center, `www.marine-geo.org`).

The Azores are a group of volcanic islands on the triple junction between the North American, Eurasian and African plates at 37°-39°N. The rate of volcanic activity in the Azores is lower than in the Canary Islands and the slope angles and height of the volcanic islands are also smaller. A devastating earthquake on October 22nd, 1522 induced several landslides over San Miguel Island. 5,000 lives were lost by the subaerial slide, which involved a volume of about 6,75x10^6 m^3 and a small tsunami has occurred. (`http://www.acri.fr/retina/Deliverables/D48_M42.htm`)

Figure

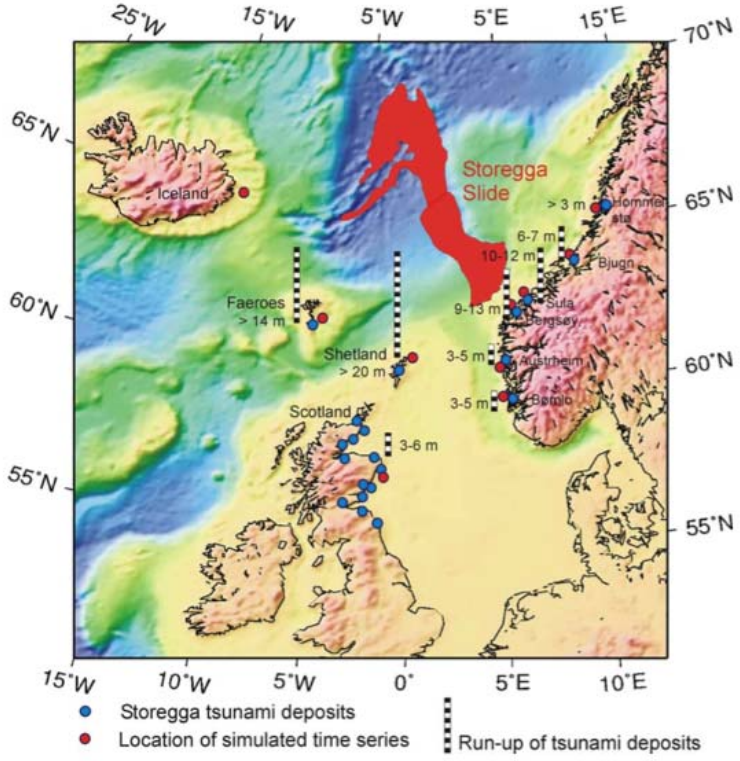

Figure 4-1: Location map of the Storegga Slide.

References:

Bondevik, S., Lovholt, F., Harbitz, C. B., Mangerud, J., Dawson, A., and Svendsen, J. I., 2005, The Storegga Slide tsunami; comparing field observations with numerical simulations: *Marine and Petroleum Geology*, *v. 22*, p. 195-208.

Bryn, P., Berg, K., Forsberg, C. F., Solheim, A., and Kvalstad, T. J., 2005, Explaining the Storegga Slide, *Marine and Petroleum Geology*, *22*, p. 11-19.

Canals, M., *et al.*, 2004, Slope failure dynamics and impacts from seafloor and shallow sub-seafloor geophysical data; case studies from the COSTA project: *Marine Geology*, *v. 213*, p. 9-72.

Gao, D., 2006, Gravitational sliding on the Mid-Atlantic Ridge at the Kane Transform; implications for submarine basin-slope degradation and deformation: *AAPG Bulletin*, *v. 90*, p. 159-176.

Gisler, G., Weaver, R., and Gittings, M. L., 2006, SAGE calculations of the tsunami threat from La Palma, *Science of Tsunami Hazards*, *24*, p. 288-301.

Kenyon, N. H., 1987, Mass-wasting features on the continental slope of Northwest Europe: *Marine Geology*, *v. 74*, p. 57-77.

Leynaud, D., Mienert, J., and Vanneste, M., *submitted*, Submarine mass movements on glaciated and non-glaciated European continental margins: Triggering mechanisms and preconditions to failure: *Marine Geology*.

Mader, C. L., 2001, Modeling the La Palma landslide tsunami: *Science of Tsunami Hazards*, *v. 19*, p. 160.

Masson, D. G., Watts, A. B., Gee, M. J. R., Urgeles, R., Mitchell, N. C., Le Bas, T. P., and Canals, M., 2002, Slope failures on the flanks of the western Canary Islands: *Earth-Science Reviews*, *v. 57*, p. 1-35.

Piper, D. J. W., and Ingram, S., 2003, Major Quaternary failures on the East Scotian Rise, Current Research: Geological Survey of Canada, 7 p.

Piper, D. J. W., and McCall, C., 2003, A synthesis of the distribution of submarine mass movements on the eastern Canadian margin, *in* Locat, J., and Meinert, J. (Editors), Submarine mass Movements and Their Consequences, Kluwer, Dordrecht, p. 291-298.

Piper, D. J. W., Mosher, D. C., Gauley, B.-J., Kimberley, J., and Campbell, D. C., 2003, The choronology and recurrence of submarine mass movements on the continental slope off southeastern Canada, *in* Locat, J., and Meinert, J. (Editors), Submarine mass Movements and Their Consequences, Kluwer, Dordrecht, p. 299-306.

Solheim, A., Berg, K., Forsberg, C. F., and Bryn, P., 2005, The Storegga Slide Complex; repetitive large scale sliding with similar cause and development: *Marine and Petroleum Geology*, *v. 22*, p. 97-107.

ten Brink, U. S., Geist, E. L., and Andrews, B. D. 2006a, Size distribution of submarine landslides and its implication to tsunami probability in Puerto Rico, *Geophysical Research Letters, v. 33*, L11307, doi:11310.11029/ 12006GL 026125.

ten Brink, U. S., Geist, E. L., Lynett, P., and Andrews, B., 2006b, Submarine slides north of Puerto Rico and their tsunami potential, *in* Mercado, A.,

and Liu, P. L.-F. (Editors), Caribbean Tsunami Hazard, World Scientific, Singapore, p. 67-90.

Tucholke, B. E., 1992, Massive submarine rockslide in the rift-valley wall of the Mid-Atlantic Ridge: *Geology*, *v. 20*, p. 129-132.

Ward, S. N., and Day, S., 2001, Cumbre Vieja Volcano; potential collapse and tsunami at La Palma, Canary Islands: *Geophysical Research Letters*, *v. 28*, p. 3397-3400.

Weaver, P. P. W., and Mienert, J., 2003, European margin sediment dynamics side-scan sonar and seismic images, Springer, New York, 310 pp.

Wynn, R. B., and Masson, D. G., 2003, Canary Island landslides and tsunami generation: can we use turbidite deposits to interpret landslide processes?, *in* Locat, J., and Meinert, J. (Editors), Submarine mass Movements and Their Consequences, Kluwer, Dordrecht, p. 325-332.

Section 2:

Earthquakes

Chapter 5: Far-field Tsunami Simulations of the 1755 Lisbon Earthquake: Implications for Tsunami Hazard to the U.S. East Coast and the Caribbean

Introduction

The Azores-Gibraltar plate boundary is the source of the largest earthquakes and tsunamis in the north Atlantic basin. These include the 1941 M8.4 and 1975 M1979 strike-slip earthquakes west of the Madeira-Tore Rise (MTR) and the 1969, Ms 8.0 earthquake in the Horseshoe Plain south-east of the Gorringe Bank (Buforn *et al.*, 1988; 2004; Fukao, 1973) (Figure 5-1). This plate boundary is also believed to have been the source region of the 1722 and 1761 tsunamigenic earthquakes (Baptista *et al.*, 2006) and of the great November 1st, 1755 Lisbon earthquake (Machado, 1966; Moreira, 1985; Johnston, 1996). The earthquake, which was estimated to be of magnitude Mw 8.5-9.0 (*e.g.*, Gutscher *et al.*, 2006), had the largest documented felt area of any shallow earthquake in Europe (Martinez-Solares *et al.*, 1979; Johnston 1996) and was the largest natural disaster to have affected Europe in the past 500 years. It inflicted up to 100,000 deaths (Chester, 2001) through destruction by ground shaking, ensuing fires and tsunami waves of 5-15 m that devastated the coasts of Southwest Iberia and Northwest Morocco and were even reported as far north as Cornwall, England (Baptista *et al.*, 1998a). Additionally, Grácia *et al.* (2003a, b) showed clear evidence of submarine landslide deposits from acoustic- backscattering, suggesting that the slope failure process could have contributed to tsunami generation and reports of tsunami waves along the European and Moroccan coasts.

The large tsunami-wave generated by the earthquake also caused damage in the eastern Lesser Antilles, as far north as Newfoundland, Canada and as far south as Brazil (Kozak *et al.*, 2005; Ruffman, 2006). However, no reports were documented from cities along the U.S. East Coast (Reid, 1914; Lockridge *et al.*, 2002; Ruffman, 2006). Table 5-1 summarizes the tsunami run-up reports from around the Atlantic Ocean (Reid, 1914; Ruffman, 1990, 2006; Baptista *et al.*, 1998a; O'Loughlin and Lander, 2003; Kozak *et al.*, 2005). Figure 5-2 shows relevant locations on the map as well as cities along the U.S. East Coast, which existed in 1755.

Although many attempts have been made to characterize the 1755 Lisbon earthquake and tsunami (Johnston 1996; Baptista *et al.*,1998a,b; Gutscher *et al.*, 2006; Grandin *et al.*, 2007) only one study (Mader, 2001) had considered the far field effects of the tsunami. Studying far field effects is advantageous in determining a possible source location and fault orientation because such effects are less influenced by near-source bathymetry and are unaffected by components of the tsunami wavefield generated by submarine landslides which are significant in the near-field (Gisler *et al.*, 2006), but attenuate rapidly. Mader (2001) generated a numerical model for a source centered at the location of the Mw 7.8, 1969 earthquake (Figure 5-1), which provided estimates of the deep water wave amplitudes along the U.S. East Coast and the Caribbean. However, the study did not attempt to characterize the earthquake's source parameters, using instead a 30-m vertical drop of a 300-km radius area as a source; nor did it endeavor to compare tsunami hazard along the U.S. East Coast and the Caribbean from different sources in the region.

In this study we first investigate constraints on the epicenter of the 1755 Lisbon earthquake from far field numerical tsunami simulations. Second, features such as fault orientation, distance from source, and near-source and regional bathymetry are tested in order to determine what governs tsunami propagation in the Atlantic Ocean. We then assess the tsunami hazard to the U.S. East Coast and the Caribbean from possible future earthquake sources located in the east Atlantic region.

Tectonic Setting and the 1755 Lisbon Earthquake

The eastern end of the Azores-Gibraltar plate boundary, which separates the Eurasian and African plates, is a region of complex bathymetry. Plate kinematic models together with focal mechanisms show that the motion between the two plates is slow (0.7-5 mm/yr) (Argus *et al.* 1989; Nocquet and Calais, 2004; Fernandes et al, 2007), changing along the boundary from extension in the Azores to compression towards the east that includes the Gorringe Bank and the Gibraltar arc (Figure 5-1, inset). The precise location of the plate boundary close to Iberia is uncertain and the plate boundary deformation there might be diffuse over a 200-330 km wide zone (Grimison and Chen, 1986; Hayward *et al.*, 1999). The dominant active structures in this region are the Gorringe Bank Fault (GBF), the Marqués de Pombal Fault (MPF), the St. Vincente Fault (SVF) and the Horseshoe Fault (HSF), which have been studied by several authors (Sartori *et al.*, 1994; Baptista et. al., 2003; Grácia *et al.*, 2003a; Terrinha *et al.*, 2003). These structures and most of the faults in this area trend NE-SW (Borges *et al.*, 2001; Zitellini *et al.*, 2004; Buforn *et al.*, 2004) (Figure 5-1).

Thus far the source of the great Lisbon earthquake remains unknown (Gutscher, 2004). A consensus attributed the origin of the earthquake to a structure located between the Gorringe Bank and the Coral Patch Ridge (Machado, 1966; Moreira, 1985; Johnston, 1996) (Figure 5-1). Yet the relatively modest surface area of this fault region makes it difficult to explain the high seismic moment of $\sim 2 \times 10^{22}$ Nm, for a reasonable set of fault

parameters (*e.g.*, co-seismic displacement, rigidity, and recurrence) (Gutscher *et al.*, 2006). Three major solutions were proposed based on seismic reflection and multibeam echosounder data, estimates of shaking intensity, and backward ray tracing of tsunami propagation. These fault solutions are shown in Figure 5-1 and will be referred later in this chapter as:

(1.) Gorringe Bank Fault (GBF) – Johnston (1996) and Grandin *et al.* (2007) suggested a NE-SW trending thrust fault (strike 060°), possibly outcropping at the base of the NW flank of the Gorringe Bank.
(2.) Marqués de Pombal Fault (MPF) – Zitellini *et al.* (2001) and Grácia *et al.* (2003a) suggested active thrusting along the MPF, located 80 km west of Cape Sao Vincente (strike 020°).
(3.) Gulf of Cádiz Fault (GCF) – Gutscher *et al.* (2002, 2006) and Thiebot and Gutscher (2006) proposed a fault plane in the western Gulf of Cádiz, possibly as part of an African plate subduction beneath Gibraltar (strike 349°).

Methodology

Tsunami model simulations

All simulations presented in this study were generated using COMCOT (Cornell Multi-grid Coupled Tsunami Model) developed by P.L.-F. Liu, X. Wang, S-B. Woo, Y-S. Cho, and S.B. Yoon, at the School of Civil and Environmental Engineering, Cornell University (Liu *et al.*, 1998). All calculations were performed on the Arctic Region Supercomputing Center in Alaska, using the Tsunami Computational Portal at: `http://tsunamiportal.nacse.org/wizard.php`. COMCOT solves both linear shallow water (LSW) and non-linear shallow water (NLSW) equations in spherical coordinates. Two simplifying assumptions were made to create the initial sea surface deformation, which serve as the initial boundary conditions for the numerical simulations. First, the sea surface responds instantaneously to seafloor earthquake deformation. Second, the initial sea surface displacement is identical to that of the seafloor (Ruff, 2003). The initial sea surface deformation, computed based upon user-provided fault parameters, is identical to the seafloor displacement generated by Coulomb 3.0 (Lin and Stein, 2004; Toda *et al.*, 2005; `http://coulombstress.org`). Aside from the governing equations, the difference in using linear vs. non-linear hydrodynamic models lies in the boundary conditions. The linear model uses reflective boundary conditions and is therefore unable to perform explicit run-up calculations at the shallow water areas along the coast. On the other hand, the non-linear model uses moving boundary conditions and is capable of explicit run-up calculations. The linear model was used in this study, because no attempt was made to calculate run-up. The output files used for all interpretations are depth and maximum wave amplitude files. The depth file contains the bathymetry of the region where

the simulation took place. An ETOPO2, 2551x1457 bathymetry grid with 2 arcmin resolution was used for all simulations. The maximum wave amplitude file contains the calculated maximum sea level amplitude for a selected region, throughout an entire simulation run (tsunami propagation time of 10-11.25 hours).

Tsunami theory and numerical model limitations

Tsunami theory has been studied by many authors. The following section sums up tsunami theory based upon Liu et al (1998) and Ward (2002). The leading wave of a tsunami has a wavelength proportional to the longitudinal dimensions of the earthquake source region, which could be several hundreds to a thousand kilometers for a major earthquake. It is considered to be a shallow water gravity wave, where the ocean depth is negligible compared to the wavelength. Its phase speed is proportional to $\sqrt{gh}$, where, g is the acceleration of gravity and h is the water depth in meters. The wave period ranges between several hundreds to several thousand seconds. During propagation in deep water, tsunami wave slope is small, resulting in insignificant convective inertia forces, which can be ignored. As tsunamis propagate into the shallower water region, the wave amplitude increases and the wavelength decreases due to shoaling. The nonlinear convective inertia force becomes increasingly important. In the very shallow water, the bottom frictional effects become significant as well. Therefore, the nonlinear shallow water equations including bottom frictional terms should be used in the description of the tsunami inundation. In principle, numerical computation of wave heights based on linear shallow water equations is sufficient and accurate as long as the modeled tsunami wavelength is much greater than water depth and the wave amplitude is much smaller than water depth. This principle holds up until the deep part of the continental shelf. Consequently, this study is unable to provide definite run-up results and only relative amplitudes can be taken into consideration.

The time step chosen for each simulation must meet the Courant-Friedrichs-Lewy (CFL) condition (Courant *et al.*, 1928) in order to assure numerical stability. The CFL condition for explicit numerical methods assures that the algorithm used for solving partial differential equations is convergent. For the COMCOT modified explicit scheme, the largest allowable Courant number is 0.8660 (Liu *et al.*, 1998). Therefore, in order to assure stability the time step used in this study never exceeded 3 seconds.

Tsunami amplitude

Two methods were used to reliably calculate wave amplitude. First, the amplitude was calculated at depths of 250 m (see 'shelf point' in Figure 5-3), similar to ten Brink *et al.* (Chapter 8, this volume), in selected sites along the U.S. East Coast, the Caribbean Islands, Europe, and Africa (Figure 5-2). This depth falls within the minimal wavelength to grid size ratio (see *Tsunami theory and numerical model limitations* for detail), allowing for accurate

propagation and amplitude calculations. Second, a rectangular patch of different sizes (Figure 5-3) was chosen seaward of each location along the Atlantic, Caribbean, African and European coasts (Figure 5-2). The average amplitude was calculated for all of the points within the depth range of 150 to 50 m in each patch. The size of the patches varied depending on the geographical locations where the amplitudes are measured. Along the U.S. East Coast for instance, where the shelf is wide, larger patches were selected to account for as many points as possible within the 150 to 50 m depth range. In the Caribbean, where the shelf is narrower, smaller patches were sufficient to incorporate a representative number of points in the same depth range. Although amplitudes calculated at such shallow depths may be inaccurate in terms of their geographical locations, averaging them out over a large area gives a good indication of the wave amplitude in that particular region. This method also verifies that the amplitude calculated at a nearby shelf edge point of 250 m depth is not anomalous. Figures 5-4a and 5-4b show a comparison between amplitudes calculated using the two methods, from an earthquake source located in location 8 (Figure 5-3). Indeed, the average amplitudes calculated in the patches in the shallower water show similar or higher amplitudes in comparison to the ones calculated in the slightly deeper shelf edge points, as one would expect from the amplification effects of shallow waters.

A method to overcome unreliable historical reports of run-up observations

Caution must be exercised when using historical reports in order to compare between possible epicenter locations. Table 5-1 shows the variability of run-up amplitudes in historical reports, particularly in the Azores, Madeira, Lisbon and Tangier. It is therefore impossible to compare our model results to individual run-up reports. Moreover, run-up amplitudes are highly sensitive to the near shore bathymetry and onshore topography whereas, because of the model limitations discussed in *Tsunami model simulations* and *Tsunami theory and numerical model limitations*, amplitudes were calculated at a water depth of 250 m. We therefore grouped together places in the Caribbean, along the Portuguese and Moroccan coast, in Madeira and the Azores, as locations representing consistent reports of high amplitudes. Earthquake sources generating high tsunami amplitudes in those locations are therefore assigned as a good fit to the 1755 Lisbon earthquake epicenter. Similarly, we joined together places along the U.S. East Coast and in Vigo and La Coruña in the northern Spanish coast, under a category of places where no historical reports were documented (*i.e.*, negative evidence). Blank, (2008) quotes a French report from 1756 about a tsunami striking La Coruña, but the report itself does not mention tsunami there (Anonyme, 1756) , we interpret the general lack of reports from this established harbor to indicate that its amplitude was small. The particular locations along the U.S. East Coast (with the exception of Virginia Key in Florida), and Vigo and La Coruña in Spain, were chosen because they were already populated at the time of the earthquake yet there were still no tsunami reports found in the literature. In places along the U.S. East Coast, the tsunami should have

struck during daylight hours. The semi-diurnal tidal ranges along the U.S. East Coast are <3 m and the difference between the times that high-tide reaches different locations along the East Coast is as large as 5 hours. Therefore, had a significant tsunami impacted the U.S. East Coast, some sites there would have experienced flooding during low tide. In NW Spain, both the time the tsunami should have struck and the tide conditions are similar to the other locations further south along the coast. Therefore, neither tidal variations nor time of the day are likely to explain the absence of reports in these locations. Table 5-2 summarizes the criteria used to group the historical reports.

In order to quantify the results we compared and normalized the amplitudes of all sources relative to source 5 (shown in Figure 5-3). For each location *j* out of a total of *n* along the coasts (shown in Figure 5-2 and Table 5-1) where no amplitudes were reported, we calculated the amplitudes of different model sources relative to that of source 5 using:

$$Amp_i^{\min} = \sum_{j=1}^{n} (Amp_5 - Amp_i) / Amp_5 \qquad (1)$$

where *i* represents the 16 model epicenter locations shown in Figure 5-3 . A better fitting epicenter location for any one of the examined model locations along the coasts would generate wave amplitudes lower than that of source 5 and, thus, receive a positive rating relative to source 5. Similarly, for each location *k* out of a total of *m* where high amplitudes were reported (shown in Figure 5-2 and Table 5-1), we calculated the amplitudes of the sources relative to that of source 5 using

$$Amp_i^{\max} = \sum_{j=1}^{n} (Amp_i - Amp_5) / Amp_5 \qquad (2)$$

where i represents the 16 epicenter locations shown in Figure 5-3. A better fitting epicenter location for any one of the locations along the coasts would generate wave amplitudes higher than source 5 and, consequently, receive a positive rating relative to source 5. As a result, the best fitting source *i* should maximize:

$$[Amp_i^{\min} + Amp_i^{\max}] \qquad (3)$$

Figures 5-5, 5-6, 5-7 and 5-17 were created using equations 1, 2 and 3. Similar results were also obtained when we excluded the Azores, Madeira and Lisbon, where there was a large variation in the reported run-up amplitude, from the calculations.

Results

Figure 5-3 and Table 5-3 show all the earthquake sources that were modeled. To facilitate a meaningful comparison among the models, and for lack of detailed geologic constraints for any of the sources, all the models used the same fault dip, dimensions, slip and rigidity (Table 5-4) as those proposed for GBF (Johnston, 1996). Gorringe Bank is the most prominent morphological feature in the area and was suggested to be capable of generating an earthquake with a moment magnitude of 1.26×10^{22} Nm, similar to the one calculated for the 1755 Lisbon earthquake (Johnston, 1996). The rigidity value used for the moment magnitude calculation was very high (6.5×10^{10} Pa), to account for a fault that is almost entirely within oceanic mantle lithosphere (Johnston, 1996). Furthermore, the use of a pure thrust fault with rake 90°, would result in the highest possible transoceanic tsunami amplitudes (see Geist, 1999), enabling us to test each individual feature that govern tsunami propagation, separately.

The effect of fault orientation on tsunami propagation and amplitudes

The first set of simulations was designed to examine the effect of strike orientation on tsunami propagation. Source 3 was chosen for this set because it is the one least susceptible to near-source bathymetric effects in the fault region. The fault strike was rotated 360° at 15° interval. Figure 5-8 shows the variations of maximum wave amplitude as a function of fault orientation, for sites along the U.S. East Coast and the Caribbean. A pattern of two maxima at fault strikes of 165°-180° and 345° yields the highest amplitudes in the Caribbean. A fault strike of 345° is the equivalent to a thrust fault dipping to the ENE (see dashed fault over source 3 in Figure 5-3) and was chosen as a reference model. In this configuration, the leading westward propagating wave is a depression phase (ocean withdrawal), followed by an elevation phase (flooding), in agreement with observations from Madeira (Reid, 1914), Brazil (Kozak *et al.*, 2005; Ruffman, 2006), Newfoundland (Ruffman, 1990), and the Caribbean (O'Loughlin and Lander, 2003). The minima are for fault strikes of 75°-90° and 270°-285°. Note that GBF, which was suggested as a possible source for the 1755 Lisbon earthquake (Johnston, 1996) has strike of 60°, close to one of the amplitude minima. Similarly, many of the tectonic features proposed by Zitellini at al. (2004), which are oriented sub-parallel to the Gorringe Bank, would have also generated low tsunami amplitudes for the Caribbean, contrary to observations.

Figure 5-6 compares fault orientations for source 5, one of our two preferred source locations for the 1755 Lisbon earthquake. It shows that according to the criteria developed in *A method to overcome unreliable historical reports of run-up observations*, source orientation of 345° fits better than source orientations of 330° and 360° and much better than a source oriented at 60°.

The effect of different source locations on tsunami propagation and amplitudes

A fault strike of 345° yields the highest amplitudes in the Caribbean in accordance with historical reports and was therefore used when searching for fault location of the 1755 Lisbon earthquake (see *The 1755 Lisbon earthquake epicenter and fault strike*). Sixteen fault locations were modeled as tsunami sources in the region of study (Figure 5-3) and tsunami amplitudes were calculated in locations along the U.S. East Coast and the Caribbean as well as along the European and African coasts. Fault orientation for all locations was assumed to be 345° following the analysis in *The effect of fault orientation on tsunami propagation and amplitudes*. Figure 5-5 shows a comparison between the different source locations relative to source 5. Based on the method outlined in *A method to overcome unreliable historical reports of run-up observations*, only source 8 fits better than source 5 and source 2 fits slightly worse. Note that source locations 8, 5, and 2 are all located within the Horseshoe Plain. Figure 5-7 shows a comparison between source 5, source 8 and the three previously suggested source locations GBF, MPF, and GCF. It is clear that these three source locations are a poorer fit to the observations than sources 5 and 8. Figures 5-9, 5-10 and 5-11 show maximum wave amplitude plots from earthquake sources located in GBF, GCF and MBF respectively. Figures 5-9 and 5-10 highlight the same conclusion that is portrayed graphically in Figure 5-7. The maximum wave amplitude generated from GBF (060°) is seen in a direction that is almost perpendicular to that observed by the historical reports. As a result, the Caribbean Islands are unaffected. Contrary to historical reports the wave amplitudes along the U.S. East Coast, generated from GCF (349°) are high (~0.5m) and spread over a relatively wide area (as far north as Charleston). MPF from Figure 5-11 cannot be discounted, because it shows that the U.S. East Coast remains relatively untouched and high wave amplitudes are seen in the direction of the Caribbean, thus in agreement with historical reports. Nevertheless, the results shown in Figure 5-7 as well as comparing between MPF and sources 5 and 8 (Figures 5-13, 5-14), indicate that MPF is less likely to be the 1755 Lisbon earthquake source.

The 1755 Lisbon earthquake epicenter and fault strike

Figures 5-5 and 5-7 indicate that the most likely epicenter of the 1755 Lisbon earthquake according to our model simulations is in the Horseshoe Plain area of sources 5 and 8 and not in the previously suggested locations: GBF, MPF and GCF. The Horseshoe Plain area is characterized by high seismicity and is cut by NE-SW trending thrust faults which reach the seafloor (*e.g.*, Sartori, 1994, Zitellini, 2004). Figures 5-6 and 5-8, however, illustrate that the fault was most likely trending NW-SE as opposed to the previously interpreted NE-SW strike orientation. The only known tectonic feature with a NW-SE trend in this area is the inferred Paleo Iberia-Africa Boundary (PIAB), the equivalent structure to the Newfoundland transform fault on the North American plate, which was formed during the opening of the central Atlantic ocean in the Late-Jurassic-Early Cretaceous (Rovere *et al.*, 2004) (Figure 5-1). However, further seismic and multibeam investigations of the west Horseshoe Plain are necessary to test if the PIAB is currently active.

Near field tsunami travel times

Constraining source location based on tsunami travel time is problematic (Gutscher *et al.*, 2006) due to the inaccuracy of historical reports (*e.g.*, a 30 minute difference in arrival time between Porto Santo and Madeira Islands which are only 50 km apart), due to the possibility of landslide-generated tsunamis, and due to the difficulties in simulating tsunami propagation at shallow depths (see *Tsunami theory and numerical model limitations*)

Nevertheless, we computed travel times to locations of historical reports assuming simple aerial distance, tsunami phase speed of $\sqrt{gh}$ with water depths ranging from 2500 m to 4500 m for sources 5 and 8 and 1000 m to 4000 m from source 2 (Table 5-5), Travel times from historical reports were listed by Baptista *et al.* (1998a) and Gutscher *et al.* (2006). Although source location 2 (near MPF) seems to be the best with respect to some of the historical reports, the overall time differences between source location 2 and sources 5 and 8 is minor, implying that an epicenter located further to the west is not unlikely.

Discussion

The effects of regional and near-source bathymetry on tsunami propagation and amplitude

Regional and near-source bathymetry have a significant effect on tsunami propagation in the Atlantic. In a hypothetical case lacking bathymetric features, a tsunami is expected to propagate uniformly in all directions along great circle paths. Figure 5-12 shows a plot of maximum wave amplitude across the Atlantic ocean from source 5. The black lines indicate great circles from earthquake source 5 to different locations along the U.S. East Coast and the Caribbean. The trace of relatively high wave amplitudes in the direction of Virginia Key in southern Florida represents the only wave packet closely following a great circle. All other wave amplitude traces relevant to the locations along the U.S. East Coast and the Caribbean suggest that the corresponding wave packets were either dispersed or deflected by various bathymetric features. Figures 5-13 and 5-14 show a maximum wave amplitude plot from sources 8 and 5 focusing on far-field and near-source effects, respectively. Figure 5-14 suggests that the wave propagating eastward toward the Portuguese coast is unaffected by deep ocean bathymetry, whereas Figure 5-13 implies that propagation westward has a fingering pattern due to wave scattering by bathymetry. The near-source bathymetric elements causing such scattering are the Gorringe Bank, the Ampere and Coral Patch seamounts as well as Madeira Island and the MTR. These bathymetric elements are much shallower than 1500 m, which is the minimal depth required to scatter a tsunami wave according to the analytical analysis of Mofjeld *et al.* (2000). The energy is first highly influenced by the Ampere and Coral Patch seamounts as well as the MTR and Madiera Island. Farther

to the west, wave propagation seems to be influenced by the Mid-Atlantic ridge; in particular the Azores and the Great Meteor and Cruiser seamounts. Higher amplitudes are shown in the vicinity of these bathymetric elements. However, the wave amplitudes decay quickly behind these bathymetric features because these features tend to attenuate the low frequency waves. On the other hand, tsunami wave energy is inferred to be traversing through the low part of the MTR (arrow in Figure 5-14) and later in between the Azores and Great Meteor and Cruiser seamounts, following a great circle toward southern Florida; this wave phase maintains its low frequency content and reaches its trans-Atlantic destination with much higher amplitude. We believe the reason why there are no reports from the 1755 tsunami in southern Florida could be attributed to the northern Bahamas Banks (NBB) which may have acted as a barrier to that area. The rest of the U.S. East Coast remains relatively protected. The northern part of the MTR may have played an important role in shielding the United States, scattering wave energy in that direction. Similarly, the Coral Patch and Ampere seamounts as well as Madeira Island seem to partially scatter the energy in the direction of the Caribbean. The same energy is later scattered a bit more by the Great Meteor and Cruiser seamounts. It is possible that the trace of relatively high amplitudes southward of the Great Meteor seamount may correspond to refracted tsunami energy, responsible for run-up reports in Brazil (Kozak *et al.*, 2005; Ruffman, 2006). Scattering energy by seamounts, however, is relatively ineffective (Mofjeld *et al.*, 2000), allowing enough energy to reach the Caribbean, thus explaining the historical reports. Additional simulations using high-resolution near-shore bathymetry could verify the historical reports claiming that some islands in the Caribbean have experienced greater run-ups than others. Historical run-up reports exist for the entire Antilles arc beginning in Santiago de Cuba and ending in Barbados with the exception of San Juan, Puerto Rico. A possible explanation for the absence of a tsunami report from San Juan is the presence of the ultra-deep Puerto Rico trench (-8350 m) north of San Juan, which may have deflected the energy of the ray path that arrived in a sub-critical angle. (Mofjeld et. al, 2000; Mei, 1999). The waves propagating northward (as indicated from the high wave amplitudes), amid the Gorringe Bank and the Josephine seamount and then passing north of the Azores, may have eventually reached Newfoundland, Canada, explaining the historical reports there. Finally, the wave energy that passed southward east of the Coral Patch seamount may explain the historical reports in the Canary Islands (Reid, 1914).

Implications to tsunami hazard to the U.S. East Coast

The effect of near-source bathymetry on tsunami propagation was tested in order to assess tsunami hazard to the U.S. East Coast from possible future earthquakes in the study area. Two sources were compared: one east and one west of the MTR because both regions have the potential to generate sufficiently strong earthquakes (Buforn *et al.*, 1988). For both sources the maximum wave amplitude was calculated for fault strike orientations varying from 0-360° at 15° interval as described in *The effect of fault orientation on*

tsunami propagation and amplitudes. The wave amplitudes were then averaged out over 360° and measured at deep water locations 3500 and 4000 km (shown by stars in Figure 5-2) from sources 16 and 3, respectively. These deep water locations lie along the azimuths of the U.S. East Coast and the Caribbean coastal sites. A 10% amplitude reduction was factored in to compensate for the difference in distance between 3500 and 4000 km (Ward, 2002) in order to properly compare between the two sources (Figure 5-15). If bathymetry had no effect on wave propagation one would expect wave amplitudes to be identical. The fact that amplitudes vary, further demonstrates the significant effect of the bathymetry on transatlantic tsunami propagation. The calculations from source 3 illustrate an amplitude distribution pattern very similar to that depicted in Figure 5-10 with a maximum in the direction of Virginia Key.). Wave amplitudes from an earthquake source west of the MTR (source 16) show an entirely different amplitude distribution pattern, revealing higher amplitudes in the direction of Baltimore and southward down to Cape Hatteras (Azimuth 292 from source), signifying possible tsunami hazard to these regions. All other places calculated from source 16 show a decrease in amplitudes, except for the waves heading towards Charleston, while the amplitude for Dominica remains relatively unchanged. Figure 5-16 shows a maximum wave amplitude plot from source 16, for a fault with a strike of 30°, west of and adjacent to the MTR. This plot may suggest a possible greater hazard to the U.S. East Coast from earthquakes located in the region west of MTR. We should note, however, that the region west of MTR has so far generated only strike-slip earthquakes (Grimison and Chen, 1986; Buforn *et al.*, 1988) and relative motion there is predicted by plate kinematic models to be strike-slip (Argus *et al.*, 1989; Nocquet and Calais, 2004). Figure 5-17 compares all the different earthquake sources relative to source 5 with respect to the U.S. East Coast only (excluding the Virgina Key), in the same way described in *A method to overcome unreliable historical reports of run-up observations*. In all cases the fault strike was 345°, because it yields the highest amplitudes in the direction of the United States, as shown in Figure 5-8. Source locations 3 and 1 in the Gulf of Cádiz and locations west and north of the Gorringe Bank are calculated to generate the highest amplitude tsunamis along the U.S. East Coast, highlighting the potential hazard from these sources. Figure 5-10 further demonstrates the potential tsunami hazard to the U.S. East Coast from earthquake sources located in the Gulf of Cádiz. Figure 5-11, on the other hand, shows low tsunami risk from an earthquake source located in the MPF. We can therefore conclude that the Gorringe Bank and the north MTR may protect the U.S. East Coast from earthquakes in the Horseshoe Plain, the MPF, the SVF and their surrounding area, but not from the Gulf of Cádiz. Finally, it is important to note that only thrust earthquakes, roughly striking northward may pose tsunami hazard to the U.S. East Coast.

Other considerations – shelf width

The continental shelf along the U.S. East Coast is much wider than along the Caribbean Islands. The large shelf width may have contributed to the

dissipation of tsunami amplitude along the U.S. East Coast and is perhaps one reason for the lack of historical reports from the 1755 Lisbon tsunami. Due to the limitations imposed by the low-resolution bathymetry (*Tsunami theory and numerical model limitations*), we were unable to quantitatively calculate the shelf width effect on wave amplitudes. Nevertheless, Figures 5-12 and 5-13 illustrate that amplitudes in southern Florida are higher than in other areas along the East Coast although the continental shelf in Florida is wider. This suggests that shelf width affects tsunami propagation and amplitudes less than the source fault strike orientation and the seafloor bathymetry along the wave paths.

Conclusions

Methodological tsunami simulations based upon historical reports of both far field and near field effects of the November 1st, 1755 Lisbon tsunami suggest three important conclusions: First, the earthquake seems to have been generated by a NW-SE trending fault located in the center of the Horseshoe Plain, south of the Gorringe Bank. This orientation is almost perpendicular to previously suggested NE-SW trending faults such as GBF and structures south of the Gorringe Bank (Zitellini, 2001). The only known tectonic structure with a NW-SE orientation in this area is the PIAB, although its potential for reactivation remains ambiguous. Moreover, the modeling results allow us to discount the GCF and to a lesser extent the MPF, because both are located too far to the east of the Horseshoe Plain. The GCF can be discounted as a tsunami source because it is predicted to generate relatively high wave amplitudes along the U.S. East Coast, and relatively low ones along the Caribbean. The orientation and location of the MPF are slightly less favorable than our preferred sources in the Horseshoe Plain, even when considering historical reports of tsunami arrival times.

Second, seafloor bathymetry is a significant factor in dictating transatlantic tsunami propagation. In particular, the bathymetry of the Gorringe Bank, the MTR (Josephine Seamount) and the Azores allows waves to reach Newfoundland, but blocks them from reaching most of the U.S. East Coast, with the exception of southern Florida. The Ampere and Coral Patch seamounts, Madeira Island, and the Great Meteor and Cruiser seamounts reduce wave propagation toward the Caribbean. The latter two features partially refract wave energy toward Brazil. Furthermore, high run-up reports in the Caribbean are most likely due to the steep rise in the bathymetry near to shore.

The third conclusion concerns tsunami hazards to the U.S. East Coast from sources located along the eastern Iberian-African plate boundary, which generate sufficiently strong thrust earthquakes. The Gorringe Bank and the north MTR act as near source barriers, protecting most of the U.S. East Coast. For sources located east of MTR and south of the Gorringe Bank, Florida might be at risk if sufficient wave energy manages to pass through the Bahamas. Sources in the Gulf of Cádiz may present a wider hazard to the U.S. East Coast, because they are sufficiently south as to not be affected by

the Gorringe Bank, north MTR, and the Azores. For sources located west of the MTR, the risk is shifted northward in the direction of Baltimore.

It is important to note that the interpretations in this report considered relative amplitudes only. High resolution near-shore bathymetry is crucial for more accurate run-up calculations and tsunami hazard assessments.

Tables

Table 5-1: Sites of historical tsunami run-up reports, sites that were populated in 1755 but did not mention tsunami impact and sites with tsunami reports but no run-up reports

Location	Latitude (°N)	Longitude (°E)	Run-up (m)	Reference
Santiago de Cuba	20.010	-75.810	NRR	OL
Samaná Bay	19.139	-69.355	NRR	OL
St. Martin	18.060	-63.050	4.5	OL
Saba	17.630	-63.230	?-7	OL, Ba2, Ru
Antigua	17.090	-61.800	3.6	OL
Dominica	15.300	-61.380	3.6	OL
Barbados	13.250	-59.530	1.5-1.8	OL,Ba2
Itamaraca (Brazil)	-7.747	-34.825	NRR	Ru
Tamandare (Brazil)	-8.760	35.105	NRR	Ru
Bonavista	49.000	-53.333	NRR	Ru ,Re
Boston	42.358	-71.060	NR	
Baltimore	39.286	-76.615	NR	
New York	40.716	-74.000	NR	
Charleston	32.783	-79.933	NR	
Virginia Key	25.787	-80.216	NR	
Cornwall	50.130	-5.425	2-3.7	Ba2
La Coruña	43.366	-8.383	NR	
Vigo	42.237	-8.721	NR	
Porto	41.150	-8.633	1	Ba
Figueira	40.140	-8.880	NRR	Ba
Porto Novo	39.100	-9.430	NRR	Ba
Lisbon	**38.700**	**-9.183**	**5-15.2**	**Ba2, OL**
Oeiras	38.683	-9.316	>6	Ba
Angra (Azores)	**38.650**	**-27.216**	**?-14.6**	**Ba2**
Huelva	37.250	-6.950	NRR	Ba
S. Vicente	37.000	-8.990	>10	Ba
Cádiz	36.533	-6.300	15-18.3	Ba, OL
Gibraltar	36.143	-5.353	2	Ba
Ceuta	35.888	-5.312	2	Ba
Tangier	**35.766**	**-5.800**	**?-15.2**	**Ba, OL**
Porto Santo	33.066	-16.330	3	Ba
Madeira	**32.630**	**-16.880**	**4-13.2**	**Ba, OL**
Safi	32.283	-9.233	>6	Ba
Canary Islands	28.135	-15.435	NRR	Re

Run-up reports from Baptista *et al.*, 1998a (**Ba1**); Baptista *et al.*, 2003 (**Ba2**); O'Loughlin and F. Lander, 2003 (**OL**); Ruffman, 1990, 2006 (**Ru**); Reid, 1914(**Re**)

Madeira, Lisbon, Angra and Tangier are bolded to indicate the large uncertainty regarding historical run-up amplitudes in those regions

NRR- Tsunami report but no run-up report

NR- No tsunami report

Table 5-2: Regions of reported tsunami run-ups (High) and regions were no run-ups were reported (Low)

	Far field	**Near field**
High run-up region	Caribbean	Lisbon to Morocco, Azores, Madeira
Low run-up region	U.S. East Coast	NW Spain

Table 5-3: Geographical coordinates of source locations shown in Figure 5-3

Source Number	**Latitude (°N)**	**Longitude (°E)**
1	35.480	-8.200
2	36.210	-9.825
3	35.144	-10.055
4	37.150	-10.110
5	36.042	-10.753
6	37.045	-10.780
7	36.940	-11.450
8	36.015	-11.467
9	37.957	-12.052
10	36.835	-12.120
11	36.789	-13.039
12	36.300	-13.051
13	37.991	-13.414
14	37.205	-13.606
15	37.507	-14.514
16	36.748	-15.929

Source locations are measured in the center of each finite fault

Bolded sources were rotated 360° and used to generate Figure 5-15

Table 5-4: Fault parameters used for all simulations

Source Depth (Km)	**Fault Length (Km)**	**Fault Width (Km)**	**Average Slip (m)**	**Dip (°)**	**Rake (°)**
5	200	80	13.1	40	90

Source depth corresponds to the top of the fault plane

Table 5-5: Comparison of historically observed tsunami arrival times with calculated arrival times from sources 5, 8 and 2 (S5, S8 and S2) in Figure 5-3 and compared to calculated arrival times from two sources (1 and 2) at the Marques de Pombal "source B"(N 160) and "source C" (N160N135) (Baptista *et al.*, 1998b) and a source in the Gulf of Cadiz (Gutscher *et al.*, 2006).

Location	Historical time	Travel time	Travel time	Depth (m)	Travel time	Depth (m)	Travel time	Travel time	Travel time GCF
St. Vincente	16 ± 7	16-17	21-22	*4000-3500*	16-19	*1500-1000*	25	21	22
Huelva	50 ± 10	39-44	45-51	*2500-2000*	39-47	*1500-1000*	80	74	52
Cadiz	78 ± 15	43-48	50-56	*2500-2000*	44-54	*1500-1000*	70	70	36
Gibraltar		52-58	59-66	*2500-2000*	55-68	*1500-1000*			53
Tangiers		48-53	54-61	*2500-2000*	50-62	*1500-1000*			54
Porto Santo	60 ± 15	48-51	44-47	*4500-4000*	58-62	*4000-3500*	68	70	59
Madeira	90 ± 15	54-57	49-52	*4500-4000*	64-68	*4000-3500*	78	78	72
Safi	26-34	35-37	37-39	*4500-4000*	37-40	*4000-3500*	75	81	55
Orieas	25 ± 10	34-38	37-42	*2500-2000*	38-47	*2000-1500*	28	22.6	51
Lisbon		35-39	38-43	*2500-2000*	39-48	*1500-1000*			
Figueira	45 ± 10	52-58	54-61	*2500-2000*	61-75	*1500-1000*	53	50	83
Porto		63-71	66-74	*2500-2000*	76-94	*1500-1000*	90	87.5	96

All times are in minutes.

Figures

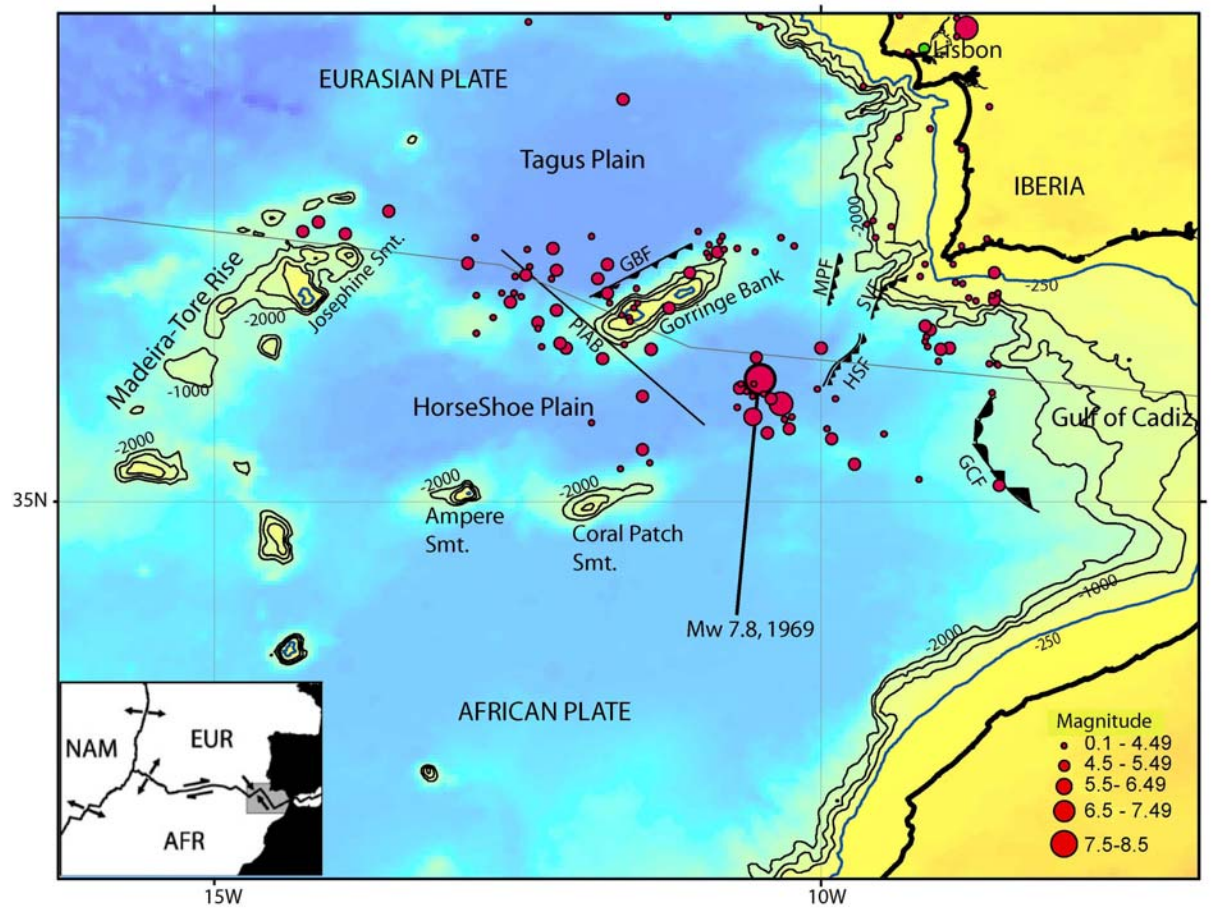

Figure 5-1: Plate tectonic setting (inset) and bathymetric map of the Iberian-African plate boundary. Depth contours: Blue – 250 m; black – 1000, 1500, and 2000 m. Barbed lines - proposed faults by previous studies: GBF - Gorringe Bank Fault; MPF - Marqués de Pombal Fault; SVF- St. Vincente Fault; HSF - Horseshoe Fault; GCF - Gulf of Cádiz Fault. PIAB refers to the Paleo Iberia- Africa Plate Boundary (Rovere *et al.*, 2004). Plates in inset: NAM – North America; EUR- Eurasia; AFR- Africa (after Grácia *et al.*, 2003a).

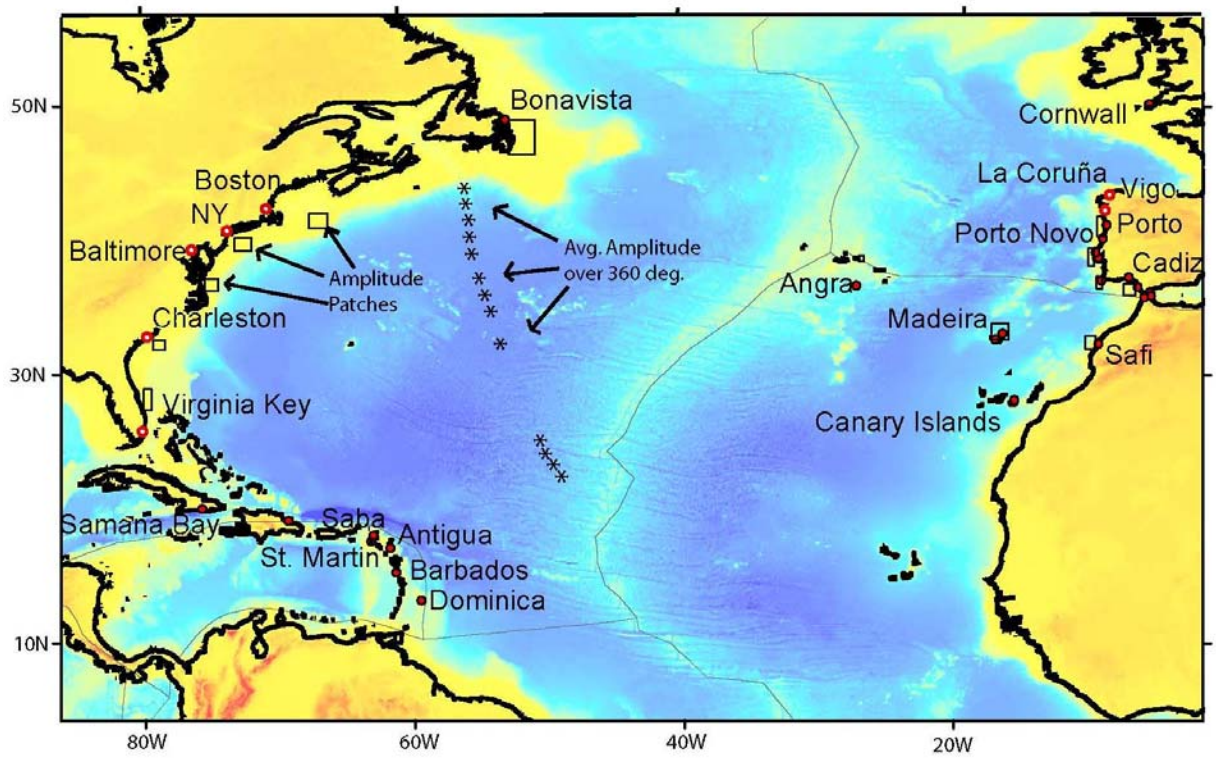

Figure 5-2: Locations of run-up reports in Table 5-1 (red circles) except for Itamaraca and Tamandare (located in Brazil). Also shown are locations along the U.S. East Coast and Spain with no historical reports (open red circles). Rectangles represent patches used to calculate average tsunami amplitudes on the shelf (see *Tsunami amplitude* for explanation). Stars indicate points where average amplitudes over 360 degrees were measured (see *Implications to tsunami hazard to the U.S. East Coast* for explanation).

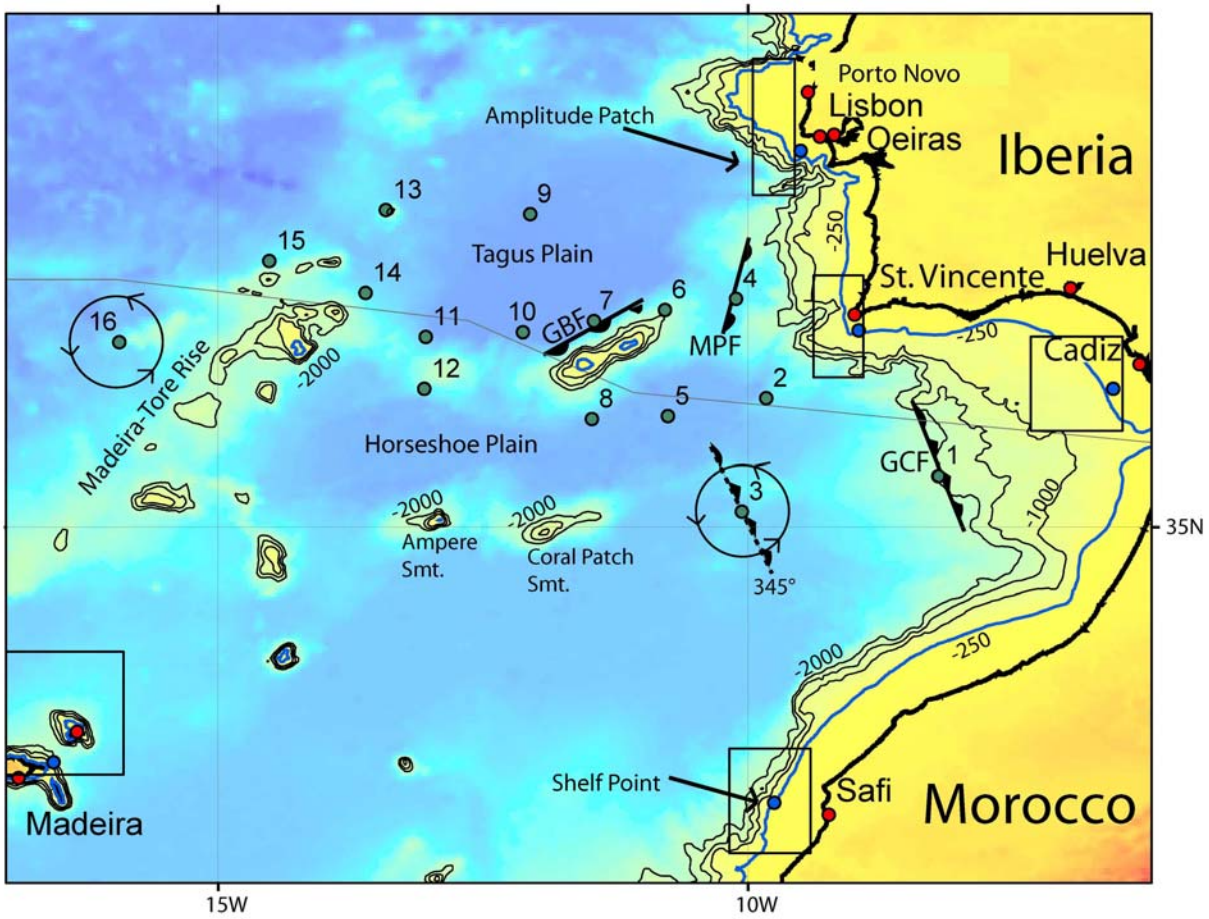

Figure 5-3: Bathymetric map of the Iberian margin. Contours- same as Figure 5-1. Epicenter (placed in the center of finite fault) used to generate tsunami simulations are shown in green circles with corresponding fault model number (see Table 5-3 for.source coordinates). Fault orientation for sources 3 and 16 were rotated 360° at 15° to test for the optimal strike angle generating maximum amplitudes in the Caribbean (see *The effect of fault orientation on tsunami propagation and amplitudes* for explanation) to assess the tsunami hazard to the U.S. East coast (see *Implications to tsunami hazard to the U.S. East Coast* for explanation). Blue circles along the 250 m contour line represent the *shelf points* where the tsunami amplitude was calculated seaward of each historical location. Rectangles- same as in Figure 5-2. Red circles represent cities with historical tsunami reports (see Table 5-1).

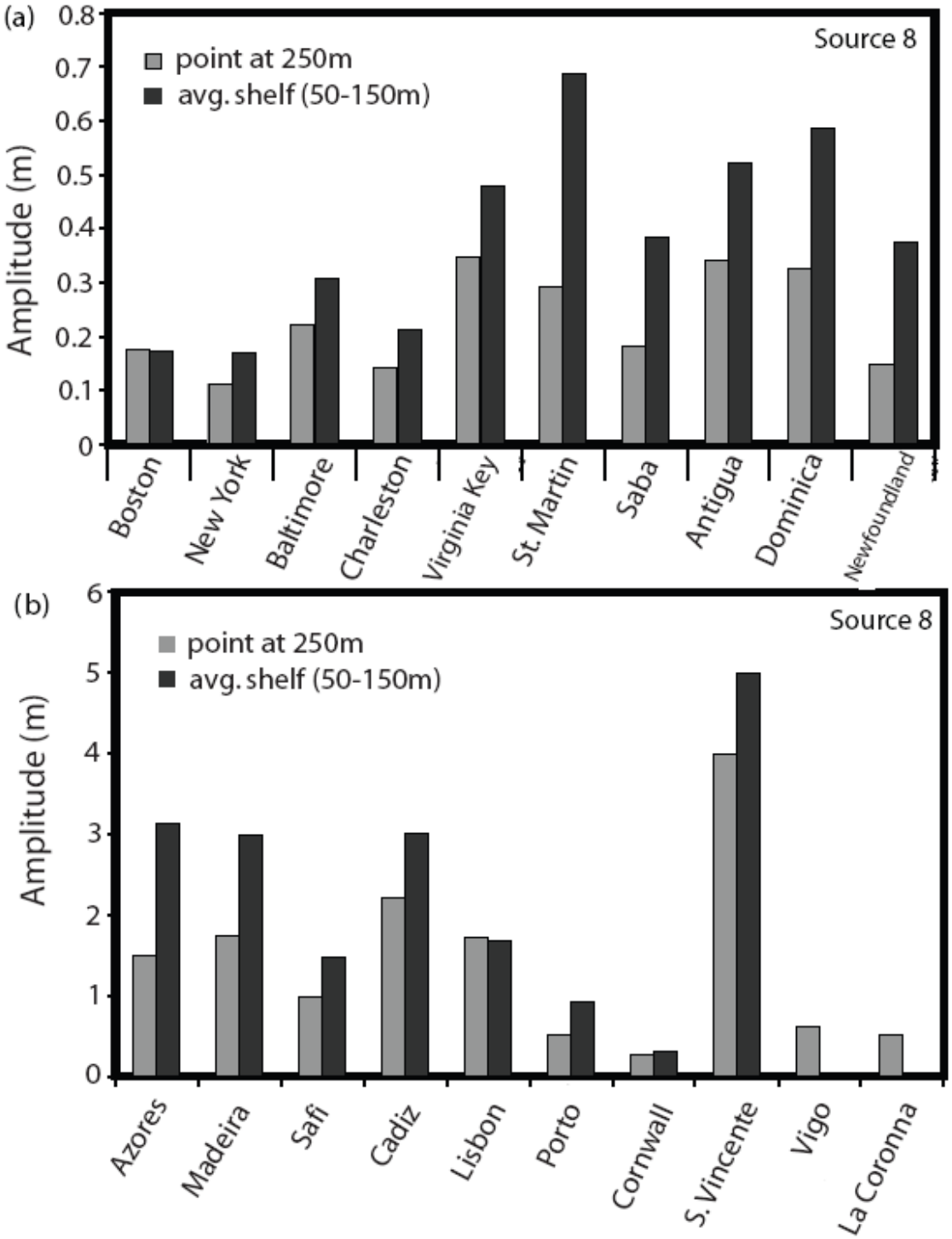

Figure 5-4: Comparison between absolute tsunami amplitudes for fault source location 8 measured at the shelf edge points at 250 m depth and averaged over rectangular patches at depths of 50-150 m (see *Tsunami amplitude* for explanation) for the Caribbean side (a) and for the European and African side (b).

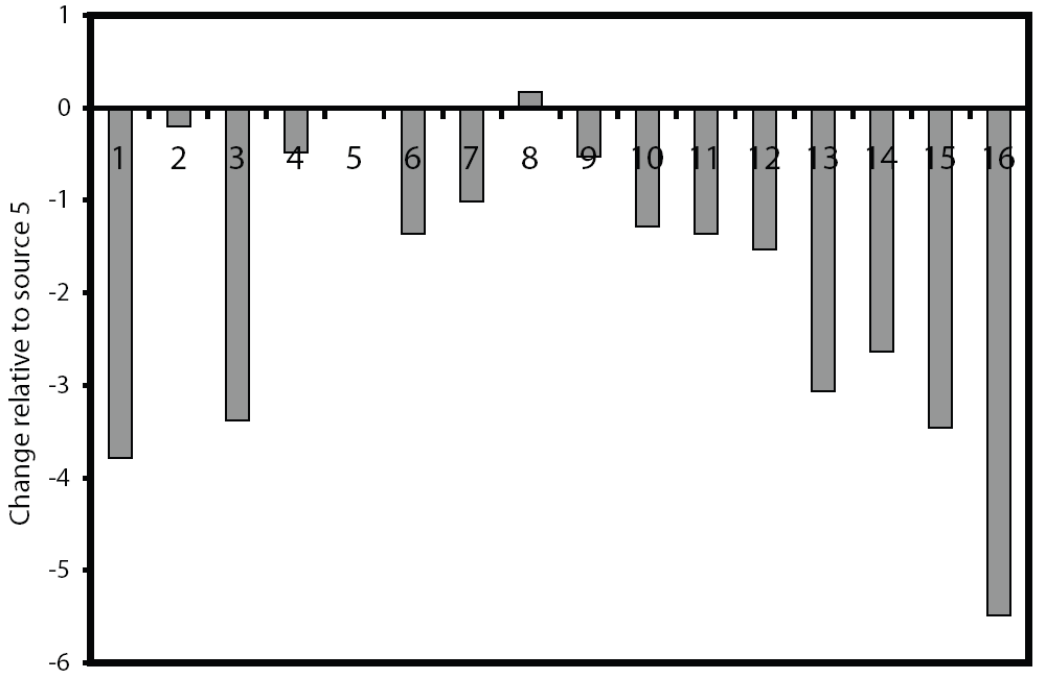

Figure 5-5: Comparison between all fault sources shown in Figure 5-3 and listed in Table 5-3. All of the faults have strike of 345° and their other parameters are listed in Table 5-4. Positive bars represent sources that are better fitting than source 5 to be the 1755 Lisbon epicenter. Negative bars represent sources that are worse fitting than source 5 to be the 1755 Lisbon epicenter (see *A method to overcome unreliable historical reports of run-up observations* for explanation). According to this test source 8 is the best candidate source for the 1755 Lisbon earthquake.

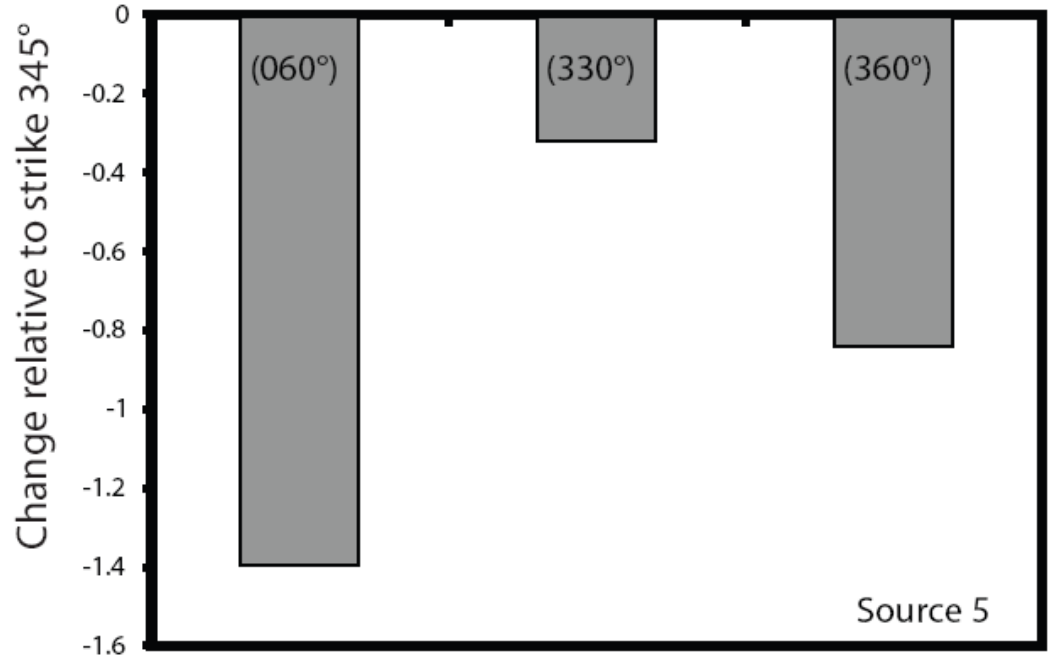

Figure 5-6: Comparison between tsunami amplitude from different fault orientations located in source 5. Negative bars represent fault orientations that do not fit as well as the model with strike of 345° (see *A method to overcome unreliable historical reports of run-up observations* for explanation). A strike of 60°, like the one suggested for GBF, has the worst fitting.

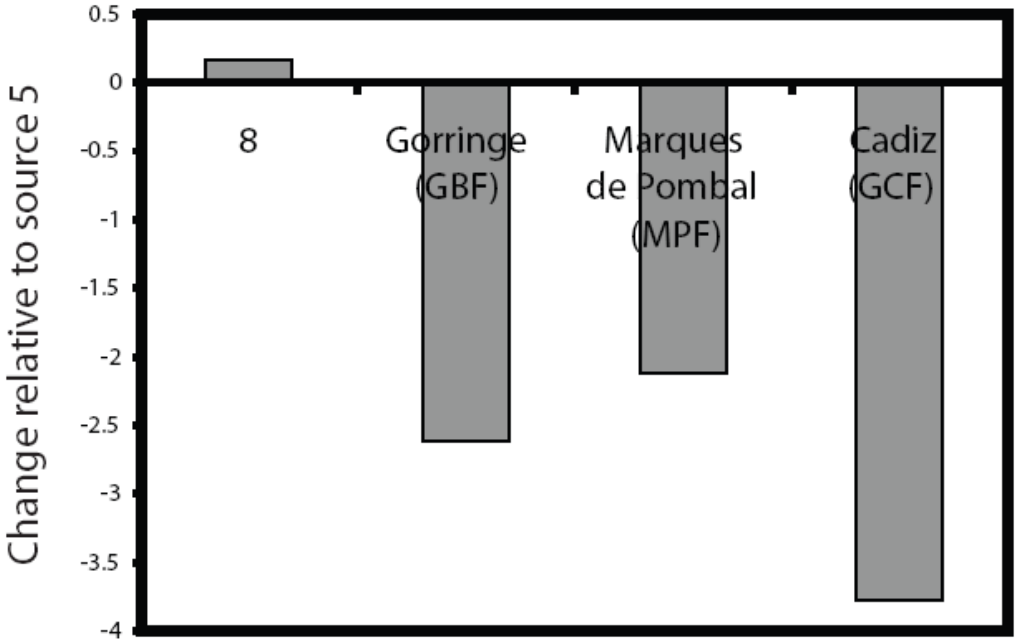

Figure 5-7: Comparison between sources 5 an 8 and the previously suggested sources of the 1755 Lisbon earthquake: GBF (Johnston, 1996); MPF (Zitellini *et al.*, 2001); and GCF (Gutscher et. al, 2006) (sources 7, 4 and1 respectively); fault strikes were 060°, 020° and 349°, respectively. Positive bars represent source locations that are better fitting than source 5 to be the 1755 Lisbon epicenter. Negative bars represent source locations that are less fitting than source 5 to be the 1755 Lisbon epicenter (see *A method to overcome unreliable historical reports of run-up observations* for explanation). Both Sources 5 and 8 are better fitting than the three previously suggested fault models.

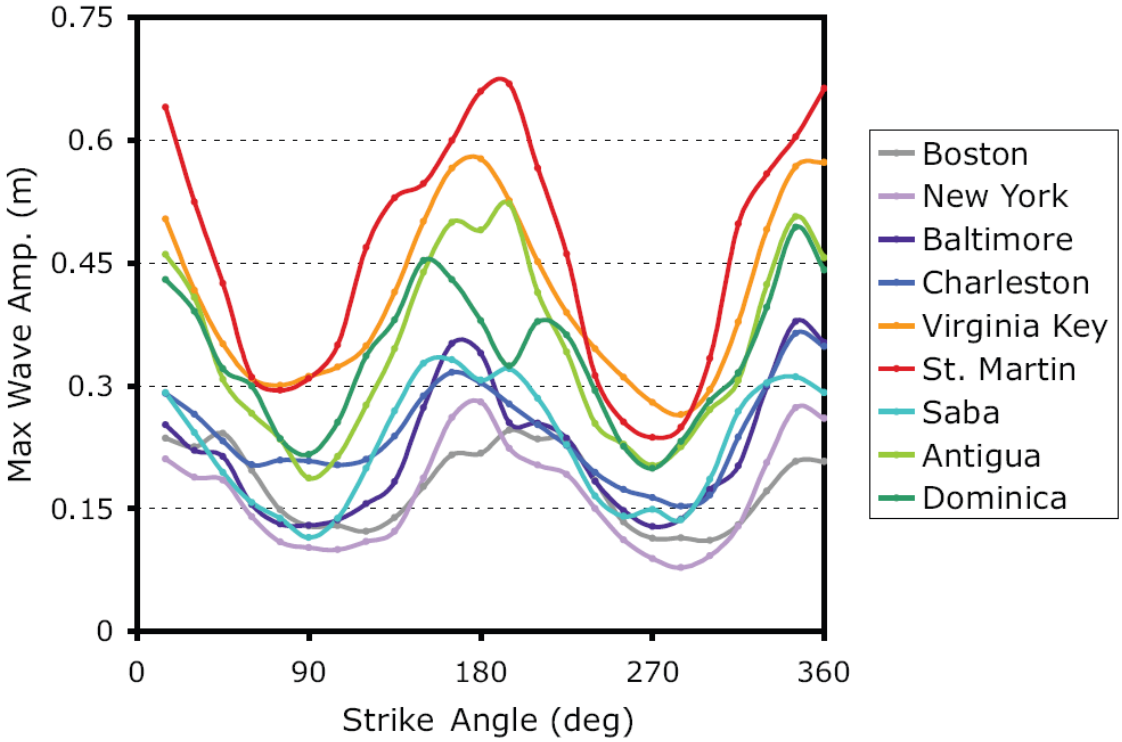

Figure 5-8: Comparison between the absolute tsunami amplitudes as a function of variation in the fault strike orientation, using source 3. Maxima are at 165°-185° and 345° and minima are at 75°-90° and 270°-285°.

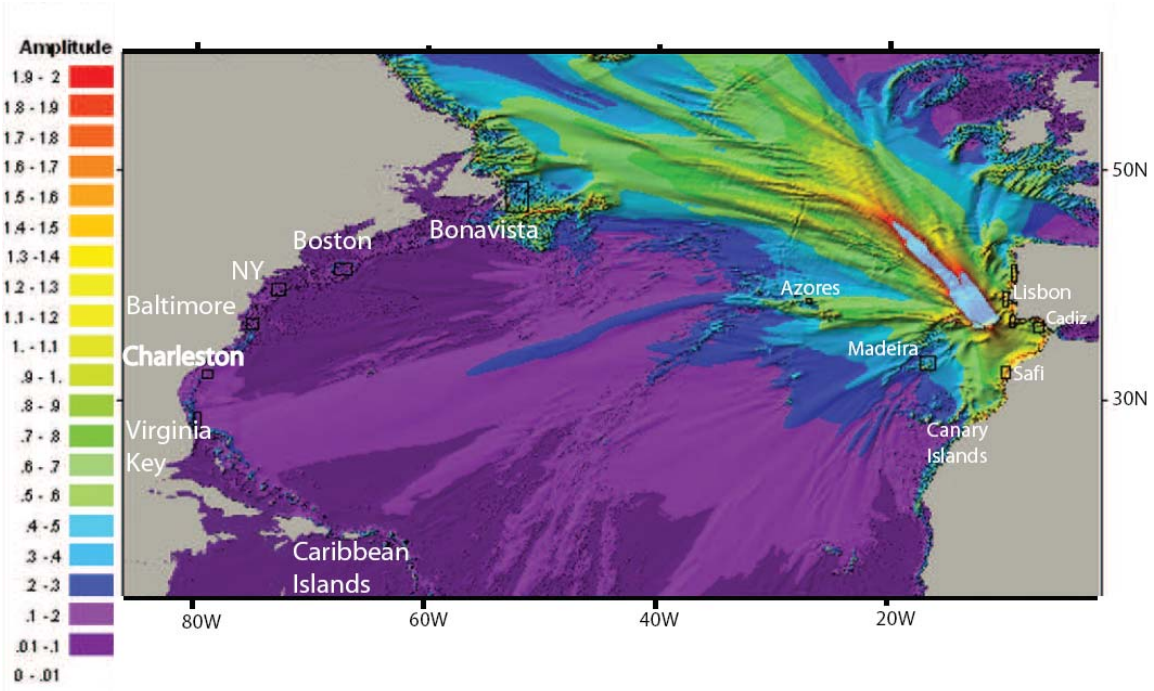

Figure 5-9: Maximum wave amplitude (m) from an earthquake source located in GBF. The strike angle used is 60° similar to that suggested by Johnston (1996) and Grandin *et al.* (2007). The scale ranges from 0-2 m, with 0.1 m intervals. The main wave energy propagates NNW, leaving the Caribbean Islands almost unaffected.

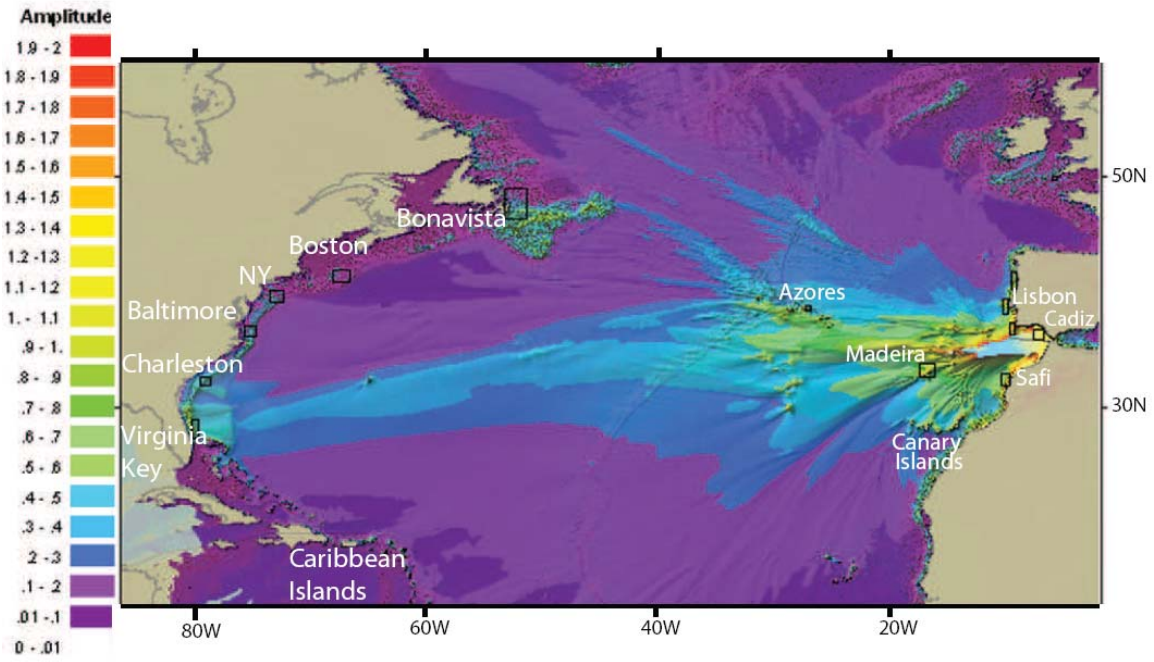

Figure 5-10: Maximum wave amplitude (m) from an earthquake source located in GCF with fault strike of 349° similar to that suggested by Gutscher *et al.* (2002; 2006) and Thiebot and Gutscher (2006). Scale- same as in Figure 5-9. Contrary to historical records low amplitudes are seen in the vicinity of the Caribbean, whereas high amplitudes are seen along the U.S. East Coast, south of Charleston.

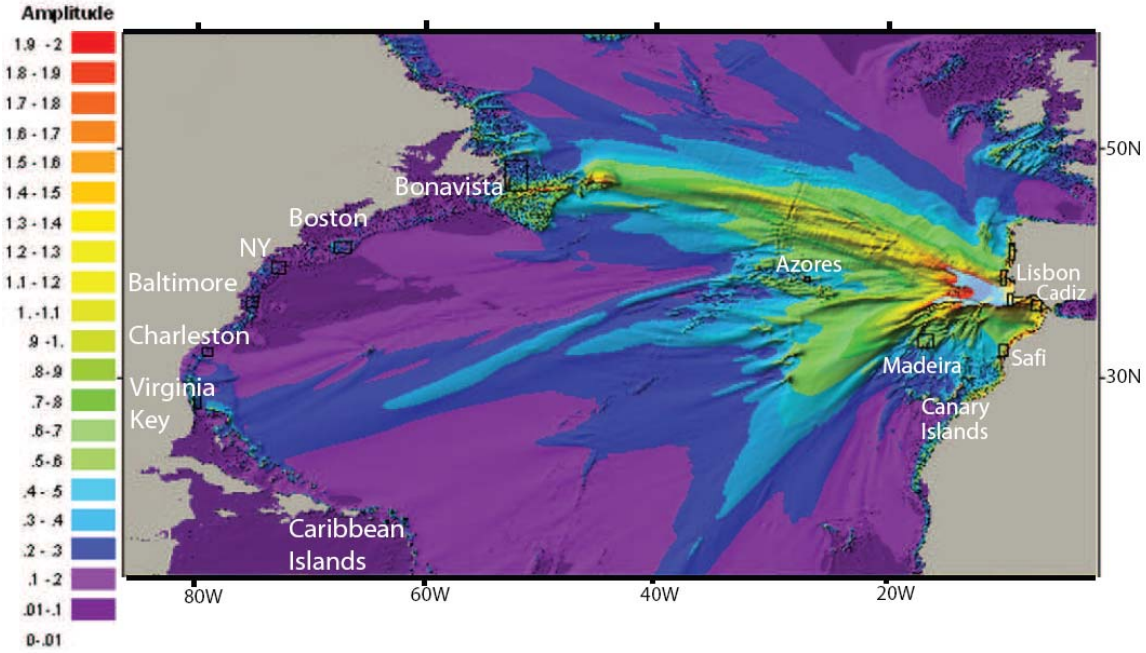

Figure 5-11: Maximum wave amplitude (m) from an earthquake source located in MPF with fault strike of 20°. Location and strike are after Zitellini *et al.* (2001) and Grácia *et al.* (2003a). Scale- same as in Figure 5-9. Note that although a tsunami generated at the MPF is not expected to affect the U.S. Atlantic coast, it predicts lower amplitude in the Caribbean and higher amplitude in northwest Spain than Figure 5-13.

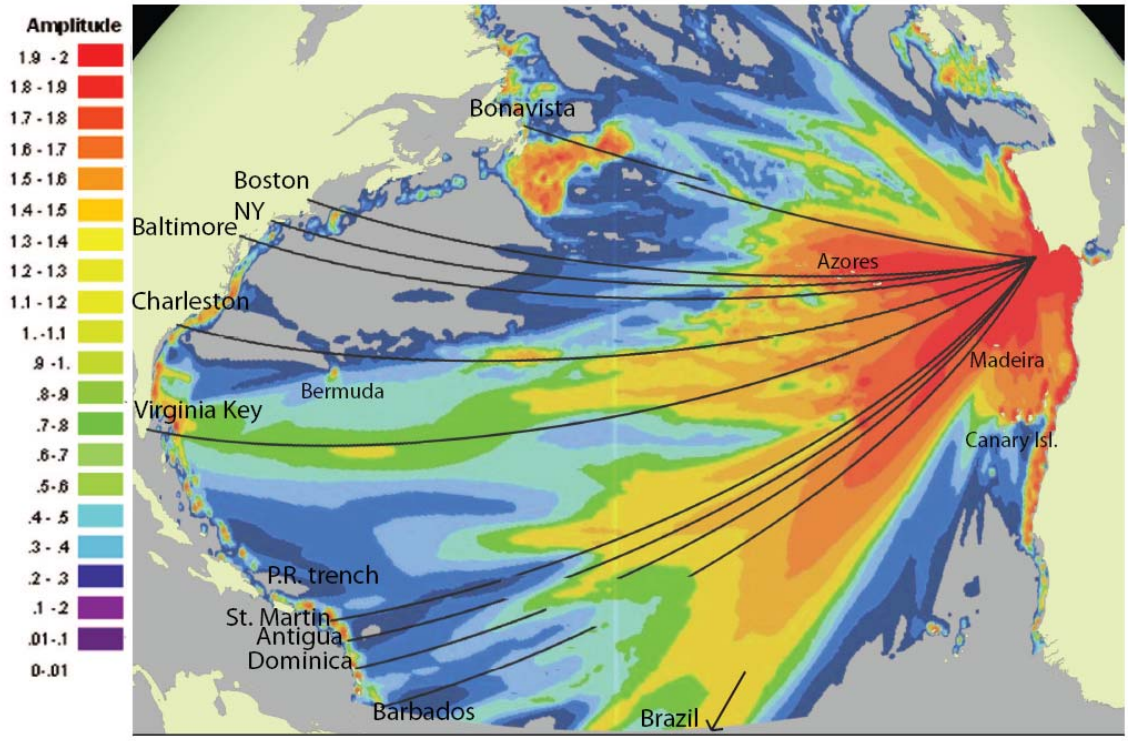

Figure 5-12: Maximum wave amplitude (m) projected on a sphere from an earthquake source located in source 5. The scale ranges from 0-1 m. Warm colors indicate high amplitudes and cold colors low amplitudes. Black lines indicate great circle paths between source 5 and locations along the U.S. East Coast and the Caribbean. The wave energy heading toward Virginia Key in southern Florida is the only one following a great circle path. All other wave energies are scattered by topography.

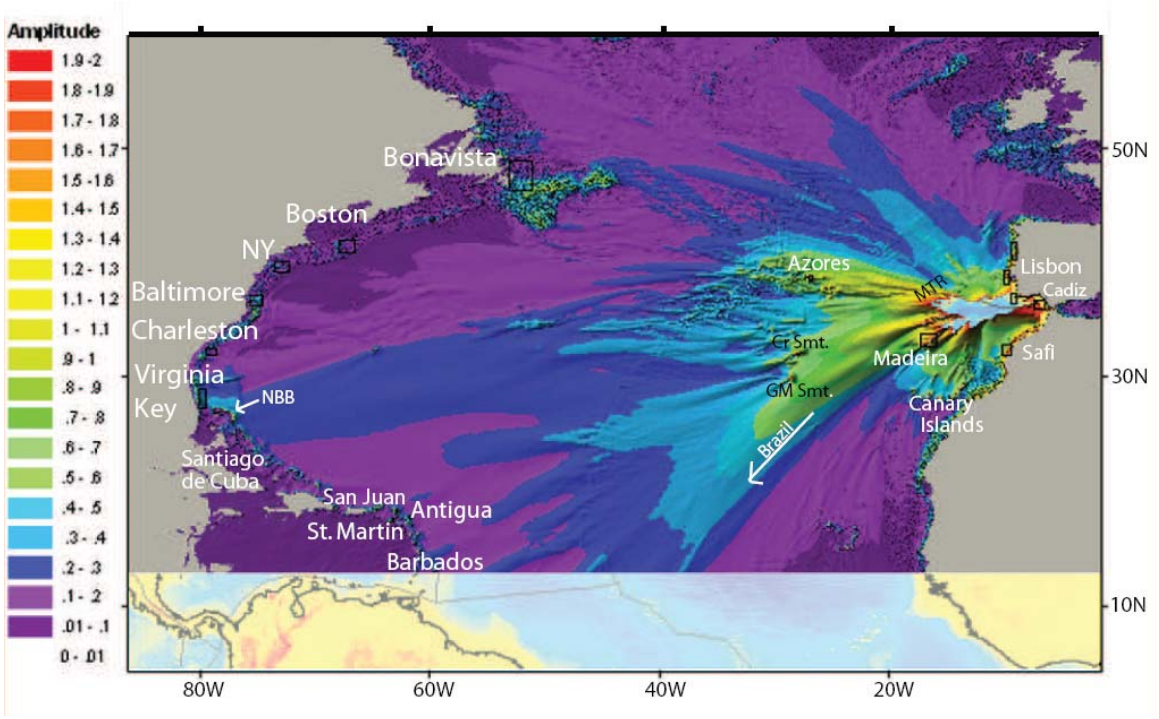

Figure 5-13: Maximum wave amplitude (m) from the best fit earthquake source located in source 8. Scale- same as in Figure 5-9. Wave scattering is mainly caused by the Madeira Island, Madeira Tore-Rise (MTR), the Azores, the Great Meteor (GM) and Cruiser (Cr) seamounts. The ray passing in between the Azores and the Great Meteor seamount reaches southern Florida. The rest of the U.S. East Coast is relatively unaffected by the tsunami. NBB-northern Bahamas Banks.

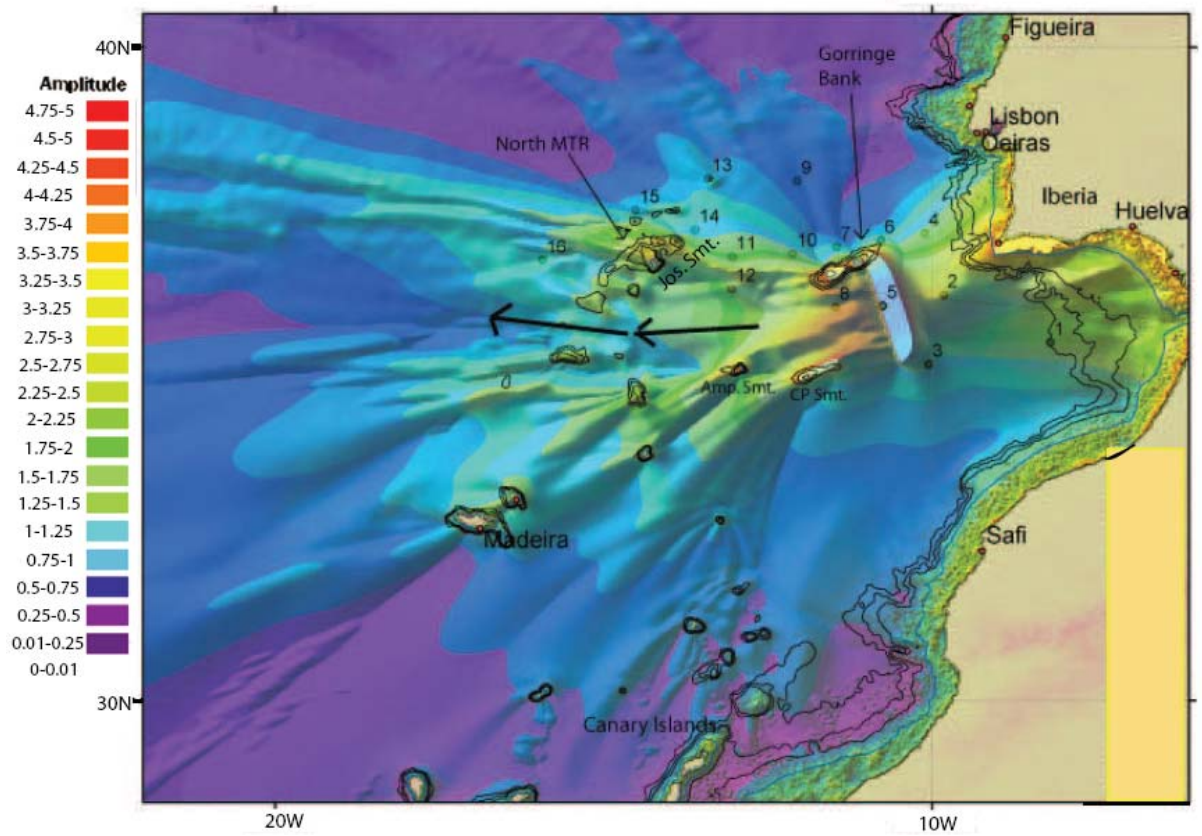

Figure 5-14: Maximum wave amplitude (m) from an earthquake source located in source 5, illustrating the effects of near-source topography. The scale ranges from 0-5 m, with 0.1 m intervals. Tsunami propagation eastward is undisturbed by topography. High amplitudes in the Gorringe Bank, Coral Patch (CP) and Ampere (Amp) seamounts, and Madeira Tore-Rise (MTR) are due to wave amplification by these relatively shallow features (> -1500 m), although these features scatter the long period component (see *The effects of regional and near-source bathymetry on tsunami propagation and amplitude* for explanation). The arrows represent a less-attenuated wave, which traverses between the Azores and the Great Meteor seamount heading toward southern Florida (see Figure 5-13). Jos. Smt.- Josephine seamount.

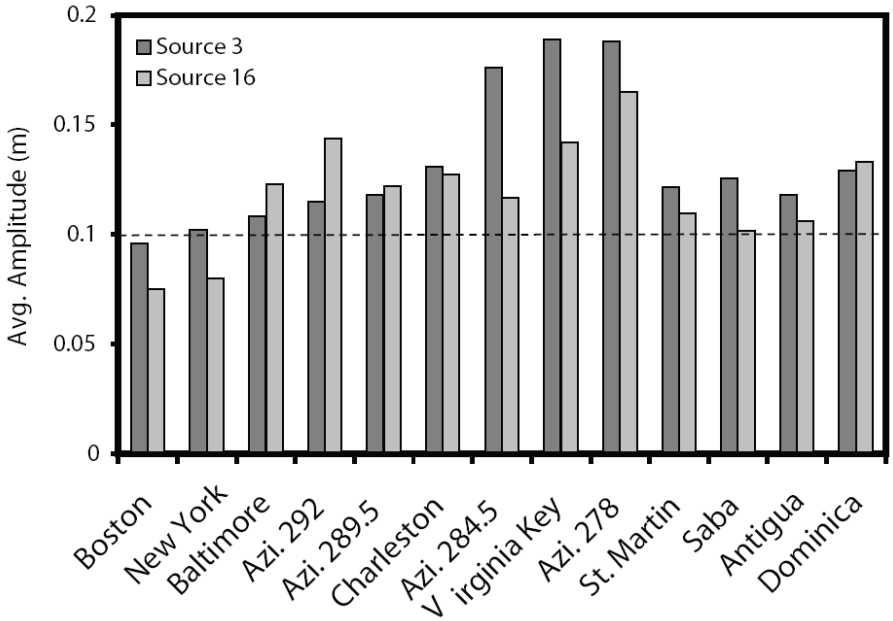

Figure 5-15: Comparison of tsunami amplitudes from sources located to the east (source 3) and the west (source 16) of the MTR. Amplitudes are measured in deep water 4000 km west from source 3 and 3500 km west from source 16 (see stars in Figure 5-2). The amplitudes are measured in the direction of sites along the U.S. East Coast and the Caribbean as indicated at the bottom of each bar. Amplitudes from source 16 were reduced by 10% in order to compensate for the 500 km shorter propagation path relative to source 3 (Ward, 2002). Amplitudes were averaged over 24 fault orientations covering 360° at 15° interval. Differences in amplitudes illustrate the effect of the bathymetry on tsunami propagation, in particular the effects of the north MTR.

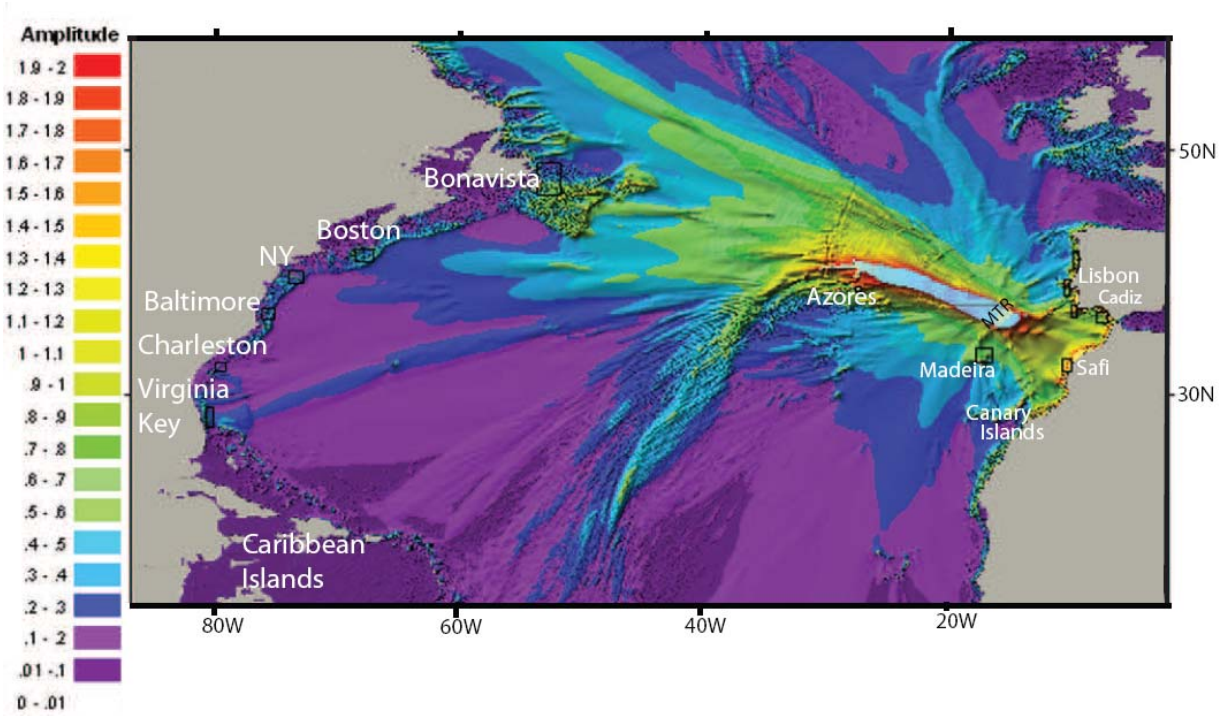

Figure 5-16: Maximum wave amplitude from an earthquake source located in source 16 and oriented 30°. Scale-same as Figure 5-9. High amplitudes are seen in a wider area along the U.S. East Coast relative to Figure 5-13, highlighting the greater hazard from earthquake sources located west of MTR.

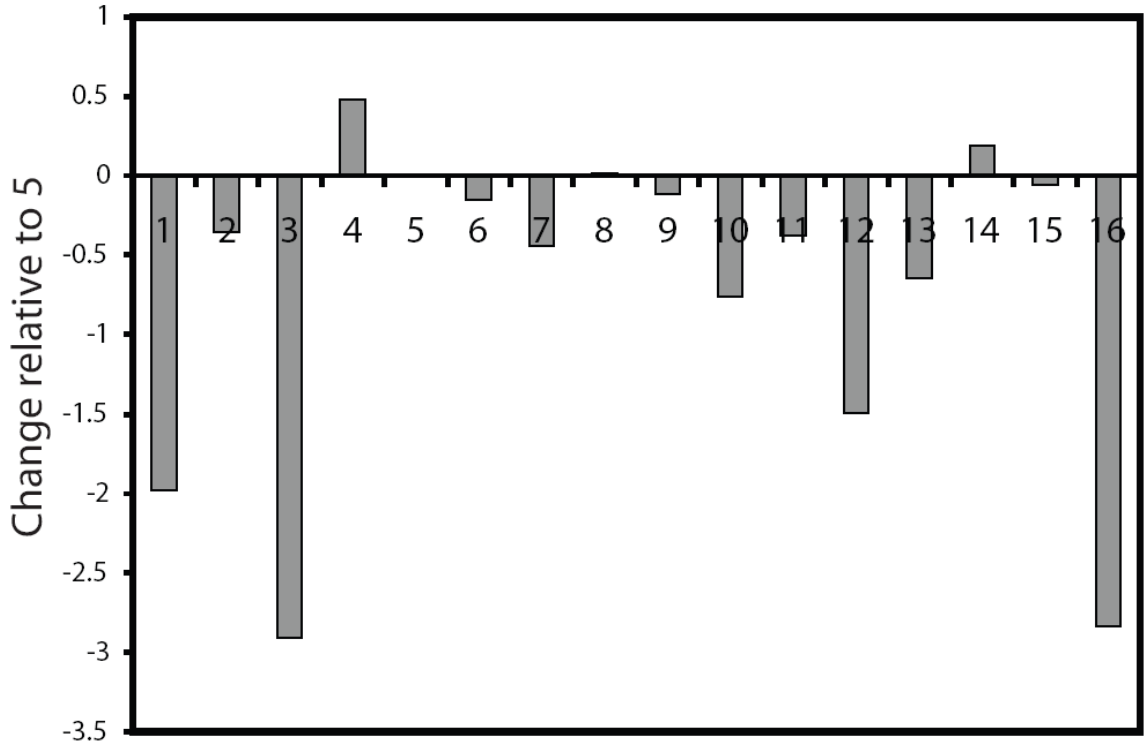

Figure 5-17: Comparison between all of the modeled sources relative to source 5, for sites along the U.S. East Coast (see *A method to overcome unreliable historical reports of run-up observations* for explanation). See Figure 5-3 and Table 5-3 for source locations. Positive bars represent sources that may have a lower impact than source 5 on the U.S. East Coast. Negative bars represent sources that are calculated to have greater impact than source 5 to the U.S. East Coast (see *Implications to tsunami hazard to the U.S. East Coast*). Sources 1, 3, 12, 16 and 10 are calculated to have the greatest impacts to the U.S. East Coast.

References

Anonyme, (1756), J. Historique sur les Matie'res du Tems (T. 79) Jan. 1756, p. 41-45 (`http://gallica.bnf.fr/ark:/12148/bpt6k105284f/f2.table`).

Argus, D.F., Gordon, R.G., DeMets, C., Stein, S., 1989, Closure of the Africa-Eurasia-North America plate motion circuit and tectonics of the Gloria fault: *Journal of Geophysical Research*, *v. 94*, p. 5585-5602.

Baptista, M.A., Heitor, S., Miranda, J.M., Miranda, P.M.A., Mendes Victor, L., 1998a, The 1755 Lisbon earthquake; evaluation of the tsunami parameters: *Journal of Geodynamics*, *v. 25*, p. 143–157.

Baptista M.A., Miranda, P.M.A., Miranda, J.M., Mendes Victor, L., 1998b, Constraints on the source of the 1755 Lisbon tsunami inferred from numerical modeling of historical data on the source of the 1755 Lisbon tsunami: *Journal of Geodynamics*, *v. 25*, p. 159–174.

Baptista, M.A., Miranda, J.M.., Chierici, F., Zitellini, N., 2003, New study of the 1755 earthquake source based on multi-channel seismic survey data and tsunami modeling: *Natural Hazards and Earth System Sciences*, *v. 3*, p. 333–340.

Baptista, M.A., Miranda, J.M.., Luis, J.F., 2006, In search of the 31 March 1761 earthquake and tsunami sources: *Bulletin of the Seismological Society of America*, *v. 96*, p. 713-721.

Blank, P.L., 2008, The tsunami in Cadiz on 1 Novermber 1755: A critical analysis of reports by Antonio Ulloa and Louis Godin, CRAS2A-2718, 11 pp.

Borges,J.F.,Fitas, A. J. S.,Bezzeghoud, M., and Teves-Costa, P., 2001, Seismotectonics of Portugal and its adjacent Atlantic area: *Tectonophysics*, *v. 337*, p. 373-387.

Buforn E., Udías, A., Mézcua, J., 1988, Seismicity and focal mechanisms in south Spain: *Bulletin of the Seismological Society of America*, *v. 78*, p. 2008-2224.

Buforn E., M. Bezzegoud, A. Udias, C. Pro, 2004, Seismic Sources on the Iberia-African Plate Boundary and their Tectonic Implications: *Pure and Applied Geophysics*, *v. 161*, p. 623-626

Chester, D.K., 2001, The 1755 Lisbon earthquake: *Progress in Physical Geography*, *v. 25*, p. 363–383.

Courant R., Friedrichs, K., Lewy, H., 1928, Über die partiellen Differenzengleichungen der mathematischen Physik: *Mathematische Annalen*, *v. 100*(1), p. 32–74.

Fernandes R.M.S, Miranda J.M., Meijninger B.M.L., Bos M.S., Noomen R., Bastos L., Ambrosius B.A.C., Riva R.E.M., 2007, Surface Velocity Field Of The Ibero-Maghrebian Segment Of The Eurasia-Nubia Plate Boundary: *Geophysical Journal International*, *v. 169*(1), p. 315-324.

Fukao, Y., 1973, Thrust faulting at a lithospheric plate boundary: The Portugal earthquake of 1969: *Earth and Planetary Science Letters*, *v. 18*, p. 205-216.

Geist, E.L., 1999, Local tsunamis and earthquake source parameters: *Advances in Geophysics*, *v. 39*, p. 117-209.

Gisler, G., Weaver, R., Gittings, M. L., 2006, SAGE calculations of the tsunami threat from La Palma: *Science of Tsunami Hazards*, *v. 24*, p. 288-301.

Grácia, E., Danõbeitia, J.J., Vergés, J., PARSIFAL team, 2003a, Mapping active faults offshore Portugal (36°N–38°N): Implications for seismic hazard assessment along the southwest Iberian margin: *Geology*, *v. 31*, p. 83– 86.

Grácia, E., Pallas, R., Casas, D., Willmot, V., Grácia -Orellan, J., Danõbeitia, J.J., The Hits Cruise Party, 2003b, Submarine landslides associated to active faulting offshore Portugal (SW Iberian Margin): Paleoseismic implications. EGS–AGU–EUG Joint Assembly, Abstracts from the meeting held in Nice, France, 6–11 April 2003, abstract #13064.

Grandin, R., Borges, J.F., Bezzeghoud, M., Caldeira, B., Carrilho, F., 2007, Simulations of strong ground motion in SW Iberia for the 1969 February 28 (Ms=8.0) and the 1755 November 1 (M~ 8.5) earthquakes – I. Velocity model. II. Strong ground motion simulations: *Geophysical Journal International*, *v. 171*(2), p. 807-822(16).

Grimison, N.L., and Chen, W., 1986, The Azores-Gibraltar plate boundary: Focal mechanisms, depth of earthquakes and their tectonical implications: *Journal of Geophysical Research*, *v. 91*, p. 2029-2047.

Gutscher, M.A., Malod, J., Rehault, J.P., Contrucci, I., Klingelhoefer, F., Mendes-Victor, L., Spackman, W., 2002, Evidence for active subduction beneath Gibraltar: *Geology*, *v. 30*, p. 1071- 1074.

Gutscher, M.-A., 2004, What caused the Great Lisbon earthquake?: *Science. v. 305*, p. 1247–1248.

Gutscher, M.-A., Baptista, M.A., Miranda, J.M., 2006, The Gibraltar Arc seismogenic zone: Part 2. Constraints on a shallow east dipping fault plane source for the 1755 Lisbon earthquake provided by tsunami modeling and seismic intensity: *Tectonophysics*, *v. 426*, p. 153-166.

Hayward, N., Watts, A.B., Westbrook, G.K., Collier, J.S., 1999, A seismic reflection and GLORIA study of compressional deformation in the Gorringe Bank region, eastern North Atlantic: *Geophysical Journal International, v. 138*, p. 831-850.

Johnston, A., 1996, Seismic moment assessment of earthquakes in stable continental regions –III New Madrid 1811-1812, Charleston 1886 and Lisbon 1755: *Geophysical Journal International*, v. 126, p. 314-344.

Kozak, J.T., Moreira, V.S., Oldroyd, D.R., 2005, Iconography of the 1755 Lisbon Earthquake: Academy of Sciences of the Czech Republic, Prague, 82 pp.

Lin, J., Stein, R.S., 2004, Stress triggering in thrust and subduction earthquakes, and stress interaction between the southern San Andreas and nearby thrust and strike-slip faults: *Journal of Geophysical Research*, *v. 109*, B02303, doi:10.1029/2003JB002607.

Liu, P.L.-F., Woo, S.-B., and Cho, Y.-S., 1998, Computer Program for Tsunami Propagation and Inundation, sponsored by National Science Foundation, `http://ceeserver.cee.cornell.edu/pll-group/comcot_down.htm`.

Lockridge, P.A., Lowell, S., Whiteside, L.A., Lander, J.F., 2002, Tsunamis and tsunami-like waves of the Eastern United States: *International Journal of the Tsunami Society*, *v. 20*(3), p. 120-157.

Machado, F., 1966, Contribução para o estudo do terremoto de 1 de Novembro de 1755: *Revista de la Facultad de Ciências de Lisbon*, ser. C, *v. 14*, p. 19-31.

Mader, C.L., 2001, Modeling the 1755 Lisbon tsunami: *Science of Tsunami Hazards*, *v. 19*, p. 93-116.

Martinez-Solares, J.M., Lopez, A., Mezcua, J., 1979, Isoseismal map of the 1755 Lisbon earthquake obtained from Spanish data: *Tectonophysics*, *v. 53*, p. 301-313.

Mei, C. C., 1989, The Applied Dynamics of Ocean Surface Waves: World Scientific, Section 3, Singapore, pp. 740.

Mofjeld, H.O., Titov, V.V., Gonzalez, F.I., Newman, J.C., 2000, Analytic Theory of Tsunami Wave Scattering in the Open Ocean With Application to the North Pacific: NOAA Technical Memorandum OAR PMEL-116.

Moreira, V.S., 1985, Seismotectonics of Portugal and its adjacent area in the Atlantic.: *Tectonophysics*, *v. 117*, p. 85-96.

Nocquet, J.M., Calais, E., 2004, Geodetic measurements of crustal deformation in the Western Mediterranean and Europe: *Pure and Applied Geophysics*, *v. 161*, p. 661-681.

O'Loughlin, K.F., Lander, J.F., 2003, Caribbean tsunamis: A 500-year history from 1498-1998: Kluwer Academic Publications, 280 pp.

Reid, H.F., 1914, The Lisbon earthquake of November 1, 1755: *Bulletin of the Seismological Society of America*, *v. 4*(2), p. 53-80.

Rovere, M., Ranero, C.R., Sartori, R., Torelli, L., Zitellini, N., 2004, Seismic images and magnetic signature of the Late Jurassic to Early Cretaceous Africa-Eurasia plate boundary off SW Iberia: *Geophysical Journal International*, *v. 158*(2), p. 554–568.

Ruff, L.J., 2003, Some aspects of energy balance and tsunami generation by earthquakes and landslides: *Pure and Applied Geophysics*, *v. 160*, p. 2155-2176.

Ruffman, A., 1990, Tsunamis of Eastern Canada, 1755- Present [Abstract], Workshop JW.1. Tsunami Sources Around Europe, European Geophysical Society, XV General Assemble, April 23-27, Copenhagen, Denmark. Annales Geophysicæ, Special issue, Abstract JW.1-11, p. 334-335.

Ruffman, A., 2006, From an Ephemerides to 'Observation on The Changes of The Air': Documenting The far-field parameters of the November 1, 1755 "Lisbon" Tsunami in the western Atlantic [Abstract]: Atlantic Geoscience Society 32nd Colloquium and Annual Meeting, February 3-4, Greenwhich, Nova Scotia. Program with Abstracts, p. 63-64, *Atlantic Geology*, *v. 42*(1), p. 111.

Sartori, R., Torelli, L., Zitellini, N., Peis, D., Lodolo, E., 1994, Eastern segment of the Azores Gibraltar line (central-eastern Atlantic): An oceanic plate boundary with diffuse compressional deformation: *Geology*, *v. 22*, p. 555–558.

ten Brink, U., Twichell, D., Geist, E., Chaytor, J., Locat, J., Lee, H., Buczkowski, B., and Sansoucy, M., 2007**,** The current state of knowledge regarding potential tsunami sources affecting U.S. Atlantic and Gulf Coasts: U.S. Geological Survey Administrative Report, 162 pp**.**

Terrinha, P., Pinheiro, L.M., Henriet, J.-P., Matias, L., Ivanov, M.K., Monteiro, J.H., Akhmetzhanov, A., Volkonskaya A., Cunha, T., Shaskin, P., Rovere, M., 2003, Tsunamigenic-seismogenic structures, neotectonics, sedimentary processes and slope instability on the southwest Portuguese Margin: *Marine Geology*, *v. 195*, p. 55-73.

Thiebot, E., Gutscher, M.A., 2006, The Gibraltar Arc seismogenic zone (part 1): Constraints on a shallow east dipping fault plane source of the 1755 Lisbon earthquake provided by seismic data, gravity and thermal modeling: *Tectonophysics*, *v. 426* (in press) 1-2, p.135-152, *Tectonophysics*, *v.426* (in press). 1-2, p.135-152.

Toda, S., Stein, R.S., Richards-Dinger, K., Bozkurt, S., 2005, Forecasting the evolution of seismicity in southern California: Animations built on

earthquake stress transfer: *Journal of Geophysical Research*, B05S16, doi:10.1029/2004JB003415.

Ward, S.N., 2002, Tsunamis. Encyclopedia of Physical Science and Technology: *Academic Press*, *v. 17*, p. 175-191. http://es.ucsc.edu/~ward/papers/tsunami_ency.pdf

Zitellini, N., Mendes-Victor, L., Córdoba, D., Dañobeitia, J., Nicolich, R., Pellis, G., Ribeiro, A,Sartori, R., Torelli, L., Bartolomé, R., Bortoluzzi, G., Calafato, A., Carrilho, F., Casoni, L., Chierici, F., Corela, C., Correggiari, A., Della Vedova, B., Gràcia, E, Jornet, P., Landuzzi, M., Ligi, M., Magagnoli, A., Marozzi, G., Matias, L.M., Penitenti, D., Rodriguez, P., Rovere, M., Terrinha, P., Vigliotti, L., and Zahinos Ruiz, A., 2001, Source of the 1755 Lisbon earthquake and tsunami investigated: *EOS Transactions of American Geophysical Union*, *v. 82*, 285 pp.

Zitellini, N., Rovere, M., Terrinha, P., Chierici, F., and Matias, L., BIGSETS team, 2004, Neogene through Quaternary tectonic reactivation of SW Iberian passive margin: *Pure and Applied Geophysics*, *v. 161*, p. 565– 587.

Chapter 6: Review of Other Tsunamigenic Earthquake Sources That May Affect the U.S. Atlantic Coast

Introduction

Earthquake-generated tsunamis generally originate by the sudden vertical movement of a large area of the seafloor during a large magnitude (M>6.5) earthquake. Such movement can be generated by reverse or thrust faulting, most often in subduction zones. The Atlantic Ocean basin is generally devoid of subduction zones or potential sources of large reverse faults. The two exceptions are the Hispaniola-Puerto Rico-Lesser Antilles subduction zone, where the Atlantic tectonic plate subducts under the Caribbean plate, and the enigmatic zone of large earthquakes west of Gibraltar. Following is a review of these two earthquake source areas and an evaluation of their tsunamigenic potential.

The 1761 Earthquake and Tsunami

The most famous earthquake to have struck Europe is the 1755 Lisbon earthquake discussed in the previous chapter. Two other large earthquakes (probably M>7) have struck the Iberian Peninsula during the 18th century. The first occurred on December 27, 1722 (Baptista and Lemos, 2000) and the second on March 31, 1761. The 1761 earthquake was felt across the Iberian Peninsula, Madeira, Agadir (Morocco), southern England, Ireland and the Netherlands (Baptista *et al.*, 2006). The earthquake generated a tsunami that was observed in Lisbon, Portugal, Cadiz, Spain, Cornwall, England, the south coast of Ireland, Terceira in the Azores, Barbados and Antigua (Baptista *et al.*, 2006, and references therein). Baptista *et al.* (2006) located the earthquake and tsunami source at 13°N 34.5°W (south of Ampere seamount) using the intersection between regions defined by back-tracking of tsunami travel time, and the intensity of the earthquake in the Iberian Peninsula (Figure 6-2). Their location contradicts previously suggested locations that the earthquake took place close to reported sea quakes (no. 1, 2, and 3, in figure 6-2), or at Gorringe Bank (marked by X in Figure 6-2).

The Northeast Caribbean

Tectonic setting

The Greater Antilles volcanic arc, which extends from Cuba to the Virgin Islands (Figure 6-3), was formed during the Cretaceous and Early Tertiary as the North American plate was subducting southwesterly beneath the Caribbean plate (Pindell and Barrett, 1990). Beginning at 49 Ma, relative plate motion changed to a more easterly direction (~250°), resulting in a more oblique subduction, a large component of left-lateral strike-slip, and the cessation of arc volcanism. This relative plate motion has been fairly stable ever since as evident from the opening of Cayman Trough between Cuba and Honduras (ten Brink *et al.*, 2002 and references therein). Presently, a typical old oceanic crust of 90-110 Ma in age subducts under Puerto Rico and the Virgin Islands, whereas the descending plate adjacent to the Hispaniola trench is a thick crust of an unknown origin, which underlies the Bahamas platform (Freeman-Lynde and Ryan, 1987). Thrust earthquakes at a shallow angle (20°) under northern Hispaniola (Dolan and Wald, 1998) indicate that subduction process is likely to be active there.

The Puerto Rico Trench

The geometry of the Puerto Rico trench with respect to relative plate motion is similar to the Sumatra-Andaman trench, where the 26 December 2004 Indian Ocean tsunami took place (Figure 6-3). Specifically, the Puerto Rico trench is curved, and the convergence angle between the subducting NOAM plate and the overlying Caribbean plate is increasingly more oblique to the west (Figure 6-3). By inference, it was suggested that perhaps the Puerto Rico Trench is capable of generating a mega-tsunami that will affect the Atlantic coast of the U.S. While more detailed modeling studies need to be carried out, it is worth pointing out some fundamental differences between the two trenches. Slip during the M=9.3 earthquake in Sumatra was sub-perpendicular to the trench, despite the highly oblique convergence angle. This indicates that additional deformation should take place in the overriding plate within the forearc and arc regions. Using numerical modeling of static stress changes, ten Brink and Lin (2004) recently showed that slip during earthquakes in the Puerto Rico Trench is highly oblique and almost parallel to the convergence direction (Figure 6-4). This finding matches evidence from GPS (Calais *et al.*, 2003) and earthquake focal mechanisms (Figure 6-4) in the area, all indicating little deformation of the overlying plate due to subduction. Therefore, only a small component of thrust motion is expected during large earthquakes, because most of the motion during a subduction earthquake will be parallel to the trench.

There is no historical record of large earthquakes along the Puerto Rico trench, although McCann (2004) proposed that the 1787 earthquake had magnitude 8 and was located north of Puerto Rico. The largest

instrumentally recorded earthquake in the area is the 1943 M_w=7.3 northwest of Puerto Rico (*e.g.*, Dolan and Wald, 1998). Although plate secular motion from GPS is limited by the paucity of landmass, available data indicate a relative displacement of 19±2 mm/y with respect to the North American plate oriented at an angle of 70° (Figure 6-4).

Using focal mechanisms for small to medium earthquakes (M_w=5.3-6) in the past 30 years and arguments discussed in ten Brink and Lin (2004), we propose the following rupture parameters: slip direction of N60E along an inclined interface with dip of 20°. The downdip length of the interface is unknown. ten Brink and Lin (2004) assumed a length of 102 km extending from depth of 5 to 40 km. The worst-case scenario for an earthquake rupture along the Puerto Rico Trench is a single rupture of a 675 km segment between 68°W (north of eastern Dominican Republic) and 62°W. For an assumed 10 m slip and shear modulus $\mu = 3 \times 10^{10}$Pa, the rupture area S = 68,850 km^2, the moment is Mo = 2.06 x 10^{22}Nm, and the moment magnitude is M_w = 8.85.

However, it should be emphasized that such a large earthquake has never been documented along the Puerto Rico trench, and the downdip length of the fault rupture is unknown. There is also significant uncertainty in scaling average slip with respect to the rupture dimensions (Geist *et al.*, 2007). In addition, the subducting plate is 90-110 m.y. old (ten Brink, 2005). Subduction zones consuming a 100 m.y. old oceanic lithosphere at a long-term convergence rate of 20 mm/y are typically associated with earthquakes < M=8 (*e.g.*, Ruff and Kanamori, 1980), although other studies (*e.g.*, Bird and Kagan, 2004) suggest little correlation between maximum earthquake magnitude and various subduction parameters. Most important, ten Brink and Lin proposed that slip during an earthquake is expected to be sub-parallel to the trench. The relatively small component of thrusting relative to strike-slip during the earthquake slip will generate a smaller tsunami compared to a pure thrust event.

The Hispaniola Trench

According to GPS measurements, slightly oblique convergence under Hispaniola is partitioned between 5.2±2 mm/y of reverse motion on the subduction interface and 12.8±2.5 mm/y and 9.0±9.0 mm/y left-lateral strike-slip on the Septentrional and Enriquillo Faults, respectively, which traverse the arc (Calais *et al.*, 2002) (Figure 6-4, Enriquillo Fault is located along the southwest side of Hispaniola beyond the map). A series of Ms = 7.0-8.1 earthquakes (M_w = 6.8-7.6; D. Wald, pers. Comm.., 2003) with mostly thrust motion took place in the eastern half of northern Hispaniola between 1946 and 1953 (Kelleher *et al.*, 1973) (Figure 6-4), presumably on a shallow dipping (~20°) subduction interface (Dolan and Wald, 1998) (Figure 6-4). Slip in these events was slightly oblique with average slip azimuth of 23° (D. Wald, pers. Comm., 2003). One of the events in 1946 was accompanied by a destructive local tsunami.

In contrast to the Puerto Rico trench, slip on the Hispaniola segment of the trench farther west, is sub-perpendicular to the trench, hence, a larger

vertical motion is expected for a given magnitude of slip. In contrast to the Puerto Rico trench, where a normal thickness oceanic crust is subducting, the crust entering the Hispaniola trench is very thick (*e.g.*, Freeman-Lynde and Ryan, 1987), and will likely allow more stress to accumulate, and therefore larger earthquakes to occur.

The Hispaniola segment may extend from 68°W to the Windward Passage 525 km to the west, where it meets the eastern end of Cayman Trough (Figure 6-3). Earthquake focal mechanisms indicate a dip of 20° (Dolan and Wald, 1998), and slip direction of N23E. The average strike of the Hispaniola segment is N95E-N102E. The downdip fault length is assumed to be 117 km assuming that rupture extend between depths of 0 - 40 km. The relocated region of the 1946-1953 aftershocks define a 95 km long downdip zone (Dolan and Wald, 1998).

Assuming a complete rupture of the Hispaniola trench with 10 m slip yields a rupture area S = 61,425 km^2; moment Mo = 1.84 x 10^{22}Nm, and moment magnitude M_w = 8.81. The easternmost 200 km long section of the subduction zone has ruptured in a series of earthquakes between 1946-1953. It is unclear, whether the western part of the subduction zone would rupture in a single earthquake and how far west the rupture would extend.

Modeling is needed to determine if the U.S. Atlantic coast would be protected from tsunamis generated in this subduction zone by the Bahamas banks which are near sea level and act as obstructions to tsunami wave propagation.

Figures

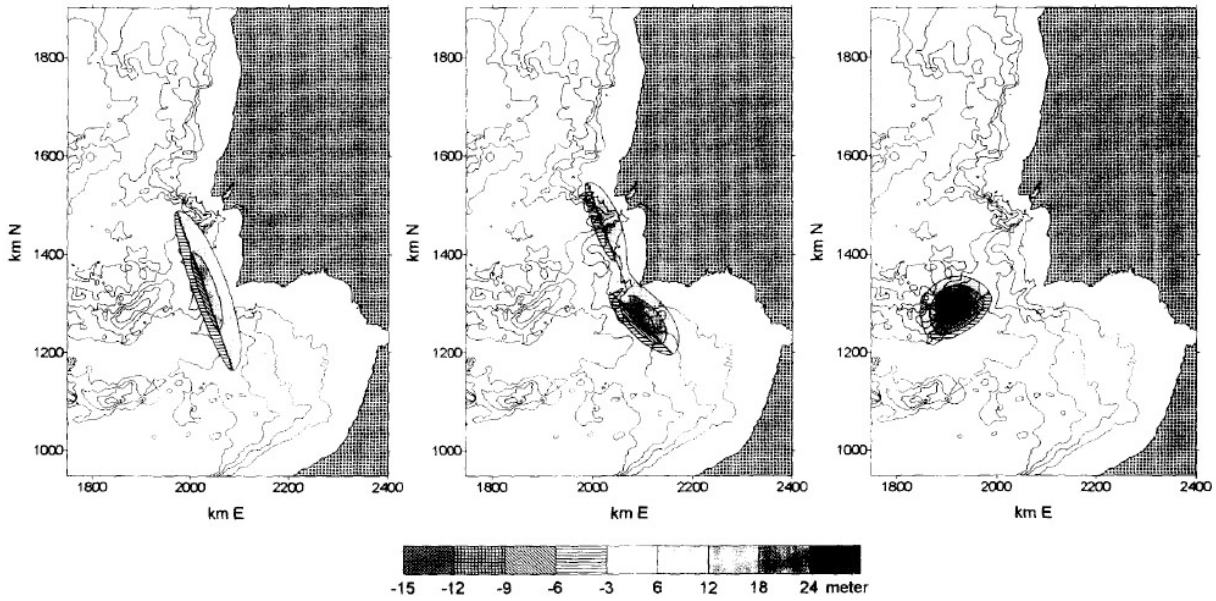

Figure 6-1: Initial displacement for shallow water simulations of the 1755 Lisbon earthquake (from Baptista *et al.*, 1998). (a) Source with strike 160°. (b) Composite source with strikes of 160° and 135° which best fits the observed tsunami travel times and amplitudes(c) Source mimicking the 1969 earthquake source with a strike of 55°, which does not fit the observations.

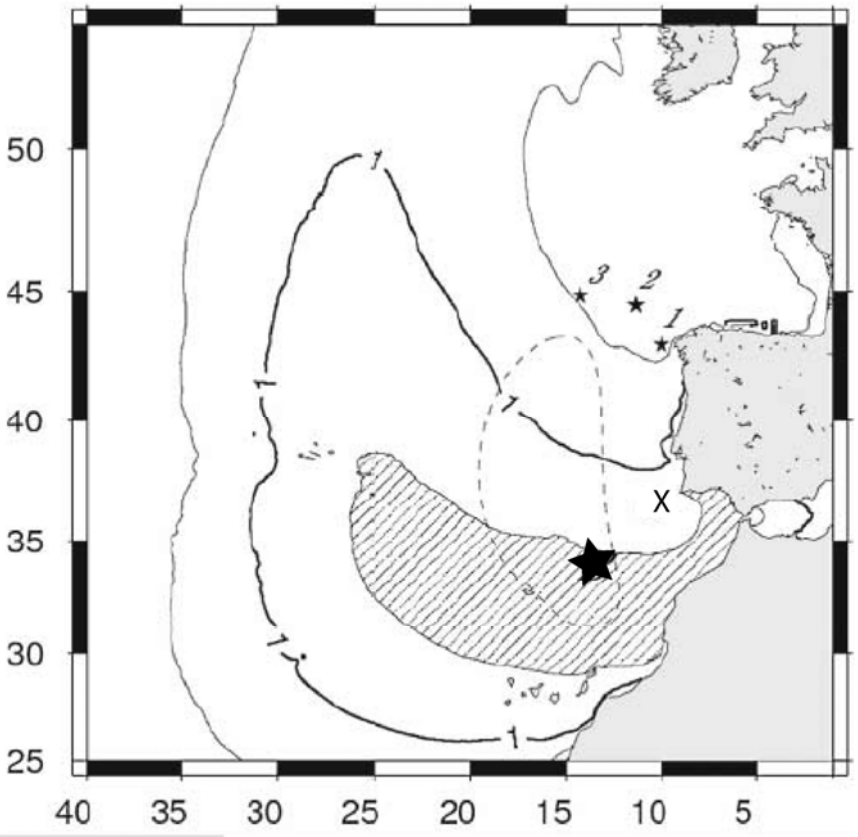

Figure 6-2: Probable location of the 31 March 1761 earthquake and tsunami (from Baptista *et al.*, 2006). Contours – average misfit (in hours) of backward tsunami ray tracing, with stripped area being < 0.5 hr. Dashed line – Enclosed area where the averaged intensity errors are minimized assuming the MSK attenuation law. Stars – locations of reported sea quakes. X- Gorringe Bank.

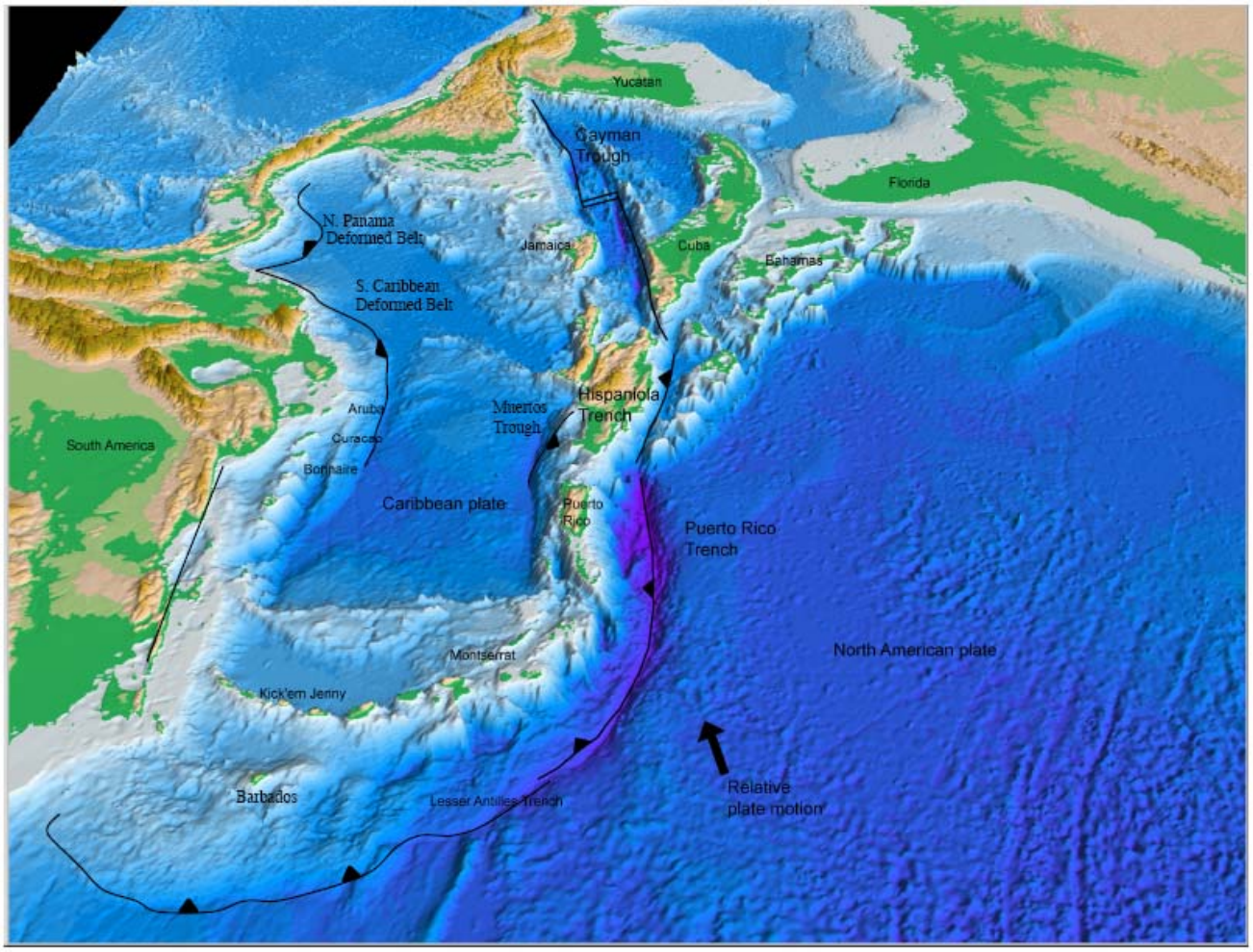

Figure 6-3: Perspective view of the tectonic elements in the Caribbean plate and seafloor topography.

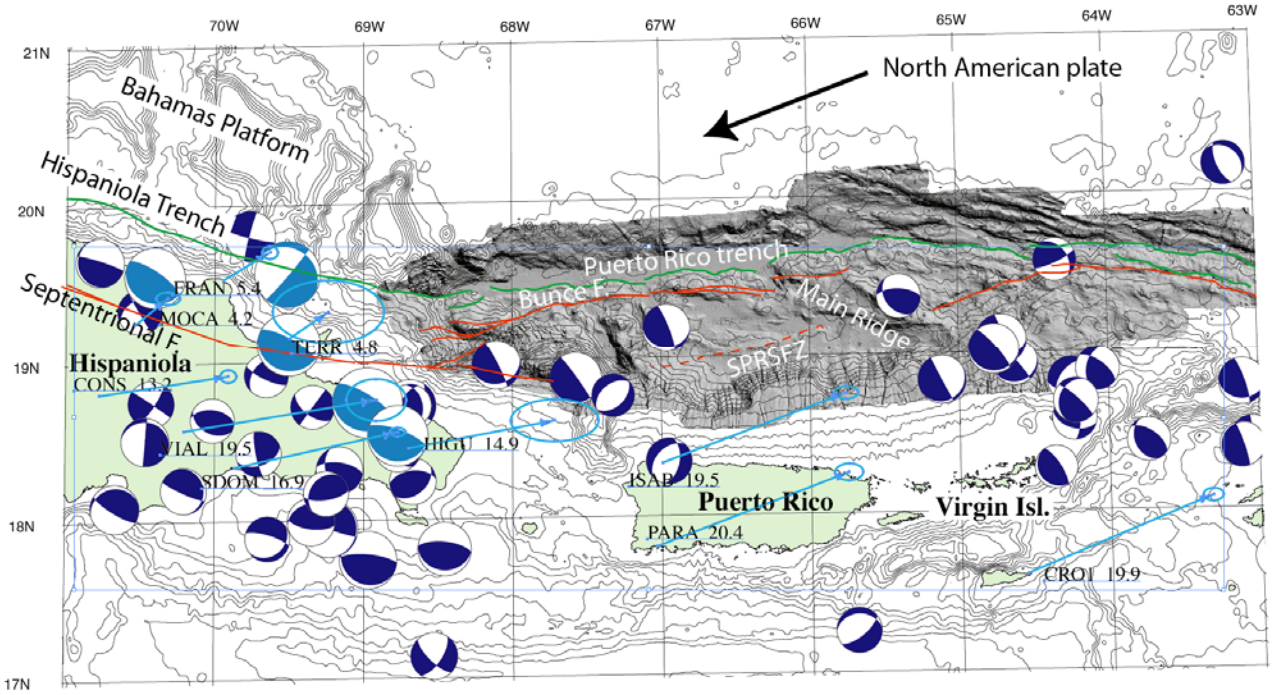

Figure 6-4: Bathymetry map of the northern Caribbean with a shaded relief map obtained from detailed multibeam bathymetry survey (ten Brink and Lin, 2004, and references therein). Solid green line – Frontal thrust of the subduction zone. Solid red line – Interpreted strike-slip faults. Blue beach balls – Focal plane solutions (lower hemisphere) of moderate earthquakes between 1977-2002 from the Harvard CMT catalog. Light blue beach balls – Same for historical earthquake sequence. Arrows – Velocity vectors relative to stable North America accompanied by rate (in mm/y) and station name, and error ellipse.

References

Argus, D. F., Gordon, R. G., DeMets, C., and Stein, S., 1989, Closure of the Africa-Eurasia-North America plate motion circuit and tectonics of the Gloria Fault: *Journal of Geophysical Research, v. 94*, p. 5585-5602.

Baptista, M. A., Miranda, J. M., and Luis, J. F., 2006, In search of the 31 March 1761 earthquake and tsunami source: *Bulletin of the Seismological Society of America, v. 96*, p. 713-721.

Baptista, M. A., and Lemos, C., 2000, The source of the 1722 Algarve earthquake, inferred from hydrodynamic modeling of the associated tsunami, European Geophysical Society, 25th general assembly, Nice, France, April 25-29, 2000.

Baptista, M. A., Miranda, P. M. A., Miranda, J. M., and Mendes Victor, L., 1998, Constraints on source of the 1755 Lisbon tsunami inferred from numerical modelling of historical data on the source of the 1775 Lisbon tsunami: *Journal of Geodynamics, v. 25*, p. 159-174.

Bird, P., and Kagan, Y. Y., 2004, Plate-tectonic analysis of shallow seismicity: apparent boundary width, beta-value, corner magnitude, coupled lithosphere thickness, and coupling in 7 tectonic settings: *Bulletin of the Seismological Society of America, v. 94*, p. 2380-2399.

Calais, E., Mazabraud, Y., Mercier de Lepinay, B., Mann, P., Mattioli, G. S., and Jansma, P. E., 2002, Strain partitioning and fault slip rates in the

northeastern Caribbean from GPS measurements: *Geophysical Research Letters, v. 29*, 1856, doi:1810.1029/2002GL015397.

Dolan, J. F., and Wald, D. J., 1998, The 1943-1953 north-central Caribbean earthquakes: Active tectonic setting, seismic hazards, and implications for Caribbean-North America plate motions: *Geological Society of America Special publications, v. 326*, p. 143-170.

Faccenna, C., Piromallo, C., Crespo-Blanc, A., Jolivet, L., and Rossetti, F., 2004, Lateral slab deformation and the origin of the western Mediterranean arcs: *Tectonics, v. 23, no.1*, p. 21.

Freeman-Lynde, R. P., and Ryan, W. B. F., 1987, Subsidence history of the Bahama Escarpment and the nature of the crust underlying the Bahamas: *Earth and Planetary Science Letters, v. 84*, p. 457-470.

Geist, E. L., 1999, Local tsunamis and earthquake source parameters: *Advances in Geophysics, v. 39*, p. 117-209.

Geist, E. L., and Dmowska, R., 1999, Local tsunamis and distributed slip at the source: *Pure and Applied Geophysics, v. 154*, p. 485-512.

Geist, E. L., Titov, V. V., Arcas, D., Pollitz, F. F., and Bilek, S. L., 2007, Implications of the December 26, 2004 Sumatra-Andaman earthquake on tsunami forecast and assessment models for great subduction zone earthquakes: *Bulletin of the Seismological Society of America, v. 97*, p. S249-S270.

Gracia, E., *et al.*, 2003, Mapping active faults offshore Portugal (36 degrees N-38 degrees N); implications for seismic hazard assessment along the Southwest Iberian margin: *Geology, v. 31*, p. 83-86.

Grimison, N. L., and Chen, W.-P., 1986, The Azores-Gibraltar plate boundary; focal mechanisms, depths of earthquakes, and their tectonic implications: *Journal of Geophysical Research, v. 91*, p. 2029-2047.

Gutscher, M. A., Baptista, M. A., and Miranda, J. M., 2006, The Gibraltar Arc seismogenic zone; Part 2, Constraints on a shallow east dipping fault plane source for the 1755 Lisbon earthquake provided by tsunami modeling and seismic intensity: *Tectonophysics, v. 426*, p. 153-166.

Hayward, N., Watts, A. B., Westbrook, G. K., and Collier, J. S., 1999, A seismic reflection and GLORIA study of compressional deformation in the Gorringe Bank region, eastern North Atlantic: *Geophysical Journal International, v. 138*, p. 831-850.

Johnston, A. C., 1996, Seismic movement assessment of earthquakes in stable continental regions; III, New Madrid 1811-1812, Charleston 1886 and Lisbon 1755: *Geophysical Journal International, v. 126*, p. 314-344.

Lander, J. F., Whiteside, L. S., and Lockridge, P. A., 2002, A brief history of tsunamis in the Caribbean Sea: *Science of Tusnami Hazards, v. 20*, p. 57-94.

McCann, W. R., Feldman, L., and McCann, M., *in press*, Catalog of felt earthquakes for Puerto Rico and neighbouring islands 1492-1899 with additional information for some 20th century earthquakes: *Tectonophysics*.

Okada, Y., 1985, Surface deformation due to shear and tensile faults in a half-space: *Bulletin of the Seismological Society of America, v. 75*, p. 1135-1154.

Pindell, J. L., and Barrett, S. F., 1990, Geological evolution of the Caribbean region; a plate tectonic perspective, edited by Dengo, G., and Case, J. E.: Geological Society of America, Boulder.

Ruff, L., and Kanamori, H., 1980, Seismicity and the subduction process: *Physics of the Earth and Planetary Interiors, v. 23*, p. 240-252.

ten Brink, U. S., Coleman, D. F., and Dillon, W. P., 2002, The nature of the crust under Cayman Trough from gravity: *Marine and Petroleum Geology, v. 19*, p. 971-987.

ten Brink, U. S., and Lin, J., 2004, Stress interaction between subduction earthquakes and forearc strike-slip faults: modeling and application to the northern Caribbean plate boundary: *Journal of Geophysical Research, v. 109*, B12310, 12310.11029/12004JB003031.

Thiebot, E., and Gutscher, M. A., 2006, The Gibraltar Arc seismogenic zone; Part 1, Constraints on a shallow east dipping fault plane source for the 1755 Lisbon earthquake provided by seismic data, gravity and thermal modeling: *Tectonophysics, v. 426*, p. 135-152.

Chapter 7: Tsunamigenic Earthquake Sources That May Affect the Gulf of Mexico

Introduction

Earthquake-generated tsunamis generally originate by the sudden vertical movement of a large area of the seafloor during an earthquake. Such movement is generated by reverse faulting, most often in subduction zones. The Gulf of Mexico basin is devoid of subduction zones or potential sources of large reverse faults. However, the Caribbean basin contains two convergence zones whose rupture may affect the Gulf of Mexico, the North Panama Deformation Belt and the Northern South America Convergent Zone. Hydrodynamic modeling is needed to evaluate the role of the Yucatan straits (between Cuba and the Yucatan Peninsula) in modifying the propagation of tsunamis into the Gulf of Mexico. The following is a review of these convergent zones.

North Panama Deformation Belt 9-12ºN, 83ºW-77ºW

Summary

The largest segment of the North Panama Deformation Belt is oriented between 60°-77°. The 1882 Panama earthquake appears to have ruptured at least 3/4 of the available length of the convergence zone, and was estimated to have a magnitude of 8 (Mendoza and Nishenko, 1989). While there was significant tsunami damage locally, there were no reports from the Gulf of Mexico of a tsunami from this earthquake (Mendoza and Nishenko, 1989). The low convergent rate (7-11 mm/y, (Trenkamp*, et al.*, 2002)) across the North Panama Deformation Belt supports long recurrence interval for large earthquakes.

Previous tsunamis

A tsunami flooded San Blas islands and the northern coast of Panama (Figure 7-1) and killed 65 people on 09/07/1882 following an offshore earthquake at about 10°N, 78°W (Mendoza and Nishenko, 1989). Mendoza and Nishenko (1989) isoseismal map (Figure 7-2) suggests that rupture occurred along almost the entire segment between longitude 80.3°W-77.8°W.

Eyewitnesses report water withdrawal before flooding. The tide gauge in Colon at the northern end of Panama Canal reported a level change of only 62 cm. The Jamaica-Panama underwater cable broke (perhaps indicating a submarine slide). The authors estimated the earthquake to be ~M=8, an increase from previous estimates (Mendoza and Nishenko, 1989).

Plafker and Ward (1992) reported an M_s=7.5 earthquake on 04/22/1991 at 9.74N 83.1W (on land), which caused uplift along 135 km of the Caribbean coast in southern Costa Rica. This earthquake was reported by the Harvard CMT catalog with location: 10.10N, 82.77W, depth: 15 km, and M_w= 7.6. It also caused a damaging tsunami, which was recorded by a tide gauge in St. Croix (Lander, *et al.*, 2002). Plafker and Ward (1992) best fit parameters of the ruptured fault from seismic and geodetic data are: thrust fault, striking between 105-120°, dipping at 30°, fault dimensions: 40 km wide and 80 km long, Their estimated recurrence time on this fault is 200-1100 y.

The parameters for this earthquake are given as:

ref.	*strike*	*dip*	*rake*
1	103°	25°	58° (oblique thrust and left-lateral)
2	123° (91°-138°)	32° (16°-39°)	89° (69°-96°)
3	107±5°	21°±10°	56°±11°

where reference 1: the Harvard CMT catalog, reference 2: Tajima and Kikuchi (1995), and reference 3: Goes, *et al.* (1993).

Other earthquakes

Within the central and eastern sections of this deformation belt, the USGS catalog lists 10 focal plane solutions, 6 of them, normal mechanisms, 4 reverse mechanisms. Their magnitudes range between 5.4-6.3. The parameters for the 4 reverse focal mechanisms are:

lat	*long*	*strike*	*dip*	*rake*	
9.7	79.7	238	70	31	(LL+ compression facing NW)
10.2	80.0	35	45	57	(compression+LL facing SE)
10.3	79.7	72	54	56	(compression+LL facing ESE)
9.0	77.4	75	26	20	(LL+compression facing ESE);

The USGS catalog lists the following earthquakes with reverse mechanism along the westernmost section (Costa Rica):

lat	*long*	*strike*	*dip*	*rake*	
9.88	-82.34	138	21	105	(compression+RL facing SW)
9.54	-82.64	151	9	108	(compression+RL facing SW)
9.65	-82.47	155	34	135	(compression+RL facing SW)
9.643	-82.3	346	34	134	(compression+RLfacing ENE)
9.91	-82.1	320	32	126	(compression+RL facing ENE)
9.69	-82.46	313	26	94	(compression facing NE)

10.1 -83.07 143 46 112 (compression+RL facing SW)

Relative motion from GPS

The relative motion between Isla San Andres (east of Nicaragua), which is considered representative of Caribbean plate motion, and Panama is 11 mm/y in azimuth 180° (Kellogg, *et al.*, 1995). Others suggest a rate of relative motion of 7±2 mm/y in direction southwest between Isla San Andres and Costa Rica and westernmost Panama (Trenkamp, *et al.*, 2002).

Northern South America Convergent Zone, 11.5°-14°N, 77°W-64°W

Summary

It is difficult to evaluate the potential tsunami hazard from the convergence zone along the north coast of South America. Although there is shortening in the SE direction between the Caribbean and South American plates, much of the shortening is probably absorbed by deformation inland within and at the boundaries of the North Andes and Maracaibo blocks (Figures 7-1, 7-3). The amount of offshore deformation is not well known. There have been only two moderate earthquakes with reverse mechanisms during the past 40 years in the offshore areas. Shallow compressional deformation is more intense west of Aruba than to the east and reaches a maximum around longitude 75°W. There is no Holocene deformation west of 76.5°W on the north/south oriented subduction segment. The shape of the subduction zone under the northwest corner of South America is in dispute, with pieces of Nazca plate entering from the west and Caribbean plate perhaps also entering from the west as well as from the north. Some workers suggest that the Caribbean plate has a dip of 17°, but the lack of seismicity does not enable a good definition of the slab. There are no historical tsunamis associated with the convergent zone.

East of 68°W, 80% of the 2 cm/y motion between Caribbean and South American plates is confined to an 80-km narrow shear zone centered around the El Pilar strike-slip fault. The expected recurrence rate there is 150-200 y with slip magnitude of 3 - 4 m. There have been several devastating tsunamis associated with the El-Pilar fault in the past 500 years, but in our opinion, those are due to local compression or submarine landslides along the strike-slip fault. Between the El-Pilar fault and Aruba, the deformation zone widens but shows signs of extension, not compression.

As a worse case scenario (probably highly unlikely), we suggest thrust faulting along a 550 km long segment of the convergent zone between 72.5°-76.5°W oriented at N53°W with a dip of 17° and an unknown downdip length and slip. Another thrust fault could exist north of Oca fault (Figure 7-1), but motion there should be fairly oblique.

Surface deformation offshore

NE-facing normal faults are found around Aruba, Bonaire, and Curacao (Taboada, *et al.*, 2000). Seismic reflection profiles perpendicular to the margin show an apron of undeformed sediments migrating northward across an older deformed belt (ibid.). The deformation zone is narrow (~45 km) and shows mild compression north of Bonaire, and the sediments of the Venezuela basin entering the trench appear sagged, as if under tension. Deformation is getting more intense and its frontal edge is steeper north of Aruba and Guajira peninsula (~71.5°W). Deformation reaches maximum intensity along the NW corner of the convergence zone, and becomes less intense farther south (Ladd, *et al.*, 1984). No deformation is observed in offshore Holocene sediments of western Columbia (from Cartagena all the way south. (Duque-Caro, 1984)

Previous tsunamis

01/17/1929 – A tsunami destroyed Cumana, Venezuela (South of Isla Margarita) following an Ms=6.9 earthquake (*Lander, et al.*, 2002). All other historical tsunamis appear to concentrate in the Gulf of Cariaco, Isla Margarita, and the Gulf of Paria, (Lander, *et al.*, 2002)) where the Pilar fault has a strike slip motion.

Earthquakes

Only four earthquakes are listed in the Harvard CMT catalog between 1976 and 2007 offshore NW South America. All four earthquakes were located east of 72.8°W and show normal fault mechanisms. Two earthquake with reverse mechanisms were quoted by Perez *et al.*, (1997):

03/12/1968	13.15°N	72.3°W	depth 58 km	Mb=5.3
04/28/1978	11.99°N	72.54°W	depth 62 km	Mb=5.2

Earthquakes around Aruba, Bonaire, and Curacao, show right-lateral strike slip.

Seismicity is shallower than 50 km deep between the northern edge of the deformation zone and the coast (200 km east of 73.5W) (Figure 7-3). The slab has a sharp corner at 73.5°W-75°W (Colmenares and Zoback, 2003).

Large historic earthquakes occurred along the coast on the El Pilar strike-slip fault system which connects to the Bocono fault system which continues inland to the southwest (McCann and Pennington, 1990). The Oca fault, a westerly continuation of the El Pilar fault (Figure 7-1) has not been active historically (Figure 7-3). There is a disagreement whether the Caribbean actually subducts under northern South America, because of lack of shallow seismicity (McCann and Pennington, 1990).

Relative block motion from GPS

The relative motion between the Caribbean plate (as measured on San Andres Island) and stable South America is 20 mm/y in direction 104° (Corredor, 2003). Perez, *et al.* (2001) and Weber, *et al.* (2001) showed that east of 68°W, 80% of the motion between Caribbean and South American plates is confined to an 80-km narrow shear zone centered around the El Pilar strike-slip fault. The expected recurrence rate of earthquakes there is estimated to be 150-200 y with a slip magnitude of 3-4 m (Perez, *et al.*, 2001). The deformation zone widens to the west. The region south of Aruba and north of Bonoco fault (the Falcon Basin) moves at 15 mm/y at N82°E, implying a very small component of N-S compression (Perez, *et al.*, 2001).

The relative block motion Caribbean (San Andres) – North Andes Block (as represented by the Bogota, Columbia station) is 14±2 mm/y in southeast direction (Trenkamp, *et al.*, 2002). However 2/3 of this motion may be taken by internal deformation of the north Andean block on shore, as evidenced by the fact that relative motion between the Caribbean and the stable South America plate is 20 mm/y, while the relative motion between Cartagena, Columbia, and stable South America is 14 mm/y at almost the same direction (Trenkamp, *et al.*, 2002). Trenkamp, *et al.*, (2002) suggested that the North Andes block escapes to the NE along the Bonoco Fault at a rate of 6 mm/y.

Stress indicators

Colmenares and Zoback (2003) show evidence for maximum horizontal compression in a southeast direction on land west of Maracaibo basin, and SW shortening, SE opening (*i.e.*, strike slip motion) in the Falcon Basin south of Aruba (Figure 7-3).

The deep structure of the convergent zone

The Caribbean subduction zone under western Columbia is suggested to be very steep. However, the shape of subduction zones under South America is in dispute, with various authors proposing that pieces of Nazca plate enter from west and the Caribbean plate perhaps entering from west as well as from north (Malave and Suarez, 1995; van der Hilst and Mann, 1994). van der Hilst and Mann (1994) proposed an average dip of 17° for Caribbean under northwest S. America.

Figures

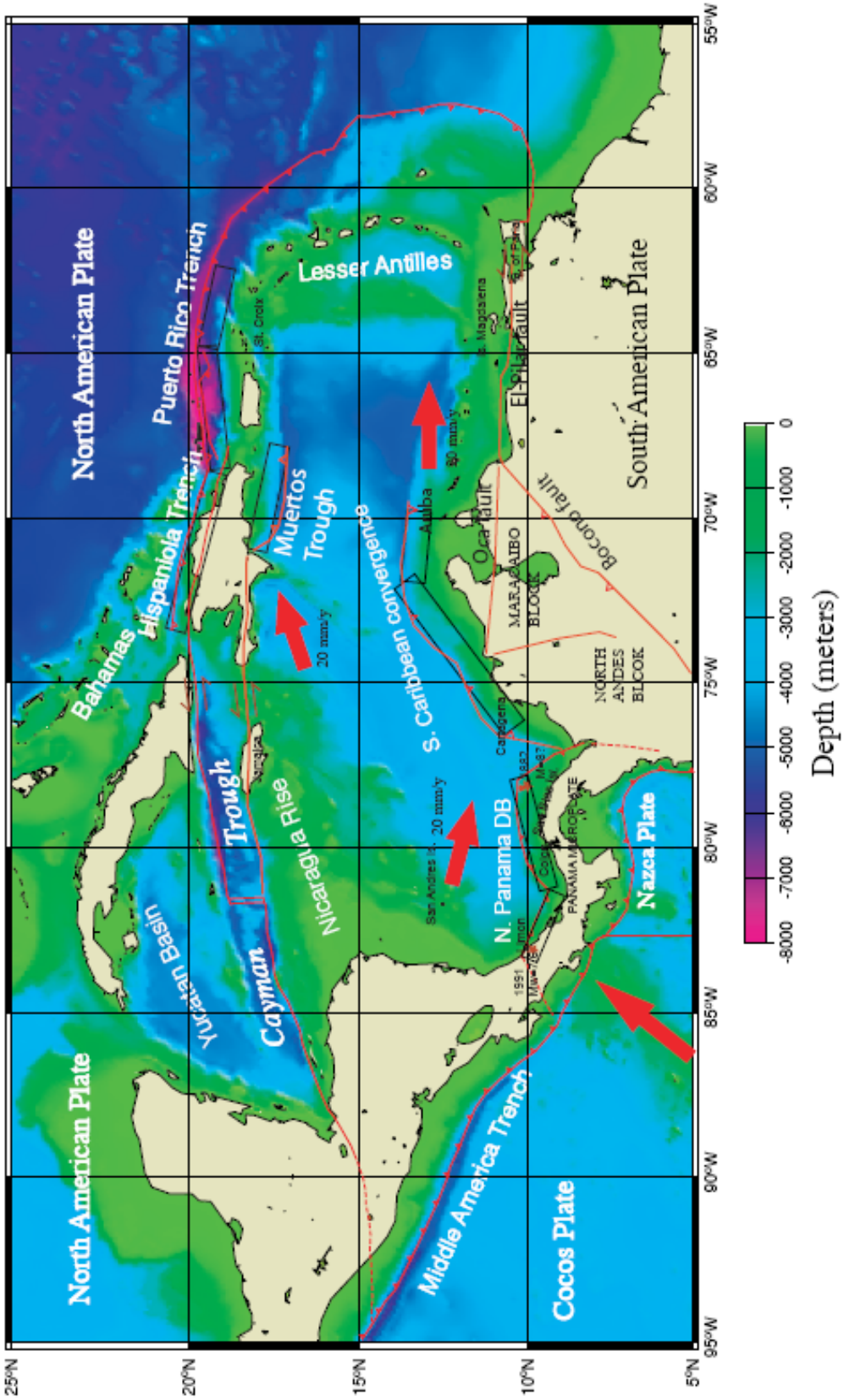

Figure 7-1: The Caribbean plate boundary and its tectonic elements.

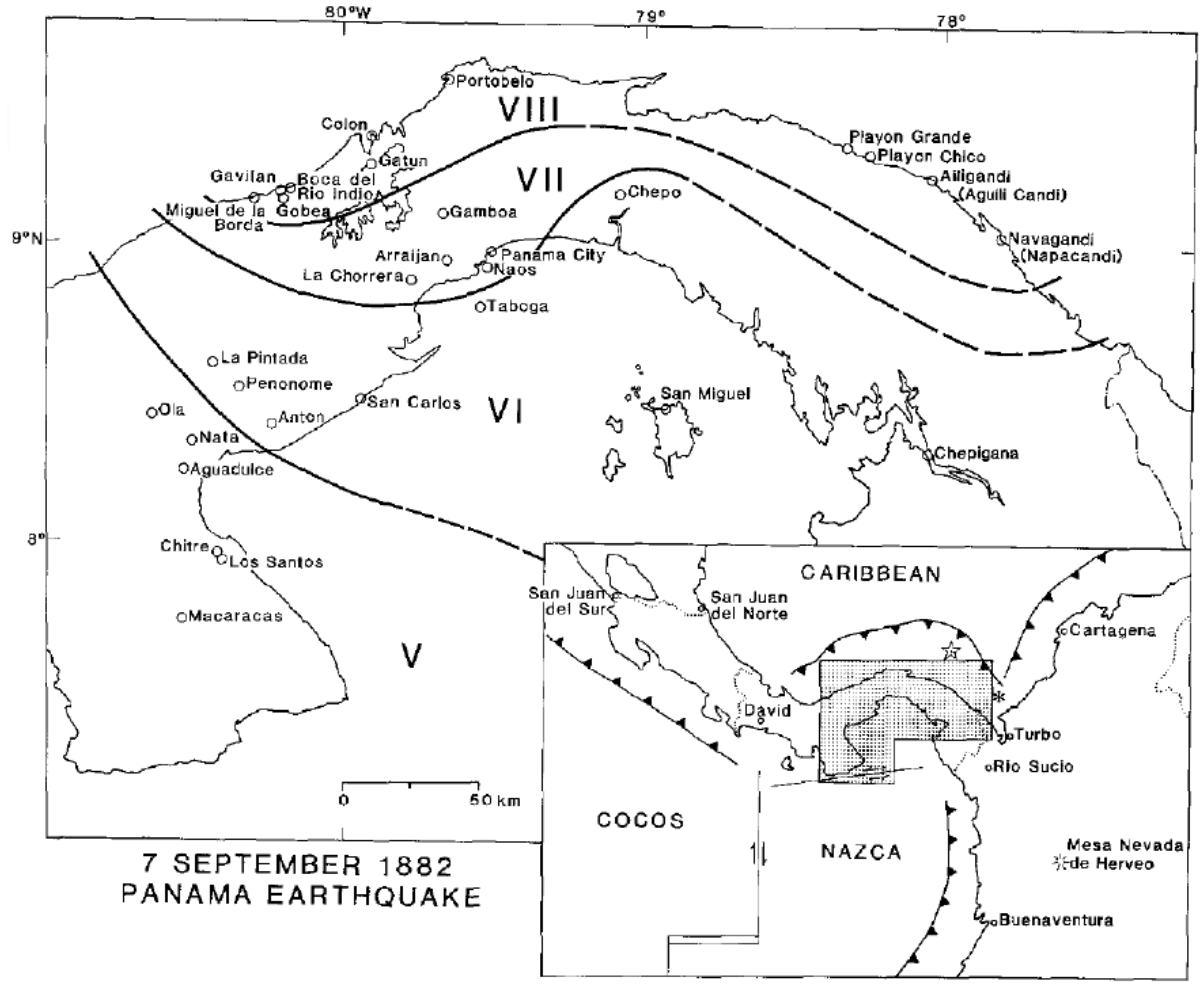

Figure 7-2: Isoseismal map of the 1882 earthquake in the North Panama Deformation Belt (from Mendoza and Nishenko, 1989). The star in the inset is their preferred epicenter.

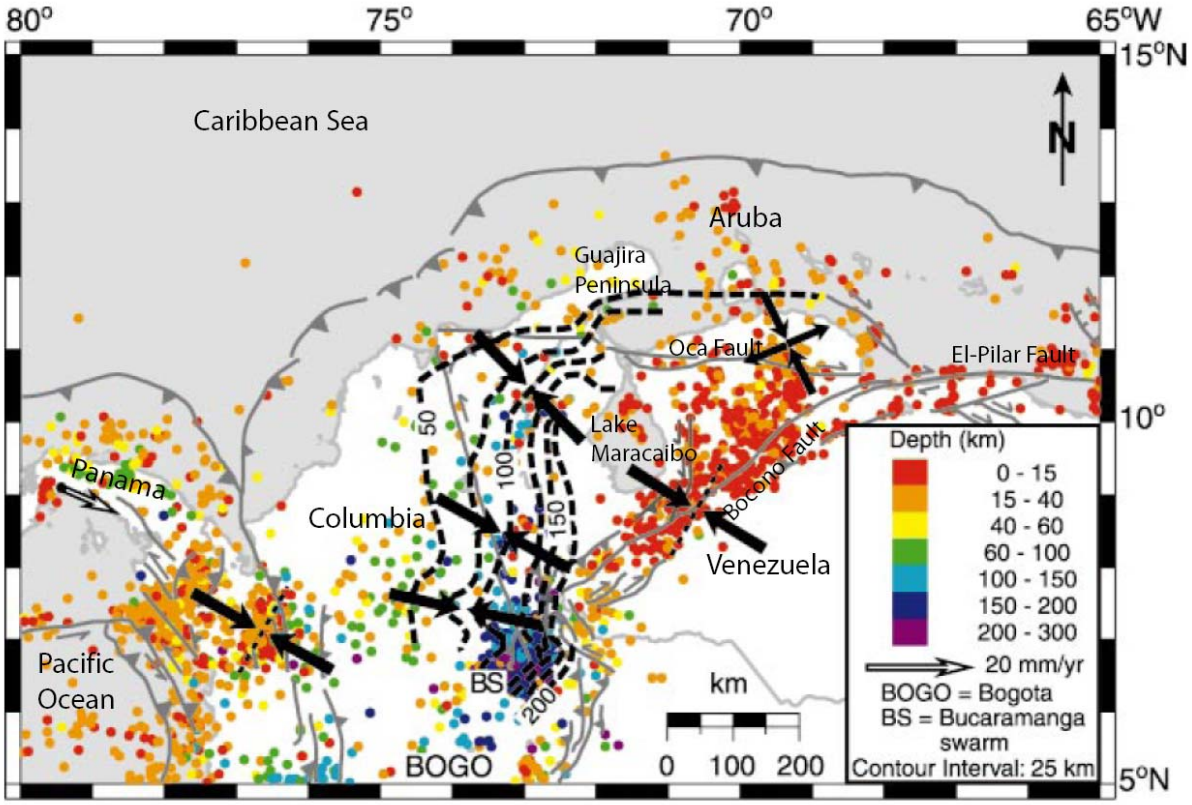

Figure 7-3: Depth of seismicity and generalized stress directions (from Colmenares and Zoback, 2003). Contour lines depths in km to top surface of inclined seismic zones.

References

Colmenares, L., and Zoback, M. D., 2003, Stress field and seismotectonics of northern South America: *Geology, v. 31*, p. 721-724.

Corredor, F., 2003, Seismic strain rates and distributed continental deformation in the Northern Andes and three-dimensional seismotectonics of northwestern South America: *Tectonophysics, v. 372*, p. 147-166.

Duque-Caro, H., 1984, Structural style, diapirism, and accretionary episodes of the Sinu-San Jacinto terrane, southwestern Caribbean borderland: *Memoir - Geological Society of America, v. 162*, p. 303-316.

Goes, S. D. B., Velasco, A. A., Schwartz, S. Y., and Lay, T., 1993, The April 22, 1991, Valle de la Estrella, Costa Rica (M (sub w) = 7.7) earthquake and its tectonic implications; a broadband seismic study: *Journal of Geophysical Research, v. 98*, p. 8127-8142.

Kellogg, J. N., Vega, V., Stallings, T. C., Aiken, C. L. V., and Kellogg, J. N., 1995, Tectonic development of Panama, Costa Rica, and the Colombian Andes; constraints from Global Positioning System geodetic studies and gravity: *Special Paper - Geological Society of America, v. 295*, p. 75-90.

Ladd, J. W., Truchan, M., Talwani, M., Stoffa, P. L., Buhl, P., Houtz, R., Mauffret, A., and Westbrook, G. K., 1984, Seismic reflection profiles

across the southern margin of the Caribbean: *Memoir - Geological Society of America, v. 162*, p. 153-159.

Lander, J. F., Whiteside, L. S., and Lockridge, P. A., 2002, A brief history of tsunamis in the Caribbean Sea: *Science of Tusnami Hazards, v. 20*, p. 57-94.

Malave, G., and Suarez, G., 1995, Intermediate-depth seismicity in northern Colombia and western Venezuela and its relationship to Caribbean Plate subduction: *Tectonics, v. 14*, p. 617-628.

McCann, W. R., and Pennington, W. D., 1990, Seismicity, large earthquakes, and the margin of the Caribbean Plate, Geol. Soc. Am. Boulder CO United States (USA).

Mendoza, C., and Nishenko, S. P., 1989, The North Panama earthquake of 7 September 1882; evidence for active underthrusting: *Bulletin of the Seismological Society of America, v. 79*, p. 1264-1269.

Perez, O. J., Bilham, R., Bendick, R., Velandia, J. R., Hernandez, N., Moncayo, C., Hoyer, M., and Kozuch, M., 2001, Velocity field across the southern Caribbean plate boundary and estimates of Caribbean/South-American plate motion using GPS geodesy 1994-2000: *Geophysical Research Letters, v. 28*, p. 2987-2990.

Perez, O. J., Jaimes, M. A., and Garciacaro, E., 1997, Microseismicity evidence for subduction of the Caribbean Plate beneath the South American Plate in northwestern Venezuela: *Journal of Geophysical Research, v. 102*, p. 17,875-817,882.

Plafker, G., and Ward S. N., 1992, Backarc thrust faulting and tectonic uplift along the Caribbean Sea coast during the April 22, 1991 Costa Rica earthquake: *Tectonics, v. 11*, p. 709-718.

Reed, D. L., and Silver, E. A., 1995, Sediment dispersal and accretionary growth of the North Panama deformed belt: *Special Paper - Geological Society of America, v. 295*, p. 213-223.

Taboada, A., Rivera, L. A., Fuenzalida, A., Cisternas, A., Philip, H., Bijwaard, H., Olaya, J., and Rivera, C., 2000, Geodynamics of the Northern Andes; subductions and intracontinental deformation (Colombia): *Tectonics, v. 19*, p. 787-813.

Tajima, F., and Kikuchi, M., 1995, Tectonic implications of the seismic ruptures associated with the 1983 and 1991 Costa Rica earthquakes: *Special Paper - Geological Society of America, v. 295*, p. 327-340.

Trenkamp, R., Kellogg, J. N., Freymueller, J. T., and Mora, H. P., 2002, Wide plate margin deformation, southern Central America and northwestern South America, CASA GPS observations: *Journal of South American Earth Sciences, v. 15*, p. 157-171.

van der Hilst, R., and Mann, P., 1994, Tectonic implications of tomographic images of subducted lithosphere beneath northwestern South America: *Geology, v. 22*, p. 451-454.

Weber, J. C., *et al.*, 2001, GPS estimate of relative motion between the Caribbean and South American plates, and geologic implications for Trinidad and Venezuela: *Geology, v. 29*, p. 75-78.

Chapter 8: Regional Tsunami Propagation Patterns from Caribbean Earthquakes

Tsunami propagation from large-magnitude earthquakes in the Caribbean is calculated to estimate deep ocean tsunami amplitudes offshore U.S. Atlantic and Gulf coasts. Sources for the tsunami calculations are discussed previously in Chapter 6: Tsunamigenic earthquake sources that may affect the Gulf of Mexico, and Chapter 5: Review of tsunamigenic earthquake sources that may affect the U.S. Atlantic Coast. This is a preliminary effort for the purpose of determining the relative severity among tsunamis from different sources and complements recent work by Knight (2006). A range of tsunami amplitudes is determined based on natural variations in slip distribution patterns expected for large magnitude earthquakes along plate boundaries in the Caribbean. This work predicts maximum wave amplitudes in 250 m of water at the shelf edge and does not predict runup nor propagation characteristics across the continental shelf.

Method

Large magnitude earthquakes in the Caribbean (Figure 8-1) were specified by determining a maximum rupture length along the following plate boundary segments (using classification scheme by Bird, 2003): (1) west Cayman oceanic transform fault (OTF), also known as Swan Island Fault, (2) east Cayman (OTF), also known as Oriente Fault, (3) northern Puerto Rico/Lesser Antilles subduction zone (SUB), (4) north Panama deformation belt, classified by Bird (2003) as an oceanic convergent boundary (OCB), and (5) the north coast of South America convergence zone classified by Bird (2003) as a subduction zone (SUB) (termed the north Venezuela subduction zone below). This classification scheme will be used to assess the probability of earthquakes along these fault zones in a later study.

Other faults in the Caribbean that can generate destructive local tsunamis, but unlikely to generate far-field tsunamis such as thrust faulting in the Muertos Trough and normal faulting in the Mona Passage were not modeled in this study. For the transform faults, the moment magnitude was estimated from rupture length using the Wells and Coppersmith (1994) empirical relationships. From this relationship and an estimate of the fault width (seismogenic thickness) from Bird and Kagan (2004), an average slip was assigned to each fault, assuming a shear modulus of 35 GPa. Fault dip and rake were estimated from analysis of past focal mechanisms from the

Global CMT database (`http://www.globalcmt.org/`). For the subduction boundary faults, geometric parameters were taken from regional studies described previously in the report and in prior publications (*e.g.*, ten Brink and Lin, 2004). Scaling of average slip from rupture length was taken from compiled databases of source parameters for subduction interplate thrust earthquakes (Lay *et al.*, 1982; Geist, 2002). Uncertainty caused by variations in slip distribution patterns is assessed by computing 100 different slip distributions that all have nearly the same average slip and slip spectrum (Herrero and Bernard, 1994; Geist, 2002; Geist *et al.*, 2007). A summary of the range of magnitude and average slip for each fault is given in Table 8-1.

Initial conditions for the propagation model are specified by the coseismic displacement of the seafloor. This includes primarily the vertical component of displacement. In addition, horizontal displacement in regions of steep bathymetric gradient will also contribute to vertical displacement of the water column in a manner described by Tanioka and Satake (1996). Since this component of the initial wavefield depends on the bathymetric gradient field near the source region, it is relatively incoherent compared to the primary component of the initial wavefield from vertical coseismic displacement. The transform faults (OTF) are much less efficient at generating tsunami waves (Figure 8-1a, b) than the thrust faults along subduction zones (SUB) and oceanic convergent boundaries (OCB) (Figure 8-1c, d, e).

Tsunami propagation was modeled using the linear long-wave equation, numerically implemented with a leap-frog, finite-difference algorithm. Only deep-ocean tsunami propagation is modeled, where linear theory is most applicable. Propagation across the continental shelf (specified by water depth less than 250 m) and runup are not modeled. As a very rough approximation, runup is approximately 3 times the tsunami amplitude at 250 m water depth, accounting for shoaling and runup amplification (Shuto, 1991; Satake, 1995, 2002), but not including energy dissipation from geometric spreading, bottom friction, and non-linear attenuation that is evident in the simulations of the Currituck landslide tsunami offshore Virginia, USA (Chapter 9). It is unclear whether the latter two dissipation mechanisms are as significant for far-field seismogenic tsunamis as they are for landslide tsunamis. Radiation boundary conditions are specified at the open-ocean boundaries, whereas reflection boundary conditions are specified at the 250 m isobath. The spatial grid size for the simulations is 2 arc-minutes and the time step is 8 s, which satisfies the Courant-Friedrichs-Lewy stability criterion (Satake, 2002). Total propagation time for each simulation is 4.4-6.6 hours, which is sufficient to capture the first few waves at the 250 m isobath within the model domain.

Results

For each fault, results from the simulation are shown in Figure 8-1 through Figure 8-4. Figure 8-1 shows the maximum tsunami amplitude in the open ocean for one of the 100 simulations for each source. Figures 8-2 and 8-3 shows the range of peak offshore tsunami amplitudes from all 100 simulations at the 250 m isobath for a latitudinal profile in the Gulf of Mexico (Figure 8-2) and a longitudinal profile along the Atlantic coast, respectively (Figure 8-3). Figure 8-4 shows the range in tsunami amplitudes as a time series (*i.e.*, marigrams) for selected offshore locations in the Gulf of Mexico and Atlantic. Tsunami characteristic for coastal regions will be different, because of nearshore propagation and runup effects.

In terms of overall severity, large earthquakes along the northern Puerto Rico subduction zone generate the largest tsunamis propagating toward the U.S. Atlantic coast, of the cases studied (Figure 8-1c). For the Gulf Coast, the largest tsunamis are generated by large earthquakes along the north Venezuela subduction zone. The absolute tsunami amplitudes are highly dependent, however, on the magnitude specified for each of these fault zones. (Distributions of earthquake magnitudes for these fault zones will be discussed in a future study. In general, these results are consistent with the findings of Knight (2006), where the far-field tsunamis generated from earthquakes located beneath the Caribbean Sea are higher along the Gulf coast than the Atlantic coast because of dissipation through the Greater Antilles islands. Conversely, tsunamis generated from earthquakes north of the Greater Antilles are higher along the Atlantic coast than the Gulf coast.

Profiles of peak offshore tsunami amplitudes along the Atlantic coast (Figure 8-3) indicate regions of focusing from variations in bathymetry. A prominent increase in tsunami amplitude between approximately 32-24°N is caused by focusing of the tsunami by the Blake Ridge (see Figure 2-1 from Chapter 2). Bathymetric ridges often act as waveguides if the ray path of the wave is within a critical angle of obliquity with respect to the orientation of the ridge (Mei, 1989; Satake *et al.*, 1992). There is also higher peak offshore tsunami amplitudes at the higher latitudes (>39°N) caused simply by the change in the orientation of the Atlantic shelf edge to a more E-W orientation.

Similarly in the Gulf of Mexico (Figure 8-2), tsunami amplitudes are higher where the shelf edge is approximately normal to the incidence of tsunami waves propagating from the south (*i.e.*, between ~83-85°W and ~87.5-88.5°W). The range in tsunami amplitudes caused by variations in slip distribution patterns is dependent on the propagation path distance from the source to the shelf edge. This distance dependence of the resulting tsunami amplitude variability is also evident on the synthetic marigrams (graph of tsunami amplitude as a function of time) (Figure 8-4). In addition, for most cases except for the northern Puerto Rico subduction zone scenario tsunami, the onset of the tsunami at the 6 marigram stations can be characterized as emergent (*i.e.*, initial tsunami waves are smaller than later ones), primarily because of obstructed propagation paths. In general, spectral characteristics

of tsunami marigrams is dependent on source characteristics, propagation path, and site response (Rabinovich, 1997).

To determine the tsunami characteristic along the coast from these sources, a more refined hydrodynamic model needs to be employed. For example, the Method of Splitting Tsunami (MOST) model (Titov and Synolakis, 1996; Titov and González, 1997; Titov and Synolakis, 1998) is specifically designed to determine propagation and runup characteristics for regional and far-field tsunamis. Source characterizations similar to what is being used for the tsunami forecasting system (Titov *et al.*, 2005) should be adequate for determining tsunami characteristics along the U.S. Atlantic and Gulf coasts.

Table

Table 8-1: Source parameters and range of average slip and moment magnitudes of earthquakes from which tsunami simulations were computed.

Fault #*	Name	Type†	Length (km)	Width (km)	strike (°)	dip (°)	rake (°)	Avg. Slip-low (m)	Avg. Slip-high (m)	M_w (low)	M_w (high)
1	W. Cayman	OTF	746	15	N73E	83N	185	10.6	12.4	8.3	8.35
2	E. Cayman	OTF	915	15	N77E	80S	175	12.1	14.2	8.4	8.45
3a	Hispaniola	SUB	525	110	N98E	20S	70				
3b	Puerto Rico	SUB	385	110	N83E	20S	23	8.2	9.4	9.11	9.15
3c	Virgin Islands	SUB	485	110	N102E	20S	42				
4a	W. Northern Panama	OCB	200	40	N113E	30S	90	3.7	4.3	8.24	8.28
4b	E. Northern Panama	OCB	350	40	N75E	35S	90				
5a	W. Southern Caribbean	SUB	550	50	N53E	17S	90	4.7	5.4	8.46	8.5
5b	E. Southern Caribbean	SUB	200	50	N95E	17S	90				

*Faults with same numeral are treated as one tsunami source.

†See Bird (2003).

Figures

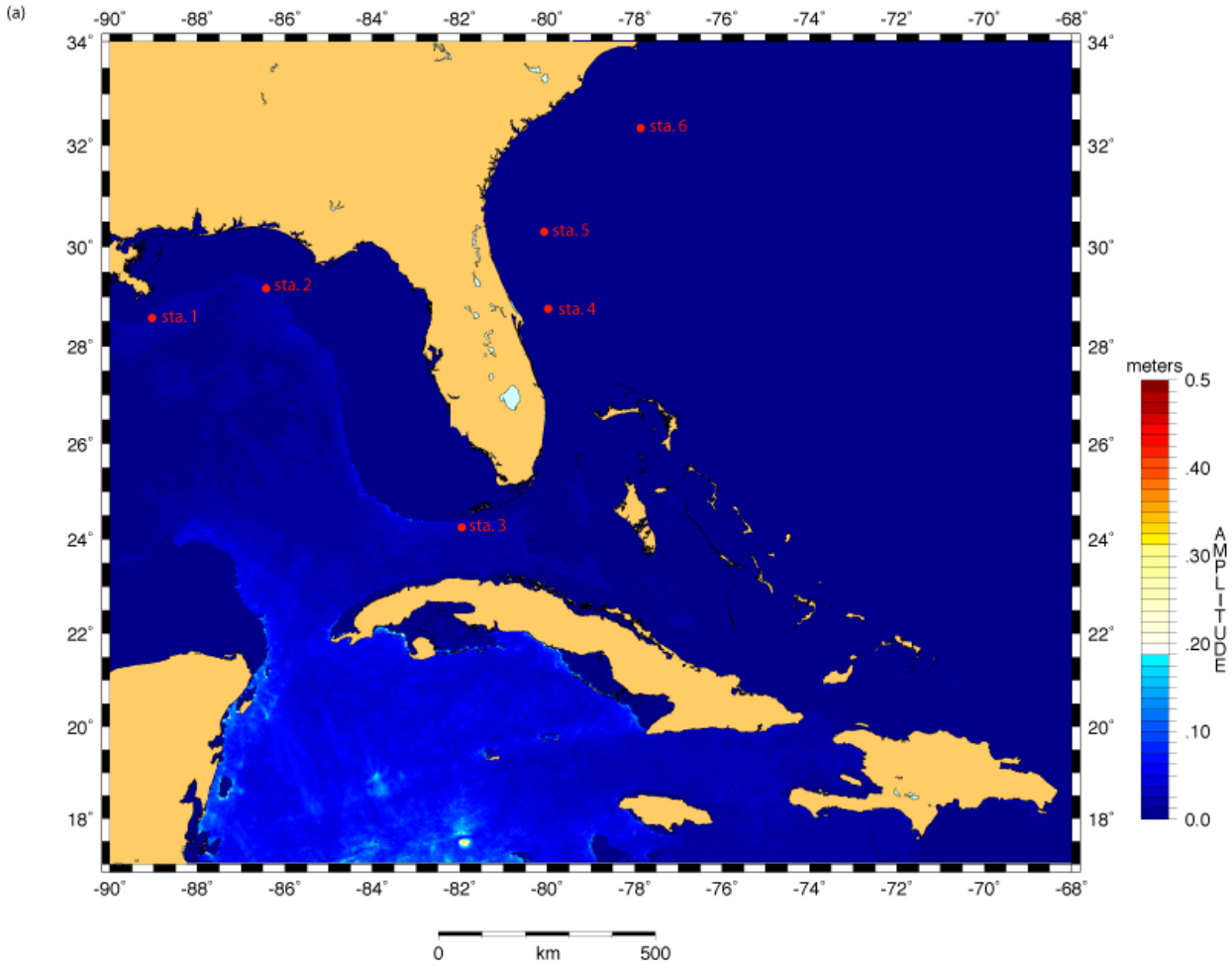

Figure 8-1: One simulation of maximum open-ocean tsunami amplitude over 4.4 hours of propagation time for each of the faults in the Caribbean: (a) W. Cayman OTF, (b) E. Cayman OTF, (c) N. Puerto Rico/Lesser Antilles SUB, (d) N. Panama OCB, (e) N. Venezuela SUB. Note change in amplitude scale for (c). Red dots indicate locations where synthetic marigrams are shown in Figure 8-4.

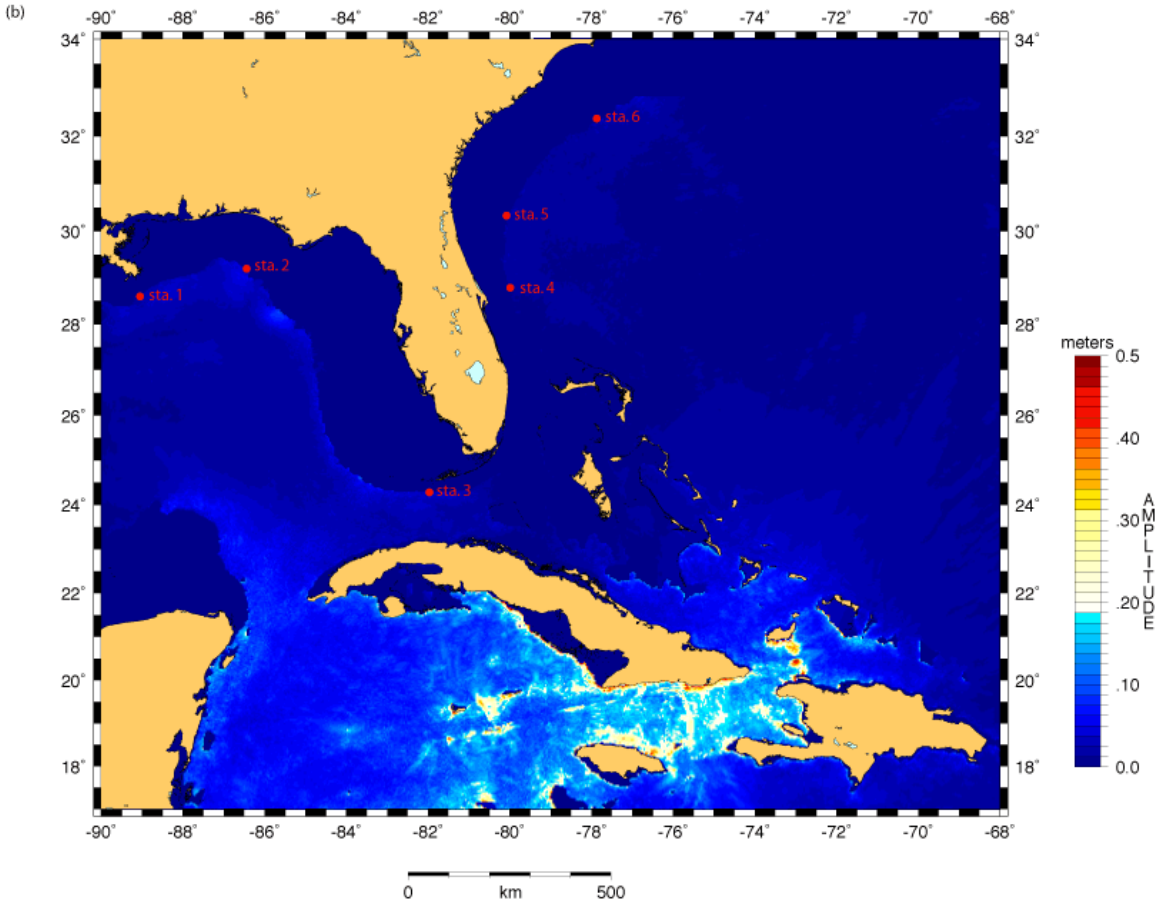
(b)
-90° -88° -86° -84° -82° -80° -78° -76° -74° -72° -70° -68°
34° 32° 30° 28° 26° 24° 22° 20° 18°
sta. 1
sta. 2
sta. 3
sta. 4
sta. 5
sta. 6
meters
0.5
.40
.30
.20
.10
0.0
AMPLITUDE
0
km
500

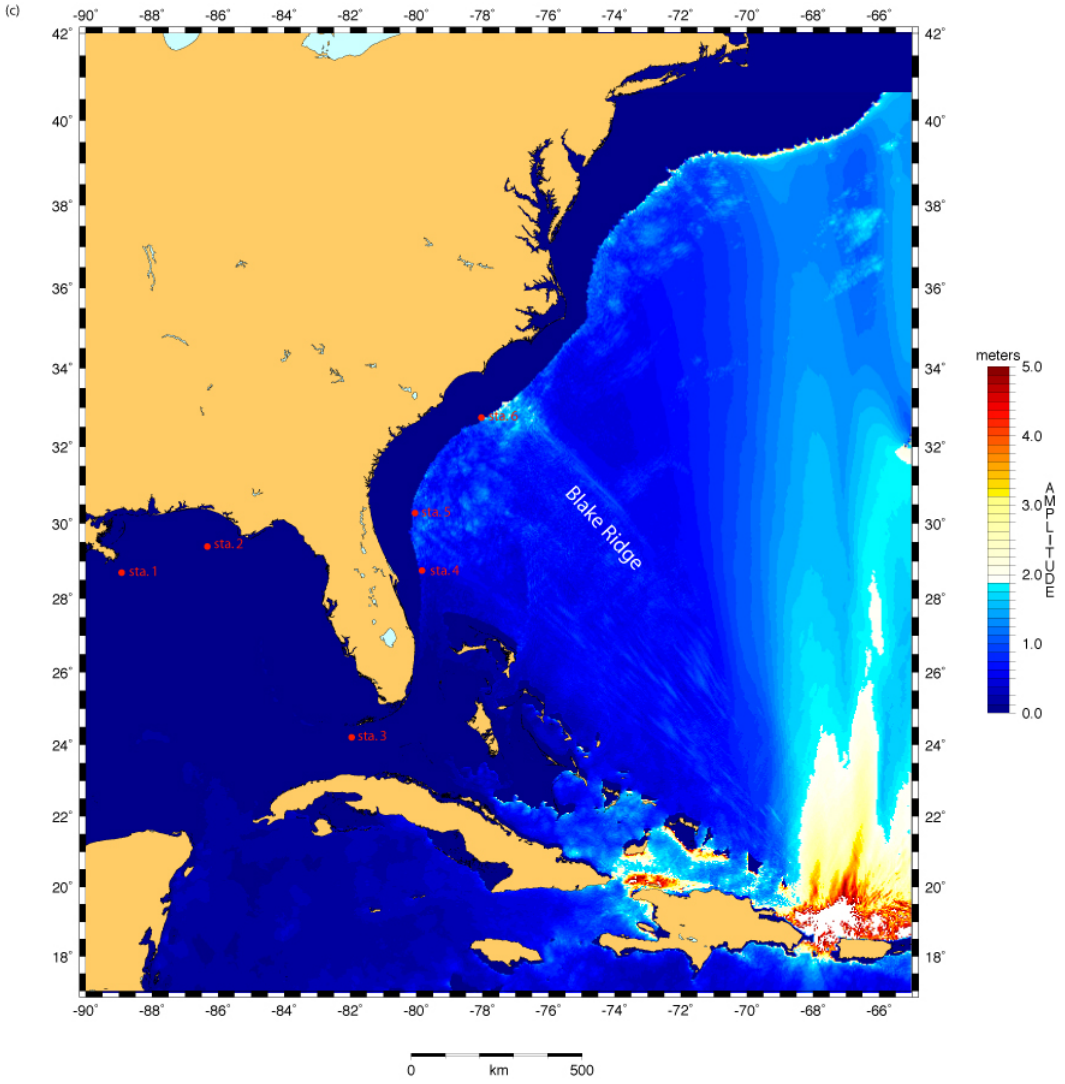
(c)
-90° -88° -86° -84° -82° -80° -78° -76° -74° -72° -70° -68° -66°
42° 40° 38° 36° 34° 32° 30° 28° 26° 24° 22° 20° 18°
sta.1
sta.2
sta.3
sta.4
sta.5
sta.6
Blake Ridge
meters
5.0
4.0
3.0
2.0
1.0
0.0
AMPLITUDE
0
km
500

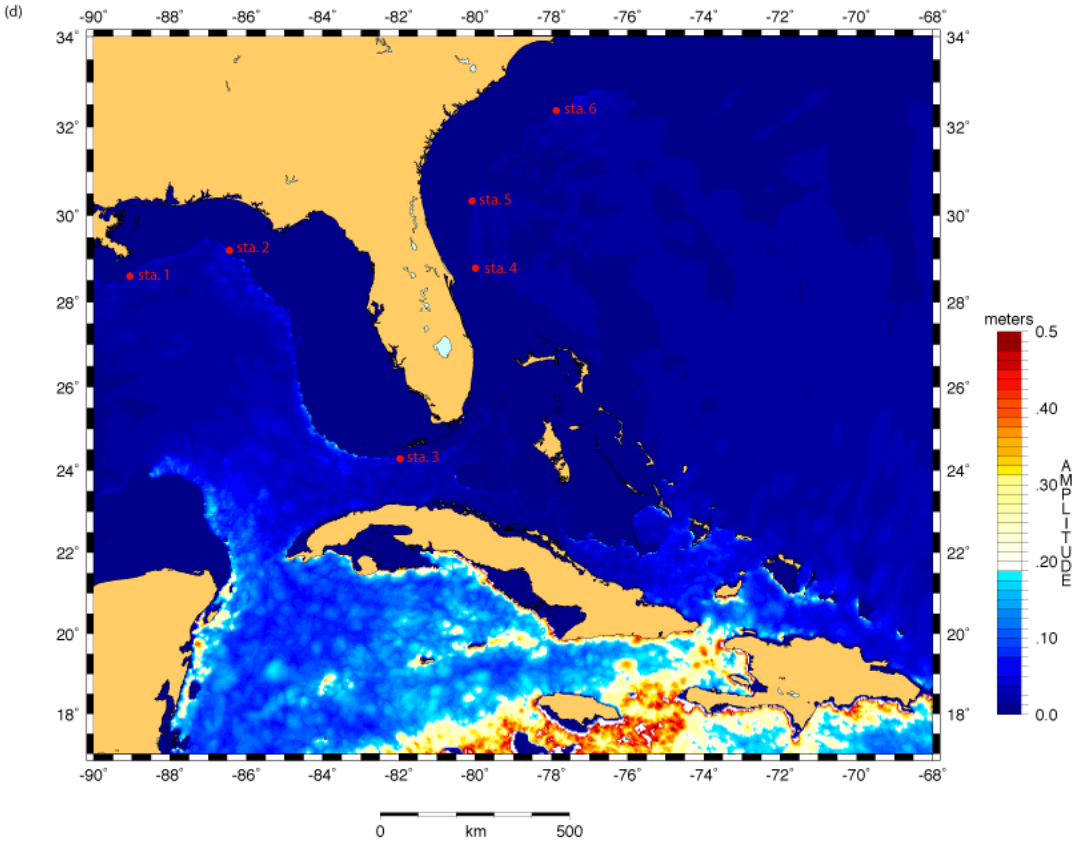
(d)
-90° -88° -86° -84° -82° -80° -78° -76° -74° -72° -70° -68°
34° 32° 30° 28° 26° 24° 22° 20° 18°
sta. 1
sta. 2
sta. 3
sta. 4
sta. 5
sta. 6
meters
0.5
.40
.30
.20
.10
0.0
AMPLITUDE
0
km
500

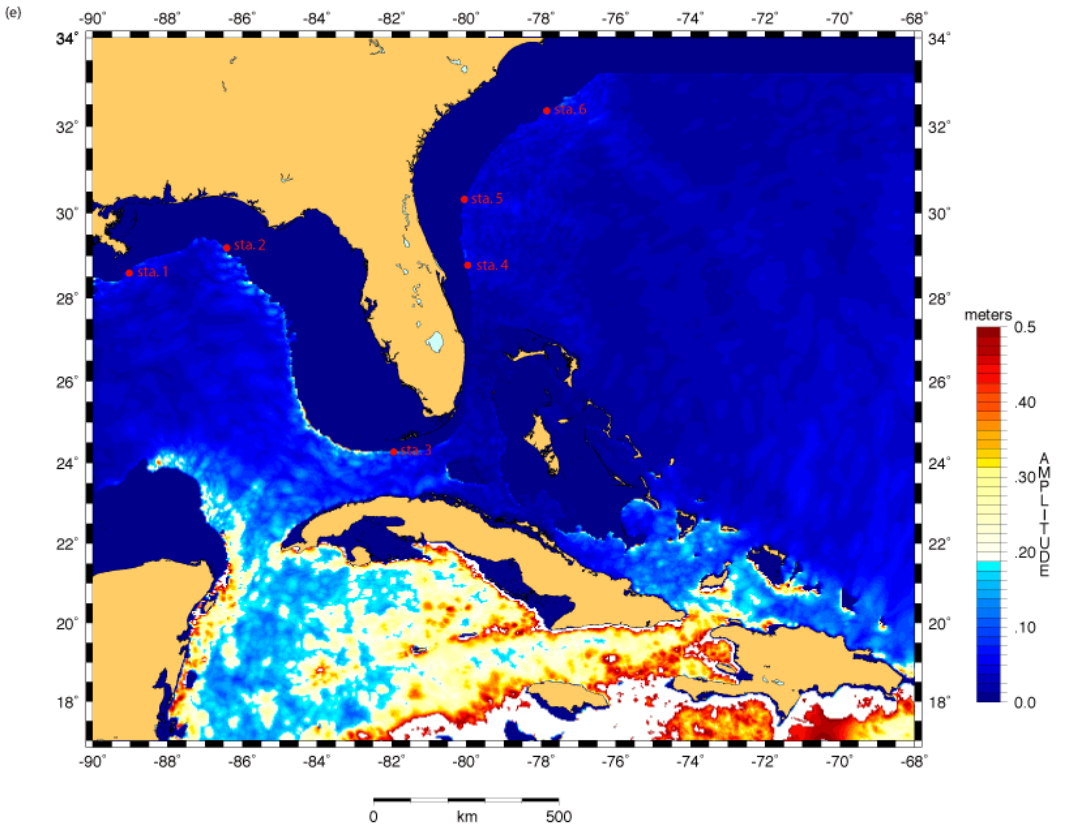
(e)
-90° -88° -86° -84° -82° -80° -78° -76° -74° -72° -70° -68°
34° 32° 30° 28° 26° 24° 22° 20° 18°
sta. 1
sta. 2
sta. 3
sta. 4
sta. 5
sta. 6
meters
0.5
.40
.30
.20
.10
0.0
AMPLITUDE
0
km
500

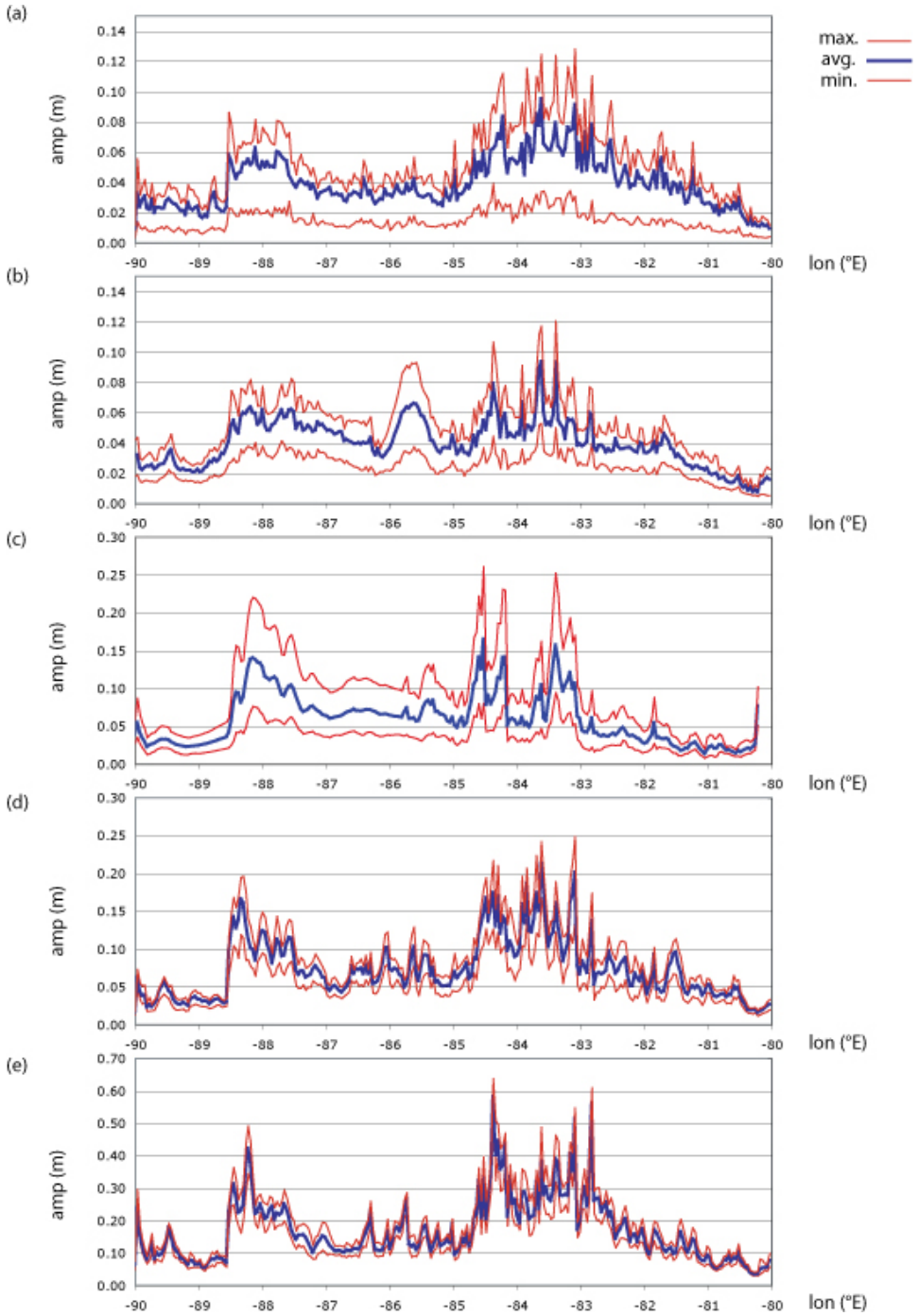

Figure 8-2: Peak offshore tsunami amplitude at the 250 isobath for 100 realizations of earthquakes on faults in the Caribbean: (a) W. Cayman OTF, (b) E. Cayman OTF, (c) N. Puerto Rico/Lesser Antilles SUB, (d) N. Panama OCB, (e) N. Venezuela SUB. Blue line shows average values; red lines extrema values. Results plotted along a latitudinal profile for the Gulf of Mexico coast. Note change in amplitude scale for (d) and (e).

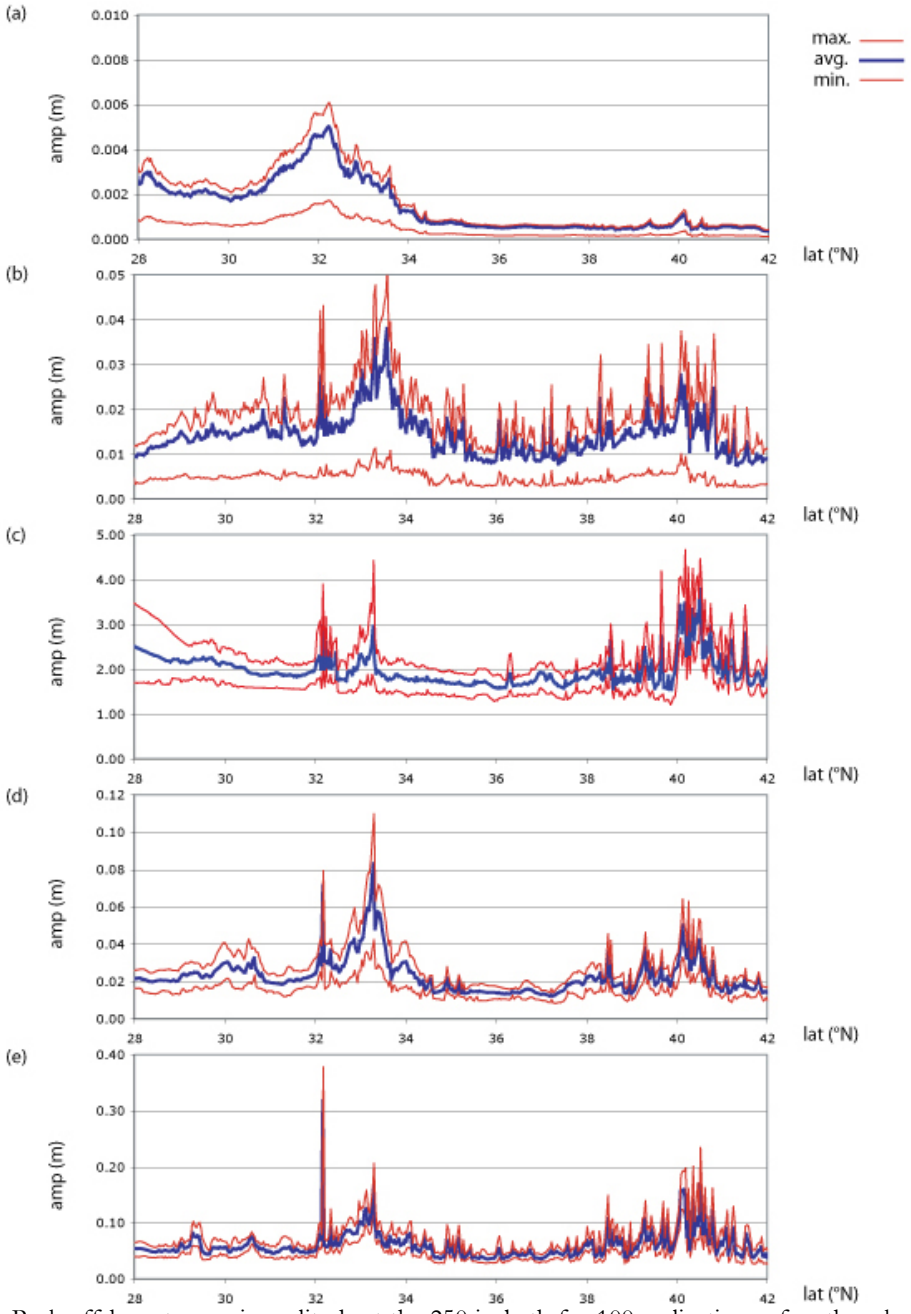

Figure 8-3: Peak offshore tsunami amplitude at the 250 isobath for 100 realizations of earthquakes on faults in the Caribbean: (a) W. Cayman OTF, (b) E. Cayman OTF, (c) N. Puerto Rico/Lesser Antilles SUB, (d) N. Panama OCB, (e) N. Venezuela SUB. Blue line shows average values; red lines extrema values. Results plotted along a longitudinal profile for the Atlantic coast. Note change in amplitude scale for each case.

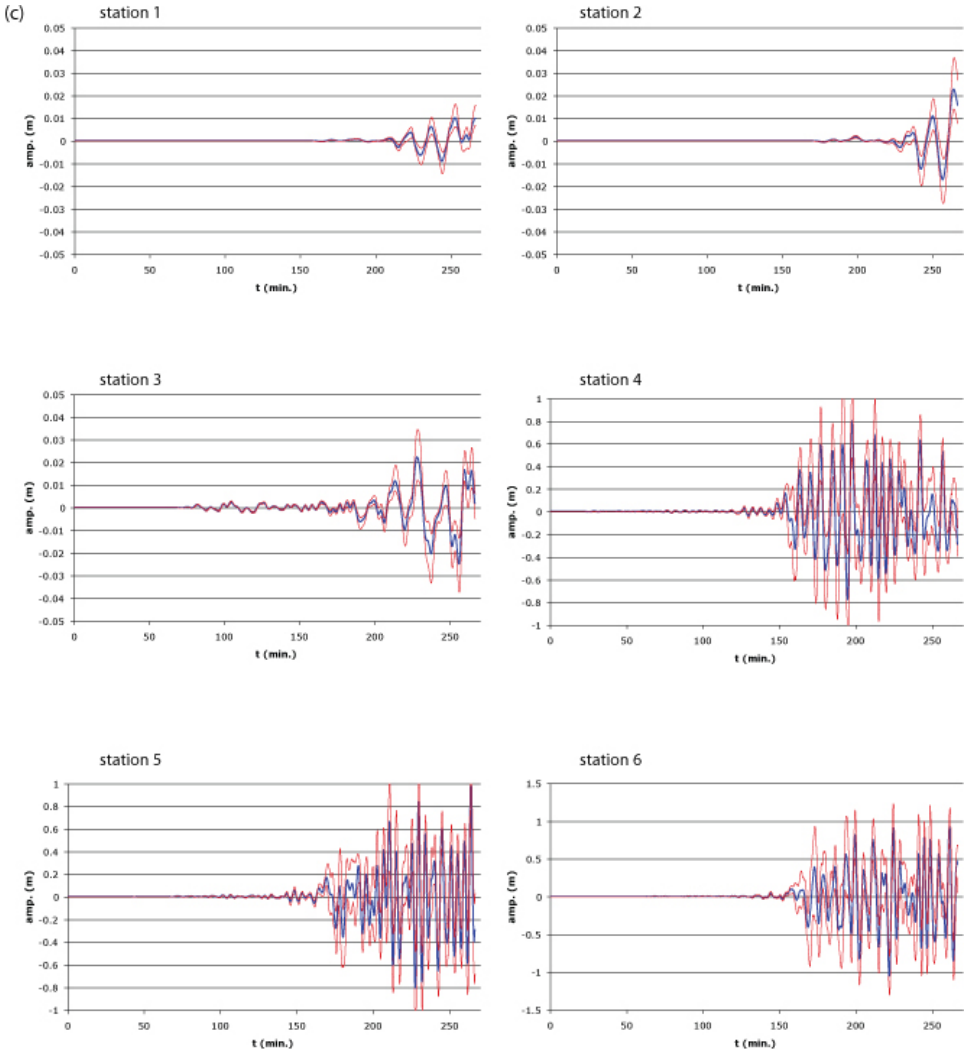

Figure 8-4: Range in synthetic marigrams (tsunami amplitude as a function of time) for six locations shown in Table 8-1. Results shown for each of the faults in the Caribbean: (a) W. Cayman OTF, (b) E. Cayman OTF, (c) N. Puerto Rico/Lesser Antilles SUB, (d) N. Panama OCB, (e) N. Venezuela SUB. Blue line shows average values; red lines extrema values. Note changes in amplitude scale.

(b)

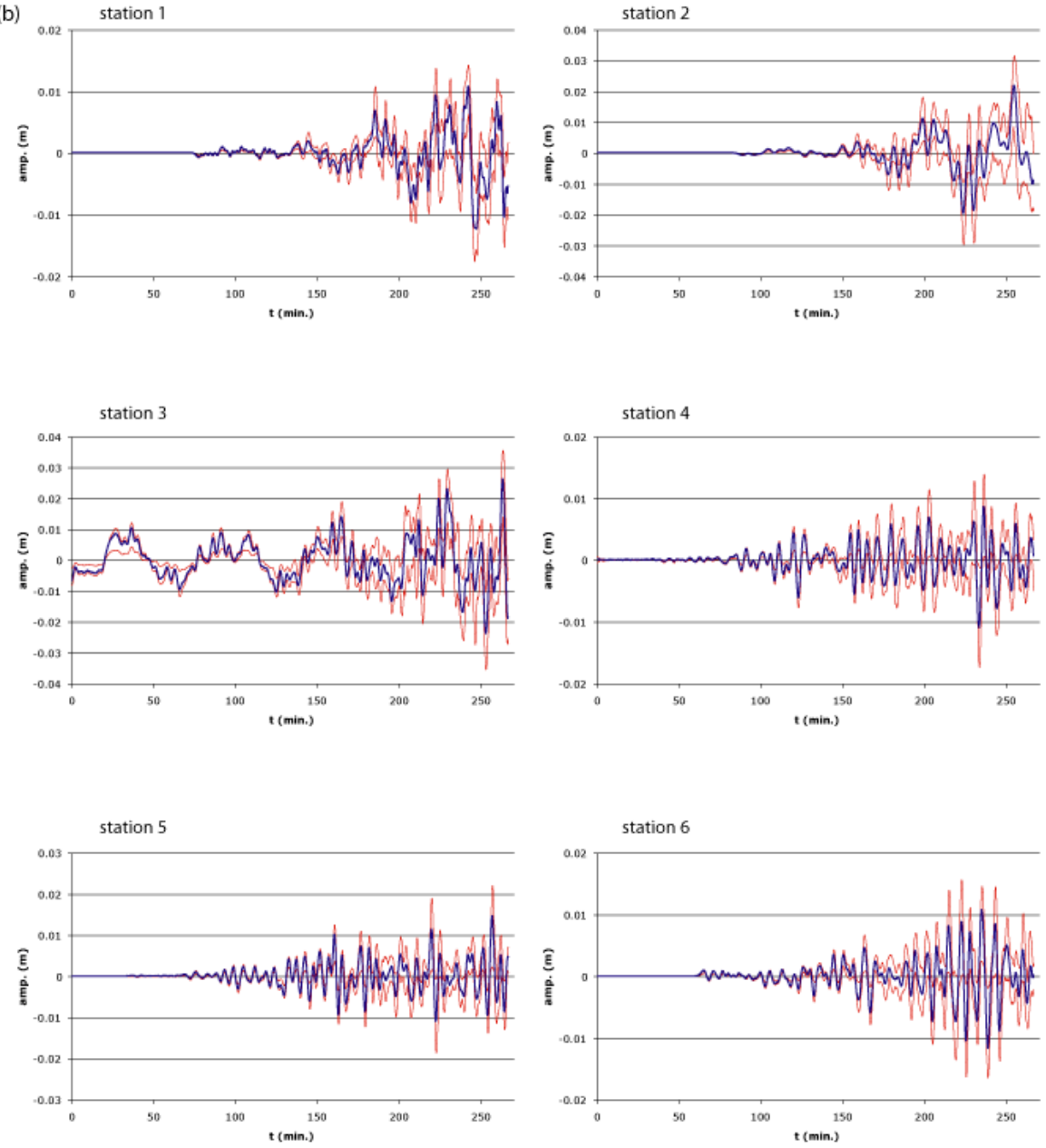
station 1
station 2
station 3
station 4
station 5
station 6
amp. (m)
t (min.)

(c)

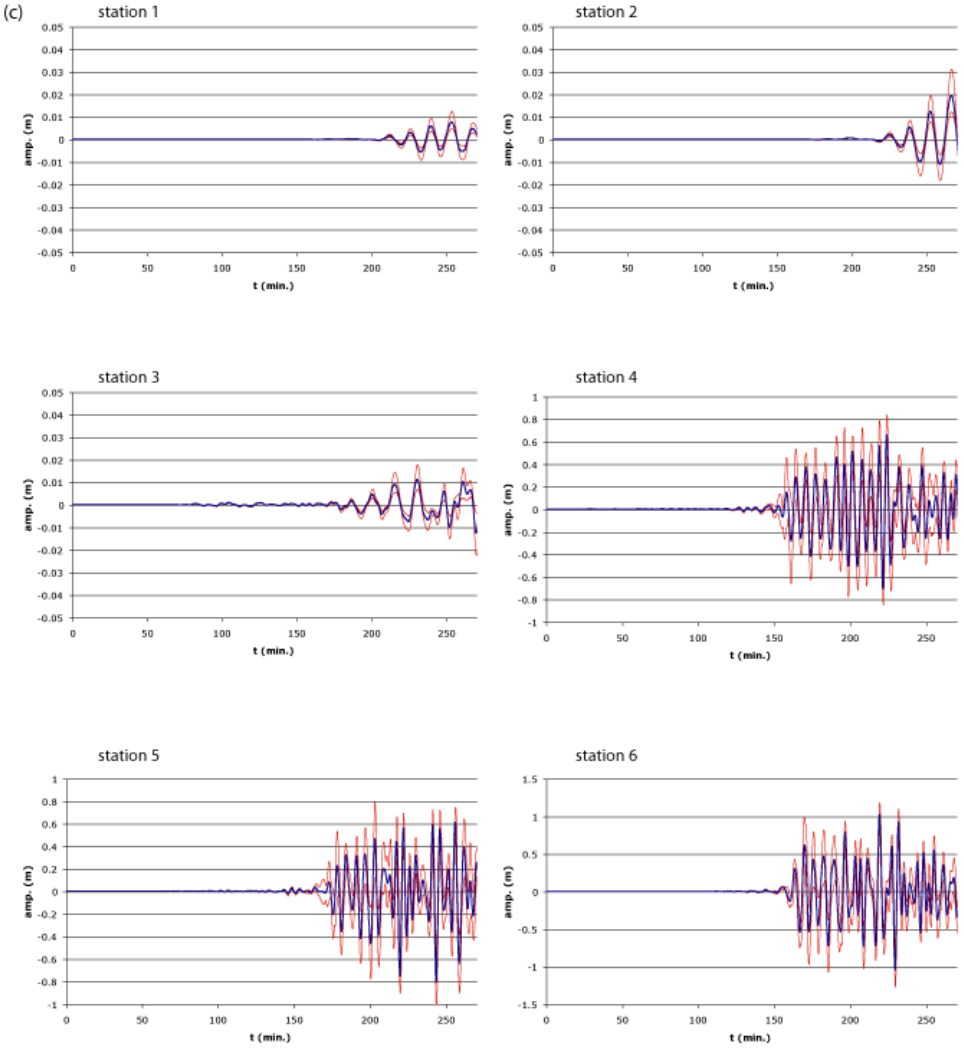
station 1
station 2
station 3
station 4
station 5
station 6
amp. (m)
t (min.)

(d)

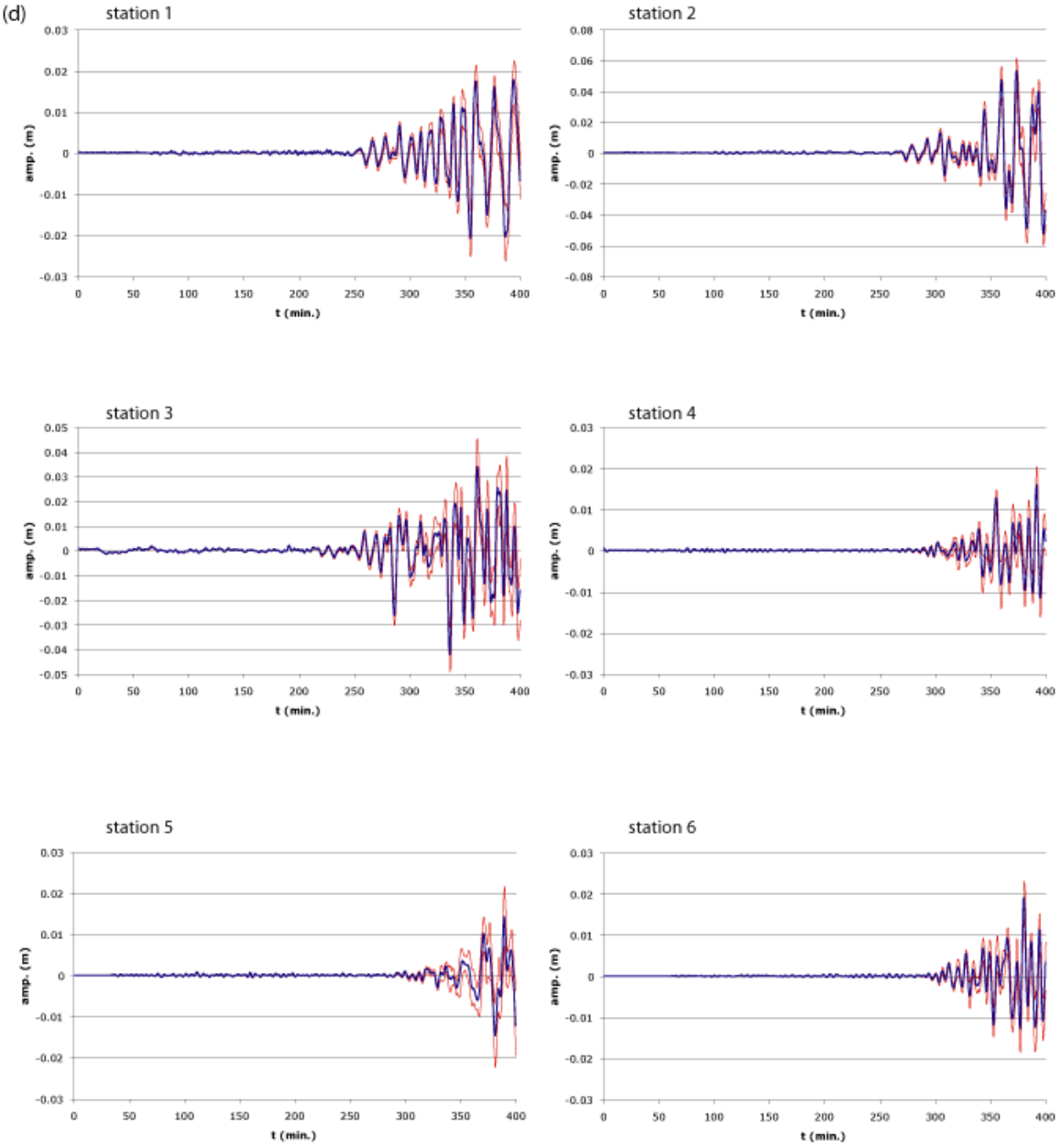
station 1
station 2
station 3
station 4
station 5
station 6
amp. (m)
t (min.)

(e)

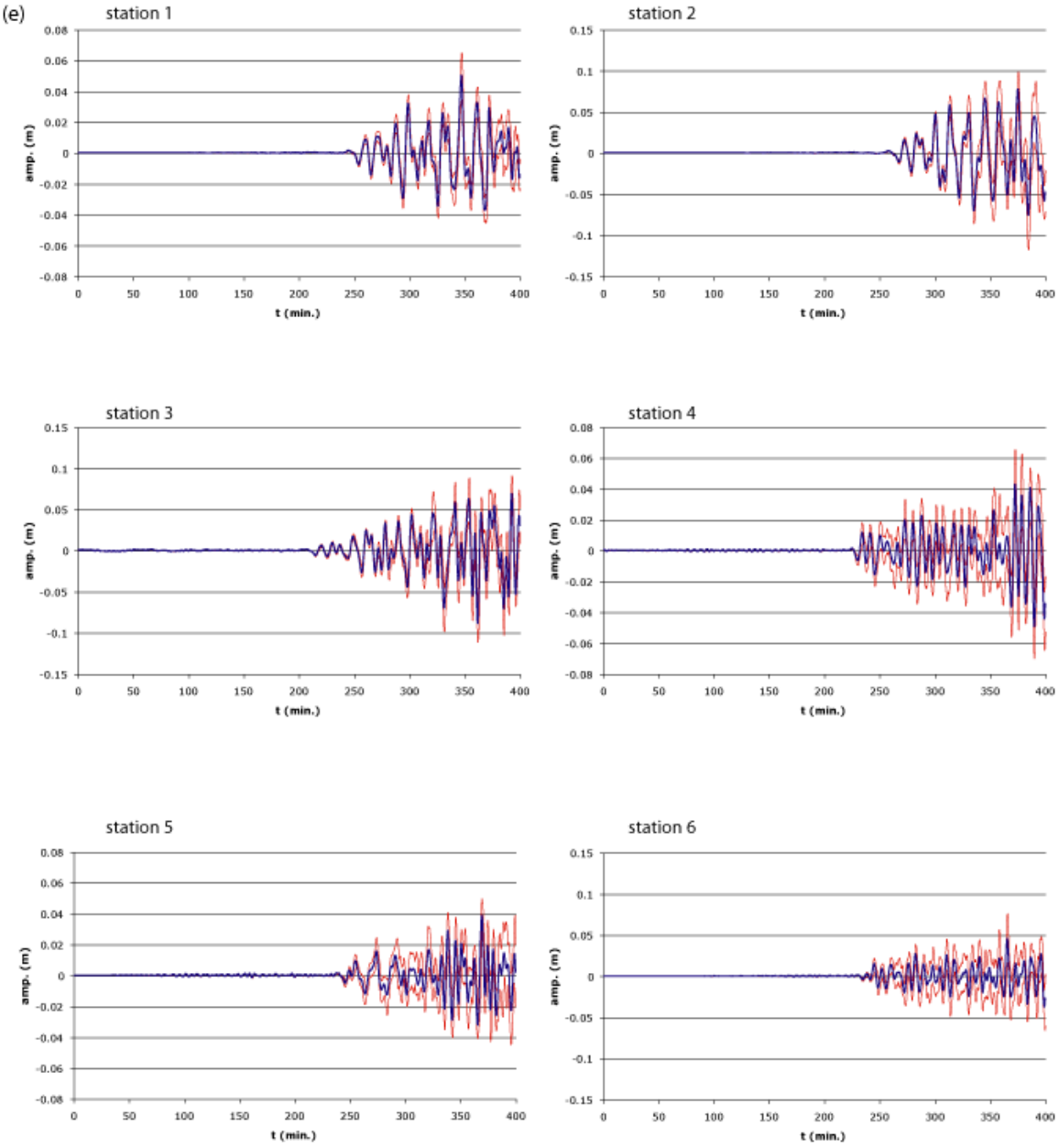
station 1
station 2
station 3
station 4
station 5
station 6
amp. (m)
t (min.)

References

Bird, P., 2003, An updated digital model of plate boundaries: *Geochemistry, Geophysics, Geosystems, v. 4*, doi:10.1029/2001GC000252.

Bird, P., and Kagan, Y. Y., 2004, Plate-tectonic analysis of shallow seismicity: apparent boundary width, beta-value, corner magnitude, coupled lithosphere thickness, and coupling in 7 tectonic settings: *Bulletin of the Seismological Society of America, v. 94*, 2380-2399.

Geist, E. L., 2002, Complex earthquake rupture and local tsunamis, *Journal of Geophysical Research, v. 107*, doi:10.1029/2000JB000139.

Geist, E. L., Titov, V. V., Arcas, D., Pollitz, F. F., and Bilek, S. L., 2007, Implications of the December 26, 2004 Sumatra-Andaman earthquake on tsunami forecast and assessment models for great subduction zone earthquakes: *Bulletin of the Seismological Society of America, v. 97*, p. S249-S270.

Herrero, A., and Bernard, P., 1994, A kinematic self-similar rupture process for earthquakes: *Bulletin of the Seismological Society of America, v. 84*, p. 1216-1228.

Knight, W., 2006, Model predictions of Gulf and southern Atlantic coast tsunami impacts from a distribution of sources: *Science of Tsunami Hazards, v. 24*, p. 304-312.

Lay, T., Kanamori, H., and Ruff, L. J., 1982, The asperity model and the nature of large subduction zone earthquakes: *Earthquake Prediction Research, v. 1*, p. 3-71.

Mei, C. C., 1989, The Applied Dynamics of Ocean Surface Waves: World Scientific, Singapore, 740 p.

Rabinovich, A. B., 1997, Spectral analysis of tsunami waves: Separation of source and topography effects: *Journal of Geophysical Research, v. 102*, p. 12,663-612,676.

Satake, K., 1995, Linear and nonlinear computations of the 1992 Nicaragua earthquake tsunami: *Pure and Applied Geophysics, v. 144*, p. 455-470.

Satake, K., 2002, Tsunamis, *in* Lee, W. H. K., *et al.* (Editors), International Handbook of Earthquake and Engineering Seismology, Part A: Academic Press, San Diego, p. 437-451.

Satake, K., Yoshida, Y., and Abe, K., 1992, Tsunami from the Mariana earthquake of April 5, 1990: Its abnormal propagation and implications for tsunami potential from outer-rise earthquakes: *Geophysical Research Letters, v. 19*, p. 301-304.

Shuto, N., 1991, Numerical simulation of tsunamis--Its present and near future: *Natural Hazards, v. 4*, p. 171-191.

Tanioka, Y., and Satake, K., 1996, Tsunami generation by horizontal displacement of ocean bottom: *Geophysical Research Letters, v. 23*, p. 861-865.

ten Brink, U. S., and Lin, J., 2004, Stress interaction between subduction earthquakes and forearc strike-slip faults: Modeling and application to the northern Caribbean plate boundary: *Journal of Geophysical Research*, *v. 109*, B12310, doi:12310.11029/12004JB003031.

Titov, V. V., and Synolakis, C. E., 1996, Numerical modeling of 3-D long wave runup using VTCS-3, *in* Yeh, H., *et al.* (Editors), Long wave runup models: World Scientific Publishing Co., Singapore, p. 242-248.

Titov, V. V., and González, F. I., 1997, Implementation and testing of the Method of Splitting Tsunami (MOST) model: NOAA Technical Memorandum, 11 p.

Titov, V. V., and Synolakis, C. E., 1998, Numerical modeling of tidal wave runup: *Journal of Waterway, Port, Coastal, and Ocean Engineering, v. 124*, p. 157-171.

Titov, V. V., González, F. I., Bernard, E. N., Ebel, J. E., Mofjeld, H. O., Newman, J. C., and Venturato, A. J., 2005, Real-time tsunami forecasting: Challenges and solutions: *Natural Hazards, v. 35*, p. 40-58.

Wells, D. L., and Coppersmith, K. J., 1994, New empirical relationships among magnitude, rupture length, rupture width, rupture area, and surface displacement: *Bulletin of the Seismological Society of America, v. 84*, p. 974-1002.

Section 3:

Case Study

Chapter 9: Geomorphology, Stability and Mobility of the Currituck Slide

Introduction

Experience with tsunamis (*e.g.* Tinti 1993) has shown that they can be caused by either movements along offshore faults (tectonic tsunamis) or by large submarine landslides (landslide tsunamis). The magnitude of landslide generated tsunamis depends strongly upon the size of the slide and how the landslide moves as it fails and flows. Submarine mass movements along the U.S. Atlantic continental margin have been recognized for many years (*e.g.* Booth *et al.* 1993; Twichell *et al.*, this volume) but it is only recently that their potential tsunamigenic contribution has been considered (ten Brink *et al.*, this volume). As is presented elsewhere, major mass movements that have taken place on the Atlantic continental margin over the last 100,000 years (Lee *et al.* this volume) may be good candidates for tsunamigenic mass movements. Many of these slides have left a clear signature which enables a minimum definition of the initial stratigraphic and physical conditions prior to failure, and also of the volume and shape of their deposits. One of them, the Currituck slide (Figure 9-1) has been selected to evaluate the tsunamigenic potential of such slides. The Currituck slide has been selected to be analyzed as part of a USGS effort sponsored by the Nuclear Regulatory Commission to perform an evaluation of the risk of damaging tsunamis impacting the U.S. East coast (ten Brink *et al.*, this volume). This paper is part of an overall effort to consider various geoscientific aspects of tsunamigenic mass movements using the Currituck slide (Figure 9-1), as a methodological example in a way similar to what has been done for the Palos Verdes slide off Los Angeles (Locat *et al.* 2004).

The Currituck slide (Figure 9-1), located northeast of Cape Hatteras, has been investigated earlier by Bunn and McGregor (1980) and Prior *et al.* (1986). Prior *et al.* (1986) presented a detailed description of the stratigraphy and morphology of the slide source area based on sidescan sonar imaging and high resolution seismic surveys. From a morphological viewpoint, the model (Figure 9-1c and d) proposed by Prior *et al.* (1986) does agree very well with what is observed from the multibeam bathymetry image obtained more recently (Figure 9-1b). They concluded that two slides could be observed (Figure 9-1d) having a total volume of 128 km^3. According to Prior *et al.* (1986) the sliding took place largely in gently seaward dipping Mid-Miocene (or younger) sediments and concluded, based on sedimentation rate

estimates, that the slide occurred 43,300 to 22,500 years BP. They also proposed that the instability could be the result of the progradation of a delta over the shelf edge but, because the failure surface is clean of deltaic sediments, they conclude that it must have taken place towards the end of the period of rapid sedimentation. A key question here is, whether or not, the slides identified by Prior et al (1986) represent different events or if they were created as part of a single event. The mobility analysis presented below suggests that they must have been a single event.

The objectives of this research effort were to complete a slope stability and mobility analysis of the Currituck slide (Figure 9-1) based on previously acquired information in order to provide input data into a tsunami analysis (Geist *et al.*, this volume). To achieve this objective there is a need to establish the following conceptual models, which are based on engineering judgment, existing geophysical, mapping, and sediment core data:

1. A morpho-stratigraphic model of the departure zone of the slide area.
2. A depositional model in the run-out zone.

These conceptual models are used as input to analyse the stability of the initial slope using SlopeW (Krahn 2004) and the mobility of the failed mass using BING Imran *et al.,* 2001b). The approach used to gather the information for these models is presented below.

Approach

The approach used follows most of the steps proposed by Locat *et al.* (2004) which includes: (1) morphological analysis, (2) estimation of geotechnical properties of the soil or rock for limit equilibrium analysis of slope failure conditions, (3) and post-failure flow dynamics (analysis of the run-out characteristics of the failed mass). At the end this analysis we provide conclusions on:

1. The geometry of the source area prior to failure.
2. The potential triggering mechanisms and potential failure scenarios.
3. An estimate of the volume of failed material and run out characteristics of the slide.
4. Inferences on initial velocity and acceleration of the failed mass obtained from the mobility analysis.

The geomorphological analysis makes use of seismic and multibeam data sets (Twichell *et al.* this volume, Chaytor *et al.* , 2007, and this volume) and also the stratigraphic interpretation provided by Prior *et al.* (1986). Since no direct geotechnical data are available for the sediments in the Currituck slide area, we used the detailed work of Dugan *et al.* (2003) from the ODP site 1073 and of Locat *et al.* (2003) on the Hudson Apron located on the continental slope some 400 km to the northeast.

The limit equilibrium state of the slope is assumed under ambient and seismic loading and for various conditions of pore pressure. It is assumed here that the material failure behavior follows a Mohr-Coulomb failure criterion such as:

$$\tau^* = c' + (\sigma - u)\tan\phi', \quad (1)$$

where τ* is the shear strength of material that can be mobilized along the failure plane, *c'* the cohesion, σ the total stress, *u* the pore pressure and φ' the friction angle. The computation was carried out using the General Limit Equilibrium (GLE) method (Krahn 2004). The role of pore pressure was evaluated using the pore pressure ratio (*ru*) calculated using the buoyant unit weight of the sediments (γ*):

$$r_u = \frac{u}{\gamma^* h}, \quad (2)$$

where *h* is the thickness of the material above the potential failure plane. For a *ru* value of 1, the pore pressure is equal to the weight of the sediments. Using the GLE method, the effects of earthquakes are taken into account by the coefficient of seismic acceleration *k*:

$$k = \frac{\alpha W}{g}, \quad (3)$$

where α represents the pseudostatic acceleration and *g* the gravitational acceleration, and *W* the total weight of the sediment, *k* can be seen as a percentage of *g*.

For post-failure analysis of the failed mass, we used a 1D-flow dynamics model, BING, presented by Imran *et al.* (2001b) which has been developed for the study of debris flows. BING can be used with various rheological models: Bingham, Herschel-Bulkley and bi-linear. In our analysis, we use both bilinear and Bingham flow models. The bi-linear model was proposed by Locat (1997) to describe the rheology of clayey silt or silt mixtures, which often present a pseudo-plastic behavior. A similar proposal was made by O'Brien and Julien (1988) also for sediments with high silt content. The bi-linear model assumes that the initial phase of the flow is Newtonian (Figure 9-4 in Locat *et al.* 2004) and evolves, after reaching a threshold shear rate value (γ*o*), into a Bingham type flow. The constitutive equation proposed by Locat (1997) for bi-linear flow is expressed by:

$$\tau = \tau_{ya} + \mu_{dh}\gamma - \frac{\tau_{ya}\gamma_o}{\gamma + \gamma_o}, \quad (4)$$

where τ is the flow resistance, τ*ya* the yield strength, μ*dh* the plastic viscosity, γ the shear rate, and γ*o* the shear strain rate at the transition from a

Newtonian to a Bingham behavior.
In BING (Imran *et al.*, 2001b), Equation 4 is re-written

$$\frac{\tau}{\tau_{ya}} = 1 + \frac{\gamma}{\gamma_r} - \frac{1}{1 + r\frac{\gamma}{\gamma_r}}, \quad (5)$$

where γr, is the strain rate defined as

$$\gamma_r = \frac{\tau_{ya}}{\mu_{dh}} \quad (6)$$

and r the ratio of the strain rates,

$$r = \frac{\gamma_r}{\gamma_o} \quad (7)$$

The Herschel Bulkley model corresponds to the following expression:

$$\tau = \tau_y + K\gamma^n \quad (8)$$

where:

$$K = \frac{\tau_y}{\gamma_r^n} \quad (9)$$

and is equivalent to a Bingham model when the exponent 'n' equals 1. For the mobility analysis both Bingham and Bilinear models are used.

For the Currituck slide, no rheological data are available. Consequently, we rely on the morphology of the source area to help estimate the yield strength. This is done using the following equation initially proposed by Johnson (1970):

$$\tau_{ya} = H_c\gamma^* \sin\beta, \quad (10)$$

where Hc is the critical thickness (in meters) of the debris flow deposit, γ^* is the buoyant unit weight (in kN/m^3) of the debris flow material and β the angle (in degrees) of the slope over which the debris flow came to rest.

The values related to the plastic viscosity, *i.e.* the strain rate, γr, and the ratio of strain rates, r, will be estimated from a parametric analysis to find the best values which can fit the observed geometric characteristics in the run-out zone, the travel distance in particular. The value of γr can also be estimated from rheological testing results which has shown that the value of γr is about 1000 for clays (Locat 1997, Locat and Lee 2002, Lee *et al.* 2007) but can be as low as 10 for sand (Jeong *et al.* 2007).

Geomorphological analysis

The initial geomorphology of the Currituck slide has been detailed by Prior *et al.* (1986) and is shown in Figure 9-1b and c. Their inferred morphology of the slope prior to failure is shown in Figure 9-1d. Details of the morphology of the source area of the slide are shown in Figures 9-1b and 9-2, which show images and profiles generated from the multibeam data that was collected subsequent to the study by Prior *et al.* (1986).

Prior *at al.* (1986) noted the presence of two slides: slide 1 (lower, assumed to have started first) with an escarpment dipping at about 15°, and slide 2 with an escarpment (upper) of about 9 top 10° and (Figure 9-3c). The actual slope morphology of the upper escarpment is similar to the adjacent areas suggesting that some sediment draping took place after the slide. The multibeam data has shown that the slope angle in the lower escarpment can reach values as high as 30°, particularly in the gullied sections (Figure 9-2). Prior *et al.* (1986) also noted that within the lower escarpment there were step like features (also revealed by the multibeam data (Figure 9-3b) showing the influence of the slope stratigraphy on shape of the failure surface. This control of the bedding on the failure surface is clearly shown in Figure 9-2 which shows bathymetry profiles more or less perpendicular to the main axis of the slide area (departure zone). In looking at the profile along line 2 in Figure 9-2b, the control of the bedding on erosion is also seen by the position of the bottom of the small canyons that are also aligned at the same orientation as the slide 2 failure surface. The multibeam bathymetry indicates the failure plane of slide 1 (lower) is not uniform but rather has a step-like shape (line 2 in Figure 9-4). Prior *et al.* (1986) assumed the surface below the lower escarpment was covered by debris coming from slide 2 (see also Figure 9-1c and d). Below the lower escarpment, the cross section shown in Figure 9-2b for line 3 reveals that there is another depression (below the so-called 'base of slide 1a') which likely represents the expression of another failure surface, more restricted laterally than the other ones and buried under some debris.

Having established the morphology of the slide area subsequent to failure, the next step is to establish the morphology prior to the slide in order to estimate the volume of material removed by the failures and construct a model for slope stability evaluation. Recreating the original surface was done by the detailed analysis of the morphology of the upper part of the slide and comparing it to the surrounding morphology. A shelf-edge delta is inferred to have formed in this area during the Pleistocene (Poag and Sevon (1989) but its offshore extension is not precisely known. The multibeam data shows what could be a partial preservation of this original feature along the southern side of the Currituck failure (Figure 9-3). The position of the toe of the delta has been taken by extending the location of the delta toe that is still preserved along the southern edge of the failure across the failed area as a smooth arc (Figure 9-3). The length of the center line of the slide is about from the upper escarpment to the proposed toe of the slide area before failure is about 30 km. Using the Fraser Delta as an example, the actual

foreslope of the delta may have been as high as 15° for depth less than 200m but less than 2° at greater depths (Christian *et al.* 1997).

The cross-section shown in Figure 9-4 was constructed considering the following elements:

1. The slide took place at a time close to the minimum sea level. This is based on Prior et al (1986) who suggested the timing of the event indicating that a delta was extending into deeper water or near the shelf. For this reason, the shoreline at the time of the event is set at an elevation about 120m below the present sea level.
2. The topset beds of the delta (having a slope of about 1°) extended as much as 5 km seaward of the present shelf edge.
3. The pre-slide surface topography is assumed to be parallel to the surface of the part of the delta that is still preserved south of the failure and extended until it intersected the present sea floor, *i.e.* at about 30 km from the actual shelf edge.

From this re-construction, it appears that the maximum thickness of the mass involved in the slide is about 750 m ('h' in Figure 9-4) at the base of the lower scarp (note that the actual height of the scarp is about 350m because the upper part has been removed when slide 2 took place, see also Figure 9-1d). Using the cross section shown in Figure 9-4 and the available bathymetry, we have estimated that the volume involved is about 108 km^3 and 57 km^3 for slide 1 and 2 respectively for a total of 165 km^3. When we look at the actual slide morphology (Figures 9-2 and 9-3) and the actual slope angles, the clean surface exposed just above the lower scarp suggests that the failure developed rapidly, much like what has been modelled for the Storegga slide (Bryn *et al.* 2004; Kvalstad *et al.* 2005). The main similarity between the Storegga and the Currituck slides is the control of the bedding on the location of the failure surface (as also pointed out by Prior *et al.* 2006, Figure 9-1c and d).

Stability analysis

Strength parameters

To evaluate the slope stability of the Currituck slide, geotechnical information is needed on strength parameters (*e.g.* Eq. [1]: cohesion and friction angle). In the absence of direct measurement on samples from the Currituck slide area, they are derived from local stratigraphic and morphological information and supplemented by the geotechnical data collected at ODP site 1073 on the continental slope 400 km to the northeast of the Currituck area (Dugan *et al.* 2003). Additional information comes from geotechnical testing of samples from the Hudson Apron immediately south of Hudson Canyon (Locat *et al.* 2003).

Strength parameters can also be estimated on the basis of equilibrium slopes angles in a given area by assuming that the slope angle may reflect the

intact strength of the sediments. This is mostly valid only for slopes which have been eroded (Locat 2001). The slopes of the area can be grouped into three categories (Figures 9-1a and 9-3). The first category is for slopes generated by sediment accumulation near the shelf edge resulting in prograding clinoforms with surface slopes varying between 4° and 10°. The second category includes slopes formed by erosional processes associated with submarine canyon development. In this case, slope angles can be as high as 30°. The third category is for slopes resulting from mass failures along failure planes that are more or less controlled by the bedding plane of sediments underlying the continental slope (Prior *et al.* 1986). The flat surface at the center of the Currituck slide is an excellent example (Figures 9-1a, 9-2 and 9-3). Therefore, eroded areas can provide indications on the strength parameters, and the friction angle in particular indicating friction angle values approaching 30° which is similar to what has been measured for the Hudson Apron sediments (Locat *et al.* 2003). The relatively low angle of canyon slopes also reveal that the cohesion does not contributes significantly to the long term strength of the slope sediments. If we assume a constant cohesion with depth, its relative contribution to the shearing resistance rapidly diminishes with depth as shown in Figure 9-6 when considering an infinite slope analysis. In the case computed in Figure 9-6, we used a cohesion of 10 kPa and 100 kPa and, in both cases, the contribution of the cohesion to the shearing resistance (Eq. [1]) reduces to less than 10% at a depth grater than 200m for a failure surface inclined at 5°.

For pore pressures, its significance can be postulated by the presence of the actual flat surface of the exposed failure surface which developed in sediment that was at least normally consolidated (according to canyon slope angles close to 30°). Such a low angle failure surface could be generated by the generation of high pore pressures (parameter u in Eq. [1]). These high pore pressures can be the result of one or a combination of the following processes: groundwater seepage forces generated by either deltaic accumulation or a particular coastal configuration of the underlying aquifer, gas hydrates, and earthquakes. Erosion alone at the base of the continental slope, which is a slow process cannot alone generate such higi excess pore pressures.

For the following back analysis of the Currituck failure, we adapted the stratigraphic model of Prior *et al* (1986) and used geotechnical parameters derived from morpho-stratigraphic information (Figure 9-4). The resulting geological model in shown in Figure 9-5 and will be used with the slope stability package SlopeW. The origin of the profile (Figure 9-5) is taken 5 km behind the actual shelf edge, and the reference datum placed at a depth of 2200m below present sea level. In order to see the stratigraphic model with greater details, the elevation is exaggerated by a factor of 3.75. Considering that the toe of the slope could be estimated from the multibeam bathymetry and from extending the stratigraphy in the escarpment to deeper waters (see Figure 9-4) we consider that the base of any deltaic accumulation could not exceed that position. Therefore, taking a foreslope angle of about 3°, the deltaic deposit (unit 1 in Figure 9-5) has been draped over the underlying sedimentary sequence. This scenario resulted in a position of the edge of the

delta, at the time of sliding, less than 1km offshore form the current shelf edge location (Figure 9-5). This also maintains volume conservation.

Figure 9-5 presents a geological cross section showing four units. Buoyant unit weights of 8, 10 and 10 kN/m^3 were selected for layers 1, 2, and 3 respectively. At the top, unit 1 represents deltaic sediments with properties taken with a friction angle of 30° and no cohesion. The other 3 units (2 to 4) are believed to consist of layered clayey sediments and rock (layer 4). Layers 2 and 3 were given a friction angle of 30° and 25° and a cohesion of 8 kPa (from Hudson Apron data of Locat *et al.* 2003) and 100 kPa respectively. For the sake of analysis with SlopeW, unit 4 is considered as a hard impermeable rock. The choice of a higher cohesion for unit 3 has been done to reflect the relative increase in strength due to aging and is within values expected for soft rocks (Barton 1976). Since the position of the failure plane are already fixed for the back analysis, the mobilized shearing resistance is constrained to these surfaces so that the remaining instability factors are link to generation of excess pore pressure or the loading (sediment progradation).

Regarding the pore pressures, in the absence of direct *in situ* measurements, we consider that the high pore pressure modeled by Dugan *et al.* (2005) for sediment in the Hudson Canyon area may be applicable here for the purpose of a parametric analysis. A similar approach has been used for the Hudson Apron by Locat *et al.* (2003).

Stability back analysis

Since the geometry of the failure surface can be approximated with some confidence and that it is considered to result from a slope failure, the overall factor of safety reached a value of 1 or less under conditions that are still to be evaluated through the following back analysis. The limit equilibrium analysis considers that the forces acting on a slope are in equilibrium when the resisting forces equal the gravitational forces so that the ratio of these forces, called the Factor of Safety (F), are at unity (F = 1).

The position of the failure surface is taken as a boundary condition for the computations so that all the evaluation is done considering failures on these surfaces (slide 1 and slide 2). Slope failures 1 and 2 are considered separately here, i.e. that slide 2 takes place with a new slope geometry created by the removal of sediments by slide 1. As it has been shown by Locat *et al.* (2003) for the Hudson Apron area to the north, instabilities which do develop on such a low natural slopes and low angle failure surfaces must involve triggering conditions requiring either very high excess pore pressures or significant earthquake acceleration or both. Since it has been proposed by Prior *at al.* 1986 that the failure could have been triggered by an excess pore pressure resulting from sediment accumulation, we included this parameter (Eq. [2]) in our analysis. In addition, observations above (see Figure 9-3) related to a potential active fault in the vicinity of the slide area, and known major historical earthquakes in the Charlestown area (M=6.9 in 1886, Bakun and Hooper 2004) lead us to also consider seismic acceleration as a potential trigger for the slide (Eq. [3]) although the aerial extent of the effect of

earthquakes may be quite limited in the region (ten Brink, this volume). This is also in agreement with the work of Keefer (1984) and Rodriguez *et al.* (1999) since significant mass movements can be initiated at a distance between 100 and 200 km for a M=7 earthquake.

As mentioned above, a back analysis was carried out to evaluate the effect of (1) excess pore pressure, (2) prograding deltaic sediment loading (only for slide 1), and (3) seismic acceleration for slide 1 and 2. Although not shown hereafter, considering a single failure event integrating slide 1 and 2 failure planes in a step like fashion yielded similar results for initiation of instability to what is presented hereafter.

The effect of excess pore pressure and delta progradation has been simulated together and the results, for slide 1, are shown in Figure 9-7 and in Figure 9-8 (for k = 0.0) for slide 2. If we consider that the estimated position of the delta at the time of sliding was less than 1km from the actual shelf edge, the factor of safety (F) would vary from a value of about 6.3 with no excess pore pressure to 1.5 for a pore pressure ration of about 0.8, which is very high, i.e. at a depth of 200m, the a pore pressure ratio of 0.8 would means a pore water pressure of about 1600 kPa. For slide 2, the factor of safety values for the same pore pressure ratios are 5.6 and about 1 respectively. The lower factor of safety values for slide 2 are largely due to the fact that the lower slope left by slide 1 is steeper than for slide 1 and also that the thickness of unit 1, relative to the lower units, is proportionally thicker.

The loading effect of a prograding delta (unit 1 in Figure 9-5) on the underlying stratigraphic formations has been estimated by considering that the base of the slope would remain at the same location and that no excess pore pressure would be generated by the sedimentary accumulation. For example, moving the delta edge seaward 20 km increases the foreslope angle from 4° near the near shelf edge to about 14° (Figure 9-5). A major consequence of moving the delta front offshore is the direct increase on the total volume of the slide up to an unrealistic level compare to the known volume. To maintain a volume similar to estimations, i.e. about 165 km^3, a realistic position of the delta edge cannot exceed 5 km seaward of the present shelf edge. Interestingly, even for a delta advancing more than 10 km (slide1 case), still significant pore pressures are required for the material to fail. The simulation in Figures 9-7 suggests that the actual impact of delta advance, considered only as a new load, is not particularly significant. It is also important to point out here that the effect of pore pressure increase, in the underlying formations, due to delta progradation, has not been considered. Still, the progradation of the delta, to a distance less than 5 km from actual shelf edge, cannot generate conditions leading to failure of the underlying sediments.

To simulate the effect of seismic acceleration (earthquake loading) on the stability of the sediments, we kept a delta advance to less than 1 km (Figure 9-8). Results are shown for both slide 1 and 2. For the same reasons as indicated above, the geometry of the remaining sediments after slide takes place is such that failure of slide 2 can take place under lower excess pore pressure or seismic acceleration than slide 1. Earthquake magnitude (M) near

7 can corresponds to a seismic acceleration coefficient between 0.15 and 0.2 which could generate a failure of slide 1 under moderate excess pore pressures (r_u = 5). For instability to be generated without existing excess pore pressures would require a very strong earthquake generating a seismic loading much in excess of 0.3.

In any case, a very large volume of sediment was mobilized by the Currituck slide under conditions likely including both existing pore pressure (or equivalent) and seismic acceleration. In the next section we will investigate the link between the run-out distance of the slide debris as a function of the volume, in the starting zone, to see weather or not the slide occurred at once or not.

Mobility analysis

The preliminary geomorphological and stability analysis of the Currituck slide indicate that the slide took place under conditions that dislodged a large volume of sediment at a pace that was fast enough to almost completely clear the failure surface above the lower scarp (see Figures 9-1 to 9-3). The multibeam map of the slide area has been analyzed in detail and its extent is shown in Figure 9-9 for which it has been possible, in most cases, to estimate volume and average thickness. The farthest distance reached by the debris was 220 km from the shelf edge and 190 km from the toe of the source area. These observations are key elements for the analysis of the mobility of the Currituck slide and provide geomorphological boundary conditions for the back analysis of the flow properties and mobility.

The bathymetry of the area inside the flow path was derived from the multibeam bathymetry, and for the purpose of modelling, we used a smoothed version of the flank profile (Figure 9-10). The slope angle along this profile varies from about 8° on the upper slope to less than 0.5° on the continental rise.

Geometry

For the mobility analysis we need to define the geometry of the slide and the properties of the flowing material. BING requires a flow path, which is provided by the bathymetry (Figure 9-10). The length, width, and thickness of the failing mass, at the onset of failure, are also needed. For simplicity, BING uses a half ellipse for the initial shape of the slide (see insert in Figure 9-10) which is very close to a long rectangle in our case. The initial geometry of the flowing mass is computed from volume estimate based on the geometry identified in Figures 9-4 and 9-5. Here we consider that the downslope length of the failed area is about 30000 m (30 km), and the width about 20 km). For example, if the initial thickness (*Hi*) in the starting zone is 250m (see insert in Figure 9-18) we get a volume of 150 km^3. So, for the computed values of Prior *et al.* (1986) at 128 km^3 and herein at 165 km^3, the value of *Hi* are 213m and 275m respectively.

Rheological parameters

Using Eq. [10], with a buoyant unit weight γ', at 8 kN/m^3, and β the potential slope angle, and thickness (*Hc*) of the debris (here considered as critical since it is the final value measured in the deposiitnal zone), a nomogram was computed to help select the appropriate yield strength. Results are shown in Figure 9-11. Considering that the slope angle in the depositional zone is between 0.2° and 0.5°, we can see that for a range in critical height (or thickness) between 20 and 50m taken from field observations of the various lobes (Figure 9-9), the yield strength could vary more or less between 2kPa and 4kPa. From the yield strength, the plastic viscosity can be estimated, according to Locat (1997) and Jeong *et al.* (2007), to vary between 0.002kPa.s and 0.02 kPa.s.

Mobility and flow volume

Using BING with the Bilinear model we then computed the relationship between the mobilized flow volume and the run-out distance of a flow over the topography given in Figure 9-10. The computation was done to cover the range in yield strength, *i.e.* between 2kPa and 4 kPa. Results are shown in Figure 9-12. On that figure, we also point out four specific volumes: slide 1 and 2 of Prior *at al.* (1986) along with the total volume estimated by Prior *et al.* (1986; 'a' in Figure 9-12) and our estimate ('b' in Figure 9-12). On Figure 9-12, we also indicate the maximum run-out distance observed from the multibeam bathymetry map of Figure 9-9.

A major element to point out here is that if slides are taken separately, results shown in Figure 9-12 indicate that they cannot generate the observed mobility. Therefore, the various features observed in the starting zone (failure area) were created more or less at the same time indicating that, for post-failure analysis, the total volume of 150 km^3 (slide 1 + slide 2) must be used, which is close to the estimated 165 km^3 reported above.

From this point on, we analyse the mobility of the Currituck slide using a single volume of 150 km^3 and a yield strength of 2000 Pa.

Flow dynamics

In order to provide some insight into the tsunamigenic potential of the Currituck slide, we use BING to estimate the velocity and acceleration profile of the failing mass. It is relevant here to point out that BING, like all other flow models, assumes that the failed mass has instantaneously reached the flow properties required for the modelling, *i.e.* there is no transition in terms of displacements between failure and post-failure. As noted by Imran *et al.* (2001a. b) this will yield initial high acceleration. Still, the observed values can be used or modified according to a flow transition model so that the initial acceleration can be adapted. For the flow dynamics, we used the two models, Bingham and Bi-linear, to describe the flow behaviour.

First, the velocity distribution of the frontal element, as a function of

distance from the toe of the slide, is shown in Figure 9-13a for both Bingham and Bilinear models. As indicated by Imran *et al.* (2001b), the Bilinear model tends to provide higher peak velocities than the Bingham model because the Bilinear model uses a very low yield strength in the first phase of the flow. With the parameters identified above, a peak velocity of 43 and 32 m/s were computed for the Bilinear and Bingham models respectively. The stretching of the failed mass is shown in Figure 9-13b for data computed using the Bingham model. The thickness varies from a maximum of 250m, in the starting zone, to less than 50m in the distal part for the depositional zone which is the the range of reported values (Twitchell *et al.*, this volume).

As we look at the change in velocity and acceleration with time (Figure 9-14) we can see that results from both models differ in the first few minutes of the event, but otherwise are quite similar. The peak velocity (or 0 acceleration) is reached at about the same time in both cases (about 7min). Since the Bilinear model has a higher peak velocity, the deceleration is also more rapid and reaches much lower values than with the Bingham model, but the timing of the maximum deceleration is about the same in both cases, *i.e.* at about 10 min (Figure 9-14b). After only 20 minutes, the deceleration proceeds very slowly until the end of the event. The initial high acceleration, expected after the above comments, is at about 12 m/s^2.

The above mobility was mostly considered for the frontal element. It is possible to extract the data to look at the behaviour of a given element as is shown in Figure 9-15 for frontal, middle and back elements. We can see that, for the first 10 minutes of the event, the absolute velocity decreases as we move away from the front (Figure 9-15a). It is interesting to note that all three elements decelerate to about 0 (or reach maximum velocity) at about the same time (*i.e.* 7 minutes).

Discussion

The analysis of the stability and mobility of the Currituck slide has been carried assuming various properties that were, in some cases, derived from field observations. The results should be treated as inferences due to assumptions that had to be made as to strength parameters, pore pressure conditions, earthquake acceleration and yield strength.

Strength parameters and pore pressures

Strength parameters were primarily derived from the known nature of the sediments involved in the slide. We feel that these are appropriate, particularly the friction angle. This is largely based on actual morphology along the upper escarpment of slide 1 and by geometry of canyons which reveal high shearing resistance required to maintain slope angles as high as 30°. The cohesion is more difficult to establish, but considering the size of the slope, even a value of 100 kPa would have little impact on the mobilized shear strength, as it is illustrated in Figure 9-6.

Choosing the appropriate pore pressure is much more difficult and can

only be ascertained by *in situ* measurements. Our approach does however illustrate how much pore pressure was required to generate a failure. Our analysis also indicates that high pore pressures have to be developed rapidly to generate a failure on such low slope angles.

As we look at the morphology of the continental slope inside the Currituck slide area, it is apparent that the scarp is quite steep and high (up to 350 m, after failure). The steepness and height of the scarp indicate that the overall strength of the sediments making up this part of the slope are likely to be at least normally consolidated and do not show signs of high *in situ* pore pressures. If the triggering of the Currituck slide was linked to the presence of high pore pressures, they clearly do not exist anymore, and if they ever existed on a more permanent basis (*e.g.* some groundwater flow regime), they must have been generated after the development of strength in the sediments. In such a case, delta construction could have lead to increase pore pressures in what otherwise would have been normally consolidated sediment but the actual estimated thickness in the upper par of the slope is small in comparison to the overall geometry of the Currituck slide (Figure 9-5).

Prior *et al.* (1986) suggest the slide took place more than 16,600 yr BP during a period of low sea level so that at that time there could have been significant changes in the groundwater flow system that may be connected to the continent. The lowering of the sea level may also have generated excess pore pressure by gas hydrates dissociation (Kayen and Lee 1991, Sultan *et al.* 2003). Since the slide could have also been triggered by an earthquake, it may be possible that the local less stable conditions around the delta may be such that sliding could only take place in this part of the slope.

Yield strength

For the mobility analysis, the yield strength is one of the main parameters and it can be estimated from the geomorphology of the debris in the run-out zone. A key assumption here is that we consider that the debris has been deposited all at once so that the estimated thickness of the debris in the depositional zone cold e used to estimate the yield strength using Eq. [10]. To that effect, more detailed seismic analysis and availability of cores may prove essential to validate this assumption and also confirm that the mobility could not be due to any channeling effect during the flow since this would tend to increase the run out distance (Locat and Lee 2005).

Conclusions

A review of previous work on the Currituck slide and the addition of recent multibeam surveys has provide an opportunity to revisit this major slide along the East Coast of the United States. The analysis presented above was based mainly on morphological interpretation and on the use of typical strength characteristics of sediments.

From the above analysis we can conclude that:

1. The Currituck slide took pace as a single event.
2. It involved a volume sediment between 150 km^3 and 165 km^3.
3. It was triggered by a catastrophic event that must have required a sudden increase in pore pressure, likely due to an earthquake.
4. The mobilized yield strength was of the order of 2000 Pa.
5. The peak velocity may have been between 30 and 40 m/s.
6. Most of the acceleration phase was completed within less than 10 minutes.
7. The acceleration of the flowing mass is not uniformly distributed with the elements at the back having a lower acceleration than the frontal element.

Appendix 1:

List of symbols

c': cohesion, kPa
c_v: coefficient of volumetric compression
E: energy
F: factor of safety
G: gravitational acceleration, m/s^2
H_c: critical height, m
H_i: initial thickness, m
H_f: final thickness, m
I_L: liquidity index
L_R: Run-out distance, m
k: coefficient of seismic acceleration
r: ratio of strain rates
r_u: pore pressure ratio ($u/\gamma H$)
St: sensitivity (ratio of intact to remoulded strength)
u: pore pressure, kPa
V: volume, m^3, km^3
W: Total weight of the sediment columns above the failure plane, kN.

Greek symbols:

α: coefficient of seismic acceleration (fraction of *g*)
β: slope angle, degree
γ: strain rate, s^{-1}
γ^*: buoyant unit weight, kN/m^3
γ_r: reference strain rate, s^{-1}
ϕ': friction angle, degree
τ^*: shear strength, kPa,
τ: flow resistance, (Pa)
τ_c: critical yield strength, Pa
τ_{ya}: yield strength considering a Bingham fluid, Pa
η: plastic viscosity, Pa.s
σ: total stress, kPa

Figures

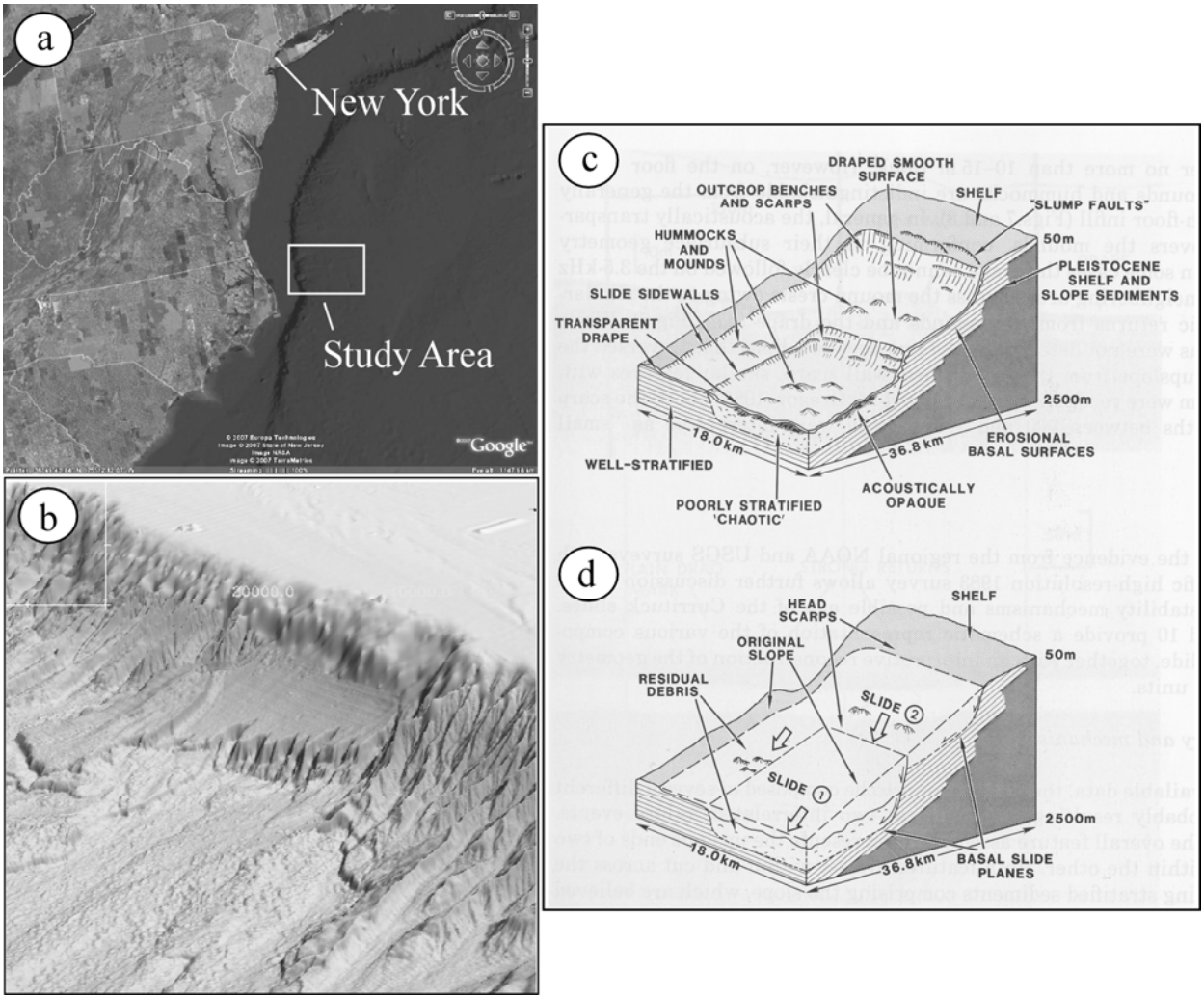

Figure 9-1: Location of the Currituck Slide., (a): study area, (b) the Currituck slide looking towards the south west, (c) and (d): schematic views of the Currituck slide taken from Prior *et al.* (1986).

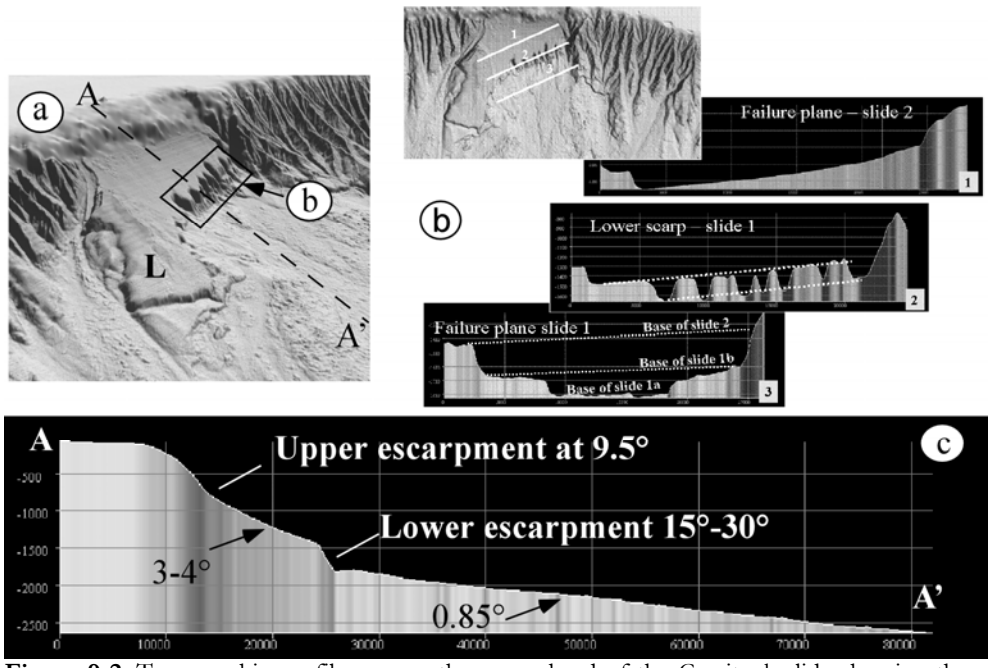

Figure 9-2: Topographic profiles across the upper head of the Currituck slide showing three potential failure planes

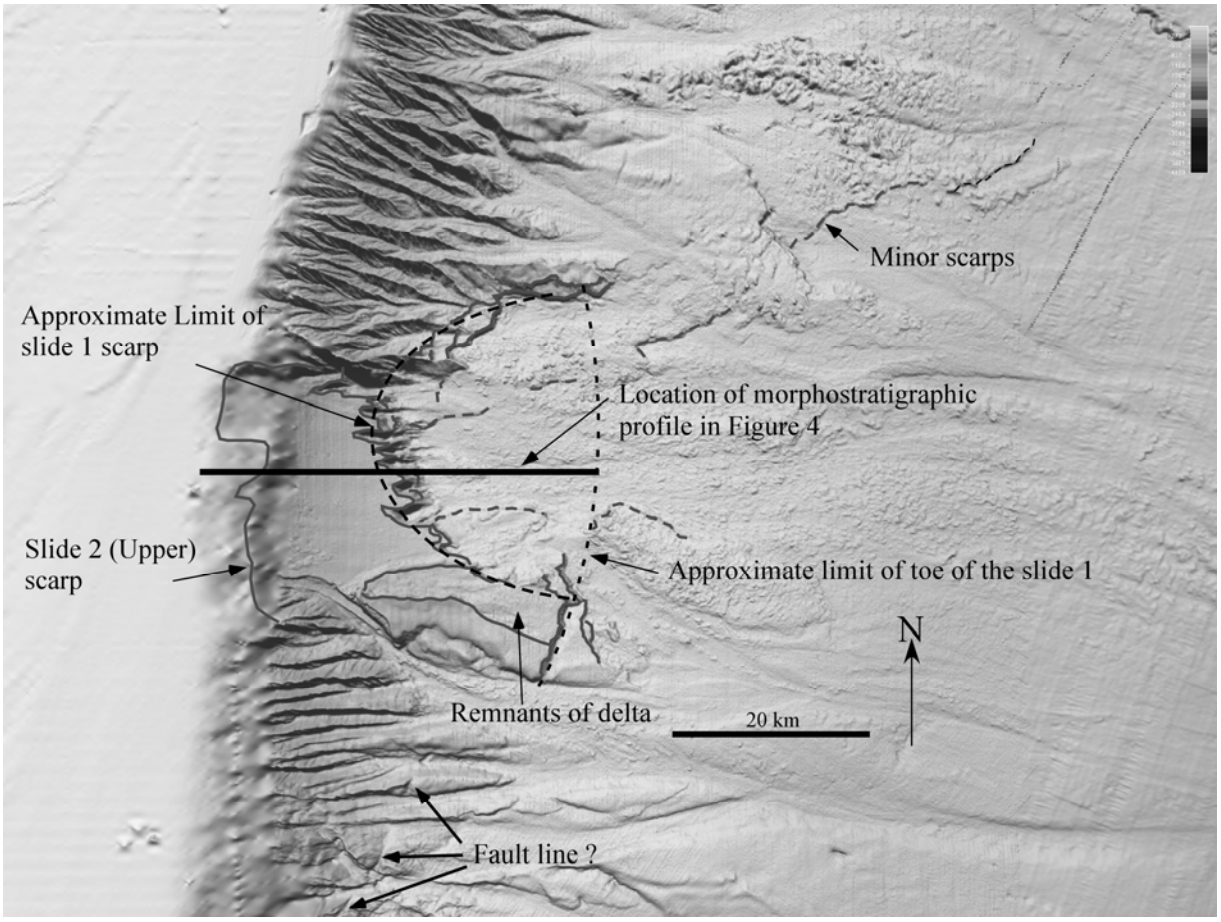

Figure 9-3: Identification of the main morphological signs used for generating the morpho-stratigraphic model shown in Figure 9-4.

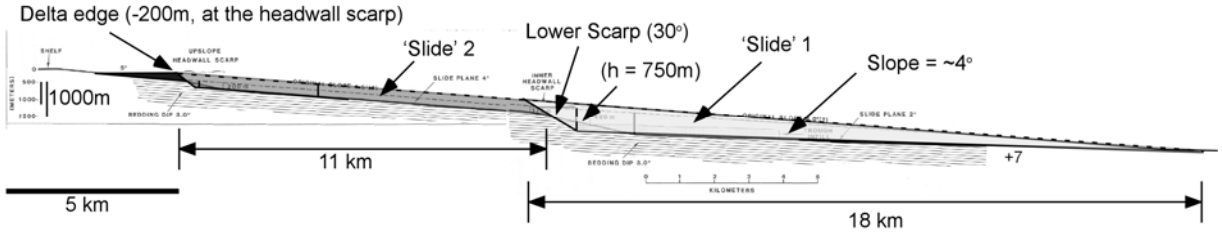

Figure 9-4: Adaptation (at scale) of the model of Prior *et al.* (1986) based on recent bathymetry data. Note that the sub-aerial part of the delta has advanced about 2.5 km over the shelf. The model also considers an scarp slope of 30°. The surface of the delta is at -200m.

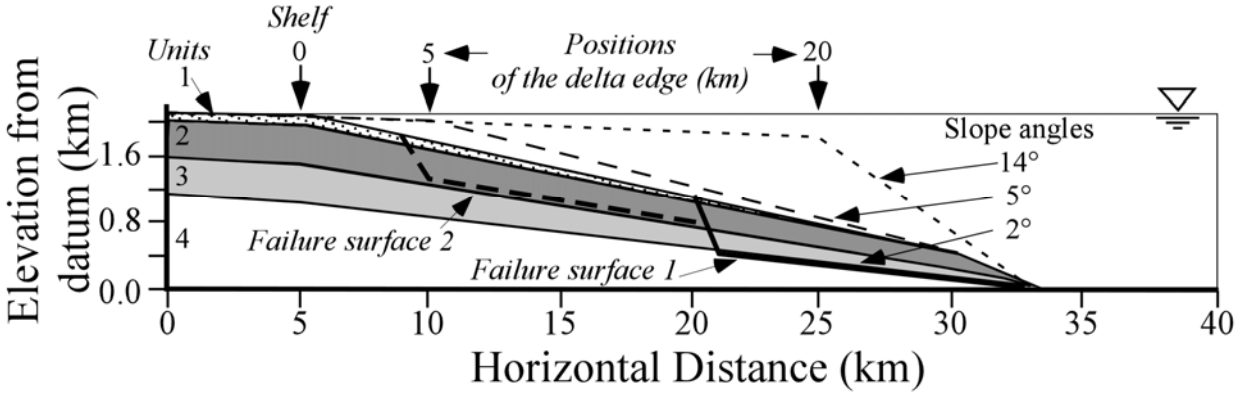

Figure 9-5: Simplified model used for slope stability analysis with SLOPEW for slide 1 and 2, showing the stratigraphic units (1 to 4, see text for explanation), the failure surfaces used for slide 1 and 2, and the hypothetical deltaic infill for a delta edge located at 0, 5 and 20 km from actual shelf break position assuming a fix position of the base of the foreslope.(vertical scale exaggeration is 3.75).

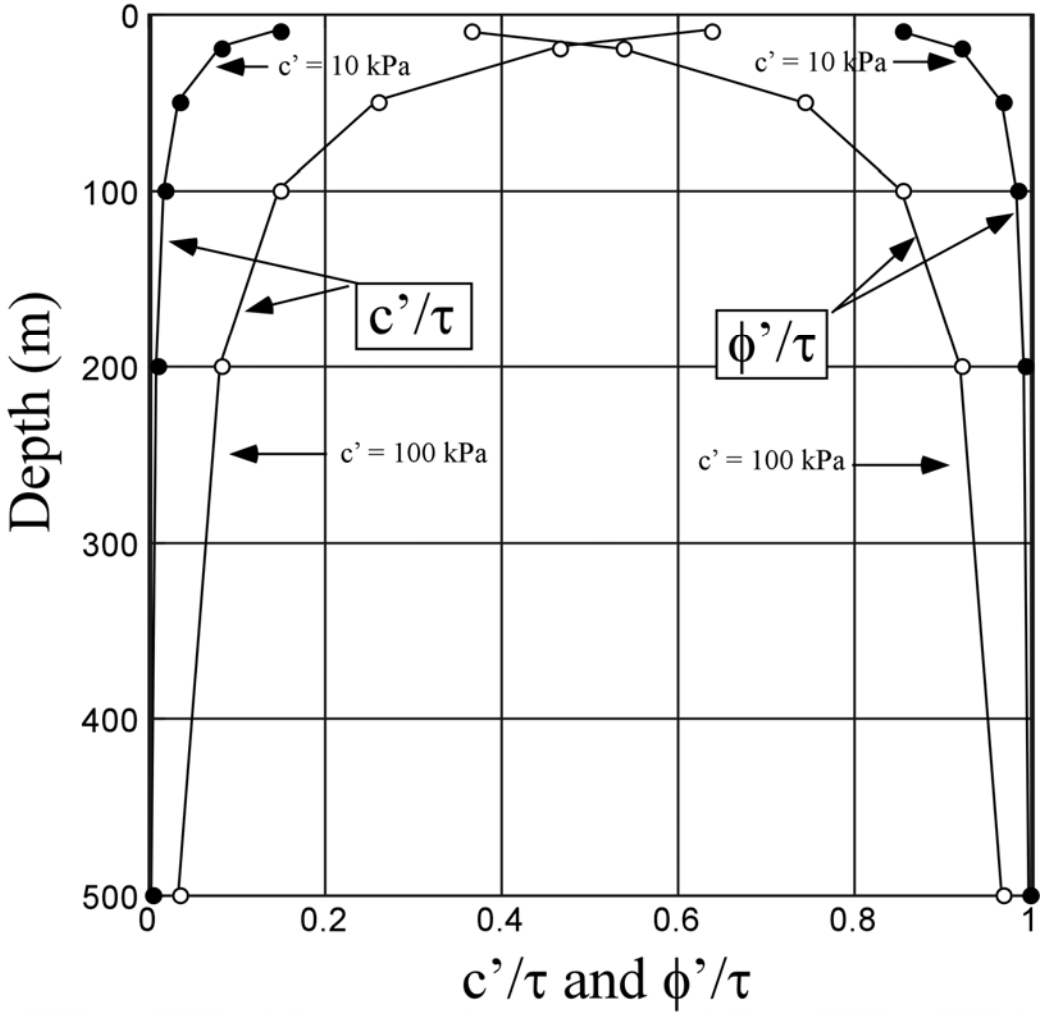

Figure 9-6: Relative contribution of the cohesion and of the friction angle on the shear strength mobilized on a failure plane (Eq [1]), considering an infinite slope approach inclined at 5° and with cohesion values of 10 kPa and 100 kPa and a friction angle of 30°.

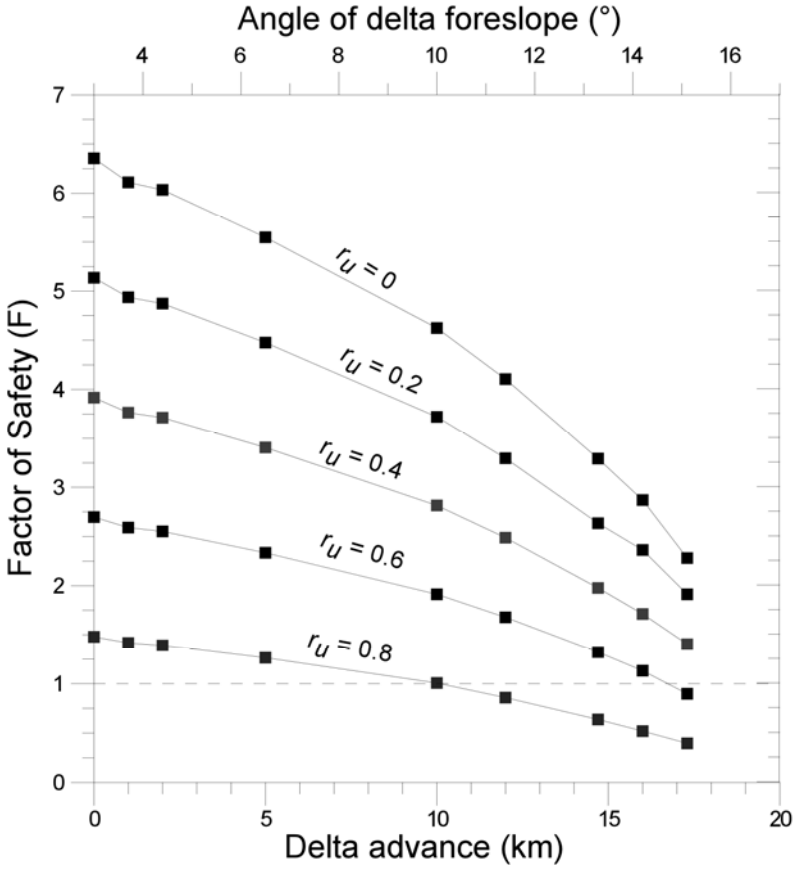

Figure 9-7: Effect of excess pore pressure (r_u) and of the position of the delta edge advance on the factor of safety of the slope for slide 1 conditions

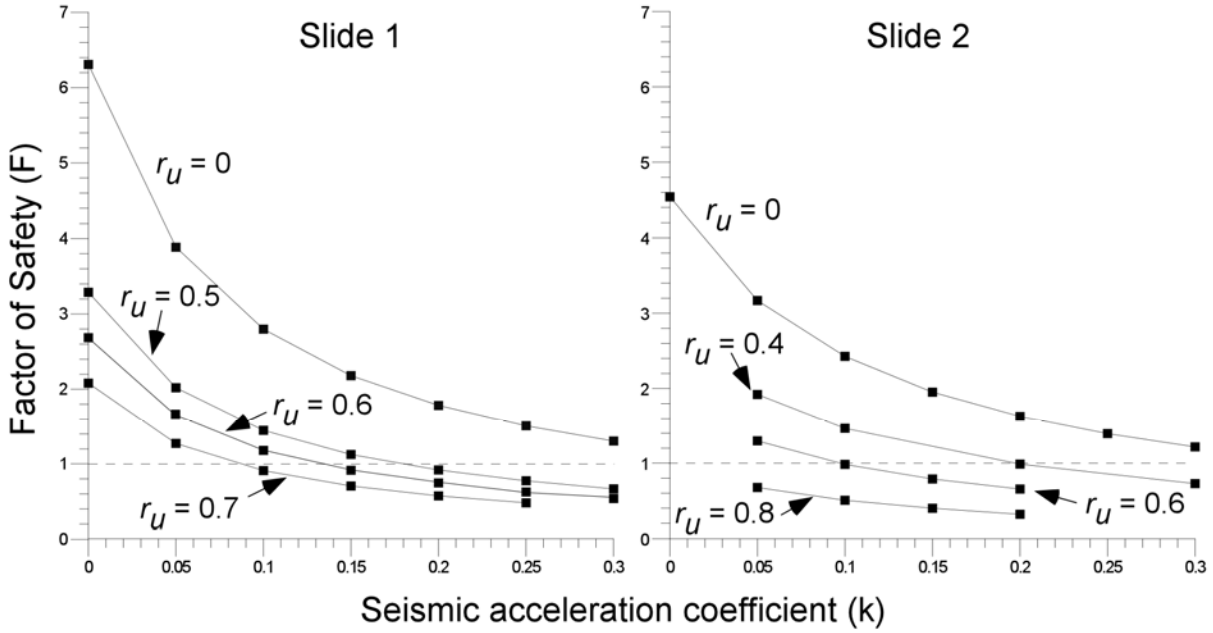

Figure 9-8: Effect of earthquake acceleration on stability conditions for slide 1 and 2 as a function of the pore pressure ratio. *k* is the seismic acceleration coefficient.

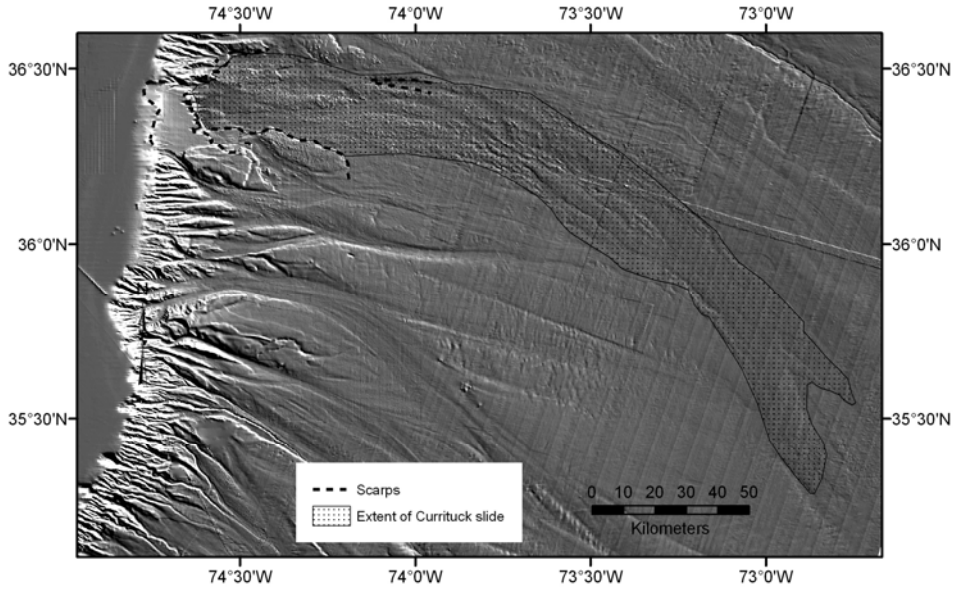

Figure 9-9: Extent of the debris generated by the Currituck slide.

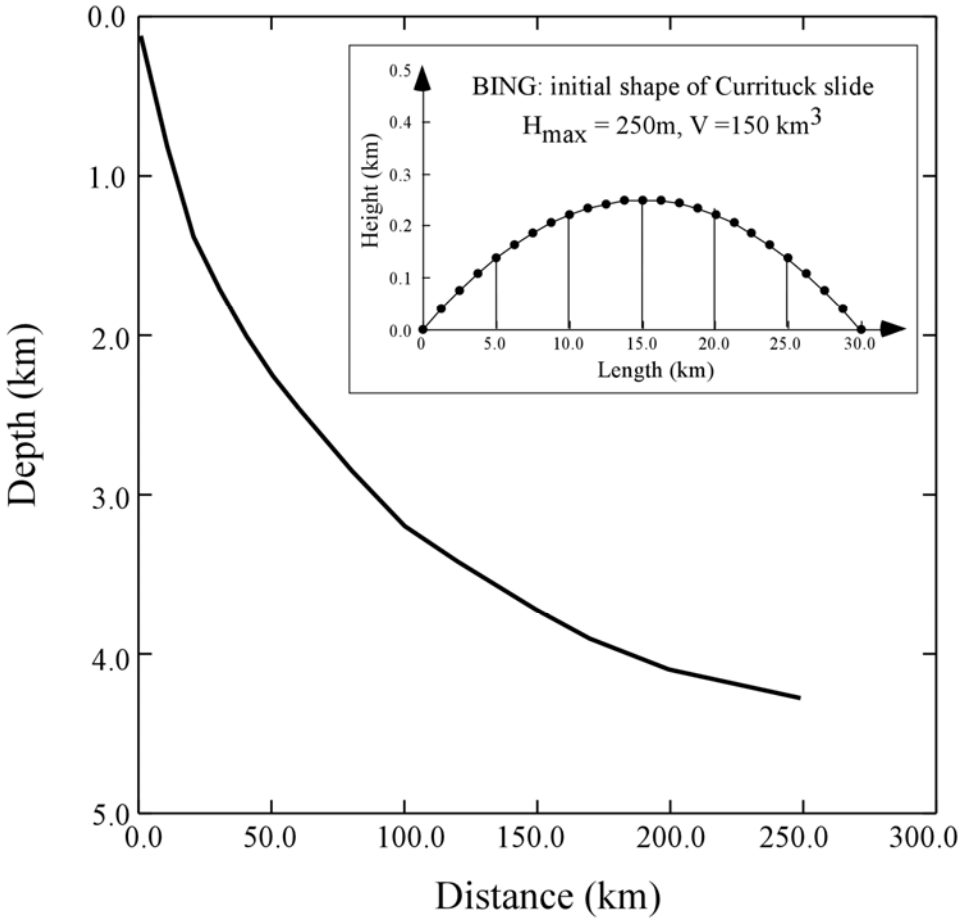

Figure 9-10: Smoothed bathymetry profile used for mobility simulation using BING. Insert shows the initial shape of the flowing material use in modelling with BING (note the scale difference).

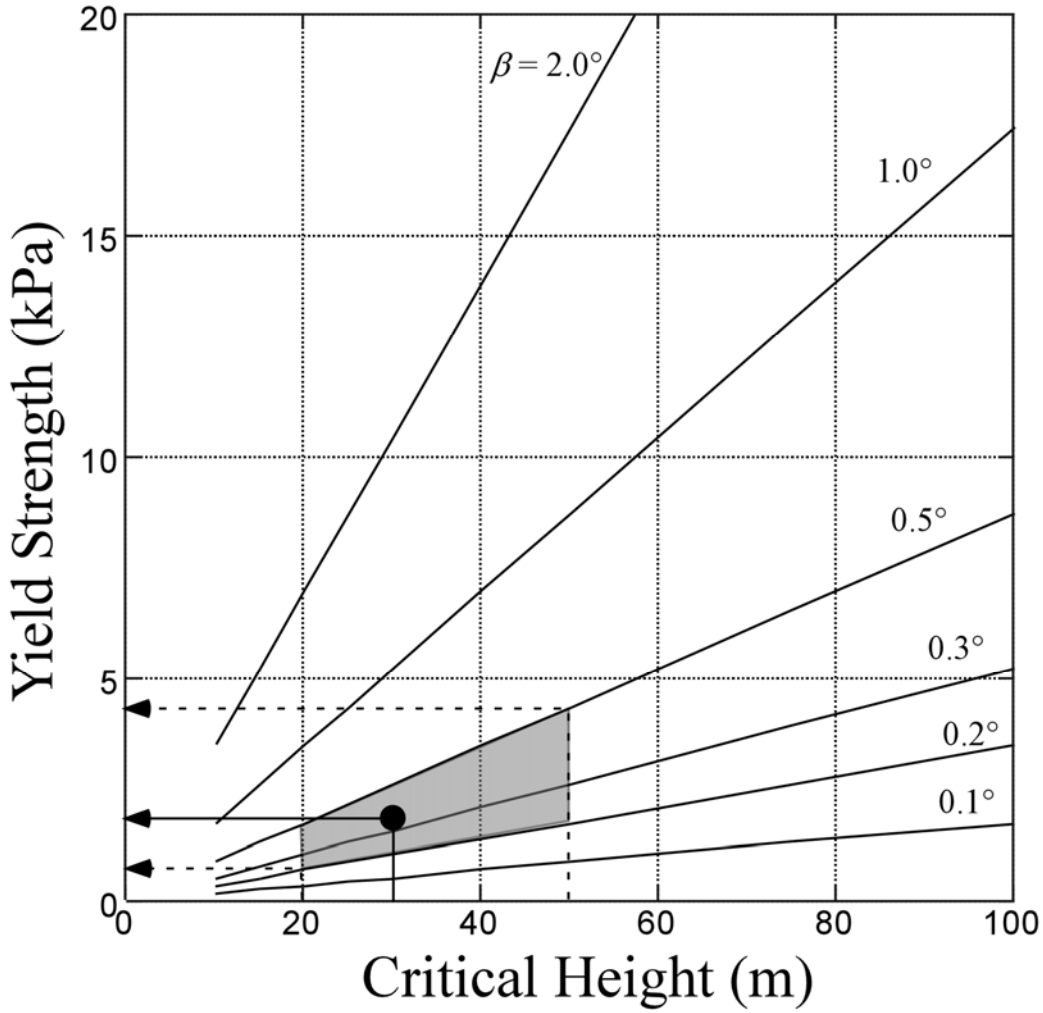

Figure 9-11: Yield strength as a function of the critical height in the depositional zone. The coloured box is for a range of reported thickness for the various depositional lobes. Black dot is for a height of 30 m and a yield strength of 2.0 kPa.

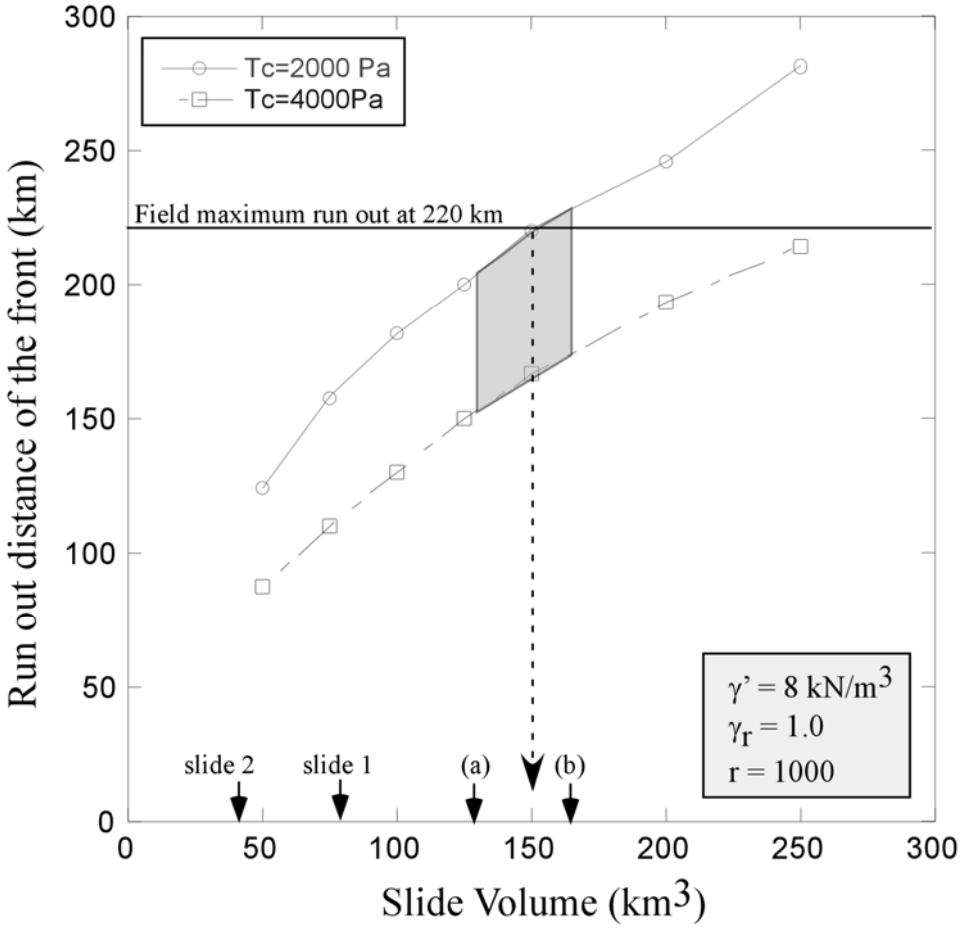

Figure 9-12: Initial volume and run out distance for two values of the yield strength. Volume at (a) is from Prior *at al.* (1986) and his taken at 128 km^3. Slide 1, and volume (b) is from herein computation at 165 km^3. Slide 1 and slide 2 are from models shown in Figure 9-5. Field maximum run out is taken from Figure 9-9.

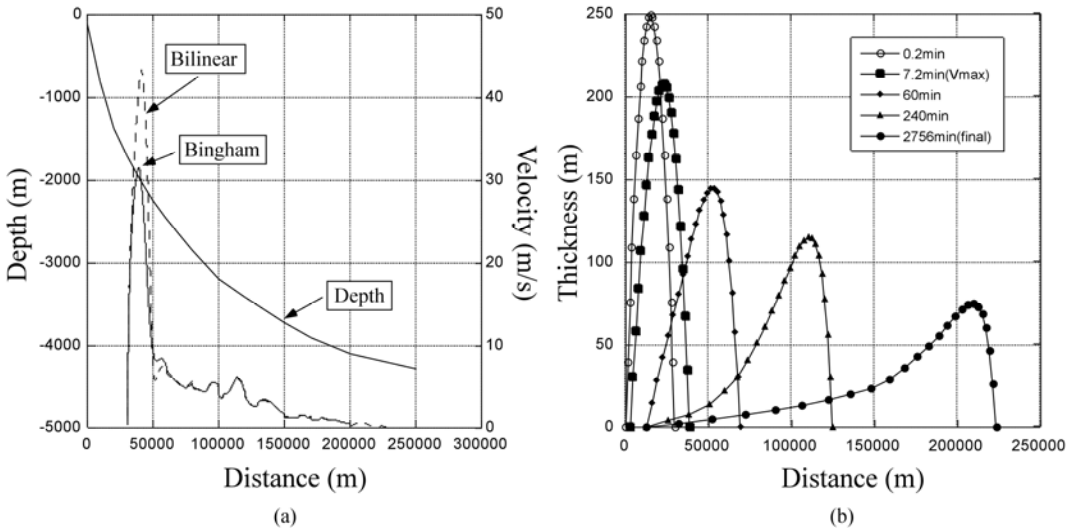

Figure 9-13: Mobility analysis for Currituck slide (a) using both Bingham and Bilinear models to illustrate the velocity profile of the frontal element as a function of distance and (b) with the shape change at various time using the Bingham parameters.

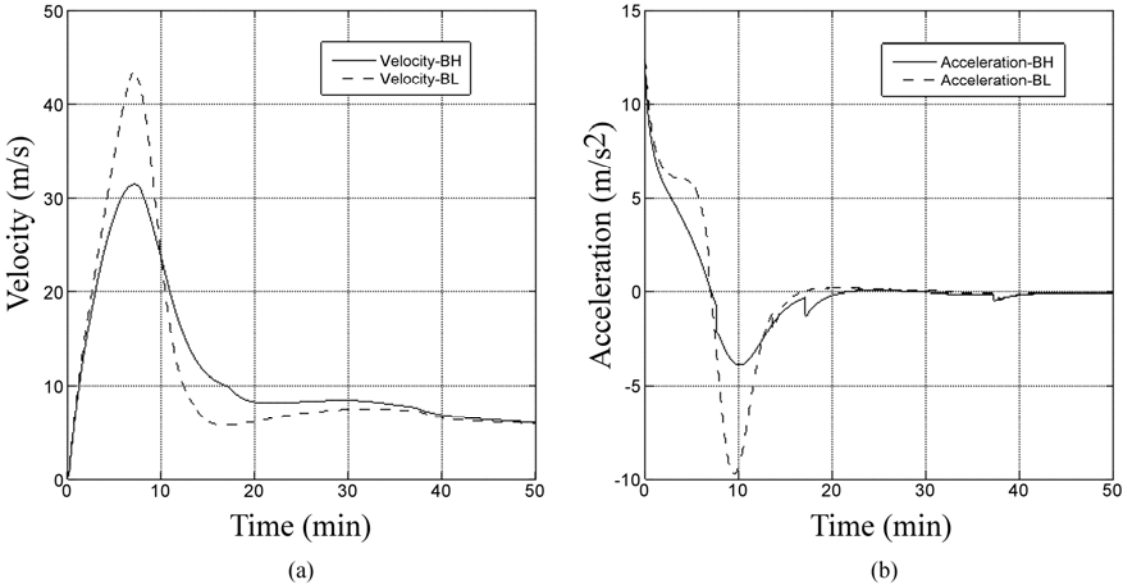

Figure 9-14: (a) Velocity and (b) acceleration profile as a function of time using both Bingham and Bilinear models (BH: Bingham; BL: Bilinear).

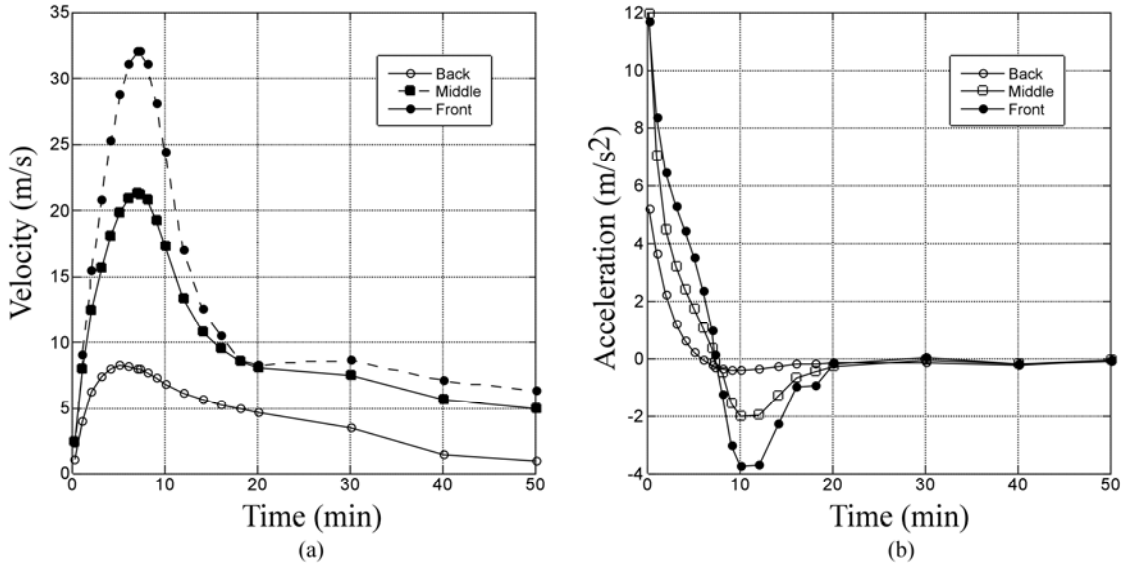

Figure 9-15: (a) Velocity profiles and (b) the acceleration profiles as a function of time for the frontal, middle and back elements using Bingham model results.

References

Bakun, W.H. and Hopper, M.G., 2004, Magnitudes and locations of the 1811-1812 New Madrid, Missouri, and the 1886 Charleston, South Carolina, earthquakes: *Bulletin of the Seismological Society of America*, *v. 94*, p. 64-75.

Barton, N.R. 1976, The shear strength of rock and rock joints: *International Journal of Rock Mechanics, Mineral Sciences and Geomechanics*, *abstract 13*(10), p. 1-24.

Booth, J.S., O'Leary, D.W., Popenoe, and P., Danforth, W.W., 1993, U.S. Atlantic Continental Slope landslides: their distribution, general attributes, and implications, *in* Submarine Landslides: Selected Studies in the U.S. Exclusive Economic Zone: U.S. Geological Survey Bulletin 2002, p. 14-22.

Bryn, P., Kvalstad, T.J., Guttormsen, T.R., Kjaernes, P.A., Lund, K.A., Nadim, F., and Olsen, J., 2004, Storegga slide risk assessment: Offshore Technology Conference, Paper 16560, 14 p.

Bunn, A.R., and McGregor, B.A., 1980, Morphology of the North Carolina continental slope, Western North Atlantic, shaped by deltaic sedimentation and slumping: *Marine Geology, v. 37*, p. 253-266.

Chaytor, J.D., Twichell, D.C., ten Brink, U.S., Buczkowski, B.J., and Andrews, B.D., 2007, Revisiting submarine mass movements along the U.S. Atlantic continental margin: Implications for tsunami hazards *in*, V. Lykousis, D. Sakellariou, and J. Locat, (Editors), Submarine Mass Movements and Their Consequences, Springer, Netherlands, p. 395-403.

Christian, H., Woeller, D.J., Robertson, P.K. and Courtney, R.C., 1997, Site investigations to evaluate flow liquefaction slides at Sand Heads, Fraser River delta: *Canadian Geotechnical Journal*, *v. 34*, p. 384-397.

Dugan, B., and Flemings, P.B., 2005, Overpressure and fluid flow in the New Jersey continental slope: implications for failure and cold seeps: *Science*, *v. 289*, p. 288-291.

Imran, J., Harff, P., and Parker, G., 2001a, A numerical model of submarine debris flow with graphical user interface: *Computers and Geosciences*, *v. 27*, p. 717-729.

Imran, J., Parker, G., Locat, J., and Lee, H., 2001b, A 1-D numerical model of muddy subaqueous and subaerial debris flows: *Journal of Hydraulic Engineering, v. 127*, p. 959-958.

Jeong, S.W, Locat, J., and Leroueil, S., 2007, Rheological properties of fine-grained sediments in modelling submarine mass movements: the role of texture. In: Proceedings of the 3rd International Symposium on Submarine Mass Movements and Their Consequences, Santorini (accepted).

Johnson, A. M., 1970, Physical processes in geology: Freeman Press, San Francisco.

Kayen, R.E. and Lee, H.J., 1991, Pleistocene slope instability of gas hydrate-laden sediment on the Beaufort sea margin: *Marine Geotechnology, v. 10*, p. 125-141.

Keefer, D.K., 1984, Landslides Caused by Earthquakes: *Geological Society of America Bulletin*, *v. 95*, p. 406-421.

Krahn, J., 2004, Stability modelling with Slope/W: an engineering methodology: GEO-SLOPE International, Calgary, Canada, 394 p.

Kvalstad, T.J., Andresen, L., Forsberg, C.F., Berg, K., Bryn, P., and Wangen, M., 2005, The Storegga slide: evaluation of triggering sources and slide mechanics: *Marine and Petroleum Geology*, *v. 22*, p. 244-256.

Lee, H.J., Locat, J., Desgagnés, P., Parson, J., McAdoo, B., Orange, D., Puig, P., Wong, F., Dartnell, P., and Boulanger, É., 2007, Chapter 6: Submarine Mass Movements *in* Nittrouer *et al.* (Editors), Continental-margin Sedimentation: Transport to Sequence.

Locat, J., 1997, Normalized rheological behaviour of fine muds and their low properties in a pseudoplastic regime. ASCE, First Conference on Debris Flows Hazards Mitigation, Mechanics, Prediction and assessment, p. 260-269.

Locat, J., 2001, Instabilities along Ocean Margins: A Geomorphological and Geotechnical Perspective. Article invite: *Marine and Petroleum Geology*, *v. 18*, p. 503-512

Locat, J., Desgagnés, P., Leroueil, S., and Lee, H.J., 2003, Stability of the Hudson Apron slope off New Jersey *in* Locat, J., and Mienert, J. (Editors), Submarine mass Movements and Their Consequences, Kluwer series on Natural and Technological Hazards, v. 19, p. 257-270.

Locat, J., and Lee, H.J., 2002. Submarine landslides: advances and challenges: *Canadian geotechnical Journal, v. 39*, p. 193-212.

Locat, J., and Lee, J., 2005, Chapter 9: Subaqueous Debris Flows *in* Mathias and Hungr (Editors), Debris-flows Hazards and Related Phenomena, Springer, p. 203-245.

Locat, J., Lee. H.J., Locat, P., and Imran, J., 2004, Numerical analysis of the mobility of the Palos Verdes debris avalanche: *Marine Geology, v. 203*, p. 269-280.

O'Brien, J.S., and Julien, P.Y., 1988, Laboratory analysis of mudflow properties: *Journal of Hydraulics Engineering, A.S.C.E., v. 114*, p. 877-887.

Poag, C.W., and Sevon, W.D., 1989, A record of Appalachian denudation in postrift Mesozoic and Cenozoicsedimentary deposits of the U.S. middle Atlantic continental margin: *Geomorphology*, *v. 2*, p. 119-157.

Prior, D.P., Doyle, E.H., and Neurauter, T., 1986, The Currituck Slide, Mid Atlantic continental slope-revisited: *Marine Geology, v. 73*, p. 25-4.

Rodríguez, C.E., Bommer, J.J., and Chandler, R.J., 1999, Earthquake-induced Landslides: 1980–1997: *Soil Dynamics and Earthquake Engineering*, *v. 18*, p. 325–346.

Sultan, N., Cochonat, P., Foucher, J.P., Mienert, J., Haflidason, H., and Sejrup, H.P., 2003, Effect of gas hydrates dissociation on seafloor slope stability, *in* Locat J., and Mienert, J., (Editors), Submarine Mass Movements and Their Consequences: *Kluwer Advances in Natural and Technological Hazards Research*, *v. 19*, p. 103-111.

ten Brink, U., this volume, On the relationships between submarine landslides and earthquakes along the U.S. Atlantic Coast.

ten Brink, U., Twichell, D., Geist, E., Chaytor, J., Locat, J., Lee, H.,

Buczkowski, B., and Sansoucy, M., 2007, Report on the Current State of Knowledge Regarding Potential Tsunami Sources Affecting the U.S. Atlantic and Gulf Coasts: U.S. Geological Survey Administrative Report, 164 p.

Tinti, S., 1993, Tsunamis in the World: Fifteenth International Tsunami Symposium, 1991: Springer Publisher, 236 p.

Twichell, D.C., Chaytor, J.B., ten Brink, U.S., and Buczkowski, B., this volume, Geologic controls on the distribution of submarine landslides along the U.S. Atlantic continental margin.

Chapter 10: Hydrodynamic Modeling of Tsunamis from the Currituck Landslide

Introduction

Potential sources for tsunamis affecting the east coast of the U.S. include submarine landslides that have been identified along the North American continental slope (Chaytor *et al.*, this volume; Twichell *et al.*, this volume). The occurrence of potentially tsunamigenic landslides off North America is infrequent, with return times measured in thousands of years and possibly waning with time since the last glacial/deglaciation period (Lee, this volume). Landslide tsunami hazards are still a present-day threat, however, as evidenced by the 1929 Grand Banks landslide tsunami (Fine *et al.*, 2005). To assess the severity of this hazard along the U.S. Atlantic coast, we model the generation, propagation, and runup from tsunamis triggered by the Currituck landslide, one of the largest landslides along the North American Atlantic offshore margin. The headwall of the landslide is located approximately 100 km offshore North Carolina and Virginia, just down slope from the continental shelf edge. The morphology, stability, and dynamics of the slide have been studied by Prior *et al.* (1986) and by studies presented in this volume (Locat *et al.*, this volume; Twichell *et al.*, this volume). The Currituck landslide complex is thought to be composed of at least two separate events, although the mobility analysis presented by Locat *et al.* (this volume) suggest that these events occurred contemporaneously. Locat *et al.* (this volume) also suggests that the landslide was triggered by a sudden increase in pore pressure, most likely from an earthquake. The geologic age of the landslide complex is 25-50 ka, occurring at a sea-level low stand (Lee, this volume). Although the Currituck landslide occurred thousands of years ago under different sea-level conditions, we can use the detailed analysis of this landslide to assess the range of potential, present-day tsunamis emanating from this type of source.

Previous studies of landslide-generated tsunamis uncovered distinct differences compared to earthquake-generated tsunamis (Lynett and Liu, 2002; Okal and Synolakis, 2004; Trifunac and Todorovska, 2002). Because of their smaller source dimensions, tsunamis from landslide sources are more affected by frequency dispersion (cf., Carrier, 1971). During open-ocean propagation, this will result in a long-wavelength leading wave with a higher-frequency wave train trailing behind. In addition, because of the large vertical displacements at the source in comparison to earthquake sources,

hydrodynamic nonlinearity also becomes a significant factor in understanding the wave evolution for landslide tsunamis in the near field. Both of these factors, as well as the potential for wave breaking, become increasingly important as tsunami waves approach and runup onshore.

With regard to landslide dynamics, it is well known that speed of the failed mass is linked to the amplitude of the out-going wave (*i.e.*, the wave propagating in the direction of slide movement) (*e.g.*, Trifunac *et al.*, 2002; Ward, 2001) as well as the initial acceleration, slide length and thickness, and whether the slide fails retrogressively (Haugen *et al.*, 2005; Løvholt *et al.*, 2005). The closer the landslide speed is to the phase speed of tsunamis (c), given in the long-wavelength limit by $c = \sqrt{gh}$ where g is the gravitational acceleration and h is the water depth, the higher the out-going tsunami amplitude. Even though a strong directivity is associated with the outgoing tsunami, the back-going tsunami propagating toward the near shore is the part of the wavefield that is potentially more dangerous, because of the shorter propagation distances (for a typical continental margin setting; fjords are a notable exception), and this is the part of the wavefield we focus on in this chapter. Because the back-going tsunami quickly leaves the source region and is not "tuned" by seafloor movement in the slide direction, it is more complexly related to initial displacement of the slide mass immediately after failure. In the past, a poor understanding of submarine landslide dynamics, in combination with the higher-order hydrodynamic theory needed to model dispersion and nonlinearity, have been major obstacles in understanding landslide tsunamis. Recent research, however, has resulted in new modeling methods to address both of these problems (*e.g.*, Elverhøi *et al.*, 2005; Imran *et al.*, 2001; Lastras *et al.*, 2005; Lynett and Liu, 2002) that will undoubtedly lead to accelerated progress in estimating the severity of this natural hazard.

Finally, the broad continental shelf also has a significant effect on the wave evolution of tsunamis (Shibata, 1983), particularly those generated from continental slope landslides. Korycansky and Lynett (2005; 2007) indicate that shallow slopes associated with continental shelves will have a marked effect on large amplitude tsunamis, such as those from asteroid impacts, through attenuation from bottom friction and wave breaking far offshore (see also Glimsdal *et al.*, 2007). One of the primary objectives in this study is to determine whether bottom friction and wave breaking are also important factors to determine the wave evolution of tsunamis generated by continental slope landslides during propagation across the continental shelf. It should be noted that the continental shelf shoreward of the Currituck landslide is one of the narrowest along the U.S. Atlantic margin (Figure 10-1). The coastal region directly across (broadside) from the Currituck landslide is characterized by barrier islands (Currituck Banks) approximately 2-4 m in elevation and a back bay (Currituck Sound).

Method

Bathymetry

Multiple sources of data were used to build a digital elevation model (DEM) and the bathymetric grid for tsunami propagation and runup modeling (Figure 10-1). These include data on the continental slope from NOAA Exclusive Economic Zone (EEZ) and University of New Hampshire Law of the Sea multibeam surveys (Gardner *et al.*, 2006) and data on the continental shelf and in the nearshore regions extracted from the NOAA National Ocean Service (NOS) hydrographic and USGS Outer Banks survey databases. Topography data for the Currituck Banks area were extracted from the Shuttle Radar Topography Mission (SRTM) finished 3-arc second (~ 90 m resolution) dataset. The areal extent of the grid encompasses the region downslope of the Currituck landslide as well as the coastal region broadside (directly across from) the landslide (Figure 10-1b). Bathymetric and topographic data were gridded at a pixel/cell resolution of 200 m with the MB-System package (Caress and Chayes, 1996), employing a weighted average gridding scheme and with empty cells filled via a 2D thin-plate spline.

A 200 m uniform grid spacing is used for the source sensitivity studies, whereas a much finer grid spacing is used to model nearshore propagation and runup. An additional DEM, also at a resolution of 200 m, was created to investigate the effects of a Curritcuk landslide tsunami over a wider section of the U.S. Atlantic coast (Section 3.3). For this larger, regional DEM (40N to 35 N), the same datasets as used in the smaller Currituck DEM were used with the addition of multibeam data covering sections of the continental slope and shelf collected on numerous survey and transit legs of the research vessels Atlantis, Knorr, and Ewing.

Hydrodynamic modeling

The model used for this study is the Cornell University Long and Intermediate Wave Modeling package (COULWAVE) (Lynett and Liu, 2002). COULWAVE was developed to model the propagation and runup of long and intermediate length waves, using fully nonlinear and dispersive wave theory (*i.e.*, the nonlinear Bousinesq equations) as described in a number of papers (Lynett and Liu, 2002; Lynett, 2006; Lynett and Liu, 2005; Lynett *et al.*, 2002). Because this wave-modeling package is computationally intensive, there are also options to use different approximations, such as weakly nonlinear, linear, and nondispersive forms of the wave equations. On the basis of initial tests, the weakly nonlinear "extended" equations (termed WNL-EXT in Lynett and Liu, 2002) were used for the multiple simulations of the Currituck landslide tsunami, including local propagation from different landslide scenarios and sensitivity tests of key parameters.

The WNL-EXT form of the wave equations described by Lynett and Liu (2002) are derived from the fully nonlinear form by assuming that the

wavelength is much greater than the water depth and that the wave amplitude and vertical seafloor displacement are much smaller than the water depth. Specifically, for the nondimensional parameters

$$\varepsilon = \frac{a_0}{h_0}, \quad \mu = \frac{h_0}{\ell_0}, \quad \delta = \frac{\Delta h}{h_0}, \tag{1}$$

where a_0 is a characteristic amplitude, h_0 characteristic water depth, ℓ_0 characteristic slide length, and Δh is the change in seafloor depth,

$$O(\varepsilon) = O(\delta) = O(\mu^2) << 1. \tag{2}$$

In addition, the conventional form of the linear dispersion relation is "extended" to an arbitrary depth (Chen and Liu, 1995; Nwogu, 1993) which improves the accuracy for modeling intermediate-depth waves.

These equations are numerically implemented using a finite-difference algorithm and an iterative, high-order predictor-corrector scheme (Lynett and Liu, 2002; Wei *et al.*, 1995). The open-ocean boundaries accommodate radiation of wave energy through a sponge layer, whereas runup on land boundaries is accommodated using a moving-boundary algorithm (Lynett *et al.*, 2002). The time step used in the finite-difference algorithm is chosen to ensure numerical stability and is always less than that required by the Courant-Friedrichs-Lewy stability criterion. We also present the results of 1D modeling below using the fully nonlinear equations (FNL-EXT) and a much finer grid spacing ($\Delta x = 5$ m) to determine the wave evolution over the continental shelf and during overland flow.

The results of preliminary sensitivity tests on many of the parameters specified by COULWAVE (*e.g.*, non-linearity, bottom friction, time and grid interval, energy dissipation from wave breaking) suggest that bottom friction and linear vs. nonlinear formulation have the greatest effect on the results. The linear assumption overestimates nearshore tsunami amplitudes for the Currituck landslide, in comparison to the more accurate nonlinear representations as shown in Figure 10-2. In general, linear models that explicitly include slope, through a mild slope approximation for example, will tend to overestimate the shoaled wave height of a nonlinear wave, as compared to nonlinear model with similar assumptions (cf., Wei *et al.*, 1995). In cases where slope is not explicitly included in propagation, such as the use of a shoaling coefficient with simple Airy wave theory, the linear models will underestimate shoaling amplification. The linear theory also underestimates the maximum amplitude in the source region, consistent with results described by Lynett and Liu (2002). For the out-going wave in deep water (*i.e.*, greater than 2km water depth; right side Figure 10-2), in contrast, there is little difference between the linear and nonlinear formulations. There is also little difference for this case study between the WNL-EXT and FNL-EXT formulations (Figure 10-2), although nonlinearity becomes increasingly important in the nearshore region, as we will demonstrate.

Tsunami generation

The landslide source for tsunami waves is parameterized by its geometry and duration of vertical displacement (Lynett and Liu, 2002; Lynett and Liu, 2005). A two-sided vertical displacement geometry (*i.e.*, dipole) is used in this study to represent the regions of excavation and deposition (Figure 10-3) (cf., Trifunac *et al.*, 2002; Trifunac *et al.*, 2003). The landslide kinematics are specified by a width of slope that fails, downslope lengths for the regions of excavation and deposition, and the maximum thickness of slide masses. Both the downslope and shore-parallel displacements are smooth functions to ensure numerical stability in the hydrodynamic calculations. Because tsunami generation is principally affected by vertical motion of the seafloor, the time history is parameterized by an overall duration of the vertical component of slide movement. Since our focus is the back-going wave propagating to the local shoreline (*i.e.*, leading-depression phase; Figure 10-4), this is interpreted as the duration of excavation during landslide movement termed "failure duration." The first elevation phase of the back-going wave is generated in the region of deposition. The out-going wave, propagating in the direction of slide movement, quickly moves out of this model domain (Figure 10-4). The resulting volumes of the regions of excavation and deposition are approximately conserved.

Results

Potential tsunamis from the Currituck landslide are examined in four different sets of simulations. First, we calculate tsunami generation and propagation for three possible failure scenarios for the Currituck landslide derived from the stability and morphology analysis of Locat *et al.* (this volume). Next, using each of the scenarios, we conduct a sensitivity analysis of two critical parameters for the local tsunami: duration of landslide failure and bottom friction of the continental shelf. The third simulation examines the regional propagation of the tsunami over a much larger area to determine whether significant energy propagates at oblique angles to the slide axis. This final simulation is a very high-resolution 1D propagation and runup model to accurately model dispersion, nonlinearity, and wave breaking as the tsunami propagates across the continental shelf and runs up onto the barrier islands broadside from the landslide.

Currituck landslide scenarios

The first tsunami simulations are computed for three landslide geometries discussed by Locat *et al.* (this volume): Slide 1 (downslope sub-event, volume=108 km^3), Slide 2 (upslope sub-event, volume=57 km^3), and a composite of Slides 1 and 2 (volume=128-165 km^3) (cf., Prior *et al.*, 1986). Previously, it has been unclear whether Slides 1 and 2 occurred as separate tsunami-generating events (relative to the phase speed of tsunami waves), although Locat *et al.* (this volume) suggest that the two sub-events occurred

simultaneously during failure (*i.e.*, the composite slide). Evolution of the tsunami wavefield is calculated for a propagation time of 100 minutes, which is approximately the time it takes the first waves to reach the nearest shoreline (Currituck Banks) at the western edge of the model domain. Results are presented in the form of (1) maps of maximum wave amplitude throughout the model domain during the entire propagation time, (2) profiles of maximum wave amplitude along a transect aligned in the middle of the slide, and (3) time series of wave amplitude (marigram) at a nearshore location (20 km offshore) broadside from the landslide. For (3), the water depth for the nearshore location is 22 m. Initial results for each slide scenario are described using a failure duration of 10 min and a bottom friction coefficient of $f = 2.5 \times 10^{-3}$ that is typical for the continental shelf (Soulsby, 1983) (Table 1). Tsunami energy dissipation from bottom turbulence is primarily important for propagation across the shallow continental shelf. The effect of variations in each of these parameters is described in the next set of simulations.

For Slide 1, the peak in tsunami amplitude is landward of the generation region and is caused by shoaling amplification of the back-going wave from the source region to the continental shelf edge (Figure 10-5a, b). Dissipation of tsunami energy as the wave propagates toward shore is caused by geometric spreading, bottom friction, and wave breaking. A secondary peak seaward of the source region is caused by the downslope directivity of the out-going tsunami. Significant off-axis tsunami energy for the back-going wave is evident in Figure 10-5a that would affect coastal sites at azimuths oblique to the landslide (outside this model domain and discussed in Section 3.3 below). The initial drawdown of the tsunami at the nearshore station starts approximately 65 minutes after landslide initiation and lasts approximately 15 minutes before the initial elevation wave arrives (Figure 10-5c).

The excavation area for Slide 2 is at shallow water depths and therefore the back-going tsunami is less affected by shoaling amplification compared to Slide 1. Because of this and because the volume of Slide 2 is smaller than that for Slide 1, the peak amplitudes are significantly less (Figure 10-6a, b). Note that the seaward peak in tsunami amplitude over the deposition region (Figure 10-6a) is slightly off the center axis profiled in Figure 10-6b. The drawdown at the nearshore station occurs slightly earlier for Slide 2 (Figure 10-6c) compared to Slide 1 (Figure 10-5c) but is otherwise similar.

For the composite scenario where Slide 1 and Slide 2 occur as a single tsunami generating event, the amplitudes near the source are much larger than for each individual slide (Figure 10-7a, b). The nearshore tsunami amplitudes for the composite slide, however, are only slightly greater than for Slide 1, owing to dissipation effects during propagation. The initial drawdown phase for the composite slide is less pronounced (Figure 10-7c) than for either Slide 1 or Slide 2.

Effect of variations in failure duration and bottom friction

For each slide scenario described above, three different values of failure duration in the excavation region are used to determine the effect on the tsunami wavefield (Table 1). In general, landslide duration is inversely proportional to the height of the generated tsunami waves, holding landslide volume constant. Two duration values are chosen according to the characteristic times, dependent on acceleration and deceleration of the moving mass, from the mobility analysis of the Currituck landslide (Locat *et al.*, this volume). The first value is the time of the maximum in slide deceleration (approximately 10 min). The second value is the time that acceleration approaches 0 after the deceleration phase starts (approximately 20 min). It is thought that the former value better accounts for the initial high acceleration of failure, whereas the latter value represents the overall total duration of slide movement in the excavation region. We also examine a very short duration time (7.2 min.) to examine the effect on tsunami amplitudes of a slide that is much more mobile than expected from the post-failure analysis (*e.g.*, from low basal shear stress, Elverhøi *et al.*, 2005).

Results shown in Figure 10-8 indicate that failure duration has a significant effect on maximum tsunami amplitudes over the source region (bottom friction held constant at $f = 2.5 \times 10^{-3}$). Because tsunami waves leave the source region at a phase speed of $\sqrt{gh}$ (long wavelength limit), slower process times will result in smaller initial tsunami amplitudes, under subcritical conditions. This effect is also evident for the out-going tsunami (right side of model domain), which is significantly affected by downslope landslide speed (Todorovska *et al.*, 2002; Trifunac *et al.*, 2002). This effect is much less significant at nearshore water depths for the back-going tsunami of interest (Figure 10-8), suggesting that landslide volume is a more significant source parameter than failure duration (*cf.*, Murty, 2003).

Bottom friction is parameterized in COULWAVE by the friction coefficient *f*. Shear stress (τ) at the bottom boundary is given by

$$\tau = \tfrac{1}{2}\rho f |\mathbf{u}_b|\mathbf{u}_b, \qquad (3)$$

where ρ is fluid density and $\mathbf{u}_b$ is the horizontal velocity field near the sea floor. Increasing the bottom friction coefficient will lead to greater dissipation of tsunami energy during propagation. The friction coefficient is related to two other parameters that describe the hydraulic roughness of the bottom boundary layer: Chézy coefficient (*C*) and Manning's roughness coefficient (*n*)

$$f = \frac{g}{C^2}$$
$$f = \frac{gn^2}{(h+a)^{1/3}}, \qquad (4)$$

where g is the gravitational acceleration, h is the water depth and a is the tsunami amplitude. Estimates of f for continental shelf environments range between approximately $1.6 - 6.1 \times 10^{-3}$, depending on the bottom type and the presence of bed forms (Soulsby, 1983). In addition, estimates of f for shoaling waves and runup are considerably higher: $f > 10^{-2}$ (Mei, 1989; Satake, 1995).

Results of using different bottom friction coefficients for the composite slide scenario are shown in Figure 10-9 (failure duration held constant at 10 min.). Above the source region, maximum tsunami amplitude decreases slightly with increasing friction coefficient. During propagation of the back-going tsunami across the continental shelf, however, higher bottom friction results in greater energy dissipation and significantly smaller tsunami amplitude estimates. Conversely, for the out-going tsunami, the effect is minimal because of the much greater water depths along the continental slope.

Bivariate analysis of the effect failure duration and bottom friction have on maximum nearshore tsunami wave height are presented for each of the slide scenarios in Figure 10-10. In each case, bottom friction has more of an effect on maximum nearshore tsunami wave height than failure duration, for the ranges tested. The curvature in the contours of maximum wave height indicate that failure duration is a more significant effect for low values of bottom friction ($f \sim 10^{-3}$). For high values of bottom friction ($f \sim 10^{-2}$), maximum nearshore wave height is less sensitive to variations in failure duration.

Regional propagation

We next examine the regional tsunami propagation pattern from the Currituck landslide using a much larger model domain. For this case, we use the scenario that produces the largest tsunami of the ones tested: the composite slide (Slide 1 plus Slide 2) and a failure duration of 7.2 min. In addition to the broadside, back-going phase that was modeled in the previous simulation set, another phase becomes apparent in the regional model (Figure 10-11). This phase originates in the region of deposition and is refracted toward the coast owing to the gradual northeastward bend in the trend of the continental slope. In contrast to the leading depression phase of the back-going tsunami that originated in the region of excavation, the refracted wave is characterized by a leading elevation phase. Thus, the leading phase of the two different waves propagating toward the coast have opposite polarities. This is analogous to the local tsunami generated from oblique fault slip that also produces a secondary tsunami phase of opposite polarity (Geist, 1999; Geist and Yoshioka, 1996). Although the refracted wave greatly increases the length of coastline affected by this tsunami, this may only apply for landslide locations near bends in the continental slope. Wave heights of the refracted wave along the more regional shorelines in this scenario are likely to be less than approximately 2 m and hence affect only the lowest lying regions.

High-resolution 1D modeling

To determine the effect that nonlinearity and dispersion have on nearshore propagation and runup, a high-resolution 1D simulation was performed along a transect aligned with the center axis of the landslide (Figure 10-12). To accurately model these effects it was determined that a grid spacing of 5 m and the fully nonlinear (FNL-EXT) equations were needed. Energy dissipation from wave breaking is also employed using an eddy viscosity scheme (Kennedy *et al.*, 2000). Runup was computed at mean sea level, noting that the tidal stage at the time of a tsunami will also influence the runup and inundation (Mofjeld *et al.*, 2007). The bathymetry was interpolated to this grid spacing from the regional DEM. Like the previous regional propagation model, the source for the 1D model is the composite slide with a 7.2 min. failure duration.

Several interesting phenomena are evident in this simulation that were not evident in the coarse-grid, regional 2D simulations. First, prior to wave breaking, the wave front fissions into a train of short-wavelength waves (~100-200 m in 30 m water depth). Wave fission is a separation process where wave energy, initially phase-locked to the primary wave or pulse, attains certain properties, such as higher or lower phase speed, that allow it to disconnect from the primary wave and propagate as a free wave. This process can sometimes lead to the formation of an undular bore (*e.g.*, Glimsdal *et al.*, 2007). . For additional description of the fission process, as well as the numerical considerations that must be taken into account to properly simulate this phenomenon, see Lynett (2008). The short-period fission waves shown in Figure 10-12 are very steep and nonlinear, individually break far offshore, and are sensitive to the bottom friction coefficient, due to their long duration of propagation (in terms of number of periods) over shallow water. The wave front breaks approximately 45 km offshore and forms a tsunami bore that continues to propagate shoreward (cf., Yeh, 1991). During runup, the tsunami overtops Currituck Banks and floods Currituck Sound, still as a breaking wave. Maximum runup is about 3 m, although water surface elevations exceed 6 m near the shoreline. The fission waves do not appear to greatly influence runup. These short waves break offshore and transfer momentum into the bore, which is clearly the dominant feature during the inundation phase.

Conclusions

Simulations of potential waves generated from the Currituck landslide yield a wide range in estimated near-shore wave heights. The primary source parameters that affect near-shore wave heights are the overall volume of the landslide and the initial acceleration and duration of vertical movement in the excavation region that generates the back-going, leading depression wave. These results are consistent with an analogous study of the Storegga landslide by Løvholt *et al.* (2005). The mobility analysis, presented by Locat *et al.* (this

volume), is key in constraining the failure duration parameter. Reasonable variations in failure duration have less of an effect on nearshore wave height estimates than the primary source parameter: landslide volume. Other source parameters of the landslide tsunami such as water depth in the excavation region, slide thickness, and downslope length also have a secondary effect on the wave characteristics. The primary hydrodynamic parameter that affects estimates of nearshore wave height is bottom friction along the continental shelf and nearshore region. Improvements to future models would incorporate different coefficients for bottom friction in the shelf and nearshore region. It is also shown that an assumption of linearity in the momentum equations overestimates the nearshore wave heights.

Potential tsunamis for the Currituck landslide are further explored using regional propagation models and high-resolution 1D models to simulate nearshore propagation and runup. Both of these models require substantial computational resources in comparison to the coarse-grid local propagation models used for the source sensitivity simulations. The regional propagation models indicate that the curvature in the trend of the continental slope refracts wave energy emanating from the landslide deposition region. This secondary wave propagates farther to the north and has the opposite leading phase polarity than the primary broadside wave emanating from the region of excavation. The high-resolution 1D simulation reveals the effect that wave breaking and combined influence of dispersion and nonlinearity (described by the Bousinesq equations) has on nearshore propagation and runup. Overall, this study demonstrates that landslide-generated tsunamis are highly complex phenomena and require multiple levels of investigation to accurately assess the hazard they pose to nearby and low-lying regional coastlines.

Table

Table 10-1: Source parameters used in tsunami simulations and corresponding maximum runup broadside from the Currituck landslide. Italics: Parameters used for scenario simulations.

Slide Scenario	Slide Volume (km^3)	Slide Duration (min)	Bottom Friction Coefficient	Runup (m)
Slide 1	108	7.2	0.001	6.10
	108	10	0.001	5.70
	108	20	0.001	4.20
	108	7.2	0.0025	4.70
	108	*10*	*0.0025*	*4.30*
	108	20	0.0025	4.00
	108	7.2	0.010	2.00
	108	10	0.010	1.90
	108	20	0.010	1.80
Slide 2	57	7.2	0.001	3.67
	57	10	0.001	3.00
	57	20	0.001	2.40
	57	7.2	0.0025	3.00
	57	*10*	*0.0025*	*3.00*
	57	20	0.0025	2.00
	57	7.2	0.010	1.60
	57	10	0.010	1.60
	57	20	0.010	1.20
Composite	165	7.2	0.001	8.80
	165	10	0.001	8.00
	165	20	0.001	6.10
	165	7.2	0.0025	6.30
	165	*10*	*0.0025*	*5.80*
	165	20	0.0025	5.00
	165	7.2	0.010	2.60
	165	10	0.010	2.50
	165	20	0.010	2.35

Figures

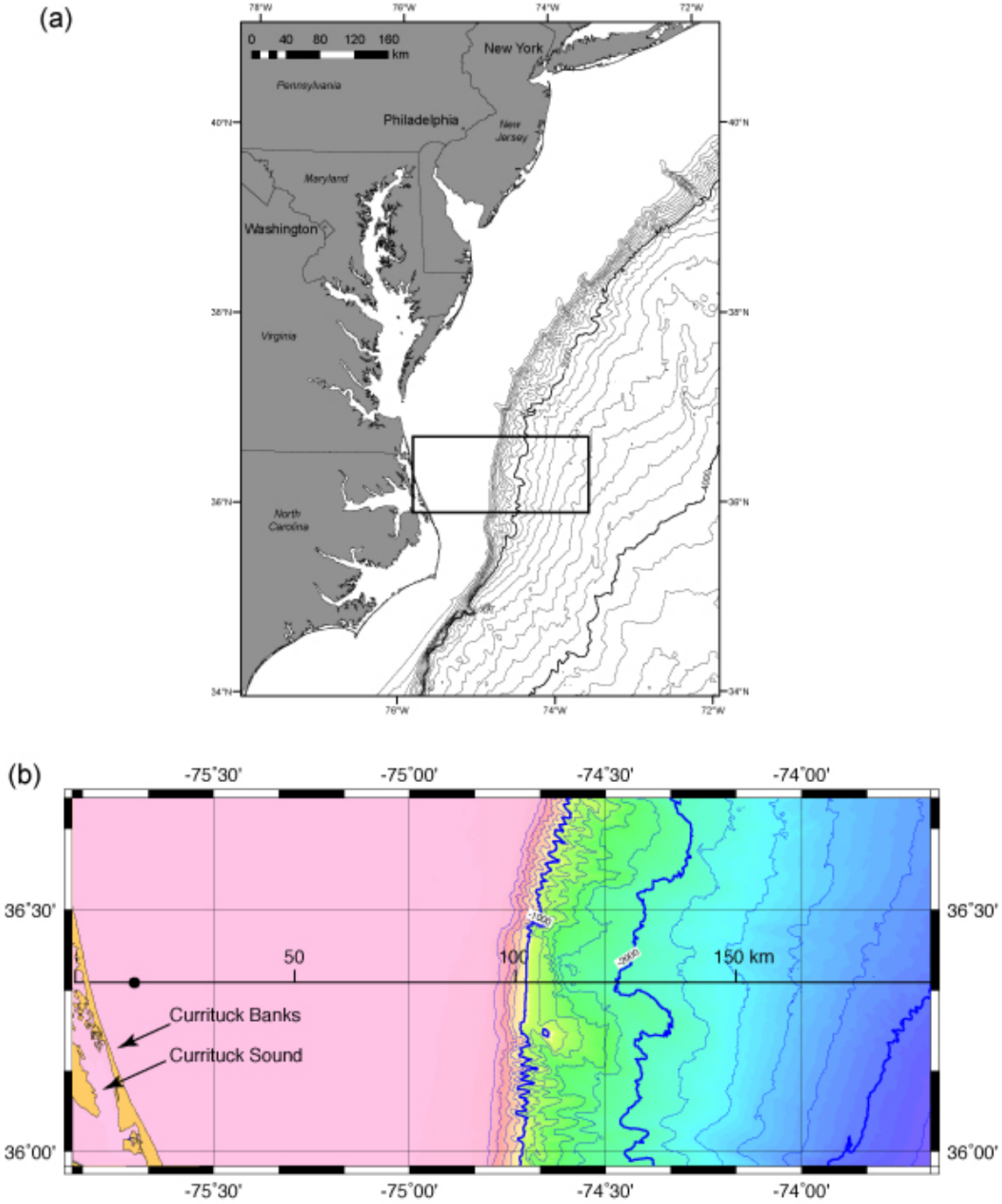

Figure 10-1: (a) Regional bathymetric setting offshore central U.S. Rectangle represents region encompassing the Currituck landslide shown in (b). (b) High resolution DEM of the Currituck landslide and nearshore region representing the model domain for local propagation models. Primary bathymetric contour interval 1000 m; secondary contour interval 200 m. Black line shows location of transect and distance scale where maximum tsunami amplitude is displayed in Figures 10-5 through 10-7; black dot, nearshore location where tsunami time series (marigram) is displayed.

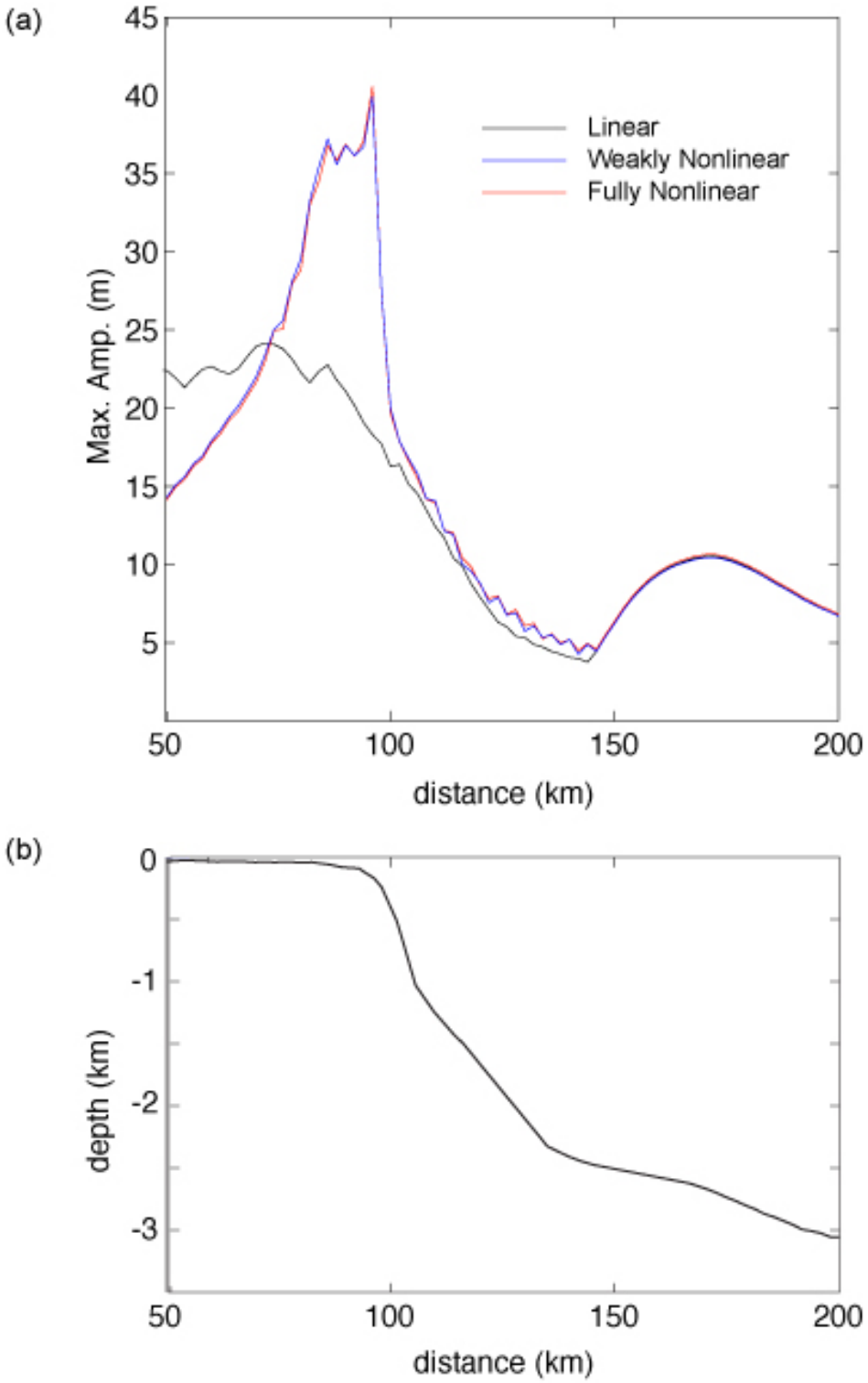

Figure 10-2: (a) Comparison of maximum amplitude profiles aligned with slide axis for the linear, weakly nonlinear (WNL), and fully nonlinear (FNL) forms of the hydrodynamic equations. Simulation for highest amplitude composite slide (duration=7.2 min., $f = 1.0 \times 10^{-3}$) using a coarse numeric grid. Nonlinear results using high-resolution grid presented in Figure 10-12. (b) Bathymetric profile aligned with maximum amplitude profiles (See Figure 10-1b).

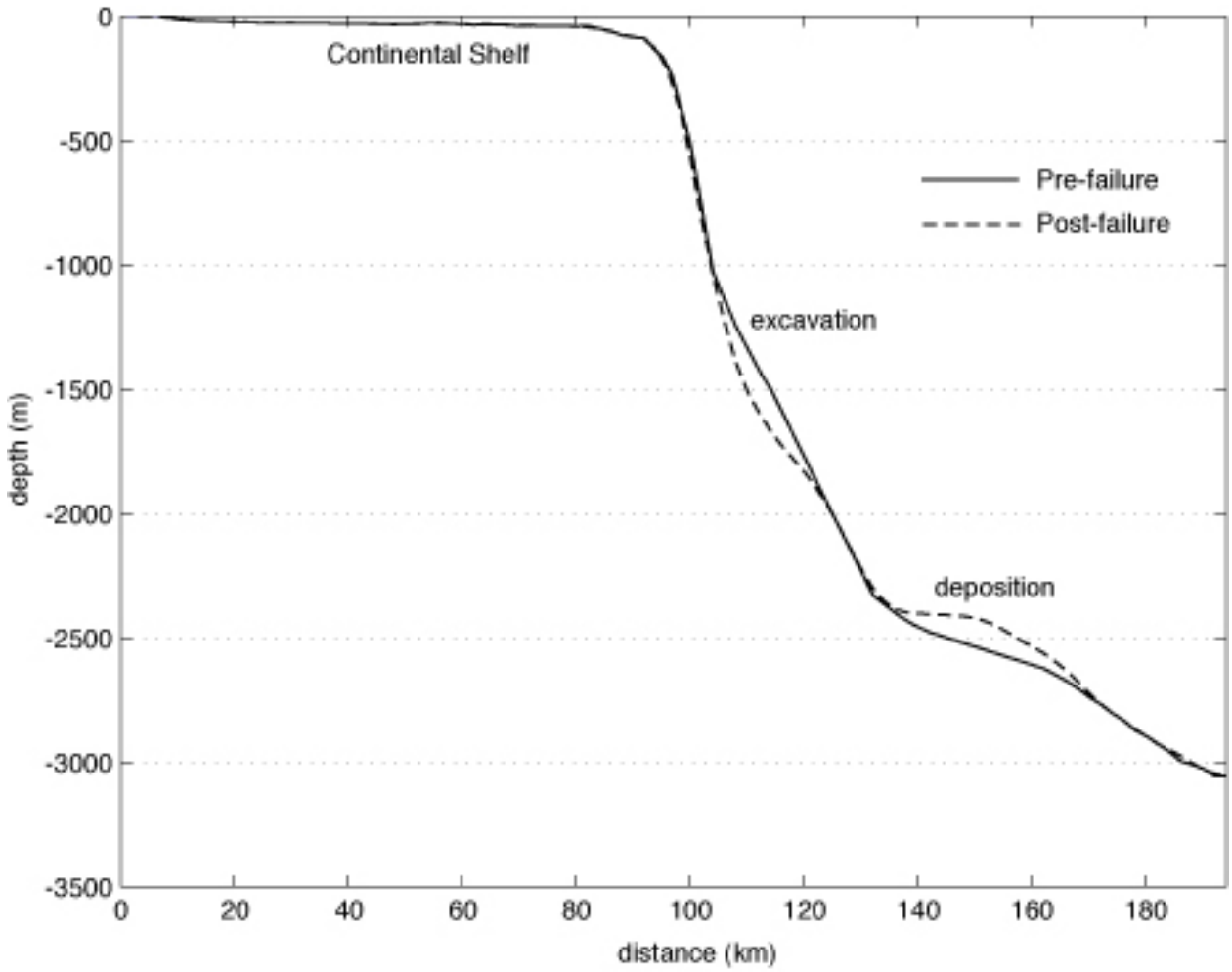

Figure 10-3: Source used for generation of landslide tsunami. Initial displacement profile (solid line) compared to displacement profile of landslide after failure has occurred (dashed line).

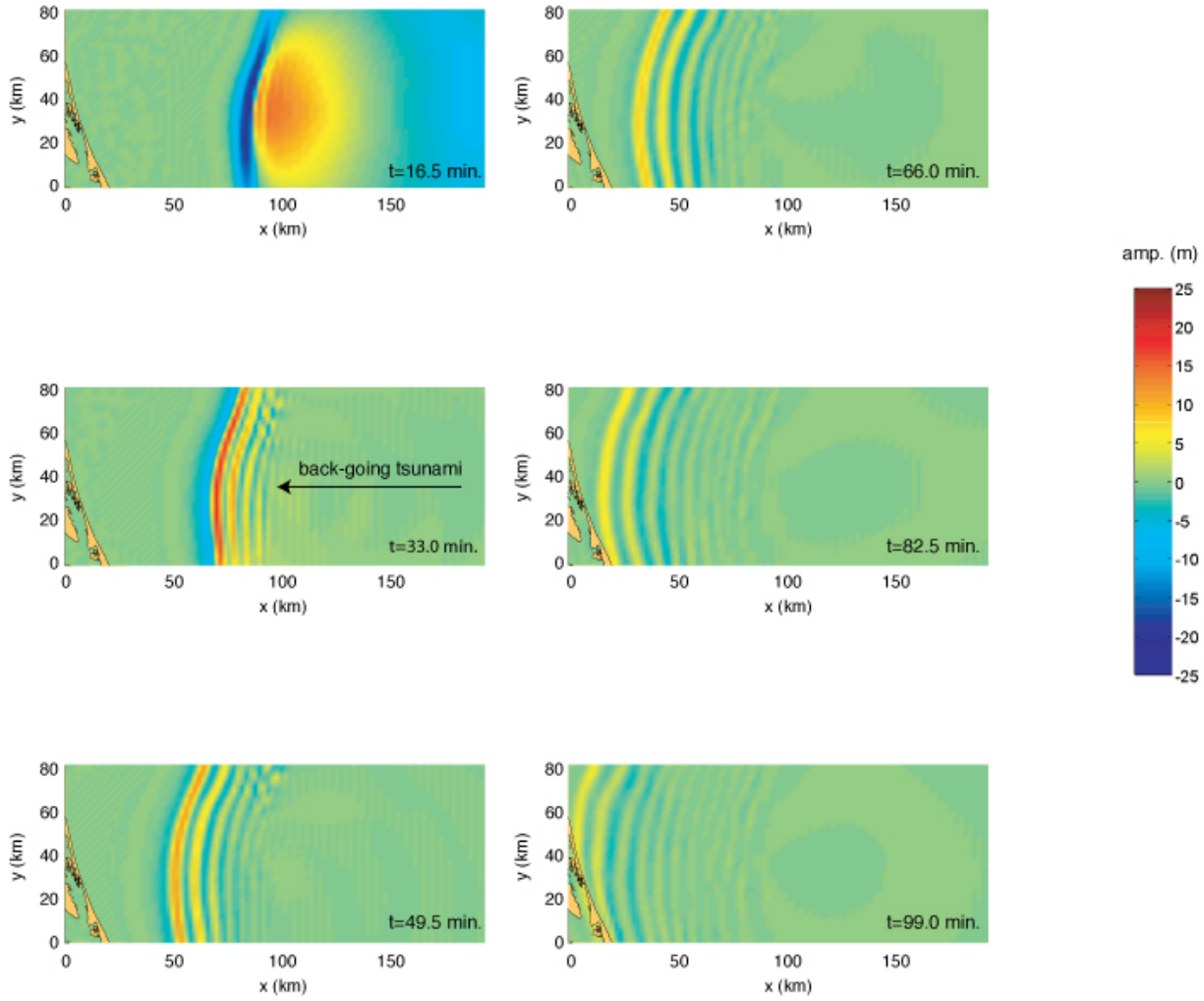

Figure 10-4: Evolution of local tsunami wavefield for composite slide (failure duration 10 min.; $f = 2.5 \times 10^{-3}$) at time intervals of 16.5 minutes. Because out-going tsunami is propagating to the right at high speeds, primarily the back-going tsunami is shown as it propagates across the continental shelf. Location of model domain shown in Figure 10-1.

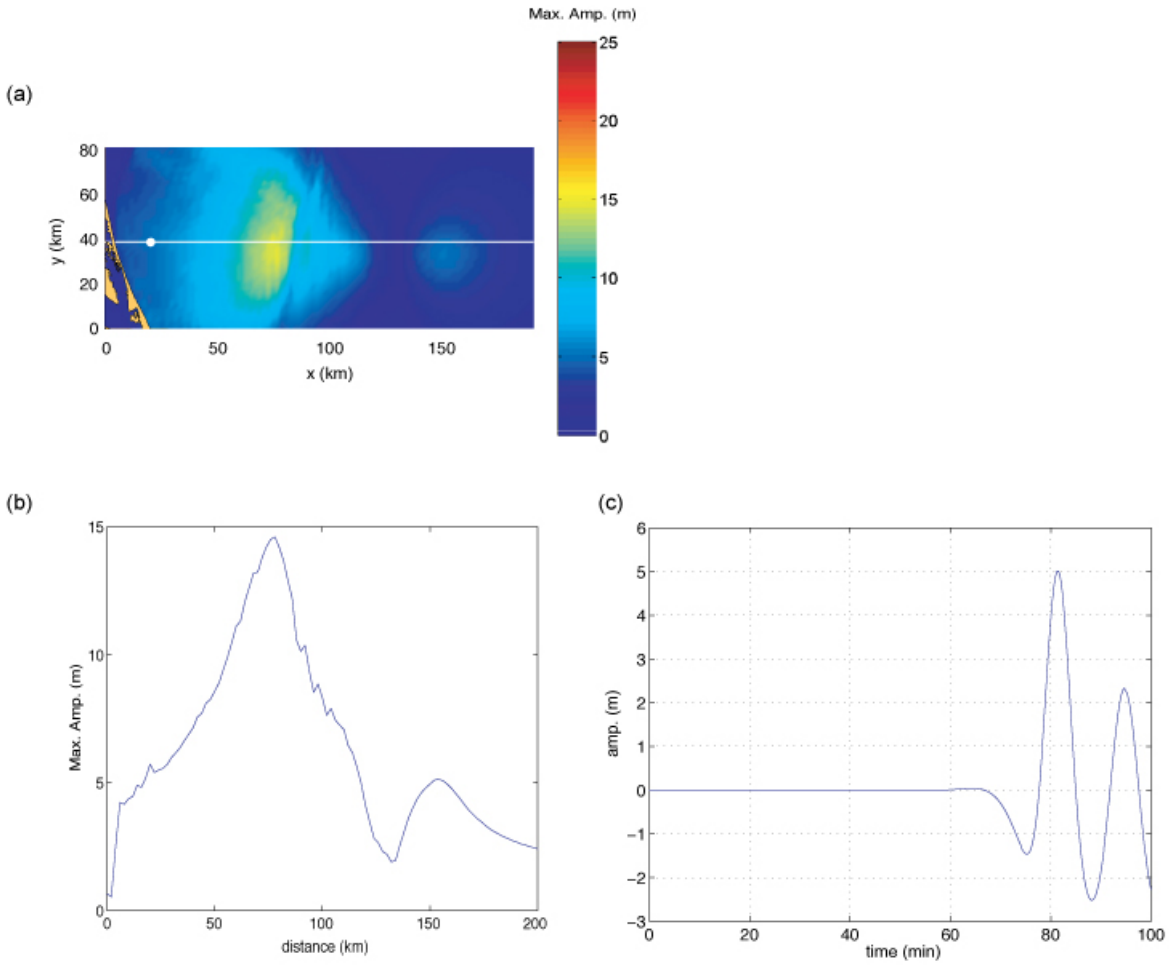

Figure 10-5: Results of hydrodynamic simulation for Slide 1 (duration=10 min., $f = 2.5 \times 10^{-3}$). (a) Maximum wave amplitude throughout model domain during 100 min. of propagation time. (b) Maximum wave amplitude profile along centerline of landslide (white line in a). (c) Time series of tsunami amplitude at a nearshore location (white dot in a; water depth 22m) broadside (directly across) from the landslide.

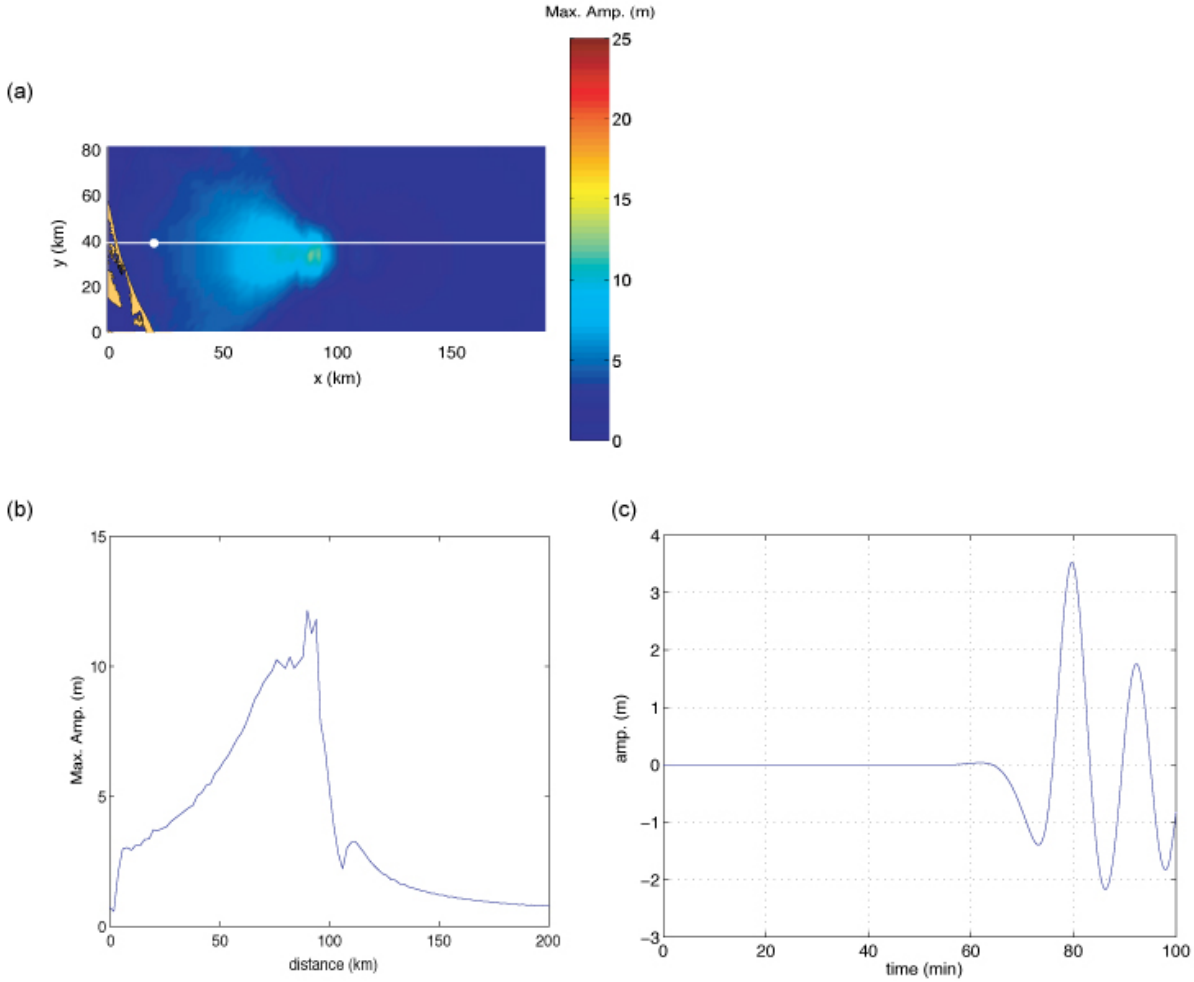

Figure 10-6: Results of hydrodynamic simulation for Slide 2 (duration=10 min., $f = 2.5 \times 10^{-3}$). (a) Maximum wave amplitude throughout model domain during 100 min. of propagation time. (b) Maximum wave amplitude profile along centerline of landslide (white line in a). (c) Time series of tsunami amplitude at a nearshore location (white dot in a; water depth 22m) broadside (directly across) from the landslide.

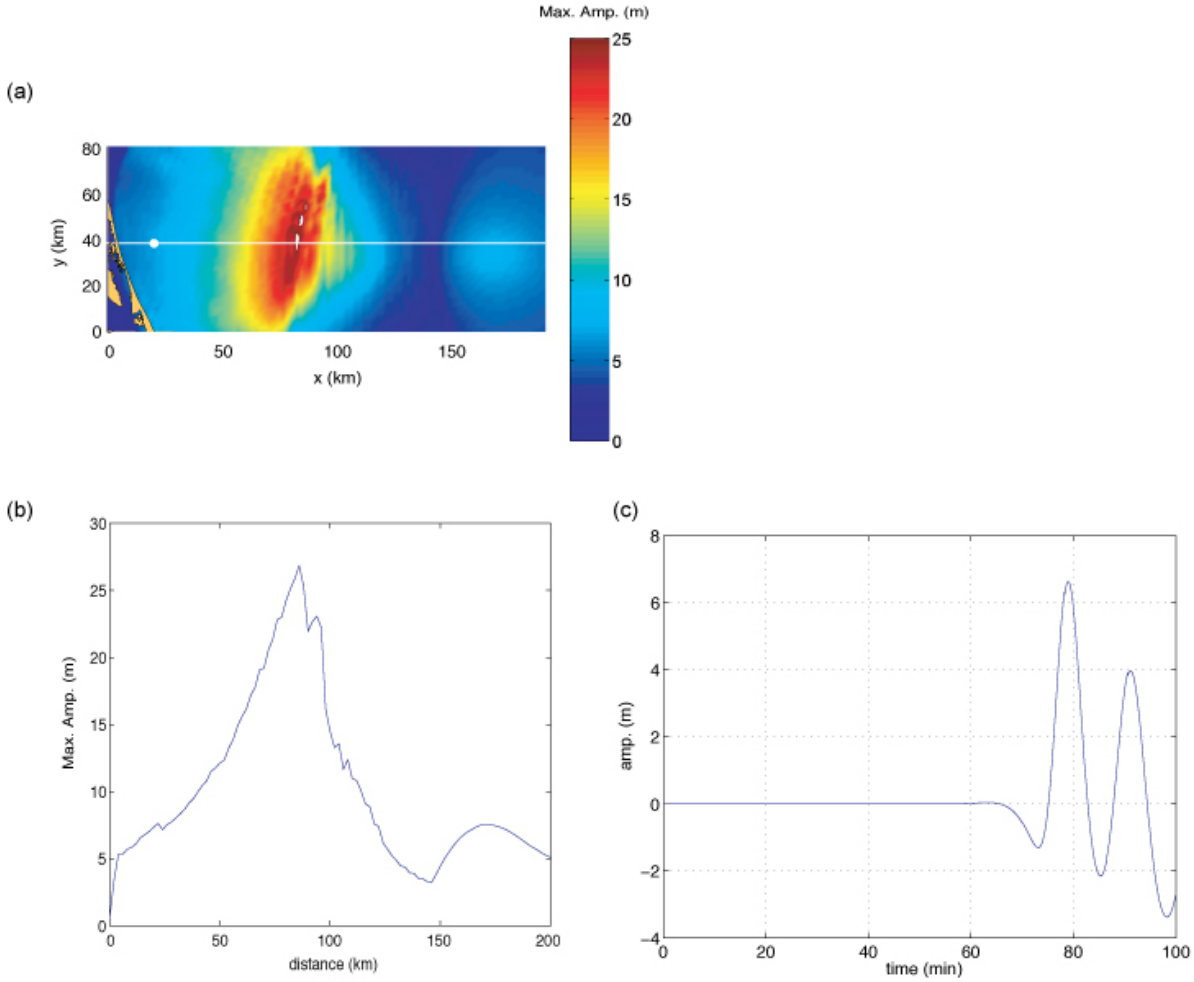

Figure 10-7: Results of hydrodynamic simulation for combined failure of both Slides 1 and 2 (duration=10 min., $f = 2.5 \times 10^{-3}$). (a) Maximum wave amplitude throughout model domain during 100 min. of propagation time. (b) Maximum wave amplitude profile along centerline of landslide (white line in a). (c) Time series of tsunami amplitude at a nearshore location (white dot in a; water depth 22m) broadside (directly across) from the landslide.

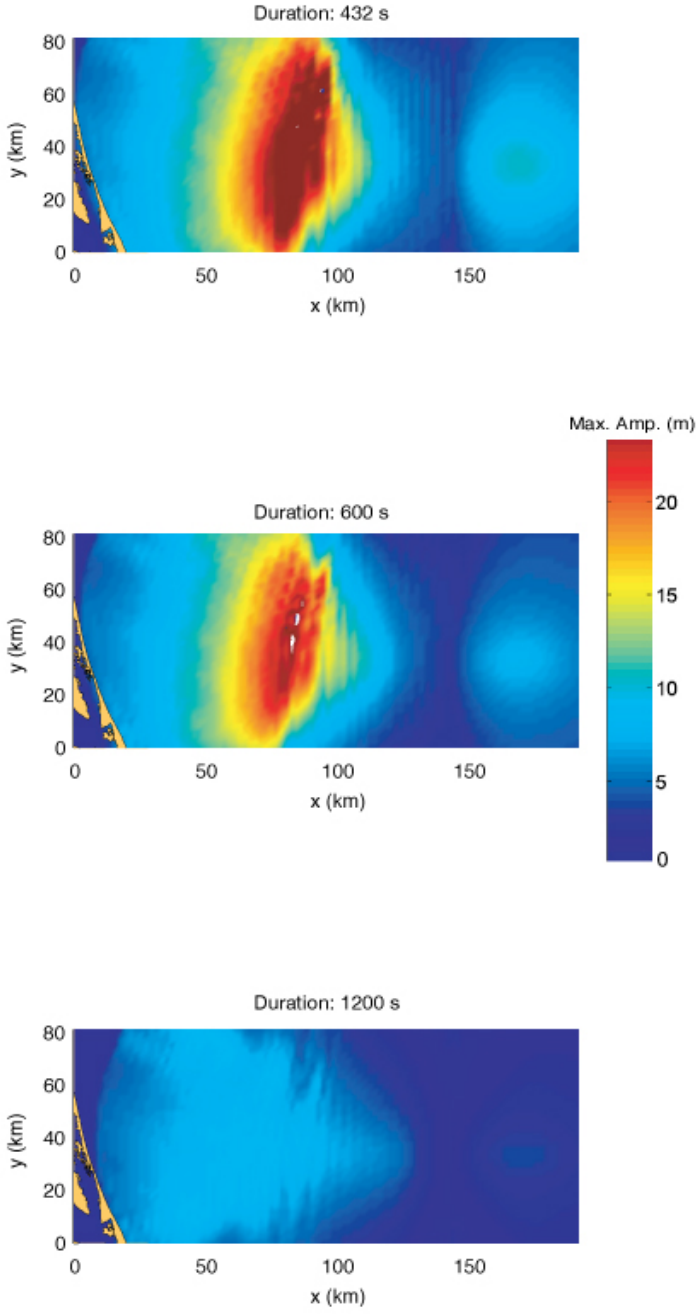

Figure 10-8: Comparison of maximum wave amplitude maps for the composite slide scenario (Slide 1 and Slide 2) using different values for failure duration in the excavation region.

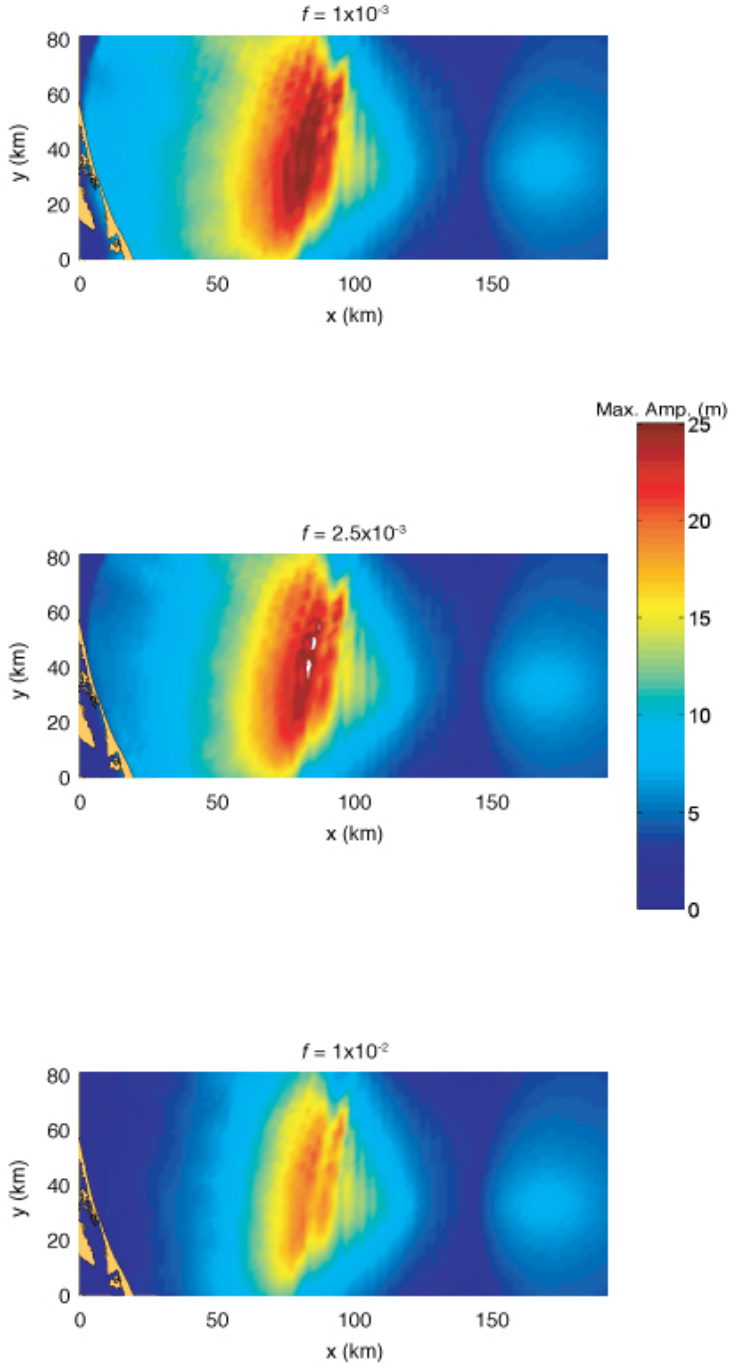

Figure 10-9: Comparison of maximum wave amplitude maps for the composite slide scenario (Slide 1 and Slide 2) using different values for the bottom friction coefficient.

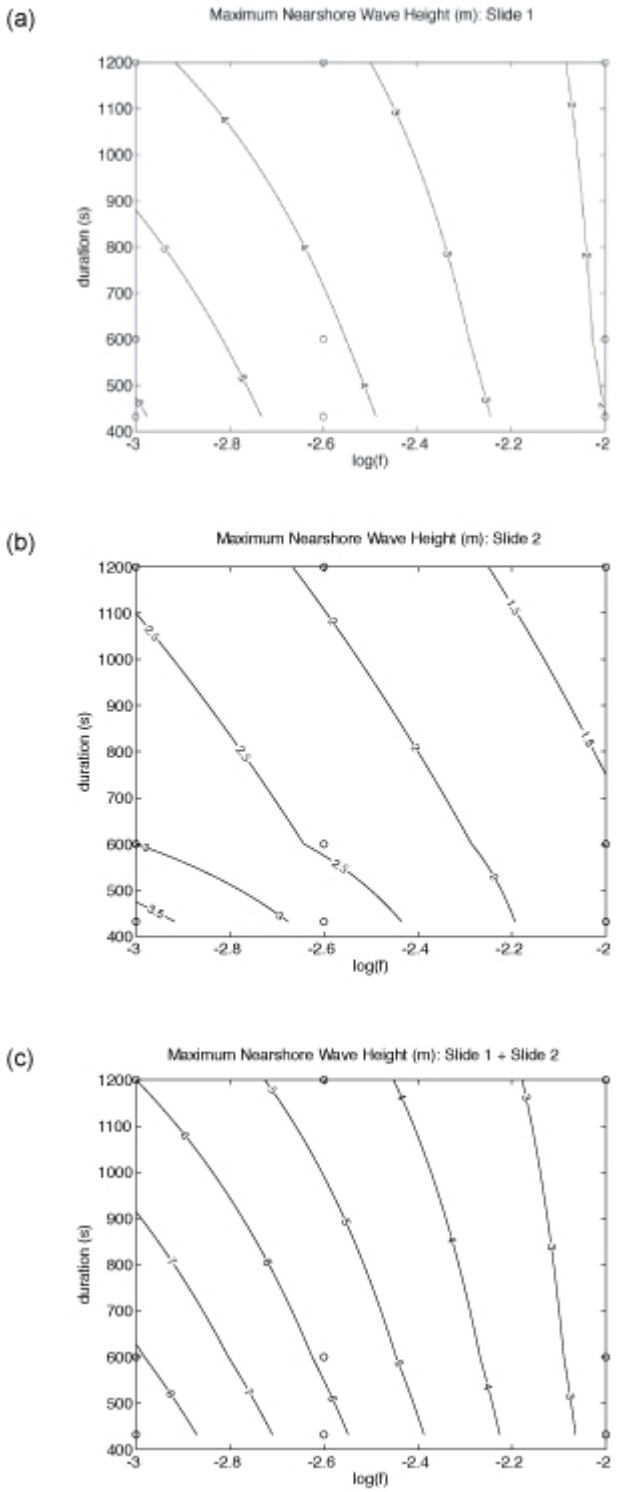

Figure 10-10: Bivariate analysis of the effect failure duration and bottom friction have on nearshore tsunami wave amplitude for (a) Slide 1; (b) Slide 2; and (c) the composite slide. Water depth where maximum wave amplitude is sampled is 18 m. Circles represent results from individual simulations.

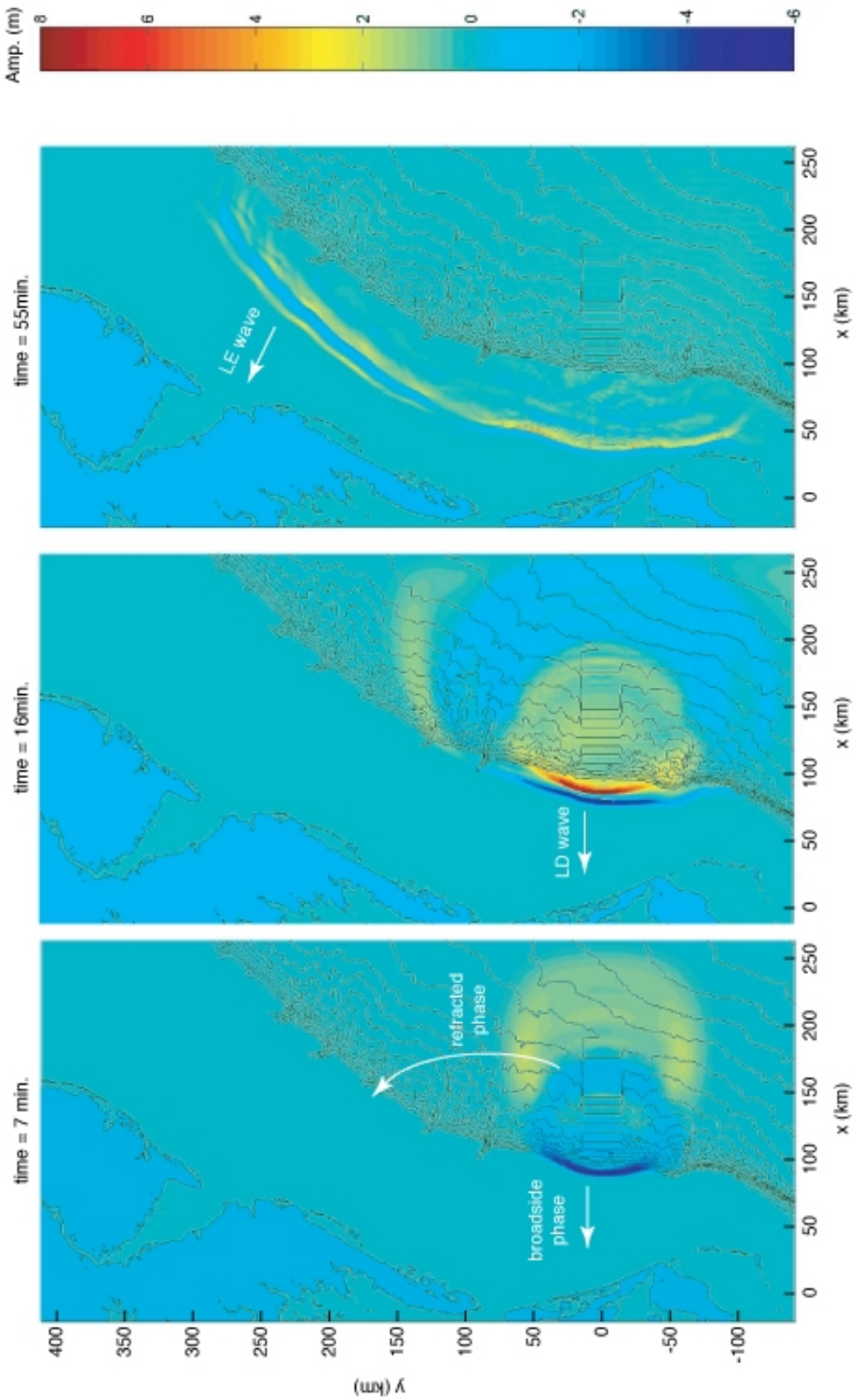

Figure 10-11: Regional wavefield of tsunami from Currituck landslide at three time steps: 7, 16, and 55 min. Evident in this simulation is a secondary wave that refracts up the continental slope and toward shore north of the Currituck landslide.

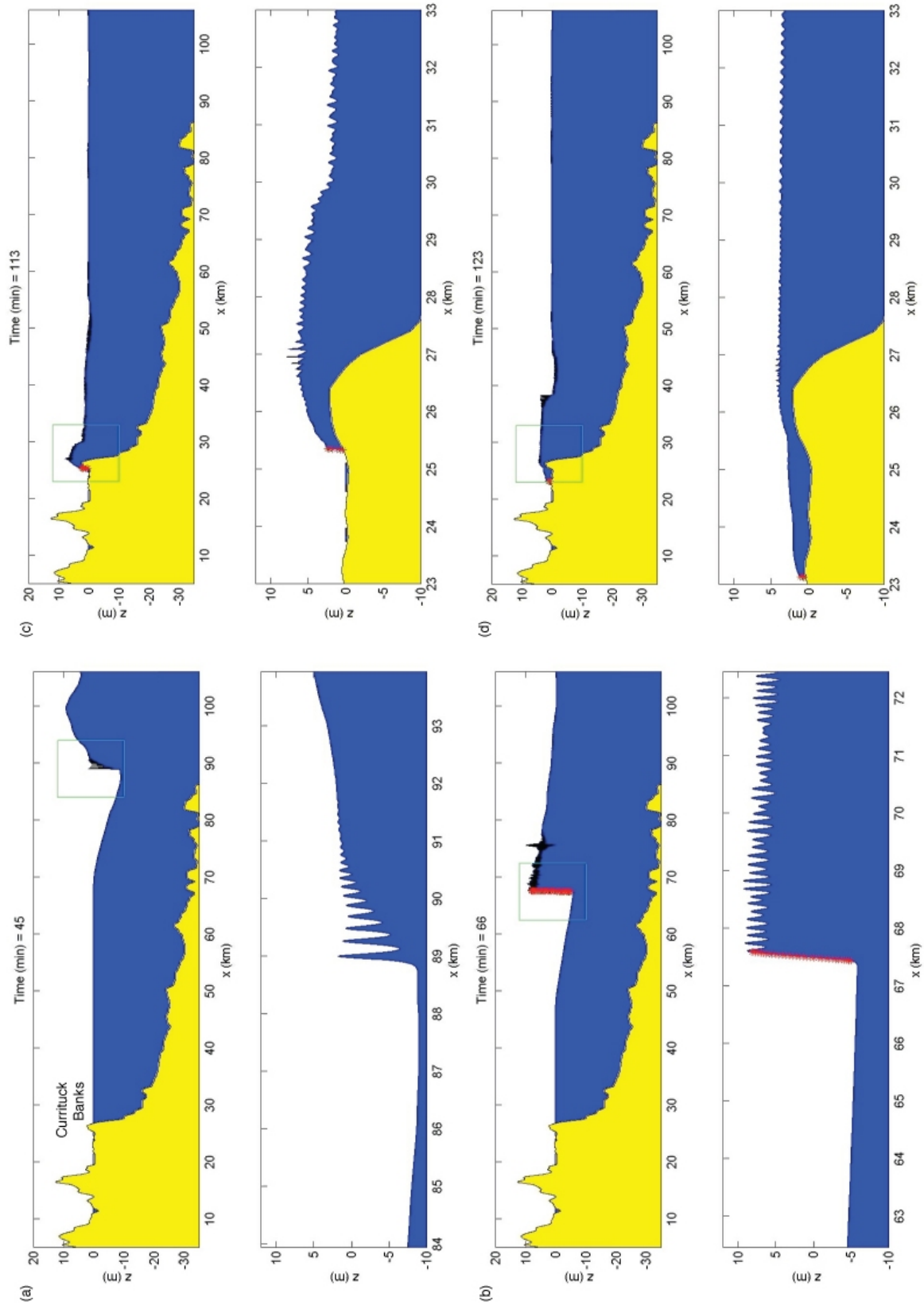

Figure 10-12: High-resolution 1D wave profile illustrating nearshore propagation and runup at four time steps: (a) 45 min.; (b) 66 min.; (c) 113 min.; and (d) 123 min. Green box in top half of each figure shows magnified area indicated in bottom half of figure. Red x's indicate wave breaking.

References

Caress, D.W. and Chayes, D.N., 1996, Improved processing of Hydrosweep DS multibeam data on the R/V Maurice Ewing: *Marine Geophysical Research*, *v. 18*, p. 631-650.

Carrier, G.F., 1971, The dynamics of tsunamis, *in* W.H. Reid (Editor), Mathematical Problems in the Geophysical Sciences. Lectures in Applied Mathematics. American Mathematical Society, Providence, Rhode Island, p. 157-187.

Chaytor, J.D., ten Brink, U.S., Solow, A.R. and Andrews, B.D., this volume. Size distribution of submarine landslides along the U.S. Atlantic Margin and its implication to tsunami hazards.

Chen, Y. and Liu, P.L.-F., 1995, Modified Boussinesq equations and associated parabolic model for water wave propagation: *Journal of Fluid Mechanics*, *v. 228*, p. 351-381.

Elverhøi, A. *et al.*, 2005, Emerging insights into the dynamics of submarine debris flows: *Natural Hazards and Earth System Sciences*, *v. 5*, p. 633-648.

Fine, I.V., Rabinovich, A.B., Bornhold, B.D., Thomson, R. and Kulikov, E.A., 2005, The Grand Banks landslide-generated tsunami of November 18, 1929: preliminary analysis and numerical modeling: *Marine Geology*, *v. 215*, p. 45-57.

Gardner, J.V., Mayer, L.A. and Armstrong, A.A., 2006, Mapping supports potential submission to U.N. Law of the Sea: *EOS Transactions American Geophysical Union*, *v. 8*7, p. 157-159.

Geist, E.L., 1999, Local tsunamis and earthquake source parameters: *Advances in Geophysics*, *v. 39*, p. 117-209.

Geist, E.L. and Yoshioka, S., 1996, Source parameters controlling the generation and propagation of potential local tsunamis along the Cascadia margin: *Natural Hazards*, *v. 13*, p. 151-177.

Glimsdal, S., Pedersen, G.K., Langtangen, H.P., Shuvalov, V. and Dypvik, H., 2007, Tsunami generation and propagation from the Mjølnir asteroid impact: *Meteoritics and Planetary Science*, *v. 42*, p. 1473-1493.

Haugen, K.B., Løvholt, F. and Harbitz, C.B., 2005, Fundamental mechanisms for tsunami generation by submarine mass flows in idealised geometries: *Marine and Petroleum Geology*, *v. 22*, p. 209-217.

Imran, J., Parker, G., Locat, J. and Lee, H., 2001, A 1-D numerical model of muddy subaqueous and subaerial debris flows: *Journal of Hydraulic Engineering*, *v. 127*, p. 959-958.

Kennedy, A.B., Chen, Q., Kirby, J.T. and Dalrymple, R.A., 2000, Boussinesq modeling of wave fransformation, breaking and runup: I. one dimension: *Journal of Waterway, Port, Coastal, and Ocean Engineering*, *v. 126*, p. 39-47.

Korycansky, D.G. and Lynett, P.J., 2005, Offshore breaking of impact tsunami: The Van Dorn effect revisited: *Geophysical Research Letters*, *v. 32*: doi:10.1029/2004GL021918.

Korycansky, D.G. and Lynett, P.J., 2007, Run-up from impact tsunami: *Geophysical Journal International*, *v. 170*, p. 1076-1088.

Lastras, G., De Blasio, F.V., Canals, M. and Elverhøi, A., 2005, Conceptual and numerical modeling of the BIG'95 debris flow, western Mediterranean Sea: *Journal of Sedimentary Research*, *v. 75*, p. 784-797.

Lee, H.J., this volume. Timing of occurrence of large submarine landslides on the Atlanic ocean margin.

Locat, J. *et al.*, this volume. Geomorphology, stability and mobility of the Currituck slide.

Løvholt, F., Harbitz, C. and Haugen, K.B., 2005, A parametric study of tsunami generated by submarine slides in the Ormen Lange/Storegga area off western Norway: *Marine and Petroleum Geology*, *v. 22*, p. 219-231.

Lynett, P., 2008, Modeling of tsunami inundation *in* W.H.K. Lee (Editor), Encyclopedia of Complexity and System Science. Springer-Verlag.

Lynett, P. and Liu, P.L.F., 2002, A numerical study of submarine-landslide-generated waves and run-up: *Proceedings of the Royal Society of London, A*, *v. 458*, p. 2885-2910.

Lynett, P.J., 2006, Nearshore wave modeling with high-order Boussinesq-type equations: *Journal of the Waterways and Harbors Division, A.S.C.E.*, *v. 132*, p. 348-357.

Lynett, P.J. and Liu, P.L.-F., 2005, A numerical study of run-up generated by three-dimensional landslides: *Journal of Geophysical Research*, *v. 10*: doi:10.1029/ 2004JC002443.

Lynett, P.J., Wu, T.-R. and Liu, P.L.-F., 2002, Modeling wave runup with depth-integrated equations: *Coastal Engineering*, *v. 46*, p. 89-107.

Mei, C.C., 1989, The Applied Dynamics of Ocean Surface Waves: Advanced Series on Ocean Engieering, 1. World Scientific, Singapore, 740 pp.

Mofjeld, H.O., González, F.I., Titov, V.V., Venturato, A.J. and Newman, A.V., 2007, Effects of tides on maximum tsunami wave heights: Probability distributions: *Journal of Atmospheric and Oceanic Technology*, *v. 24*, p. 117-123.

Murty, T.S., 2003, Tsunami wave height dependence on landslide volume: *Pure and Applied Geophysics*, *v. 1160*, p. 2147-2153.

Nwogu, O., 1993, Alternative form of Boussinesq equations for nearshore wave propagation: *Journal of Waterway, Port, Coastal, and Ocean Engineering*, *v. 119*, p. 618-638.

Okal, E.A. and Synolakis, C.E., 2004, Source discriminants for near-field tsunamis: *Geophysical Journal International*, *v. 158*, p. 899-912.

Prior, D.B., Doyle, E.H. and Neurauter, T., 1986, The Currituck Slide, Mid-Atlantic continental slope; revisited: *Marine Geology*, *v. 73*, p. 25-45.

Satake, K., 1995, Linear and nonlinear computations of the 1992 Nicaragua earthquake tsunami: *Pure and Applied Geophysics*, *v. 144*, p. 455-470.

Shibata, M., 1983, One-dimensional dispersive deformation of tsunami with typical initial profiles on continental topographies, *in* K. Iida and T. Iwasaki (Editors), Tsunamis: Their Science and Engineering: Terra Science Publication Company, Tokyo, pp. 241-250.

Soulsby, R.L., 1983, The bottom boundary layer of shelf seas, *in* B. Johns (Editor), Physical Oceanography of Coastal and Shelf Seas: Elsevier, Amsterdam, pp. 189-266.

Todorovska, M.I., Hayir, A. and Trifunac, M.D., 2002, A note on tsunami amplitudes above submarine slides and slumps: *Soil Dynamics and Earthquake Engineering*, *v. 22*, p. 129-141.

Trifunac, M.D., Hayir, A. and Todorovska, M.I., 2002, A note on the effects of nonuniform spreading velocity of submarine slumps and slides on the near-field tsunami amplitudes: *Soil Dynamics and Earthquake Engineering*, *v. 22*, p. 167-180.

Trifunac, M.D., Hayir, A. and Todorovska, M.I., 2003, A note on tsunami caused by submarine slides and slumps spreading in one dimension with nonuniform displacement amplitudes: *Soil Dynamics and Earthquake Engineering*, *v. 23*, p. 223-234.

Trifunac, M.D. and Todorovska, M.I., 2002, A note on differences in tsunami source parameters for submarine slides and earthquakes: *Soil Dynamics and Earthquake Engineering*, *v. 22*, p. 143-155.

Twichell, D., Chaytor, J.D., ten Brink, U.S. and Buczkowski, B., this volume, Controls on the distribution of submarine landslides along the U.S. Atlantic continental margin.

Ward, S.N., 2001, Landslide tsunami: *Journal of Geophysical Research*, *v. 106*, p. 11,201-11,215.

Wei, G., Kirby, J.T., Grilli, S.T. and Subramanya, R., 1995, A fully nonlinear Boussinesq model for surface waves. Part 1. Highly nonlinear unsteady waves: *Journal of Fluid Mechanics*, *v. 294*, p. 71-92.

Yeh, H.H., 1991, Tsunami bore runup: *Natural Hazards*, *v. 4*, p. 209-220.

Section 4:

Toward the Development of Quantitative Probabilistic Hazard Assessment

Chapter 11: Assessment of Tsunami Hazard to the U.S. East Coast Using Relationships between Submarine Landslides and Earthquakes

Introduction

Recent tsunamigenic landslides (*e.g.*, Papua New Guinea, Tappin *et al.*, 2001) and re-analysis of historical tsunamis (*e.g.*, the 1918 western Puerto Rico, Lopez *et al.*, in press) have contributed to the realization that landslides can locally generate high-amplitude tsunamis. Along the Atlantic margin, a landslide-generated tsunami in 1929 resulted in loss of life and property along the Newfoundland coast (*e.g.*, Piper and Aksu, 1987; Fine *et al.*, 2005). The U.S. Atlantic coast is particularly vulnerable to devastation from tsunamis because of the high density of population and infrastructure along its low-lying coastal areas and estuaries. Seafloor observations show large landslide scars and debris fields on the continental slope (*e.g.*, Booth, *et al.*, 1993; Chaytor *et al.*, 2007**;** Twichell *et al.*, this volume). Evaluation of the spatial and temporal distributions of submarine landslides should therefore help estimate the probability of landslides; however, it is sometimes difficult to determine whether each of the scars and debris fields represents single or composite landslides (Twichell *et al.*, this volume), and the ages of the slope failures are often not well constrained (Lee, this volume). To overcome the paucity of knowledge about the spatial and temporal distributions of landslides along the U.S. continental slope, we propose here an indirect approach. The approach is to derive relationships between the sizes of submarine landslides and earthquakes and use published earthquake recurrence intervals to estimate the maximum sizes of submarine landslides and their recurrence. The minimum landslide size that can cause a devastating tsunami can be estimated from tsunami runup models of selected landslides of different sizes along the margin. While this approach does not accurately provide the size of individual landslides, it provides an upper bound to the landslide size and to the probability of recurrence of tsunamigenic landslides. We focus here on the relationship between earthquakes and submarine landslides, because, although other triggering mechanisms have been proposed for submarine landslides (*e.g.*, gas hydrate dissociation, excess pore pressure, salt movement;

see Lee, this volume), to date, observed landslide-generated tsunamis have all been triggered by earthquakes.

Three methods to derive the relationship between submarine landslides and earthquakes are presented. The first method, which is introduced in Sections 3 and 4, is based on slope stability analysis. The other two, which are introduced in Section 5, are based on subaerial analogs. In section 5 we compare between the three methods, and compare the predictions based on these methods to the only historical earthquake-generated landslide along the Atlantic coast, namely the 1929 Grand Banks. In Section 6, we estimate the minimum earthquake magnitude that could cause a devastating tsunami (*i.e.*, one that will overtop a barrier island or a sand berm) resulting from a submarine landslide. In Section 7, we extrapolate earthquake recurrence rates for the Canadian margin to the U.S. margin, and define the region, where earthquakes could induce large landslides. This approach may help estimate the potential for landslide-generated tsunamis along the U.S. Atlantic margin.

Slope Stability

The first method to relate earthquake magnitude to the distance from the ruptured fault to the submarine failure (henceforth, fault-to-failure distance) and to the landslide area, is presented in the next two sections. The method is based on calculating catastrophic slope failure conditions due to horizontal acceleration by earthquakes**.** By catastrophic failure we mean a failure that causes downhill mass movement of a finite distance. In engineering literature, finite distance is taken to be at least 1 m (*e.g.*, Hynes-Griffin and Franklin, 1984; , Newmark, 1965), which is assumed to be sufficient for continued downhill movement.

Methodology

We assume that earthquake-induced landslides, at least in soft sediments, may occur when the shear stress τ on a slip surface exceeds the undrained shear strength *Su* of the sediment (*e.g.*, Morgenstern, 1967). This condition is expressed as

$$F = Su/\tau \leq 1 \qquad (1)$$

where *F* is known as the Factor of Safety.

The downslope shear stress in a pseudo-static representation consists of the downslope component of gravitational stress added to a pseudo-static horizontal stress related to earthquake loading (Morgenstern, 1967).

$$\tau = \gamma' z \sin\beta \cos\beta + k\gamma z \cos^2\beta \qquad (2)$$

where γ' is the submerged (buoyant) unit weight in an infinite slope with an angle β, k denotes the horizontal acceleration due to an earthquake (as a

fraction of the gravitational acceleration), z represents the vertical thickness of the landslide, and γ is the unit total weight of the slide.

Setting F=1 as the failure condition yields:

$$Su/(\gamma' z) = \cos\beta \sin\beta + k(\gamma/\gamma') \cos^2\beta \qquad (3)$$

The ratio $Su/(\gamma' z)$ is defined as the c/p ratio and can be measured in the laboratory by subjecting samples to cyclic loading in triaxial tests and observing their failure (*e.g.*, Seed and Lee, 1966, Lee *et al.*, 2000). Rearranging (3), the critical acceleration, corresponding to the earthquake acceleration k_y at which the pseudostatic stress just equals the shear strength, is:

$$k_y = (c/p)(\gamma'/\gamma)/(\cos^2\beta) - (\gamma'/\gamma) \tan\beta. \qquad (4)$$

In other words, the peak earthquake acceleration has to be equal to or exceed k_y to overcome the shear strength of the sediment.

However, the failure condition will lead to a catastrophic slope failure only if the shaking causes the slope to be displaced a finite distance (Newmark, 1965). A catastrophic slope failure will be affected not only by the pseudo-static condition (1), but also by the cyclic nature of earthquake acceleration and its duration. During an earthquake, the ground seldom experiences maximum acceleration in the direction of slope failure. The resultant response may be non-linear and dependent on a transient buildup of pore pressure (Newmark, 1965), the magnitude of shaking (Makdisi and Seed, 1978) and on variations of shaking with depth (Cetin, *et al.*, 2004). Model tests (Makdisi and Seed, 1978, Newmark, 1965) have shown that the peak earthquake acceleration necessary to cause a catastrophic displacement must be much larger than the undrained shear strength.

Empirical and hybrid empirical attenuation relationships for the horizontal component of peak spectral acceleration (PSA) have been derived using databases of hundreds of accelerograms (Abrahamson and Silva, 1997, and references therein). For eastern North America, these relationships take the general form of

$$\ln Y = c + f_1(M) + f_2(M,r) + f_3(r) , \qquad (5)$$

(Campbell, 2003)

where Y is the 5% damped peak spectral acceleration (PSA), M is the moment magnitude, r is the distance from the fault to the site, c is a constant, and f is a function.

Selection of parameters

The c/p ratio was measured in samples from a 38 m deep hole at water depth of 639 m on the Hudson Apron offshore New Jersey (Locat *et al.*, 2003). The c/p ratio decreases from 0.5 near the surface to ≤ 0.2 at depths greater than 10 m, and is 0.15 at the base of the hole (Locat *et al.*, 2003). Based on a

compilation of 106 landslides along the U.S. Atlantic slope, the relationship between landslide volume V and area A is found to be $V = 0.0163\ A^{1.1}$ (Chaytor *et al.*, this volume), suggesting that the average landslide thickness is ~16 m. Therefore, the slide plane depth is likely to be greater than 10 m, justifying the use of c/p=0.2. The relatively low value of c/p may indicate sediment overpressure or the presence of aquifers, which were suggested for the New Jersey margin (Dugan and Flemings, 2000). However, in the absence of direct measurements of pore pressure and cyclic loading measurements of the cored sediments, it is possible that the low c/p values represent coring disturbance. We therefore also calculated the potential slope failure with a more typical c/p value of 0.3. A soil density of 1600 kg/m^3 was measured in this hole (Locat, *et al.*, 2003), resulting in a weight ratio, γ'/γ = 0.375.

The ratio of the critical acceleration necessary to induce catastrophic displacement (taken as 1 m) k_y to the peak spectral acceleration K_{PSA} was calculated by a sliding block analysis for 348 horizontal-component records from earthquakes in California and was found to be k_y/K_{PSA}= 0.17 (Hynes-Griffin and Franklin, 1984). By comparing observations of landslide scarps offshore California to peak seismic acceleration from shake maps and equating a catastrophic failure with a displacement of at least 1 m, Lee *et al.* (2000) derived a ratio of $k_y/K_{PSA} \leq 0.15$. Similar empirical relationships have so far not been derived for the U.S. Atlantic continental margin. We therefore use k_y/K_{PSA} = 0.15 in our calculations.

We calculate PSA using Campbell's (2003) hybrid empirical ground motion attenuation relationships for hard rock in eastern North America. In contrast to the western U.S., this attenuation model is not completely empirical because of the paucity of large earthquakes in the eastern North America. There is no previous guidance for the choice of the fundamental period of shaking. For a soil layer with constant velocity and density, the fundamental period T depends on the layer thickness H, and the shear wave velocity Vs:

$$T = 4H / Vs \qquad (6)$$

(Dorby *et al.*, 1976)

Shallow (<100 m) Pliocene and Quaternary marine sediments on the New Jersey shelf have a shear wave velocity of 200-400 m/s (Ewing *et al.*, 1992), and the thickness of the sliding layer is typically 20-100 m. Hence, T may vary between 0.2 and 2.0 s, and we choose T=~ 0.75 s as an overall best estimate.

The expected site amplification in shallow (top 30 m) soft sediments with Vs = 310 m/s relative to hard rock sites (Vs = 2800 m/s) is ≥ 3.5 (Boore and Joyner, 1997). Hynes-Griffin and Franklin (1984) derived an amplification factor of approximately 3. Consequently, we multiply the calculated peak spectral acceleration by 3.5 to account for site amplification.

Results of Slope Stability Analysis

Maximum distance to failure

The calculated maximum distance r_{max} from a rupturing fault to sites where submarine slope failure is expected is that distance at which the modified peak spectral acceleration of the earthquake, k_{PSA}, is equal or smaller than the critical acceleration, necessary to cause catastrophic displacement, k_y,

$$0.15 \times 3.5 \times K_{PSA\ (T=0.75)} \leq k_y \qquad (7)$$

This distance increases with seabed slope angle and earthquake magnitude (Figure 11-1a). The distance is larger for $c/p = 0.2$ than for $c/p=0.3$ (compare Figures 11-1a and 11-1c), but does not exceed 62 km for slopes ≤ 2°, and 102 km for slopes ≤ 6° even for an earthquake with a magnitude M_w = 7.5. Following Frankel, *et al.* (1996) and Mazzotti and Adams (2005), we used M_w = 7.5 as the estimated largest expected event along the U.S. Atlantic coast. Except along canyon walls and on the flanks of seamounts, the lower continental slope and continental rise have slopes < 2° (Figure 11-3).

Based on the results in Figure 11-1a, an M7.5 earthquakes occurring inland from the Atlantic coast are unlikely to cause sediment failure on the continental slope because of the great distance (>100 km) between them. Therefore, historical earthquakes such as the 1888 Charleston and 1755 Cape Ann earthquakes (Figure 11-2) would not have caused a slope failure on the continental slope. The only exception could be the area around Cape Hatteras where the shelf is 50 km wide (Figure 11-2). An M7.5 earthquake located up to 102 km from the upper slope could cause failure on slopes of 6°, but such high slope angles are confined to only small portions of the continental margin (Figure 11-3). Failures on the more typical slopes of 2° require the epicenter to be within 62 km of the shelf edge. An M6.5 earthquake could cause a landslide only if located within 28 km of the continental slope of 2° and within 42 km of a 6° slope and n M5.5 only if located within 7 and 14 km, respectively.

Mosher *et al.* (1994) have arrived at a similar conclusion from their geotechnical analysis of cores from landslides on the Scotian shelf, namely, that an earthquake would have to be local to generate sufficient ground acceleration for slope failure. Their calculated distance to failure, however, was larger than derived here (40 km for M5 and 100 km for M6.7; Mosher *et al.*, 1994) probably because catastrophic failure was not factored in their analysis.

Note that a finite distance to failure is predicted even on flat ground β=0°. Sediment strength will decline with continued shaking, but in the absence of a slope, the weakened sediments will not move appreciably.

Maximum slope failure area

The maximum slope failure area A_L can be calculated by assuming that the area is defined by the maximum distance to failure, r_{max}. Hence, the maximum failure area is a rectangle containing the fault trace, whose length is the fault length L and whose half-width is r_{max}, plus two half circles with a radius r_{max} at either end of the fault (Figure 11-4a), as given by:

$$A_L = \pi r_{max}^2 + L * 2 r_{max} \quad (8)$$

The fault length as a function of magnitude is given by the empirical relationship

$$\log (L) = -2.44 + 0.59M \quad (9)$$

(Wells and Coppersmith, 1994)

The maximum failure area reaches 24,100 km^2 for slope angles < 2° and M=7.5 (Figure 11-1b). The maximum slope failure area refers to an "ideal" position of a fault within the slope area and parallel to its strike, in which case the fault lengths L in equations 8 and 9 are the same. The expected failure area will be smaller if the fault is not parallel to the margin and/or if the fault is located on the shelf or in the abyssal plain (Figure 11-4b). Note that we assume no catastrophic failure on the shelf, where the slope is ~0°.

Slope angles > 2° along the Atlantic coast of the U.S. are generally limited to a <30 km wide zone of the upper slope as well as some submarine canyons (Figure 11-3). Hence, failure area will likely deviate from the simple shape in equation (8), such that a longer portion of the steep upper slope will fail during an earthquake, compared to the lower slope (Figure 11-4b). The maximum total failure area will therefore be slightly larger than that for a 2° slope. For example, for an M7.2 earthquake, the total area will be about 15,900 km^2 instead of 14,200 km^2 due to the added contribution of the upper slope. The maximum observed landslide area along the Atlantic margin is 15,240 km^2 and is located off southern New England (Twichell *et al.*, this volume).

Comparison with the 1929 Grand Banks landslide

The modeling results can be compared with observations of the 1929 Grand Banks landslide, that caused the only historical tsunami along the Atlantic margin of North America. On the basis of the area encompassing the instantaneous breaks of communication cables along the sea floor during the earthquake, Piper *et al.* (1985) and Mosher and Piper (2007) estimated the region where at least 10% of the sea floor failed to be 22,700 km^2. Using side-scan sonar they estimated the region where 100% of the sea floor failed to be 7200 km^2. Piper and Aksu (1987) and Piper *et al.* (1999) estimated the average failure thickness as 20 m and the volume of failed material to be >150 km^3. McCall *et al.* (2005) estimated the total volume of failed material in

the area of 100% seafloor failure to be 93.5 km^3. Hughes Clarke, *et al.* (1990) pointed out that a small volume of debris flow (<15 km^3) appears to post-date the turbidity flow, and could have been triggered by aftershocks.

The Mw=7.2±0.3 1929 Grand Banks earthquake was located in the middle of the steep upper slope (Bent, 1995). For a 2° average slope and c/p ratio of 0.2, the predicted area of the entire possible failure region from an M7.2 earthquake, is 14,200 km^2 (Figure 11-1b). With a 30-km-wide steeper (6°) upper slope replacing part of the predicted failure area of a 2° slope, the total predicted maximum failure is 15,900 km^2. This value is similar to the observed slide failure area associated with the 1929 earthquake within the uncertainties of the model parameters, the earthquake magnitude and the observations of the failure area. (For example, the predicted area from M7.5 earthquake is 24,100 km^2; Figure 11-5b). The ~30 km wide upper slope is steeper (~6°), hence a longer part of the upper slope is expected to fail along strike compared to the less steep lower slope (Figure 11-4b). The region with 100% failure indeed extends along 210 km of the upper slope, whereas the length of lower slope failure is half of that (Mosher and Piper, 2007). The area with at least 10% sea floor failure has a maximum failure length of 245 km in the upper slope and is also narrower on the lower slope (Piper, *et al.*, 1985, Mosher and Piper, 2007). The calculated length of upper slope failure for M7.2 is 200 km, which is within the observed estimates.

Additional notes

The choice of attenuation relationship also affects the prediction of seismic acceleration. Using different attenuation relationships for eastern North America (Tavakoli and Pezeshik, 2005), the predicted distance to failure and slope failure area are slightly larger than those predicted by Campbell's (2003) relationships (Figure 11-5). The difference becomes considerably larger for large magnitude earthquakes (M7), because of changes in the functional relationship of Tavakoli and Pezeshik (2005) at distances of 70 and 130 km.

Predictions of landslide susceptibility were made for two regions offshore California by coupling slope stability analysis with the predicted peak seismic acceleration. (Lee, *et al.*, 2000). Published maps of peak seismic acceleration with 10% probability of exceedance in the next 50 years were used to estimate the peak ground acceleration along the margin (Lee, *et al.*, 2000). The California continental slope is generally much closer to land than the Atlantic continental slope of the U.S., and the frequency of earthquakes is much higher; therefore the use of such maps is justified there. Peak acceleration maps of the U.S. Atlantic coast (Figure 12 of Frankel *et al.*, 1996) do not extend into the continental margin and are heavily skewed at the 50-year exposure time toward the two large historical earthquakes in the U.S. East Coast--Cape Ann (1755) and Charleston (1888). Hence, we had to infer the seismic acceleration directly from the maximum magnitude (M_{max}) of hypothetical earthquakes, with the intention of calculating the probability of occurrence of earthquakes of certain magnitude along the margin in the future. At present, however, microseismicity monitoring along the continental margin (≤M3.5) is incomplete due to the lack of dense

instrument coverage, the large distance from shore, and the relatively short measurement period in comparison to rates of seismic moment release.

Other Methods - Using Land-based Empirical Relationships

Empirical estimates of landslide effects due to earthquakes have been carried out on land, where these effects can be easily observed and surveyed (Keefer, 1984; Ambraseys, 1988; Rodriguez *et al.*, 1999; Keefer, 2002), and references therein). Ambraseys (1988) proposed a curve that bounds the maximum distances from the fault rupture to liquefaction sites, which we call the maximum liquefaction distance r_{liq}.

$$Mw = 0.18 + 9.2 * 10^{-8} r_{liq} + 0.9 \log (r_{liq}). \qquad (10)$$

Liquefaction on land is indicative of catastrophic soil failure in the absence of a topographic slope and in the presence of a water table close to the surface. Hence, these observations can probably be compared to the distance of failure of submarine sediments from the triggering fault, predicted by slope stability analysis, because of the generally low submarine slopes (Figure 11-5a). The maximum observed liquefaction distance falls within the predicted distance from slope stability analysis for slopes between 2° - 6° and c/p=0.2, but is higher than the predicted distance from slope stability analysis for c/p=0.3 (Figure 11-5a).

Based on post-earthquake observations, Keefer (1984) and Rodriguez *et al.* (1999) defined an upper bound curve for the total area in which earthquake-triggered landslides occur (Figure 11-5b). Their compilations of landslide areas do not differentiate between different slope angles or landslides types, such as rock falls, disrupted and coherent rock slides, soil spreads, and flows. As with maximum distance to failure, the area calculated from slope stability analysis for slopes between 2°-6° is similar to or slightly less than Keefer (1984) and Rodriguez *et al.* (1999) curves. An expected maximum failure area can also be calculated by combining the maximum observed distance from the fault r_{liq} to liquefaction (cf. equation (10), Ambraseys, 1988) and equation (9). The expected maximum failure area from the maximum distance to liquefaction (A in Figure 11-5b) appears to be similar to the observed maximum landslide area by Rodriguez *et al.* (1999, R in Figure 11-5b).

The maximum subaerial failure area resulting from a M7.2 earthquake is between 21,000 km^2 (when using Keefer, 1984, relationship) and 36,000 km^2 (when using Rodriguez *et al.*, 1999, relationship), and the maximum area using the liquefaction distance is 33,800 km^2. These estimates are within, or larger than, observed failure area of the 1929 Grand Banks landslide (Mw=7.2±0.3, area=7,200-22,700 km^2, Figure 11-5b).

At present, it is unclear whether the use of slope stability analysis or the subaerial observations is the more valid method for estimating the relationship between earthquakes and submarine landslides. The empirical

relationships of Ambraseys (1988), Keefer (1984), and Rodriguez *et al.* (1999) are based on observations from around the world, with variable drainage conditions, slope direction and angle, and lithology within a single affected area, whereas the slope stability analysis uses a specific attenuation relationship for the U.S. East Coast, a monotonous and fairly low slope, and observed geotechnical parameters for the Atlantic continental slope. However, the PSA may not account for the duration of shaking, which increases with magnitude. In addition, the ratio of the peak spectral acceleration K_{PSA} to the acceleration k_y necessary to induce catastrophic displacement (taken as 1 m) was assumed here to be constant (Haynes-Griffin and Franklin, 1984), but it may in fact increase with magnitude (Makdisi and Seed, 1978). One way to explicitly account for the increase in the duration of shaking is by using Arias intensity instead of PSA. The Arias intensity is the integral of the acceleration-time history (Travasarou *et al.*, 2003, and references therein). However, an Arias intensity relationship for the eastern U.S. has not yet been developed.

Magnitude Threshold for Devastating Tsunamis

The morphology of the U.S. East Coast is variable with many coastlines having sand berms or barrier islands. Detailed LIDAR elevation maps of the coast stretching from North Carolina to southern Florida show that elevations typically vary from 2-8 meters above the NAVD88 88 reference level (Elko *et al.*, 2002). The NAVD88 reference level is on average 0.5-1.25 m below the mean highest high water level (Weber *et al.*, 2005) hence this amount has to be subtracted from the dune height in a worst-case scenario. Similar detailed information of dune height or of a maximum elevation close to shore is lacking north of North Carolina. Hydrodynamic modeling shows that a tsunami can overtop a sand dune or barrier island even if the tsunami's wave amplitude is lower than the sand dune elevation (Geist *et al.*, this volume, their Figure 12) because of the large wavelength of the tsunami relative to that of the sand dune. Tsunami wave amplitude from the 1929 Grand Banks tsunami was estimated at 3-8 and the maximum runup was 13 m (Fine *et al.*, 2005). Recognizing that dune elevation is highly variable in space, we assume in this analysis a tsunami with wave height of 2 m offshore, as one that can overtop many of the dunes and can therefore be potentially damaging.

The maximum calculated area of slope failure is sufficiently large for earthquakes magnitudes greater than M=5.5-6 to cause a devastating tsunami (inset in Figure 11-5) if the epicenter is optimally located at the base of the upper slope and if the entire area indeed fails. This estimate is based on the calculated wave amplitude at 22 m water depth from hydrodynamic modeling of the Currituck slide offshore Virginia (Geist *et al.*, this volume). The modeling suggests that, for the particular characteristics of the Currituck region and for a near-shore bottom friction of $0.25\text{-}1\text{x}10^{-2}$, a failure area of 300 km^2 would generate a wave amplitude of 1.6-2.4 m, which is probably not enough to cause a devastating tsunami, but a failure area of 1240 km^2

would generate a wave amplitude of 2-4.5 m, which could overtop the sand berms (inset in Figure 11-5; Geist *et al.*, this volume). A larger earthquake magnitude may be necessary to cause a devastating tsunami from a submarine landslide along the southern New England margin, because the shelf there is twice as wide as the 80-km-wide Currituck shelf. The amplitude of tsunami waves is expected to decay as they travel over the shelf because of bottom friction and dispersion, the latter caused by the long propagation time across the shallow shelf. At present, there are no hydrodynamic models for this region.

Probability of Earthquake Recurrence

Analysis of the rates of deformation in eastern Canada (Mazzotti and Adams, 2005) suggests that the continental slope of eastern Canada from the Arctic to Georges Bank is associated with a relatively high average annual seismic moment release (2-10 x 10^{17} N-M/yr) for an intraplate setting. The annual moment release is the equivalent of an M_w7 earthquake occurring somewhere along this ~6000 km long margin every 40 –200 years. The source of the seismicity is unclear but some workers have suggested that seismicity is due to glacial unloading of the Laurentide ice sheet (Mazzotti and Adams, 2005, and references therein). Seismicity offshore the U.S. Atlantic coast is mostly concentrated offshore New England (Figure 11-3), the only sector to have undergone glacial unloading. It is possible therefore that the same seismic regime present on the eastern Canadian margin extends from the Canadian continental slope south along the 400-km-long New England margin. Using Canadian seismicity as a guide and assuming equal probability for the spatial distribution of earthquakes (*e.g.*, Swafford and Stein, 2007), the rate of seismic moment release along the New England margin is 1/15 that of the Canadian estimate, which is equivalent to an M=7.0 earthquake occurring every 600-3000 yr. However, the frequency of submarine landslide-induced destructive tsunamis is likely smaller than this because of additional conditions such as optimally located epicenter within the vulnerable area, catastrophic failure of much of the vulnerable area, and rapid slide movement, that are necessary to generate a destructive tsunami.

South of the New England margin, the seismicity rate appears lower than to the north (Figure 11-2). Nevertheless, possible faults have been identified on the slope south of the Cape Fear area (Hornbach *et al.*, 2007) and south of the Currituck slide (Locat *et al.*, this volume). These faults may be related to salt movement at depth and may be associated with the slides (Hornbach *et al.*, 2007). The recurrence interval on these faults is unknown.

Conclusions

It is clear from the analysis above that there are large uncertainties in estimating tsunami probability with this approach. These uncertainties are attributed to the choice of the spectral acceleration period, the amplification due to soft sediments, the choice of c/p, sediment thickness, the presence of

over-pressured or liquefiable sediments, and the recurrence interval of seismicity. Likewise, the applicability of land-based empirical relationship of heterogeneous lithologies and slopes to submarine slopes has not been established. Nevertheless, the fit of the predictions of landslide area from magnitudes of earthquakes for all three methods to the observed area of the 1929 Grand Banks landslide is encouraging, keeping in mind that this is a single example, and the total area of the Grand Banks slide is still not well-constrained.

With these uncertainties in mind, we can reach several conclusions:

(a) Slope stability analysis suggests that the upper slope of the continental margin (slope angle ≤6°) will be affected by earthquakes with magnitudes of 5.5, 6.5, and 7.5, only if the earthquakes occur at distances less than 14, 42, and 102 km from the upper slope, respectively. For the lower, more shallowly dipping slope (≤ 2°), the distances are much smaller (*i.e.*, 7, 28, and 62 km, respectively). These distances represent maximum distances will be smaller if c/p=0.3 is assumed in the analysis. This analysis suggests that, with the exception of Cape Hatteras, only offshore earthquakes may be able to trigger submarine landslide-generated tsunamis.

(b) The maximum calculated area of slope failure is sufficiently large for earthquakes with magnitude greater than M5.5 to cause a devastating tsunami if the epicenter is optimally located at the base of the upper slope and if the entire area indeed fails.

(c) Based on extrapolation of results from the Canadian margin, the rate of release of seismic moment along the New England margin is estimated to be equivalent to an M7.0 earthquake occurring every 600-3000 y. If these earthquakes are located at the base of the upper slope so as to maximize the failure area, or if slope sediments are overpressured, the resultant landslide area (and volume) will be sufficient to cause a destructive tsunami. The paucity of earthquakes south of the New England margin suggest that landslides there are either less frequent or they are generated by other mechanisms.

(d) Slope stability analysis predicts similar or smaller maximum distance from fault to failure and maximum failure area than compilations of subaerial landslides and liquefactions. Both predictions from slope stability analysis and the extrapolation from land compilations fit the observations of the 1929 Grand Banks event, but other events are needed to validate these methods.

In summary, mapping entire continental margins and determining the age of submarine landslides is difficult and costly. We present here an approach to estimate the maximum size and recurrence interval of potentially-tsunamigenic submarine landslides from the size and recurrence interval of earthquakes in the near vicinity of the said landslides. We also suggest that

the minimum landslide size that will cause a devastating tsunami can be estimated from tsunami runup models of selected landslides of different sizes. This information can help in the design of infrastructure facilities to withstand the effects of tsunamis. A successful implementation of this approach may require improvement in the seismic monitoring of continental margins.

Figures

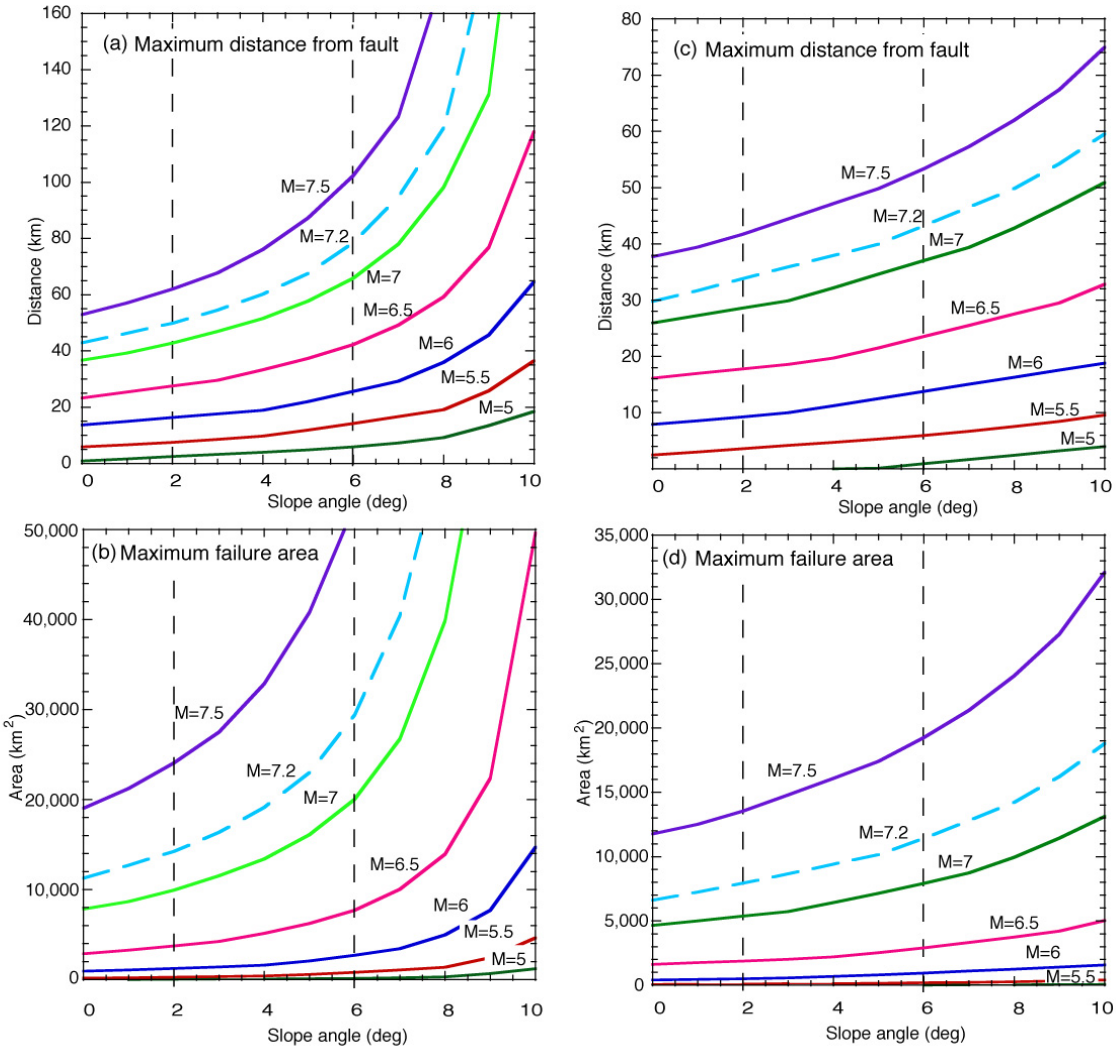

Figure 11-1: (a) Calculated maximum distance from a fault to sites where failure is expected, as a function of slope angle and earthquake moment magnitude. The following parameters were used: c/p = 0.2, k_y/K_{PSA} = 0.15, γ'/γ = 0.375, and peak seismic acceleration (PSA) relationship of Campbell (2003) for T = 0.75 s. Vertical dashed lines mark 2° and 6° (b) Calculated maximum failure area as a function of slope angle and earthquake moment magnitude using the same parameters as in (a). (c) Same as (a) with c/p = 0.3. (d) Same as (b) with c/p = 0.3.

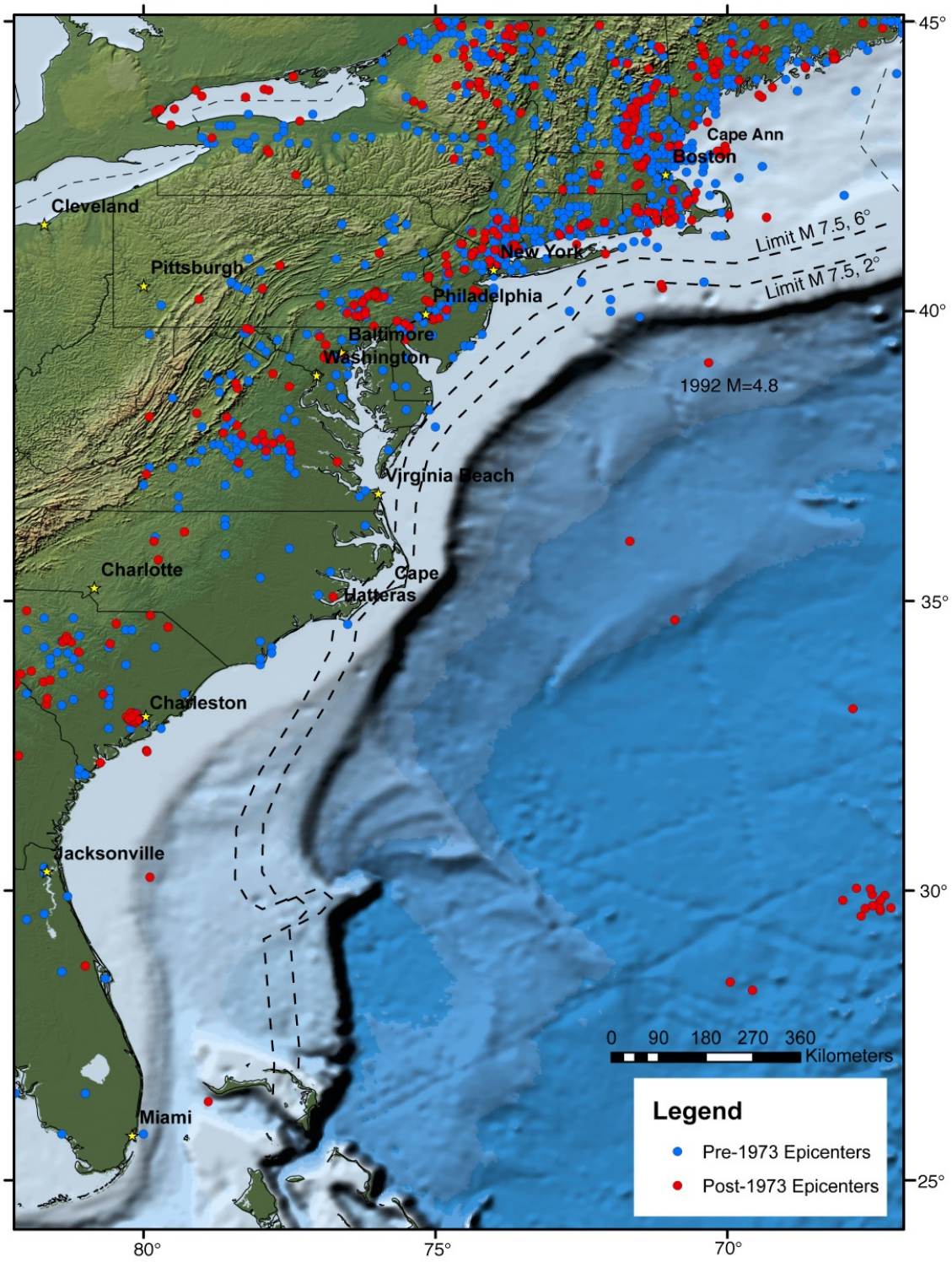

Figure 11-2: Earthquake epicenters along the U.S. Atlantic coast from the NEIC catalog (`http://neic.usgs.gov/neis/epic/epic.html`). Blue dots: earthquakes between 1534-1973. Red dots: earthquakes post-1973 catalog. Dashed lines: distances of 62 and 102 km from the top of the continental slope. These are the maximum predicted distances based on slope stability analysis, for an M7.5 earthquake, to cause a catastrophic failure of the continental slope with slope angles of 2° and 6°, respectively. Smaller magnitude earthquakes will have to be located closer to the shelf edge to cause catastrophic slope failures.

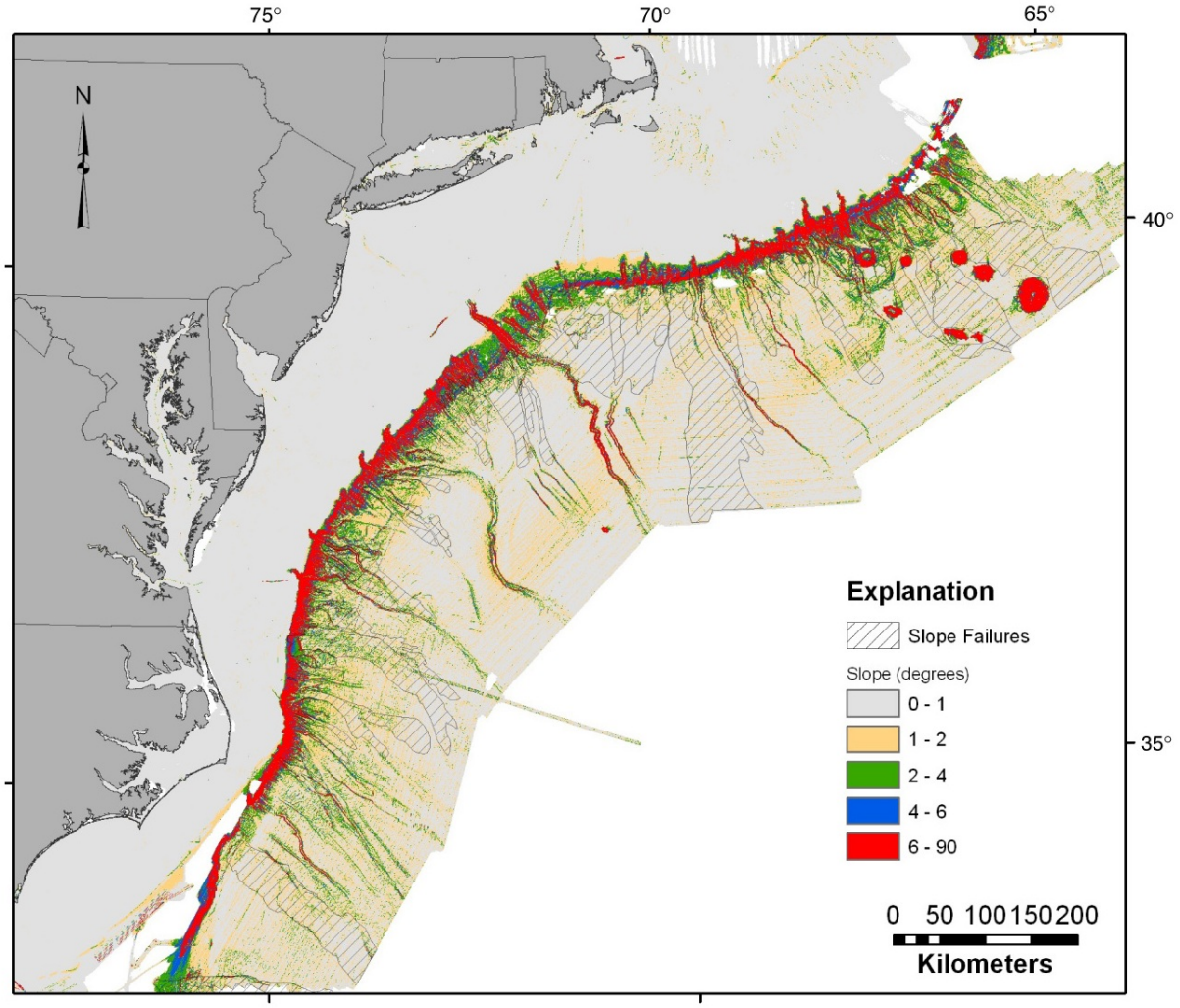

Figure 11-3: Slope angle of the U.S. Atlantic continental margin and overlays of interpreted slope failures (Twichell *et al.*, this volume).

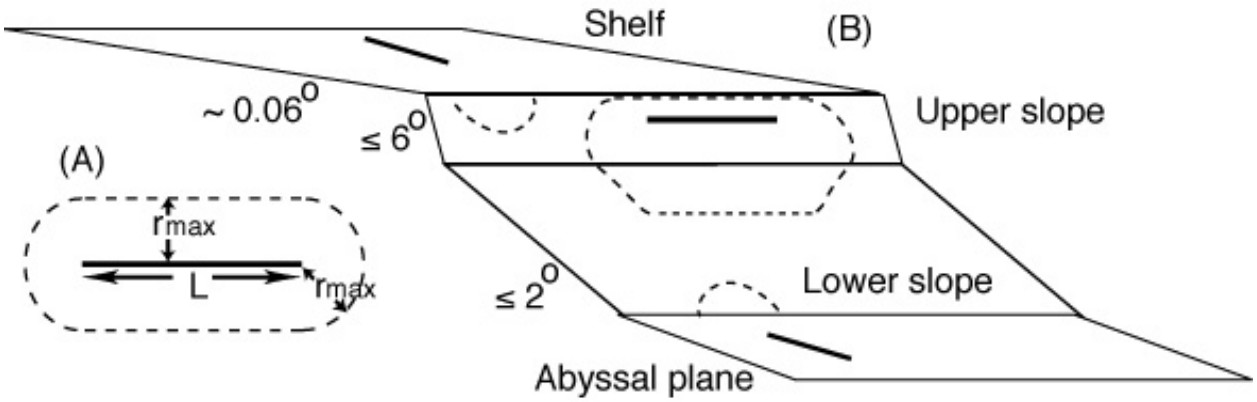

Figure 11-4: (a) Schematic diagram showing the geometry of a slope failure, including fault length *L*, maximum distance from fault to failure r_{max}, and maximum failure area (dashed line). (b) Schematic diagram of the continental margin. Heavy lines – different fault orientations with dashed lines enclosing their associated maximum failure areas.

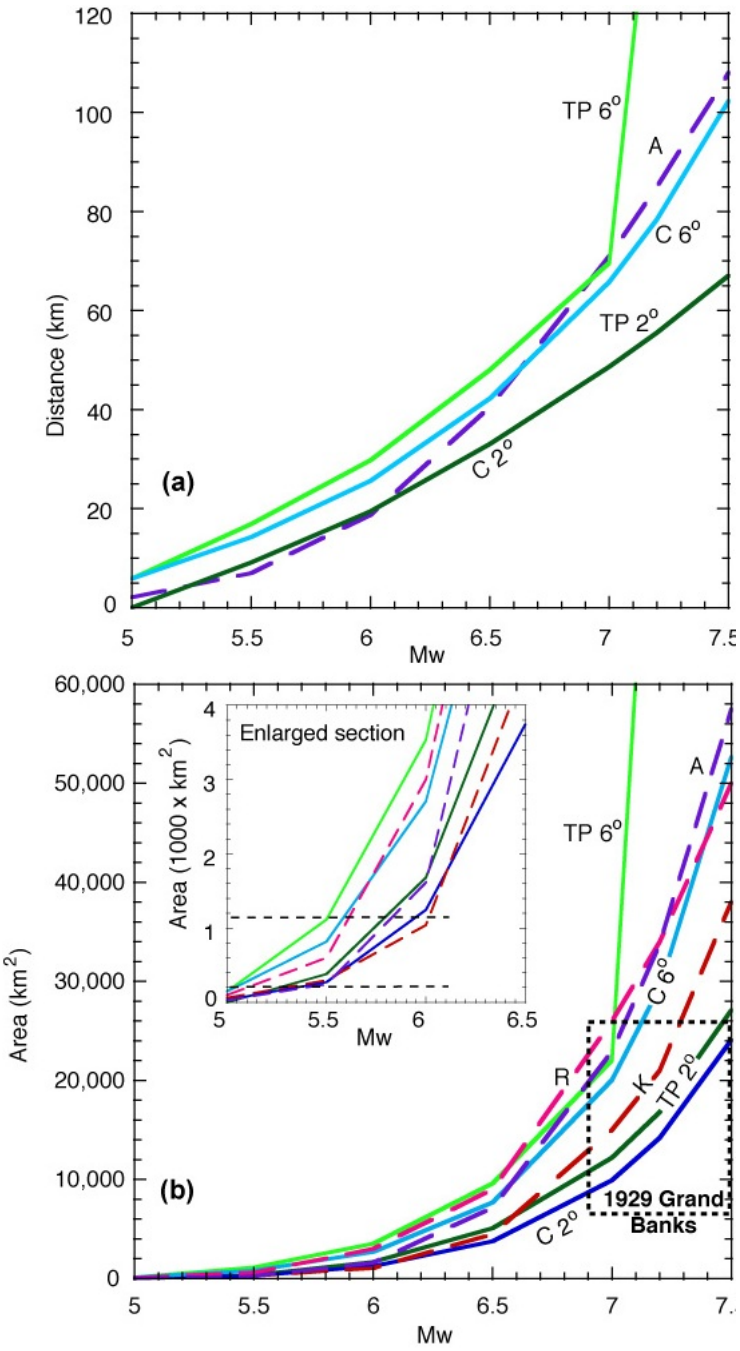

Figure 11-5: (a) Comparison between three methods to derive relationship between earthquakes and submarine landslides. Two parameters are compared as a function of earthquake magnitude: (a) maximum distance to slope failure from fault rupture, and (b) maximum area of slope failure. Methods to derive maximum area of slope failure are compared to the observed 1929 Grand Banks landslide, with the uncertainty in area and magnitude shown as a dashed rectangle. Solid curves were calculated by the slope stability analysis method for seabed slopes of 2° and 6° with the PSA relationships of *Campbell* (2003) (C2° and C6°) and Tavakoli and Pezeshk (2005) (TP2° and TP6°). Dashed curves are empirical relationships of maximum distance to liquefaction on land, A (Ambraseys, 1988), and observed maximum failure area on land, K (Keefer, 1984) and R (Rodriguez *et al.*, 1999). Also shown in (b) is a curve (marked A) of the expected maximum failure area using Ambraseys' (1988) empirical relationship for maximum distance to liquefaction. Inset shows enlargement of maximum failure area as a function of earthquake magnitude for low magnitudes. Horizontal dashed lines in inset mark the areas of two submarine slides within the Currituck slide complex, the larger area is expected to cause a destructive tsunami and the smaller one is not. See text for further explanations.

References

Abrahamson, N.A., Silva, W.J., 1997, Empirical response spectral attenuation relations for shallow crustal earthquakes: *Seismological Research Letters*, *v. 68*, p. 94-127.

Ambraseys, N.N., 1988, Engineering seismology: *Earthquake Engineering and Structural Dynamics*, *v. 17*, p. 1-105.

Bent, A.L., 1995, A complex double-couple source mechanism for the Ms 7.2 1929 Grand Banks earthquake, *Bulletin of the Seismological Society of America*, *v. 85*, p. 1003-1020.

Boore, D.M., Joyner, W.B., 1997, Site amplifications for generic rock sites. *Bulletin of the Seismological Society of America*, *v. 87*, p. 327-341.

Booth, J.S., O'Leary, D.W., Popenoe, P. and Danforth, W.W., 1993, U.S. Atlantic continental slope landslides; their distribution, general attributes, and implications, *in* Schwab, W.C., Lee, H.J., and Twichell D.C. (Editors), Submarine landslides, Selected studies in the U.S. Exclusive Economic Zone. USGS Bulletin, p. 14-22.

Campbell, K.W., 2003, Prediction of strong ground motion using the hybrid empirical method and its use in development of ground-motion (attenuation) relations in Eastern North America: *Bulletin of the Seismological Society of America*, *v. 93*, p. 1012-1033.

Cetin, K.O., *et al.*, 2004, Standard penetration test-based probabilistic and deterministic assessment of seismic soil liquefaction potential: *Journal of Geotechnical and Geoenvironmental Engineering*, *v. 130*, p. 1314-1340.

Chaytor, J.D., Twichell, D.C., ten Brink, U.S., Buczkowski, B.J. and Andrews, B.D., 2007, Revisiting submarine mass movements along the U.S. Atlantic continental margin, Implications for tsunami hazards, *in* V. Lykousis, D. Sakellariou and J. Locat (Editors), Submarine Mass Movements and Their Consequences: Springer, Dordrecht, p. 395-403.

Chaytor, J.D., ten Brink, U.S., Solow, A.R. and Andrews, B.D., this volume, Size distribution of submarine landslides along the U.S. Atlantic margin and its implication to tsunami hazards.

Dorby, R., Oweis, I. and Urzua, A., 1976, Simplified procedures for estimating the fundamental period of a soil profile: *Bulletin of the Seismological Society of America*, *v. 66*, p. 1293-1321.

Dugan, B. and Fleming, P.B., 2000, Overpressure and fluid flow in the New Jersey continental slope: Implications for slope failures and cold seeps: *Science*, *v. 289*, p. 288-291.

Elko, N.A., Sallenger, A.H., Jr., Guy, K., Morgan, K.L.M., 2002, Barrier island elevations relevant to potential storm impacts; 2, South Atlantic: USGS Open-File Report 02-0288.

Ewing, J.I., Carter, J.A., Sutton, G.H., Barstow, N., 1992, Shallow water sediment properties derived from high-frequency shear and interface waves*: Journal of Geophysical Research*, *v. 97*, p. 4739-4762.

Fine, I.V., Rabinovich, A.B., Bornhold, B.D., Thomson, R.E., Kulikov, E.A., 2005, The Grand Banks landslide-generated tsunami of November 18, 1929; preliminary analysis and numerical modeling: *Marine Geology*, *v. 215*,

p. 45-57.
Frankel, A.D., Mueller, C.S., Barnhard, T.P., Perkins, D.M., Leyendecker, E.V., Dickman, N., *et al.*, 1996, National seismic-hazard maps; documentation June 1996: USGS Open-File Report 96-532.
Geist, E.L., Parsons, T.A., this volume, Assessment of Source Probabilities for Potential Tsunamis Affecting the U.S. Atlantic Coast.
Hornbach, M.J., Lavier, L.L., Ruppel, C.D., 2007, Triggering mechanism and tsunamigenic potential of the Cape Fear slide complex: *Geochemistry, Geophysics, and Geosystems*, *v. 8*(12), Q12008, 10.1029/ 2007GC001722.
Hughes Clarke, J.E., Shor, A.N., Piper, D.J.W., Mayer, L.A., 1990, Large-scale current-induced erosion and deposition in the path of the 1929 Grand Banks turbidity current: *Sedimentology*, *v. 37*, p. 613-629.
Hynes-Griffin, M.E., Franklin, A.G., 1984, Rationalizing the seismic coefficient method: U.S. Army Engineer Waterways Experiment Station Misccelaneous Paper, GL-84-13, 21 pp.
Keefer, D.K., 1984, Landslides caused by earthquakes: *Geological Society of America Bulletin*, *v. 95*, p. 406-421.
Keefer, D.K., 2002, Investigating landslides caused by earthquakes; a historical review: *Surveys in Geophysics*, *v. 23*, p. 473-510.
Lee, H.J., this volume, Timing of occurrence of large submarine landslides on the Atlantic Ocean margin.
Lee, H.J., Locat, J., Dartnell, P., Minasian, D., Wong, F., 2000, A GIS-based regional analysis of the potential for shallow-seated submarine slope failure: Proceedings of the 8th International Symposium on Landslides, Cardiff, Wales, June 26-30, p. 917-922.
Locat, J., Desgagnes, P., Leroueil, S., Lee, H.J., 2003, Stability of the Hudson Apron slope off New Jersey, *in* Locat, J., and Meinert, J. (Editors), Submarine mass Movements and Their Consequences: Kluwer series on Natural and Technological Hazards, Kluwer, Dordrecht, p. 257-270.
Locat, J., Lee, H.J., ten Brink, U., Twichell, D., Geist, E., Sansoucy, M., this volume, Geomorphology, stability, and mobility of the Currituck slide.
Lopez, A.M., ten Brink, U.S., Geist, E.L., *in press*, Submarine landslide as the source for the 1918 Mona Passage tsunami: Observations and modeling: *Marine Geology*.
Makdisi, F.I., Seed, H.B., 1978, Simplified procedure for estimating dam and embankment earthquake-induced deformations: *Journal of the Geotechnical Engineering Division*, *v. 104* (GT7), p. 849-867.
Mazzotti, S., Adams, J., 2005, Rates and uncertainties on seismic moment and deformation in eastern Canada: *Journal of Geophysical Research*, *v. 110*, B09301, doi:10.1029/2004JB003510.
McCall, C., Morrison, M.L., Piper, D.J.W., 2005, Geological data from the St. Pierre Slope around the epicenter of the 1929 Grand Banks earthquake, Morgenstern, N.R., 1967: submarine slumping and the inititation of turbidity currents, *in* A.F. Richards (Editor), Marine Geotechnique, University of Illinois Press, Urbana, IL, p. 189-210
Mosher, D.C., Moran, K., Hiscott, R.N., 1994, Late Quaternary sediment, sediment mass flow processes and slope stability on the Scotian Slope, Canada: *Sedimentology*, *v. 41*, p. 1039-1061.

Mosher, D.C., Piper, D.J.W., 2007, Analysis of multibeam seafloor imagery of the Laurentide Fan and the 1929 Grand Banks landslide area, *in* V. Lykousis, D. Sakellariou, J. Locat (Editors), Submarine mass movements and their consequences. Springer, Dordrecht, p. 77-88.

Newmark, N.M., 1965, Effects of earthquakes on dams and embankments: *Geotechnique*, *v. 15*, p. 139-159.

Piper, D.J.W., Aksu, A.E., 1987, The source and origin of the 1929 Grand Banks turbidity current inferred from sediment budgets: *Geo-Marine Letters*, *v. 7*, p. 177-182.

Piper, D.J.W., Cochonat, P., Morrison, M.L., 1999, The sequence of events around the epicentre of the 1929 Grand Banks earthquake; initiation of debris flows and turbidity current inferred from sidescan sonar: *Sedimentology*, *v. 46*, p. 79-97.

Piper, D.J.W., Shor, A.N., Farre, J.A., O'Connell, S., Jacobi, R., 1985, Sediment slides and turbidity currents on the Laurentian Fan; sidescan sonar investigations near the epicenter of the 1929 Grand Banks earthquake: *Geology*, *v. 13*, p. 538-541.

Rodriguez, C.E., Bommer, J.J., Chandler, R.J., 1999, Earthquake-induced landslides: 1980-1997: *Soil Dynamics and Earthquake Engineering*, *v. 18*, p. 325-346.

Seed, H.B., Lee, K.L., 1966, Liquefaction of saturated sands during cyclic loading: *Journal of the Soil Mechanics and Foundations Division*, *ASCE*, *v. 92* (SM6).

Swafford, L., Stein, S., 2007, Limitations of the short earthquake record for seismicity and seismic hazard studies, *in* S. Stein, S. Mazzotti (Editors), Continental Intraplate Earthquakes: Geological Society of America Special Paper 425, Geological Society of America, Boulder, p. 49-58.

Tappin, D.R., Watts, P., McMurtry, G.M., Lafoy, Y., Matsumoto, T., 2001, The Sissano, Papua New Guinea tsunami of July 1998; offshore evidence on the source mechanism: *Marine Geology*, *v. 175*, p. 1-23.

Tavakoli, B., Pezeshk, S., 2005, Empirical-stochastic ground-motion prediction for eastern North America: *Bulletin of the Seismological Society of America*, *v. 95*, p. 2283-2296.

Twichell, D.C., Chaytor, J.D., ten Brink, U.S., Buczkowski, B., this volume, Geologic controls on the distribution of submarine landslides along the U.S. Atlantic continental margin.

Travasarou, T., Bray, J.D., Abrahamson, N.A., 2003, Empricial attenuation relationship for Arias intensity: *Earthquake Engineering and Structural Dynamics*, *v. 32*, p. 1133-1155.

Weber, K.M., List, J.H., Morgan, K.L.M., 2005, An operational mean high water datum for determination of shoreline position from topographic lidar data: USGS Open-File Report 2005-1027.

Wells, D.L., Coppersmith, K.J., 1994, New empirical relationships among magnitude, rupture length, rupture width, rupture area, and surface displacement: *Bulletin of the Seismological Society of America*, *v. 84*, p. 974-1002.

Chapter 12: Size Distribution of Submarine Landslides along the U.S. Atlantic Margin

Introduction

Recent evidence has shown landslide-generated destructive to be of increasing importance in evaluating the hazard posed to coastal areas (*e.g.*, Fine *et al.*, 2005; Greene *et al.*, 2006; López *et al.*, 2008; Maramai, *et al.*, 2005; Synolakis *et al.*, 2002). By understanding the amount of material released in individual landslides, the distribution of landslides within a given geographic region, the recurrence time of landslides of particular sizes, and the mechanisms responsible for the generation of the landslides, we may be better able to determine that potential hazard of these events. Additonally, the derivation of size-distribution relationships for submarine landslides in many different geological environments provides valuable insight into the fundamental processes of landslide dynamics and margin evolution. Ultimately, the continued development of distribution relationships in areas of dense data coverage may aid in the estimation of the expected number of landslides of a particular size in a region from low data quality or incomplete observations.

Over the past several years, it has been suggested that the cumulative number-area and cumulative number-volume relationships of subaerial landslides can be described by inverse power-law distributions based on the dimensions of the failure scarp, slide deposits, or headwall length (*e.g.*, Dai and Lee, 2001; Dussauge *et al.*, 2003; Guthrie and Evans, 2004; Malamud *et al.*, 2004; Sugai *et al.*, 1994). In the marine environment, the limited application of these statistical techniques for landslide analysis has resulted in only a few examples of such distribution relationships being observed (*e.g.*, Issler *et al.*, 2005; Micallef *et al.*, 2008; ten Brink *et al.*, 2006). Although power-law scaling is widely invoked to describe the distribution of subaerial and submarine landslide inventories, in the majority of these cases however, an inverse power-law distribution only applies to a truncated portion of mapped inventories. Undersampling of a particular range of magnitudes of landslide size is commonly suggested to account for the portion of the data that is not described by the inverse-power law function (see Guthrie *et al.*, 2008 for a detailed discussion of this topic). Several methods have been employed to extend the fit of a power-law distribution to entire landslide datasets including the use of modified-pareto (*e.g.*, Stark and Hovis, 2001) and gamma (*e.g.*, Guzzetti *et al.*, 2005) distributions and the application of different

statistical techniques such as noncumulative analysis and data binning (*e.g.*, Burroughs and Tebbens, 2001; Guzzetti *et al.*, 2002; Malamud and Turcotte, 2006). To date only a few examples of non power-law distributions have been reported for landslides (*e.g.*, logarithmic, Issler *et al.*, 2005; log-normal, Dunning *et al.*, 2007).

In this chapter we investigate the cumulative size distribution of submarine landslide source zone (landslide failure scarps) volumes identified along the different geologic provinces of the U.S. Atlantic continental margin (Figure 12-1). Because this distribution differs from the classic inverse power-law usually determined for both subaerial and submarine landslides, we investigate potential causes of the departure, including variation of geologic conditions along the margin and observational bias. To obtain a more direct measure of the amount of material initially mobilized at the time of single failure we calculate volume and area of the failure scarp, rather than the entire landslide (source and deposition regions) or the failure deposit only, as done in other similar studies (*e.g.*, Issler *et al.*, 2005). We have chosen this approach because many of the mapped landslide deposits are composite features resulting from multiple failures (Twichell *et al.*, this volume). The generic term "landslide" throughout this paper encompasses all forms of submarine mass movement as described by Locat and Lee (2002) (i.e., slides, topples, spreads, falls, and flows).

Regional setting

The U.S. Atlantic margin (shelf, slope and rise) is covered by large volumes of Quaternary sediments eroded from the North American continent by glacial and fluvial processes. These sediments were deposited on a mix of Middle Jurassic carbonate, Eocene chalk, and other Mesozoic to Cenozoic siliclastic sedimentary formations that lie on the remnants of Triassic-Jurassic age rift basement (see Twichell *et al.*, this volume for a more detailed overview of the margin's geology). Glacially-derived sediments deposited by large river systems are found along the Georges Bank shelf edge (Schlee and Fritsch, 1983) and along the shelf and slope/rise south of southern New England. South of the extent of glaciers, the large river systems that underlie the present Hudson, Delaware, and Chesapeake estuaries extended across the shelf with shelf-edge deltas built off the Virginia and Delaware coasts, while the Hudson Canyon system transferred sediment to a deep-sea fan (Poag and Sevon, 1989).

For the purpose of this study, we have separated the margin into five sub regions (Figure 12-1), to explore the possibility of geologic control on the cumulative size distribution. Two of these regions are characterized by surficial glacial deposits on the shelf/slope (Georges Bank and Southern New England), one a mix of Quaternary fluvial deposits and exposed Eocene rock (Northern Baltimore Canyon Trough-NBCT), and the remaining two are characterized by surficial sediments of fluvial origin (Southern Baltimore Canyon Trough-SBCT) and from sediments carried by bottom currents that are deposited out of suspension (Carolina Trough).

Data and Methods

We used a bathymetric Digital Elevation Model (DEM) with a grid-cell resolution of 100 m, derived from the compilation of multibeam swath bathymetry data from different sources and hydrographic soundings surveys (see Twichell *et al.*, this issue for a full description of the bathymetry data) as the primary geographic dataset to identify the landslide source zones. The near-complete coverage of the U.S. Atlantic continental slope and rise by multibeam bathymetry provides a more uniform and detailed view of the geomorphology of submarine landslides than has been previously available. Although coverage is excellent, several significant gaps within the dataset totaling an area of approximately 26,000 km^2 (~ 8% of the total area) are present along the continental slope. Several major data gaps or areas of reduced resolution are present along the shelf edge and upper slope in the Georges Bank, Southern New England, and NBCT regions preventing the detailed or complete mapping of landslides that are only partially observed in these areas. In most cases, the identified failure scarps appear to have been created by single evacuation events, but several of the scarps, especially in the NBCT slope area, may have been created as either a single event or part of a larger retrogressive slide. In these cases, during the analysis, these slides were examined both as individual slides and as combined, larger single slides.

Landslide failure scarps are identified through examining multiple perspective views of the bathymetry DEM using different illuminations, and the evaluation of seafloor slope maps derived from the DEM. The area of the failure scarp is calculated as the planar area within a manually digitized bounding polygon that encompasses the region of negative elevation within the landslide's headwall and sidewalls. The downslope end of the failure scarp is digitized as a straight line connecting the bounding sidewalls on either flank of the landslide, done in this way because the toe is usually obscured by slide deposits or cannot otherwise be identified on the bathymetry. Failure volumes were calculated using a method similar to ten Brink *et al.* (2006), in which a smooth upper surface is interpolated from the polygon that defines the boundary of each failure scarp and is then subtracted from the extracted bathymetric data (lower surface) within a GIS (Figure 12-2). The grid cell sizes of the upper and lower surfaces are each 100 m.

Landslide Failure Scarps

A total of 141 landslide failure scarps were identified within the ~ 347,000 km^2 investigated area of the U.S. Atlantic margin. Of these, 106 had sufficient data coverage and quality to assign high confidence values to their boundaries and as such they were used in the analysis (Figures 12-3 and 12-4). The remaining failure scarps that were not included in this analysis have only partial or lower-resolution coverage, with the area and volume values less reliable, but on average appear to be within the same size range as those used in the analysis. Measured areas for the scarps range in size from 0.89

km^2 to a maximum of ~ 2410 km^2; with a total area for all scarps of 15,275 km^2. Volumes range from as low as 0.002 km^3 up to ~ 179 km^3, with a margin-wide total removed volume of 862 km^3. It is currently not possible to determine if adjacent failure scarps failed independently, together, or in a retrogressive manner. Booth *et al.* (1993) recognize that along the margin, landslides fall into two categories: 1) those with source areas on the continental slope and rise ("open-slope"); and 2) those that are sourced in submarine canyon and channel systems. In general, the largest values are from sources that displaced material on the open-slope rather than from the headwall and sidewalls of canyon and channel systems. While canyon/channel sources account for a significant portion of the total number of excavations that were identified and mapped (~ 30%) they constitute only ~6.5% and 7.1% of the total margin-wide mapped source zone area and volume, respectively.

Although the range of source zone area values is distributed across the margin, some local geographic clustering of values is noted (Figure 12-5a), which may be a reflection of differing geological or geotechnical conditions along the margin, or a result of different regional triggering mechanism. The largest scarp areas (> 500 km^2) are found in three of the five geologic provinces, Georges Bank, SBCT, and the Carolina Trough regions (Figures 12-3a and 12-3b). All of these large scars are slope rather than canyon sources, although limited data availability in the Southern New England region prevents a full evaluation of that area. In the southernmost part of the SBCT and Carolina Trough regions (Figure 12-3b), area values greater than 1000 km^2 are found, with few, if any, small-area sources. In contrast, failure scarps with small areas (~ < 100 km^2) dominate the continental slope offshore of New York and New Jersey south of Hudson Canyon. Area values in the southern New England region are distributed well below 500 km^2, but the region may actually contain a greater number of landslide scarps than currently observed, some with area values greater than 1000 km^2, especially along the sections of the slope where multibeam bathymetry data are missing or of limited resolution.

The full range of source zone volumes are also distributed across the margin (Figures 12-4 and 12-5b), but with less obvious clustering than with the area values. Except for the two very large scarps off Georges Bank, source volumes are characteristically in the 0.1 to 10 km^3 size range in the Georges Bank, southern New England, and NBCT regions,. The dominant range of source volumes in the southern NBCT, SBCT, and Carolina Trough regions covers the 0.1-100 km^3 range. As with the area values, the largest source volumes, those greater than 100 km^3, are found in the Georges Bank, SBCT, and Carolina Trough regions, but there is not a 1:1 relationship between regions with the largest areas and those with the largest volumes.

The area/volume relationship for Atlantic margin landslide source zones (Figure 12-6; $V_L=0.0163A_L^{1.099}$, $R^2=0.711$) is similar to that calculated for the submarine Storegga Slide [$V_L=0.0267A_L^{1.032}$, calculated by ten Brink *et al.* (2006) from data in Haflidason *et al.* (2005)], which, like the Atlantic margin landslides, primarily involved the failure of a thin (10's of meters thickness) layer unconsolidated clay-rich material. This differs from area/volume

relationships previously calculated for both subarial landslides (*e.g.*, $V_L=0.0240A_L^{1.368}$, Simonett, 1967; $V_L=0.1549A_L^{1.0905}$, Guthrie and Evans, 2004) and submarine slope failures of carbonate rock around Puerto Rico (*e.g.*, $V_L=0.0263A_L^{1.292}$, ten Brink *et al.*, 2006). The different exponent values can be explained by differences in the failed material and landslide processes or by the presence of saturated or overpressured sediments in the submarine environment. For small exponent values, such as that calculated for the Atlantic margin sources, volumes increase almost linearly with area, possibly resulting from a thin and relatively constant evacuation depth for each landslide, with the majority of landslides only mobilizing material within the unconsolidated Quaternary sedimentary section. This is in contrast to areas characterized by larger exponents, such as landslides on the margin of the Puerto Rico Trench area and numerous subaerial slides, where thick sections of unconsolidated and consolidated material are evacuated during each event, resulting in the formation of rotational landslides, rock slides and falls, and debris avalanches. Such a marked difference in excavation depth in the source zone has important implications for scarp preservation and is discussed in the following section.

Size Distribution of Submarine Landslides

Log-normal distribution

Because the volume of material that is released during a submarine landslide is one of the critical parameters controlling the amplitude of a landslide-generated tsunami (Geist *et al.*, this volume; Murty, 2003; Pelinovsky and Poplavsky, 1997; Watts and Grilli, 2003), the following analysis is focused predominantly on the volumes of the failure scarps. The observed volumes of the identified failure scarps on the U.S. Atlantic margin plotted as a cumulative number on a log scale (Figure 12-7) show a very good fit ($R^2=0.985$) of a log-normal distribution across the entire dataset with a standard deviation (σ) and sample mean (μ) of log volume of 2.27 and 6.60, respectively. For the entire dataset, an inverse power-law provides a poor fit ($R^2=0.611$). That said, in some cases it has been possible to differentiate the mechanisms by which landslides are initiated and to describe complete landslide inventories by several power-law distributions (Van Den Eeckhaut *et al.*, 2007). Attempts to describe the Atlantic margin landslide data in this way (Figure 12-8) using arbitrary break-points loosely based on changes in the shape of cumulative data curve, show that a robust inverse power-law distribution ($R2 \geq 0.9$), can at best, only be applied over two orders of magnitude, providing a weak description of the entire inventory.

The differences in distributions of landslides along the U.S. Atlantic margin when compared to other regions mentioned above (i.e., log-normal vs. inverse power law) may reflect observational limitations or error, or it may be due to a more fundamental characteristic of the study area, such as geologic control on the landslides or it may be related to a dynamic feature of the landslide processes that controls their size. For example, in many

regions, the variation of geomorphic, lithologic, or structural characteristics can be a critical factor in controlling the differences in the rate and magnitude of landscape modification by slope failure (Burbank and Anderson, 2001). The region under study here encompasses a very large geographic area, with variations in geology (*e.g.*, Quaternary glacial and non-glacial fluvial deposits), seafloor slope, and potential local triggering mechanisms such as: 1) salt diapirism south of Cape Hatteras (Dillon *et al.*, 1982); 2) water discharge movement along the slope off New Jersey (Robb, 1984); 3) sediment thickness and composition changes (*e.g.*, Pratson and Laine, 1989); and 4) hydrate destabilization (Carpenter, 1981) which may provide some control on the size of landslides and hence their distribution.

Analysis of the individual geologic and geographic regions shown in Figure 12-1 for power-law behavior shows that over limited orders of magnitude or for truncated portions of data from these regions, inverse power-laws can be fit (Figure 12-9). However, the power-law exponents do not vary with geology in any discernable pattern. For example, the inverse power-law exponents for the Georges Bank and southern New England regions, both characterized by surficial glacial deposits, differ significantly (Figure 12-9a, b) even though they are geologically similar regions. On the other hand, the exponents for the southern New England and NBCT regions are similar (Figure 12-9b, c), yet they are characterized by surficial glacial deposits and a mix of fluvial deposits and exposed Eocene chalk, respectively. Note also the small number of samples in a number of the regions, which makes the fit statistically less robust.

While the dynamic processes involved in the initiation and evolution of each landslide likely play a role in determining the size of a landslide, similar processes are likely to be operating in areas of common geology and physical setting (*e.g.*, surface slope, geomorphic setting). That said, although there are marked differences in the landslide process between canyon- and open slope-sourced slides that may influence the distribution of the combined dataset as a result of differences in sediment availability, seafloor slope, and triggering mechanism, no strong power-law relationship was obtained when canyon or slope landslides were analyzed separately (Figure 12-10a). Similarly, the cumulative volume distribution of landslides originating in both glacially and non-glacially derived Quaternary sediments follow a similar distribution to that of the complete inventory (Figure 12-10b)

Test for a power law distribution

Another explanation for the observed log-normal distribution is that it has been modified by a conditional probability to observe only certain-sized excavations. The ability to observe a landslide depends on several factors such as the quality and resolution of data used to observe it and the level of preservation (*e.g.*, morphology, age, type of material which evacuated) of the individual landslides. The horizontal resolution depends on grid size, which in this analysis is 100 m by 100 m. Therefore, the minimum size of failure scarp that can be identified from these data, given that it must be visible in three or more cells, is 0.09 km^2. Vertical resolutions of modern deep water

multibeam systems are commonly on the order of 1-2% of water depth, which therefore affects both the ability to identify the failure scarp and the calculation of volumes.

Equally important in determining the observational potential is the temporal distribution of the landslides and the level of preservation of the features within the failure scarp zone (Malamud *et al.*, 2004). Given sufficient time, the morphology of the failure scarps and the entire landslide as a whole will change shape or degrade to a level where they will become unrecognizable as the remnant of a landslide, introducing a size bias into the observed landslide dataset. Several processes acting individually or together are responsible for this size bias including pelagic/hemipelagic sedimentation, turbidite sedimentation and erosion, and the masking of older, smaller landslide features by newer, larger landslides (but not vice-versa). Although smaller landslides are most likely to be affected or even completely removed by these mechanisms, the morphology of large landslides may be altered enough with time to change their dimensions and prevent close estimation of their original area and volume. On the U.S. Atlantic margin, all but one of the landslides that have reliable age information is pre-Holocene (Lee, this volume) so enough time may have passed for significant alteration of many of the failure scarps. Additionally, the failure scarp areas of the majority of the slides are wholly within the unconsolidated Quaternary sediment deposits on the continental slope, or within previously failed material on the outer rise, material that is more unstable and likely to degrade at a faster rate than slides sourced in a more coherent material such as a granite (Dussauge *et al.*, 2003) or carbonate rock (ten Brink *et al.*, 2006).

Let us assume that the cumulative-volume data should conform to a Pareto distribution for X, the volume of a landslide scarp, with an inverse power-law exponent, θ:

$$F(x) = prob(X \le x) = 1 - \left(\frac{x}{x_o}\right)^{-\theta} \qquad (1)$$

where x_o is half of the minimum observed volume (x_o = 0.001 km^3 for U.S. Atlantic margin submarine landslides). Under this model:

$$\log prob(X \le x) = \log(1 - F(x)) = \psi - \theta \log x \qquad (2)$$

where $\psi = \theta \log x_o$.

To quantitatively investigate the possibility that those data presented here are size or observationally biased a conditional probability function is introduced. Observational bias means that the ability to identify landslide failure scarps depends on the size of the scarp. Using Y= log x, the conditional probability density function of y, or the probability of identifying the failure scarp, is:

$$g(y|obs) \propto p(obs|y)g(y) \quad (3)$$

where p(obs|y) is the probability that a landslide scarp of log volume y will be observed and g(y) is the unconditional probability density of y, or the true size distribution of the landslide scarps. If X has a Pareto distribution, then y has a truncated exponential distribution with a density function of:

$$g(y) = \theta e^{(-\theta(y-\ln x_o))} \qquad y \geq \ln x_o \quad (4)$$

The shape of the conditional probability function p(obs|y) for alternate values of the inverse power-law exponent θ, is derived from (3):

$$p(obs \mid y) \propto \frac{g(y \mid obs)}{g(y)} \quad (5)$$

For a fixed value of x_o and θ, p(obs|y) can be determined up to a scale constant by the ratio of an estimate of g(obs|y) and g(y). As previously mentioned, Figure 12-7a shows the probability distribution of the observed log volume to be normal. Therefore under the normal approximation:

$$p(obs \mid y) \propto e^{(\theta y - \frac{1}{2}(\frac{y-\mu}{\sigma})^2)} \quad (6)$$

In other words, the observational probability will increase with increasing log landslide scarp size y up to the point where $y = \mu+\sigma^2\theta$, then decline with increasing values of y (Figure 12-11a). The standard deviation (σ) and sample mean (μ) of the log volume are 2.27 and 6.60, respectively.

Using Figure 12-11a, some assumptions can be made to help determine a power-law exponent (θ) for the distribution the submarine slides. Given that the median values of the landslide failure scarp volume is 0.86 km^3, it is highly likely that a landslide failure scarp volume of 1 km^3 or greater should be observed (i.e., a probability of observation > 0). Any exponent (θ) with a probability of observation of ~ 0 for failure scarp volumes of 1 km^3 can therefore be rejected, which in this case occurs for $\theta \geq 1.6$ (Figure 12-11a). Because the maximum possible size of landslides failure scarps along the U.S. Atlantic margin is unknown, the maximum observed volume is used to define the minimum θ. If it is assumed that the maximum failure scarp should always be observed (probability of observation ~ 1), then only two values of θ have probabilities of observation high enough (> 0.9) at this volume to satisfy the requirement, 1 and 1.2. Taking 1 as the minimum and 1.6 as the maximum, the estimated value of θ for landslide failure scarps on the U.S. Atlantic margin is 1.3±0.3. A similar plot analysis of observation probability for the Puerto Rico data (Figure 12-11b) yields a value of θ of ~ 0.6, as is indicated by the near flattening of that curve at 1, very close to the 0.64 value calculated by ten Brink *et al.* (2006).

This range of exponent values is similar to the range of average cumulative distribution exponent values for the volumes of mixed-type subaerial landslides ($\theta = 1.2 \pm 0.3$) predicted by Dussauge *et al.* (2003). Furthermore, the calculated U.S. Atlantic margin distribution exponent is noticeably larger than that determined for submarine landslide sources in the carbonate platform surrounding Puerto Rico ($\theta = 0.64$; ten Brink *et al.*, 2006), and for subaerial rockfall volumes ($\theta = 0.5 \pm 0.2$; Dussauge *et al.*, 2003). The differences between the exponent values points toward the differences in cohesion and internal friction within the failed materials (Densmore *et al.*, 1998; ten Brink *et al.*, 2006). This may imply differences in inherent strength between consolidated rock versus unconsolidated sediment, and in the dynamics of failure within each of these materials. Provided that the distribution of landslides along the U.S. Atlantic margin can be described by a conditional probability of landslide observation, the inference of a large exponent value ($\theta > 1$) strengthens the interpretation that only the unconsolidated, mostly Quaternary, sediments and reworked landslide material (Twichell *et al.*, this volume) are failing along the U.S. Atlantic Margin.

Possible Causes for Log-Normal Behavior

Figure 12-7a shows that a log-normal distribution fits very well the cumulative volume distribution of submarine landslides along the U.S. Atlantic margin. Log-normal behavior has been observed in the frequency of natural events such erosion and depositional processes responsible for the creation of geomorphic features (Wolman and Miller, 1960), turbidite deposit bed volumes (Talling *et al.*, 2007), in numerous biological mechanisms (Limpert *et al.*, 2001), and earthquake recurrence (Nishenko and Buland, 1987). Except for a few cases (*e.g.*, Dunning *et al.*, 2007; Guthrie and Evans, 2007) log-normal behavior has not been invoked to describe landslide distributions even though both the landslides north of Puerto Rico (Figure 12-7b) and especially those within the Storegga Slide complex (Figure 12-7c) could be fit with log-normal distributions. Ultimately, one of the main reasons for examining the distribution of submarine landslides is to unravel the physical processes responsible for the distribution.

The nature of these controlling physical processes, both for subaerial and submarine landslides, are still under debate. For landslide distributions displaying power-law scaling, the concepts of self-organized criticality (SOC; Bak *et al.*, 1988) or self-similarity have become popular (e.g, Guzzetti *et al.*, 2002; Micallef *et al.*, 2008; Noever, 1993; Van Den Eeckhaut *et al.*, 2007). In this framework, landslides size distributions within the same system are thought to be scale invariant; essentially each landslide is a scaled copy of other landslides within a system that is in a critical state. But Gisiger (2001) and Solow (2005) show that power scaling cannot simply be taken as evidence for SOC, but rather criticality must be determined on a region-by-region basis. The fact that without modification, the entire identified landslide inventory along the U.S. Atlantic margin is not fit by an inverse

power-law distribution may imply that the failure process in the area does not obey SOC, but is indicative of a different processes. What these processes are remains to be determined, the answer may is likely to be the result of the interplay of a number variables, including the geology and geotechnical characteristics of a region, the nature of the triggering mechanism, and the dynamic behavior of the landslide once it has been initiated.

Conclusions

We showed that landslide source zone volumes along the U.S. Atlantic margin have a log-normal size distribution. This result, which is fit across the entire data set, is in contrast to most analyses of landslide size distributions, which interpret an inverse power-law distribution over a truncated portion of the data. Reanalysis of landslide debris-lobe volumes from the Storegga Slide were also to found to show log-normal behavior across the entire inventory. A log-normal distribution suggests that landslides along the U.S. Atlantic margin have a characteristic volume of approximately 1 km^3. Both large landslides and small landslides of less that 1 km^3 are less common along the margin, which may be a reflection of changes in geologic and geotechnical conditions along the margin or the type and magnitude of triggering mechanisms. To explore the possibility of size-dependant observational bias in identifying landslide failure scarps in the bathymetry data, a conditional probability function is used together with an inverse power-law distribution to fit these data. The inverse power-law has an exponent value of 1.3 ± 0.3, which is close to that established for subaerial and submarine landslides in low cohesive, poorly consolidated material suggesting a similarity in excavation processes. In terms of the hazard posed by submarine landslides along the U.S. Atlantic margin, both the log-normal distribution of the observed source zone volumes suggest that large landslides, and the tsunamis that they can generate (*e.g.*, 1929 Grand Banks landslide and tsunami; Piper *et al.*, 1988), occur infrequently. Evaluation of this hypothesis awaits the collection of additional age data.

Figures

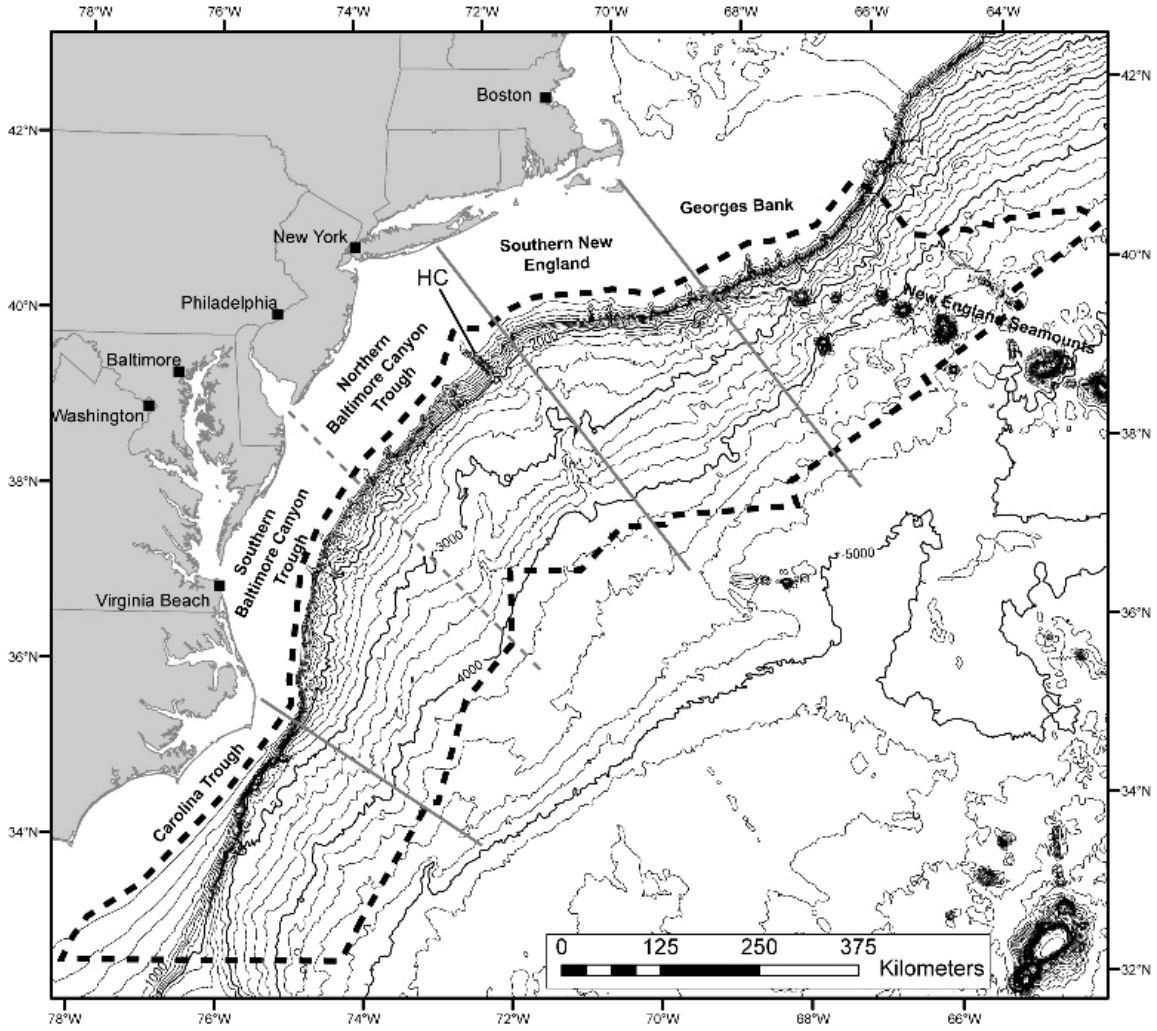

Figure 12-1: Map of the U.S. Atlantic margin. The thick dashed line encloses the region in which source volume excavations were identified. The 5 geographic/geologic provinces as discussed in the text are also highlighted. HC – Hudson Canyon. Contour interval is 200 m.

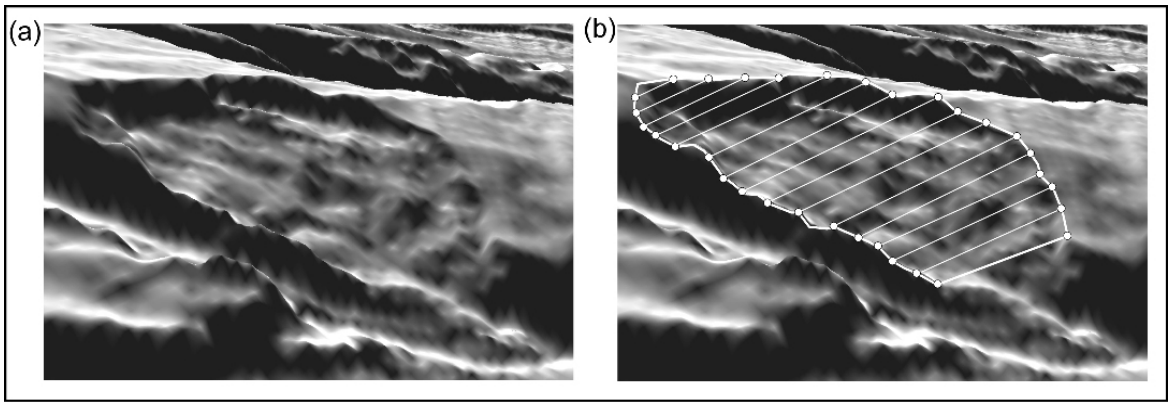

Figure 12-2: Perspective view of a failure scar area (grey shaded bathymetry; ~ 10x vertical exaggeration) on the left, with a schematic example of the smooth-surface that was fit within the perimeter and used as the upper surface to estimate the excavated volume on the right.

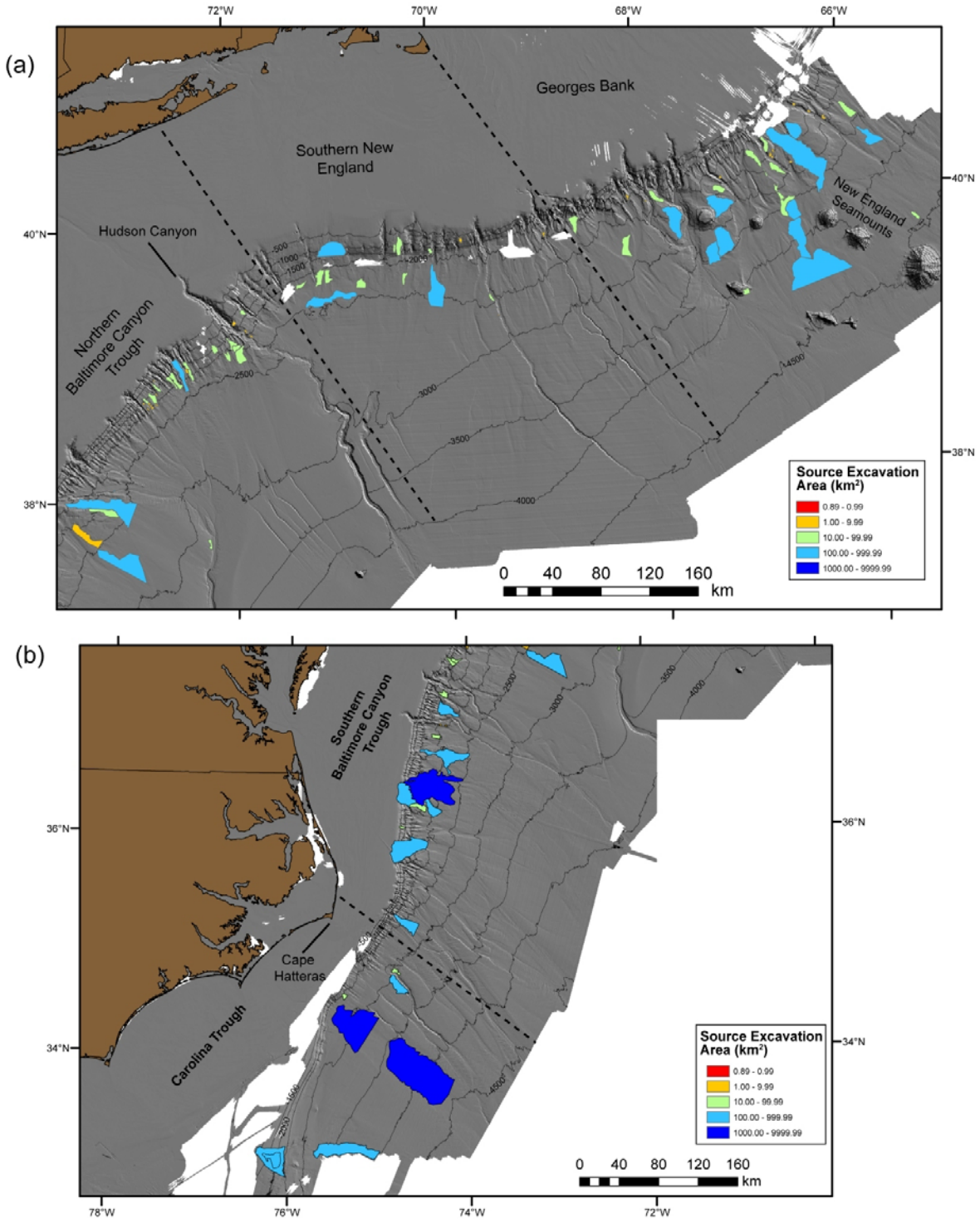

Figure 12-3: Map showing the distribution of landslide failure scar area values across the (a) northern U.S. Atlantic margin and (b) southern U.S. Atlantic margin. Dashed black lines mark the boundaries of the geographic areas from Figure 12-1. Contour interval is 500 m. DEM illumination is from the NE, with 2x vertical exaggeration.

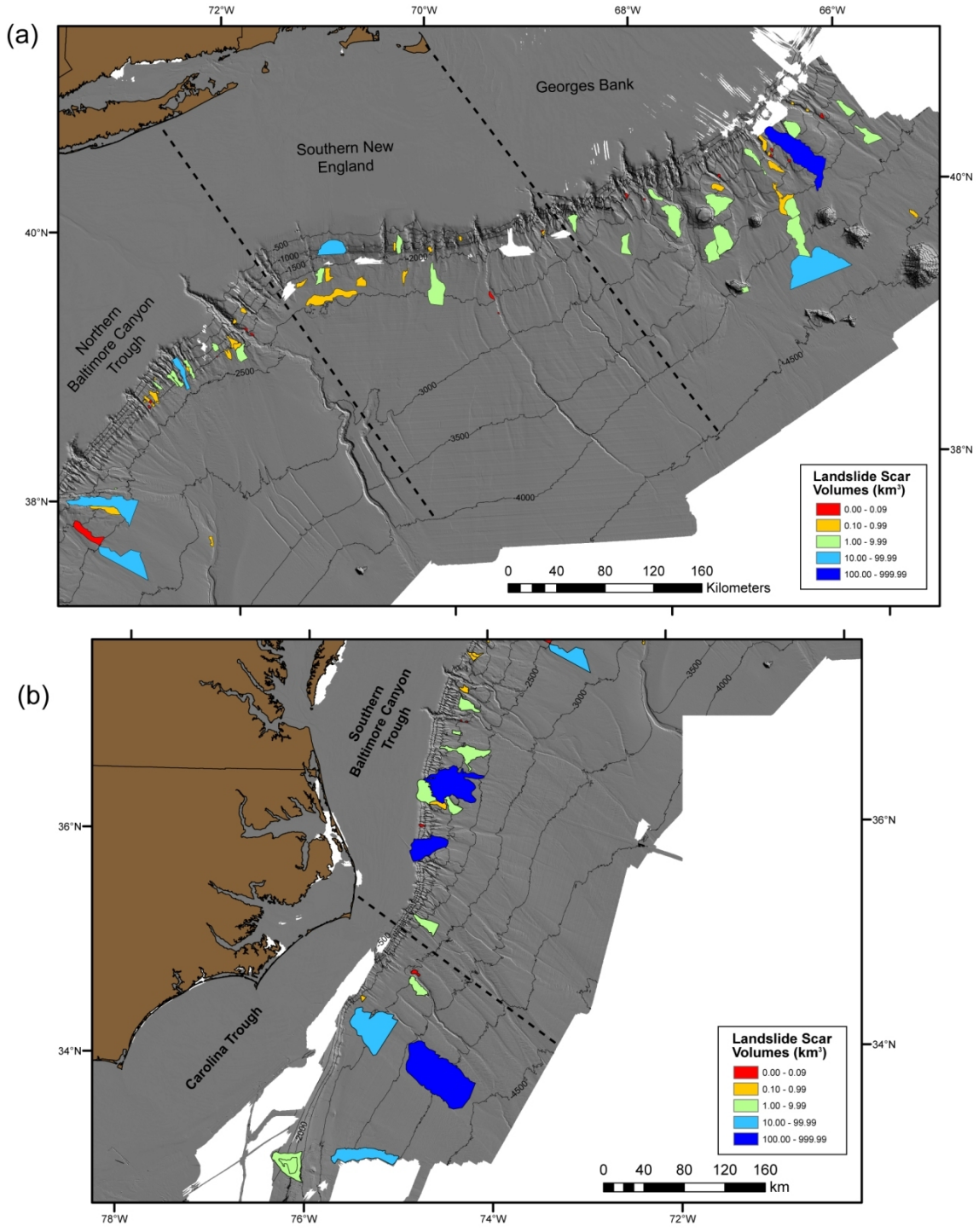

Figure 12-4: Map showing the distribution of landslide failure scar volume values across the (a) northern U.S. Atlantic margin and (b) southern U.S. Atlantic margin. Dashed black lines mark the boundaries of the geographic areas from Figure 12-1. Contour interval is 500 m. DEM illumination is from the NE, with 2x vertical exaggeration.

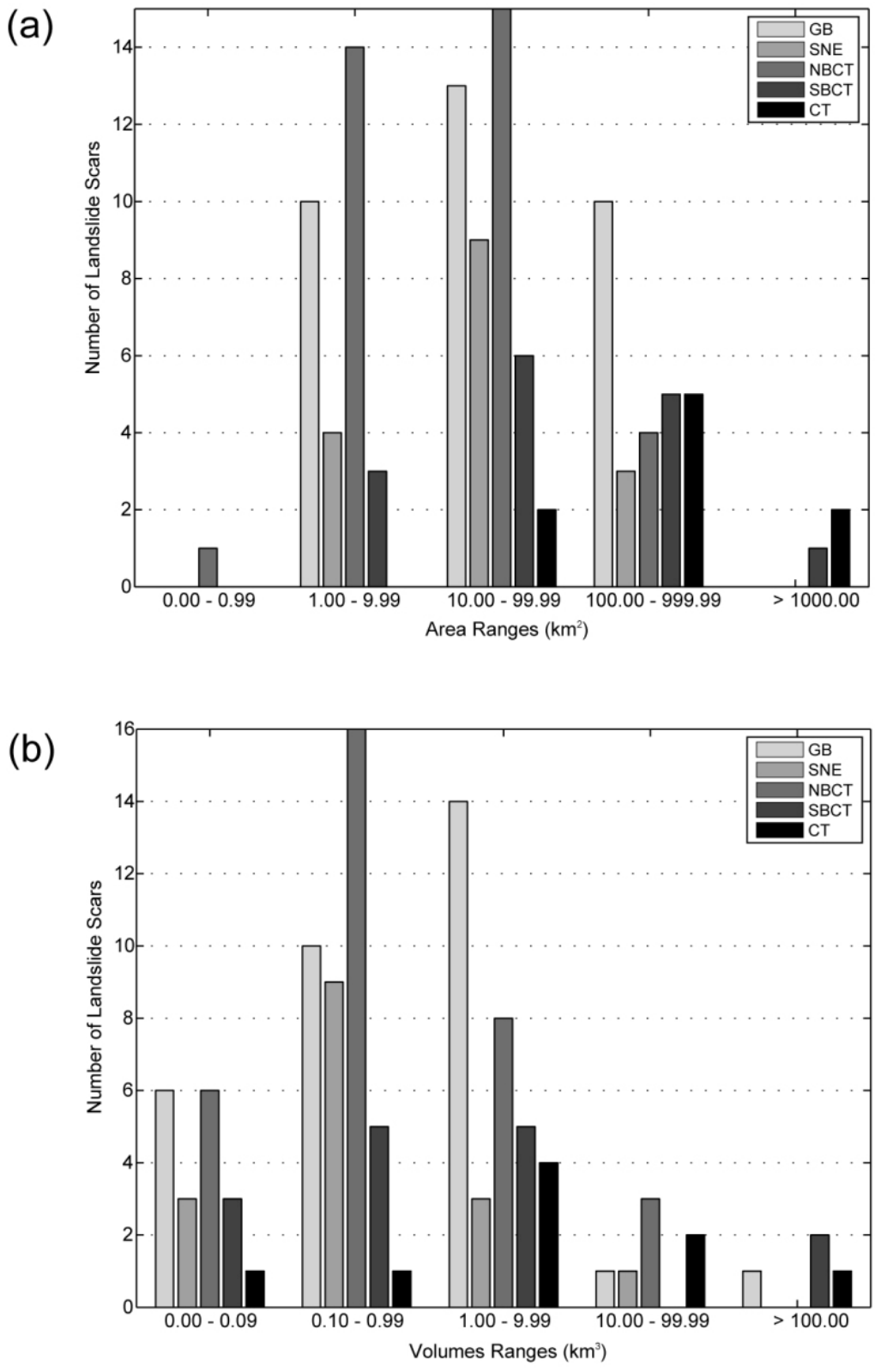

Figure 12-5: Histograms of landslide source zone areas (a) and source zone volume (b) separated based on the five geographic regions shown in Figure 12-1.

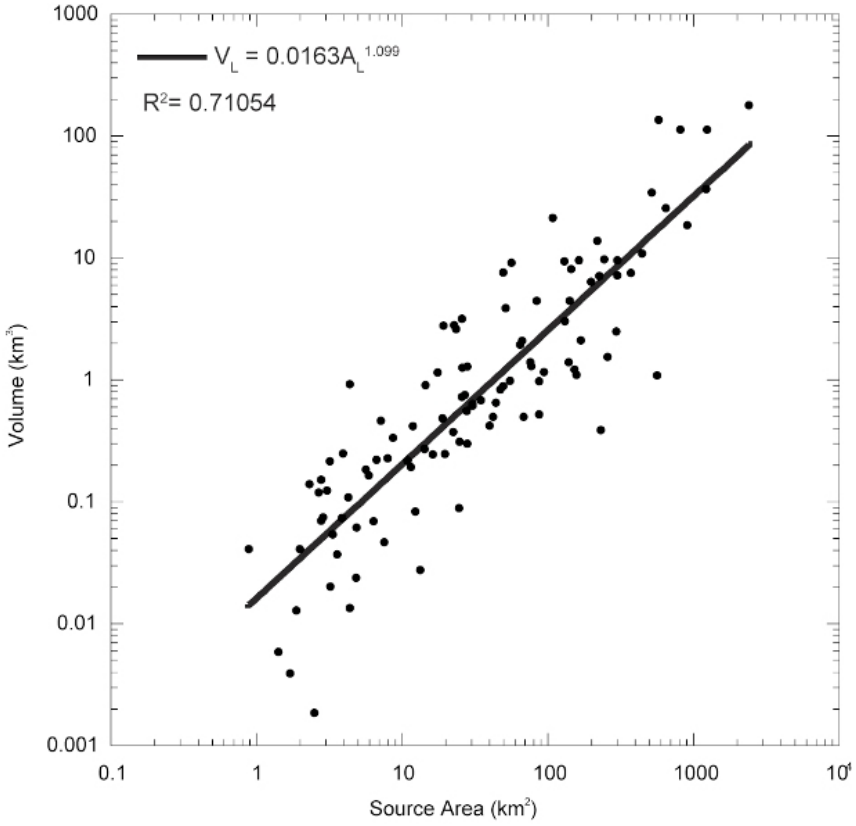

Figure 12-6: Relationship between area and volume of the 106 failure scars along the U.S. Atlantic margin.

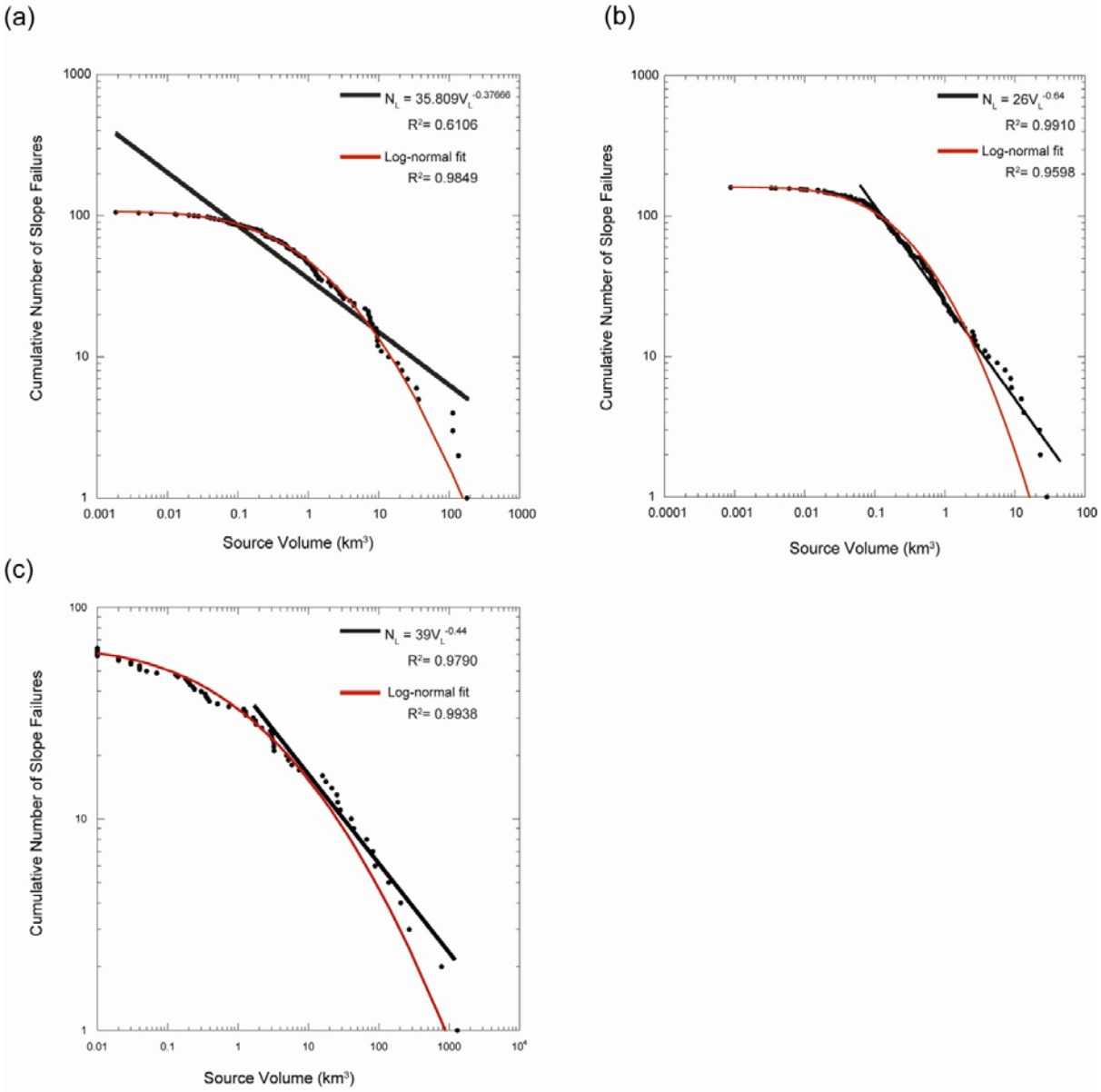

Figure 12-7: (a) Log-log plot showing the cumulative volume distribution of 106 observed failure scars overlain by the poorly fitting calculated inverse power-law distribution (black line) and well-fit log-normal distribution (red line). (b) Log-log plot showing the cumulative volume distribution of landslide sources from Puerto Rico (data from ten Brink *et al.*, 2006), showing the good fit of an inverse power-law distribution for volumes greater than ~0.1 km^3 (black lines) and the modeled log-normal distribution (red line). (c) Log-log plot showing the cumulative volume distribution of landslide sources from the Storegga Slide (data from Haflidason *et al.*, 200), showing the good fit of an inverse power-law distribution for volumes greater than ~ 2 km^3 (black lines) and the good fit of those data to a log-normal distribution (red line).

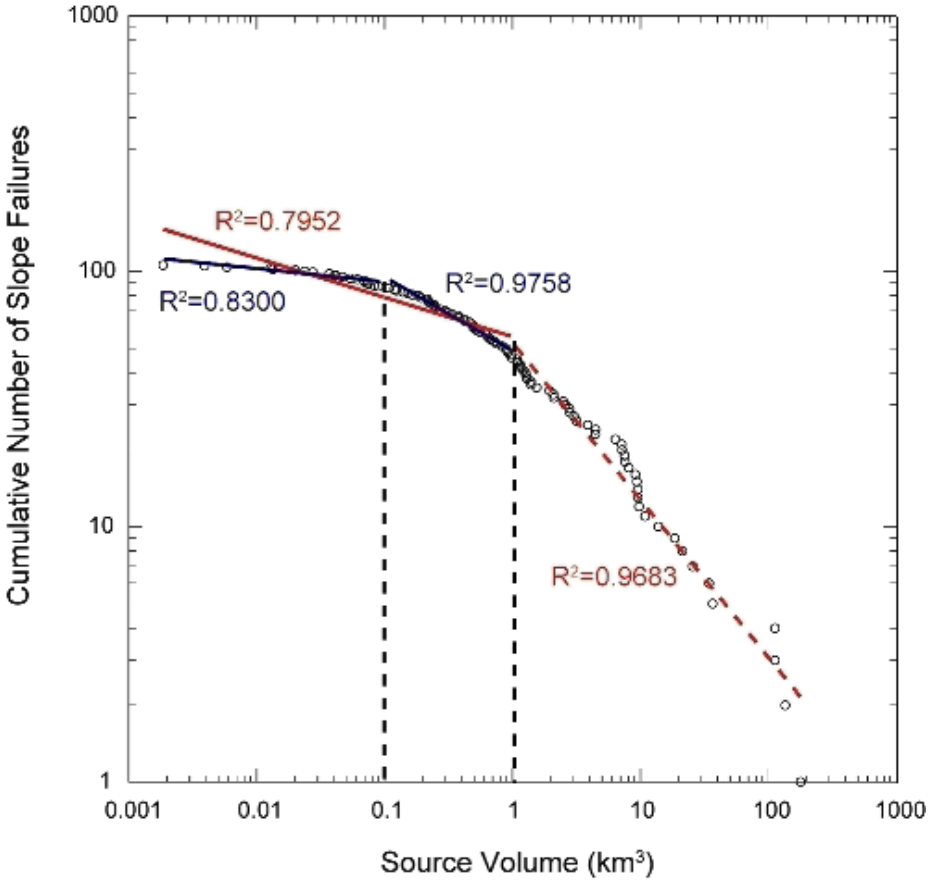

Figure 12-8: Cumulative volume distribution of the 106 observed failure scars described by two (red solid and dashed line) and three (blue solid lines and red dashed line) showing that at best, a inverse power-law can only describe a truncated portion of the distribution over two or fewer orders of magnitude.

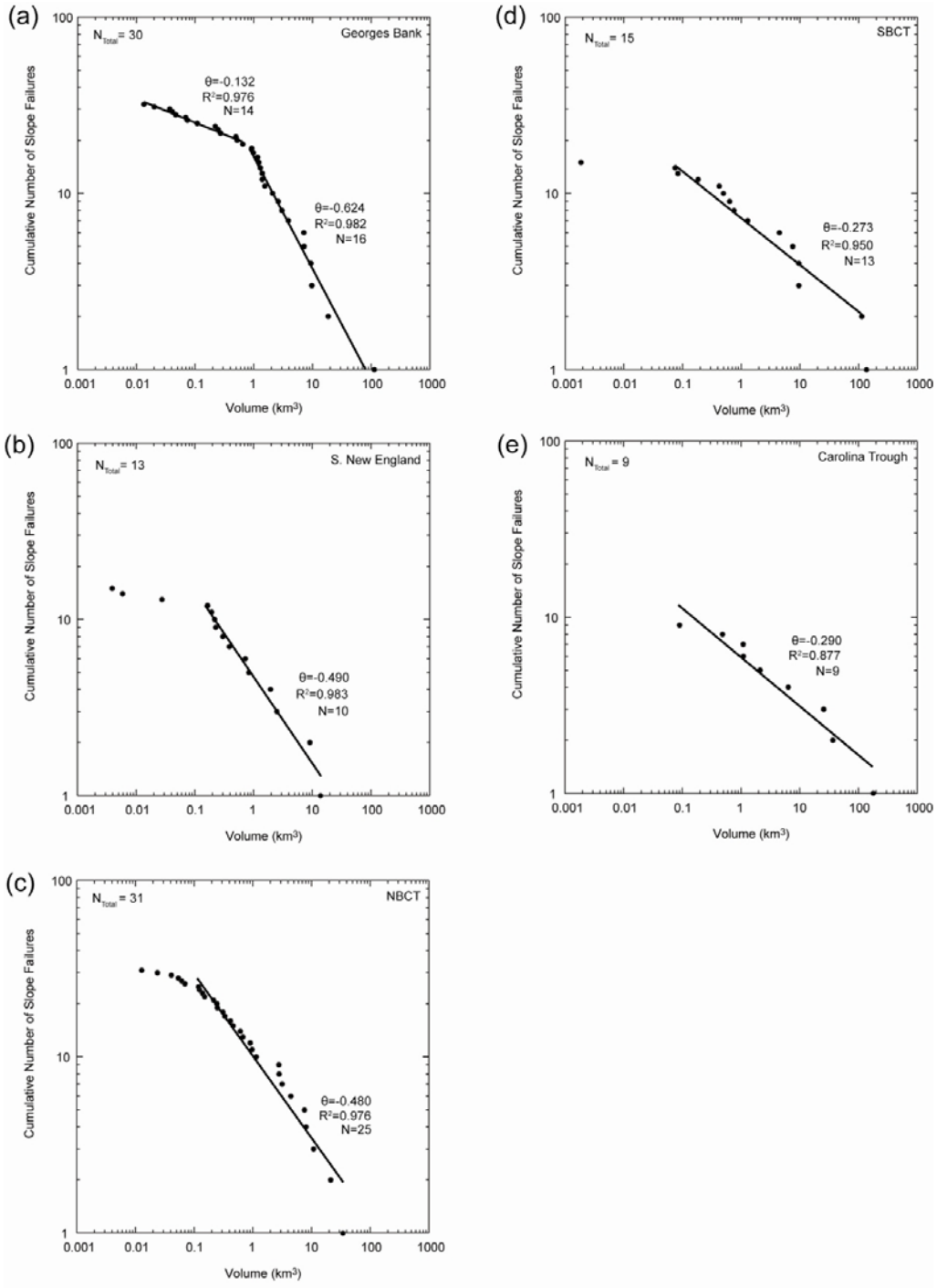

Figure 12-9: Cumulative volume distributions of slope failures scars from the five geographic/geologic regions as shown in Figure 12-1 with the calculated goodness of fit and exponent of fitted inverse power-law: (a) Georges Bank, (b) Southern New England, (c) Northern Baltimore Canyon Trough (NBCT), (d) Southern Baltimore Canyon Trough, (e) Carolina Trough.

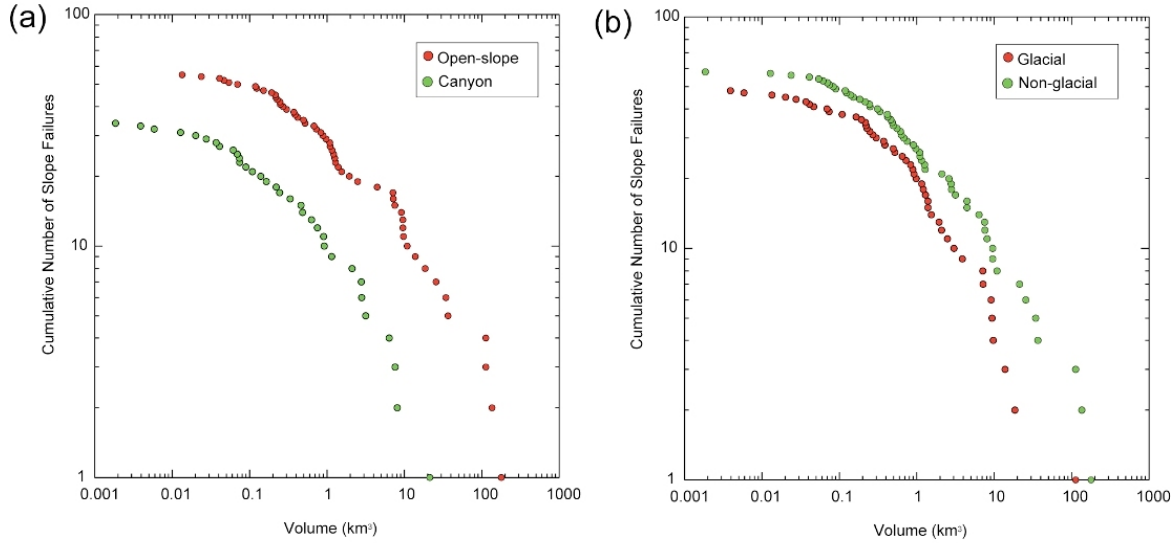

Figure 12-10: Cumulative volume distributions of slope failures scars from (a) open-slope and submarine canyon environments and (b) glacial and non-glacial influenced depositional environments.

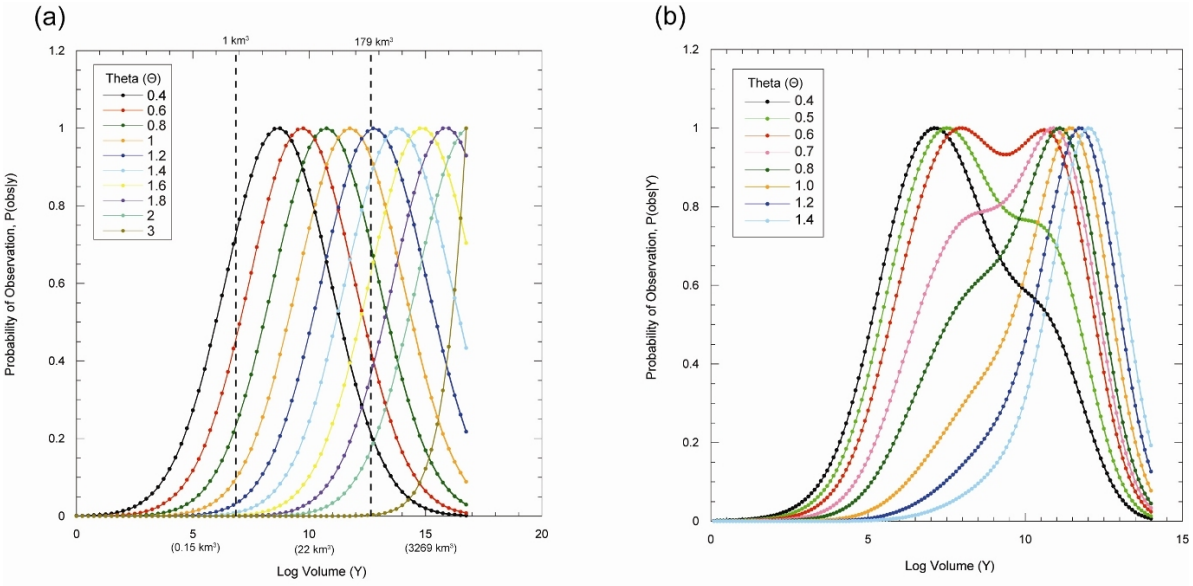

Figure 12-11: (a) Probability of observation (normalized) versus log volume (Y) for U.S. Atlantic margin failure scar volumes for different power-law exponent values (θ). Values of θ that have an ~ 0 probability of observation above a volume of 1 km³ are likely too high, while those that are not close to 1 for the maximum volume observed along the Atlantic margin are likely too small. Values in parentheses on the x-axis are the excavation volumes that correspond to the values of Y (*i.e.*, $x = 0.001e^{Y}$). (b) Similar plot for the Puerto Rico data of ten Brink, *et al.* (2006), where the flattening of the curves highlights the approximate best-fit value of θ (~ 0.6).

References

Bak, P., Tang, C., Wiesenfield, K., 1988, Self-organized criticality: *Physical Review*, *v. A. 38*, p. 364-374.

Booth, J.S., O'Leary, D.W., Popenoe, P., Danforth, W.W., 1993, U.S. Atlantic continental slope landslides: Their distribution, general

attributes, and implications, *in* Schwab, W.C., Lee, H.J., and Twichell, D.C. (Editors), Submarine landslides: Selected studies in the U.S. Exclusive Economic Zone: U.S. Geological Survey Bulletin no. 2002, p. 14-22.

Burbank, D. W. and Anderson, R. S., 2001, Tectonic Geomorphology: Blackwell Science, Malden, 274 p.

Burroughs, S.M., Tebbens, S.F., 2001, Upper-truncated power laws in natural systems: *Pure and Applied Geophysics*, *v. 158*, p. 741-757.

Carpenter, G., 1981, Coincident sediment slump/clathrate complexes on the U.S. Atlantic continental slope: *Geo-Marine Letters*, *v. 1*, p. 29-32.

Dai, F.C., Lee, C.F., 2001, Frequency-volume relation and prediction of rainfall-induced landslides: *Engineering Geology*, *v. 59*, p. 253-266.

Densmore, A.L., Ellis, M.A., Anderson, R. S., 1998, Landsliding and the evolution of normal-fault-bounded mountains: *Journal of Geophysical Research*, *v. 103 (B7)*, 15,203-15,219.

Dillon, W.P., Popenoe, P., Grow, J.A., Klitgord, K.D., Swift, B.A., Paull, C.K., Cashman, K.V., 1982, Growth faulting and salt diapirism: Their relationship and control in the Carolina Trough, eastern North America, *in* Watkins, J. S. and Drake, C. L. (Editors), Studies in continental margin geology: American Association of Petroleum Geologists Memoir 34, p. 21-46.

Dunning, S.A., Mitchell, W.A., Petley, D.N., Rosser, N.J., Cox, N.J., 2007, Landslides predating and triggered by the 2005 Kashmir earthquake: rockfall to rock avalanches: *Geophysical Research Abstracts*, *v. 9*, 06376.

Dussauge, C., Grasso, J., Helmstetter, A., 2003. Statistical analysis of rockfall volume distributions: Implication for rockfall dynamics: *Journal of Geophysical Research*, *v. 108 (B6)*, 2286, doi: 10.1029/2001JB000650.

Fine, I.V., Rabinovich, A.B., Bornhold, B.D., Thomson, R.E., Kulikov, E.A., 2005, The Grand Banks *landslide*-generated *tsunami* of November 18, 1929: preliminary analysis and numerical modeling: *Marine Geology*, *v. 215*, p. 45-57.

Geist, E.L., Lynette, P.J., and Chaytor, J.D., this volume, Hydrodynamic modeling of tsunamis from the Currituck Landslide.

Gisiger, T., 2001, Scale invariance in biology: coincidence or footprint of a universal mechanism?: *Biological Reviews*, *v. 76*, p. 161-209.

Greene, H.G., Murai, L.Y., Watts, P., Maher, N.A., Fisher, M.A., Paull, C.E., and Eichhubl, P., 2006, Submarine landslides in the Santa Barbara Channel as potential tsunami sources: *Natural Hazards and Earth System Sciences*, *v. 6*, p. 63-88.

Guthrie, R.H., and Evans, S.G., 2004, Analysis of landslide frequencies and characteristics in a natural system, coastal British Columbia: *Earth Surface Processes and Landforms*, *v. 29*, p. 1321-1339.

Guthrie, R.H., and Evans, S.G., 2007, Work, persistence, and formative events: The geomorphic impact of landslides: *Geomorphology*, *v. 88*, p. 266-275.

Guthrie, R.H., Deadman, P.J., Cabrera, A.R., and Evans, S.G., 2008, Exploring the magnitude-frequency distribution: a cellular automata model for landslides: *Landslides*, *v. 5*, p. 151-159.

Guzzetti, F., Malamud, B.D., Turcotte, D.L., and Reichenbach, P., 2002, Power-law correlations of landslide areas in central Italy: *Earth and Planetary Science Letters*, *v. 195*, p. 169-183.

Guzzetti, F., Reichenbach, P., Cardinali, M., Galli, M., and Ardizzone, F., 2005, Probabilistic landslide hazard assessment at the basin scale: *Geomorphology*, *v. 72*, p. 272-299.

Haflidason, H., Lien, R., Sejrup, H.P., Forsberg, C.F., and Bryn, P., 2005, The dating and morphometry of the Storegga Slide: *Marine and Petroleum Geology*, *v. 22*, p. 123-136.

Issler, D., De Blasio, F. V., Elverhoi, A., Bryn, P., and Lien, R., 2005, Scaling behavior of clay-rich submarine debris flows: *Marine and Petroleum Geology*, *v. 22*, p. 187-194.

Lee, H.J., this volume, Timing of occurrence of large submarine landslides on the Atlantic Ocean margin.

Limpert, E., Stahel, W.A., and Abbt, M., 2001, Log-normal distributions across the sciences: keys and clues: *Bioscience*, *v. 51* (5), p. 341-352.

Locat, J., and Lee, H.J., 2002, Submarine landslides: advances and challenges: *Canadian Geotechnical Journal*, *v. 39*, p. 193-212.

Lopez-Venegas, A.M., ten Brink, U.S., and Geist, E.L., 2008, Submarine landslide as the source for the October 11, 1918 Mona Passage tsunami: Observations and modeling: *Marine Geology*, doi: 10.1016/j.margeo. 2008.05.001.

Malamud, B.D., and Turcotte, D.L., 2006, An inverse cascade explanation for the power-law frequency-area statistics of earthquakes, landslides and wildfires, *in* Cello, G., and Malamud, B. D. (Editors), 2006, Fractal Analysis for Natural Hazards: *Geological Society, London, Special Publications*, *v. 261*, p. 1-9.

Malamud, B.D., Turcotte, D.L., Guzzetti, F., and Reichenbach, R., 2004, Landslide inventories and their statistical properties: *Earth Surface Processes and Landforms*, *v. 29*, p. 687-711.

Maramai, A., Graziani, L., Alessio, G., Burrato, P., Colini, L., Cucci, L., Nappi, R., Nardi, A., and Vilardo, G., 2005, Near- and far-field survey report of the 30 December 2002 Stromboli (Southern Italy) tsunami: *Marine Geology*, *v. 215*, p. 93-106.

Micallef, A., Berndt, C., Masson, D G., and Stow, D.A.V., 2008, Scale invariant characteristics of the Storegga Slide and implications for large-scale submarine mass movements: *Marine Geology*, *v. 247*, p. 46-60.

Murty, T.S., 2003. Tsunami wave height dependence on landslide volume: *Pure and Applied Geophysics*, *v. 160*, p. 2147-2153.

Nishenko, S.P., and Buland, R., 1987, A generic recurrence interval distribution for earthquake forecasting: *Bulletin of the Seismological Society of America*, *v. 77*, p. 1382–1399.

Noever, D.A., 1993, Himalayan sandpiles: *Physical Review E*, *v. 47*, p. 724-725.

Pelinovsky, E., and Poplavsky, A., 1997, Simplified model of tsunami generation by submarine landslides: *Physics and Chemistry of the Earth*, *v. 21*, p. 13-17.

Piper, D.J.W., Shor, A.N., and Hughes Clarke, J.E., 1988, The 1929 Grand Banks earthquake, slump and turbidity current, *in* Clifton, H.E. (Editor),

Sedimentologic consequences of convulsive geologic events: Geological Society of America Special Paper 229, p. 77-92.

Poag, C.W., and Sevon, W.D., 1989, A record of Appalachian denudation in postrift Mesozoic and Cenozoic sedimentary deposits of the U.S. middle Atlantic continental margin: *Geomorphology*, *v. 2*, p. 119-157.

Pratson, L.F., and Laine, E.P., 1989, The relative importance of gravity-induced versus current-controlled sedimentation during the Quaternary along the mideast U.S. Outer continental margin revealed by 3.5 kHz echo character: *Marine Geology*, *v. 89*, p. 87-126.

Robb, J.M., 1984, Spring sapping on the lower continental slope, offshore New Jersey: *Geology*, *v. 12*, p. 278-282.

Schlee, J.S., Fritsch, J., 1983, Seismic stratigraphy of the Georges Bank basin complex, offshore New England, *in* Watkins, J.S., and Drake, C.L. (Editors), Studies in continental margin geology, American Association of Petroleum Geologists Memoir, 34, p. 223-251.

Simonett, D.S., 1967, Landslide distribution and earthquakes in the Bewani and Torricelli Mountains, New Guinea; a statistical analysis, *in* Jennings, J. N. and Mabbutt, J. A. (Editors), Landform Studies From Australia and New Guinea: Cambridge University Press, Cambridge. p. 68-84.

Solow, A. R., 2005, Power laws without complexity: *Ecology Letters*, *v. 8*, p. 361-363.

Stark, C.P., and Hovius, N., 2001, The characterization of landslide size distributions: *Geophysical Research Letters*, *v. 28*, p. 1091-1094.

Sugai, T., Ohmori, H., and Hirano, M., 1994, Rock control on magnitude-frequency distribution of landslides: *Transactions of the Japananese Geomorphological Union*, *v. 15*, p. 233-251.

Synolakis, C.E., Bardet, J-P., Borrero, J.C., Davies, H.L., Okal, E.A., Silver, E.A., Sweet, S., and Tappin, D.R., 2002, The slump origin of the 1998 Papua New Guinea tsunami: *Proceedings of the Royal Society of London A*, *v. 458*, p. 763-789.

Talling P.J., Amy, L.A., and Wynn, R.B., 2007, New insight into the evolution of large-volume turbidity current: comparison of turbidite shape and previous modeling results: *Sedimentology*, *v. 54*, p. 737-769.

ten Brink, U.S., Giest, E.L., and Andrews, B.D., 2006, Size distribution of submarine landslides and its implication to tsunami hazard in Puerto Rico: *Geophysical Research Letters*, *v. 33*, L11307, doi: 10.1029/ 2006GL026125.

Twichell, D.C, Chaytor, J.C., ten Brink, U.S., and Buczkowski, B., this volume, Geologic Controls on the distribution of submarine landslides along the U.S. Atlantic continental margin.

Van Den Eeckhaut, M., Poesen, J., Govers, G., Verstraeten, G., and Demoulin, A., 2007, Characteristics of the size distribution of recent and historical landslides in a populated hilly region: *Earth and Planetary Science Letters*, *v. 256*, p. 588-603.

Watts, P., and Grilli, S.T., 2003, Tsunami Generation by Deformable Underwater Landslides: Proceedings of the 13th Offshore and Polar Engineering Conference (ISOPE03, Honolulu, USA, May 2003), p. 364-371.

Wolman, M. G., and Miller, J. P., 1960, Magnitude and frequency of forces in geomorphic processes: *Journal of Geology*, *v. 68*, p. 54-74.

Chapter 13: Timing of Occurrence of Large Submarine Landslides on the Atlantic Ocean Margin

Introduction: Submarine Landslide Territories and Times

Landslide territories

As noted by Hampton *et al.* (1996) submarine landslides commonly occur in areas with thick sedimentary deposits, sloping seafloor and high environmental stresses. These "landslide territories" are most common in five specific environments: (1) fjords, (2) active river deltas on the continental margin, (3) submarine canyon-fan systems, (4) the open continental slope, and (5) oceanic volcanic islands. Note that these "territories" exclude much of the continental shelves and deeper water basins. All five of these "territories" occur along the margins of the Atlantic Ocean, but on the east coast of the United States at present, the most common of these are submarine canyons and open slopes. In a survey of almost 200 submarine landslide deposits from the US Atlantic margin, Booth *et al.* (1993) reported that somewhat more landslides occurred on the open slope than in canyons and that a much larger area is covered by open-slope landslide deposits than canyon landslide deposits (although the data set may be somewhat biased against canyon landslides because of resolution difficulties in complex canyon morphologies). Accordingly, open-slope landslides are much larger. Because the likelihood of tsunami generation varies directly with landslide size, open-continental-slope landslides clearly deserve the greatest attention in any submarine-landslide tsunami evaluation. The only exception might be the partial collapse of volcanic islands, such as the Canary Islands, which could serve as a far-field tsunami source.

Landslide times

There are a number of large submarine landslide deposits associated with the open continental slope off the east coast of the US with volumes in the range of several hundred km^3 and areas exceeding 500 km^2 (Booth *et al.*, 1993, Maslin *et al.*, 2004, Edgers and Karlsrud, 1982), These large landslides most

likely generated significant tsunamis when they occurred. However, just as some areas of the sea floor are more prone to failure than others, the environmental conditions that cause landslides of this nature are also not uniformly distributed with geologic time. There are most likely some time periods when the probability of failure is greater, and some periods when the probability is less. If we can evaluate when these periods occur, we can either reduce or increase our estimate of the likelihood of landslide tsunamis for the present period in geologic history.

Many temporally varying factors influence submarine slope stability. These include the following:

(1) Quantities and types of sediment delivered to the margins. As the quantity of sediment delivered increases, the likelihood of formation of thick, potentially unstable sedimentary deposits also increases. The influence of sediment type is less clear. Sandy sediment is more vulnerable to failure during cyclic loading events but fine-grained sediment, if deposited rapidly, can form weak, gassy, pore-water pressure-charged material. During glacial periods, the input of sediment to the continental margins generally increases, particularly near the edges of continental ice sheets

(2) Locations of depocenters; particularly slope vs. shelf. Thick, relatively weak sediment deposits on the continental slope clearly have a greater potential for producing open-slope failures than similar deposits on the shelf. Likewise, during glacial periods, when sea level is lowered to near the shelf break, the likelihood of deposition on the slope increases (formation of shelf-edge deltas) vs. interglacial periods when river deltas are commonly located on the shelf. Catastrophic drainage of glacial lakes (Uchupi *et al.*, 2001) can also occur during glacial periods and can bring large quantities of sediment to the outer shelf and continental slope. According to Uchupi *et al.* (2001) such floods can trigger gravity flows on the upper slope and carry coarse debris into the deep sea.

(3) Changes in seafloor pressures and temperatures, which can influence hydrate stability and the possible generation of free gas (Kayen and Lee, 1992). Changes in sea level alter hydrostatic pressures on the seafloor and can cause destablilization of gas hydrates contained within some bottom sediment. Global oceanic temperature changes and redirection of warm and cold currents can have a similar effect. When gas hydrate is destabilized, it can release free gas, increase pore-water pressure, and reduce sediment strength. Critical times in geologic history include sea-level falls during the onset of continental glaciation, the beginning and end of glacial cycles when the locations of major currents, such as the Gulf Stream, change their course and other periods of extensive environmental change.

(4) Variations in seismicity related to isostatic loading or unloading of coastal and near-coastal regions by ice (or to a lesser extent by large sea level changes) (Bungum *et al.*, 2005). The formation and melting of thick sheets of ice produce large changes in crustal stresses.

Particularly in areas near the margins of ice sheets, the crust may respond to strong induced stress gradients by internal failure and the generation of earthquakes that are larger than would generally be expected for these areas. Crustal stress changes related to ice loading and sea-level changes may also play a role in the frequency of island and coastal volcanism (McGuire *et al.*, 1997). Variations in volcanism could lead to variations in volcanic island collapses.

(5) Changes in groundwater flow conditions within the continental slope and shelf (Dugan and Fleming, 2000). Some sediment beds within continental margins can become pressurized for a variety of reasons, including flow from higher elevations, tectonic activity, direct loading by ice and gas reservoirs. Pressure gradients in these beds induce groundwater flow, commonly from the continents into the offshore. Sea-level changes during the waxing and waning of ice sheets alter these conditions and rates of flow. This in turn alters the pore water pressure regime within the slope and can, under some conditions, contribute to slope failure.

Although all of the above conditions can occur on a small scale, because of local effects (*e.g.*, river course changes, tectonic activity, opening and closing of straits, etc.), the dominant factor that can influence the times of occurrence of significant submarine landslides is glaciation. Pleistocene glacial and interglacial cycles include several phases (see Figure 13-1 for a conceptual diagram of these effects) that can cause or impede the development of large submarine landslides:

(1) Initiation of glaciation. With the onset of a glacial cycle, large, thick ice sheets form over high latitude continental areas. The resulting impoundment of water causes sea level to fall worldwide in the range of 100 m, and the fronts of the ice sheets advance toward the coast. The ice erodes large quantities of geologic material, and meltwater from the front of the ice sheets increases in flow rate and sediment concentration. Deposits of rapidly accumulating sediment form near the shelf break and these increase in thickness with time. With sea level lowered, a result is the development of more extensive and potentially more unstable shelf-edge deltas, even in areas far removed from continental ice sheets. Shifting the weight of large amounts of water from the ocean to land changes crustal stresses and can create an environment of increased seismicity, particularly near the edges of the ice sheets where the stress gradients are highest.

Most of these effects increase the likelihood of submarine slope failure. Lowering sea level immediately decreases seafloor pressure and this can lead to gas-hydrate dissociation and the development of high excess pore-water pressures in some places. The resulting decreased shear strength can lead to failure. Increased seismicity can load continental slope sediment bodies and also potentially cause them to fail. The development of thick sediment bodies near the shelf break, including shelf-edge deltas, can clearly also

increase the risk of failure. However, this last process extends throughout a glacial cycle and the problem progressively worsens as the cycle continues. Groundwater flow conditions can change. Certainly the head difference between groundwater levels in near coastal highlands and the ocean is increased, owing to sea-level fall. In the absence of other changes this can reduce stability.

(2) Full glaciation. After the ice sheets have reached their maximum extent, seismicity at the margins may begin to decline and the tendency toward hydrate dissociation will be reduced. Both of these factors will, in themselves, lead to reduced slope instability. However, rapidly deposited sediment bodies will continue to form on the slope and as they become thicker the tendency towards excess pore-water pressure development will actually increase. Likewise, enhanced groundwater flow and resulting elevated pore-water pressures may also continue. The net effect of all of these factors is unclear. Almost certainly the likelihood of slope instability is greater during full glaciation than during interglacial times although it may well be less than during the transition period between interglacials and glacials.

(3) Transition from glacial to interglacial time. As continental ice sheets melt and sea levels rise, increased seismicity near the margins of areas that were heavily glaciated will begin to occur as a result of isostatic readjustment. Shelf-edge deltas will be near their maximum extent and may have pore-water pressures that are near their greatest values owing to long periods of rapid deposition during the glacial period. Major current systems such as the Gulf Stream may readjust, bringing warmer water to areas like northern Europe and possibly altering the stability of gas hydrates. This effect, of course, is countered by larger seafloor pressures produced by greater water depths on the slope. Groundwater flow may be slowed owing to higher sea levels, and new deposition will tend to occur more commonly on the shelf than on the slope. The net effect of these changes is not immediately obvious, although, as will be seen below, the geologic record shows many large submarine landslides occurring in the early Holocene.

(4) Interglacial time. After sea level has risen, seismicity near the margins of the former ice sheets will slowly decline. Unstable shelf edge deltas formed during the glacial period will either already have failed or will become gradually less likely to fail. Enhanced stability occurs because of a lack of new sediment and the dissipation of excess pore-water pressures produced during rapid deposition. Conditions of hydrate stability will become less variable and elevated pore-water pressures related to groundwater flow will decline. The period well after the end of a glacial cycle is most likely one in which the likelihood of submarine slope failure is lowest, except on deltas of large rivers that have prograded across the shelf, *e.g.*, the Mississippi River Delta.

Field Data

Techniques

The data base of reliable ages of submarine landslides is limited. To properly date a landslide, one generally must have a sample of sediment from immediately above either the landslide debris itself or the surface along which sediment has been completely removed (landslide scar). Datable materials (*e.g.*, calcareous microfossils, mollusks) from within the sediment above the slide are separated and dated using a variety of techniques, among which radiocarbon methods are most popular. For very recent (last 100 years) landslides, measurements of short-half-life radioisotopes such as ^{210}Pb or ^{137}Cs can be used (Lee *et al.*, 2007). Dating landslide debris itself is not as reliable because the sediment that failed may be relatively old. Likewise the sediment preserved below the failure may have been eroded and may also have a date that is greater than that of the failure. Another technique that has been used is to observe acoustic reflectors in seismic-reflection profiles across the front of a landslide extending into unfailed areas. If identified reflectors can be dated within a nearby boring (*e.g.*, an ODP hole), then the age of the critical reflector associated with the top of the landslide deposit can be taken as the age of the slide. Another common but less reliable dating method is to determine the thickness of post-landslide sediment above a landslide scar or landslide debris, estimate a representative sediment accumulation rate, and convert the sediment thickness into time.

Canadian Margin

One area where a relatively large number of landslides have been dated is southeast Canada (Piper *et al.*, 2003). For this area, the investigators have estimated the ages of 23 failures extending back to about 125,000 years before present, although most (20) are younger than 50,000 years. The methodology used for determining the chronology of piston cores taken in the vicinity of the failures included radiocarbon dating of mollusks or foraminifera, comparison of oxygen-isotope profiles with accepted oxygen-isotope stage data, and the observation of indicators of Heinrich events in the cores (Piper and Skene, 1998). Heinrich layers are periodic beds of detrital carbonate transported by ice rafting and proglacial plumes that come from the vicinity of Hudson Strait. They were clearly laid down during glacial times and their mechanism for development is likely related to oscillations in the Laurentide ice sheet. The exact cause is relatively unimportant; Canadian scientists are well acquainted with the events and their ages and their presence can be used as a chronologic indicator. With dated cores, the investigators could date landslides directly, follow acoustic reflectors from coring sites into the zones of failure or use a dated stratigraphy to recognize a set of key reflectors that could be used regionally to date landslide features. On the basis of these various dating techniques, Piper *et al.* (2003) developed a graph showing the distribution of failures vs.

time and general location (Figure 13-2). The graph shows only two dated failures in the last 10,000 years, one of them being the Grand Banks earthquake event of 1929. These failures occurred under post-glacial conditions. In contrast the graph shows 14 dated failures for the preceding 20, 000 years (30,000 to 10,000 years before present). This period generally corresponds to glacial conditions. Fewer events are identified for times before 30,000 years before present, but this may relate to the difficulty of identifying older failures that may be buried deeply in the sediment column. In any case, the rate of dated landslide occurrence is 2 per 10,000 years during the present interglacial cycle and roughly 7 per 10,000 for the later stages of the last glacial cycle. From these data one can estimate a roughly 350% increase in submarine landslide occurrence during glacial periods vs. interglacial periods, at least for a high-latitude, glaciated margin like Canada's.

A more recent study of the continental slope off Nova Sotia (Jenner *et al.*, 2007) shows a similar trend. Mass-transport deposits were sampled by six piston cores in the vicinity of a series of submarine canyons. The mass-transport deposits were dated using radiocarbon methods and the resulting stratigraphic information showed that failure deposits in more than one core had roughly the same age. In fact there were apparently four or five episodes of mass wasting that have occurred in this area over the last 17,000 years. These are at 5-8 ka, 12.7 ka, 13.8 ka, 17.9 ka and possibly 14.0 ka. Again the ratio of failure numbers during the period 20 ka to 10 ka to failures during the period 10 ka to 0 is roughly 4:1. Jenner *et al.* (2007) suggest that the landslides were caused by seismic events because they occurred over a broad area such that they could be sampled at locations that are distant from each other. Although there are some active salt tectonics features along the Canadian margin there is no apparent relationship between salt tectonics and failure (Piper *et al.*, 2003).

U.S. Margin

Not as many landslides along the US margin have been dated as along the Canadian margin. However, estimates of ages have been obtained for two large failure deposits: the Currituck slide (Prior *et al.*, 1986) and the Cape Fear slide (Popenoe *et al.*, 1993; Paull *et al.*, 1996; Rodriguez and Paull, 2000; see Figure 13-3 for locations).

Currituck Slide

The Currituck slide (Locat *et al.*, this volume) was first described by Bunn and McGregor (1980). Prior *et al.* (1986) described the feature in detail and showed that the deposits actually represent at least two separate slides, one within the other. They estimated that the volume of the inner, presumably first, slide is greater than 78 km^3 and the volume of the outer, later slide is greater than 46 km^3. Locat *et al.* (this volume) also estimated the volumes of these two slides and obtained 108 km^3 and 57 km^3, respectively. The failure deposits are covered with a fairly thick sediment drape that clearly postdates the event. The drape is 5-9 m thick over a deeper trough part of the feature

and 4-6 m thick over the shallower and steeper headwall. Deposition rates are likely about 5 cm/ky for the Holocene and about 20 cm/ky for the Late Pleistocene. According to Prior *et al.* (1986), these rough numbers indicate that the age of the Currituck Slide is between 25 and 50 ky, Such values would clearly indicate a period of glaciation and lowered sea level. Prior *et al.* (1986) suggest that the landslide may have been associated with a shelf-edge delta created by the ancestral James and Roanoke Rivers, which would have deposited sediment rapidly on the upper slope during periods of sea-level lowering.

Cape Fear Slide

The Cape Fear slide is the largest submarine slope failure off the east coast of North America, having a volume that is likely in excess of 200 km^3. The failure deposits were discovered in the late 1970s (Embley, 1980) and have been studied extensively (Popenoe *et al.*, 1993, Paull *et al.*, 1996, Rodriguez and Paull, 2000, Schmuck and Paull, 1993, Hornbach *et al.*, 2007) in subsequent years. Gravity and piston core samples taken from within the landslide source area show a 1- to 2-m-thick surface layer of brown clay overlying sediment with a fabric suggestive of mass-movement deposits (inclined beds, small convolutions and clasts within a finer matrix and a relatively large proportion of sand). Embley (1980) and Poponoe *et al.* (1993) reported ^{14}C dates from the base of the younger brown clay in two cores; these were about 21 and 12 ky, respectively. Paull *et al.* (1996) obtained sediment ages from 9 cores that pass through the sole of the slide within 50 km of the headwall; these consistently yielded ages of 9 to 14.5 ka at locations 5 to 50 cm above the unconformity. Directly below the unconformity, the ages are all greater than 29 ka. Finally, a recent ODP boring (Site 991) sampled the sole of the landslide and recovered 2.09 m of post slide material above a distinct contact (Rodriguez and Paull, 2000). Five ^{14}C dates above the contact show a uniform rate of sedimentation (27 cm/ky) above the hiatus. Below the hiatus the age of sediment is about 27 ky years. Accordingly, numerous radiocarbon dates show that the landslide occurred between 8 and 14.5 years ago. The one older age (about 21 ky years) reported by Embley (1980) most likely has been affected by contamination by material below the unconformity. The age of the material below the unconformity (*i.e.*, age of slip surface) is in the range of 20 ky to greater than 29 ky.

The results above show that the Cape Fear slide occurred near the transition between the last major glacial cycle and the present interglacial. The Cape Fear slide is clearly younger than the Currituck slide as suggested by these radiocarbon dates and the significantly less post-failure drape on top of the failed material (1-2 m vs. 4-9 m). The Cape Fear slide is also older than the Cape Lookout Slide to the north as indicated by GLORIA records that show the Cape Fear Slide cutting across it (Booth *et al.*, 1993).

At least one of the causes for the Cape Fear slide is salt tectonics and diapirism. A salt body was deposited during the period of rifting that marked the birth of the North Atlantic. Subsequent loading by sediment from the

North American continent caused the salt to mobilize and move seaward (Poponoe *et al.*, 1993). This mobility caused the development of salt diapirs and the formation of normal faults (Cashman and Poponoe, 1985; Poponoe *et al.*, 1993, Hornbach *et al.*, 2007). Recent high-resolution multibeam and chirp surveys show that a single massive normal fault, related to salt intrusion, intersects the main Cape Fear headwall. These data suggest that slide failure initiated along this fault (Hornbach *et al.*, 2007). If salt tectonics and normal faulting are the basic cause of the slide, then temporally varying environmental conditions (*e.g.*, glacial and sea level cycles) might have played a smaller role than they did along the Canadian Atlantic margin or at the location of the Currituck slide.

Investigators have also observed indicators of gas hydrates (*e.g.*, bottom simulating reflectors, BSRs) and gas accumulations below the hydrate seal. These factors could induce excess pore-water pressures and possibly trigger failure (Poponoe *et al.*, 1993; Schmuck and Paull, 1993). If so, environmental conditions related to glacial stages could conceivably play a role because hydrate stability is known to be influenced by sea-level stands and bottom-water temperatures (Carpenter, 1981). However, the most likely period for hydrate-destabilization-induced failure is during sea-level falls (Kayen and Lee 1992) and the Cape Fear slide apparently occurred during a period of sea-level rise.

Mid-Atlantic Slope

The mid-Atlantic slope between roughly the entrance to Chesapeake Bay and Hudson Canyon has been studied intensively for the locations and mechanics of submarine landslides (Embley and Jacobi, 1977; Cardinell *et al.*, 1982; McGregor, 1977; Robb *et al.*, 1982; Malahoff *et al.*, 1980; McGregor and Bennett, 1977). This is mainly because the area was a focus for possible Outer Continental Shelf (OCS) energy resource development in the late 1970s and early 1980s prior to moratoria on offshore drilling in the area passed in the 1980s. Submarine landslides played a major role in assessing whether or not lease sale areas were safe for development. According to W. Menard, USGS Director at the time (Folger and Hathaway, 1986), "because of the uncertainty of whether or not there were large submarine landslides or scars that might be reactivated off the area (Baltimore Canyon Trough), we were unable to tell the Bureau of Land Management that it was safe to go ahead and develop….Some of the most promising tracts, as far as the oil companies were concerned, were simply eliminated because we didn't know whether it was safe to develop them."

The Mid-Atlantic slope is complex with many small to medium canyons incising the slope and, in some cases, the shelf break. Distributed among the canyons and extending out onto the continental rise are a number of mapped submarine landslide deposits, some of them quite large. For example, Embley and Jacobi (1977) report a slide on the slope and rise off Maryland with a scar and deposit area of about 2000 km^2. GLORIA imagery shows an almost continuous series of landslides all along the mid-Atlantic margin (Booth *et al.*, 1993). Surprisingly, given the importance of this area and the

number of investigations that have been conducted, few reliable landslide ages are available. Embley and Jacobi (1986) note that the existing data set of more than 40 cores suggests that all of the mass-wasting events with initial water depths shallower than 3000 m are of Wisconsin or early Holocene age. Embley (1980) presents several of these landslide ages that are consistent with the observations of Embley and Jacobi (1986). Four cores taken between Baltimore and Norfolk Canyons sampled homogeneous brownish-gray silty clay without primary structures overlying distinct clasts, suggestive of failure deposits, below 80-120 cm. Radiocarbon dates for the bases of the homogeneous clay layer, presumed to be post-landslide sediment, were 5,500 yrs, 7,285, 10,080 and 6,680 years before present. These ages correspond to the early Holocene, a period during or shortly after the latest sea-level rise following the last glacial cycle. No dates more recent than 5,000 years ago are reported although the data base is clearly incomplete.

New England Slope

The continental slope south and southeast of New England is an area of extensive mass wasting processes (O'Leary, 1986; O'Leary, 1993; Booth *et al.*, 1993). GLORIA imagery shows generally greater backscatter for this part of the US margin, likely indicating the presence of more coarse grained material introduced by landslides, and much of the margin has been mapped as landslide terrain (Embley and Jacobi, 1986; Booth *et al.*, 1993; O'Leary, 1993). Since this is the part of the US Atlantic margin that bounds the region of major continental glaciation, there likely is a connection between glacial processes and the prevalence of submarine landslides, much as there is farther to the north in Canada (Piper *et al.*, 2003). However, the marine community has gathered scant information regarding the ages of the failures. Embley (1980) notes that cores from a landslide area southeast of Long Island, first discussed by Uchupi (1967), all contain an apparently undisturbed hemipelagic section overlying mass-flow units, indicating that failure did not occur in the very recent past. One published age for landslide deposits south of New England, in the area identified by O'Leary (1993) as the Southeast New England Landslide Complex, is given by Embley (1982) as 23,440 years old. Such an age is near the last glacial maximum, further supporting the premise that slope failure processes were most active south of New England during glacial times. The lack of an extensive data base prevents us from drawing any definite conclusions.

European and North African Margins

The European and North African margins (Figure 13-4) have been studied extensively for submarine landslides. This results in part from the many active marine science institutions in the countries bordering the North Atlantic in Europe, the presence of the largest gas field in Norway in the source region of the largest landslide, and a general interest on the part of the European Union in funding submarine landslide research. The EU-funded COSTA (continental slope stability) Project (Mienert, 2004) extended from

2000 to 2004 and involved a large group of scientists from many countries (including Norway, UK, Belgium, France, Spain, Portugal, Italy and Canada).

Within the COSTA Project, a review was made contrasting the characteristics of submarine landslides in the western and eastern North Atlantic (Huhnerbach and Masson 2004). The reviewers found that submarine landslides are more abundant in the western North Atlantic (off Canada and the US) than in the eastern North Atlantic (off Europe) and that, with the exception of a few huge failure complexes, the slides in the west are generally smaller than those in the east. A majority of slides on both sides of the Atlantic seem to originate in water depths between 1000 and 1300 m.

Weaver *et al.* (2000) reviewed sedimentation processes along the European and North African margins and prepared a map that summarizes the distribution of landslides. The authors noted that sedimentary environments can be divided into three general sections: a glaciated margin north of 56° N (southern tip of Norway), a "glacially-influenced" margin from 26° N to 56° N, and a non-glaciated margin south of 26° N. Large-scale mass movements are a prominent feature along the glaciated margins of Norway and the Faeroe Islands and some of these are known to have occurred in the Holocene (following the last glacial period). However, a major causal factor for the Holocene failures may have been high sedimentation rates occurring during the glacial period. The intermediate or "glacially influenced" margin has surprisingly few instances of mass movements but is rather cut by a large number of canyons, which funnel sediment to the deep sea by means of turbidity currents. South of 26° N (North Africa) upwelling produces elevated sediment accumulation rates and the area is subject to infrequent but large-scale debris flows.

Canals *et al.* (2004) reviewed the dating work that has been done on the North Atlantic landslides studied by the COSTA project. These include (from north to south) Traenadjupet, Finneidfjord, Storegga, Afen and Canary (Figure 13-4). The first four of these are in the section that Weaver *et al.* (2000) terms a glaciated margin west of Norway, and the Canary slide is in a clearly non-glaciated margin off North Africa.

Traenadjupet Slide

The Traenadjupet slide occurred off northern Norway, extends from the shelf break to more than 3000 m water depth, and has a scar and deposit area of about 14,000 km^2 (Laberg and Vorren, 2000). Failure was initiated either at the present headwall or retrogressed landward from a deeper site. Apparently, a combination of events led to the slope failure. Sedimentation rates were high within the failure zone during the glacial maxima. Such high sedimentation could have led to high pore-water and gas pressures which would have produced relatively low shear strength. Although smaller slides were likely initiated during the glacial maxima through sediment loading, the main Traenadjupet slide was probably caused by seismicity related to postglacial coastal uplift (Laberg and Vorren, 2000),

Two gravity cores from the Traenadjupet slide scar show post-slide sediment overlying what is apparently the slide basal plane. Radiocarbon

dating of the post-slide sediment (Laberg *et al.*, 2002) shows that the slide likely occurred about 4000 years ago, after significant glaciation in Norway had stopped but during a time when post-glacial isostatic readjustment could have led to increased seismicity.

Deposits from an older slide, the Nyk slide (Lindberg *et al.*, 2004) occur south of the Traenadjupet slide and have a mapable area of 2200 km^2, although parts of the slide are buried by subsequent debris flows and parts of the slide were removed by the Traenadjupet slide. The slide has been dated at greater than 16.3 ka BP, which is synchronous with fluctuations of a major ice sheet near the shelf edge. Lindberg *et al.* (2004) suggest that the slide was triggered by loading and unloading of the ice front.

Storegga Slide

The Storegga slide occurred off the coast of Norway and has a headwall that is about 310 km wide and a runout of over 800 km. Accordingly, with a volume of between 2500 and 3500 km^3 (Bryn *et al.*, 2005), the Storegga slide is one of the world's largest submarine landslides. The Ormen Lange gas field, the largest in Norway, lies in the scar left by the slide and this coincidence has led to what has certainly been the most extensive submarine-landslide investigation ever conducted. The Storegga slide was a component of the COSTA project (Mienert, 2004, Haflidason *et al.*, 2004) and was also the center of a major industry-supported thrust that is summarized in a special publication of the journal Marine and Petroleum Geology (Solheim *et al.*, 2005), containing 26 individual papers.

Dating the Storegga slide has involved the analysis of 89 cores from within a number of identified slide lobes within the larger slide deposit (Haflidason *et al.*, 2005). In all, about 80 dates were obtained, most of them allowing the determination of the age of the base of post-slide sediment. Although more than 60 individual lobes were identified, the dating results show that all of the main lobes represent slide phases that took place within a very short time interval. Indeed most of the lobes evidently intermingled into each other during the failure phase. The lobes become progressively smaller upslope, showing that the Storegga slide has the classic character of a retrogressive slide process. The dating results show that all of the retrogressive phases of the main slide event are clustered within an age interval from 6400 ^{14}C to 7800 ^{14}C yrs BP. The average of all the dates is 7249 ^{14}C yrs BP with a standard deviation of 239 yrs. A few younger lobes were dated with ages that clustered around 5000 and between 2000 to 3000 ^{14}C yrs BP. However, these events were very small in comparison with the main event, having volumes less than 0.1% of the total volume of the slide debris. The general conclusion of the dating study (Haflidason *et al.*, 2005) is that the main Storegga slide is one retrogressive event dated to be 7250 $\pm$ 250 ^{14}C yrs BP or about 8100 $\pm$ 250 cal. yrs BP. A few minor events have occurred more recently along the northern escarpment and are dated to be 5000 ^{14}C yrs BP and 2500-3000 ^{14}C yrs BP (5700 and 2200-2800 cal. yrs. BP).

The investigators of the Storegga slide have developed a good understanding of how it occurred (Bryn *et al.*, 2005). First, it was not the first

megaslide to occur at this location (Evans *et al.*, 2005). Rather, similar slides have occurred periodically with intervals of approximately 100 ky since the onset of continental shelf glaciation about 500 ky ago. The repeated sliding seems to be a response to climatic variability, and the seismic stratigraphy indicates that sliding occurs at the end of a period of glaciation or soon after the glaciation. Destabilization prior to the slide is related to rapid loading from glacial deposits with generation of excess pore pressure and development of relatively low shear strength in underlying clays. The slide was likely triggered by a strong earthquake and initiated in an area downslope from the present head scar. The failure then developed into a retrogressive slide and the head propagated shoreward. The earthquake, in turn, was likely related to glacio-isostatic rebounding following the deglaciation of Scandinavia. Bryn *et al.* (2005) claim that a new ice age with infilling of glacial sediment on top of marine clays in the slide scar will be needed to create a new unstable situation at the site of the Storegga slide.

The Storegga slide clearly produced a tsunami, the deposits of which have been observed around the Norwegian Sea and North Sea and along the northeast coast of England (Bondevik *et al.*, 2005). The deposits are found at onshore elevations of up to 10-12 m in Norway, 3-6 m in northeast Scotland and above 20 m on the Shetland Islands above the estimated sea level of the time of failure. A model of a tsunami resulting from a retrogressive slide that descends at 25-30 m/s is in good agreement with the observed deposits (Bondevik *et al.*, 2005, Ward, 2001).

Slides off the British Isles

A series of relatively large landslides has been surveyed off the north and northwest coasts of the British Isles. Several large slides are found on the slopes of the Norwegian Basin northeast of the Faeroe Islands (van Weering *et al.*, 1998). One of the most recent failures has been dated from one box core at 9850 ± 140 years BP. Farther south, the Afen slide, located about 100 km northwest of the Shetland Islands, is relatively small (area of scar and deposit~40 km^2, volume~0.2 km^3) but has been studied extensively (Wilson *et al.*, 2004) as part of the COSTA project. One dated core shows that it occurred more recently than 5800 yrs BP. On the Barra Fan, in Rockall Trough, west of Scotland and northwest of Ireland, the Peach slide (Holmes *et al.*, 1998) has had multiple failure events extending back to the mid-Miocene. The most recent event is thought to have occurred after the last glacial cycle. An age of 10,500 yrs is given by Maslin *et al.* (2004). In the same general area, failures have been mapped on the east side of Rockall Bank and these appear to have ages in the range of 15,000-16,000 (Flood *et al.*, 1979). In general, and with the exception of the small Affen slide, the failures on slopes to the north and northwest of the British Isles appear to have occurred either shortly after the last period of glaciation or during it.

Southern Europe

The section of the continental margin between the British Isles and West Africa is dominated by submarine canyons and deep sea fans. The fans are likely accumulations of turbidites, mass flow deposits that originate in many cases in slope failures in the upper parts of submarine canyons. A study of the Horseshoe fan off Portugal (Lebreiro *et al.*, 1997) shows that significantly more turbidites are deposited during glacial periods than during interglacial. Lebreiro *et al.* (1997) estimate that there were about 2.7 times as many turbidity currents during glacial periods than during inter-glacials.

West Africa

A surprisingly large number of mass-wasting deposits are found in the area off West Africa and surrounding the Canary Islands (Figure 13-4, Urgeles *et al.*, 1997, 1999, Krastel *et al.*, 2001, Masson *et al.*, 2002). The landslides appear to have two distinctly different origins (Gee *et al.*, 1999). The first type consists of pelagic sediment deposited off the coast of northwest Africa. This sediment results from highly productive surface waters that produce large quantities of biologic material deposited fairly rapidly on the slope. This biogenic sediment is augmented by dust blown off the Sahara Desert. The second type of landslide consists of volcaniclastic debris derived from collapses of parts of the Canary Islands. Both types of failure have long runouts and can involve large quantities of sediment. Volcanic collapse occurring on La Palma Island has been suggested as a potential source of a huge tsunami that could strike the coasts of the Americas with waves in the range of 3-8 m (Ward and Day, 2001). Recent, more realistic analyses of such a collapse (Gisler *et al.*, 2006) show that high amplitude waves could be produced that would be dangerous to the Canary Islands themselves and the shores of Morocco, Spain and Portugal. However, waves striking the coast of Florida would be more in the range of 1 to 77 cm.

Many studies have been conducted to date Saharan and Canary Island landslide deposits (*e.g.*, Krastel *et al.*, 2001). An event about 60,000 years ago (Gee *et al.*, 1999) apparently initially involved a failure of the pelagic sediment off Africa. The debris flow proceeded downslope and ultimately loaded and destabilized volcaniclastic material in the vicinity of the western Canary Islands. The combined flow continued for a distance of 400 km. More common are Canary Island debris avalanches (Urgeles *et al.*, 1997, 1999). The most recent significant event likely occurred off the island of El Hierro about 15 ka ago (Masson, 1996, Carracedo *et al.*, 1999) and probably involved the failure of a subaqueous lava platform. A much older (~130 ka) failure caused a collapse that removed a substantial subaerial part of the island as well (Carracedo *et al.*, 1999). Major debris avalanches related to partial island collapses appear to be correlated with turbidity-current deposits in the Madeira Abyssal Plain. If so, there have been seven major landslides in the Canary Islands in the last 750 ka, yielding a recurrence interval of about 100 ka. Canals *et al.* (2004) suggested a slightly shorter recurrence interval of 75 ka. There may be a correlation between eruptions of island volcanoes and

sea level (McGuire *et al.*, 1997), and this could lead to a possible temporal effect on volcanic island collapses. Also, Saharan debris flows might be slightly more common during glacial periods and sea-level lowstands because of the greater sediment production in Africa.

Amazon Fan

Seismic reflection profiles through the Amazon fan show at least four major mass-transport deposits (Piper *et al.*, 1997). Deep-sea drilling has shown that all of the deposits date from the late Pleistocene. Each deposit extends over an area on the order of 10^4 km^2 and is 50-100 m thick. According to Piper *et al.* (1997), the failures initiated in upper-fan levee sediment and occurred because the sediment was underconsolidated due to rapid deposition during marine lowstand, as well as the presence of shallow gas and gas hydrates. The exact timing of the failures is not completely clear (Piper *et al.*, 1997, Maslin and Mikkelsen, 1997, Maslin *et al.*, 1998), but the two most recent deposits appear to date between the time of peak glaciation and the early Holocene. Maslin *et al.* (1998) suggest the failures occurred at about the same time, with ages of 14-17 ka. The two more deeply buried and older failures date to about the periods of 35 ka and 42-45 ka. These times predate the last glacial maximum but still correspond to sea levels much lower than today's. Maslin *et al.* (1998, 2004) suggest that the ages of these Amazon fan (and other North Atlantic) failures are associated with short periods (few thousand years) of relatively lower sea level and that these low sea levels produced hydrate dissociation. Although such a mechanism is possible, the accuracy of dating landslide deposits does not seem to be high enough to confirm a strong correlation.

Other large failures worldwide

Probably most of the world's large submarine landslides that have been dated are located in the North Atlantic. However, a few examples of dated large landslides are noted in other areas. The BIG'95 slide, whose deposits cover an area of about 2000 km^2 in the Mediterranean Sea off the east coast of Spain, has been dated at about 11.4 ka (Canals *et al.*, 2004, Lastras *et al.*, 2004). Off Southern California, the Goleta slide covers about 100 km^2 and contains three surface lobes, two of which have been dated at 8 and 10 ka (Fisher *et al.*, 2005). Older failure deposits lie below one of the lobes and have been dated at 75, 130, and 164 ka, indicating a recurrence interval of failure of about 50 ka for this lobe (Lee *et al.*, 2004). The Palos Verdes debris avalanche, off Los Angeles (Bohannon and Gardner, 2004, Normark *et al.*, 2004) has a deposit with an area of about 50 km^2. The most recent major failure of the Palos Verdes debris avalanche has been dated at 7.5 ka (Normark *et al.*, 2004), but seismic-reflection profiles indicate that numerous failures have occurred at the location of this failure zone in the past. The Sur submarine slide off central California (Normark and Gutmacher, 1988) has an area (scar and deposit) of more than 1000 km^2. The slide has not been

dated directly, but by observing the thickness of post-failure deposits in piston cores along with sediment accumulation rates obtained from a core taken 50 km away, Normark and Gutmacher (1988) estimated that the latest phase of the slide occurred 1.5 to 6 ka. The Hawaiian Islands are surrounded by very large landslide deposits that resulted from partial collapses of the islands (Moore *et al.*, 1989). One of the youngest, the Alika 2 slide (Lipman *et al.*, 1988, Normark *et al.*, 1993, McMurtry and Herrero-Bervera, 2003) has an age of around 120 ka and the two largest failures (Nuuanu and Wailau) have ages between 1 and 2 Ma.

Historic landslide tsunamis

Several tsunamis from the last 100 years are known to have been caused by submarine landslides. These include the 1929 Grand Banks event, the 1964 Alaskan earthquake, which caused major submarine landslides and tsunamis in many places including Seward and Valdez (Lee *et al.*, 2006), the 1970 aseismic submarine-landslide at Nice, France (Seed *et al.*, 1988), the 1975 landslide in Kitimat, British Columbia (Prior *et al.*, 1982), the 1975 Kalapana event in Hawaii (Goff *et al.*, 2006), and the 1998 earthquake-related Papua-New Guinea landslide tsunami which killed approximately 2,000 people (Tappin *et al.*, 2003). A large landslide that might have caused an anomalously large tsunami following the 1946 Aleutian earthquake (Fryer *et al.*, 2004) has been suspected, but a definitive deposit has yet to be found. In general, a fairly large number of tsunamigenic submarine-landslide deposits have been found at locations where tsunamis have been observed, corresponding to one century of historic time. Most likely few, if any, of these landslide deposits would have been discovered by routine surveys if the occurrence of the tsunamis had not focused the attention of researchers on specific locations. Accordingly, one must be wary of the completeness of any list of submarine-landslide dates such as that presented in the main text of this chapter. Many times more tsunamigenic-submarine landslides likely have not been mapped or dated. All mapped landslide deposits do not necessarily correspond to tsunami generation at the time of occurrence. The landslides could have moved slowly or as a series of smaller pluses. Conclusions regarding timing and significance of past events need to be tempered with the knowledge that the available data are very limited and incomplete.

Modeling

Hutton and Syvitski (2004) report on numerical modeling of the role of sediment failure in the development of continental margins. The authors use the *SedFlux* model (Syvitski and Hutton, 2001) to simulate the lithologic character of basin stratigraphy through the use of a series of process-based event modules to distribute sediment through surface or subsurface plumes, ocean storm events, slope failures, turbidity currents or debris flows. The model can change accommodation space (space available for sediment

deposition) as a result of subsidence, tectonics or compaction. The model produces distributions of grain size, bulk density, porosity and permenability.

Hutton and Syvitski (2004) applied the model to a representative 2-D continental margin and allowed the margin to develop over a period of one million years, incorporating many glacial and sea level cycles. The authors related the modeled sedimentologic properties to geotechnical properties and used the results to predict how earthquake-loading influenced slope stability of the margin as a function of time over this large time span. The model simulates many of the factors thought to be important in continental margin stability and allows an additional check on the role of glacial cycles in affecting margin stability. The results show a strong association between slope stability and sea-level stand. Although failures were modeled to occur at any sea-level position, depending on the prior depositional history, many more (by a factor of 3-5) occur during periods of falling or low sea level than during comparable periods of rising or high sea level. The largest number of failures was modeled to occur during falling sea level. The model showed that most of the failures are located on the upper continental slope in 500±250 m water depth. The model also showed that most of the failures have a thickness less than 10 m although some can exceed 30 m. The thickness of sediment failure increases during periods of rising or high sea level.

Findings and Conclusions

Table 13-1 summarizes the ages of submarine landslides reviewed in this chapter (including failures in both the Atlantic Ocean and elsewhere but excluding those from the last 100 years), and these results are plotted in Figure 13-5. Also provided in the table is a brief description of the bases used for making age estimates. As can be seen, many different age estimate strategies have been applied, and the reliability of the estimates varies greatly. Conclusions drawn from these results must be considered as tentative. If these ages are binned in groups of 5,000 years for the last 20,000 years (using the mean age for landslides that show a range of possible ages), we find the following: two slides in the last 5,000 years, five from 5 to 9.9 ka, four from 10 to 14.9, and five from 15 to 19.9. Using 10,000 years ago as a crude approximation for the end of the last glacial cycle and 20,000 year ago as a crude approximation for the last glacial peak, these results imply that the occurrence of large landslides was roughly evenly distributed with time from the last glacial maximum until about five thousand years after the end of glaciation. In the past 5,000 years the occurrence of submarine landslides has been less frequent. Note that the last 100 years were excluded because landslide-tsunamis are now directly observed and these observations lead us to conduct surveys and find landslides. Some, perhaps most, of the very recent tsunamigenic landslides would not have been seen if we had not know where to look. However, possibly the Grand Banks event, which laid down a 1-m-thick turbidite over large parts off the Sohm Abyssal Plain (Heezen *et al.*, 1954), would still have been observed even if observers had not been

available to experience the earthquake, tsunami, and cable breaks. If so, then we can increase the apparent number of large landslides of the last 5,000 years from two to three. We could then conclude that ratio of landslide occurrence during and shortly after glacial cycles to landslide occurrence well into an interglacial period is about 5:3.

These observations regarding large landslides are supported by other data. For example, as discussed above, Piper *et al.* (2003) show that glacial periods produce about 3.5 times as many submarine landslides on the Canadian margin as do non-glacial periods. Likewise, Lebreiro *et al.* (1997) estimate that there were about 2.7 times as many turbidity currents during glacial periods off the coast of central Europe. Although at least part of the reason for reduced turbidity current activity during interglacial periods is that some canyon heads become stranded at the shelf break, an association is still likely between turbidity-current deposits on deep-sea fans and abyssal plains and submarine-slope failures on the slope and within canyons. In summary, all these field results appear to indicate an increase in the frequency of large landslides by about a factor of 1.7 to 3.5 during and shortly after glacial periods, relative to times well after glaciation.

Model results (Hutton and Syvitski, 2004) support the idea that significantly more submarine landslides occur during falling or lowered sea level than during rising or high sea level. The model, in fact, suggests that occurrences are 3 to 5 times more likely under falling or lowered conditions, with the greatest number corresponding to the time when sea level is falling.

A plausible explanation for field observations that many more landslides occur during and shortly after glacial periods is that during glacial periods and the associated lowstands of sea level, thick deposits of sediment form readily on the upper continental slope, often in shelf-edge deltas. When glaciation ends, seismicity is increased near previously glaciated areas, serving as a trigger for causing these thick slope deposits to fail. Even in regions that were not glaciated, relatively thick, potentially weak deposits may have been preferentially deposited on the upper slope. These deposits might be more susceptible to failure during glacial cycles or shortly thereafter than similar slopes at times farther into an interglacial cycle (after most of the potentially unstable slopes have failed, probably during large earthquakes).

The role of hydrate dissociation in the initiation of submarine landslides has been discussed extensively in the literature (*e.g.*, Maslin *et al.*, 2004, Paull *et al.*, 1996, Kayen and Lee, 1992) but there are few definitive studies that show that this process indeed caused a landslide. One problem is that most of the landslides reported are from the last 20,000 years, which is a period of mostly stable or rising sea level, a time when significant hydrate dissociation might not be expected. Also, the relatively poor accuracy of landslide dates makes it difficult to associate failure events with relatively short periods of sea level fall (Maslin et al., 2004). Large landslides such as the Storegga slide were at one point thought of as possibly having been caused by hydrate dissociation but more recent studies appear to show that hydrates were not a major factor in causing failure (Bryn *et al.*, 2005).

Clearly, not all tsunamigenic landslides involve failures of sediment deposits that were emplaced on the slope during lowstands or were failures

triggered by isostatic-rebound related seismicity. Collapses of volcanic islands and other mechanisms for steepening slopes, such as the salt tectonics associated with the Cape Fear slide and some failures in the Gulf of Mexico, may be less influenced by glacial stands, although even for these cases, crustal stress changes associated with sea level change may play a role (McGuire *et al.*, 1997). Likewise, as evidenced by the Grand Banks event, there is a continuing possibility of slope failures in previously glaciated areas that are initiated through the residual effects of the last ice age. Such failures could possibly occur off the southern margin of New England where we know many submarine landslides have occurred in the past but where we have little knowledge of their chronology.

In summary, a risk of tsunamigenic submarine landslides exists off the east coast of the US. and likely elsewhere along the margin of the Atlantic Ocean. The probability of occurrence is less during the present interglacial period, perhaps by a factor of 1.7 to 3.5. Most likely areas where future tsunamigenic landslides could occur include volcanic islands (which are possibly too distant to have a significant impact on the eastern US), within salt tectonics areas such as near the head of the Cape Fear slide, and off previously glaciated margins such as southern New England.

Table

Table 13-1: Distribution of ages of several large submarine landslides. Non-Atlantic Ocean landslides are in italics.

Name of landslide	Age in 1000's of years	References	Basis for age determination
Sur slide	*1.5-6*	*Normark and Gutmacher (1988)*	*Sediment thickness and published deposition rates from nearby cores.*
Traenadjupet	4	Laberg *et al.*, 2002	^{14}C with a reservoir age of 440 yrs; calibrated using CALIB 4.0
Afen	5.8	Wilson *et al.*, 2004	AMS ^{14}C and biostratigraphy
Storegga	8.1	Haflidason *et al.*, 2005	^{14}C with a reservoir age of 400 yrs
Palos Verdes	*7.5*	*Normark et al., 2004*	^{14}C with a reservoir age of 800 yrs; calibrated using CALIB 4.3
Goleta west	*8*	*Fisher et al., 2005*	*Stratigraphic correlation with ODP 893; ^{14}C dating of ODP samples, corrected to calendar years using methods of Ingram and Kennett (1995)*
Faeroe	9.9	Van Weering *et al.*, 1998	^{14}C with a reservoir correction
Goleta middle lobe	*10*	*Fisher et al., 2005*	*Stratigraphic correlation with ODP 893; ^{14}C dating of ODP samples, corrected to calendar years using methods of Ingram and Kennett (1995)*
Peach	10.5	Holmes *et al.*, 1998; Maslin *et al.*, 2004	Regional stratigraphy based on dated cores and borings
BIG'95	*11.4*	*Canals et al., 2004; Lastras et al., 2004*	^{14}C with a reservoir age of 402 yrs; calibrated using CALIB 3.0
Cape Fear	8-14.5	Embley, 1980; Poponoe *et al.*, 1993; Paull ert al., 1996; Rodriguez and Paull, 2000	Recently obtained dates (Rodriguez and Paull, 2000; Paull *et al.*, 1996) are uncalibrated ^{14}C
Amazon Shallow East	14-17	Maslin *et al.*, 1998	Radiocarbon dating and oxygen isotope correlation with Leg 155 sediment and piston cores. Radiocarbon years corrected to calendar years.
Amazon Shallow West	14-17	Maslin *et al.*, 1998	Radiocarbon dating and oxygen isotope correlation with Leg 155 sediment and piston cores. Radiocarbon years corrected to calendar years.
Rockall	15-16	Flood *et al.*, 1979	Carbonate and cocccolith stratigraphy
Canary	15	Masson , 1996	Calibrated ^{14}C dating of turbidites; K/Ar dating of volcanic events
Nyk	16.3	Lindberg *et al.*, 2004	^{14}C with a reservoir age of 440 yrs
Amazon Deep Eastern	35	Maslin *et al.*, 1998	Biostratigraphy, seismic stratigraphy, magnetostratigraphy, and sedimentation rate constraints
Currituck	25-50	Prior *et al.*, 1986	Sediment thickness and published deposition rates from nearby cores
Amazon Deep Western	42-45	Maslin *et al.*, 1998	Biostratigraphy, seismic stratigraphy, magnetostratigraphy, and sedimentation rate constraints
Saharan	60	Gee *et al.*, 1999	Coccolith assemblage analysis using the method of Weaver (1994)

Figures

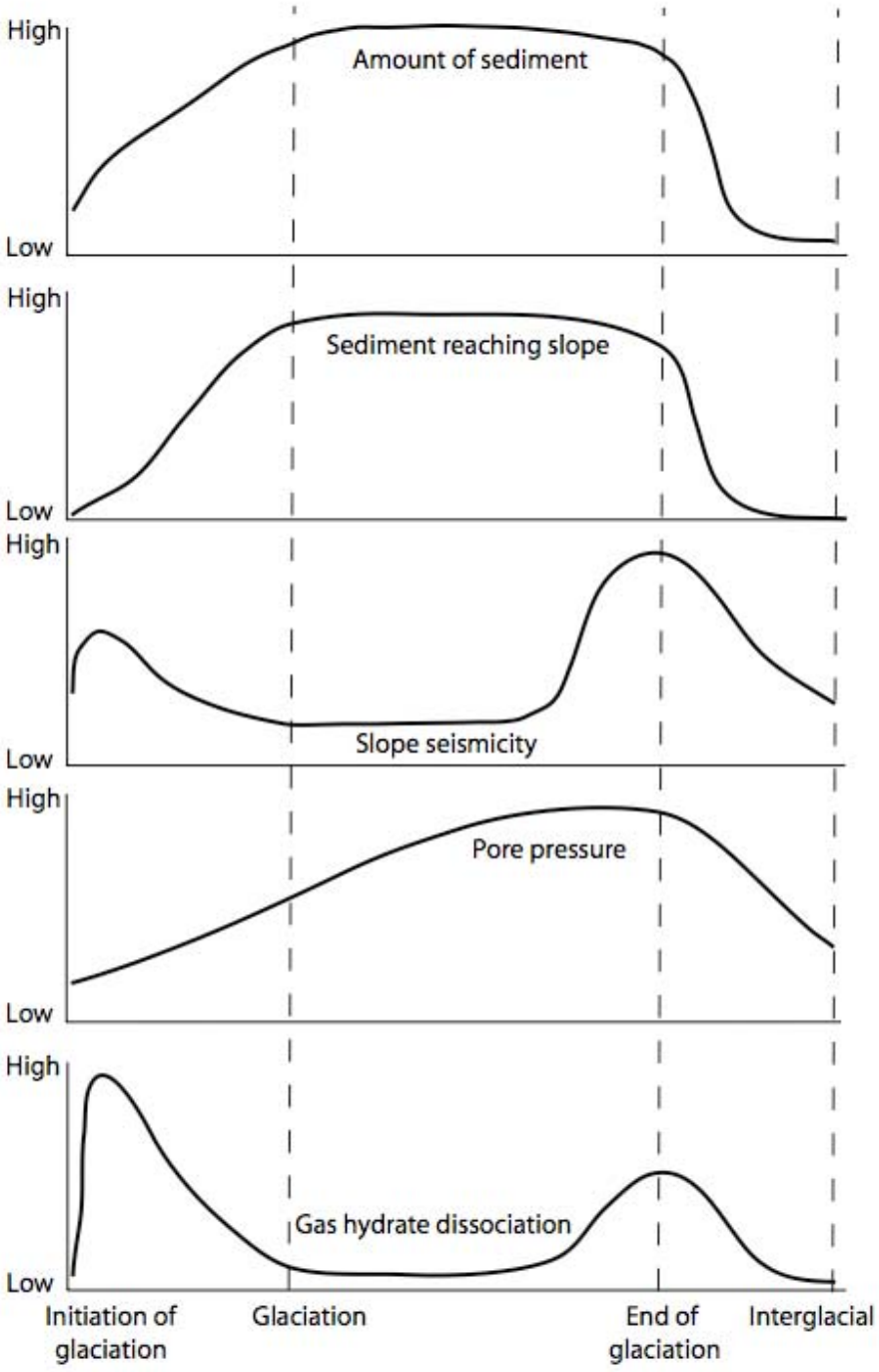

Figure 13-1: Approximate impact of time on several factors that impact the stability of submarine slopes.

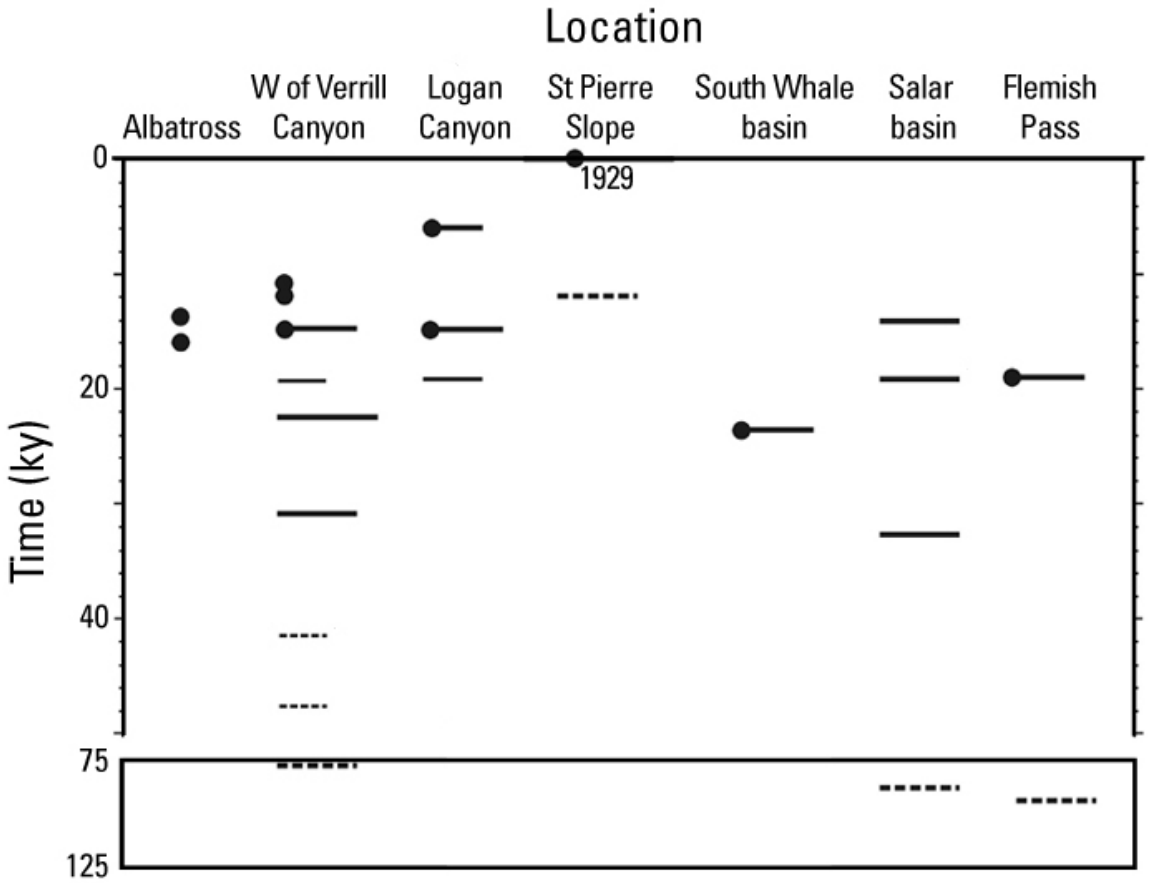

Figure 13-2: Occurrence of submarine landslides off eastern Canada by time and general location (after Piper *et al.*, 2003). Dots indicate direct dates of unconformities or failure deposits in a core. Solid lines indicate chronology established using sparker profiles and a set of key reflectors that have been dated back to 36 ka. Dashed lines represent an extrapolation of this sparker reflector chronology to older ages (Mosher *et al.*, 2004).

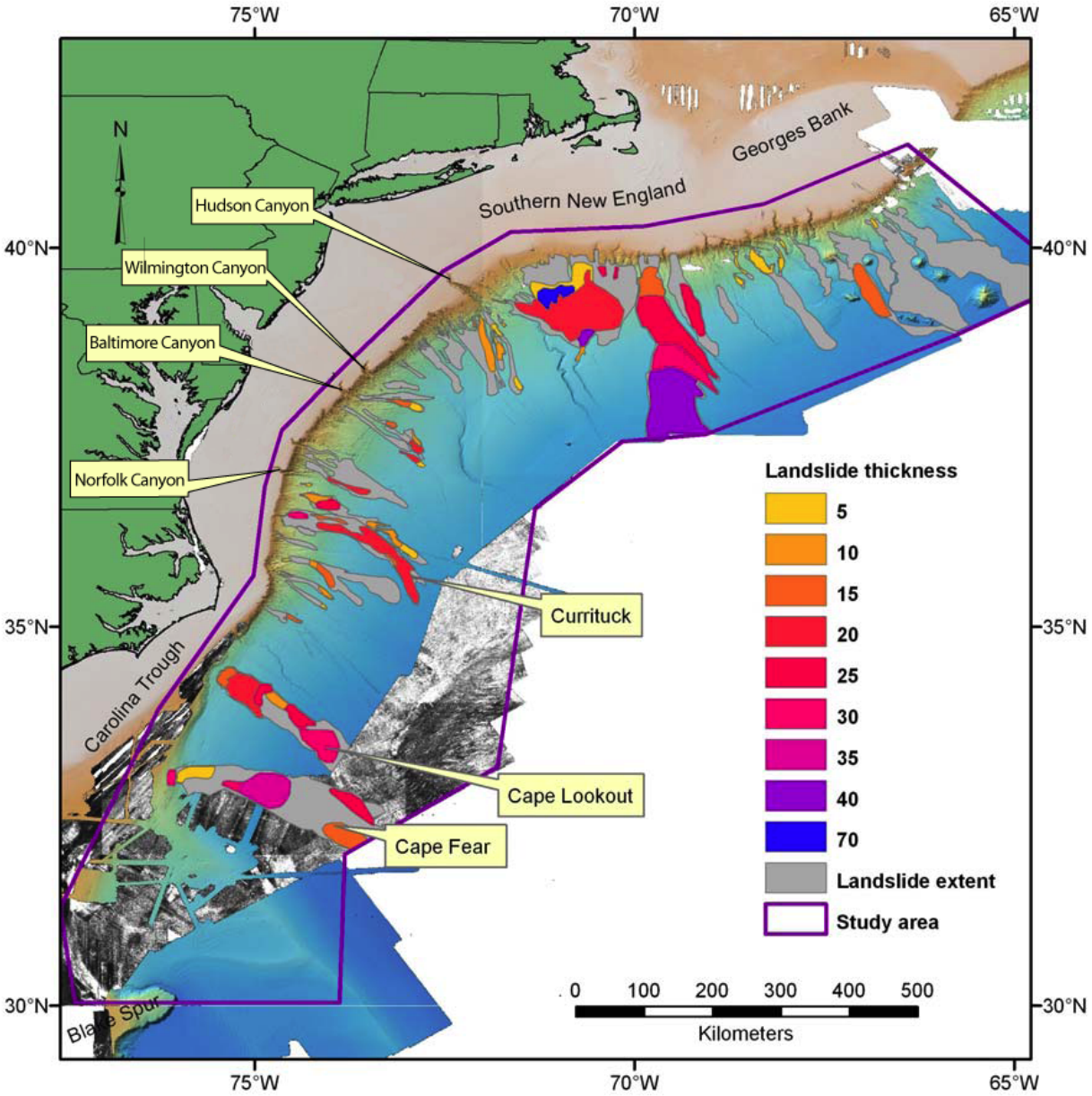

Figure 13-3: Locations of east coast submarine landslides discussed in the text, and based on information in Chapter 2. Deposit thicknesses shown for several of the large landslides.

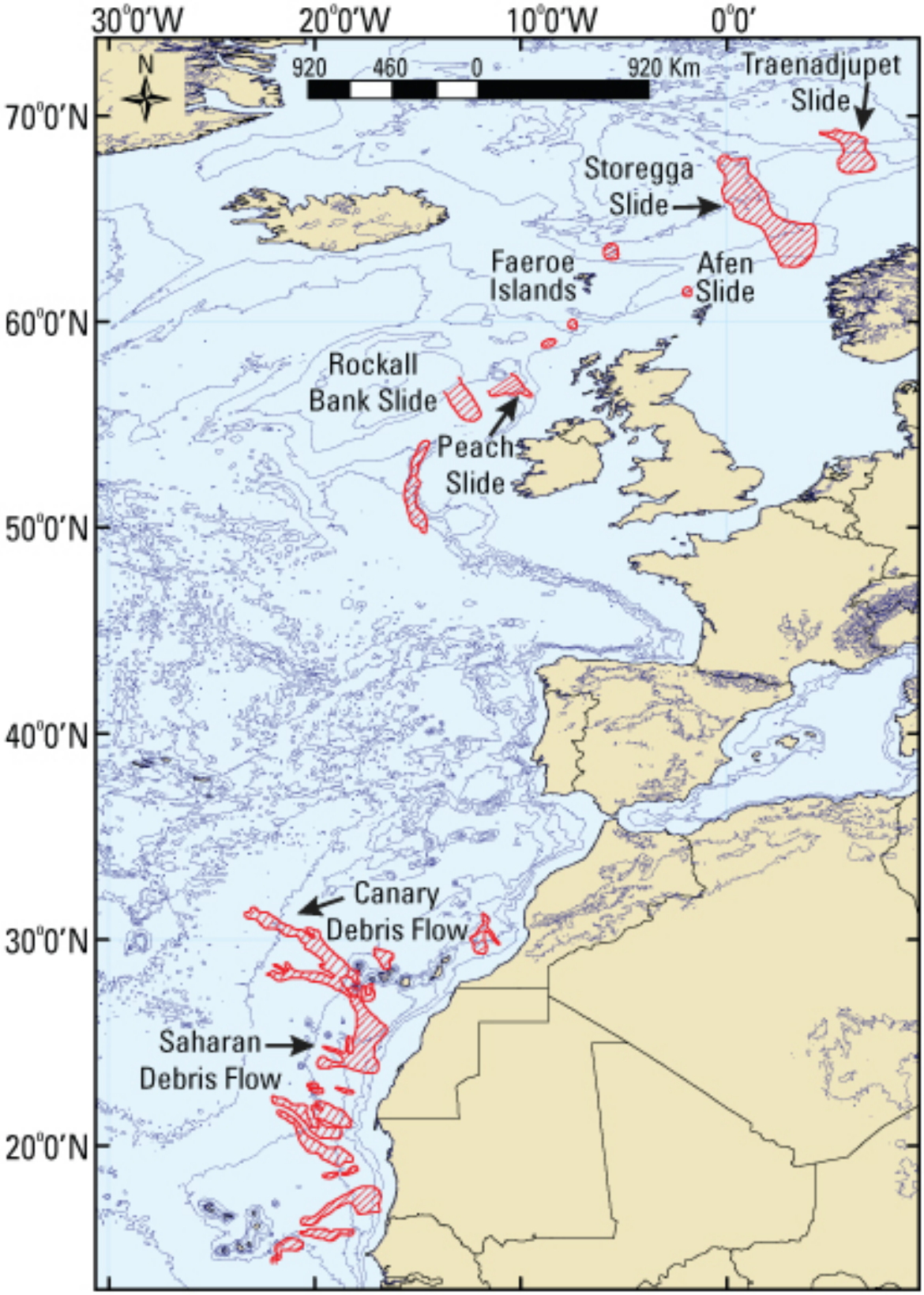

Figure 13-4: Locations of submarine landslides discussed in the text off Europe and North Africa.

Figure 13-5: Plot showing the distribution of ages of landslides younger than 20 ky and listed in Table 13-1. The figure shows a reduced occurrence of landslides during the last 5 ky.

References

Bohannon, R.G. and Gardner, J.V., 2004, Submarine landslides of San Pedro Escarpment, southwest of Long Beach, California: *Marine Geology*, *v. 203*, p. 261-268.

Bondevik, S., Lovholt, F., Harvitz, C., Mangerud, J., Dawson, A., and Svendsen, J.I., 2005, The Storegga slide tsunami—comparing field observations with numerical simulations: *Marine and Petroleum Geology*, *v. 22*, p. 195-208.

Booth, J.S., O'Leary, D.W., Popenoe, P., and Danforth, W.W., 1993, U.S. Atlantic continental slope landslides: their distribution, general attributes, and implications, *in* Schwab, W.C., Lee, H.J., and Twichell, D.C. (Editors), Submarine landslides: Selected studies in the U.S. EEZ: USGS Bulletin 2002, p.14-22.

Bryn, P., Berg, K., Forsberg, C.F., Solheim, A., and Kvalstad, T.J., 2005, Explaining the Storegga slide: *Marine and Petroleum Geology*, *v. 22*, p. 11-19.

Bungum, H., Lindholm, C. and Faleide, J.I., 2005, Postglacial seismicity offshore mid-Norway with emphasis on spatio-temporal-magnitudal variations: *Marine and Petroleum Geology*, *v. 22*, p. 137/148.

Bunn, A.R. and McGregor, B.A., 1980, Morphology of the North Carolina continental slope, western north Atlantic, shaped by deltaic sedimentation and slumping: *Marine Geology*, *v. 37*, p. 253-266.

Canals, M., Lastras, G., Urgeles, R., Casamor, J.L., Mienert, J., Cattaneo, A., De Batist, M., Haflidason, H., Imbo, Y., Laberg, J.S., Locat, J., Long, D., Longva, O., Masson, D.G., Sultan, N., Trincardi, F., and Bryn, P., 2004, Slope failure dynamics and impacts from seafloor and shallow sub-seafloor geophysical data: case studies from the COSTA project: *Marine Geology*, *v. 213*, p. 9-72.

Cardinell, A.P., Keer, F.R., and Good, L.K., 1982, Hazard analysis on the mid-Atlantic continental slope, OCS Lease Sale 59 area: Proceedings of the 14th annual OTC, Paper OTC 4173.

Carpenter, G., 1981, Coincident sediment slump/clathrate complexes on the U.S. Atlantic continental slope: *Geo-Marine Letters*, *v. 1*, p. 29-32.

Carracedo, J.C., Day, S. J., Guillou, H., And Perez Torrado, J., 1999, Giant Quaternary landslides in the evolution of La Palma and El Hierro, Canary Islands: *Journal of Volcanology and Geothermal Research*, *v. 94*, p. 169-190.

Cashman, K.V. and Poponoe, P., 1985, Slumping and shallow faulting related to the presence of salt on the continental slope and rise off North Carolina: *Marine and Petroleum Geology*, *v. 2*, p. 260-271.

Dugan, B. and Flemings, P.B., 2000, Overpressure and fluid flow in the New Jersey continental slope: implications for slope failure and cold seeps: *Science*, *v. 289*, p. 288-291.

Edgers, L., and Karlsrud, K., 1982, Soil flows generated by submarine slides: case studies and consequences, *in* Chryssostomomidis, C. and Connor, J.J (Editors), Proceedings of the 3rd International Conference on the Behavior of Offshore Structures, Hemisphere Publishing Corporation, volume 2, p. 425-437.

Embley, R.W., 1980, The role of mass transport in the distribution and character of deep-ocean sediments with special reference to the North Atlantic: *Marine Geology*, *v. 38*, p. 23-50.

Embley, R.W., 1982, Anatomy of some Atlantic margin sediment slides and some comments on ages and mechanisms, *in* Saxov, S. and Nieuwenhuis, J.K. (Editors), Marine Slides and other Mass Movements: Plenum Press, New York, p. 189-213.

Embley, R.W. and Jacobi, R., 1977, Distribution and morphology of large submarine sediment slides and slumps on Atlantic continental margins: *Marine Geotechnology*, *v. 2*, p. 205-228.

Embley, R.W. and Jacobi, R., 1986, Chapter 29, Mass wasting in the western north Atlantic, *in* Vogt, P.R. and Tucholke, B.E. (Editors), The Geology of North America, Volume M: the Western North Atlantic Region, Geological Society of America, p. 479-490.

Evans, D., Harrison, Z., Shannon, P.M., Laberg, J.S., Nielsen, T., Ayers, S., Holmes, R., Hoult, R.J., Lindberg, B., Haflidason, H., Long, D., Kuijpers, A., Andersen, E.S., and Bryn, P., 2005, Paleoslides and other mass failures of Pliocene to Pleistocene age along the Atlantic continental margin of NW Europe: *Marine and Petroleum Geology*, *v. 22*, p. 1131-1148.

Fisher, M.A., Normark, W.R., Greene, H.G., Lee, H.J., and Sliter, R.W., 2005, Geology and tsunamigenic potential of submarine landslides in Santa Barbara Channel, southern California: *Marine Geology*, *v. 224*, p. 1-22.

Flood, R.D., Hollister, C.D., and Lonsdale, P., 1979, Disruption of the Feni sediment drift by debris flows from Rockall Bank: *Marine Geology*, *v. 32*, p. 311-334.

Folger D.W. and Hathaway, J.C., 1986, Conference on Continental Margin Mass Wasting and Pleistocene Sea-Level Changes, August 13-15, 1980: USGS Circular 961, 133 pp.

Fryer, G.J., P. Watts, and L.F. Pratson, 2004: Source of the great tsunami of 1 April 1946: A landslide in the upper Aleutian forearc: *Marine Geology*, *v. 203*, p. 201-218.

Gee, M.J.R., Masson, D.G., Watts, A.B. and Allen, P.A., 1999, The Saharan debris flow: an insight into the mechanics of long runout submarine debris flows: *Sedimentology*, *v. 46*, p. 317-335.

Gisler, G., Weaver, R., and Gittings, M.L., 2006, SAGE calculations of the tsunami threat from La Palma: *Science of Tsunami Hazards*, *v. 24*, p. 288-301.

Goff, J., Dudley, W.C., deMaintenon, M.J., Cain, G., and Coney, J.P., 2006, The largest local tsunami in 20th century Hawaii: *Marine Geology*, *v. 226*, p. 65-79.

Haflidason, H., Lien, R., Sejrup, H.P., Forsberg, C.F., and Bryn, P., 2005, The dating and morphometry of the Storegga slide: *Marine and Petroleum Geology*, *v. 22*. p. 123-136.

Haflidason, H., Sejrup, H.P., Nygard, A., Mienert, J., Bryn, P., Lien, R., Forsberg, C.F., Berg, K., and Masson, D., 2004, The Storegga slide; architecture, geometry and slide development: *Marine Geology*, *v. 213*, p. 201-234.

Hampton, M.A., Lee, H.J., and Locat, J., 1996, Submarine landslides: *Reviews of Geophysics*, *v. 34*, p. 33-59.

Heezen, B.C., Ericsson, D.B., Ewing, M., 1954, Further evidence of a turbidity current following the 1929 Grand Banks earthquake: *Deep Sea Research*, *v. 1*, p. 193-202.

Holmes, R., Long, D., and Doded, L.R., 1998, Large-scale debrities and submarine landslides on the Barra Fan, west of Britain, *in* Stoker, M.S., Evans, D. and Cramp, A. (Editors), Geological Processes on Continental Margins: Sedimentation, Mass-Wasting and Stability: *Geological Society, London, Special Publications*, *v. 129*, p. 67-79.

Hornbach, M.J., Lavier, L.L., and Ruppel, C.E., 2007, Active faulting coincident with the Cape Fear slide headwall: Implications for slope stability and tsunamis along the U.S. East Coast: Geological Society of America Abstracts with Programs, volume 39. 1, 83.

Huhnerbach, V., and Masson, D.G., 2004, Landslides in the North Atlantic and its adjacent seas: an analysis of their morphology, setting and behaviour: *Marine Geology*, *v. 213*, p. 343-362.

Hutton, E.W.H. and Syvitski, J.P.M., 2004, Advances in the numerical modeling of sediment failure during the development of a continental margin: *Marine Geology*, *v. 203*, p. 367-380.

Ingram, B.L. and Kennett, J.P., 1995, Radiocarbon chronology and planktonic-benthic foraminiferal ^{14}C age differences in Santa Barbara Basin sediments, Hole 893A, *in* Kennett, L.P., Baldauf, J.G., and Lyle, M. (Editors), Proceedings of the Ocean Drilling Program, Scientific Results 146 (Pt. 2), p. 19-27.

Jenner, K.A., Piper, D.J.W., Campbell, D.C., and Mosher, D.C., 2007, Lithofacies and origin of late Quaternary mass transport deposits in submarine canyons, central Scotian slope, Canada: *Sedimentology*, *v. 54*, p. 19-38.

Kayen, R.E. and Lee, H.J., 1992. Pleistocene slope instability of gas hydrate-laden sediment on the Beaufort Sea margin, in Lee, H.J. (Ed.), Special Issue on Marine Slope Stability, Marine Geotechnology 10, 125-142.

Krastel, S., Schmincke, H.-U., Jacobs, C.L., Rihm, R., Le Bas, T.P. and Alibes, B., 2001, Submarine landslides around the Canary Islands: *Journal of Geophysical Research*, *v. 106*, p. 3977-3997.

Laberg, J.S. and Vorren, T.O., 2000, The Traenadjupet slide, offshore Norway – morphology, evacuation and triggering mechanisms: *Marine Geology*, *v. 171*, p. 95-114.

Laberg, J.S., Vorren, T.O., Mienert, J., Evans, D., Lindberg, B., Ottesen, D., Kenyon, N.H., and Henriksen, S., 2002, Late Quaternary palaeoenvironment and chronology in the Traenadjupet slide area offshore Norway: *Marine Geology*, *v. 188*, p. 35-60.

Lastras, G., Canals, M., Urgeles, R., de Batist, M., Calafat, A.M. and Casamor, J.L., 2004, Characterisation of the recent BIG'95 debris flow deposit on the Ebro margin, Western Mediterranean Sea, after a variety of seismic reflection data, *Marine Geology*, *v. 213*, p. 235-255.

Lebreiro, S.M., McCave, N.I., and Weaver, P.P.E., 1997, Late Quaternary turbidite emplacement on the Horseshoe abyssal plain (Iberian Margin): *Journal of Sedimentary Research*, *v. 67*, p. 856-870.

Lee, H.J., Normark, W.R., Fisher, M.A., Greene, H.G., Edwards, B.D. and Locat, J., 2004, Timing and extent of submarine landslides in Southern California: Offshore Technology Conference proceedings, Houston TX, OTC Paper 16744, 11 pp.

Lee, H., Ryan, R.E., Haeussler, H., Kayen, R.E., Hampton, M.A., Locat, J., Suleimani, E. and Alexander, C.R., 2007, Reassessment of seismically induced tsunamigenic submarine slope failures in Port Valdez, Alaska, USA, *in* Lycousis, V., Sakellarion, D., and Locat, J. (Editors), Submarine Mass Movements and Their Consequences: Kluwer Academic Publishers, The Netherlands, p. 357-365.

Lee, H., Ryan, H., Kayen, R.E., Haeussler, P.J., Dartnell, P., and Hampton, M.A., 2006, Varieties of submarine failure morphologies of seismically-induced landslides in Alaskan fjords: *Norwegian Journal of Geology*, *v. 86*, p. 221-230.

Lindberg, B., Laberg, J.S. and Vorren, T.O., 2004, The Nyk Slide—morphology, progression, and age of a partly buried submarine slide offshore northern Norway: *Marine Geology*, *v. 213*, p. 277-289.

Lipman, P.W., Normark, W.R., Moore, J.G., Wilson, J.B.G., and Gutmacher, C.E., 1988, The giant submarine Alika debris slide, Mauna Loa, Hawaii: *Journal of Geophysical Research*, *v. 89*, p. 4279-4299.

Malahoff, A., Embley, R.W., and Perry, R.B., 1980, Submarine mass –wasting of sediments on the continental slope and upper rise south of Baltimore Canyon: *Earth and Planetary Science Letters*, *v. 49*, p. 1-7.

Maslin, M. and Mikkelsen, N., 1997, Amazon Fan mass-transport deposits and underlying interglacial deposits: age estimates and fan dynamics, *in* Flood, R.D., Piper, D.JW., Klaus, A., and Peterson (Editors), Proceedings of the Ocean Drilling Program, Scientific Results, volume 155, p. 353-365.

Maslin, M., Mikkelsen, N., Vilela, C., and Haq, B., 1998, Sea-level and gas-hydrate-controlled catastrophic sediment failures of the Amazon Fan: *Geology*, *v. 26*, p. 1107-1110.

Maslin, M., Owen, M., Day, S. and Long, D., 2004, Linking continental-slope failures and climate change: testing the clathrate gun hypothesis: *Geology*, *v. 32*, p. 53-56.

Masson, D.G., 1996, Catastropic collapse of the volcanic island of Hierro 15 ka ago and the history of landslides in the Canary Islands: *Geology*, *v. 24*, p. 231-234.

Masson, D.G., Watts, A.B., Gee, M.J.R., Urgeles, R., Mitchell, N.C., Le Bas, T.P. and Canals, M., 2002, Slope failures on the flanks of the western Canary Islands, *Earth-Science Reviews*, *v. 57*, p. 1-35.

McGregor, B.A, 1977, Geophysical assessment of submarine slide northeast of Wilmington Canyon: *Marine Geotechnology*, *v. 2*, p. 229-244.

McGregor, B.A. and Bennett, R.H., 1977, Continental slope instability northeast of Wilmington Canyon: *American Association of Petroleum Geologists Bulletin*, *v. 61*, p. 918-928.

McGuire, W.J., Howarth, R.J., Firth, C.R., Solow, A.R., Pullen, A.D., Saunders, S.J., Stewart, I.S. and Vita-Finzi, C., 1997, Correlation between rate of sea-level change and frequency of explosive volcanism in the Mediterranean: *Nature*, *v. 389*, p. 473-476.

McMurtry, G.M. and Herrero-Bervera, E., 2003, Dating of submarine landslides and their tsunami deposits using Hawaii as an example: American Geophysical Union Fall Meeting, Abstract OS314A-01.

Mienert, J. (Editor), 2004, COSTA-Continental slope stability: *Marine Geology*, *Special Issue*, *v. 213*, p. 1-497.

Moore, J.G., Clague, D.A., Holcomb, R.T., Lipman, P.W., Normark, W.R., Torresan, M.E., 1989, Prodigious submarine landslides on the Hawaiian Ridge: *Journal of Geophysical Research*, *v. 94* (B12), p. 17465-17484.

Mosher, D.C., Piper, D.J.W., Campbell, D.C. and Jenner, K.A., 2004, Near-surface geology and sediment-failure geohazards of the central Scotian Slope: *AAPG Bulletin*, *v. 88*, p. 703-723.

Normark, W.R. and Gutmacher, C.E., 1988, Sur submarine slide, Monterey Fan, central California: *Sedimentology*, *v. 35*, p. 629-647.

Normark, W.R., McGann, M. and Sliter, R.W., 2004, Age of Palos Verdes submarine debris avalanche, southern California: *Marine Geology*, *v. 203*, p. 247-259.

Normark, W.R., Moore, J.G., and Toresan, M.E., 1993, Giant volcano-related landslides and development of the Hawaiian Islands, *in* Schwab, W.C., Lee, H.J., and Twichell, D.C. (Editors), Submarine Landslides: Selected Studies in the U.S. EEZ: USGS Bulletin 2002, p. 184-196.

O'Leary, D.W., 1986, The Munson-Nygren slide: a major lower-slope slide off Georges Bank: *Marine Geology*, *v. 72*, p. 101-114.

O'Leary, D.W., 1993, Submarine mass movement, a formative process of passive continental margins: the Munson-Nygren landslide complex and the southeast New England landslide complex, *in* Schwab. W.C., Lee, H.J., and Twichell, D.C. (Editors), Submarine Landslides: Selected Studies in the U.S. EEZ: USGS Bulletin 2002, p. 23-39.

Paull, C.K., Buelow, W.J., Ussler, W., III, and Borowski, W.S., 1996, Increased continental-margin slumping frequency during sea-level lowstands above gas hydrate-bearing sediments: *Geology*, *v. 24*, p. 143-146.

Piper, D.J.W., Mosher, D.C., Gauley, B.-J., Jenner, K., and Campbell, D.C., 2003, The chronology and recurrence of submarine mass movements on the continental slope off southeastern Canada, *in* Locat, J., and Mienert (Editors), Submarine Mass Movements and their Consequences: Kluwer Academic Publishers, The Netherlands, p. 299-306.

Piper, D.J.W., Pirmez, C., Manley, P.L., Long, D., Flood, R.D., Normark, W.R., and Showers, W., 1997, Mass-transport deposits of the Amazon Fan, *in* Flood, R.D., Piper, D.JW., Klaus, A., and Peterson (Editors), Proceedings of the Ocean Drilling Program, Scientific Results, volume 155, p. 109-146.

Piper, D.J.W. and Skene, K.I., 1998, Latest Pleistocene ice-rafting events on the Scotian margin (eastern Canada) and their relationship to Heinrich events: *Paleoceanography*, *v. 13*, p. 205-214.

Popenoe, P., Schmuck, E.A., and Dillon, W.P., 1993, The Cape Fear landslide: slope failure associated with salt diapirism and gas hydrate decomposition, *in* Schwab. W.C., Lee, H.J., and Twichell, D.C. (Editors), Submarine Landslides: Selected Studies in the U.S. EEZ: USGS Bulletin 2002, p. 40-53.

Prior, D.G., Bornhold, B.D., Coleman, J.M, and Bryant, W.R., 1982, Morphology of a submarine slide, Kitimat Arm, British Columbia: *Geology*, *v. 10*, p. 588-592.

Prior, D.B., Doyle, E.H., and Neurauter, T., 1986, The Currituck slide, mid-Atlantic continental slope-revisited: *Marine Geology*, *v. 73*. p. 25-45.

Robb, J.M., Hampson, J.C., and Kirby, J.R., 1982, Surficial studies of the continental slope in the northern Baltimore Canyon Troough area—techniques and findings, Proceedings of the 14th Annual Offshore Technology Conference, paper OTC 4170.

Rodriguez, N.M. and Paull, C.K., 2000, Data Report: ^{14}C dating of sediment of the uppermost Cape Fear slide plain: constraints on the timing of this massive submarine landslide, *in* Paull, C.K., Matsumoto, R., Wallace, P.J., and Dillon, W.P. (Editors), Proceedings of the Ocean Drilling Program, Scientific Results, volume 164, p. 325-327.

Schmuck, E.A., and Paull, C.K., 1993, Evidence for gas accumulation associated with diapirism and gas hydrates at the head of the Cape Fear Slide: *Geo-Marine Letters*, *v. 13*, p. 145-152.

Seed, H.B., Seed, R.B., Schlosser, F., Blondeau, F., and Juran, I., 1988, The landslide at the Port of Nice on October 16, 1979: Earthquake Engineering Research Center (University of California, Berkeley), Report No. UCB/EERC-88/10, 68 pp.

Solheim, A., Bryn, P., Berg, K., Sejrup, H.P., and Mienert, J. (Editors), 2005, Ormen lange, An integrated study for the safe development of a deep-water gas field within the Storegga slide complex, NE Atlantic continental margin: *Marine and Petroleum Geology*, *Special Issue*, *v. 22*, nos. 1-2.

Syvitski, J.P.M., and Hutton, E.W.H., 2001, SEDFLUX 1.0C: An advanced process-response numerical model for the fill of marine sedimentary basins, *Computers and Geosciences*, *v. 27*, p. 731-754.

Tappin, D.R., Watts, P., and Matsumoto, T., 2003, Architecture and failure mechanism of the offshore slump responsible for the 1998 Papua New Guinea tsunami, *in* Locat, J., and Mienert (Editors), Submarine Mass Movements and their Consequences, Kluwer Academic Publishers, The Netherlands, p. 383-389.

Uchupi, E., 1967, Slumping on the continental margin southeast of Long Island, New York: *Deep-Sea Research*, *v. 14*, p. 635-639.

Uchupi, E., Driscoll, N., Ballard, R.D. and Bolmer, S.T., 2001, Drainage of late Wisconsin glacial lakes and the morphology and late quaternary stratigraphy of the New Jersey—southern New England continental shelf and slope: *Marine Geology*, *v. 172*, p. 117-145.

Urgeles, R., Canals, M., Baraza, J., Alonso, B. and Masson, D., 1997, The most recent megalandslides of the Canary Islands: El Golfo debris avalanche and Canary debris flow, west El Hiero Island: *Journal of Geophysical Research*, *v. 102*, B9, p. 20,305-20,323.

Urgeles, R., Masson, D.G., Canals, M., Watts, A.B. and Le Bas, T., 1999, Recurrent large-scale landsliding on the west flank of La Palma, Canary Islands: *Journal of Geophysical Research*, *v. 104*, B11, p. 25,331-25,348.

Van Weering, T., Nielsen, T., Kenyon, N.H., Akentieva, K., and Kulipers, A.H., 1998, Large submarine slides on the NE Faeroe continental margin, *in* Stoker, M.S., Evans, D. and Cramp, A. (Editors), Geological Processes on Continental Margins: Sedimentation, Mass-Wasting and Stability: *Geological Society, London, Special Publications*, *v. 129*, p. 5-17.

Ward, S.N., 2001, Landslide tsunami. *Journal of Geophysical Research*, *v. 106*, p. 11,201-11,215.

Ward, S.N. and Day, S., 2001, Cumbre Vieja Volcano – potential collapse and tsunami at La Palma, Canary Islands: *Geophysical Research Letters*, *v. 28*, p. 3397-3400.

Weaver, P.K., Wynn, R.B., Kenyon, N.H. and Evans, J., 2000, Continental margin sedimentation, with special reference to the north-east Atlantic margin: *Sedimentology*, *v. 47* (Supplement 1), p. 239-256.

Wilson, C.K., Long, D. and Bulat, J., 2004, The morphology, setting and processes of the Afen Slide: *Marine Geology*, *v. 213*, p. 149-167.

Chapter 14: Assessment of Source Probabilities for Potential Tsunamis Affecting the U.S. Atlantic Coast

Introduction

A probabilistic approach is the best method to fully assess the hazard posed by tsunamis for a wide range of sizes. Tsunami probability is calculated from the distribution of earthquake or landslide sizes and the recurrence distribution of events in time. For coastal locations that have a long record of tsunamis, the size distribution is best described as a power-law (Burroughs and Tebbens, 2005), similar to the distribution of many other natural hazards such as earthquakes, landslides, and forest fires (*e.g.*, Hergarten, 2002). In oceans such as the Pacific, tsunamigenic earthquakes from many different subduction zones influence tsunami probability at any given location because of the slowly attenuating nature of tsunamis during propagation over long distances. In the Atlantic Ocean, however, the number of tsunami source zones is much more limited. As such, it is unclear whether the size distribution and recurrence distribution of tsunamis along the U.S. Atlantic coast is similar in functional form to sites around the Pacific.

Because tsunami records along the Atlantic coast are sparse in both space and time, empirical approaches to define tsunami probabilities from, for example, tsunami catalogs are of limited use. In this study, we first describe the general framework for a computational approach to probabilistic tsunami hazard analysis (PTHA). We then focus on different approaches for determining source probabilities for both landslides and earthquakes and for both locally-generated and transoceanic tsunamis. Like tsunamis themselves, source probabilities are described by size and recurrence distributions. The applicable size parameter in this case is the primary source parameter for generating tsunamis. For earthquakes, this parameter is seismic moment m, where moment magnitude M_w is given by $M_w = (2/3)(\log(m) - 9.05)$, with secondary influence on tsunami generation from earthquake source depth and focal mechanism (*e.g.*, Okal, 1988; Ward, 1980). For landslides, the primary source parameter is volume V, although landslide thickness (which may not scale with volume), landslide speed, and submergence depth also significantly affects tsunami generation (*e.g.*, Fritz, 2006; Fritz *et al.*, 2004; Geist *et al.*, this volume; Grilli and Watts, 2005; Harbitz, 1992; Liu *et al.*, 2005;

Løvholt *et al.*, 2005; Lynett and Liu, 2002; Murty, 2003). Secondary parameters such as these can be determined from mobility analysis (*e.g.*, Locat *et al.*, this volume) or scaling relations, with their attendant uncertainty included directly into probabilistic calculations. In terms of the recurrence distribution, a common assumption is that the recurrence rate is independent of time and that inter-event times are uncorrelated because source zones are physically uncorrelated. In statistical terms, this is the temporal description of a Poisson process. In addition to assessing the size distribution for tsunami sources, we briefly review evidence to determine whether earthquakes and landslides behave as a Poisson process.

General Framework of Probabilistic Tsunami Hazard Analysis (PTHA)

Probabilistic tsunami hazard analysis (PTHA) (Geist and Parsons, 2006; Geist *et al.*, in press) is directly derived from probabilistic seismic hazard analysis (PSHA) (Senior Seismic Hazard Analysis Committee (SSHAC), 1997) with some significant modifications. Like PSHA, there are essentially three steps involved: (1) define the source parameters, including source probabilities for all relevant tsunami sources; (2) calculate wave heights and other hydrodynamic parameters for each source; and (3) aggregate the results to determine the tsunami hazard curve for a particular coastal site or the probabilistic inundation map for a particular coastal region. The source parameters specified in step (1) are those that directly relate to the volume of water displaced during a submarine earthquake or landslide. These include primary geologic parameters such as the moment magnitude (M_w) of the earthquake or volume (V) of the landslide, as well as secondary source parameters such as landslide thickness and speed and the water depth above the source. Unlike PSHA, sources at much larger distances are considered for PTHA, because of the slowly-attenuating propagation characteristics of tsunami waves. As a notable example of the far-traveled nature of tsunamis, the M_w 9.2 2004 Sumatra-Andaman earthquake along the Sunda subduction zone in the Indian Ocean resulted in small tsunami amplitudes recorded along the U.S. Atlantic coast (Titov *et al.*, 2005).

Step (2) in PTHA can be implemented using numerical models and the known bathymetry of the world's ocean. For PSHA, in contrast, step (2) linking the source and site is often implemented using empirical and stochastic attenuation relationships (and their attendant uncertainty). Because the horizontal dimensions of seafloor deformation near the tsunami source are typically much greater than the water depth, tsunami propagation is modeled using the shallow-water or long-wave equations (Liu, 2008). For landslide tsunamis, however, high-order hydrodynamic equations that incorporate dispersion and non-linearity are often necessary (Lynett and Liu, 2002). These equations can be implemented using finite-difference or finite-element methods and accurately simulate many aspects of wave propagation, such as focusing, dispersion, shoaling amplification, etc. As tsunami waves approach shore and inundate coastal regions, the hydrodynamics become

considerably more complex (Imamura, 2008; Yeh, 2008). Inundation models need to account for non-linearity in wave propagation, bottom friction, turbulence, and other site specific factors. The size of a tsunami at a particular coastal location can be measured by the amplitude (*amp*) of the offshore wave (determined from propagation models) or more accurately, by runup (R), which is the water level height above ambient sea level at the point of farthest onshore inundation (determined from inundation models).

To calculate the probability that a tsunami with runup greater than a specified minimum value (R_0) will occur at a coastal location for an exposure time T (step 3 in PTHA), it is first necessary to know the distribution of recurrence times. Most often, an exponential distribution that is associated with a Poisson process is assumed such that

$$P(R > R_0, T) = 1 - e^{-\lambda T} \quad (1)$$

where P is the probability that one or more tsunamis with $R>R_0$ will occur in time T, and λ is the rate at which these tsunamis occur. To test whether or not tsunamis are best described by a Poisson process, Geist and Parsons (2008) examine the distribution of inter-event times from the National Geophysical Data Center (NGDC) global tsunami catalog (`http://www.ngdc.noaa.gov/hazard/tsu_db.shtml`). Results indicate that the observed distribution deviates from that expected for a Poisson process at short recurrence times, indicative of a temporal clustering effect that is also observed for earthquake inter-event times (Corral, 2004). Therefore, the hazard rate increases slightly immediately after an event, but is otherwise that of a Poisson process.

The equation to calculate the Poisson rate (λ) at which tsunamis will exceed a certain runup (R_0) at a coastal location from all relevant sources is

$$\lambda(R > R_0) = \sum_{\text{type}=i} \sum_{\text{zone}=j} \nu_{ij} \int P(R > R_0 \mid \psi_{ij}) f(\psi_{ij}) d\psi, \quad (2)$$

where the index i refers to the type of tsunami source (*e.g.*, i=1 for earthquakes, i=2 for landslides, etc.), index j identifies the zone in which that source occurs (according to some particular zonation scheme), $\nu_{i,j}$ the mean rate for each source (i,j) where $R>R_0$, $\psi_{i,j}$ is the tsunami source parameters for source (i,j) (Ward, 2001), f_ψ is the probability distribution for tsunami source parameters, and $P(R > R_0 \mid \psi_{ij})$ is the probability that runup will exceed R_0 at the coastal location for a given source parameter or set of source parameters (Geist *et al.*, in press). The propagation distance and other propagation factors such as ray path are implicitly included in the term $P(R > R_0 \mid \psi_{ij})$ since this term is computed by numerical propagation models (step 2). In the absence of any uncertainty, this term is simply $1 - H(R)$ for a given set of source parameters, where H is the Heaviside step function. For earthquakes, the primary source parameter is seismic moment m such that $f(\psi_{1j})$ is the size distribution $f(m_j)$, whereas for landslides it is volume V

such that $f(\psi_{2j}) = f(V_j)$. Other source parameters can be included in the probabilistic analysis through the f_{ψ} term, although size (*i.e.*, seismic moment or volume) distributions are best constrained by the available data. Secondary parameters such as slip distribution (earthquakes) and landslide time history can alternatively be included as sources of uncertainty in the $P(R > R_0 \mid \psi_{ij})$ term (Geist *et al.*, in press) as described below. This method can be expanded from just examining runup (R) as the hazard variable to producing probabilistic tsunami inundation maps in which wave height and damage metrics are the hazard variables, as discussed in the Seaside, Oregon, Tsunami Pilot Study (Tsunami Pilot Study Working Group, 2006).

An graphic example of how probabilities are aggregated at a particular coastal location is shown in Figure 14-1. For this simple case, three source zones are included: two seismogenic zones (i=1, j=1,2) generating transoceanic tsunamis and one landslide zone (i=2, j=1) generating local tsunamis. Zonation for the landslides is primary geographic in this example, based on observed occurrence and distance to the coastal location. More sophisticated zonation schemes can be developed based on geologic factors described by Lee (this volume) and Chaytor *et al.* (this volume). Zonation for earthquakes in this example is according to plate boundary type (Bird and Kagan, 2004). Source probabilities are given by the rate term ν_{ij} and the size distribution $f(m_j)$ or $f(V_j)$.

If tsunami sources behave in a time dependent manner (either clustered in time or as a quasiperiodic process), then an aggregation equation other than equation (2) needs to be used. The tsunami probability during time T corresponding to each of N sources is calculated and aggregated according to the following equation (Rikitake and Aida, 1988; Ward, 1994):

$$P(R \geq R_0 \mid T) = 1 - \prod_{j=1}^{N} \left[1 - P(R \geq R_0 \mid \psi_j, T) \right]. \qquad (3)$$

In this case, the set of source parameters ψ_{ij} includes the parameters for the source recurrence distribution.

In the next two sections (3 and 4), we will examine methods to determine the probabilities for both earthquake and landslide tsunami sources, respectively. This includes methods to determine the size distribution f_{ψ}, overall rate ν_{ij}, and where possible, whether or not earthquakes and landslides are adequately described by a Poisson process in terms of their recurrence distribution.

Earthquake Tsunamis

In this section, we review different approaches to define the parameters for earthquake size distributions $f(m_j)$. We first focus on earthquake zones in the Caribbean and eastern Atlantic that can potentially generate transoceanic

tsunamis and then examine the possibility of seismogenic tsunamis generated locally to the U.S. Atlantic coastline.

Transoceanic seismogenic tsunamis

For transoceanic tsunamis, seismic moment is the controlling source parameter that determines tsunami amplitude with other parameters having a secondary effect (Abe, 1995; Okal, 1988; Pelayo and Wiens, 1992; Titov *et al.*, 2001). In addition, because only large earthquakes (M_w approximately greater than 8) will result in significant tsunami amplitudes in the far-field, we can focus our attention on earthquakes that occur along plate boundaries, particularly subduction zones and oceanic convergent boundaries (as defined by Bird, 2003). Accordingly, source probabilities can be based on previous statistical work defining seismic moment and recurrence distributions along plate boundaries (Bird and Kagan, 2004; Kagan, 1997).

Subduction zone boundaries

The Caribbean subduction zone extending from Hispaniola in the west through the Lesser Antilles Islands in the east is the closest plate boundary to the U.S. Atlantic coast along which transoceanic tsunamis can be generated (Figure 14-1). Tsunamis generated from large earthquakes along other plate boundary zones in the Caribbean, for example along the northern Venezuela subduction zone and the northern Panama oceanic convergent zone (Bird, 2003) (Figure 14-1), are greatly attenuated and scattered as they propagate northward through the Greater Antilles Islands (Knight, 2006), but may result in small tsunami amplitudes at the U.S. Atlantic coast. Most of the historic locally damaging tsunamis recorded along the Greater Antilles segment of the Caribbean subduction zone have been generated by intra-plate events, both along transverse structures such as the Mona rift and back arc structures such as the Muertos and Anegada troughs. Exceptions are the 1946 M~8 Hispaniola interplate thrust earthquake and subsequent events (Dolan and Wald, 1998; Doser *et al.*, 2005; ten Brink and Lin, 2004). The low rate of subduction earthquakes along this segment can be linked to the highly oblique relative plate motion and slow convergence rates.

The standard Gutenberg-Richter size distribution (G-R) for earthquakes is a power-law magnitude-frequency relationship: $\log \nu(M_w) = a - bM_w$, where ν is the rate of earthquakes $\geq M_w$. The tail of the distribution at large sizes is specified in one of two ways: using a sharp truncation specified by a maximum seismic moment m_{max} or using a gradual taper using a corner moment m_{cm} (Kagan, 2002a) as described below. For the former, the size distribution $f(m)$ in equation (2) is given by the truncated G-R distribution:

$$f(m) = \beta \frac{(m_{\max} m_t)^{\beta}}{m_{\max}^{\beta} - m_t^{\beta}} m^{-(1+\beta)}, \quad m_t \leq m \leq m_{\max}, \quad (4)$$

where m_t is a minimum threshold moment and the power-law exponent $\beta = \frac{2}{3}b$. A similar size distribution with a hard maximum cutoff is specified for tsunamis themselves based on historic data by Burroughs and Tebbens (2005). The maximum moment m_{max} is determined from knowledge of the fault geometry, physical properties, and rupture kinematics such that for a planar fault in an isotropic Earth with no variation in rake

$$m_{\max} = \int_{\Sigma} \mu u_s d\Sigma, \tag{5}$$

where μ is the shear modulus and u_s is the static slip for the largest event integrated over the maximum fault area Σ. This is often simplified by using spatial averages of shear modulus ($\overline{\mu}$) and static slip ($\overline{u}_s$) for the largest earthquake such that

$$m_{\max} = \overline{\mu}\,\overline{u}_s \Sigma. \tag{6}$$

Unfortunately, there is significant uncertainty in a parametric approach such as this to determine m_{max}, owing to strong variations in physical properties and kinematics as indicated by past earthquake inversion studies. Often, moment is estimated from scaling relationships with source dimensions (*e.g.*, Mai and Beroza, 2000), rather than using a purely parametric approach. Maximum moment can also be determined from past seismicity as discussed by Kijko (2004). A similar type of distribution is the one in where a large "characteristic" earthquake is identified separately from the background G-R distribution (Wesnousky, 1994). It is unlikely that any of the plate boundary faults in the Atlantic have enough dated paleoseismic horizons to make a statistically meaningful estimate of characteristic magnitude or recurrence (cf., Geist *et al.*, in press).

A size distribution based on a "soft" corner moment (m_{cm}) is an alternative to the truncated distribution (equation 4) that is more consistent with the available empirical data and with the physics of extreme earthquakes (Kagan, 2002a; Sornette and Sornette, 1999). An example of this type of distribution model that has been fit to global subduction zone seismicity is the tapered G-R distribution (Bird and Kagan, 2004; Kagan, 2002a; Kagan and Jackson, 2000; Vere-Jones *et al.*, 2001):

$$\Phi(m) = \left(\frac{m_t}{m}\right)^{\beta} \exp\left(\frac{m_t - m}{m_{cm}}\right), \quad m_t \le m, \tag{7}$$

where $\Phi(m)$ is the survivor function ($\Phi(m)$ = 1-$F(m)$; $F(m)$ is the cumulative distribution of $f(m)$). The two distribution parameters, β and corner moment m_{cm} are estimated by Kagan (1997; 2002a; b) and Bird and Kagan (2004) from the historic earthquake catalog using a maximium log-likelihood method. The difference between the two studies is the way earthquakes are grouped together (*i.e.*, the zonation index j used in this chapter): Kagan (2002a; b) analyzes seismicity based on different geographic

zonation schemes, whereas Kagan (1997) and Bird and Kagan (2004) group events together based on common plate boundary types. Using the Harvard CMT catalog, the corner moment magnitude M_{cm} = 8.76±0.65 and β = 0.93±0.43 for the Lesser Antilles subduction zone (Kagan, 2002b), with the high uncertainty related to the sparse number of events in this region. For global subduction zones using a 20th century earthquake catalog, M_{cm} = $9.58^{+0.48}_{-0.46}$ and β = 0.64±0.04 (Bird and Kagan, 2004).

Unlike the size distribution $f(m_j)$, the rate term υ_{1j} in equation (2) that is proportional to the seismic moment rate $\dot{M}_t$ varies substantially among subduction zones, depending principally on relative plate convergence rate and seismic coupling (Bird and Kagan, 2004; Kagan, 2002b; Kreemer *et al.*, 2002; McCaffrey, 1994). The rate term can be related to the seismic moment rate ($\dot{M}_{s(j)}$) for size distributions indicated in equations (4) and (7), respectively, as described by Kagan (2002b) (cf., McCaffrey, 1994):

$$\upsilon_j(m) = \frac{(1-\beta)\dot{M}_{s(j)}\left(m_{\max}^{\beta} - m^{\beta}\right)}{\beta m^{\beta} m_{\max}} \qquad (8)$$

and

$$\upsilon_j(m) = \frac{(1-\beta)\dot{M}_{s(j)}}{m^{\beta} m_{cm}^{1-\beta}\Gamma(2-\beta)e^{m/m_{cm}}}, \qquad (9)$$

where Γ is the gamma function. The "tectonic" moment rate ($\dot{M}_{t(j)}$) is given by

$$\dot{M}_{t(j)} = \mu_j L_j W_j \dot{S}_j, \qquad (10)$$

where μ is the shear modulus, L is the length of the fault zone, W is the width of the seismogenic part of the fault zone, and $\dot{S}$ is the long-term slip rate along the fault determined from geodetic and plate motion studies (McCaffrey, 1994; Ward, 1994). It should be noted that there is a strong depth dependence in μ for subduction zones (Bilek and Lay, 1999), such that the value used in equation (10) is an average over the entire zone. $\dot{M}_s$ and $\dot{M}_t$ are related by a seismic coupling parameter ($0 \le \chi \le 1$): $\dot{M}_s = \chi \dot{M}_t$. For a fault that has no aseismic slip at seismogenic depths, χ=1. For the Caribbean subduction zone, $\dot{M}_s$ is more than an order of magnitude less than $\dot{M}_t$ (4.0×10^{18}Nm/yr compared to $49. \times 10^{18}$ Nm/yr) (Kagan, 2002b), suggesting that either χ is very low or that the historic catalog is under-sampled, particularly with respect to large magnitude earthquakes that dominate estimates of $\dot{M}_s$ (cf., Parsons and Geist, in review). Compounding this discrepancy, Caribbean subduction zone slip rates may be considerably higher than the NUVEL-1A (DeMets *et al.*, 1994) plate rate model used by Kagan (2002b). For example, Dixon *et al.* (1998) and DeMets *et al.* (2000)

calculated a Caribbean plate rate of 21±1 mm/yr and 18-20±3 mm/yr , respectively, from GPS measurements, nearly twice the NUVEL-1A estimate of 11±3 mm/yr.

A comparison of several different frequency-magnitude distributions for the Caribbean subduction zone using the tectonic moment rate derived from regional slip rates and a seismic coupling parameter χ=1 is shown in Figure 14-2. For the truncated G-R distribution (equation 4), a maximum 1100 km fault length was assumed (from Hispaniola to the Caribbean-N. America-S. America triple junction) and three different methods were considered to determine M_{max}. The light solid line represents moment-length scaling (Mai and Beroza, 2000), the short-dashed line moment-area scaling (Wyss, 1979), and the long-dashed line a parametric approach with $\overline{\mu}$=30 GPa and $\overline{u}_s$=9 m (equation 6). The heavy solid line represents the tapered G-R distribution (equation 7) with the maximum-likelihood estimate for M_{cm} from the Bird and Kagan (2004) study. (It should be noted that this study also provides 95% confidence interval estimates for M_{cm}) For a higher M_{max} or M_{cm}, the overall activity (*a*-value) has to decrease to balance the overall moment rate.

For a given source size, the probability that runup will exceed R_0 at a coastal location for source parameters ψ_{ij} is given by the term $P(R > R_0 \mid \psi_{ij})$ in equation 2. Shown in Figure 14-3, for example, is the maximum tsunami wavefield from a M_w~9 earthquake along the Caribbean subduction zone computed using a finite-difference approximation to the linear long-wave propagation equations. Details of the tsunami generation and propagation methods used to construct Figure 14-3 are described in Geist (2002) and Geist *et al.* (2007). To determine the uncertainty from different slip distribution patterns $u(x,y)$ during earthquake rupture on tsunami amplitude, $P_{M=9}(amp > amp_0 \mid u(x,y))$ was calculated for two points offshore the U.S. Atlantic coast spaced 230 km apart, where maximum offshore amplitude (*amp*) is used as the hazard variable rather than runup (*R*) (Figure 14-4). The histograms for each site show the maximum amplitude from 100 different slip distributions. Uncertainty caused by this source parameter can be approximated by a normal distribution (green line), though in some cases (*e.g.*, Point B in Figure 14-4) the distribution of wave amplitudes is multi-modal. The exceedance probability $P_{M=9}(amp > amp_0 \mid u(x,y))$ varies significantly between the two points shown, owing to wave propagation—particularly the waveguide effect of the Blake Ridge (Figure 14-1). Multiple sources of uncertainties in evaluating $P(R > R_0 \mid \psi_{ij})$ can be accommodated using Monte Carlo techniques (Geist and Parsons, 2006).

Finally, the recurrence distribution for subduction zone earthquakes most closely follows an exponential distribution (equation 1), with some exceptions. Several studies (Kagan and Jackson, 1991; 1995; Rong *et al.*, 2003) test the seismic gap hypothesis based on time-dependent recurrence against a Poisson null hypothesis related to the exponential distribution of recurrence times and found that in most cases the Poisson null hypothesis passed most of the statistical tests. Clustering of earthquakes in time as characterized by greater number of short inter-event times than expected

from an exponential distribution is evident in most global earthquake catalogs. This is usually attributed to aftershocks and other triggered earthquakes (Parsons, 2002) and has been explained using a negative binomial distribution (Kagan and Jackson, 2000) or a gamma distribution (Corral, 2004).

Non-subduction zone boundaries

Other non-subduction zone boundaries in the Atlantic where tsunamigenic earthquakes can occur include the Azores-Gibraltar oceanic convergence boundary (Figure 14-1). It was here that the 1755 and 1761 Lisbon earthquakes generated transoceanic tsunamis recorded in the Lesser Antilles Islands (Baptista, 2006; O'Loughlin and Lander, 2003). This boundary is structurally complex with convergence in the eastern part indicated from deformation modeling (Jiménez-Munt *et al.*, 2001) and the mechanism of the M_w =7.8, 1969 Cape St. Vincent (Portugal) earthquake (Fukao, 1973). Sources for the tsunamis in this zone include the Gorringe Bank faults and the shallow, eastward dipping thrust faults in the Horseshoe abyssal plain and the Gulf of Cadiz (Baptista *et al.*, 2003; Gjevik *et al.*, 1997; Gràcia *et al.*, 2003; Gutscher *et al.*, 2006; Terrinha *et al.*, 2003; Thiebot and Gutscher, 2006; Zitellini *et al.*, 2004). The geometry of the fault zone and its position relative to mid-ocean topographic features that scatter tsunami energy have important controls on tsunami amplitudes along the U.S. Atlantic coast (Barkan *et al.*, this volume). Although there is insufficient seismic activity along this zone to determine the seismic moment distribution, for oceanic convergent zones on a global basis, $M_{cm} = 8.04^{+0.52}_{-0.22}$ and $\beta = 0.53 \pm 0.13$ (Bird and Kagan, 2004). Determination of M_{ma} for the truncated G-R size distribution would entail determining the interaction of the different fault strands that make up this plate boundary (cf., Ward, 1997).

Gutscher *et al.* (2006) indicate that for a 1 cm/yr convergence rate, an event similar to the M_w 8.6-8.8 1755 earthquake would occur with a mean return time of 1000-2000 years. This estimate may be on the low side, as recent GPS surveys indicate lower convergence rates, ranging from 1 to 5 mm/yr (Fernandes *et al.*, 2003; Nocquet and Calais, 2004). Using the lower convergence rate and a tapered G-R distribution results in a much higher mean return time for an event like the 1755 earthquake (Figure 14-5), though there is significant uncertainty in magnitude distributions for OCB boundaries. This demonstrates the critical effect that corner moment and plate-rate estimates have on estimating seismogenic tsunami source probabilities.

Mid-ocean spreading ridges, such as the mid-Atlantic ridge, are unlikely to generated transoceanic tsunamis because of a low corner magnitude $M_{cm} = 5.82 \pm 0.07$ (Bird *et al.*, 2002). Oceanic transform faults have a higher corner magnitude, but because there is little vertical displacement associated with strike-slip earthquakes, tsunamis emanating from theses fault zones are typically very small.

Local tsunamigenic earthquakes

In addition to earthquakes generating transoceanic tsunamis, it is possible that offshore earthquakes within the North American plate may generate local tsunamis. Seismicity is broadly distributed along the U.S. Atlantic coast and not concentrated on identified fault zones (Kafka, 2002; Kafka and Levin, 2000). Compared with active tectonic margins, which are often dominated seismically by one-to-several faults, earthquake magnitudes and rates of seismicity are significantly smaller along the passive margin of the eastern U.S. In this region, recent seismicity is relatively greater along the northern Atlantic seaboard than the southern (with the exception of the 1886 Charleston earthquake and aftershocks), as are strain rates determined from seismic and GPS observations (Anderson, 1986; Gan and Prescott, 2001). This in turn can be linked to isostatic rebound following glaciation in the north as well as overall differences in the crustal structure between the two regions (Wheeler, 1996). Kafkin and Levin (2000) suggest that the broad seismicity patterns defined by small earthquakes tend to delineate where large earthquakes may occur. In addition, Ebel and Kafka (2002) indicate that earthquakes are more clustered in time than predicted by a Poisson process.

The size distribution for this region based on past seismicity patterns (Frankel, 1995; Frankel *et al.*, 1996; Frankel *et al.*, 2002; Wheeler and Frankel, 2000) has been described using a truncated Gutenberg-Richter distribution where the moment rate and power-law exponent (β) are determined from gridded and smoothed seismicity. In these studies, the G-R distribution is truncated (in the cumulative form of the distribution) at M_W=7.5. As an alternative, one may choose a smooth taper using distributions described, for example, by Kagan (2002a). Like transoceanic tsunamis, estimating the tail of the distribution becomes a critical issue for calculating local tsunami probabilities, since only earthquakes of M_W > 6.5-7.0 generate significant local tsunami amplitudes (Geist, 1999).

The studies indicated above were designed for assessing onshore seismic hazard and were not intended to extend offshore (Frankel *et al.*, 1996). A persistent problem in determining the rates of seismicity in the offshore region (υ_{1j}) is catalog completeness. Mazzotti and Adams (2005) address this problem offshore eastern Canada by comparing different zonation schemes based either on patterns of historic seismicity or on geologic and tectonic boundaries. For the latter model, they indicate relatively high seismic moment rates along the eastern continental margin where the 1929 Grand Banks earthquake occurred. Analysis of seismicity can be combined with geodetic studies (*e.g.*, Gan and Prescott, 2001) to help reduce the uncertainty in estimating the rate of earthquake activity. ten Brink *et al.* (this volume) estimates a wide range of return times (600-3,000 years) for M_W > 7.0 earthquakes using the available data and analyses. In terms of seismic moment rates, the maximum rate in the coastal region estimated by Gan and Prescott (2001) is approximately 6×10^{16} Nm/yr, *i.e.* several orders of magnitude less that the $\sim10^{20}$ Nm/yr rate for the Caribbean subduction zone.

Although earthquake magnitude is the primary source parameter, other parameters such as average slip, fault mechanism, and focal depth also significantly affect local tsunami amplitudes (Geist, 1999). Stress drops associated with intra-plate earthquakes, particularly in the eastern U.S., are variable but do not indicate a distinct scaling relationship with seismic moment relative to western U.S. earthquakes (Hartzell *et al.*, 1994; Somerville *et al.*, 1987). Most focal solutions for eastern North American earthquakes indicate a predominantly near horizontal axis of compression with a mixture of reverse, strike slip, or composite mechanisms (Bent, 1995; Du *et al.*, 2003; Hartzell *et al.*, 1994; Mazzotti and Adams, 2005). Focal depths are typically shallow for U.S. events (2-8 km) and slightly deeper for Canadian events (5-28 km) (Du *et al.*, 2003).

Landslide Tsunamis

Like submarine earthquakes, only large landslides can potentially generated significant tsunamis. Although we focus on submarine landslides here, it should be recognized that subaerial landslides can generate impact tsunami with dramatic runup in the near field (Fritz, 2006; Fritz *et al.*, 2001). In contrast to submarine earthquakes, submarine landslide probabilities are more difficult to determine because a lack of an instrumental catalog of occurrence. From the NGDC global tsunami catalog, less than 10% of all tsunamis are estimated to have a landslide-generation component, though observations of landslide sources are likely to be incomplete. Recent marine geophysical surveys have helped define the volume distribution of landslides in specific regions (Booth *et al.*, 1993; Chaytor *et al.*, this volume), but the lack of a complete catalog of age dates for individual landslides precludes accurate assessment of the recurrence distribution and overall activity rate υ_{2j}. One advantage over earthquake tsunami sources is that landslide probabilities typically only have to be determined for sources local to the coastal location, rather than throughout an entire ocean basin. Although the largest landslides may generate transoceanic tsunamis of significant amplitude, recent studies (*e.g.*, Gisler *et al.*, 2006 for the Canary Islands landslide tsunami) indicate that non-linear and dispersive effects greatly attenuate tsunami energy at far-field distances in comparison to seismogenic tsunamis.

Empirical methods

Empirical methods to determine the source rate term υ_{2j} or the recurrence distribution of offshore landslides have primarily been hampered by a lack of age dates. As an initial hypothesis, we can assume that the recurrence distribution is that of a Poisson process, although an initial study of onshore landslides in Italy (Rossi *et al.*, 2007) suggests that landslides are more clustered in time than predicted by an exponential distribution (1). Clustering of terrestrial landslides may result in part from climatic conditions and/or seismic triggers (*e.g.*, Chleborad, 1997; Kang and Wang, 1995; Trauth *et al.*, 2003): processes that may influence temporal distributions of submarine

landslides as well. As such, nearshore processes might depart from a Poisson process at short inter-event times . Given a minimum number of landslide ages, we may be able to adapt recently developed methods to establish source probabilities from observed, uncertain event times for earthquakes (Ogata, 1999; Parsons, 2008) to landslide probabilities if the form of the inter-event distribution can be assumed and some temporal record exists.

It should be noted that results described by Maslin *et al.* (2004) and Lee (this volume) suggests that the long-term recurrence rate of landslides may be dependent on glacial cycles. For the U.S. and Canadian Atlantic margin, Lee (this volume) indicates dates for two of the largest landslides: the Cape Fear landslide (9-14.5 kyr) and the Currituck landslide (25-50 kyr) (Figure 14-1). From the available age dates, relatively few landslides occur in more recent times (*i.e*, >5,000 years after the end of glaciation). The tsunamigenic 1929 Grand Banks landslide (Piper *et al.*, 1999) is a notable exception. Lee (this volume) estimates that the rate of landslide occurrence during the last 5,000 yrs. is 2.5-3.5 times less than during the last glacial, deglaciation period. Therefore, over 10's of thousands of years the distribution of landslide occurrence times is likely that of a non-stationary Poisson process such that the rate term υ_{2j}, decreases with time since the last glacial period. Adapting either Ogata's (1999) Bayesian inference approach or Parsons' (2008) Monte Carlo approach to landslide probabilities would require, therefore, that the inter-event distribution class for which parameter estimation is conducted be non-stationary.

Statistical studies of onshore landslides have indicated that the size distribution is essentially a power law over a large range of volumes ($f(V_j)$ in equation 2 above). Taking into account very small and very large volumes, more complex size distributions that span the observed range of volumes are described by a number of authors (Chaytor *et al.*, this volume; Dussauge *et al.*, 2003; Guzzetti *et al.*, 2002; Malamud *et al.*, 2004; Stark and Hovius, 2001).The origin of power-law scaling appears to require a state variable that results in a long-term, time-weakening effect (Hergarten, 2003; Hergarten and Neugebauer, 1998), arising from, for example, strain softening, creep, and pore pressure redistribution. In addition, it appears that the power-law exponent of the distribution is dependent on the type of failure (*e.g.*, rock fall, slump, etc.) and the lithology of the failed material (Dussauge *et al.*, 2003; Malamud *et al.*, 2004). In the offshore region, examination of landslides north of Puerto Rico have established that landslide volumes (V) also follow a power-law relationship, with an exponent similar to that observed for onshore rock falls (ten Brink *et al.*, 2006).

Link to earthquake ground motions

Because the majority of (but not all) tsunamigenic landslides are triggered by earthquakes (Bardet *et al.*, 2003), landslide probabilities can also be inferred from earthquake ground motions and a slope stability model as an alternative to a direct empirical approach. From an earthquake scenario-based mode, Jibson *et al.* (2000) shows that if the topography, geology, shear strength and

seismic shaking for a given earthquake are known, then one can determine the probability of failure over a certain region. Shear strength is likely one of the greatest unknowns, particularly in the marine environment where direct tests over a given region may be limited. More generally, landslide probabilities can be linked to probabilistic ground motions based on a distribution of earthquake magnitudes. We can think of the probability that a landslide of a certain size will occur (P_V) in terms of the probability of the triggering event E (*i.e.*, seismic ground motion above a certain level: $P(E)$) and the conditional, time-dependent probability of threshold or preparatory conditions leading to an outcome O of slope failure (cf., Lee *et al.*, 2001):

$$P_V = P(E)P(O \mid E,t) \qquad (8)$$

Threshold conditions would include slope angle, shear strength, groundwater flow conditions, sediment load, gas hydrate dissociation, etc. (Biscontin and Pestana, 2006; Biscontin *et al.*, 2004; Lee, this volume; Locat and Lee, 2002; Maslin *et al.*, 2004) . $P(E)$ can be determined straightforwardly from PSHA, using an appropriate spectral acceleration relative to the thickness of the near surface layer that can fail (Biscontin and Pestana, 2006; Biscontin *et al.*, 2004). The probability $P(O \mid E)$, however, would have to be computed using a complex event tree in which the uncertainties are likely to be large. For example Wright and Rathje (2003) and Biscontin et al (2004) indicates that the nature of pore-pressure redistribution following an earthquake that can cause delayed initiation of a failure is related to the physical properties of the near surface layer. Hence, the preparatory conditions for landslide failure are likely to be time dependent as indicate in equation (8).

This problem can be simplified by using empirical relationships between earthquake magnitude and ensemble landslide statistics such as total area or volume, maximum distance to failure, etc. (Keefer, 1994; 2002). ten Brink *et al.* (this volume) adapts this type of approach to determine the minimum magnitude and maximum distance from the continental shelf edge for earthquakes to trigger landslides of tsunamigenic size. That study indicates that the width of a potential landslide hazard zone is dependent on the magnitude of the earthquake. The rate at which landslides above a certain volume occur along the continental slope can then be tied to the rate of earthquake occurrence within the zone where triggering may occur. Although there are large uncertainties with this approach, it is a useful way to estimate the rate of landslide occurrence until more age dates become available.

Discussion

Comparative analysis of different tsunami sources

Assessment of source probabilities for tsunamis affecting the U.S Atlantic coast yield comparative information with which to better define the scope of

the hazard. For example, the mean return time for M_w>8.0 earthquakes that potentially can generate transoceanic tsunamis along the Caribbean subduction zone (Figure 14-2) is greater than that along Azores-Gibraltar convergence zone (Figure 14-5). If we use source rates for each of these zones of $\sim 2.5 \times 10^{-3}$ yr^{-1} and $\sim 1.0 \times 10^{-3}$ yr^{-1} respectively, then the mean return time of a tsunami exceeding $R_0(M_w>8.0)$ (where, R_0 is the minimum runup from either of the two source zones) is ~285 years. For M_w>8.5 earthquakes along these two source zones, and considering the significant uncertainty in the size distribution for the Azores-Gibraltar convergence zone, the mean return time of a tsunami exceeding $R_0(M_w>8.5)$ is 800-1,000 years. Because runup scales directly with seismic moment, $R_0(M_w>8.5)$ will typically be greater than $R_0(M_w>8.0)$.

In comparison to the previous example, the few available age dates of large landslides that might generate tsunamis local to the northern U.S. Atlantic coast suggest that the mean rate is ~10^{-4} yr^{-1}, with higher rates along the Canadian Atlantic coast (Lee, this volume). As indicated by Lee (this volume), the mean rate may be decreasing with time since the last glacial period. It should be stressed, however, that there are currently few age dates for landslides along the Atlantic margin, such that the observed rate may be biased (undersampled). Even so, there is likely little contribution from landslide tsunamis according to the aggregation equation (2), if one were concerned about tsunamis occurring at, for example, an annual probability of P=0.005 (*i.e.*, a 200-year return time tsunami). This is consistent with the overall low incidence of landslides tsunamis from the global historic catalog. The mean return time for local seismogenic sources (M_w>7) in the northern U.S. Atlantic coast is 600-3000 years (ten Brink *et al.*, this volume) and thus may span the mean recurrence rates of transoceanic sources and local landslide sources.

Uncertainties

For an accurate tsunami probabilistic assessment, however, there is still significant uncertainty in these source probabilities. Probabilistic methods accommodate model and parameter uncertainty by classifying them as either epistemic (uncertainty that will decrease with the acquisition of additional data) or aleatory (natural or stochastic uncertainty) (Toro *et al.*, 1997). Examples of epistemic uncertainty alluded to in this study include different methods to determine M_{ma} (Figure 14-2a), different estimates of the seismic coupling parameter χ, and different estimates of fault slip rates. Epistemic uncertainty is typically accommodated in PTHA through the use of logic trees (*e.g.*, Geist and Parsons, 2006) or a Bayesian weighting scheme (Parsons and Geist, in review). Examples of aleatory uncertainty include slip distribution (Figure 14-4) and tidal stage at the time of tsunami arrival (Mofjeld *et al.*, 2007). Aleatory uncertainty is typically accommodated by integration in the $P(R > R_0 \mid \psi_{ij})$ term in equation 2 (Geist *et al.*, in press). Special considerations need to be taken in probabilistic methods when

different sources of uncertainty are dependent on one another (Page and Carlson, 2006).

For tsunamis affecting the U.S. Atlantic coast, the greatest uncertainty is associated with landslide probabilities. Not only is there little information on the shape of the recurrence distribution, but even information on the overall mean rate of occurrence is lacking because of few available age dates. There are statistical methods to estimate recurrence rates from sparse and uncertain data (Ogata, 1999; Parsons, 2008). These techniques have been designed for estimating earthquake recurrence rates using paleoseismic horizons associated with a range of age dates. Similarly, these techniques can be applied to landslides, once a range of age dates is obtained from strata above and below a landslide geologic unit (Lee, 2005).

Future directions

In contrast to determining landslide recurrence rates, determining the size distribution for landslides is currently a tractable problem. Modern marine geophysical methods and GIS tools permit a fairly accurate determination of landslide volumes over broad reaches of seafloor (Chaytor, this volume). Moreover, recent advances in modeling the dynamics and mobility of submarine landslides (Imran *et al.*, 2001; Locat *et al.*, this volume; Locat *et al.*, 2004) permit a reasonable determination of landslide motion—a significant parameter affecting tsunami generation (Brandshaw *et al.*, 2007; Grilli and Watts, 2005; Harbitz, 1992; Løvholt *et al.*, 2005; Ward, 2001). Development of tsunami models that explicitly solve for landslide and wave dynamics as part of a coupled system will provide even more accurate estimates of wave heights and runup.

For earthquakes, although the earthquake catalog for the Caribbean subduction zone and the Azores-Gibraltar oceanic convergence zone is sparse and incomplete, seismic moment rate can be inferred from tectonic motions and geodetically determined fault slip rates. In addition, the parameters for the size distribution can be estimated using global earthquakes specific to different plate boundaries as performed by Kagan (1997) and Bird and Kagan (2004). However, generation of transoceanic tsunamis occurs for earthquakes of large magnitude ($M_w \geq 8$) and is therefore sensitive to the shape of the size distribution tail and corner moment magnitude M_{cm} as indicated in Figures 14-2 and 14-5. Further work is needed to better constrain these parameters, especially for oceanic convergent boundaries. In terms of the recurrence distribution, whereas the exponential distribution associated with a Poisson process is a good first approximation, there appear to be cases of time-dependency which may also affect tsunami probability calculations.

Conclusions

Because of the sparse record of tsunamis along the U.S. Atlantic coast, tsunami probability needs to be determined from a computational PTHA

approach, rather than using only empirical methods based on tsunami catalogs. Key ingredients in the computational approach are the probability distribution of tsunami source sizes and source recurrence. For the most frequent source of tsunamis, earthquakes along subduction and oceanic convergent plate boundaries in the Atlantic, the shape of these distributions can be inferred from studies of global seismicity (*e.g.*, Bird and Kagan, 2004). For other less frequent sources of local tsunamis, including offshore intra-plate earthquakes and landslides, it is more difficult to determine the size and inter-event distribution because of a lack of recorded events and the geographically distributed nature of these events. For landslides, the size distributions and overall rate of occurrence can be determined from the available sparse age dates in combination with global comparison of potentially tsunamigenic landslides (*e.g.*, Lee, this volume), and through an association with triggering earthquakes (*e.g.*, ten Brink *et al.*, this volume).

The highest rate of earthquake activity that could produce transoceanic tsunamis in the Atlantic occur along Caribbean subduction zone and Azores-Gibraltar oceanic convergence zones. For $M_{w\geq}$8.0 earthquakes, for example, rates along the Caribbean subduction zone are approximately 2.5 times that for the Azores-Gibraltar oceanic convergence zone, with an aggregate return time of ~285 years for transoceanic tsunamis. For $M_{w\geq}$8.5 earthquakes, the rate along the Caribbean subduction zone is at least 5 times greater than that for the Azores-Gibraltar oceanic convergence zone, resulting in an aggregate return time of ~800-1,000 years. Local landslide tsunamis, may occur at rates approximately an order of magnitude less than for transoceanic tsunamis, although there are few age dates of submarine landslides to validate this estimate. In terms of the recurrence distribution, deviations from the standard Poisson assumption for source inter-event times include clustering for earthquake sources and non-stationarity for landslide sources. There is currently a high level of uncertainty associated with tsunami probabilities in the Atlantic that can be improved with the acquisition of additional marine geologic and geophysical data and further statistical analyses.

Figures

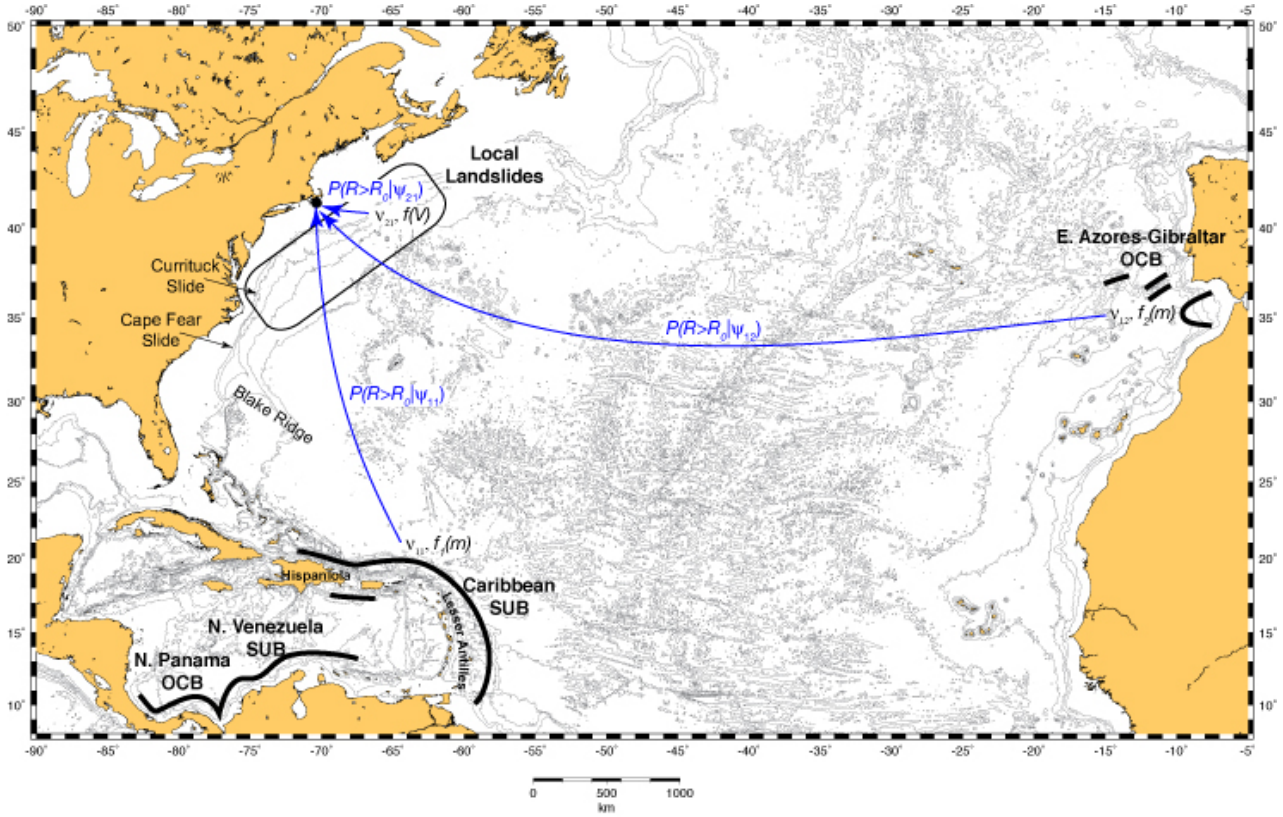

Figure 14-1: Schematic diagram of how tsunami probabilities are aggregated for a particular coastal location. Two types of sources (earthquakes and landslides: index i = 1, 2, respectively) are indicated. Each source is associated with a particular zonation scheme (index j). For landslides in this example, zonation is geographic, whereas for earthquakes the zonation is according to plate boundary type and location.

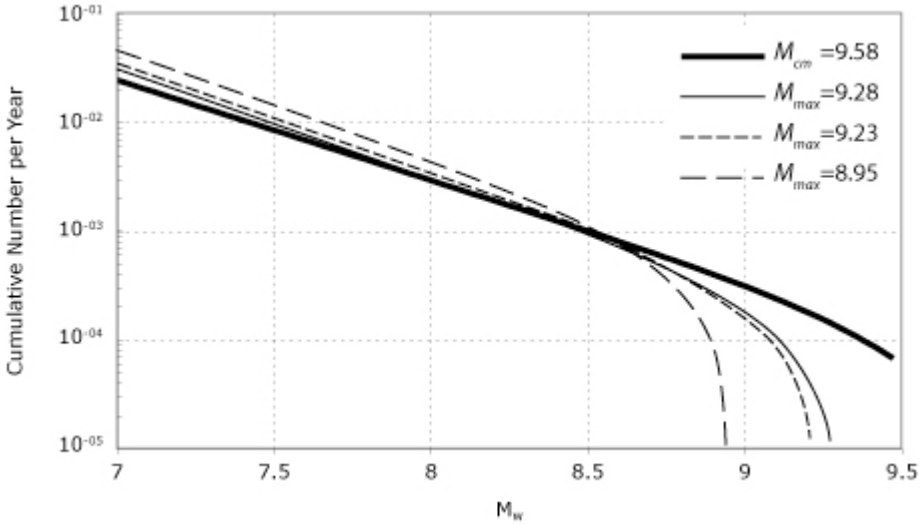

Figure 14-2: Comparison of size distributions for earthquakes along the Caribbean subduction zone (Greater Antilles segment). In each case, tectonic moment rates and complete coupling ($\chi = 1$) are used. Truncated G-R distributions computed using three different method to determine M_{max} and a constant rupture length of 1100 km: moment-length scaling (light solid); moment-area scaling (short dashed); parametric (long dashed). Heavy solid line represents tapered G-R distribution with a maximum-likelihood estimate for M_{cm} from the global earthquake catalog (Bird and Kagan, 2004).

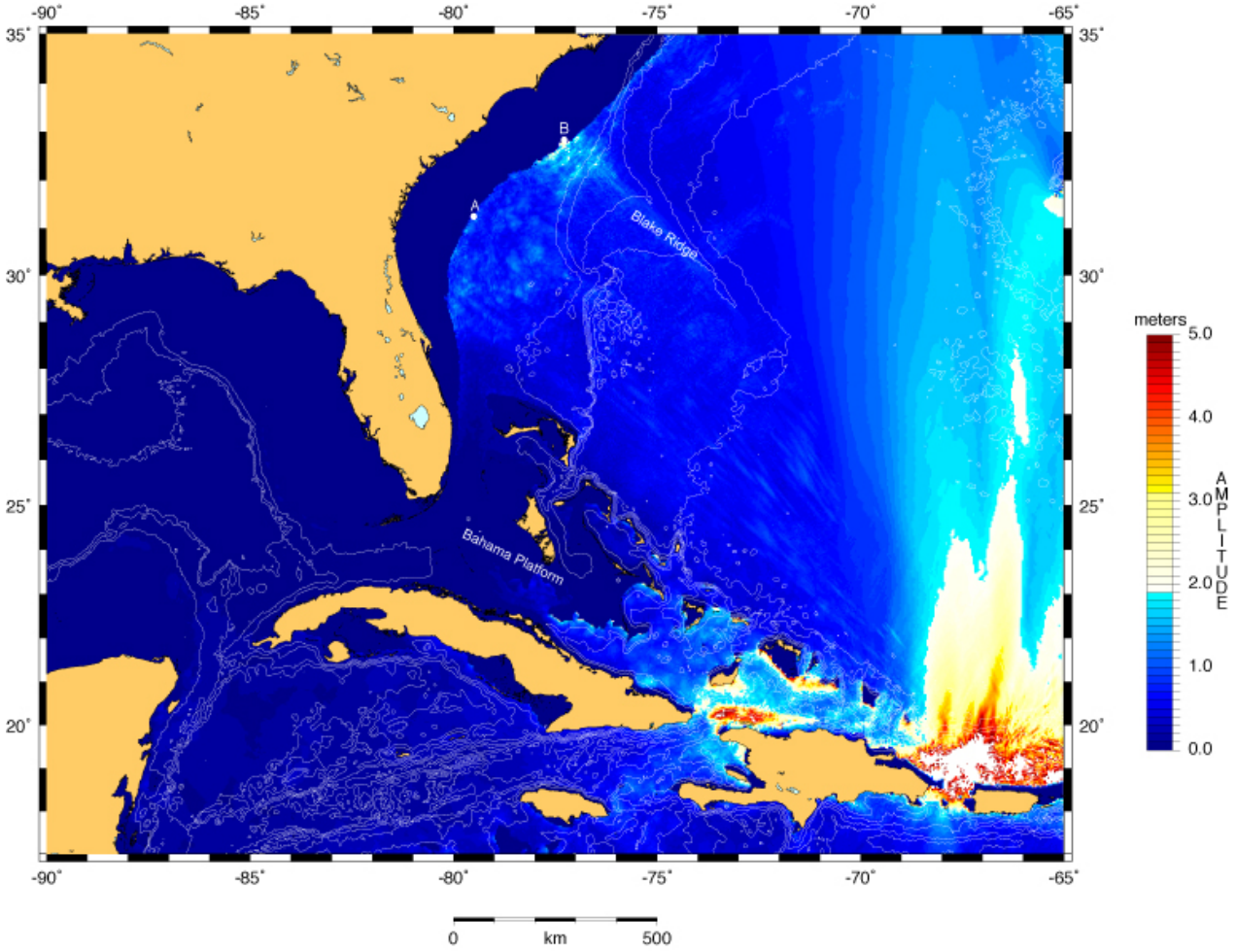

Figure 14-3: Example of maximum tsunami amplitude during 4.4 hours of total propagation time for a *M*~9 earthquake on the Caribbean subduction zone. Tsunami beaming is apparent along an azimuth perpendicular to strike, although the Blake Ridge acts as a waveguide to locally focus tsunami energy. Points A and B discussed in Figure 14-4 shown for reference.

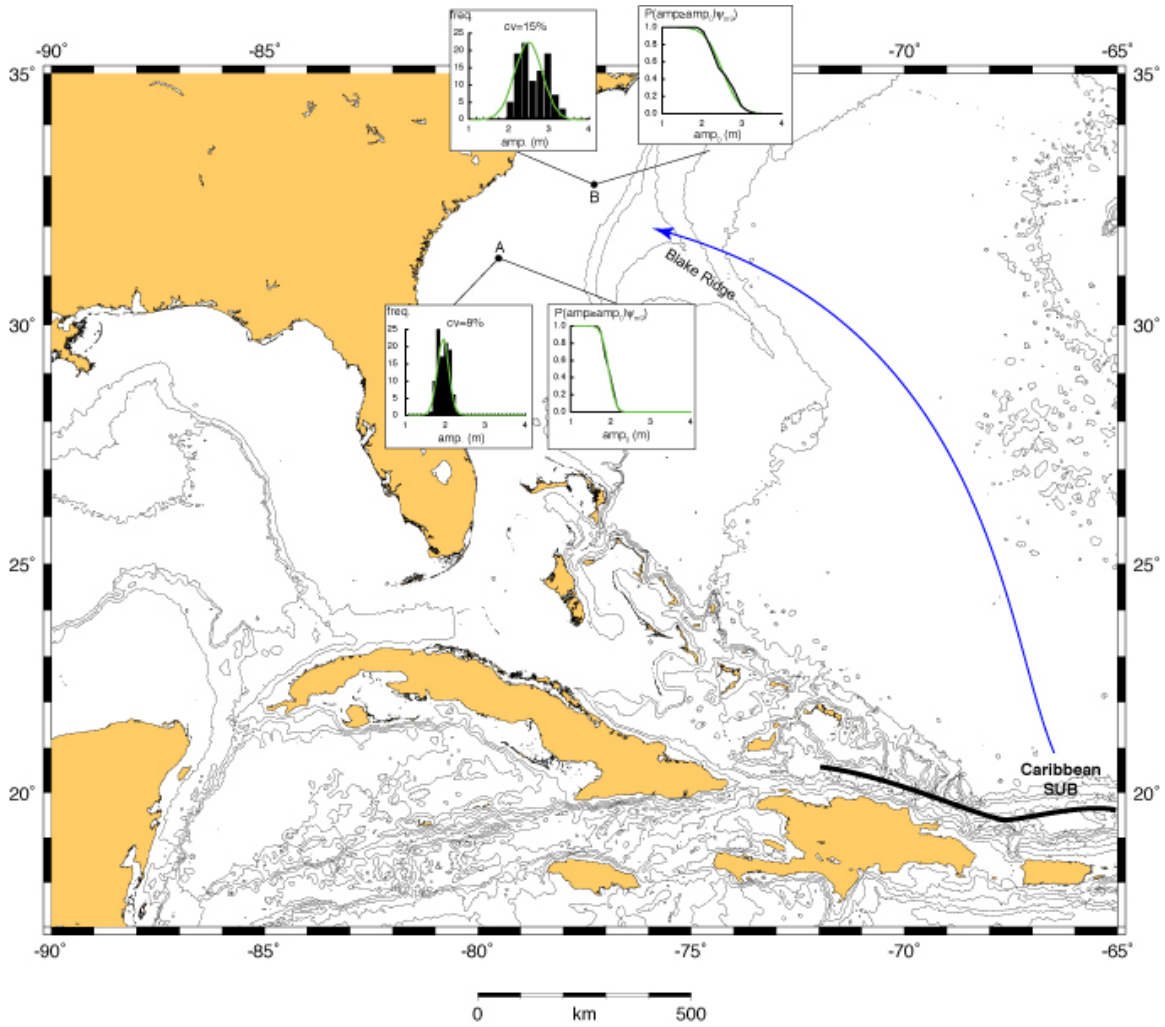

Figure 14-4: Examples of the probability that tsunami amplitude will exceeded a given value $P(amp \geq amp_0 \mid \psi_{M\,9})$, for 2 different sites (A and B) along the Atlantic coast and the same *M*~9 earthquake along the Caribbean subduction zone. Left plot: histogram of amplitude values as a results of varying slip distribution patterns for the source earthquake (cv-coefficient of variation). Green line represents normal distribution approximation. Right: Probability of exceeding amplitude value amp_0 using the histogram values (black line) and the normal distribution approximation (green line).

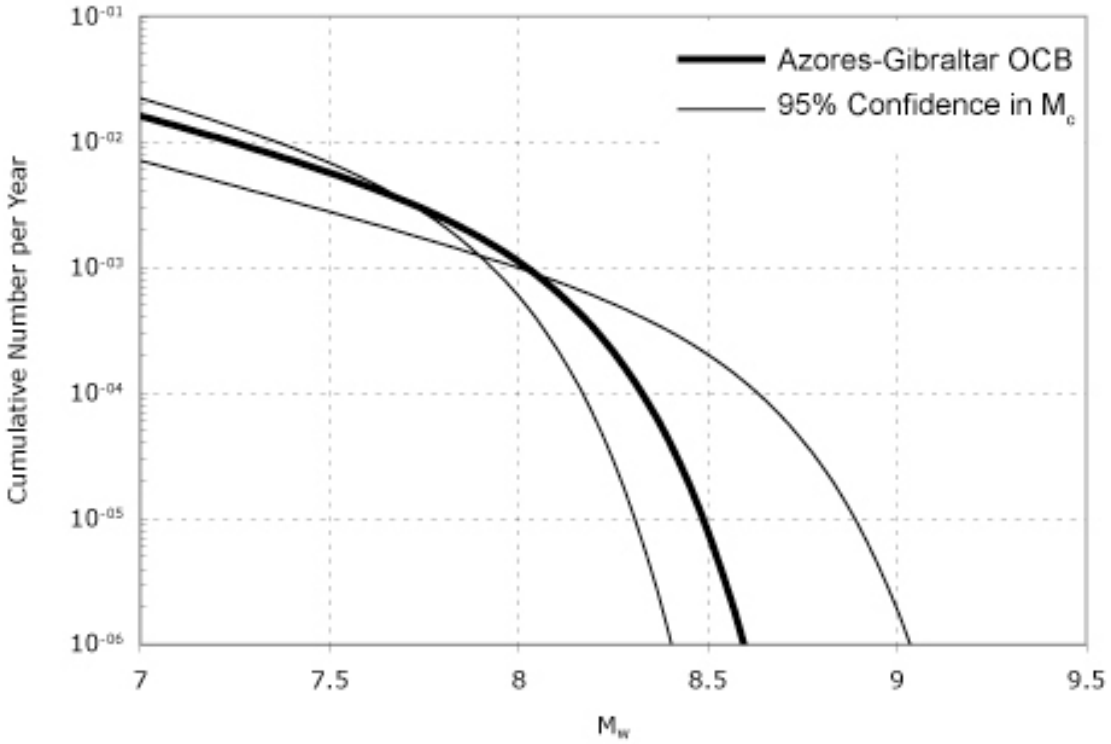

Figure 14-5: Comparison of size distributions for earthquakes along the Azores-Gibraltar oceanic convergence boundary. Size distributions were computed using tectonic moment rates and distribution shape parameters from Bird and Kagan (2004). Heavy line represents tapered G-R distribution with a maximum-likelihood estimate for M_c from the global earthquake catalog; thin lines represent distributions for 95% confidence interval in M_c (Bird and Kagan, 2004).

References

Abe, K., 1995, Estimate of tsunami run-up heights from earthquake magnitudes. In: Y. Tsuchiya and N. Shuto (Editors), Tsunami: Progress in Prediction, Disaster Prevention and Warning: Kluwer Academic Publishers, Dordrecht, p. 21-35.

Anderson, J.G., 1986,. Seismic strain rates in the central and eastern United States: *Bulletin of the Seismological Society of America*, *v. 76*, p. 273-290.

Baptista, M.A., 2006, In search of the 31 March 1761 earthquake and tsunami source: *Bulletin of the Seismological Society of America*, *v. 96*, p. 713-721.

Baptista, M.A., Miranda, J.M., Chierici, F. and Zitellini, N., 2003, New study of the 1755 earthquake source based on multi-channel seismic survey data and tsunami modeling: *Natural Hazards and Earth System Sciences*, *v. 3*, p. 333-340.

Bardet, J.-P., Synolakis, C.E., Davies, H.L., Imamura, F. and Okal, E.A., 2003, Landslide tsunamis: Recent findings and research directions: *Pure and Applied Geophysics*, *v. 160*, p. 1793-1809.

Barkan, R., ten Brink, U.S. and Lin, J., this volume, The source of the 1755 Lisbon earthquake: Implications for tsunami hazard to the U.S. Atlantic coast.

Bent, A.L., 1995, A complex double-couple source mechanism for the Ms 7.2 1929 Grand Banks earthquake: *Bulletin of the Seismological Society of America*, *v. 85*, p. 1003-1020.

Bilek, S.L. and Lay, T., 1999, Rigidity variations with depth along interplate megathrust faults in subduction zones: *Nature*, *v. 400*, p. 443-446.

Bird, P., 2003, An updated digital model of plate boundaries: *Geochemistry, Geophysics, Geosystems*, *v. 4*: doi:10.1029/ 2001GC000252.

Bird, P. and Kagan, Y.Y., 2004, Plate-tectonic analysis of shallow seismicity: apparent boundary width, beta-value, corner magnitude, coupled lithosphere thickness, and coupling in 7 tectonic settings: *Bulletin of the Seismological Society of America*, *v. 94*, p. 2380-2399.

Bird, P., Kagan, Y.Y. and Jackson, D.D., 2002, Plate tectonics and earthquake potential of spreading ridges and oceanic transform faults, *in* S. Stein and J.T. Freymueller (Editors), Plate Boundary Zones: American Geophysical Union, Geodynamic Series, Washington, D.C., p. 203-218.

Biscontin, G. and Pestana, J.M., 2006, Factors affecting seismic response of submarine slopes: *Natural Hazards and Earth System Sciences*, *v. 6*, p. 97-107.

Biscontin, G., Pestana, J.M. and Nadim, F., 2004, Seismic triggering of submarine slides in soft cohesive soil deposits: *Marine Geology*, *v. 203*, p. 341-354.

Booth, J.S., O'Leary, D.W., Popenoe, P. and Danforth, W.W., 1993, U.S. Atlantic continental slope landslides: Their distribution, general attributes, and implications, *in* W.C. Schwab, H.J. Lee and D.C. Twichell (Editors), Submarine Landslides: Selected Studies in the U.S. Exclusive Economic Zone: U.S. Geological Survey Bulletin 2002, p. 14-22.

Brandshaw, A.S., Baxter, C.D.P., Taylor, O.-D.S. and Grilli, S.T., 2007, Role of soil behavior on the initial kinematics of tsunamigenic slides, *in* V. Lykousis, D. Sakellariou and J. Locat (Editors), Submarine Mass Movements and Their Consequences. Springer, p. 387-394.

Burroughs, S.M. and Tebbens, S.F., 2005, Power law scaling and probabilistic forecasting of tsunami runup heights: *Pure and Applied Geophysics*, *v. 162*, p. 331-342.

Chaytor, J.D., ten Brink, U.S., Solow, A.R. and Andrews, B.D., this volume, Size distribution of submarine landslides along the U.S. Atlantic Margin and its implication to tsunami hazards.

Chleborad, A.F., 1997, Temperature, snowmelt, and the onset of spring season landslides in the central Rocky Mountains: U.S. Geological Survey Open-File Report 97-27, 18 pp.

Corral, A., 2004, Long-term clustering, scaling, and universality in the temporal occurrence of earthquakes: *Physical Review Letters*, *v. 92*, doi: 10.1103/ PhysRevLett.92.108501.

DeMets, C., Gordon, R.G., Argus, D.F. and Stein, S., 1994, Effect of recent revisions to the geomagnetic reversal time scale on estimates of current plate motions: *Geophysical Research Letters*, *v. 21*, p. 2191-2194.

DeMets, C. *et al.*, 2000, GPS geodetic constraints on Caribbean-North America plate motion: *Geophysical Research Letters*, *v. 27*, p. 437-440.

Dixon, T.H. *et al.*, 1998, Relative motion between the Caribbean and North American plates and related boundary zone deformation from a decade

of GPS observations: *Journal of Geophysical Research*, *v. 103*, p. 15,157-15,182.

Dolan, J.F. and Wald, D.J., 1998, The 1943-1953 north-central Caribbean earthquakes: Active tectonicc setting, seismic hazards, and implications for Caribbean-North America plate motions, *in* J.F. Dolan and P. Mann (Editors), Active Strike-Slip and Collisional Tectonics of the Northern Caribbean Plate Boundary Zone: *Geological Society of America, Special Paper 326*, Boulder, Colorado, p. 143-169.

Doser, D.I., Rodriguez, C.M. and Flores, C., 2005, Historical earthquakes of the Puerto Rico-Virgin Islands region (1915-1963), *in* P. Mann (Editor), Active tectonics and seismic hazards of Puerto Rico, the Virgin Islands, and offshore areas: *Geological Society of America, Special Paper 385*, Boulder, Colorado, p. 103-114.

Du, W.-X., Kim, W.-Y. and Sykes, L.R., 2003, Earthquake source parameters and state of stress for the northeastern United States and southeastern Canada from analysis of regional seismograms: *Bulletin of the Seismological Society of America*, *v. 93*, p. 1633-1648.

Dussauge, C., Grasso, J.R. and Helmstetter, A., 2003, Statistical analysis of rockfall volume distributions: Implications for rockfall dynamics: *Journal of Geophysical Research*, *v. 108*, doi:10.1029/ 2001JB000650.

Ebel, J.E. and Kafka, A.L., 2002, A non-Poissonian element in the seismicity of the northeastern United States: *Bulletin of the Seismological Society of America*, *v. 92*, p. 2040-2046.

Fernandes, R.M.S., Ambrosius, B.A.C. and Noomen, R., 2003, The relative motion between Africa and Eurasia as derived from the ITRF2000 and GPS data: *Geophysical Research Letters*, *v. 30*, doi:10.1029/ 2003GL017089.

Frankel, A.D., 1995, Mapping seismic hazard in the central and eastern United States: *Seismological Research Letters*, *v. 66*, p. 8-21.

Frankel, A.D. *et al.*, 1996, National seismic-hazard maps: Documentation June 1996. 96-532: U.S. Geological Survey, 41 pp.

Frankel, A.D. *et al.*, 2002, Documentation for the 2002 Update of the National Seismic Hazard Maps. 02-420: U.S. Geological Survey, 33 pp.

Fritz, H.M., 2006, Physical modeling of landslide generated tsunami, *in* A. Mercado and P.L.F. Liu (Editors), Caribbean Tsunami Hazard: World Scientific Publishing Co., Singapore, p. 308-324.

Fritz, H.M., Hager, W.H. and Minor, H.E., 2001, Lituya Bay case: rockslide impact and wave run-up: *Science of Tsunami Hazards*, *v. 19*, p. 3-22.

Fritz, H.M., Hager, W.H. and Minor, H.E., 2004, Near field characteristics of landslide generated impulse waves: *Journal of Waterway, Port, Coastal, and Ocean Engineering*, *v. 130*, p. 287-302.

Fukao, Y., 1973, Thrust faulting at a lithospheric plate boundary: The Portugal earthquake of 1969: *Earth and Planetary Science Letters*, *v. 18*, p. 205-216.

Gan, W. and Prescott, W.H., 2001, Crustal deformation rates in central and eastern U.S. inferred from GPS: *Geophysical Research Letters*, *v. 28*, p. 3733-3736.

Geist, E.L., 1999, Local tsunamis and earthquake source parameters: *Advances in Geophysics*, *v. 39*, p. 117-209.

Geist, E.L., 2002, Complex earthquake rupture and local tsunamis: *Journal of Geophysical Research*, *v. 10*7, doi:10.1029/ 2000JB000139.

Geist, E.L., Lynett, P.J. and Chaytor, J.D., this volume. Hydrodynamic modeling of tsunamis from the Currituck landslide.

Geist, E.L. and Parsons, T., 2006, Probabilistic analysis of tsunami hazards: *Natural Hazards*, *v. 37*, p. 277-314.

Geist, E.L. and Parsons, T., 2008, Distribution of tsunami inter-event times: *Geophysical Research Letters*, *v. 35*, L02612, doi:101029/ 2007GL032690.

Geist, E.L., Parsons, T., ten Brink, U.S. and Lee, H.J., in press, Tsunami Probability, *in* E.N. Bernard and A.R. Robinson (Editors), The Sea: Harvard University Press, Cambridge, Massachusetts.

Geist, E.L., Titov, V.V., Arcas, D., Pollitz, F.F. and Bilek, S.L., 2007, Implications of the December 26, 2004 Sumatra-Andaman earthquake on tsunami forecast and assessment models for great subduction zone earthquakes: *Bulletin of the Seismological Society of America*, *v. 97*, p. S249-S270.

Gisler, G., Weaver, R. and Gittings, M.L., 2006, SAGE calculations of the tsunami threat from La Palma: *Science of Tsunami Hazards*, *v. 24*, p. 288-301.

Gjevik, B. *et al.*, 1997, Modeling tsunamis from earthquake sources near Gorringe Bank southwest of Portugal: *Journal of Geophysical Research*, *v. 102*, p. 27,931-27,949.

Gràcia, E., Dañobeitia, J., Vergés, J. and PARSIFAL Team, 2003, Mapping active faults offshore Portugal (36°N-38°N): Implications for seismic hazard assessment along the southwest Iberian margin: *Geology*, *v. 31*, p. 83-86.

Grilli, S.T. and Watts, P., 2005, Tsunami generation by submarine mass failure. I: Modeling, experimental validation, and sensitivity analyses: *Journal of Waterway, Port, Coastal, and Ocean Engineering*, *v. 13*1, p. 283-297.

Gutscher, M.-A., Baptista, M.A. and Miranda, J.M., 2006, The Gibralter Arc seismogenic zone (part 2): Constraints on a shallow east dipping fault plane source for the 1755 Lisbon earthquakes provided by tsunami modeling and seismic intensity: *Tectonophysics*, *v. 426*, p. 153-166.

Guzzetti, F., Malamud, B.D., Turcotte, D.L. and Reichenbach, P., 2002, Power-law correlations of landslide areas in central Italy: *Earth and Planetary Science Letters*, *v. 195*, p. 169-183.

Harbitz, C.B., 1992, Model simulations of tsunamis generated by the Storegga slides: *Marine Geology*, *v. 105*, p. 1-21.

Hartzell, S.H., Langer, C. and Mendoza, C., 1994, Rupture histories of eastern North American earthquakes: *Bulletin of the Seismological Society of America*, *v. 84*, p. 1703-1724.

Hergarten, S., 2002, Self-Organized Criticality in Earth Systems: Springer, Berlin, 272 pp.

Hergarten, S., 2003, Landslides, sandpiles, and self-organized criticality: *Natural Hazards and Earth System Sciences*, *v. 3*, p. 505-514.

Hergarten, S. and Neugebauer, H.J., 1998, Self-organized criticality in a landslide model: *Geophysical Research Letters*, *v. 25*, p. 801-804.

Imamura, F., 2008, Tsunami modeling - inundation, *in* A.R. Robinson and E.N. Bernard (Editors), The Sea: Harvard University Press, Cambridge, Massachusetts.

Imran, J., Parker, G., Locat, J. and Lee, H., 2001, A 1-D numerical model of muddy subaqueous and subaerial debris flows: *Journal of Hydraulic Engineering*, *v. 127*, p. 959-958.

Jibson, R.W., Harp, E.L. and Michael, J.A., 2000, A method for producing digital probabilistic seismic landslide hazard maps: *Engineering Geology*, *v. 58*, p. 271-289.

Jiménez-Munt, I., Fernàndez, M., Torne, M. and Bird, P., 2001, The transition from linear to diffuse plate boundary in the Azores-Gibraltar region: results from a thin-sheet model: *Earth and Planetary Science Letters*, *v. 192*, p. 175-189.

Kafka, A.L., 2002, Statistical analysis of the hypothesis that seismicity delineates areas where future large earthquakes are likely to occur in the central and eastern United States: *Seismological Research Letters*, *v. 73*, p. 992-1003.

Kafka, A.L. and Levin, S.Z., 2000, Does the spatial distribution of smaller earthquakes delineate areas where larger earthquakes are likely to occur?: *Bulletin of the Seismological Society of America*, *v. 90*, p. 724-738.

Kagan, Y.Y., 1997, Seismic moment-frequency relation for shallow earthquakes: Regional comparison: *Journal of Geophysical Research*, *v. 102*, p. 2835-2852.

Kagan, Y.Y., 2002a, Seismic moment distribution revisited: I. Statistical Results: *Geophysical Journal International*, *v. 148*, p. 520-541.

Kagan, Y.Y., 2002b, Seismic moment distribution revisited: II. Moment conservation principle: *Geophysical Journal International*, *v. 149*, p. 731-754.

Kagan, Y.Y. and Jackson, D.D., 1991, Seismic gap hypothesis: Ten years after: *Journal of Geophysical Research*, *v. 96*, p. 21,419-21,431.

Kagan, Y.Y. and Jackson, D.D., 1995, New seismic gap hypothesis: Five years after: *Journal of Geophysical Research*, *v. 100*, p. 3943-3959.

Kagan, Y.Y. and Jackson, D.D., 2000, Probabilistic forecasting of earthquakes: *Geophysical Journal International*, *v. 143*, p. 438-453.

Kang, L.X. and Wang, J.R., 1995, Episodes and ages of seismic landslides along the Changma fault zone: *Acta Seismologica Sinica*, *v.* 8, p. 491-496.

Keefer, D.K., 1994, The importance of earthquake-induced landslides to long-term slope erosion and slope-failure hazards in seismically active regions: *Geomorphology*, *v. 10*, p. 265-284.

Keefer, D.K., 2002, Investigating landslides caused by earthquakes--A historical review: *Surveys in Geophysics*, *v. 23*, p. 473-510.

Kijko, A., 2004, Estimation of the maximum earthquake magnitude, m_{max}: *Pure and Applied Geophysics*, *v. 161*, p. 1655-1681.

Knight, W., 2006, Model predictions of Gulf and southern Atlantic coast tsunami impacts from a distribution of sources: *Science of Tsunami Hazards*, *v. 24*, p. 304-312.

Kreemer, C., Holt, W.E. and Haines, A.J., 2002, The global moment rate distribution within plate boundary zones, *in* S. Stein and J.T. Freymueller

(Editors), Plate Boundary Zones: American Geophysical Union, Geodynamic Series, Washington, D.C., pp. 173-202.

Lee, E.M., Hall, J.W. and Meadowcroft, I.C., 2001, Coastal cliff recession: the use of probabilistic prediction methods: *Geomorphology*, *v. 40*, p. 253-269.

Lee, H.J., 2005, Undersea landslides: extent and significance in the Pacific Ocean, an update: *Natural Hazards and Earth System Sciences*, *v. 5*, p. 877-892.

Lee, H.J., this volume, Timing of occurrence of large submarine landslides on the Atlanic ocean margin.

Liu, P.L.-F., 2008, Tsunami modeling - propagation, *in* A.R. Robinson and E.N. Bernard (Editors), The Sea: Harvard University Press, Cambridge, Massachusetts.

Liu, P.L.F., Wu, T.-R., Raichlen, F., Synolakis, C.E. and Borrero, J.C., 2005, Runup and rundown generated by three-dimensional sliding masses: *Journal of Fluid Mechanics*, *v. 536*, p. 107-144.

Locat, J. *et al.*, this volume, Geomorphology, stability and mobility of the Currituck slide.

Locat, J. and Lee, H.J., 2002, Submarine landslides: advances and challenges: *Canadian Geotechnical Journal*, *v. 39*, p. 193-212.

Locat, J., Lee, H.J., Locat, P. and Imran, J., 2004, Numerical analysis of the mobility of the Palos Verdes debris avalanche, California, and its implication for the generation of tsunmis: *Marine Geology*, *v. 203*, p. 269-280.

Løvholt, F., Harbitz, C. and Haugen, K.B., 2005, A parametric study of tsunami generated by submarine slides in the Ormen Lange/Storegga area off western Norway: *Marine and Petroleum Geology*, *v. 22*, p. 219-231.

Lynett, P. and Liu, P.L.F., 2002, A numerical study of submarine-landslide-generated waves and run-up. *Proceedings of the Royal Society of London, A*, *v. 458*, p. 2885-2910.

Mai, P.M. and Beroza, G.C., 2000, Source scaling properties from finite-fault-rupture models: *Bulletin of the Seismological Society of America*, *v. 90*, p. 604-615.

Malamud, B.D., Turcotte, D.L., Guzzetti, F. and Reichenbach, P., 2004, Landslide inventories and their statistical properties: *Earth Surface Processes and Landforms*, *v. 29*, p. 687-7111.

Maslin, M., Owen, M., Day, S. and Long, D., 2004, Linking continental-slope failures and climate change: Testing the clathrate gun hypothesis: *Geology*, *v. 32*, p. 53-56.

Mazzotti, S. and Adams, J., 2005, Rates and uncertainties on seismic moment and deformation in eastern Canada: *Journal of Geophysical Research*, *v. 110*, doi:10.1029/ 2004JB003510.

McCaffrey, R., 1994, Dependence of earthquake size distributions on convergence rates at subduction zones: *Geophysical Research Letters*, *v. 21*, p. 2327-2330.

Mofjeld, H.O., González, F.I., Titov, V.V., Venturato, A.J. and Newman, A.V., 2007, Effects of tides on maximum tsunami wave heights: Probability distributions: *Journal of Atmospheric and Oceanic Technology*, *v. 24*, p. 117-123.

Murty, T.S., 2003, Tsunami wave height dependence on landslide volume: *Pure and Applied Geophysics*, *v. 1160*, p. 2147-2153.

Nocquet, J.-M. and Calais, E., 2004, Geodetic measurements of crustal deformation in the Western Mediterranean and Europe: *Pure and Applied Geophysics*, *v. 161*, p. 661-681.

O'Loughlin, K.F. and Lander, J.F., 2003, Caribbean Tsunamis: A 500-Year History from 1498-1998: Advances in Natural and Technological Hazards Research, 20. Kluwer Academic Publishers, Dordrecht, The Netherlands, 280 pp.

Ogata, Y., 1999, Estimating the hazard of rupture using uncertain occurrence times of paleoearthquakes: *Journal of Geophysical Research*, *v. 104*, p. 17,995-18,014.

Okal, E.A., 1988, Seismic parameters controlling far-field tsunami amplitudes: A review: *Natural Hazards*, *v. 1*, p. 67-96.

Page, M.T. and Carlson, J.M., 2006, Methodologies for earthquake hazard assessment: Model uncertainty and the WGCEP-2002 forecast: *Bulletin of the Seismological Society of America*, *v. 96*, p. 1624-1633.

Parsons, T., 2002, Global Omori law decay of triggered earthquakes: Large aftershocks outside the classical aftershock zone: *Journal of Geophysical Research*, *v. 107*, p. 2199, doi:10.1029/ 2001JB000646.

Parsons, T., 2008, Monte Carlo method for determining earthquake recurrence parameters from short paleoseismic catalogs: Example calculations for California: *Journal of Geophysical Research*, *v. 112*, doi:10.1029/2007JB004998.

Parsons, T. and Geist, E.L., in review, Tsunami probability in the Caribbean region: *Pure and Applied Geophysics*.

Pelayo, A.M. and Wiens, D.A., 1992, Tsunami earthquakes: Slow thrust-faulting events in the accretionary wedge: *Journal of Geophysical Research*, *v. 97*, p. 15,321-15,337.

Piper, D.J.W., Cochonat, P. and Morrison, M.L., 1999, The sequence of events around the epicentre of the 1929 Grand Banks earthquake: initiation of debris flows and turbidity current inferred from sidescan sonar: *Sedimentology*, *v. 4*6, p. 79-97.

Rikitake, T. and Aida, I., 1988, Tsunami hazard probability in Japan: *Bulletin of the Seismological Society of America*, *v. 78*, p. 1268-1278.

Rong, Y., Jackson, D.D. and Kagan, Y.Y., 2003, Seismic gaps and earthquakes: *Journal of Geophysical Research*, *v. 108*, p. ESE 6-1 - 6-14.

Rossi, M. *et al.*, 2007, Statistical and temporal properties of 596 triggered landslide events in the Emilia-Romagna region of Italy: 2007 Eurpoean Geosciences Union General Assembly: *Geophysical Research Abstracts*, *v. 9*.

Senior Seismic Hazard Analysis Committee (SSHAC), 1997, Recommendations for Probabilistic Seismic Hazard Analysis: Guidance on Uncertainty and Use of Experts: NUREG/CR-6372 UCRL-ID-122160 Vol. 1, U.S. Nuclear Regulatory Commission, 256 pp.

Somerville, P.G., McLaren, J.P., LeFevre, L.V., Burger, R.W. and Helmberger, D.V., 1987, Comparison of source scaling relations of eastern and western North American earthquakes: *Bulletin of the Seismological Society of America*, *v. 77*, p. 322-346.

Sornette, D. and Sornette, A., 1999, General theory of the modified Gutenberg-Richter law for large seismic moments: *Bulletin of the Seismological Society of America*, *v. 89*, p. 1121-1130.

Stark, C.P. and Hovius, N., 2001, The characterization of landslide size distributions: *Geophysical Research Letter*s, *v. 28*, p. 1091-1094.

ten Brink, U.S., Geist, E.L. and Andrews, B.D., 2006, Size distribution of submarine landslides and its implication to tsunami hazard in Puerto Rico: *Geophysical Research Letters*, *v. 33*, doi:10.1029/ 2006GL026125.

ten Brink, U.S., Lee, H.J., Geist, E.L. and Twichell, D., this volume, Assessment of tsunami hazard to the U.S. Atlantic Coast using relationships between submarine landslides and earthquakes.

ten Brink, U.S. and Lin, J., 2004, Stress interaction between subduction earthquakes and forearc strike-slip faults: Modeling and application to the northern Caribbean plate boundary: *Journal of Geophysical Research*, *v. 109*, B12310, doi:10.1029/ 2004JB003031.

Terrinha, P. *et al.*, 2003, Tsunamigenici-seismogenic structures, neotectonics, sedimentary processes and slope instability on the southwest Portuguese Margin: *Marine Geology*, *v. 195*, p. 55-73.

Thiebot, E. and Gutscher, M.-A., 2006, The Gibraltar Arc seismogenic zone (part 1): Contraints on a shallow east dipping fault plane source for the 1755 Lisbon earthquake provided by seismic data, gravity and thermal modeling: *Tectonophysics*, *v. 426*, p. 135-152.

Titov, V.V., Mofjeld, H.O., González, F.I. and Newman, J.C., 2001, Offshore forecasting of Alaskan tsunami in Hawaii, *in* G.T. Hebenstreit (Editor), Tsunami Research at the End of a Critical Decade: Kluwer Academic Publishers, Dordrecht, The Netherlands, p. 75-90.

Titov, V.V., Rabinovich, A.B., Mofjeld, H.O., Thomson, R. and González, F.I., 2005, The global reach of the 26 December 2004 Sumatra tsunami: *Science*, *v. 309*, p. 2045-2048.

Toro, G.R., Abrahamson, N.A. and Schneider, J.F., 1997, Model of strong ground motions from earthquakes in central and eastern North America: Best estimates and uncertainties: *Seismological Research Letters*, *v. 68*, p. 41-57.

Trauth, M.H., Bookhagen, B., Marwan, N. and Strecker, M.R., 2003, Multiple landslide clusters record Quaternary climate changes in the northwestern Argentine Andes: *Palaeogeography, Palaeoclimatology, and Palaeoecology*, *v. 194*, p. 109-121.

Tsunami Pilot Study Working Group, 2006, Seaside, Oregon Tsunami Pilot Study--Modernization of FEMA Flood Hazard Maps: U.S. Geological Survey.

Vere-Jones, D., Robinson, R. and Yang, W., 2001, Remarks on the accelerated moment release model: problems of model formulation, simulation and estimation: *Geophysical Journal International*, *v. 14*4, p. 517-531.

Ward, S.N., 1980, Relationships of tsunami generation and an earthquake source: *Journal of Physics of the Earth*, *v. 28*, p. 441-474.

Ward, S.N., 1994, A multidisciplinary approach to seismic hazard in southern California: *Bulletin of the Seismological Society of America*, *v. 8*4, p. 1293-1309.

Ward, S.N., 1997, More on M_{max}: *Bulletin of the Seismological Society of America*, *v. 87*, p. 1199-1208.

Ward, S.N., 2001, Landslide tsunami: *Journal of Geophysical Research*, *v. 106*, p. 11,201-11,215.

Wesnousky, S.G., 1994, The Gutenberg-Richter or characteristic earthquake distribution, which is it?: *Bulletin of the Seismological Society of America*, *v. 84*, p. 1940-1959.

Wheeler, R.L., 1996, Earthquakes and the southeastern boundary of the intact Iapetan margin in eastern North America: *Seismological Research Letters*, *v. 67*, p. 77-83.

Wheeler, R.L. and Frankel, A.D., 2000, Geology in the 1996 USGS seismic-hazard maps, central and eastern United States: *Seismological Research Letters*, *v. 71*, p. 273-282.

Wright, S.G. and Rathje, E.M., 2003, Triggering mechanisms of slope instability and their relationship to earthquakes and tsunamis: *Pure and Applied Geophysics*, *v. 160*, p. 1865-1877.

Wyss, M., 1979, Estimating maximum expectable magnitude of earthquake from fault dimensions: *Geology*, *v. 6*, p. 336-340.

Yeh, H., 2008, Tsunami impacts on coastlines, *in* A.R. Robinson and E.N. Bernard (Editors), The Sea: Harvard University Press, Cambridge, Massachusetts.

Zitellini, N. *et al.*, 2004, Neogene through Quaternary tectonic reactivation of SW Iberian passive margin: *Pure and Applied Geophysics*, *v. 161*, p. 565-587.

Section 5:

Summary and Future Directions

Chapter 15: Summary of the Evaluation of Tsunami Sources with the Potential to Impact the U.S. Atlantic and Gulf Coasts

This report is divided into five sections: the first section addresses submarine landslides on the continental slope. It includes analysis of recently released detailed bathymetry along the Atlantic continental margin (Chapter 2), preliminary mapping of three potential tsunamigenic landslides in the Gulf of Mexico, and review of previous work pertaining to landslide earthquake sources (Chapters 3 and 4). Section 2 addresses earthquake hazards. It includes reviews of potential tsunamigenic earthquakes in the Atlantic (Chapter 6), the Gulf of Mexico (Chapter 7), and propagation models of the 1755 Lisbon earthquake (Chapter 5), as well as the Puerto Rico Trench and other Caribbean earthquakes (Chapter 8). Section 3 analyzes in detail one submarine landslide offshore North Carolina: a morphological, geotechnical and mobility analysis of the Currituck landslide (Chapter 9), and tsunami propagation models for this slide (Chapter 10) were performed as examples of more in-depth work that is necessary to quantify the tsunami hazard from submarine landslides along the U.S. Atlantic continental margin. Section 4 addresses efforts to develop tsunami probability, given the lack of known tsunamis. An indirect method is proposed to estimate the recurrence of landslide tsunamis using relationships between submarine landslides and earthquakes (Chapter 11). The size distribution of submarine landslides along the Atlantic Continental Slope is analyzed (Chapter 12), and a survey of the temporal distribution of submarine landslides in the Atlantic, as well as worldwide, is presented (Chapter 13). A preliminary tsunami probability approach for the U.S. Atlantic Coast is offered using the Probabilistic Tsunami Hazard Analysis (PTHA) method and information provided in previous chapters (Chapter 14).

Following is a more detailed summary of each chapter:

Section 1: Landslides

Chapter 2

Submarine landslides are recognized as an important hazard on continental margins, and the increased availability of multibeam bathymetry and sidescan sonar imagery along nearly the entirety of the U.S. Atlantic continental slope and rise provides an opportunity to evaluate the controls on their formation and distribution. Landslide distribution is strongly, although not exclusively, controlled by proximity to areas covered by continental glaciers. Landslides cover 33% of the continental slope and rise of the glacially influenced New England margin, 16% of the sea floor offshore of the fluvially dominated Middle Atlantic margin, and 13% of the sea floor south of Cape Hatteras. Quaternary shelf-edge deltas are common on the glacially influenced New England margin, scattered on the Middle Atlantic margin, which is influenced by a few large rivers, and absent south of Cape Hatteras. The headwall scarps of landslides are most common on the lower slope, and the deposits are thin (mostly 20-40 m thick) and comprised primarily of Quaternary material. The largest failures along the margin were sourced on the open slope offshore of the shelf-edge deltas. Two exceptions are large failures south of Cape Hatteras that are sourced on the open slope near salt domes that breach the sea floor. Faults that breach the sea floor and the occurrence of small earthquakes from this section of the margin may have been the triggers for these landslides. Landslides occur on the walls of submarine canyons as well, but the volumes of the deposits from canyon source areas are much smaller than those from open-slope source areas. The distribution of landslides suggests that depositional processes during the Quaternary shaped the shallow stratigraphy and morphology of this margin, and these in turn had a strong control on the stability of the slope.

Chapter 3

Landslides in the Gulf of Mexico occur in all three depositional provinces (carbonate, salt, and canyon/fan). The largest failures are found in the canyon/fan province. The largest failures were excavated from the Mississippi Canyon and covered large parts of the Mississippi and Eastern Mississippi Fans. Available information suggests they occurred during the early part of the Holocene (7,500-11,000 yr BP). The resumption of hemipelagic sedimentation in the head of Mississippi Canyon at 7,500 yr BP indicates that at least the largest of these landslide complexes had ceased being active by mid-Holocene time.

Landslides within the salt province are in general considerably smaller than those in the canyon/fan province, many of them are confined to the walls of mini-basins, but some occupy the Sigsbee escarpment. These landslides appear to be driven by salt movement. Available information on the age of these small landslides suggests that they are mostly older than 18,000 years. Landslides in the carbonate provinces that fringe the eastern and southern Gulf of Mexico appear to have been derived from both the steep West Florida and Campeche Escarpments as well as from the gentler slope above the escarpments. The northern part of the Florida Escarpment

has probably undergone little erosion since it originally formed during the Cretaceous, but the southern part of the Florida Escarpment shows sign of active erosion. The largest failures appear to be from the slope above the escarpment, with the volume of one excavation event exceeding 16 km^3.

Chapter 4

Far-field submarine landslide sources have been quoted as potential sources for trans-oceanic tsunamis. The most widely known is the threat of a large-volume landslide caused by an imminent eruption of Cumbre Vieja volcano in the Canary Island. However, models of tsunami propagation, which take into account dispersion and non-linearity of the landslide-generated waves, show rapid amplitude decay with distance and predict <1 meter of flooding in Florida. In addition, the recurrence time of a major eruption-related landslide is 10^5 yr. The giant Storegga landslide offshore Norway caused large tsunami waves within 600 km radius in the northeast Atlantic, but the waves are not known to have propagate to the U.S. East Coast. Some large landslides have been identified along the Scotian margin north off New England. Most of them are Holocene and older in age and appear to be related to the expansion and contraction of the Laurentide ice sheet. The 1929 Grand Banks landslide generated a damaging tsunami locally, but not in New England. However, larger landslides than the 1929 Grand Banks landslide have been identified in the stratigraphic record of the Scotian Margin.

Section 2: Earthquakes

Chapter 5

The great Lisbon earthquake of November 1st, 1755 with an estimated moment magnitude of 8.5-9.0 was the most destructive earthquake in European history. The associated tsunami run-up was reported to have reached 5-15 m along the Portuguese and Moroccan coasts and the run-up was significant at the Azores and Madeira Island. Run-up reports from a trans-oceanic tsunami were documented in the Caribbean, Brazil and Newfoundland (Canada). No reports were documented along the U.S. East Coast. Many attempts have been made to characterize the 1755 Lisbon earthquake source using geophysical surveys and modeling the near-field earthquake intensity and tsunami effects. Studying far field effects, as presented here, is advantageous in establishing constraints on source location and strike orientation because trans-oceanic tsunamis are less influenced by near source bathymetry and are unaffected by triggered submarine landslides at the source. Source location, fault orientation and bathymetry are the main elements governing transatlantic tsunami propagation to sites along the U.S. East Coast, much more than distance from the source and continental shelf width. Results of our far and near-field tsunami simulations based on relative amplitude comparison limit the earthquake source area to a region located

south of the Gorringe Bank in the center of the Horseshoe Plain. This is in contrast with previously suggested sources such as Marqués de Pombal Fault, and Gulf of Cádiz Fault, which are farther east of the Horseshoe Plain. The earthquake was likely to be a thrust event on a fault striking ~345° and dipping to the ENE as opposed to the suggested earthquake source of the Gorringe Bank Fault, which trends NE-SW. Gorringe Bank, the Madeira-Tore Rise (MTR), and the Azores appear to have acted as topographic scatterers for tsunami energy, shielding most of the U.S. East Coast from the 1755 Lisbon tsunami. Additional simulations to assess tsunami hazard to the U.S. East Coast from possible future earthquakes along the Azores-Iberia plate boundary indicate that sources west of the MTR and in the Gulf of Cadiz may affect the southeastern coast of the U.S. The Azores-Iberia plate boundary west of the MTR is characterized by strike-slip faults, not thrusts, but the Gulf of Cadiz may have thrust faults. Southern Florida seems to be at risk from sources located east of MTR and South of the Gorringe Bank, but it is mostly shielded by the Bahamas. The Gulf of Cádiz is another source area of potential tsunami hazard to the U.S. East Coast. Higher resolution near-shore bathymetry along the U.S. East Coast and the Caribbean as well as a detailed study of potential tsunami sources in the central west part of the Horseshoe Plain are necessary to verify our simulation results.

Chapter 6

The Atlantic Ocean is generally devoid of subduction or convergent zones. Two exceptions are the area west of Gibraltar: the location of the 1755 Lisbon earthquake, and the Hispaniola-Puerto Rico-Lesser Antilles subduction zone. The 1755 Lisbon earthquake, as well as an earthquake in 1761 in that area, generated a transoceanic tsunami recorded along the European and African coasts, islands in the Atlantic, and the Caribbean islands. The source of these earthquakes is still debatable, and the previous chapter offers a novel approach to assess the source of the 1755 tsunami and its impact on the U.S. East Coast.

The northern Caribbean subduction zone has the potential to cause a major tsunami similar to the 2004 Sumatra tsunami. However, detailed work in the Puerto Rico Trench indicates that slip there is highly oblique and the subducting lithosphere is very old, two indications that perhaps the subduction zone is not capable of generating very large earthquakes. The Hispaniola segment of this subduction zone, while perhaps capable of very large earthquakes, is fringed to the north by an almost continuous line of islands and shallow banks that obstruct, but not completely block, propagating tsunami waves.

Chapter 7

Convergent or subduction zones in the southern Caribbean are reviewed and

do not appear to be capable of generating very large earthquakes, and thus do not appear to pose a significant tsunami hazard to the Gulf of Mexico coastal zones.

Chapter 8

Tsunamis arising from the Caribbean earthquake sources outlined in Chapters 7 and 8, as well as from the transform faults along Cayman Trough were modeled using linear long-wave equation. Tsunami propagation was modeled only in deep water and up to a depth of 250 m in the continental margin of the Atlantic and the Gulf of Mexico. Tsunami propagation did not extend to shallower water, to avoid addressing energy dispersion, bottom friction, and non-linear attenuation. The models suggest that rupture of the Puerto Rico trench is the only Caribbean source capable of causing damaging tsunamis along U.S. coasts. High wave amplitude from rupture of the Puerto Rico trench is predicted to concentrate along the New England and New Jersey margin, and in the vicinity of Wilmington, N.C. and Myrtle Beach, S.C.

Section 3: Case Study

Chapter 9

Over the last 100,000 years, the U.S. Atlantic continental margin has experienced various types of mass movements some of which are believed to have taken place at times of low sea level. At one of these times of low sea level, a significant trigger caused a major submarine mass movement off the coast of Virginia: the Currituck slide. This slide removed a total volume of about 165 km^3 from this section of the continental slope. The departure zone still shows a very clean surface that dips at 4° and is only covered by a thin veneer of Holocene sediment. Multibeam bathymetric data suggest that this slide took place along three failure surfaces. The morphology of the source area suggests that the sediments were already at least normally consolidated at the time of failure. The slide debris covers an area as much as 55 km wide that extends 180 km from the estimated toe of the original slope. The back analysis of slide initiation indicates that very high pore pressure, a strong earthquake, or both had to be generated to trigger slides on such a low failure plane angle. The shape of the failure plane, the fact that the surface is almost clear of any debris, and the mobility analysis, all support the argument that the slides took place nearly simultaneously. Potential causes for the generation of high pore pressures could be seepage forces from coastal aquifers, delta construction and related pore pressure generation due to the local sediment loading, gas hydrates, and earthquakes. This slide, and its origin, is a spectacular example of the potential threat that submarine mass movements can pose to the US Atlantic coast and underline the need to further assess the potential for the generation of such large slides, like the Grand Banks 1927 landslide of similar volume.

Chapter 10

Tsunami generation from the Currituck landslide offshore North Carolina and propagation of waves toward the U.S. coastline are modeled based on recent geotechnical analysis of slide movement. A long and intermediate wave modeling package (COULWAVE) based on the non-linear Boussinesq equations is used to simulate the tsunami. This model includes procedures to incorporate bottom friction, wave breaking, and overland flow during runup. Potential tsunamis generated from the Currituck landslide are analyzed using four approaches: (1) tsunami wave history is calculated from several different scenarios indicated by geotechnical stability and mobility analyses; (2) a sensitivity analysis is conducted to determine the effects of both landslide failure duration during generation and bottom friction along the continental shelf during propagation; (3) wave history is calculated over a regional area to determine the propagation of energy oblique to the slide axis; and (4) a high-resolution 1D model is developed to accurately model wave breaking and the combined influence of nonlinearity and dispersion during nearshore propagation and runup. The primary source parameter that affects tsunami severity for this case study is landslide volume, with failure duration having a secondary influence. Bottom friction during propagation across the continental shelf has a strong influence on the attenuation of the tsunami during propagation. The high-resolution 1D model also indicates that the tsunami undergoes nonlinear fission prior to wave breaking, generating independent, short-period waves. Wave breaking occurs approximately 40-50 km offshore where a tsunami bore is formed that persists during runup. These analyses illustrate the complex nature of landslide tsunamis, necessitating the use of detailed landslide stability/mobility models and higher-order hydrodynamic models to determine their hazard.

Section 4: Toward the Development of Quantitative Probabilistic Hazard Assessment

Chapter 11

Submarine landslides along the continental slope of the U.S. Atlantic margin are potential sources for tsunamis along the U.S. East coast. The magnitude of potential tsunamis depends on the volume and location of the landslides, and tsunami frequency depends on their recurrence interval. However, the size and recurrence interval of submarine landslides along the U.S. Atlantic margin is poorly known. Well-studied landslide-generated tsunamis in other parts of the world have been shown to be associated with earthquakes. Because the size distribution and recurrence interval of earthquakes is generally better known than those for submarine landslides, we propose here to estimate the size and recurrence interval of submarine landslides from the size and recurrence interval of earthquakes in the near vicinity of the said landslides. To do so, we calculate maximum expected landslide size for a given earthquake magnitude, use recurrence interval of earthquakes to

estimate recurrence interval of the landslide, and assume a threshold landslide size that can generate a destructive tsunami. The maximum expected landslide size for a given earthquake magnitude is calculated in 3 ways: by slope stability analysis for catastrophic slope failure on the Atlantic continental margin, by using a land-based compilation of maximum observed distance from earthquake to liquefaction, and by using a land-based compilation of maximum observed area of earthquake-induced landslides. We find that the calculated distances and failure areas from the slope stability analysis is similar or slightly smaller than the maximum triggering distances and failure areas in subaerial observations. The results from all three methods compare well with the slope failure observations of the M_w=7.2, 1929 Grand Banks earthquake, the only historical tsunamigenic earthquake along the North American Atlantic margin. The results further suggest that a M_w=7.5 earthquake (the largest expected earthquake in the eastern U.S.) must be located offshore and within 100 km of the continental slope to induce a catastrophic slope failure. Thus, a repeat of the 1755 Cape Anne and 1881 Charleston earthquakes are not expected to cause landslides on the continental slope. The observed rate of seismicity offshore the U.S. Atlantic coast is very low with the exception of New England, where some micro-seismicity is observed. An extrapolation of annual strain rates from the Canadian Atlantic continental margin suggests that the New England margin may experience the equivalent of a magnitude 7 earthquake on average every 600-3000 years. A minimum triggering earthquake magnitude of 5.5 is suggested for a sufficiently large submarine failure to generate a devastating tsunami and only if the epicenter is located within the continental slope.

Chapter 12

Assessment of the probability for destructive landslide-generated tsunamis depends on the knowledge of the number, size, and frequency of large submarine landslides. This paper investigates the size distribution of submarine landslides along the U.S. Atlantic continental slope and rise using the size of the landslide source regions (landslide failure scarps). Landslide scarps along the margin identified in a detailed bathymetric Digital Elevation Model (DEM) have areas that range between 0.89 km^2 and 2410 km^2 and volumes between 0.002 km^3 and 179 km^3. The area to volume relationship of these failure scarps is almost linear (inverse power-law exponent close to 1), suggesting a fairly uniform failure thickness of a few 10s of meters in each event, with only rare, deep excavating landslides. The cumulative volume distribution of the failure scarps is very well described by a log-normal distribution rather than by an inverse power-law, the most commonly used distribution for both subaerial and submarine landslides. A log-normal distribution centered on a volume of 0.86 km^3 may indicate that landslides preferentially mobilize a moderate amount of material (on the order of 1 km^3), rather than large landslides or very small ones. Alternatively, the log-normal distribution may reflect an inverse power law distribution modified by a size-dependent probability of observing landslide scarps in the

bathymetry data. If the latter is the case, an inverse power-law distribution with an exponent of 1.3±0.3, modified by a size-dependent conditional probability identifying more failure scarps with increasing landslide size, fits the observed size distribution. This exponent value is similar to the predicted exponent of 1.2±0.3 for subaerial landslides in unconsolidated material. Both the log-normal and modified inverse power-law distributions of the observed failure scarp volumes suggest that large landslides, which have the greatest potential to generate damaging tsunamis, occur infrequently along the margin.

Chapter 13

Submarine landslides are distributed unevenly both in space and time. Spatially, they occur most commonly in fjords, active river deltas, submarine canyon-fan systems, the open continental slope and on the flanks of oceanic volcanic islands. Temporally, they are influenced by the size, location, and sedimentology of migrating depocenters, changes in seafloor pressures and temperatures, variations in seismicity and volcanic activity, and changes in groundwater flow conditions. The dominant factor influencing the times of submarine landslide occurrence is glaciation. A review of known ages of submarine landslides along the margins of the Atlantic Ocean, augmented by a few ages from other submarine locations shows a relatively even distribution of large landslides with time from the last glacial maximum until about five thousand years after the end of glaciation. During the past 5000 years the frequency of occurrence is less by a factor of 1.7 to 3.5 than during or shortly after the last glacial/deglaciation period. Such an association likely exists because of the formation of thick deposits of sediment on the upper continental slope during glacial periods and increased seismicity caused by isostatic readjustment during and following deglaciation. Hydrate dissociation may play a role, as suggested previously in the literature, but the connection is unclear.

Chapter 14

Estimating the likelihood of tsunamis occurring along the U.S. Atlantic coast critically depends on knowledge of tsunami source probability. We review available information on both earthquake and landslide probabilities from potential sources that could generate local and transoceanic tsunamis. Estimating source probability includes defining both size and recurrence distributions for earthquakes and landslides. For the former distribution, source sizes are often distributed according to a truncated or tapered power-law relationship. For the latter distribution, sources are often assumed to occur in time according to a Poisson process, simplifying the way tsunami probabilities from individual sources can be aggregated. For the U.S. Atlantic coast, earthquake tsunami sources primarily occur at transoceanic distances along plate boundary faults. Probabilities for these sources are constrained from previous statistical studies of global seismicity for similar

plate boundary types. In contrast, there is presently little information constraining landslide probabilities that may generate local tsunamis. Though there is significant uncertainty in tsunami source probabilities for the Atlantic, results from this study yield a comparative analysis of tsunami source recurrence rates that can form the basis for future probabilistic analyses.

Chapter 16: Future Directions to Increase the State of Knowledge

The systematic evaluation of tsunami sources that may impact the U.S. Atlantic Coast and the Gulf of Mexico has revealed gaps in our knowledge and the need for additional directions of investigations to help in a quantitative assessment of the hazard.

Probability analysis

(1) Probability hazard assessment of earthquakes along the Atlantic continental margin and the northern Caribbean plate boundary.

Understanding specific hazards

(1) Analysis of the geomorphology, stability, and mobility of a slide off New England, which may reveal different characteristics than the Currituck slide.
(2) Hydrodynamic modeling of the potential tsunami hazard from a slide offshore New England.
(3) Quantitative analysis of large failures and their mobility in the Gulf of Mexico and modeling their potential tsunami hazard.

Data gaps

(1) The source areas of the landslide complexes along the Georges Bank and southern New England margin need to be adequately imaged with multibeam sonar. This region houses the largest landslide complexes off the U.S. Atlantic coast, and understanding the depth of the source area, relief and nature of the headwall scarps, would help explain the causes of these failures, and the volume of material removed is each failure episode.
(2) Careful age dating on cores recovered from within and adjacent to several of the landslides in order to constrain the timing of the submarine landslides.
(3) Mapping of the Campeche Bank, Mexico. Potential landslides along the Campeche Bank margin may pose an equal or higher threat to the U.S. Gulf coast than proximal landslides, but little has been published about them.

(4) Further age dating to refine the timing of the landslides derived from the Mississippi Canyon area. These dates are needed to determine if they are associated with meltwater floods discharged into the Gulf of Mexico during the early part of the Holocene or whether they were triggered by other processes at a later time when conditions were more similar to present conditions.
(5) Increase our knowledge on the characteristics of coastal aquifers and their influence on slope stability.